Institute of Thermomechanics

International Workshop on Physical Modeling of Flow and Dispersion Phenomena

Book of Abstracts

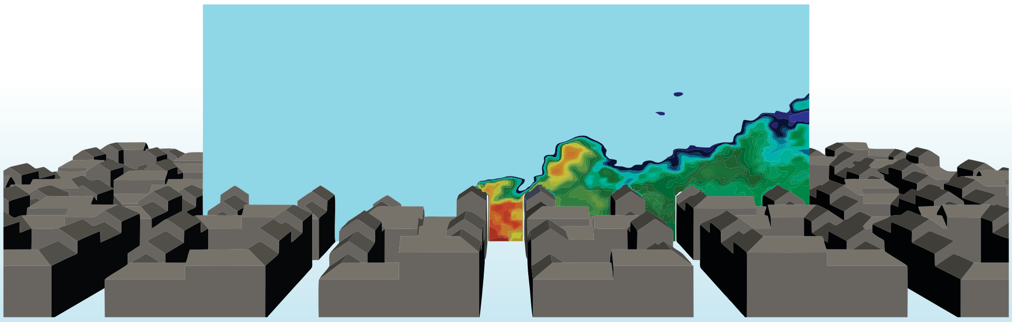

August 29 - 31, 2022
Prague, Czech Republik

PHYSMOD 2022 – International Workshop on Flow and Dispersion Phenomena
Book of extended abstracts

Editors Klára Jurčáková & Radka Kellnerová
Institute of Thermomechanics of the Czech Academy of Sciences
Dolejškova 1402/5
182 00 Prague
Czech Republic

ISBN 978-80-87012-81-9

Dear colleagues,

We are very glad that after two and half years of very limited opportunities for onsite scientific meetings we can hold **PHYSMOD 2022** in Prague at the Institute of Thermomechanics of the Czech Academy of Sciences. There are still limitations for some regions, so we decided to organize a hybrid meeting with a majority of participants on-site and a minority online. The workshop consists of 43 oral and 4 poster contributions, 11 talks will be given by remote speakers. We have very strong student representation – 18 presentations will be given by students. Altogether 73 participants have registered.

The objective of **PHYSMOD** is to bring together the community active in physical and numerical modeling of flow and dispersion processes occurring in the lowest part of the atmosphere using wind tunnels, water channels, or CFD models. The history of the biennial workshop starts in 1999 here in Prague and attracts a growing number of experts, scientists, and students active in the field.

PHYSMOD provides a forum where the most recent advances in fluid modeling, state-of-the-art in experimental work, and newly emerging research areas are discussed in an open-minded and friendly atmosphere. One of the main purposes is to encourage broader collaboration between researchers and transfer the knowledge between the laboratories as well as generations. We will be very happy to welcome students who present their work and incorporate them into our community.

Klára Jurčáková
On behalf of the scientific and organizing committee

Scientific Committee:
Jeroen van Beeck, *von Karman Institute for Fluid Dynamics, Sint-Genesius-Rode, Belgium*
Matteo Carpentieri, *University of Surrey, Guilford, United Kingdom*
Klára Jurčáková, *Institute of Thermomechanics, Prague, Czech Republic*
Bernd Leitl, *University of Hamburg, Germany*
Chun-Ho Liu, *The University of Hong Kong*
Laurent Perret, *Ecole Centale de Nantes, Nantes, France*
Eric Savory, *University of Western Ontario, London, Canada*

Organizing committee:
Klára Jurčáková, chair
Hana Chaloupecká
Michala Jakubcová
Radka Kellnerová
Zuzana Kluková
Štěpán Nosek

PHYSMOD 2022
TABLE OF CONTENTS

PROGRAM OF THE WORKHOP

LIST OF PARTCIPANTS

EXTENDED ABSTRACTS [In the alphabetical order of the presenting authors]

PHYSMOD 2022
PROGRAM OF THE WORKSHOP

Legend: **Invated talk**
Student presentation
Online presentation

[Affiliation concerns the first author]

Monday, 29 August, 2022

8:20 – 8:50	**Registration**
8:50 – 9:00	**Welcome** *Klára Jurčáková*, Institute of Thermomechanics of the Czech Academy of Sciences
	Session 1 - Scale interactions and correlations, Chair: Eric Savory
9:00 – 9:30	**Scale interaction and the large-scales influence in the urban canopy** *Laurent Perret*, Centrale Nantes, Nantes, France
9:30 – 9:50	**Roughness Sublayer effect on the law of the wall modeled by a "co-spectral link"** *Yardena Bohbot-Raviv, V. Babin, G. G. Katul,* Institute for Biological research, Ness Ziona, Israel
9:50 – 10:10	**Surface pressure, velocity and concentration correlations in an urban canopy layer** *David Birch, J. Wingrave, M. Placidi,* University of Surrey, Guildford, United Kingdom
10:10 – 10:30	**Scale analysis of turbulent statistics over real urban surface: A wind tunnel study** *Fei Li, Ziwei Mo, Chun-Ho Liu,* The University of Hong Kong, Hong Kong
10:30 – 11:00	**Coffee break**
	Session 2 - Urban canopy and buildings 1, Chair: Matteo Carpentieri
11:00 – 11:20	**Turbulent flows around multi-scaled buildings - a comparative study of wind tunnel experiments and Large Eddy Simulations** *Benedikt Seitzer, F. Harms, B. Leitl,* University of Hamburg, Germany
11:20 – 11:40	**Lattice-Boltzmann Large-Eddy Simulations of the flow field and dispersion around a bidimensional obstacle** *Sofia Fellini, G. Lamaison, E. Lévêque, P. Salizzoni, L.Soulhac,* Ecole Centrale Lyon, France
11:40 – 12:00	**The influence of building structures on ground level air movement and pollutant input in courtyards** *Frank Harms, T. Szyszka, B. Leitl,* University of Hamburg, Germany
12:00 – 12:20	**Modelling Airflow over Pitched-Roof Buildings** *Matthew Coburn, S. Herring, Z-T. Xie,* University of Southampton, United Kingdom
12:20 – 12:40	**Tall buildings drag: the effect of multiscale urban morphologies** *Cameron Southgate-Ash, M. Placidi,* University of Surrey, Guildford, United Kingdom
12:40 – 12:50	**Poster presentations**
12:50 – 14:20	**Lunch break**

Session 3 - Urban canopy and buildings 2, Chair: Laurent Perret

14:20 – 14:40	**Cyclists Exposure to Vehicle Emissions in Urban Canyons** *Joy Wingrave (Schmeer), M. Placidi,* University of Surrey, Guildfor, United Kingdom
14:40 – 15:00	**Effect of an upstream tall building on a street canyon flow** *Haoran Du, Eric Savory, Laurent Perret,* University of Western Ontario, London, Canada
15:00 – 15:20	**Wake Flows of a Cluster of Tall Buildings** *Saad Inam, C. H. Nguyen, D. Lasagna, Z-T. Xie,* University of Southampton, United Kingdom
15:20 – 15:40 .	**New guideline – better guideline? The new VDI code of practice for wind tunnel modeling of atmospheric flow and dispersion processes** *Bernd Leitl, W. Bächlin, W. Theurer, F. Harms, R. Lieb, R. Höffer, C. Kalender-Wevers, V. Hildebrand, B Bauhofer,* University of Hamburg, Germany

15:40 – 16:10	**Coffee break**

Session 4 - Non-neutral stratification, Chair: Bernd Leitl

16:10 – 16:30	**Wind Tunnel Modelling of the Jack Rabbit II Mock Urban Environment Chlorine Releases** *Tom Spicer, Chad T. Smith,* University of Arkansas, Fayetteville, USA
16:30 – 16:50	**Struggles of Heavy Gas Dispersion Experiments** *Simon Michel, B. Leitl, F. Harms,* University of Hamburg, Germany
16:50 – 17:10	**Effect of non-neutral stratification on urban flow and dispersion** *Matteo Carpentieri, D. Marucci, P. Hayden,* University of Surrey, Guildford, United Kingdom
17:10 – 17:30	**Wake flows of wind turbines in stably stratified boundary layers** *Marco Placidi, C. Deebank, M. Bastankhah,* University of Surrey, Guildford, United Kingdom

19:00 – 21:00	**Dinner on the boat**

Tuesday, 30 August, 2022

Session 5 - Vegetation, Chair: Márton Balczó

8:40 – 9:10 .	**Using Doppler wind lidars to measure kinematic quantities across the lower atmosphere** *Markus Kayser, E. Päschke, C.Detring, F. Beyrich, C. Becker, V. Lehman, R. Leinweber,* Lindenberg Meteorological Observatory, Tauche OT Lindenberg, Germany
9:10 – 9:30 .	**Influence of vegetation on urban canyon ventilation. Part I : experimental and numerical investigation of averaged concentration and bulk exchange velocity.** *Marilina Barulli, S. Fellini , A. Del Ponte , L. Ridolfi , L. Shoulhac , M. Marro , A. Emmanuelli , P. Salizzoni,* Politecnico di Torino, Turin, Italy
9:30 – 9:50 .	**Influence of vegetation on urban canyon ventilation. Part II: velocity field and turbulent mass fluxes** *Annika Vittoria Del Pont, S. Fellini, M. Barulli, L. Ridolfi, L. Shoulha, M. Marro, P. Salizzoni,* Politecnico di Torino, Turin, Italy
9:50 – 10:10	**Dry deposition of particulate matter on urban green infrastructure with parameterised drag effects** *Tess Ysebaert, R. Samson, S. Denys,* University of Antwerp, Belgium
10:10 – 10:30	**Wind tunnel measurement on the flow and traffic emission dispersion around roadside building with green vegetation belt** *Bao-Shi Shiau, H.P. Huang,* National Taiwan Ocean University, Taiwan
10:30 – 10:50	**A comparison of turbulent flows over idealized urban and vegetation canopy** *Ruiqi Wang, Ziwei Mo and Chun-Ho Liu,* The University of Hong Kong, Hong Kong

10:50 – 11:20	**Coffee break**

Session 6 - Methodology, Chair: Frank Harms

11:20 – 11:40	**Measuring wall shear forces with a simple pressure transducer?** *Nikhil Raghuvanshi, F. Harms, B. Leitl, T. Glanert,* University of Hamburg, Germany
11:40 – 12:00	**Prediction of turbulence generated by non-homogeneous grids for applications to experimental atmospheric boundary layer generation** *Thomas Huret, G.Tanguy, C. Vassilicos, L. Jacquin, Q. Gallas, ONERA, Lille, France*
12:00 – 12:20	**Evaluation of differences between DMD and OPD in coherent structures detection** *Zuzana Kluková, Š. Nosek, Z. Jaňour,* Institute of Thermomechanics , Prague, Czechia
12:20 – 12:40	**Statistical assessment of the ventilation of street canyons based on time-resolved wind tunnel experiments** *Bálint Papp, B. Istók, M. Koren, M. Balczó, G. Kristóf,* Budapest University of Technology and Economics, Hungary
12:40 – 13:00	**Transient Wind Forcing: a method for modelling wind shear in building-scale Large Eddy Simulations** *Márton Koren, M. Balogh, G. Kristóf,* Budapest University of Technology and Economics, Hungary

13:00 – 14:30 **Lunch break**

14:45 **Bus departure**

16:00 – 17:30 **Excursion in the Aerodynamical laboratory in Nový Knín**

18:00 – 21:30 **Dinner on the Dobříš Chateu**

22:30 **Return to Prague**

Wednesday, 31 August, 2022

Session 7 - Urban canopy and buildings 3, Chair: Yardena Bohbot-Raviv

8:40 – 9:00	**Predicting mean wind profiles and pollutant dispersion inside urban canopies** *Huanhuan Wang, E. Furtak-Cole, K. Ngan,* City University of Hong Kong, Hong Kong
9:00 – 9:20	**Large-Eddy Simulation of the Atmospheric Boundary Layer Flows over Different Urban-Like Morphologies** *Wai-Chi Cheng,* Sun Yat-sen University, Zhuhai, China
9:20 – 9:40	**Application of a microscale ship plume parameterization in a city-scale air quality model** *Ronny Badeke, V. Matthias, M. Karl, M.O.P. Ramacher, D.A. Schwarzkopf, D. Grawe,* Helmholtz-Zentrum Hereon, Geesthacht, Germany
9:40 – 10:00	**Coarse grid and implicit LES for urban pollutant dispersion** *Tom Lauriks, W. Munters, J. van Beeck, Siegfried Denys,* University of Antwerp, Belgium
10:00 – 10:20	**Turbulent Flows in the Inertial- and Roughness-sublayer over Real Urban Morphology: A Comparison of Wind tunnel Experiment and Large-eddy Simulation** *Ziwei Mo, Chun-Ho Liu,* The University of Hong Kong, Hong Kong

10:20 – 10:50 **Coffee break**

Session 8 - Urban canopy and buildings 4, Chair: Marco Placidi

10:50 – 11:10	**Experimental investigation of the heat removal and air ventilation in urban area using simultaneous PIV-LIF measurement in water tunnel** *Yunpeng Xue, Y. Zhao, S. Mei, Y. Chao, J. Carmeliet,* Singapore-ETH Centre, Singapore
11:10 – 11:30	**PIV-PLIF measurements of pollutant dispersion in atmospheric boundary layer flow in a water channel** *Desmond Lim, C. Vanderwel,* University of Southampton, United Kingdom
11:30 – 11:50	**Quadrant Analysis of Two-height Canopy Flow Modeled in a Wind Tunnel** *Valery Babin, L. Shig, E. Fattal, R. Shnapp, A. Liberzon and Y. Bohbot-Raviv,* Institute for Biological Research, Ness Ziona, Israel
11:50 – 12:10	**Different boundary conditions for LES solver PALM 6.0 used for ABL in tunnel experiment** *Hynek Řezníček, J. Geletič, M. Bureš, P. Krč, J. Resler, K. Vrbová, A.Trush,P. Michálek, L. Beneš, M. Sühri,* Institute for computer science, Prague, Czechia
12:10 – 12:30	**Computational Simulations of Gases Dispersion in Built-up Environment under changes in Roof Shape configurations** *Mohamed Yassin, M. Jasem, M.Shlash,* Kuwait Institute for Scientific Research, Kuwait

12:30 – 14:00 **Lunch Break**

Session 9 - Applications, Chair: Klára Jurčáková

14:00 – 14:20	**Use of atmospheric boundary-layer LES fields for an operational Lagrangian dispersion model** *Ariane Emmanuelli, G. Lamaison, L.Soulhac,* Ecole Centrale Lyon, France
14:20 – 14:40	**Wind tunnel measurements of airflows and gas concentrations downwind a naturally-ventilated pig building model** *Qianying Yi, D. Janke, L. Thormann, S. Hempel, B. Amon, T. Amon,* Leibniz Institute for Agricultural Engineering and Bioeconomy (ATB), Postdam, Germany
14:40 – 15:00	**Operational dispersion model for emergency services** *Hana Chaloupecká,* Institute of Thermomechanics , Prague, Czechia
15:00 – 15:20	**Aspects of dosage from short and long duration emissions** *Alan Robin, P. Hayden, D. Gallacher, S. Pace, H. Chaloupecka,* University of Surrey, Guildford, United Kingdom
15:20 – 16:00	**Final discussion and the best student presentation award**

POSTERS

	Concentration fluctuations in atmospheric boundary layer *Claudia Schiavini, L. Soulhac, P. Salizzoni, M. Marro,* Ecole Centrale Lyon, France
	The control of buoyant smoke in transversally ventilated tunnels with the presence of a longitudinal flow *Cosimo Peruzzi, P. Salizzoni, M. Marro, P. Cingi, D. Angeli, T. Kubwimana, A. Mos,* Ecole Centrale Lyon, France
	Experimental study of natural ventilation in realistic urban environments *Matteo Carpentieri, Hayden, P. Singh, L. Morina, M. Mian Muhammad,* University of Surrey, Guildford, United Kingdom
	Temporal, Spatial, and Spatio-temporal correlation of the velocity fluctuations *Klára Jurčáková,* Institute of Thermomechanics , Prague, Czechia

ON-SITE PARTICIPANTS

Valery	Babin	babinv79@gmail.com	Israel Institute for Biolofical Research	Ness Ziona	IL
Ronny	Badeke	Ronny.Badeke@hereon.de	Helmholtz-Zentrum Hereon	Geesthacht	DE
Marton	Balczo	balczo.marton@gpk.bme.hu	Budapest University of Technology and Economics	Budapest	HU
Miklós	Balogh	czetka350@gmail.com	Budapest University of Technology and Economics	Budapest	HU
Marilina	Barulli	s269581@studenti.polito.it	Politecnico di Torino	Turin	IT
David	Birch	d.birch@surrey.ac.uk	University of Surrey	Guildford	GB
Yardena	Bohbot Raviv	yardena.raviv@gmail.com	Institute for Biological research	Ness Ziona	IL
Matteo	Carpentieri	m.carpentieri@surrey.ac.uk	University of Surrey	Guildford	GB
Hana	Chaloupecká	hchaloupecka@seznam.cz	Institute of Thermomechanics of the CAS	Prague	CZ
Matthew	Coburn	matthew.coburn.20@gmail.com	University of Southampton	Southampton	GB
Annika Vittoria	Del Ponte	annikavittoria@gmail.com	Politecnico di Torino	Torino	IT
Haoran	Du	hdu59@uwo.ca	University of Western Ontario	London	CA
Ariane	Emmanuelli	ariane.emmanuelli@ec-lyon.fr	Ecole Centrale Lyon	Lyon	FR
Sofia	Fellini	sofia.fellini@ec-lyon.fr	Ecole Centrale Lyon	Lyon	FR
Frank	Harms	frank.harms@uni-hamburg.de	University of Hamburg	Hamburg	DE
Saad	Inam	si1a22@soton.ac.uk	University of Southampton	Southampton	GB
Balázs	Istók	istok.balazs@gpk.bme.hu	Budapest University of Technology and Economics	Budapest	HU
Michala	Jakubcová	michala@it.cas.cz	Institute of Thermomechanics, AS CR, v.v.i.	Prague	CZ
David	Janke	djanke@atb-potsdam.de	Leibniz Institute for Agricultural Engineering and Bioeconomy	Potsdam	DE
Zbyněk	Jaňour	janour@it.cas.cz	Institute of Thermomechanics of the CAS	Prague	CZ
Klára	Jurčáková	klara.jurcakova@it.cas.cz	Institute of Thermomechanics of the CAS	Prague	CZ
Markus	Kayser	Markus.Kayser@dwd.de	Lindenberg Meteorological Observatory	Lindenberg	DE
Zuzana	Kluková	klukovaz@it.cas.cz	Institute of Thermomechanics of the CAS	Prague	CZ
Márton	Koren	koren.marton@gpk.bme.hu	Budapest University of Technology and Economics	Budapest	HU
Gergely	Kristóf	kristof.gergely@gpk.bme.hu	Budapest University of Technology and Economics	Budapest	HU
Tom	Lauriks	tom.lauriks@uantwerpen.be	University of Antwerp	Antwerpen	BE
Bernd	Leitl	bernd.leitl@uni-hamburg.de	University of Hamburg	Hamburg	DE
Simon	Michel	simon.michel@uni-hamburg.de	University of Hamburg	Hamburg	DE
Štěpán	Nosek	nosek@it.cas.cz	Institute of Thermomechanics of the CAS	Prague	CZ
Bálint	Papp	papp.balint@gpk.bme.hu	Budapest University of Technology and Economics	Budapest	HU
Laurent	Perret	laurent.perret@ec-nantes.fr	Centrale Nantes	Nantes	FR
Marco	Placidi	m.placidi@surrey.ac.uk	University of Surrey	Guildford	GB
Nikhil	Raghuvanshi	nikhil.raghuvanshi@studium.uni-hamburg.de	University of Hamburg	Hamburg	DE
Hynek	Řezníček	reznicek@cs.cas.cz	Institute for computer science of the CAS	Prague	CZ
Pietro	Salizzoni	pietro.salizzoni@ec-lyon.fr	Ecole Centrale Lyon	Lyon	FR
Eric	Savory	esavory@uwo.ca	University of Western Ontario	London	CA
Claudia	Schiavini	claudia.schiavini@etu.univ-lyon1.fr	Ecole Centrale Lyon	Lyon	FR
Benedikt	Seitzer	benedikt.seitzer@uni-hamburg.de	University of Hamburg	Hamburg	DE
Cameron	Southgate-Ash	cs00879@surrey.ac.uk	University of Surrey	Guildford	GB
Huret	Thomas	thomas.huret@onera.fr	ONERA	Lille	FR
Lars	Thormann	lthormann@atb-potsdam.de	Leibniz Institute for Agricultural Engineering and Bioeconomy	Potsdam	DE
Mohamed	Yassin	mohamed_f_yassin@hotmail.com	Kuwait Institute for Scientific Research	Kuwiat	KW
Qianying	Yi	qyi@atb-potsdam.de	Leibniz Institute for Agricultural Engineering and Bioeconomy	Potsdam	DE
Tess	Ysebaert	tess.ysebaert@uantwerpen.be	University of Antwerp	Antwerpen	BE

ONLINE PARTICIPANTS

Desmond	Lim	h.d.lim@soton.ac.uk	University of Southampton	Southampton	GB
Bao-Shi	Shiau	bsshiau@gate.sinica.edu.tw	National Taiwan Ocean University	Keelung	TW
Michael	Pirhalla	pirhalla.michael@epa.gov	US Environmental Protection Agency	Durham	US
Yunpeng	Xue	yunpeng.xue@sec.ethz.ch	ETH Zurich	Singapore	SG
David	Heist	heist.david@epa.gov	US Environmental Protection Agency	Durham	US
Chris	Owen	owen.chris@epa.gov	US Environmental Protection Agency	Durham	US
Joy	Wingrave (Shmeer)	j.wingrave@surrey.ac.uk	University of Surrey	Guildford	GB
William	Patino	william.patino@chmi.cz	Czech Hydrometeorological Institute	Prague	CZ
Fei	Li	lifei9524@outlook.com	The University of Hong Kong	Hong Kong	HK
Ruiqi	Wang	rwangbz@connect.ust.hk	The University of Hong Kong	Hong Kong	HK
Huanhuan	Wang	huanhwang3-c@my.cityu.edu.hk	City University of Hong Kong	Hong Kong	HK
Ziwei	Mo	mozw7@mail.sysu.edu.cn	Sun Yat-sen University, China	Guangzhou	CN
Wai-Chi	Cheng	zhengwzh7@mail.sysu.edu.cn	Sun Yat-sen University	ZhuHai	CN
Cosimo	Peruzzi	cosimo.peruzzi@ec-lyon.fr	Ecole Centrale Lyon	Lyon	FR
Zheng-Tong	Xie	z.xie@soton.ac.uk	University of Southampton	Southampton	GB
Tom	Spicer	tos@uark.edu	University of Arkansas	Fayetteville	US
Cung	Nguyen	c.h.nguyen@salford.ac.uk	University of Salford	Manchester	GB
Davide	Lasagna	davide.lasagna@soton.ac.uk	University of Southampton	Southampton	GB
Perrine	Charvolin-Volta	perrine.charvolin@ec-lyon.fr	Ecole Centrale Lyon	Lyon	FR
Hiromasa	Nakayama	nakayama.hiromasa@jaea.go.jp	Japan Atomic Energy Agency	Ibraki	JP
Christina	Vanderwel	c.m.vanderwel@soton.ac.uk	University of Southampton	Southampton	GB
Tomos	Rich	tjr1u19@soton.ac.uk	University of Southampton	Southampton	GB
Alan	Robins	a.robins@surrey.ac.uk	University of Surrey	Guildford	GB
Paul	Hayden	p.hayden@surrey.ac.uk	University of Surrey	Guildford	GB
Jonathan	Retter	jretter92@gmail.com	US Environmental Protection Agency	Durham	US
Abhishek	Mishra	a.mishra@surrey.ac.uk	University of Surrey	Guildford	GB
Shanshan Ding	Ding	s.ding@surrey.ac.uk	University of Surrey	Guildford	GB
Pavel	Sedlák	sedlak@ufa.cas.cz	Institute of Atmospheric Physics of the CAS	Prague	CZ
Michioka	Takenobu	michioka@mech.kindai.ac.jp	Kindai University	Higashiosaka	JP

PHYSMOD 2022

International Workshop on Flow and Dispersion Phenomena

Extended abstracts

In the alphabetical order of the presenting authors

QUADRANT ANALYSIS OF TWO-HEIGHT CANOPY FLOW MODELED IN A WIND TUNNEL

V. Babin[1], L. Shig[2], E. Fattal[1], R. Shnapp[3], Alex Liberzon1[2] and Y. Bohbot-Raviv[1]

[1]Israel Institute for Biological Research (IIBR), Ness-Ziona Israel
[2]School of Mechanical Engineering, Tel Aviv University, Tel Aviv, Israel
[3]Department of Physics of Complex System, Weizmann Institute, Rehovot, Israel

Abstract

The atmospheric boundary layer over urban areas is often described as a heterogeneous canopy layer, in terms of its height and/or spatial distribution. In the present study, specific heterogeneity made of two-height flat-plate roughness elements form two horizontal layers of different density, drag, and alignment. The turbulent flow above the roughness was modeled in the environmental wind tunnel at IIBR. Extensive particle image velocimetry (2D2C-PIV) measurements within and above the modeled canopy were performed. The quadrant analysis of sweeps and ejections of the Reynolds stress, known to dominate the turbulent transport in canopies is presented. The results are compared with two common models of the joint statistics of the velocity components (CEM and ICEM), designed to reproduce the imbalance in the stress contribution of sweeps and ejections to momentum transfer. Both models were found to reproduce the measured values well above the canopy top, while deviate inside the canopy. A local increase in momentum transfer between the two canopy layers was observed, indicating the existence of a second inflection in profile of momentum transfer.

Introduction

Turbulent canopy flows contribute an essential part to the heat and mass transport budgets in cities and forests. In the past few decades, large number of field and laboratory measurements, combined with numerical and theoretical studies, have investigated the unique and fundamental features of canopy turbulence [Brunet, 2020].

Some features of canopy flow, such as an inflection point in the mean velocity profile at the top of the canopy, the turbulence transport term in the turbulent kinetic energy (TKE) balance, support the representation of canopy flow using the so-called "mixing-layer analogy" [Raupach et al., 1996]. The canopy turbulence, especially near the canopy top, is populated with coherent motions entitled as "sweeps" and "ejections", at length scales of the order of the canopy height. These coherent motions were found to be responsible for the larger fraction of the momentum and scalar fluxes [Raupach et al., 1986a, Brunet et al., 1994].

The contribution of coherent motions to the momentum transfer is typically quantified using conditional sampling and a so-called "quadrant analysis" of the joint statistics of turbulent streamwise (u) and vertical (w) velocity components [Lu and Willmarth, 1973, Antonia, 1981].

Some of the key challenges in turbulent canopy flow modeling is due to difficulty of simple turbulent models, such as eddy-viscosity models, to simulate flows with significant non-local momentum exchange, as is the case within the canopy top [Wilson and Shaw, 1977, Finnigan, 2000]. For the higher order closure models, the joint statistics u, w need to be modeled. The joint probability density function (JPDF) of u, w can be modeled by two-dimensional Gram-Charlier *cumulant expansion method* (CEM) [Nakagawa and Nezu, 1977, Raupach, 1981], and its simplified version, the *incomplete cumulant expansion method* (ICEM) [Katul et al., 1997a, Katul et al., 1997b]. Both methods were employed successfully to reproduce measured difference in stress fraction contributions of quadrant 2 and quadrant 4 [Poggi et al., 2004, Katul et al., 2006].

Although most plant and urban canopies on Earth are heterogeneous (spatially varying in density, height and shape), yet a physical representation of heterogeneity and its effect on canopy turbulence remain unclear [Brunet, 2020]. In particular, the effects of heterogeneity on the coherent structures (sweeps and ejections) are not well understood [Katul et al., 2006], and it is not known how the CEM and ICEM models perform in non-uniform canopies. In this study these questions are addressed using an experimental study of a heterogeneous canopy, modeled in a wind tunnel.

Experimental setup

The flow measurements within and above the heterogeneous canopy model were conducted in the Environmental Wind Tunnel Laboratory (EWTL) at IIBR. This is an open-circuit wind tunnel, with a closed 15 m long 2×2 m ^{2} uniform rectangular cross section test section. The canopy layer was constructed using spires, fence at the test section entrance and ground-mounted roughness elements spanning an area of $\sim 12 \times 2$ m ^{2} (Fig. 1a). The reference velocity is determined via a Pitot-Prandtl tube placed at the test section entry, above the developing boundary layer.

The measurements have been performed for two reference wind speeds, 4.6 and 9.0 m s $^{-1}$ (bulk Reynolds number of $\delta u_e/\nu = Re_1 = 2.3 \times 10^5$ and $Re_2 = 4.9 \times 10^5$, where δ is boundary layer height of about 80cm, respectively). The roof and lateral walls near the testing regions of the canopy model are transparent to allow an optical access to the flow. The heterogeneous canopy model is composed of vertical metal plates of two heights, 50 mm ($H/2$) and 100 mm (H) in equal amounts, resulting in an average canopy height of 75 mm ($\frac{3}{4}H$). The roughness elements were arranged in a staggered configuration. Each lateral row of elements consists of either tall or short elements only as illustrated in Fig.1b.

(**a**) (**b**)

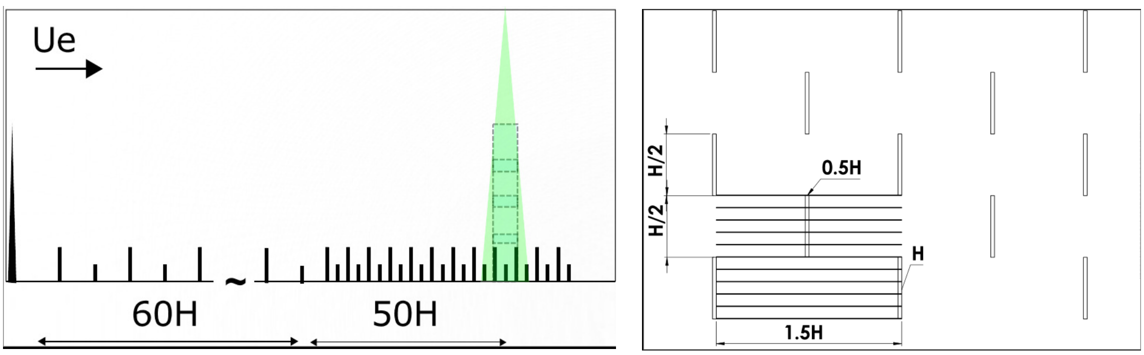

Fig.1: (a) Side view of the experimental section of the wind tunnel and layout of the canopy roughness elements, and (b) top-view of the roughness elements and PIV-planes obtained in the measurement region.

Velocity fields measurements in the $x - z$ planes (streamwise and floor-normal direction plane, $x = 0$ defined at the entrance to the measurement cell) were performed with a planar (2D/2C) Particle Image Velocimetry (PIV) system (LaVision, Gmbh). The system consisted of a Imager sCMOS camera with

2560X2160 pixels sensor and Zeiss Milvus 100mm f2M ZF lens, 15Hz double pulsed EverGreen Nd:Yag laser (200 mJ/pulse). A vertical light sheet with thickness of about 1 mm was generated at 11 different (x,y) locations and 4 different heights with 50 mm overlap between each two successive heights, aligned in the streamwise direction. FoV was about 20X20 cm^2 with pixelsize of about 0.08 mm/pixel. All the measurements were repeated for the two Reynolds number flows. For each PIV plane 1000 double frame images were obtained at 15 Hz. PIV analysis was preformed using 2 passes of 64×64 window size and 50% overlap and a final pass with 32×32 window size and 75% overlap obtaining resolution of a velocity vector per 1.2 mm. Outliers were removed using median filter, removing neighboring vector that were more than three standard deviations away from the local median.

Conditional sampling and analysis

Conditional sampling and quadrant analysis of the main Reynolds stress component $-\langle u'w' \rangle$ [Lu and Willmarth, 1973, Wallace, 2016] is applied, following studies of uniform canopies [Raupach et al., 1986a, Poggi et al., 2004, Zhu et al., 2007].

The maps of $-\langle u'w' \rangle$ are divided into four quadrants (Q_k) according to the signs of u' and w': *ejections*, or Q_2 represent $u' < 0, w' > 0$; *sweeps* Q_4, $u' > 0, w' < 0$), inward Q_1 and outward Q_3 interactions. Note that we use a zero threshold to define a quadrant and in the common notation it is sometimes marked with a subscript zero [Raupach, 1981].

The fraction number of quadrant k instances out of all measured planes at each point $D_k$is defined as:

$$D_k(\vec{x}) = \frac{1}{N} \sum_{i=0}^{N} I_k(\vec{x}, t_i) \tag{1}$$

with

$$I_k(\vec{x}, t_i) = \begin{cases} 1, & u'w'(\vec{x}, t_i) \quad in \ quadrant \ k \\ 0, & else. \end{cases} \tag{2}$$

The contribution of a certain quadrant to the total ensemble average of $-\langle u'w' \rangle$ is defined as:

$$u'w'_k(\vec{x}) = \frac{1}{N} \sum_{i=0}^{N} u'w'(\vec{x}, t_i) I_k(\vec{x}, t_i) \tag{3}$$

The relative contribution of Q_i to the total stress $-\langle u'w' \rangle$ can be quantified by the fractional stress term:

$$S_k = \frac{u'w'_k}{\langle u'w' \rangle}, \tag{4}$$

Note that $\sum_{k=1}^{4} D_k = 1$ and $\sum_{k=1}^{4} S_k = 1$.

A common measure to quantify the relative importance of ejections and sweeps to $\langle u'w' \rangle$ is the imbalance in the contribution of sweeps and ejections to momentum transfer using the difference in stress fraction contributions which can be defined as in Raupach (1981):

$$\Delta S = S_4 - S_2 \tag{5}$$

To link ΔS and quadrant analysis with the TKE budgets and RANS models, work of Nakagawa and Nezu (1977) and Raupach (1981) that successfully employed the third-order cumulant expansion method (CEM) were followed:

$$\Delta S = \frac{1 + R_{uw}}{R_{uw}\sqrt{2\pi}} \left(\frac{2C_1}{(1 + R_{uw})^2} + \frac{C_2}{1 + R_{uw}} \right) \tag{6}$$

where:

$$C_1 = (1 + R_{uw})(\frac{M_{03}-M_{30}}{6} + \frac{M_{12}-M_{21}}{2}) \quad (7)$$

$$C_2 = -\frac{2R_{uw}(M_{03}-M_{30})}{6} - \frac{(M_{12}-M_{21})}{2} \quad (8)$$

and $R_{uw} = \frac{\langle u' w' \rangle}{\sigma_u \sigma_w}$, $M_{ij} = \frac{\langle u'^i w'^j \rangle}{\sigma_u^i \sigma_w^j}$, $\sigma_s = \sqrt{s'^2}$.

Katul et al. (1997a) conducted a sensitivity analysis on the relative importance of the mixed moments and the velocity skewness on ΔS. They demonstrated that the mixed moments $M_{12} - M_{21}$ contribute much more than $M_{03} - M_{30}$. Hence, based on this finding, a further simplification was suggested referred to as the incomplete CEM (ICEM) given by:

$$\Delta S = \frac{1}{2R_{uw}\sqrt{2\pi}}(M_{21} - M_{12}) \quad (9)$$

Results

Example for two instantaneous sweep and ejection events at Re_1 are presented in Fig. 0. The PIV realizations are chosen such that at least 70% of the image is dominated by either ejections (a) or by sweep event (b). The black arrows indicate fluctuating flow-field (u', w'), superimposed on the normalized color map representing turbulent shear stress $u'w'$ normalised by $u_* = \sqrt{\langle u'w' \rangle_H}$, within the heterogeneous canopy and up to the height of $\approx 1.8H$. Note the different scale of the color bars, adjusted to the events for clarity. The wind direction is from left to right.

Fig. 2(a) shows an instantaneous ejection event (black arrows pointing upward in the opposite direction of the main flow), which demonstrates transport of momentum out of the canopy by a slower (than the mean velocity) upward-moving coherent motion. Higher shear regions (yellow color) during ejection events was observed mainly above the canopy height, e.g $z/H > 1$, consistently throughout all the measured planes. Fig. 2(b) shows a sweep event (black arrows pointing downwards), spreading over the whole measurement domain, demonstrating the instantaneous penetration of momentum into the canopy by a fast, downward moving gust. During sweep events high shear events (yellow color) were observed inside the canopy ($z/H < 1$) with higher magnitude, but less common and smaller in size as compared to ejection events. Conversely, in both realisations, the scale of the observed coherent motions seem to exceed the size of the measurement volume. Such large scale and violent events are persistent and were observed in numerous PIV images.

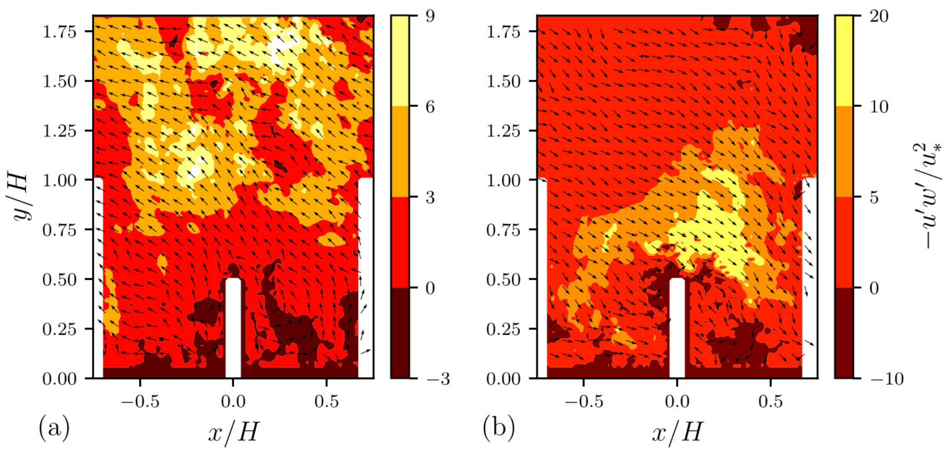

Fig.2: Example turbulent fluctuating velocity fields (u', w') (arrows) a) dominated by ejections $(u' < 0, w' > 0)$ and b) sweeps $(u' > 0, w' < 0)$, superimposed on the normalized turbulent shear stress $(u'w')$ for Re_1 at plane 8 ($y/H = 0.7$). Flow is from left to right.

Horizontal averaged duration fraction profiles for each quadrant are shown in Fig. 3 (a). Ejection and sweep events are the most abundant, in agreement with the previous studies of Raupach (1981) and Zhu et al. (2007). The duration of sweeps is about $D_4 \approx 0.36$ above the canopy and decreases sharply below, while the ejection duration has a peak right below the canopy top ($z/H = 1$) and decreases at higher elevations. At $z/H \approx 1.5$, the ejection and sweep events have the same duration values. These trends are consistent with the results of homogeneous canopies of Raupach (1981) and Zhu et al. (2007). One should keep in mind, though, that the frequent occurrence of ejections near and below the canopy top does not necessarily imply that they dominate over other variables, since the characteristic magnitudes in each quadrant are considerably different.

The stress fraction profiles are shown in Fig. 3(b). Below and around the canopy top, the sweep events are the most dominant contributors to the shear stress. Thus, in spite of the high duration fraction of ejections at $z/H < 1$ the sweeps dominate the contribution to shear stress. At $z/H > 1.5$, the ejections become the largest contributors. This latter trend is consistent with previous observations in homogeneous canopies [Harman et al., 2016; Raupach, 1981; Zhu et al., 2007].

Despite this difference in interpretation, one key characteristic of the development sequence is that the resulting coherent motions retain the initial spatial structure of the eigenfunctions of the inflected free shear layer, which are set up by the drag in the upper layers of the canopy.

Vertical profile of ΔS are shown in Fig. 3(c). Above the canopy ($z > H$) the profile appear similar in shape to the profiles obtained in homogeneous canopies. This similarity further supports the idea that the drag in the upper layer of the canopy dominates the inflected velocity profile height and the instability associated with it [Brunet, 2020]. Another interesting feature, which has not been observed in previous canopy studies, occurs near the short element height $H/2$, where a sudden increase in ΔS follows a local decrease in $H/2 < z < H$. This sudden increase might be associated with the weak instability induced by the short element height, rather than the canopy as a whole (inflected double average velocity at H) creating a double inflected profile.

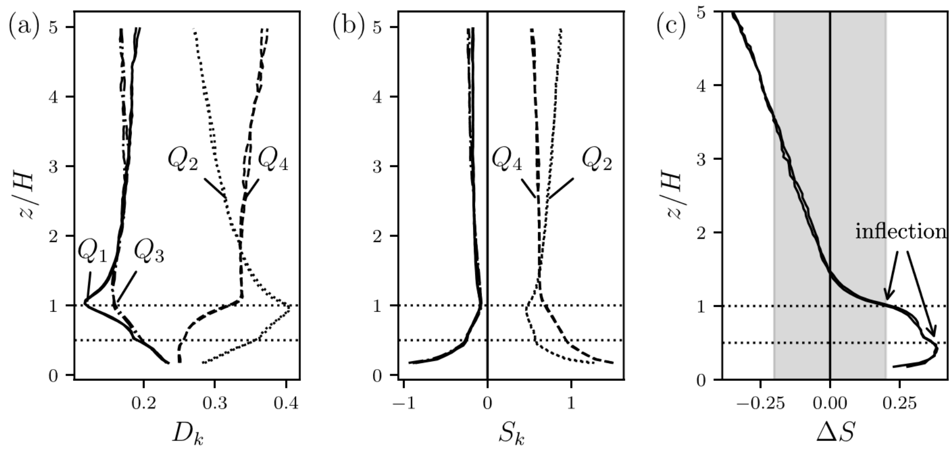

Fig 3: (a) Duration fraction vertical profiles, D_k, for each quadrant at both Re numbers, (b) Stress fraction vertical profiles S_k for each Re number and (c) Profile of measured ΔS. Horizontal dotted line indicate the height of the plates.

In Fig. 4 CEM and ICEM models to the directly measured ΔS comparison is presented. Both models don't deviate substantially from the measurements in agreement with Katul et al. (2006) and Zhu et al. (2007), with exception of deviation deeper inside the canopy ($z/H < 1$), resulting in larger positive values ($\Delta S > 0.25$). In this region the ICEM deviates strongly from the measured data visible by different slopes of the linear fit: CEM ≈ 1.03 while ICEM ≈ 0.8. The deviation is due to the non-negligible values of $M_{03} - M_{30}$ (not shown here for the sake of brevity). Conversely the range $|\Delta S| < 0.2$ (gray area in 0(c)), corresponds to the layer slightly below and above the canopy top, at which both models are in great agreement with the measured data.

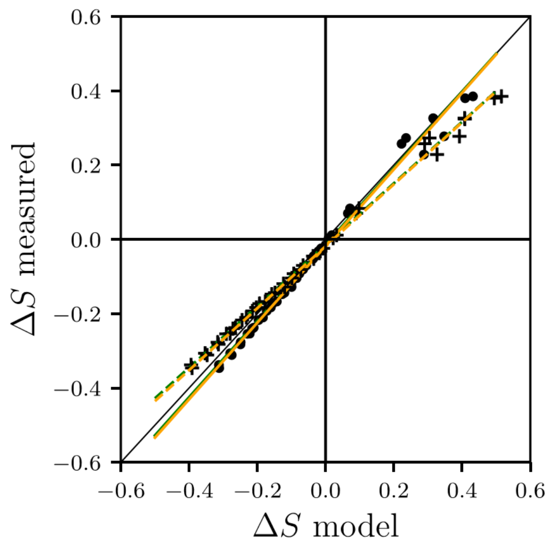

Fig. 4: Comparison of the CEM (o) and ICEM (+) models with the measured values of ΔS at Re_1 (green) and Re_2 (orange). Dashed line indicated linear fitted line for ICEM model comparison and solid line for CEM model comparison.

Summary

PIV measurements were performed for a wind-tunnel model of a heterogeneous canopy boundary layer in order to examine the characteristics of the turbulence within and above the heterogeneous canopy. The turbulence characteristics of the model found to be similar but not identical to uniform canopies [Raupach, 1981, Zhu et al., 2007, Harman et al., 2016]. Conditional sampling based on the quadrant analysis, based on the signs of velocity fluctuations, reveals some interesting features of the flow structure, especially during the sweep and ejection events, which are shown to dominate in this case the momentum fluxes. During the sweeps, the downward flow generates small, concentrated, high intensity ($-u'w'/u_*^2 > 10$) shear layers, right below the canopy top. The flow above is distinctly less intense in terms of turbulence shear stress. During ejections, the shear layers at lower intensity cover large areas above the canopy top.

Consistent with previous studies, ejections occur most frequently, having the highest duration inside and above the canopy top, while sweeps are more frequent above the canopy, at $z/H > 1.5$. The sweeps, nevertheless, contribute more significantly to the turbulent shear stress at heights up to $z/H > 1.5$. This is consistent with the high shear layers near the canopy top observed during sweep events.

Interestingly, for this heterogeneous canopy comprising of elements of two heights and also of the layers of staggered versus aligned elements – at heights above the canopy the sweeps and ejections exhibit similar behavior to uniform canopies [Raupach, 1981; Raupach et al., 1986b; Zhu et al., 2007]. This can be explained by the fact that the upper layer (which in our case is an aligned array of plates), contributes more significantly to the total drag and responsible for the height and strength of the mean velocity profile. Further study with different types of heterogeneous canopy layers are needed to validate this hypothesis.

In terms of ΔS, above the canopy top very similar profiles to the previous cases of uniform, homogeneous canopies were observed. The interesting feature that is specific to this type of canopy is the sudden increase in ΔS at the height of short elements, which might be associated with the local instability that is induced by the short element which created a double inflected canopy velocity profile. It was shown that the incomplete third-order cumulant expansion (ICEM) approach reproduces the sign and magnitude of ΔS above the canopy surprisingly well, but deviates substantially inside the canopy ($z/H < 1$), while the full CEM model seems to predict the measured values well below and above the canopy top. A follow up step to this, is to check the gradient diffusion formulation obtaining the ΔS with the second moments, which could allow second order models to calculate ΔS and through it reproduce the statistical properties of the ejection–sweep cycle. This approach was shown to work well in uniform canopies [Katul et al., 2006] but not in canopies with heterogeneity of some sort.

Acknowledgments

The experimental study was supported by the PAZY grant, number 2403170.

References

Antonia, R. A. (1981). Conditional sampling in turbulence measurement. *Annual Review of Fluid Mechanics*, 13:131–156.

Brunet, Y., Finnigan, J. J., and Raupach, M. R. (1994). A wind tunnel study of air flow in waving wheat: Single-point velocity statistics. *Boundary-Layer Meteorology*, 70:95–132.

Brunet, Y. (2020). Turbulent flow in plant canopies: Historical perspective and overview. *Boundary-Layer Meteorology*, 177:315–364.

Finnigan, J. (2000). Turbulence in plant canopies. *Annu Rev Fluid Mech*, 32(1):519–571.

Harman, I., Böhm, M., Finnigan, J., and Hughes, D. (2016). Spatial variability of the flow and turbulence within a model canopy. *Boundary-Layer Meteorol.*, 160(3):375–396.

Katul, G., Hsieh, C.-I., Kuhn, G., Ellsworth, D., and Nie, D. (1997a). Turbulent eddy motion at the forest-atmosphere interface. *Journal of Geophysical Research: Atmospheres*, 102:13409–13421.

Katul, G., Kuhn, G., Schieldge, J., and Hsieh, C.-I. (1997b). The ejection-sweep character of scalar fluxes in the unstable surface layer. *Boundary-Layer Meteorology*, 83:1–26.

Katul, G., Poggi, D., Cava, D., and Finnigan, J. (2006). The relative importance of ejections and sweeps to momentum transfer in the atmospheric boundary layer. *Boundary-Layer Meteorology*, 120:367–375.

Lu, S. S. and Willmarth, W. W. (1973). Measurements of the structure of the reynolds stress in a turbulent boundary layer. *Journal of Fluid Mechanics*, 60:481–511.

Nakagawa, H. and Nezu, I. (1977). Prediction of the contributions to the reynolds stress from bursting events in open-channel flows. *Journal of Fluid Mechanics*, 80:99–128.

Poggi, D., Porporato, A., Ridolfi, L., Albertson, J. D., and Katul, G. G. (2004). The effect of vegetation density on canopy sub-layer turbulence. *Boundary-Layer Meteorology*, 111:565–587.

Raupach, M. R., Coppin, P. A., and Legg, B. J. (1986a). Experiments on scalar dispersion within a model plant canopy part i: The turbulence structure. *Boundary-Layer Meteorology*, 35:21–52.

Raupach, M. R., Finnigan, J. J., and Brunet, Y. (1996). Coherent eddies and turbulence in vegetation canopies: the mixing-layer analogy. *Boundary-Layer Meteorology*, 78:351–382.

Raupach, M. R. (1981). Conditional statistics of reynolds stress in rough-wall and smooth-wall turbulent boundary layers. *Journal of Fluid Mechanics*, 108:363–382.

Raupach, M., Coppin, P., and Legg, B. (1986b). Experiments on scalar dispersion within a model plant canopy part i: The turbulence structure. *Boundary-Layer Meteorol*, 35(1-2):21–52.

Wallace, J. M. (2016). Quadrant analysis in turbulence research: History and evolution. *Annual Review of Fluid Mechanics*, 48:131–158.

Wilson, N. and Shaw, R. (1977). A higher order closure model for canopy flow. *J. Appl. Meteorol.*, 16(11):1197–1205.

Zhu, W., van Hout, R., and Katz, J. (2007). On the flow structure and turbulence during sweep and ejection events in a wind-tunnel model canopy. *Boundary-Layer Meteorology*, 124:205–233.

Application of a microscale ship plume parameterization in a city-scale air quality model

R. Badeke[1], V. Matthias[1], M. Karl[1], M.O.P. Ramacher[1], D.A. Schwarzkopf[1] and D. Grawe[2]

[1]Institute of Coastal Environmental Chemistry, Chemistry Transport Modeling, Helmholtz-Zentrum Hereon, Max-Planck-Str. 1, 21502 Geesthacht, Germany
[2]CEN, Met. Inst., University of Hamburg, Bundesstr. 55, 20146 Hamburg, Germany

Abstract

This work presents an advanced method for vertical ship emission distribution in Eulerian city-scale models. The emissions are distributed based on a parameterized exponentially modified Gaussian function. This parameterization was derived from model results of a microscale model, taking into account effects of thermal plume rise and obstacle-induced turbulence in the near-field of a ship. A complex city-scale chemistry transport modeling study for the inner-city of Hamburg, Germany is performed with the newly derived parameterization and compared against a static distribution and measurements from the Hamburg air monitoring network. Results show improved model accuracy compared to measurements of crucial air quality components NO, NO_2, and O_3. For example, at the representative station Altona-Elbhang, mean hourly biases of NO are reduced from 11.35 µg m^{-3} to 1.57 µg m^{-3} and from 13.36 µg m^{-3} to 6.69 µg m^{-3} in January and August 2018, respectively. Modeling with a zero-out method also shows the potential of reaching WHO air quality guideline values for mean daily NO_2 concentrations of 25 µg m^{-3} by reducing ship emissions close inside the harbor.

Introduction

The negative impacts of shipping emissions on human health and the environment remain an ongoing problem in coastal cities. Regarding air quality, the most problematic combustion products are oxides of nitrogen (NO_x = NO + NO_2) and particulate matter (PM), followed by oxides of sulfur (SO_x), carbon monoxide CO and volatile organic compounds (VOCs).
When using Eulerian models, precise estimation of ship emissions is only possible if the absolute emission values are determined correctly and when they are distributed correctly into the model domain (Matthias et al., 2018).
Of special importance is the consideration of plume rise and turbulent downward dispersion when modeling concentrations in the near field of a ship (Badeke et al., 2021). This can be done by using the microscale chemistry, transport and stream model (MITRAS) (Schlünzen et al., 2003, 2018). Badeke et al. (2022) used MITRAS results to calculate parameterizations for the vertical ship emission profile. This study applies these parameterizations in a complex urban air quality modeling study with the city-scale model EPISODE-CityChem (Karl et al., 2019) and compares the model performance against measurements.

Methods

Previous model setups with EPISODE-CityChem used a static vertical ship emission distribution into the model domain (Ramacher et al., 2019). Emissions were distributed evenly into the lowest four model layers, i.e., 25% each layer. This is referred here as “Fixplume”.

In this study, a new flexible plume ("Flexplume") is applied, in which the vertical ship emission distribution corresponds to the exponentially modified Gaussian (Expgauss) function, following Badeke et al. (2022):

$$c(h) = \frac{\lambda_1}{2}\exp\left(\frac{\lambda_1}{2}(2\lambda_2 + \lambda_1\lambda_3^2 - 2h)\right)\cdot \mathrm{erfc}\left(\frac{\lambda_2 + \lambda_1\lambda_3^2 - h}{\sqrt{2}\lambda_3}\right),$$

where c(h) is the vertical concentration profile depending on the height (h) and λ_1, λ_2 and λ_3 are shape parameters of the Expgauss function. The shape parameters can be calculated as:

$$\lambda_1 = -0.00445 + 0.002\ v_{wind} - 0.00575\ \Gamma$$

$$\lambda_2 = 27.6 + h_{fleet} - 52.7\ \log_{10}(v_{wind}) + 2.86\ \cos(\phi) + 0.023\ T_{exh} + 3.86\ \Gamma$$

$$\lambda_3 = 20.4 - 8.28\cos(\phi) - 0.0135\ T_{exh} - 6.0\ \Gamma,$$

where v_{wind} is the wind speed given dimensionless in [m s^{-1}], h_{fleet} is the average ship height given dimensionless in [m], T_{exh} is the exhaust temperature given dimensionless in [K], ϕ is the flow angle in [°], and Γ is the atmospheric stability given dimensionless in [K · 100 m^{-1}]. Currently, all ships in the EPISODE-CityChem model have the same height, exhaust temperature and flow angle. These were set to 25 m, 300°C and 0°, respectively. With the update of EPISODE-CityChem v1.6 (Karl, 2022), it is possible to include the effects of wind speed and stability on the vertical ship emission distribution. EPISODE-CityChem calculates the ship emission distribution at every x-y position inside the domain where ship emissions occur and generates individual Expgauss emission profiles, depending on the local meteorological conditions.

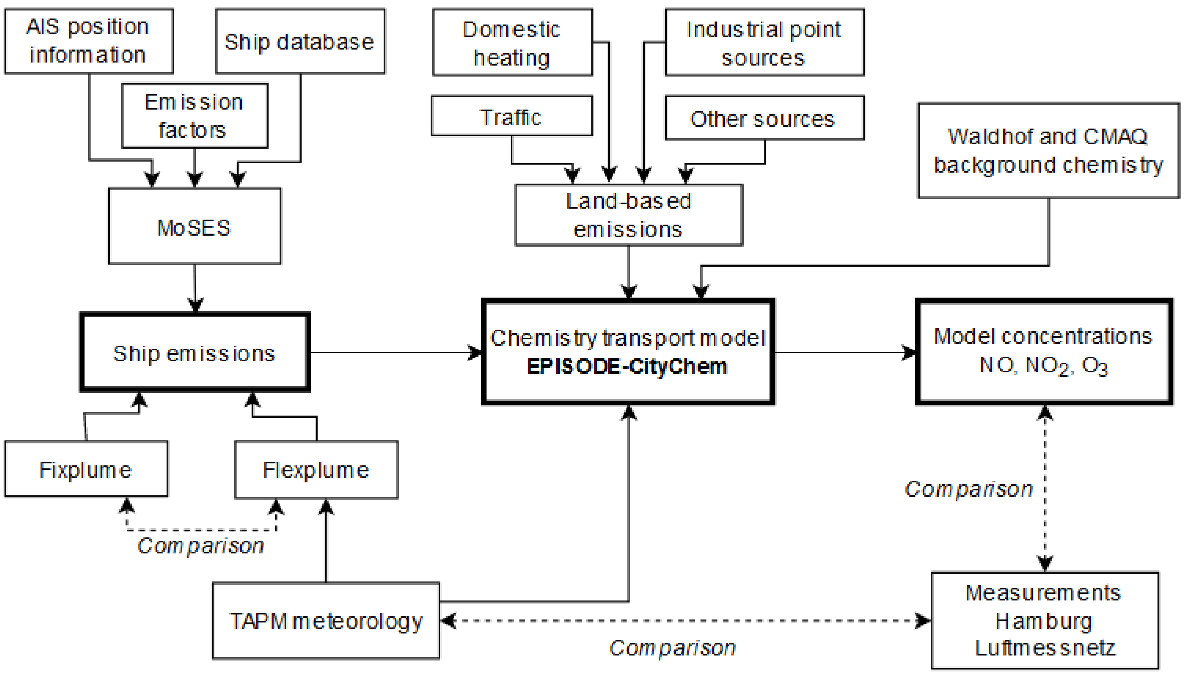

Figure 1: Schematic overview of the model setup for this study.

The new Flexplume approach is tested in a complex chemistry transport modeling study with the EPISODE-CityChem model system (Fig. 1). Results are calculated for two months, January and August 2018. The horizontal resolution was set to 250 m × 250 m to match with the resolution of the meteorological input data from the Australian air quality model TAPM (The Air Pollution Model) (Hurley, 2008; Hurley et al., 2005).

Background concentrations were gathered primarily from the background station Waldhof, which is part of the European Monitoring and Evaluation Programme (EMEP, 2022). Background chemicals that were not measured in Waldhof, were taken as monthly mean concentrations from the Community Multiscale Air Quality Model (CMAQ) from a previous study (Matthias et al., 2021).

Ship emissions are calculated with the bottom-up modular ship emission modeling system (MoSES, Schwarzkopf et al., 2021). The emission calculation is based on information about the ship (e.g., ship type, fuel type, engine power) that is gathered from the IHS Markit 2020 ship database.

This study further accounts for land-based emissions from industrial point sources, road traffic, commercial and industrial combustion, domestic heating, agriculture, waste and solvent emissions.

Modeled concentrations for NO, NO_2 and O_3 are compared against measurements from stations of the air quality measurement network (Hamburger Luftmessnetz, 2022, Fig. 4). A variety of statistical measures have been tested (e.g., bias, regression and root mean square error (RMSE)).

Results

Model performance with Fixplume and Flexplume

For modeled NO concentrations compared to measured concentrations, almost all statistical parameters show improvements for the new Flexplume algorithm compared to the Fixplume, both on an hourly and daily scale.

The largest improvement is found at the stations Altona-Elbhang (80KT) and Finkenwerder West (72FI) as expected since they are closest to the river Elbe and not dominated by traffic emissions.

Figure 2 presents the corresponding time series for Altona-Elbhang, based on daily trimmed mean values. Trimmed means that only values from percentile 10 to percentile 90 (i.e., 20 hours per day) are used for the calculation of daily means to reduce the effect of outliers that cannot be captured by the model. Outliers may be caused by local activity, e.g., people smoking close to the instruments or short-time construction works nearby. Trimming was done for both measured and modeled values to maintain consistency and work with the same amount of data.

For hourly data in January, the bias in Altona-Elbhang is reduced from 11.35 $\mu g\ m^{-3}$ to 1.57 $\mu g\ m^{-3}$ compared to the Fixplume. The RMSE improves from 45.34 $\mu g\ m^{-3}$ to 19.99 $\mu g\ m^{-3}$. The correlation coefficient R increases from 0.76 to 0.86 (based on daily trimmed mean data). In August, the NO model performance is lower, but still an improvement can be seen when comparing Flexplume to Fixplume. The bias is reduced from 13.36 $\mu g\ m^{-3}$ to 6.89 $\mu g\ m^{-3}$ (hourly data). However, correlation does not show a significant improvement in Altona-Elbhang in August and lies at approximately R = 0.45 (daily trimmed mean).

For NO_2 in January, the Flexplume algorithm shows an overall worse statistical agreement with measurements compared to the Fixplume assumption. However, the positive change in bias and negative impact on regression bias are small. The highest additional absolute bias is ~3.0 µg m^{-3} more compared to the Fixplume in Finkenwerder-West (from -3.3 to -6.14 with hourly data). The strongest loss in correlation is -0.03 points, also in Finkenwerder West (from 0.89 to 0.86 based on daily trimmed mean data). In August, NO_2 model results improve statistically. The bias from Altona-Elbhang is reduced from 5.81 µg m^{-3} to 3.05 µg m^{-3} for the Flexplume algorithm.

Overall the positive effect for NO modeling outweigh the loss in model performance for NO_2 in January.

The differences of Flexplume and Fixplume algorithms are clearly located in the harbor area (Fig. 3). For NO the highest differences between the algorithms occur close to the shipping lanes and at the shipping terminals, since NO is quickly oxidized. For NO_2 and O_3, the differences occur more evenly distributed over the whole harbor area.

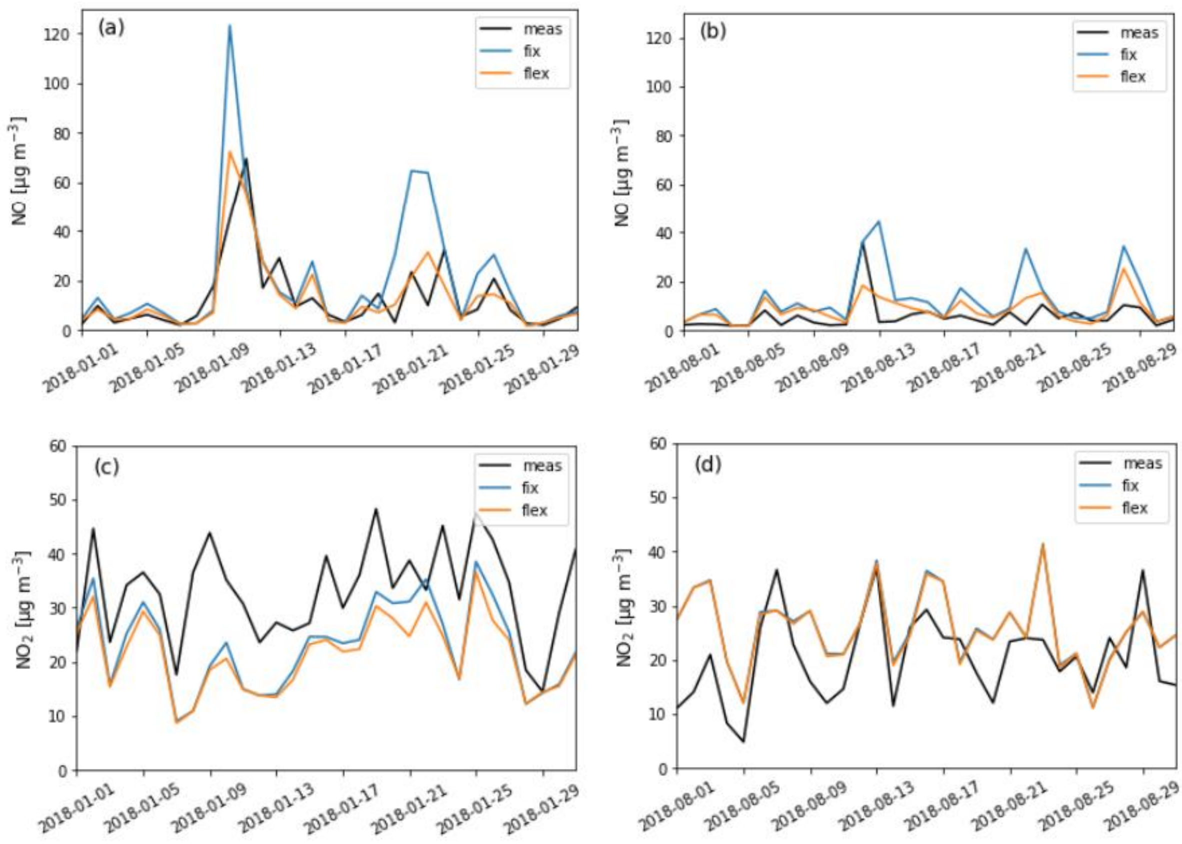

Figure 2: Time series (daily, trimmed mean) for the station Altona-Elbhang (NO, NO_2) in January (left) and August (right) 2018. Comparison of measurements with the Fixplume and Flexplume model algorithm for ship emissions.

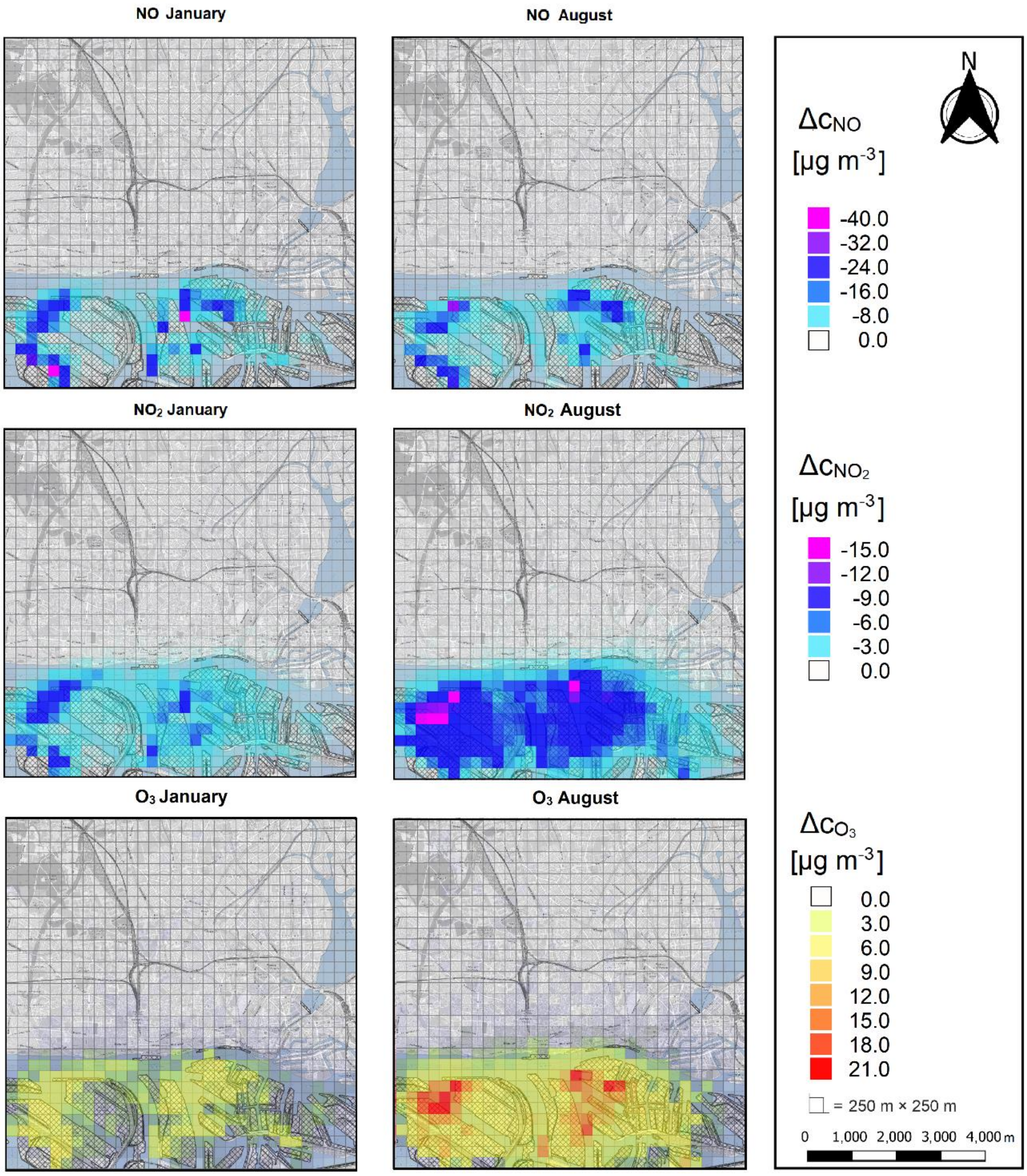

Figure 3: Concentration maps of the investigated domain showing the difference of the Flexplume approach to the Fixplume ($\Delta c = c_{Flex} - c_{Fix}$) for mean monthly concentrations of NO, NO_2 and O_3. Maps were created using © QGIS-Version 3.22.1-Białowieża with a topographic base map by © OpenStreetMap contributors 2022 and © Copernicus Urban Atlas 2012 land use and land cover data. Distributed under a Creative Commons BY-SA License.

Wind direction effects

In both months, the main wind sector was southwest occurring 40−50% of the time followed by southeast and northwest. Wind from northeast occurred only 5−7% of the time.

An overview on the model performance based on the modeled bias is presented in Fig. 4 for the Flexplume approach.

The model performance is evaluated exemplary for the station Altona-Elbhang (80KT), which both close to the city center and affected by ship emissions. For NO, the best results compared to measurement data were found for wind conditions from the southwest sector (e.g., bias -0.07 µg m^{-3} in January and 2.38 µg m^{-3} in August). In comparison, the lowest model performance at this station were found for winds from the northeast sector with biases of 7.82 µg m^{-3} in January and a large bias of 47.18 µg m^{-3} in August.

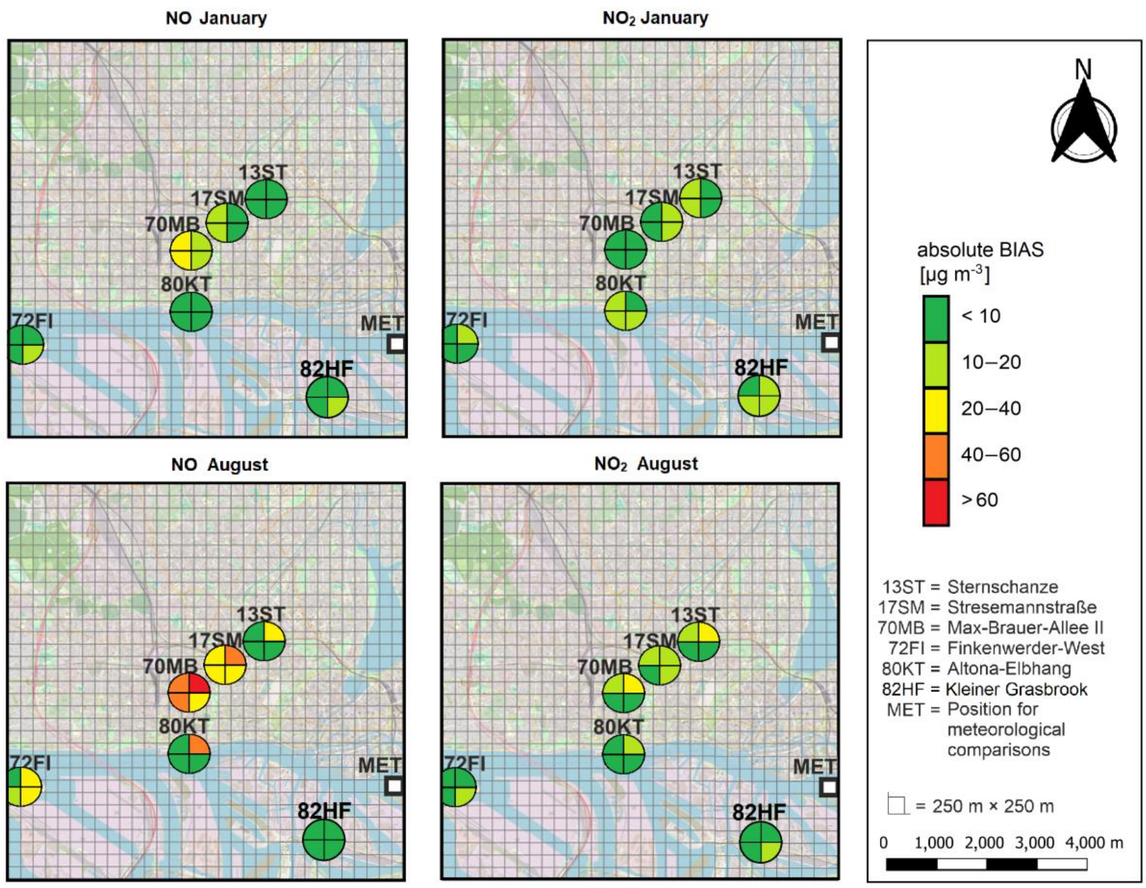

Figure 4: Overview on the EPISODE-CityChem performance (bias) in NO_2 and NO depending on the wind sector in January and August based on the Flexplume approach. Maps were created using © QGIS-Version 3.22.1-Białowieża with a topographic base map by © OpenStreetMap contributors 2022 and © Copernicus Urban Atlas 2012 land use and land cover data. Distributed under a Creative Commons BY-SA License.

NO_2 results show the best performance for winds from the northeast sector (bias: -8.64 µg m^{-3}) in January and from the southeast (0.35 µg m^{-3}) and southwest (-0.35 µg m^{-3}) in August. The largest biases occurred from the southeast sector in January (-11.95 µg m^{-3}) and from the northeast sector in August (15.21 µg m^{-3}).

Notably, northeast conditions showed the best regression results for NO_2 (R = 0.72 in January and 0.52 in August).

Since the station Altona-Elbhang lies close to the Elbe at the northern shore, good performance for winds from the southern sectors are attributed to good representation of shipping emissions in this study. Air masses from the northwest represent mainly urban background conditions, which are also well represented. The larger errors from the northeast sector are attributed to strong traffic emissions. The low model performance can also be attributed to the low occurrence of winds from this sector. In this way, few very strong peaks can raise the model error very high.

A general overview on the Flexplume performance on all available stations is given in Fig. 4.

Shipping effect on the urban pollutant concentration

The contribution of shipping emissions to the total modeled concentration of air pollutants was determined based on the zero-out method, i.e., the difference between model runs including all emissions (= with ships and using the Flexplume approach) and runs without ship emissions (Table 1). Results shown here are given for the position of Altona-Elbhang.

The ship emission contribution to mean daily NO concentration is 7.0 µg m^{-3} and 5.8 µg m^{-3} in January and August, respectively. This is an increase of 109−114% compared to a situation without ships. The main contribution is from direct NO emission by ships, which form 95% of their total NO_x emission. Another source for NO concentrations is NO_2 photolysis during daytime, which also intensifies due to direct ship emission of NO_2.

Mean daily NO_2 concentration contribution by ships is 9.5 µg m^{-3} and 8.5 µg m^{-3} for January and August, respectively, which corresponds to an increase of 77% and 44%, respectively. The main reaction for increased NO_2 by ship emissions are the production from NO and O_3, as well as reactions of NO with peroxy radicals like HO_2 and CH_3O_2. The seasonal difference in mean concentrations might be caused by the underestimation of NO_2 concentrations in winter, probably due to uncertain numbers for NO_2 emissions from domestic or industrial heating in winter.

O_3 concentrations are reduced by reaction with NO emissions by ships. In January and August the mean reduction due to ship emissions on a daily basis is -9.1 µg m^{-3} and -8.7 µg m^{-3}, respectively. This corresponds to -28% in January and -16% in August compared to a situation without ships.

For NO_2, the EU limit value for 24-hour mean concentrations is 200 µg m^{-3} (European Union, 2008), that shall not be exceeded more than 18 times per year. This value is not exceeded in this study. The corresponding WHO recommendation is 25 µg m^{-3} (World Health Organization, 2021). Table 1 shows the potential to comply with the WHO recommendation values for NO_2 when ship emissions are reduced in the future.

Table 1: Overview on shipping effect on mean monthly concentration of various chemical substances, modeled for the position of Altona-Elbhang. Absolute ship effect is calculated as $\Delta c = \bar{c}_{\text{with ships}} - \bar{c}_{\text{without ships}}$, and relative ship effect is calculated as $c_{\text{rel}} = (\bar{c}_{\text{with ships}} - \bar{c}_{\text{without ships}})/\bar{c}_{\text{without ships}} \cdot 100\%$.

Substance	Month	$\bar{c}_{\text{with ships}}$	$\bar{c}_{\text{without ships}}$	Δc	c_{rel}
NO	January	14.6	7.0	7.6	109%
[µg m^{-3}]	August	12.4	5.8	6.6	114%
NO_2	January	21.8	12.3	9.5	77%
[µg m^{-3}]	August	27.7	19.2	8.5	44%
O_3	January	23.0	32.1	-9.1	-28%
[µg m^{-3}]	August	46.4	54.7	-8.7	-16%

Conclusion

The Flexplume distribution showed an improved model accuracy, especially for NO close to the shipping lanes. The model bias was reduced by up to ~10 µg m^{-3} NO based on hourly data. The modeled NO_2 concentrations showed slightly lower statistical accuracy with the new Flexplume approach in January, but better results in August. The model results also indicate that the effect of the new Flexplume approach mainly affects the harbor area and approximately 2 km around it. Due to the lower modeled NO concentrations, the modeled O_3 concentrations are up to 20 µg m^{-3} higher in the harbor area than with the Fixplume approach.

The model improvement for shipping emissions was further shown by analyzing model biases depending on the wind direction, showing that for most measurement stations the modeled bias in NO and NO_2 now lies below 10 µg m^{-3} when the wind transported air from the harbor area to the measurement instrument. This often delivered better results than from other sectors (e.g., when the wind blows from traffic or industrial areas).

The results of this study have strong implications on the chemical feedback and a high relevance for compliance with air quality regulations.

References

Badeke, R., Matthias, V., and Grawe, D.: Parameterizing the vertical downward dispersion of ship exhaust gas in the near field, Atmos. Chem. Phys., 21, 5935–5951, https://doi.org/10.5194/acp-21-5935-2021, 2021.

Badeke, R., Matthias, V., Karl, M., and Grawe, D.: Effects of vertical ship exhaust plume distributions on urban pollutant concentration – a sensitivity study with MITRAS v2.0 and EPISODE-CityChem v1.4, Geosci. Model Dev. 4077–4103, https://doi.org/10.5194/gmd-15-4077-2022, 2022.

EMEP: European Monitoring and Evaluation Programme, https://www.emep.int/ (last access: 25 May 2022), 2022.

European Union: Directive 2008/50/EC of the European Parliament and of the Council of 21 May 2008 on ambient air quality and cleaner air for Europe. Off. J. Eur. Union 51, 1–44, https://eur-lex.europa.eu/legal-content/EN/TXT/PDF/?uri=OJ:L:2008:152:FULL&from=EN (last access: 24 May 2022), 2008.

Hamburger Luftmessnetz: Messstationen, https://luft.hamburg.de/ (last access: 01 June 2022), 2022.

Hurley, P.: TAPM v.4. Part 1: Technical Description. CSIRO Marine and Atmospheric Research Paper No. 25, Aspendale, Vic., Australia, ISBN: 9781921424717, https://www.cmar.csiro.au/research/tapm/docs/tapm_v4_technical_paper_part1.pdf (last access: 24 May 2022), 2008.

Hurley, P. J., Physick, W. L., and Luhar, A. K.: TAPM – A practical approach to prognostic meteorological and air pollution modelling, Environ. Modell. Softw., 20, 737–752, https://doi.org/10.1016/j.envsoft.2004.04.006, 2005.

Karl, M.: City-scale Chemistry Transport Model EPISODE-CityChem (Release version 1.6), Zenodo [code], https://doi.org/10.5281/zenodo.6573059, 2022.

Karl, M., Walker, S.-E., Solberg, S., and Ramacher, M. O. P.: The Eulerian urban dispersion model EPISODE - Part 2: Extensions to the source dispersion and photochemistry for EPISODE-CityChem v1.2 and its application to the city of Hamburg, Geosci. Model Dev., 12, 3357–3399, https://doi.org/10.5194/gmd-12-3357-2019, 2019.

Matthias, V., Arndt, J. A., Aulinger, A., Bieser, J., Denier van der Gon, H., Kranenburg, R., Kuenen, J., Neumann, D., Pouliot, G. and Quante, M.: Modeling emissions for three-dimensional atmospheric chemistry transport models, J. Air Waste Manage., 68, 763–800, https://doi.org/10.1080/10962247.2018.1424057, 2018.

Matthias, V., Quante, M., Arndt, J. A., Badeke, R., Fink, L., Petrik, R., Feldner, J., Schwarzkopf, D., Link, E.-M., Ramacher, M. O., et al.: The role of emission reductions and the meteorological situation for air quality improvements during the COVID-19 lockdown period in Central Europe, Atmospheric Chemistry and Physics, 21, 13 931–13 971, 2021.

Ramacher, M. O. P., Karl, M., Bieser, J., Jalkanen, J.-P., and Johansson, L.: Urban population exposure to NO_x emissions from local shipping in three Baltic Sea harbour cities - a generic approach, Atmos. Chem. Phys., 19, 9153–9179, https://doi.org/10.5194/acp-19-9153-2019, 2019.

Schlünzen, K. H., Hinneburg, D., Knoth, O., Lambrecht, M., Leitl, B., López, S., Lüpkes, C., Panskus, H., Renner, E., Schatzmann, M., Schoenemeyer, T., Trepte, S., and Wolke, R.: Flow and transport in the obstacle layer: First results of the micro-scale model MITRAS, J. Atmos. Chem., 44, 113–130, https://doi.org/10.1023/A:1022420130032, 2003.

Schlünzen, K. H., Boettcher, M., Fock, B. H., Gierisch, A., Grawe, D., and Salim, M.: Scientific documentation of the Multiscale Model System M-SYS, MEMI Tech. Rep. 4, CEN, Univ. Hambg., 153 p., https://www.mi.uni-hamburg.de/en/arbeitsgruppen/memi/modelle/dokumentation/msys-scientific-documentation-20180706.pdf (last access: 24 May 2022), 2018.

Schwarzkopf, D. A., Petrik, R., Matthias, V., Quante, M., Majamäki, E., & Jalkanen, J. P.: A ship emission modeling system with scenario capabilities. Atm. Environment: X 12, 100132, https://doi.org/10.1016/j.aeaoa.2021.100132, 2021.

World Health Organization: WHO global air quality guidelines: particulate matter ($PM_{2.5}$ and PM_{10}), ozone, nitrogen dioxide, sulfur dioxide and carbon monoxide, https://apps.who.int/iris/bitstream/handle/10665/345329/9789240034228eng.pdf?sequence=1&isAllowed=y (last access: 25 March 2022), 2021.

Influence of vegetation on urban canyon ventilation. Part I : experimental and numerical investigation of averged concentration and bulk exchange velocity.

M. Barulli[1] , S. Fellini[2] , A. Del Ponte[3] , L. Ridolfi[3] , L. Shoulhac[2] , M. Marro[4] , A. Emmanuelli[4] , P. Salizzoni[4]

[1] Department of Mathematical Sciences "Giuseppe Luigi Lagrange", Politecnico di Torino, Corso Duca Degli Abruzzi 24, 10129, Turin, Italy
[2]Univ Lyon, INSA Lyon, CNRS, Ecole Centrale de Lyon, Univ Claude Bernard Lyon 1, LMFA, UMR5509, 69621, Villeurbanne France
[3] Department of Environmental, Land, and Infrastructure Engineering, Politecnico di Torino, Corso Duca Degli Abruzzi 24, 10129, Turin, Italy
[4]Laboratoire de Mécanique des Fluides et D'Acoustique, UMR CNRS 5509, Université de Lyon, Ecole Centrale de Lyon, INSA Lyon, Université Claude Bernard Lyon I, 36, Avenue Guy de Collongue, 69134, Ecully, France

Abstract

The urban environment represents an area with particular microclimatic characteristics, due to human activities and to the geometry of the buildings. Urbanization processes can alter the processes of heat, mass and exchange momentum between the ground and the atmosphere. The most important phenomenon is the formation of the so-called heat island (Cancelli et al., 2006), a limited region above the city with higher temperature with respect to that of the surrounding atmosphere. Among the main reason for the formation of the heat island, there are the absorption of the solar radiation, which is higher for the materials used in the city (concrete, asphalt etc.) with respect to the rural environment, and the reduction of phenomena of evaporation and transpiration that, for a surface protected from vegetation, counteract the increase of temperature. The positive effects of vegetation on temperature and humidity, known as "urban cool island", are clearly visible during the afternoon and the evening, when the evaporative cooling has a greater impact. Despite its positive effect on urban microclimate, vegetation can negatively affect the pollutant concentration in urban areas. In fact, vegetation can play a dual role. On one side, foliage helps the deposition and the absorption of pollutants and on the other side, vegetation can cause an obstruction, inhibiting the ventilation in the canyon. Therefore, in the context of urban pollution and prevention of the risks on human health, the main goal of the present work is to advance the understanding of the effect of the presence of trees on the dispersion of pollutants in an urban geometry. To this purpose, the results obtained from an experimental campaign conducted in a wind tunnel are compared to the results obtained from RANS two-dimensional numerical simulations. The urban geometry considered consists in a street canyon placed perpendicular to the wind direction. Three configurations are analysed, namely: no trees, two rows of scattered trees and two dense rows of trees. A source emitting a mixture of ethane and air is used to simulate the pollutant and concentration measurements are performed by means of a Flame Ionization Detector (FID).

The obtained results show how the presence of trees modifies the pollutant concentration field (*Figure 1*). In particular, the configuration without trees results in a nearly two-dimensional concentration field, while the two configurations with trees present a three-dimensional field.

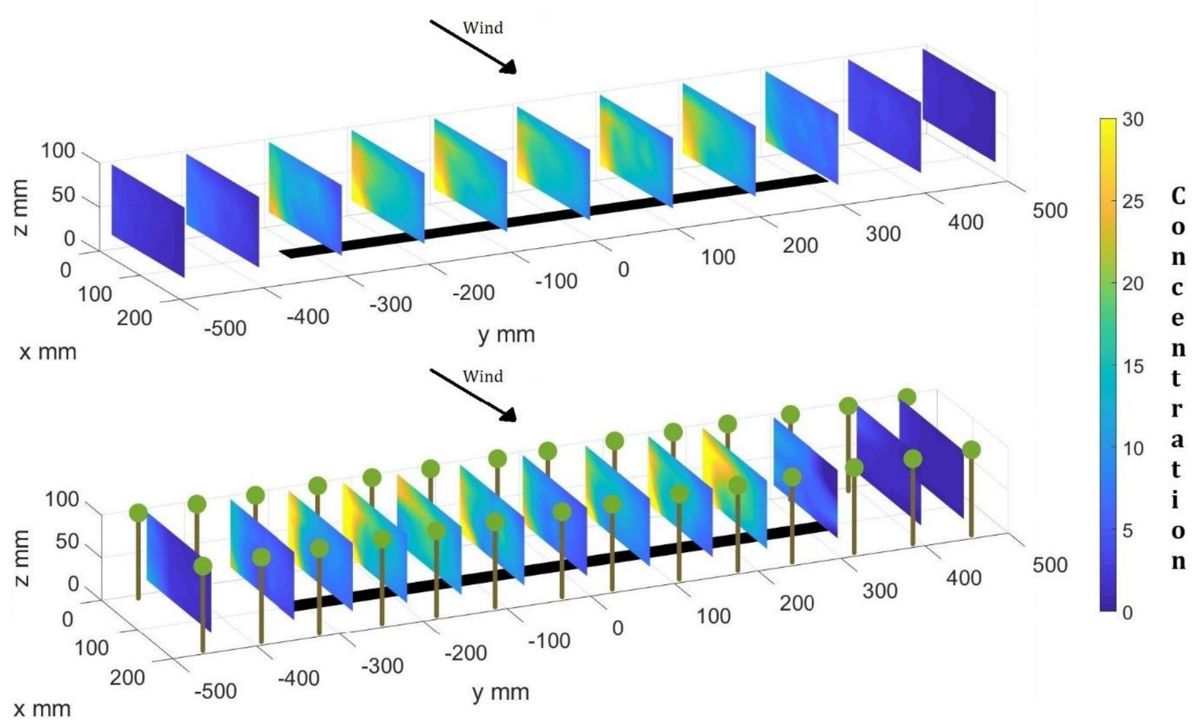

Figure 1 – *Concentration field at different sections along y direction. Configuration without trees (top) and with trees (bottom). The black bar on the ground represents the ethane source, the green dots represent the crowns of the trees, and the brown lines represent the trunks.*

Furthermore, the results from the computation of the vertical mass transfer velocity (*Figure 2*), as defined in (Salizzoni et al., 2009) and (Fellini et al., 2020), did not show any significant difference among the configurations analysed, therefore suggesting that the presence of trees does not affect the ventilation in the canyon. In the light of these experimental evidences, the outputs of simulations are analysed and their reliability in reproducing the processes responsible for the ventilation of the canyon is critically discussed. The obtained numerical results (*Figure 3*) are in a good agreement with the experimental campaign conducted in the wind tunnel. However, due to the inherent constraints of the RANS approach, they have provided only a qualitative behaviour of the concentration field.

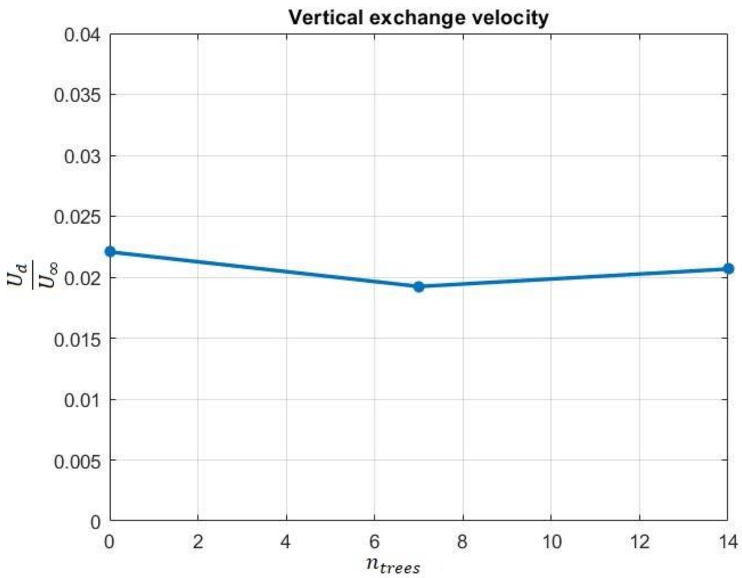

Figure 2 – *Vertical exchange velocity computed for the three different configurations analysed. The velocity is normalized with respect to the horizontal velocity at the top of the boundary layer, i.e., U_∞. The number of trees 0, 7 and 14 stay for the configurations with no trees, with two rows of scattered trees and with two dense rows of trees respectively.*

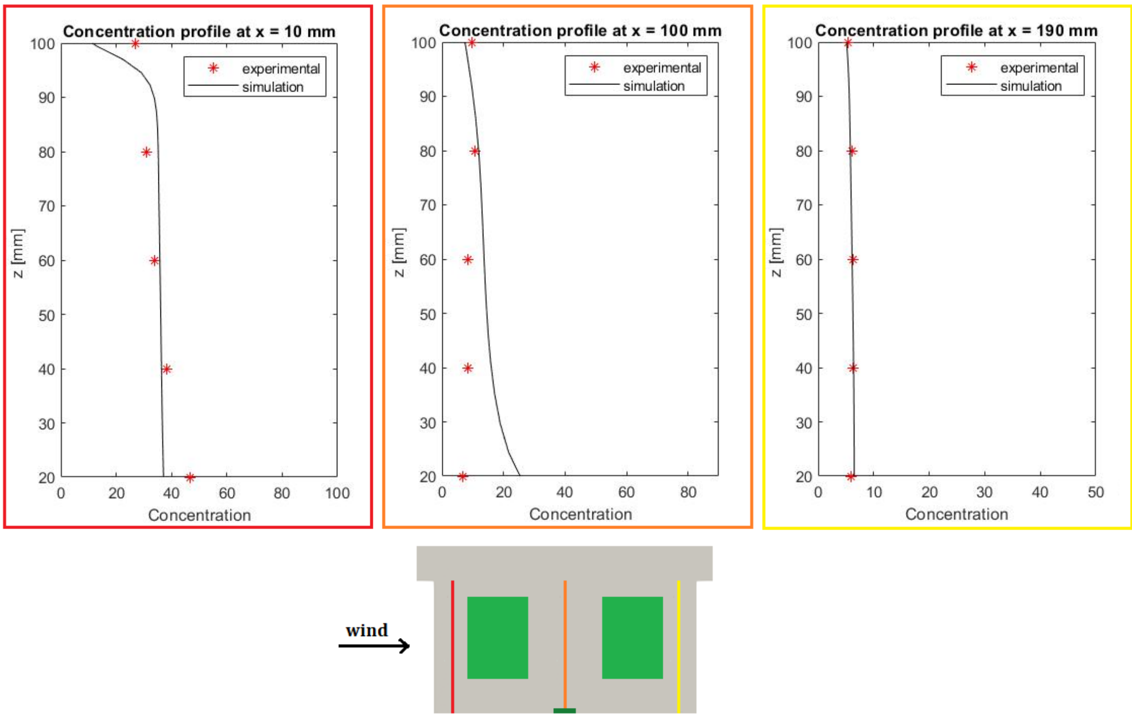

Figure 3 – *Profiles of concentration field obtained from numerical simulations compared to experiments. Red, orange, and yellow lines represent the different positions along x direction in the cavity where the profiles are compared. At the bottom part of the figure, sketch of the section of the cavity along the wind direction. The green boxes represent the trees.*

References

Cancelli, C., Boffadossi, M., and Salizzoni, P. (2006). *Fluidodinamica ambientale: Turbolenza e dispersione*. Otto Editore.

Fellini, S., Ridolfi, L., and Salizzoni, P. (2020). *Street canyon ventilation: Combined effect of cross-section geometry and wall heating*. Quarterly Journal of the Royal Meteorological Society, 146(730):2347–2367.

Salizzoni, P., Soulhac, L., and Mejean, P. (2009). *Street canyon ventilation and atmospheric turbulence*. Atmospheric Environment, 43(32):5056–5067.

Surface pressure, velocity and concentration correlations in an urban canopy layer

J. Wingrave, M. Placidi and D. M. Birch

Centre for Aerodynamics & Environmental Flow, University of Surrey, Guildford, Surrey, GU2 7XH

Abstract

Experimental measurements were collected using a highly instrumented cube model (of height h = 150 mm) within a canonical cube array to represent an urban canopy layer within the EnFlo environmental flow wind tunnel at the University of Surrey. Correlations between instantaneous surface pressure, velocity and concentration were used to examine the mechanisms of passive scalar transport within the canopy sublayer ($z < 5h$).

The instrumented cube featured 500 pressure tappings, simultaneously sampled using ultra-low range pressure sensors that had been dynamically calibrated *in situ* (by means of a novel Fourier-reconstruction technique) and high-speed wall-embedded pressure sensors. Velocity field measurements collected using a 2D laser-Doppler anemometry system and tracer gas concentrations measured with a high-bandwidth fast-flame ionization detector may then be spatially and temporally correlated to the pressure fields around the cube, providing some insight into the relative importance of the advection, pressure and diffusion terms in the transport equation. Sensitivity to source location and type will also be examined.

1 Introduction

Urban air quality is an area of increasing global concern, as populations and population densities increase. Globally, air pollution has now overtaken poor sanitation as the leading environmental cause of premature death (Kelly & Fussell 2015), and prolonged exposure to PM2.5 from emissions has been found to directly reduce life expectancy and increase the incidence of required medical interventions (Pope *et al*. 2009; Seaton *et al*. 2009). The understanding and modelling of transport phenomena within the complex, buoyant, three-dimensional and turbulent urban canopy layer has, therefore, received a lot of recent attention.

Wind tunnel measurements remain a very valuable tool in modelling the complexity of passive scalar transport within the urban canopy layer; they provide a flexibility and controllability of the parametric space unavailable from field studies, and - for more complex cases or those with large variations in scales - can be faster and less resource-intensive than computational simulations. However, there remain a number of serious challenges in the experimental characterisation of dispersion.

First, to achieve reasonable approximations of both the Reynolds number and Prandtl number, experiments typically must be carried out at very low dimensional velocities. Since high-resolution surface pressures are required to obtain critical turbulence scaling parameters (and are likewise often used in the flow to infer velocities), a dense array of pressure transducers with extremely high gain are required. Second, spatially-resolved measurements of concentration fields are also required- and all measurements need to be collected at sufficient bandwidth to at least resolve the dominant scales within the roughness sublayer. The technologies to address these two critical measurement requirements exist, but can be too expensive for large arrays (needed for spatial correlations) to be tractable.

A technique has therefore been developed to enable the simultaneous dynamic calibration of 512 low-cost, ultrasensitive pressure sensors enabling experimental time-domain surface pressure measurement over a generic cube-shaped urban roughness element with a spatial resolution of 10×10 measurement points on each exposed face- something which, to our knowledge, has not yet been demonstrated. With this capability, it then becomes possible to explore correlations between surface pressure and concentration, in both time and space.

2 Methodology

Experiments were carried out using the NERC Smart Cube facility- a 150 mm cube fitted with 100 pressure taps logarithmically spaced on each face. Pressure taps were connected to a 512-channel Surrey Sensors Ltd. DPS14-160P pressure scanner array (having a full-scale range of 160 Pa and a sensor bandwidth of 1 kHz), by means of lengths of 1 mm ID silicone hoses nominally 1.5 m long. The Smart Cube is also fitted with 20 embedded analogue pressure sensors having a full-scale range of 6.9 kPa and a bandwidth of 150 Hz. Measurements were collected in the EnFlo Stratified Atmospheric Wind Tunnel at the University of Surrey, a UK national Atmospheric Measurement and Observation Facility, at $Re \sim 1.7 \times 10^4$ based on cube side length (resulting in a maximum available total pressure of approximately 2.5 Pa). The facility is also equipped with 2D and 3D laser-Doppler anemometry (LDA) hardware for pointwise velocity measurement, and fast-flame ionization detectors (FFID) for pointwise concentration measurement (with a bandwidth of 200 Hz).

2.1 Dynamic calibration

Since one of the aims of this project is to obtain correlations between surface pressures and concentrations, the effect of the lengths of tubing on the time-domain pressure measurements from the cube needed to be characterised and compensated for. For this, a direct, *in situ* Fourier-reconstruction technique was used.

Once the model was installed in the floor of the wind tunnel, a sealed calibration enclosure was placed around it (see Figure 1). One side of the enclosure was fitted with a speaker cone, so that the actuation of the cone would change the volume of the enclosure, and thereby the pressure inside. The enclosure was also equipped with a direct-reading pressure sensor with a bandwidth of less than 1 kHz. The speaker provided sinusoidal pressure oscillations of approximately 10 Pa in amplitude, at frequencies from 2 Hz (DC) to 150 Hz to include the bandwidths of interest. Each pressure channel was compared to the reference pressure in Fourier space, and a unique frequency-dependent gain and phase shift obtained.

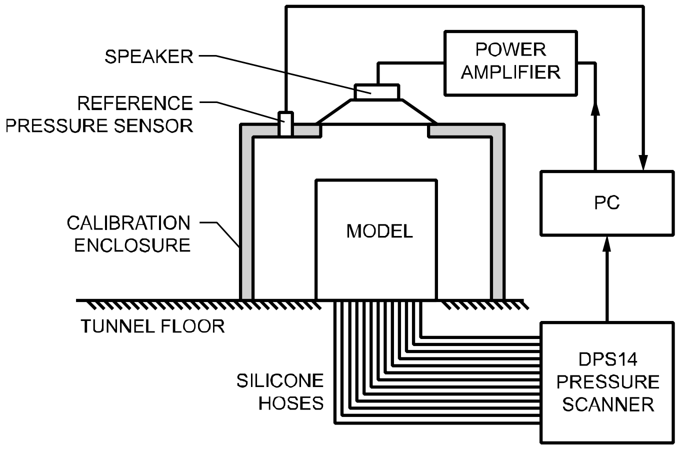

Figure 1: Calibration setup

During measurement, signals were converted to the Fourier domain, the gain and phase shift were applied, and the signals were then converted back to the time domain. Surprisingly, despite the uniformity of the tubing and the care taken in ensuring identical lengths of tubing, variabilities in gain of over 60% were observed. Figure 2 shows the variability in signals before and after dynamic calibration. Calibration was also validated using random white-noise signals to ensure that there were no significant nonlinearities.

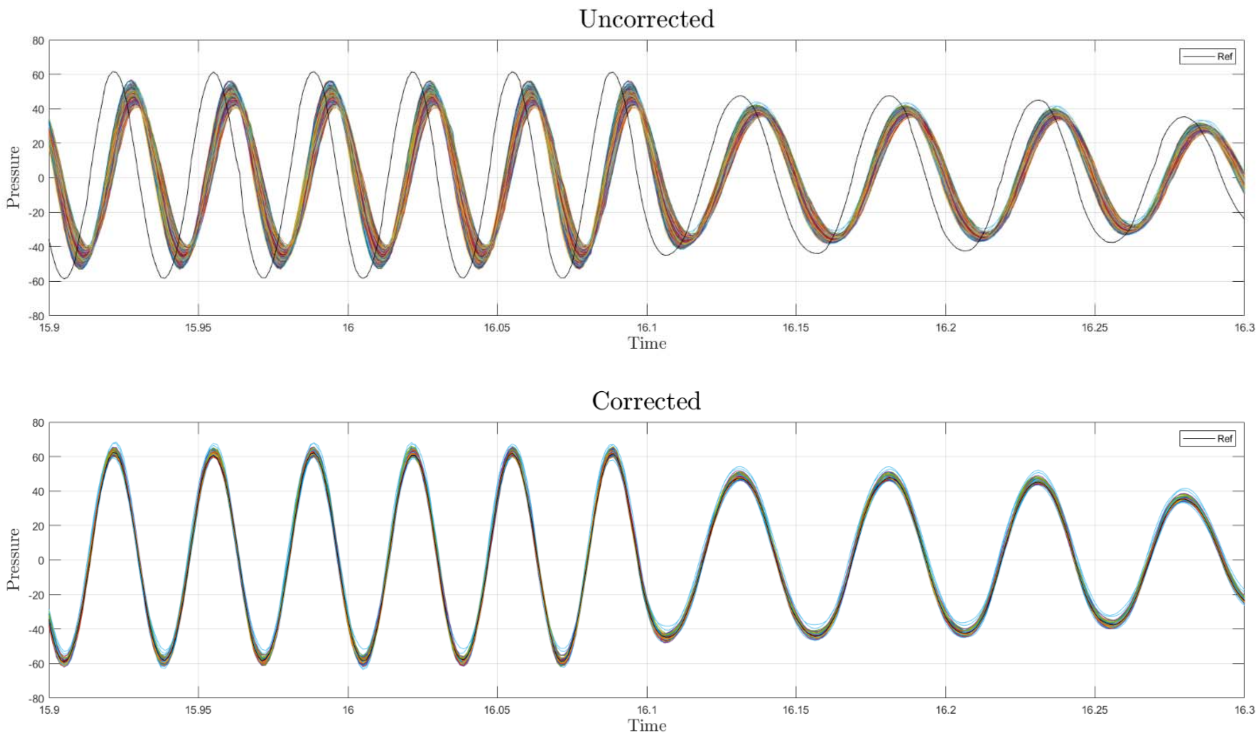

Figure 2: Demonstration of dynamic calibration of 500 channels. Top, uncalibrated arbitrary signals; bottom, same signals after calibration. Solid black line is high-bandwidth dynamic reference signal.

2.2 Validation

Mean surface pressures from the single cube model were obtained in different facilities at free-stream speeds of 3 m/s and 10 m/s (corresponding to Re $\sim 2.6 \times 10^4$ and 8.8×10^4, respectively), and compared to the well-accepted results of Castro & Robins (1997) and the field data of Richards *et al.* (2001) from the Silsoe site. Figure 3 compares pressures along vertical cross sections over the cube at incidences of 0° and 45°, and shows reasonably good agreement, noting that the upstream boundary layer conditions were not necessarily well-matched.

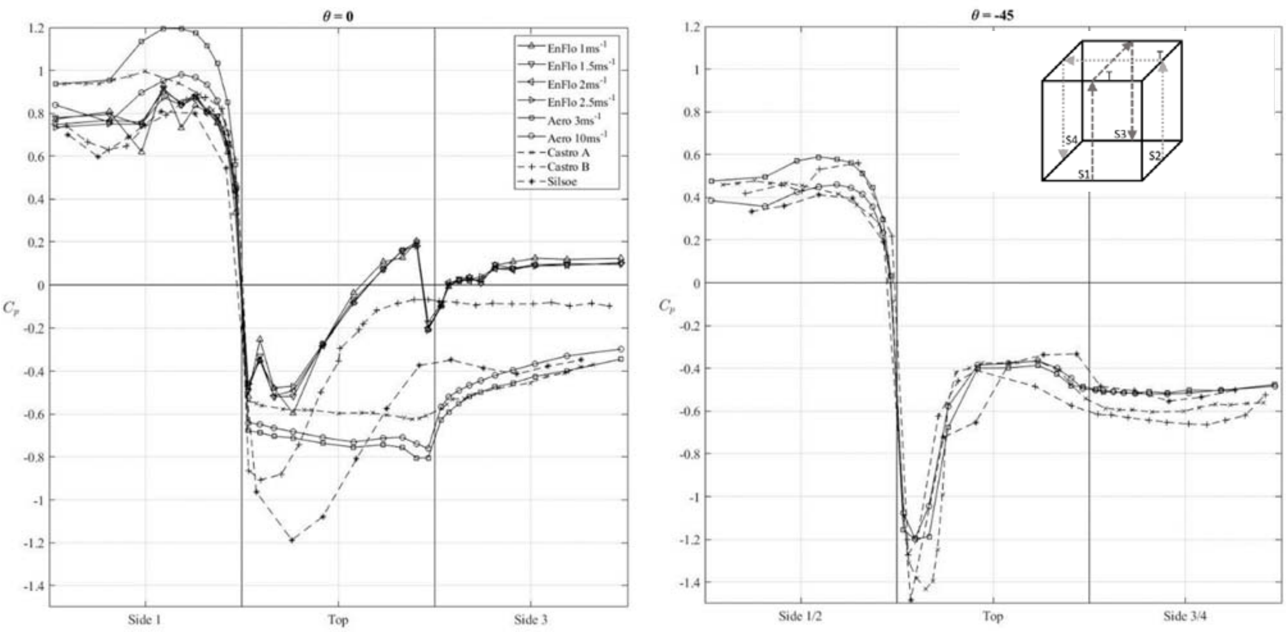

Figure 3: Comparison of mean pressure profiles along cube face centrelines at Re ~ 2.6×10^4 and 8.8×10^4 against data of Castro & Robins (1977) and the Silsoe data of Richards *et al.* (2001), at incidences of 0° (left) and 45° (right).

3. Results

Figure 4 shows a map of the mean pressure coefficients C_P over the surface of the cube at an incidence of 0° and Re $\sim 1.7 \times 10^4$, taking advantage of the high spatial resolution afforded by the model. Results are consistent with expectation, showing a maximum $C_P \sim 1$ on the front face above the boundary layer, and $C_P \sim -0.6$ in the separation region around the forward corners.

The value of the spatially- and temporally-resolved measurements is demonstrated by Figure 5, which shows a map of the mean-square of pressure coefficient fluctuation over the surface. Areas of high $\overline{C_P'^2}$ are apparent on the left side, suggesting that despite the symmetry of the mean pressures, the cube was likely to have been slightly out of alignment (yielding an adverse pressure gradient over that surface), with higher values in the lower-speed flow nearer to the floor. A horse-shoe of high $\overline{C_P'^2}$ is also apparent on the top surface, corresponding to the expected location of flow reattachment, which would be unsteady (and, therefore,

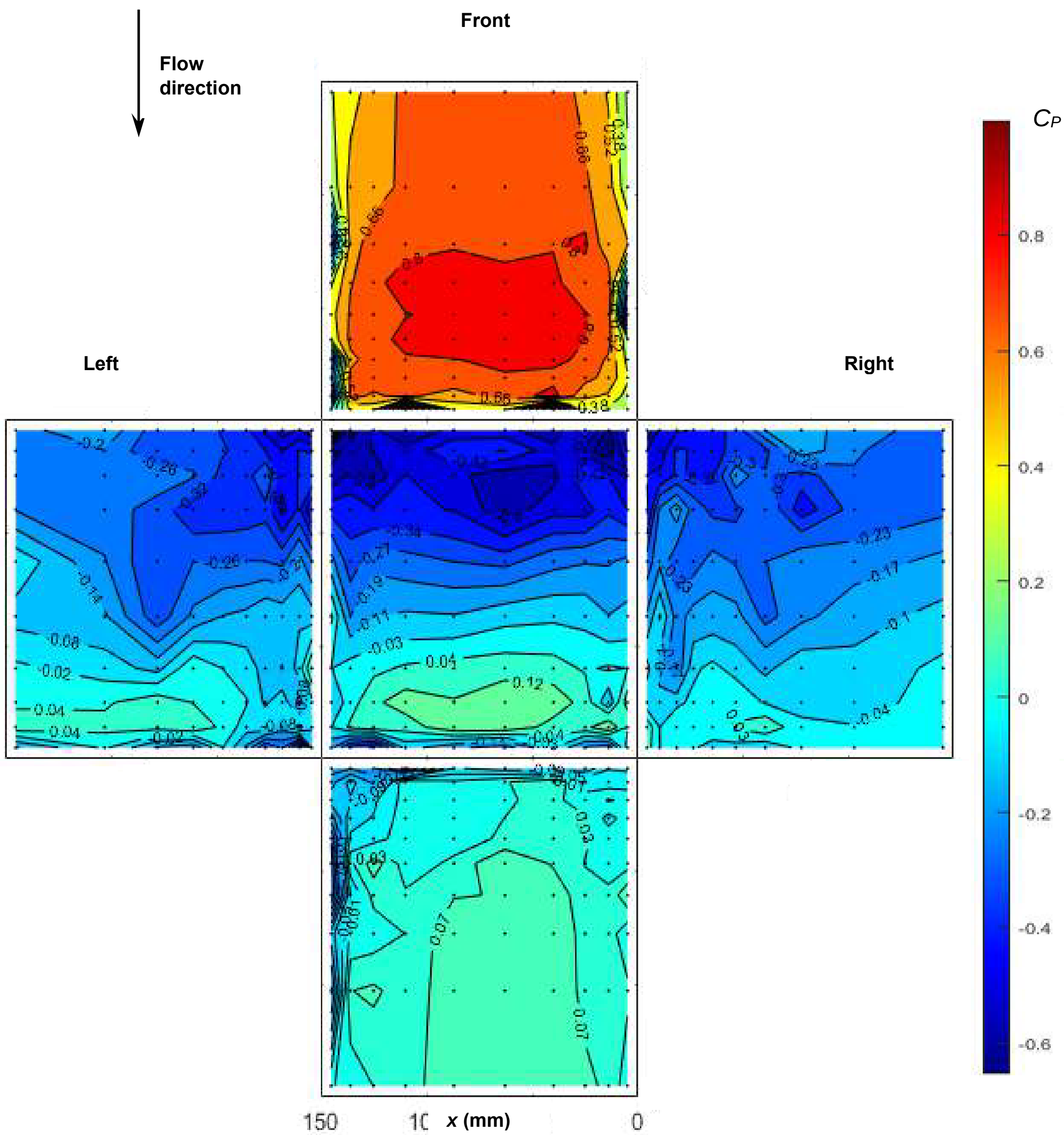

Figure 4: Contours of C_P over a development of the cube surfaces. Dots denote locations of pressure taps.

contributing to high variations). Some isolated spots of high $\overline{C_P'^2}$ are also evident on the front and rear faces of the cube, but these are likely the result of experimental error (leaks in the model) and are under investigation.

4. Conclusions and further work

Despite the extremely challenging parametric space, the Smart Cube is returning validated surface pressure data resolved in both space and time. A dynamic calibration process based on Fourier-reconstruction has compensated for variations in the second-order response of the tubing, which has been found to be significant despite the care taken in minimizing variations, and may be due to wide manufacturing tolerances on the diameter of the tubes themselves.

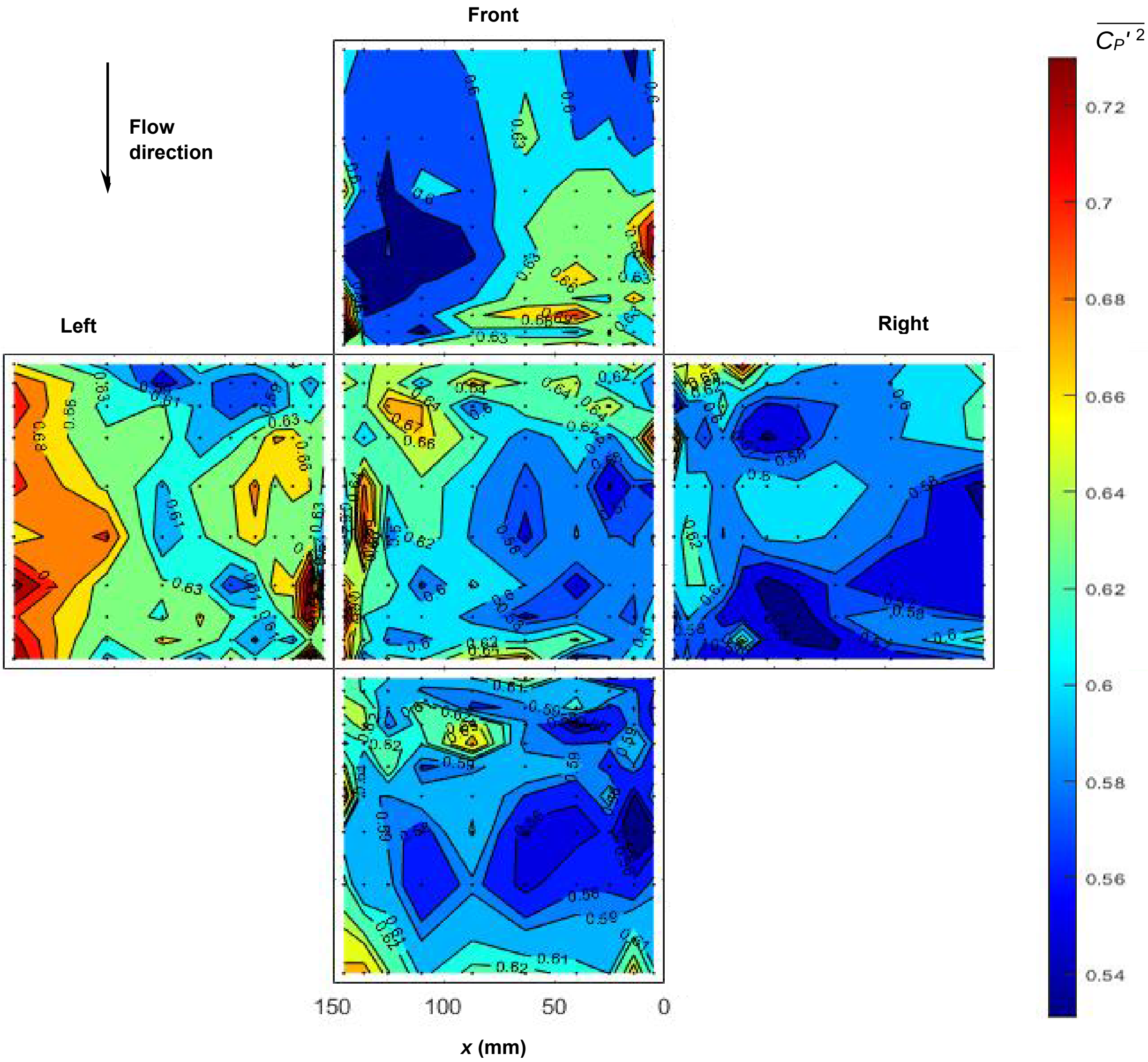

Figure 5: Contours of standard deviation over the cube surface.

Simultaneous, time-domain measurements of surface pressure together with velocity and concentration within the flow around the cube in an array are currently underway, and further progress will be reported.

Acknowledgements

This project was supported by the UK Natural Environment Research Council through grant NE/T009101/1 and the SCENARIO Doctoral Training Centre.

References

Castro, I. P. and Robins, A. G. (1977) "The flow around a surface-mounted cube in uniform and turbulent streams". J. Fluid Mech. 79, 307-335.

Kelly, F. J. and Fussell, J. C. (2015) "Air pollution and public health: emerging hazards and improved understanding of risk". Environ. Geochem. & Health 37.4, 631-649.

Pope, C. Arden, M. E., and Dockery, D. W. (2009) "Fine-Particulate Air Pollution and Life Expectancy in the United States". New England J. of Med. 360.4, 376-386

Richards, P. J., Hoxey, R. P. and Short, L. J. (2001) “Wind pressures on a 6m cube”. J. Wind Eng. & Ind. Aero. 89, 1553–1564.

Seaton, A., MacNee, W., Donaldson, K., and Godden, D. (1995) "Particulate air pollution and acute human health". Lancet 345, 176-178.

Roughness Sublayer effect on the law of the wall modeled by a "co-spectral link"

Y. Bohbot-Raviv[1,2], V. Babin[2] and G. G. Katul[1]

[1]Duke University, Department of Civil and Environmental Engineering, Durham, North Carolina 27708, USA
[2]Israel Institute for Biological Research, Department of Applied Mathematics, Ness Ziona, 9410001, Israel

Abstract

Fully developed turbulent flows near walls, regardless of their roughness, are commonly studied based on the law of the wall originally proposed by Prandtl and von Kármán in the early part of the 20th century. The derivation of the law of the wall has traditionally been based on theoretical and scaling arguments, under which a balance between dissipation and production (negligible advection terms) of turbulent kinetic energy and a nearly constant shear stress with distance from the wall are assumed in a thin layer of fluid, accommodating about 10% of the boundary layer (i.e., separation of scales). One of the hallmarks of this theory is the von Kármán constant (=0.4) valid across many wall-roughness and boundary layer flow configurations. In many situations, however, the separation of scales required to observe a log-layer is hardly realizable, especially in tall and fully rough canopy flows as in submerged aquatic vegetation and urban centres under certain atmospheric conditions. In recent years, several spectral- and co-spectral -based theories have revealed a "link" between the law of the wall and the energy spectrum of turbulent eddies. This link is exploited here to derive roughness sublayer adjustments to the law of the wall in canopy boundary layers. A simplified co-spectral model and flow data collected from wind tunnel experiments above a rough canopy are used to examine the effect of finite Reynolds number and intermittency on the von Kármán constant, from which the scales dominating the law of the wall in the roughness sublayer are proposed.

Effect of non-neutral stratification on urban flow and dispersion

M. Carpentieri[1], D. Marucci[1], P. Hayden[1]

[1]University of Surrey, EnFlo laboratory, School of Mechanical Engineering Sciences, GU2 7XH Guildford, UK

1 Introduction

Understanding flow and dispersion in urban areas is becoming increasingly important due to rapid urbanisation and related health and economic issues. One aspect of urban flow and dispersion that is still not very well studied is atmospheric stratification, despite the fact that cities very often present either stable or convective conditions (see Wood et al., 2010, for example). Wind tunnel simulations that include the effects of approaching flow stratification are rare. Only a few studies can be listed, since only few facilities worldwide are capable of simulating non-neutral flows and the development of the correct experimental methodology is very time-consuming (Marucci at al., 2018). In this work we investigate this subject by using an array of rectangular buildings rotated by 45 degrees and multiple stable (SBL) and convective boundary layer (CBL) strengths.

2 Methodology

The experiments were carried out in the EnFlo meteorological wind tunnel at the University of Surrey. Two different sets of Irwin's spires and roughness elements on the tunnel floor were employed to artificially thicken the boundary layer in the stable and convective cases. When stratified boundary layers were simulated, a vertical temperature profile was imposed at the inlet section. In the SBL cases a negative surface heat flux was generated with floor-cooling panels by means of recirculating water. In the CBL cases the floor was heated by means of electrical mats added on top of additional insulating panels. The details about the development and optimisation of the experimental techniques were reported by Marucci et al. (2018). The urban model was constituted by a regular array of more than 350 rectangular ($H \times 2H \times H$) blocks with equal height and spacing (H = 70 mm). Such configuration represents a significant departure from the more studied cube array, introducing a geometrical asymmetry which makes it more typical of street canyons in real urban regions (Castro et al., 2017), but at the same time remaining an organised and regular geometry. All the experiments reported here were performed using a wind direction of 45 degrees. Temperatures and two components of velocity were measured simultaneously using, respectively, a fast-response cold-wire probe (CW) and a laser Doppler anemometer (LDA). Tracer concentrations, as well as mass fluxes, were measured using a fast flame ionisation detector (FFID).

3 Results

The level of stability of the approaching flow is here labelled with the bulk Richardson number, estimated as $Ri_{app} = g(\bar{\theta}_\delta - \theta_0)\delta/\left(\theta_0 \overline{U}_\delta^2\right)$, where g is the gravity acceleration, δ the boundary layer depth, θ_0 is the temperature at z = 2 mm (approximately equivalent to the aerodynamic roughness length). Six stratification levels were considered, corresponding to Ri_{app} 0.29, 0.21, 0.14, 0, -0.5 and -1.5. The reference neutral case was repeated with the SBL and CBL setup. For all the cases, a horizontal scan of the plume was performed at two heights inside and above the canopy (z/H = 0.5 and 1.5, respectively), as well as vertical scans along the centreline of the plume.

	CBL			SBL			
Ri_δ^{app}	-1.5	-0.5	0	0	0.14	0.21	0.29
U_{ref} (m/s)	1.0	1.25	1.25	1.25	1.25	1.25	1.15
u_*/U_{ref}	0.118	0.105	0.081	0.078	0.063	0.061	0.059
z_0 (mm)	6.2	6.3	4.0	3.4	2.5	2.6	2.9
d (mm)	21	23	51	52	53	54	55
Ri_H	-0.19	-0.15	0	0	0.10	0.19	0.28

Table 1 – Urban array cases parameters at wind direction 45 degrees.

Table 1 summarises some important parameters. The friction velocity (u_*), aerodynamic roughness length (z_0) and displacement height (d) are measured, as described in Marucci *et al.* (2018), from a fitting of the roughness sub- layer region over the array, found here to happen in the range $z/H = 2 \div 4$. All of these quantities show a dependency from the stratification. Finally also a Richardson number Ri_H measured over the array is shown, in which the reference height and velocity are the building height and the averaged velocity measured at this height, while the temperature difference is the difference between the averaged values measured at roof height and a reference sampled at 10 mm in the canopy.

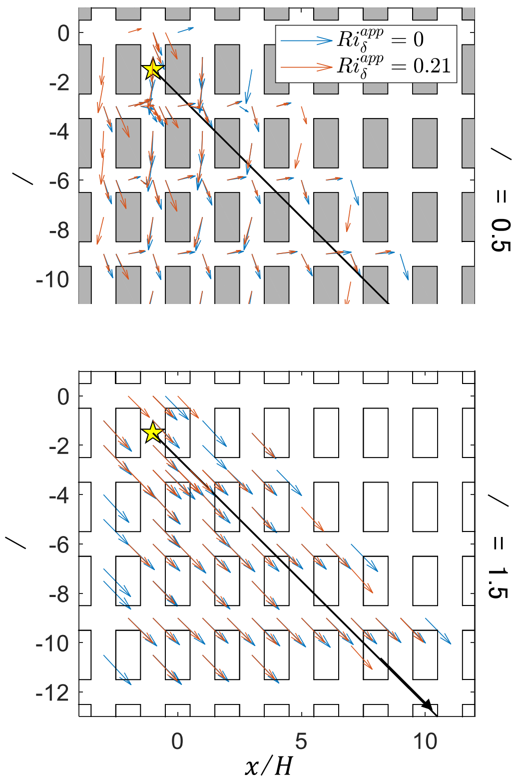

Figure 1 – Planar view of mean horizontal velocity vectors inside and above the canopy for SBL and NBL and wind 45 degrees. Black arrow is free-stream wind direction while the yellow star is the location of the pollutant source.

Figure 1 shows the vectors of horizontal velocity for a neutral and stable case. No effects on the channelling inside the streets are experienced by the flow, while the module of the velocity appears generally reduced by stratification. At a height of 1.5H the flow is already aligned with the free stream, both in the NBL and in SBL case. In Figure 2 the horizontal contour plots of the non-dimensional mean concentration inside the canopy for SBL, NBL and CBL are presented. At *z/H* = 0.5 inside the canopy the axis of the plume is not affected by the stable stratification (being deviated of about 15 degrees for both SBL and NBL). Differently, in the CBL such angle is increased to 18 degrees). Above the canopy at *z/H* = 1.5 both the non-neutral stratification cases show an increment of about 2 degrees in the angle respect to the neutral case. The concentrations appear increased by the application of the stable stratification and reduced by the convective one, effects which become more and more evident farther from the source.

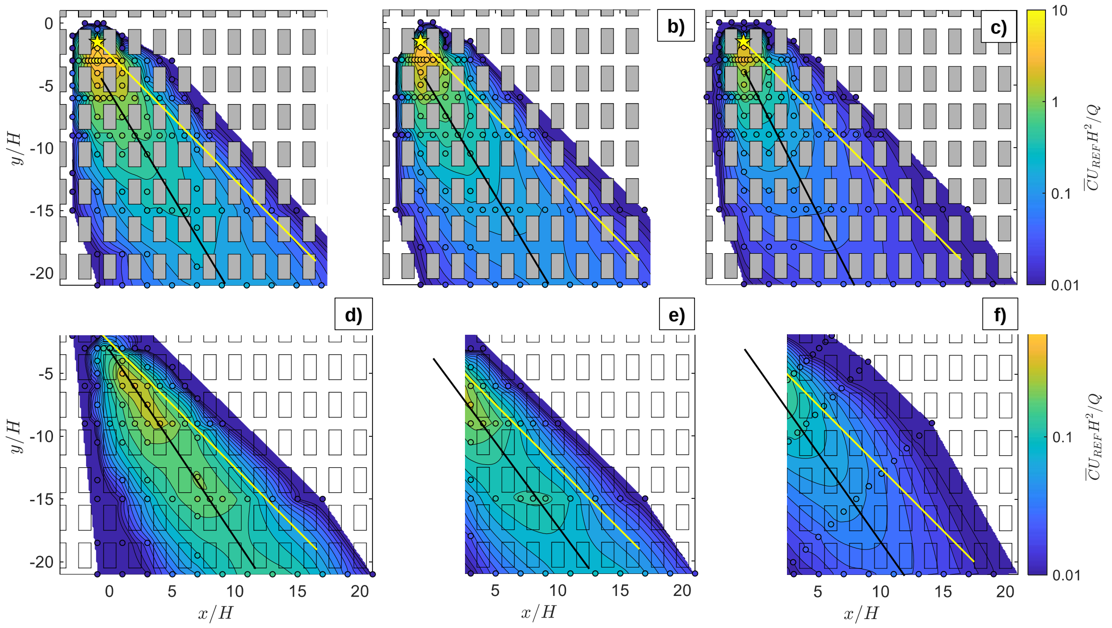

Figure 2 - Contour plots of non-dimensional mean concentration for different level of stability at z/H = 0.5 (a-c) and z/H = 1.5 (d-f). $Ri_\delta^{app} = 0.21$ (a, d), $Ri_\delta^{app} = 0$ (b, c), $Ri_\delta^{app} = -1.5$ (c, f).Yellow line is free-stream wind direction, yellow star is the ground source location, black line is the estimated plume axis. For brevity only the reference neutral case measured with the SBL setup is shown in (b,e). Q is the pollutant tracer flow rate from the source.

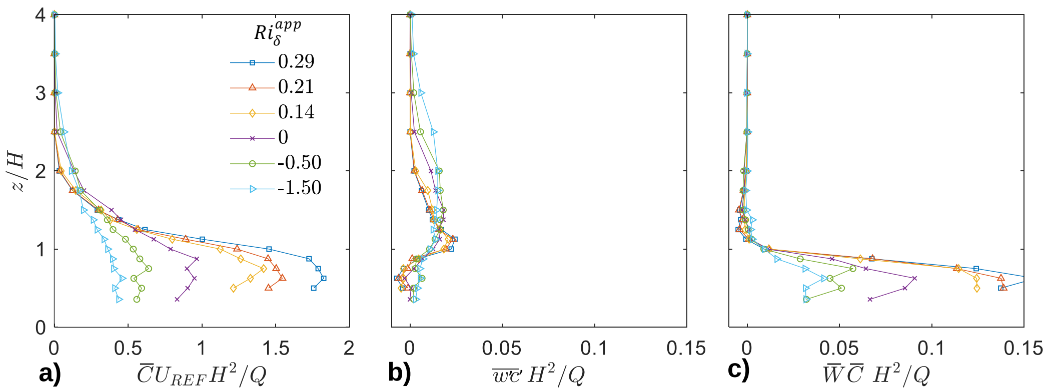

Figure 3 - Vertical profiles of non-dimensional mean concentration (a), turbulent (b) and mean (c) vertical pollutant fluxes for different level of stability at the centre of an intersection (x/H = 1, y/H = −6). For brevity only the reference neutral case measured with the CBL setup is shown.

Figure 3 shows vertical profiles of mean concentration at the centre of an intersection 6*H* far from the source. The concentrations within the canopy are doubled for the strongest SBL, compared to the reference NBL, and one half for the CBL. The plume height is affected as well, with a reduction of 20% for the SBL (independently from the intensity) and an increment of the same amount for the CBL. Such profiles were fitted with a Gaussian curve to find the σ_z coefficient representative of the plume height. The same was done for the lateral profiles perpendicular to the plume axis (extrapolated from the contour graphs of Figure 2) to find σ_h, representative of the plume width. Very small stratification effects were found on σ_h, compared to the effects experienced by σ_z, which was up to 40% lower in the most stable case and up to 150% larger in the most unstable, compared to the reference neutral. This is in agreement with what observed by Briggs (1973) in field experiments over urban roughness. On the contrary, Kanda & Yamao (2016) found an opposite behaviour, with the plume height almost unaffected and the width sensibly reduced by the application of stable stratification. They were not able to explain such a peculiar behaviour.

In Figure 3 also the vertical fluxes at the centre of an intersection are shown. Inside the canopy the fluxes are strongly dependent on the location, hence a generalization is difficult. Nevertheless, it can be noted that at least at the centre of the intersection the turbulent component is negligible, while at the roof level it becomes roughly equivalent to the mean flux for all the stratification conditions. Above the canopy the turbulent flux is then predominant. The latter appears to scale with the vertical mean concentration gradient in all the stability cases investigated, as already found for the NBL by Carpentieri *et al.* (2012).

4 Conclusions

An extensive wind tunnel experimental campaign was conducted in order to investigate the effect of thermal stratification on flow and dispersion in an urban array. From the regular array of rectangular building case with wind direction 45◦ it can be concluded that in both SBLs and CBLs the plume width and axis are only slightly modified by the applied stratification. Differently, the plume height as well as the mean concentration values are clearly affected in a specular way. In SBL the vertical displacement is reduced, and the pollutant is trapped close to the canopy more than doubling the concentration level and reducing the plume height. In CBL, instead, the opposite behaviour was found, with lower concentration (up to three times respect to NBL) and taller plumes. A deeper analysis and discussion of the results can be found in Marucci & Carpentieri (2020a and2020b). The produced dataset represents valuable validation cases for models and CFD simulations.

References

Briggs, Gary A. 1973 Diffusion Estimation for Small Emissions. *Tech. Rep.*. Atmospheric Turbulence and Diffusion Laboratory. NOAA/ATDL ATDL-106.

Carpentieri, Matteo, Hayden, Paul & Robins, Alan G. 2012 Wind tunnel measurements of pollutant turbulent fluxes in urban intersections. *Atmospheric Environment* 46, 669–674.

Kanda, Isao & Yamao, Yukio 2016 Passive scalar diffusion in and above urban-like roughness under weakly stable and unstable thermal stratification conditions. *Journal of Wind Engineering and Industrial Aerodynamics* 148, 18– 33.

Marucci, D., Carpentieri, M. & Hayden, P. 2018 On the simulation of thick non-neutral boundary layers for urban studies in a wind tunnel. *International Journal of Heat and Fluid Flow* 72, 37–51.

Marucci, D. & Carpentieri. M. (2020a). Stable and convective boundary-layer flows in an urban array. *Journal of Wind Engineering and Industrial Aerodynamics* 200, 104140.

Marucci, D. & Carpentieri. M. (2020b). Dispersion in an array of buildings in stable and convective atmospheric conditions. *Atmospheric Environment* 222, 117100.

Wood, C. R., Lacser, A., Barlow, J. F., Padhra, A., Belcher, S. E., Nemitz, E., Helfter, C., Famulari, D. & Grimmond, C. S. B. (2010). Turbulent Flow at 190 m Height Above London During 2006-2008: A Climatology and the Applicability of Similarity Theory. *Boundary-Layer Meteorology* 137 (1), 77–96.

Experimental study of natural ventilation in realistic urban environments

M. Carpentieri[1], P. Hayden[1], P. Singh[1], L. Morina[1], M. Mian Muhammad[1]

[1]University of Surrey, EnFlo laboratory, School of Mechanical Engineering Sciences, GU2 7XH Guildford, UK

Abstract

Wind-tunnel measurements to study the effectiveness of natural ventilation for different window arrangements were performed. Decay of indoor pollutants, wind-driven alone and with the addition of buoyancy, was tested within a room placed in a. realistic urban configuration. Different cross-ventilation single-sided ventilation arrangements were investigated using tracer concentration measurements.

The results from this study displayed a clear influence of wind direction on the calculated decay constants. It was found that for the cross-ventilation cases and the single-sided 'front open' case, 45° and 90° provided the best ventilation, whereas, for the single-sided 'back open' case, the best ventilation was at 0°. In general, the 'back open' case was the least ventilated exhibiting the highest steady-state concentrations and lowest decay constants. The 'all windows open' case showed the lowest steady- state concentrations and best decay at each wind direction. The addition of buoyancy showed minimal change which was attributed to the position of the openings being at the same height. It was shown by the temperature stratification within the room that displacement was prevalent during these cases, while the wind-driven cases leaned towards mixing.

Operational dispersion model for emergency services

H. Chaloupecká[1]

[1]Institute of Thermomechanics, Czech Academy of Sciences, Dolejškova 1402/5, 18200, Praha 8, Czech Republic

Abstract

The paper introduces a model enabling to predict a situation after a gas leakage. The model predicts both, the situation after the long and short gas leakage. It is under development and currently two versions of the model exist.

Both versions of the model utilize a sub-model enabling to recalculate the concentrations predicted for the continuous source into those valid for the short-term leakages. This sub-model was developed using data from wind tunnel modeling and has two modes – for an urban area or for a rural region.

The difference in the versions is in the prediction of the concentrations valid for a continuous leakage. The first version utilizes a simple Gaussian model based on the Industrial Source Complex model (ISC2) developed by U.S. Environmental Protection Agency (EPA). The second version of the model uses a simple mass-consistent model to estimate all the inputs needed by a lagrangian model, which is then utilized to predict the dispersion of the concentration in the exposed area.

The paper introduces both versions of the model and shows their results compared to wind tunnel data. Standard validation procedures were used – e.g., fractions within a factor of two, fractional bias.

PHYSMOD 2022 – International Workshop on Physical Modeling of Flow and Dispersion Phenomena
Institute of Thermomechanics of the CAS, Prague, Czech Republic – August 29-31, 2022

Large-Eddy Simulation of the Atmospheric Boundary Layer Flows over Different Urban-Like Morphologies

Wai-Chi Cheng

Sun Yat-sen University, Atmospheric Sciences, 519082, Zhuhai, China

Abstract

In the study of urban flows, idealized urban morphologies are usually used to investigate the basic flow characteristics and to develop flow parameterizations in the urban canopy layer. However, how these urban-like morphologies affect the flow statistics in the atmospheric boundary layer flows above is currently less well understood. In this study, in order to understand these impacts, a set of large-scale large-eddy simulations are performed to simulate the fully-developed atmospheric boundary layer flows over a flat surface, two-dimensional street canyons, uniform and non-uniform heightened building block (aligned and staggered) arrays, and a realistic urban morphology in neutral thermal conditions. The overall flow and turbulence characteristics of the different cases will be first compared and the differences in the turbulence production patterns will be discussed. After that, the time-and horizontally-space-averaged profiles of the mean wind and turbulence statistics will be calculated to identify the similarities and differences in the different profiles among the various test cases. Lastly, based on the mean profiles of the Prandtl's mixing length, new insights will be provided on how to parametrize the turbulent shear stress in the roughness and inertial sublayers over the urban-like surfaces.

Introduction

The characterizations of flows in the roughness sublayer (RSL) and the inertial sublayers (ISL) of the atmospheric boundary layer over urban surfaces are important for weather forecasting and for air quality predictions. Due to the drag exerted by the individual buildings on the wind flows, the velocity distribution in the RSL is generally spatially heterogeneous and characterized by flow recirculations and building wakes. Over the years, a large number of studies have been conducted to understand the flow and scalar transport in the RSL over urban surfaces (see Barlow 2009). In particular, different urban canopy models (UCMs) have been proposed to predict the time-and horizontally space-averaged wind profiles within and above idealized urban canopies (Nazarian et al. 2020, Cheng and Porté-Agel 2021). Currently, more results for realistic urban canopies and a better understanding of the depth of RSL above urban surfaces are still needed.

Above the RSL in the ISL, the flow is homogeneous and, in neutral conditions, the time-averaged wind profile is expected to be described by the logarithmic profile as

$$\frac{\langle \overline{u}(z)\rangle}{u_*} = \frac{1}{\kappa} ln\left(\frac{z-d}{z_0}\right) \quad [1]$$

where $\langle \overline{u}\rangle$ is the time-and horizontally-space-averaged streamwise velocity component, u_* is the friction velocity, z is the height, d is the zero-plane displacement, z_0 and the aerodynamic roughness length, and κ is the von Karman constant. In the literature, different models have been proposed to predict the parametric dependence of z_0 and d over different urban morphologies (Kanda et al. 2013, Zhu et al. 2017). However, accurately identifying the ISL over urban surfaces remains challenging. The computational fluid dynamics method large-eddy simulation (LES), which can resolve the detailed spatial and temporal distributions of turbulent flows has been a popular and useful tool to study the urban ISL and RSL flow characteristics to complement experimental measurement data. However, to simulate a deep urban boundary layer with explicit-resolved buildings at the ground is still computing resource-demanding. This has caused difficulty in the investigations of the ISL dynamics as a deep boundary layer and a large computational domain are essential to accurately reproduce the ISL flow over urban surfaces. In this study, by performing large-scale LESs of urban boundary layer flows with explicitly-resolved building morphologies for different representative urban surfaces, the characteristics of the ISL and RSL over different urban surfaces are investigated.

LES setups

The open-source CFD code OpenFOAM is used to perform the LESs in this study. A total of seven LES cases of turbulent boundary layer flow over (1) a flat surface, (2) a 2D street canyon, (3) a uniform array of cubes, (4) a uniform staggered array of cubes, (5) a non-uniform height aligned array of building blocks, (6) a non-uniform height staggered array of building blocks, and (7) a realistic urban surface are considered (Figure 1). The sizes of the LES domains and the grid resolutions are shown in Table 1. Periodic boundary conditions are used in the horizontal directions with a uniform driving force prescribed in the x direction. A wall boundary condition based on a wall function for rough surfaces is used for all the ground and building surfaces. Symmetry boundary conditions are used at the top surface. The one k-equation subgrid-scale (SGS) model is used to parametrize the SGS stresses. Flow statistics are collected after the flows achieve the quasi-static state.

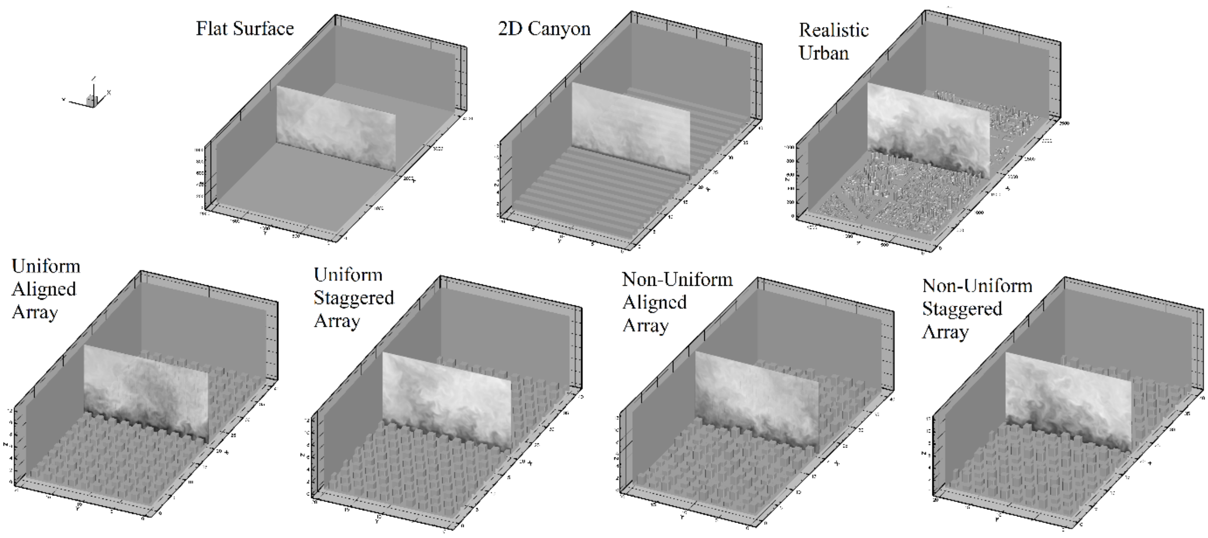

Figure 1. LES domains for the different cases.

The plan area fractions (Λ_p) of the different surfaces are provided in Figure 2. For 2D canyon, the typical setting of building width equal to street width is used, which corresponds to $\Lambda_p = 0.5$ within the canopy. For both uniform and non-uniform aligned and staggered arrays of building blocks, typical ground-level values of $\Lambda_p = 0.25$ are used. For the cases of non-uniform building heights, two different building heights are considered. For the realistic urban surface, the urban morphology is obtained using the building map data of Shenzhen, China. the value of Λ_p is found to be smaller than the other cases.

Table 1. LES domain sizes ($L_x \times L_y \times L_z$) and cell sizes ($\Delta x \times \Delta y \times \Delta z$) for the different cases.

Case	Geometry	$L_x \times L_y \times L_z$	$\Delta x \times \Delta y \times \Delta z$	Total cell numbers
1	Flat Surface	4000m×2000m×1000m	10m× 10m × 10m	8,140,701
2	2D Canyon	40h×20h×12h	$h/12 \times h/12 \times h/10$	13,496,241
3	Uniform Aligned Array	40h×20h×12h	$h/12 \times h/12 \times h/12$	16,518,145
4	Uniform Staggered Array	40h×20h×12h	$h/12 \times h/12 \times h/12$	16,516,825
5	Non-uniform Aligned Array	40h×20h×12h	$h/12 \times h/12 \times h/12$	16,533,633
6	Non-uniform Staggered Array	40h×20h×12h	$h/12 \times h/1h \times h/12$	16,532,401
7	Realistic Urban surface	3430m×1720m×1000m	6.6m× 6.6m × 8.3m	16,385,050

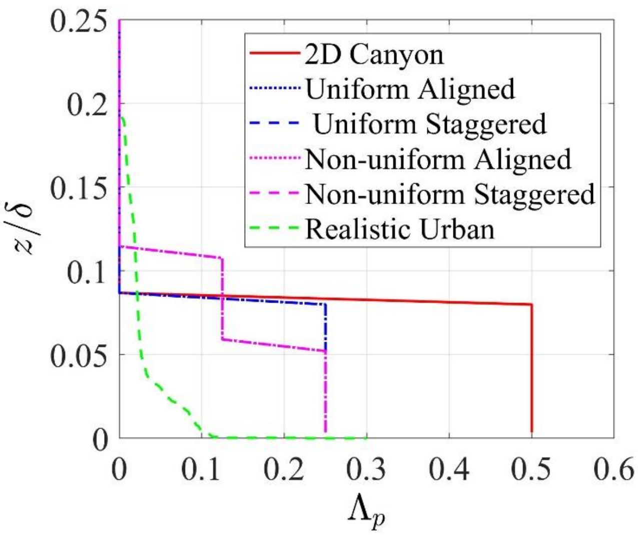

Figure 2. Vertical profiles of the plan area fractions (Λ_p) for the urban surfaces.

Results

Figure 3 shows the vertical contours of the mean streamwise velocity component ($\bar{u}$) at the selected plane for the different cases. Obvious differences in the magnitudes of $\bar{u}/u_*$ among different cases are found. In particular, a large value of $\bar{u}(z=\delta)/u_* \approx 25$ is found in the 2D canyon cases, which is even larger than that found in the flat surface case. This is followed by the uniform aligned array and realistic urban cases with $\bar{u}(z=\delta)/u_* \approx 16$. In comparison, for the uniform staggered array and the two non-uniform arrays cases, the values of $\bar{u}(z=\delta)/u_*$ in the free-stream region are about 10. These results indicate that the considered 2D canyon surface with $\Lambda_p = 0.5$ is relatively smooth and only exerts a small drag on the flow compared with the other considered urban morphologies. In comparison, non-uniform building height and staggered array arrangement of buildings are found to exert larger drags on the flows. For the realistic urban geometry, the relatively low drag exerted by the surface compared to the building block array is believed to be due to the lower building density in the realistic urban case (Figure 2).

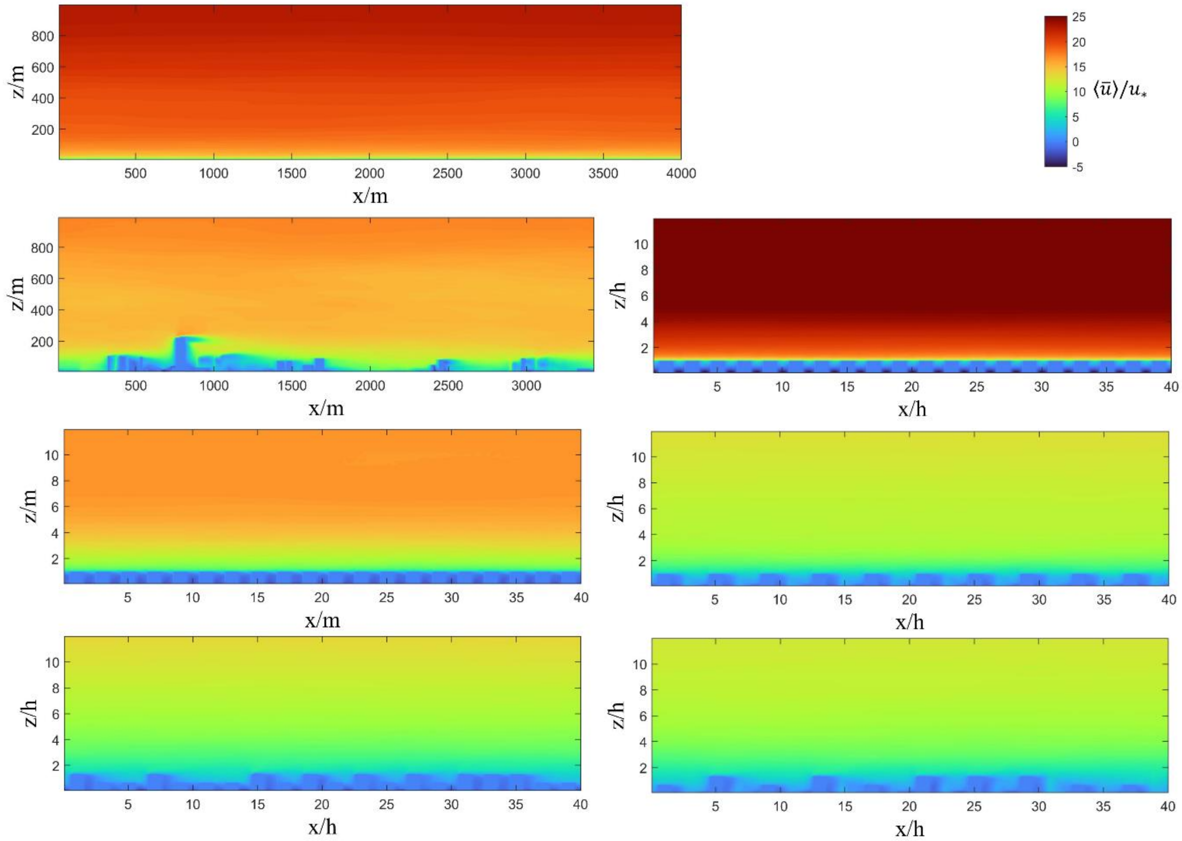

Figure 3. Vertical contours of normalized mean streamwsie velocity component $\bar{u}/u_*$ at the selected plane for the different cases.

The heterogeneous of $\bar{u}$ just above the ground or urban surface in the different cases is also shown in Figure 3. As expected, the highest heterogeneity of flow is found in the realistic urban surface cases due to the irregular building morphology. The non-uniform building array cases also show heterogeneity in $\bar{u}$ at the region just above buildings. In comparison, for the 2D canyon and the uniform aligned array cases, the heterogeneous of $\bar{u}$ is not obviously observed at the above-canopy region in the contour plots.

Figure 4 shows the vertical profiles of the time-and horizontally-averaged $\langle\bar{u}\rangle$ and turbulent shear stress $\langle\overline{u'w'}\rangle$ in the different cases. Consistent with the results in Figure 3. A large magnitude of $\langle\bar{u}\rangle$ is found in the boundary layer for the 2D canyon case, which is even larger than the reference case of a flat surface. For the realistic urban surface, higher wind speed is found within the urban canopy ($z/\delta <$ ~ 0.1) than in the cases of building block arrays. This is due to the smaller Λ_p in the realistic urban geometry case. For the $\langle\overline{u'w'}\rangle$ profiles, it is found that a peak magnitude of $\langle\overline{u'w'}\rangle$ is found at the building roof level for the street canyon and the two uniform building array cases. For the non-uniform building cases, $\langle\overline{u'w'}\rangle$ is found to be peaked at the roof level of the taller buildings. For the realistic urban geometry cases, $\langle\overline{u'w'}\rangle$ is found to be peaked at about $z/\delta \sim 0.1$. More discussions on the flow characteristics in the ISL and RSL flows will be given in the presentation.

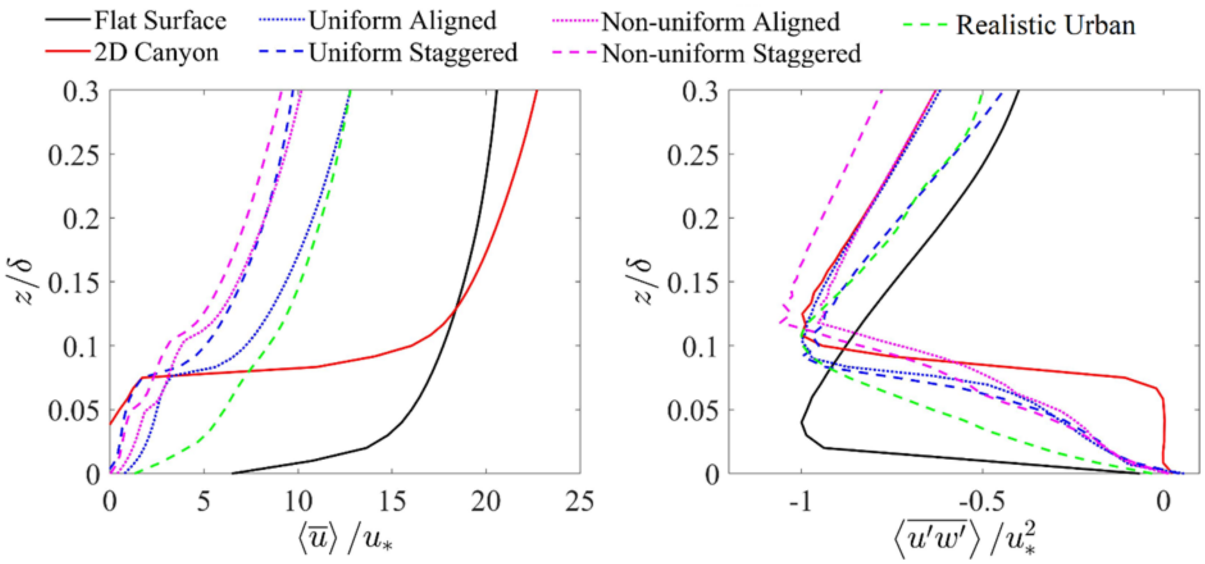

Figure 4. Vertical profiles of the normalized time-and horizontally-averaged streamwise velocity component $\langle\bar{u}\rangle/u_*$ and turbulent shear stress $\langle\overline{u'w'}\rangle/u_*^2$ for the different cases.

References

Barlow J, Coceal O (2009) A review of urban roughness sublayer turbulence. Technical Report, Met Office, Department of Meteorology, Reading University.

Cheng WC, Porté-Agel F (2021) A simple mixing-length model for urban canopy flows. Boundary-Layer Meteorol 181:1-9.

Y Yang, WC Cheng (2021), Impacts of realistic urban geometry heterogeneity on the turbulent transport in urban roughness sublayer using large eddy simulation. Asia Oceania Geosciences Society (AOGS) 18th Annual Meeting, 01-08 August 2021, Singapore.

Kanda M, Inagaki A, Miyamoto T, Gryschka M, Raasch S (2013) A new aerodynamic parametrization for real urban surfaces. Boundary-Layer Meteorol 148:357-377.

Nazarian N, Krayenho ES, Martilli A (2020) A one-dimensional model of turbulent flow through “urban” canopies (MLUCM v2.0: updates based on large-eddy simulation). Geosci Model Dev 13:937-953.

Zhu X, Lungo GV, Leonardi S, Anderson W (2017) Parametric study of urban-like topographic statistical moments relevant to a priori modelling of bulk aerodynamic parameters. Boundary-Layer Meteorol 162:231-253.

Modelling Airflow over Pitched-Roof Buildings

M. Coburn [1], Steven Herring [2], Z-T. Xie [1]

[1]University of Southampton, Engineering, Aerodynamics and Flight Mechanics, Burgess Road, SO16 7QF, UK
[2]AWE, Reading, RG7 4PR

Abstract

Arrays of buildings with pitched roofs are common in urban and suburban areas of European cities. Large eddy simulations were performed to predict the flows over flat and pitched-roof cuboids to gain a greater understanding of the impact of pitched roofs on urban boundary layers. The simulation methodology was validated for an array of flat roof cuboids. Comparisons of turbulent and surface pressure statistics, and dispersive stresses, were carried out between flat and pitched roof cuboid arrays at two different packing densities, 17% and 33%. It is concluded that the interactions between pitched-roof buildings and their effect on the urban boundary layer are considerably different to those of flat-roof buildings. The pitched roofs at packing density 33% lead to significant changes in the mean flow field, the Reynolds stresses, and the aerodynamic drag. Further work investigated the effects of turbulence level and atmospheric thermal stratification in the approaching flow. Importantly, it was shown that in comparison to a flat-roof array, the pitched-roof one at a packing density 33% evidently increases the friction velocity and greatly reduces the effects of stable stratification condition and inflow turbulence level. The pitched roof greatly affects the Inetnal boundary layer growth and it's eventual height.

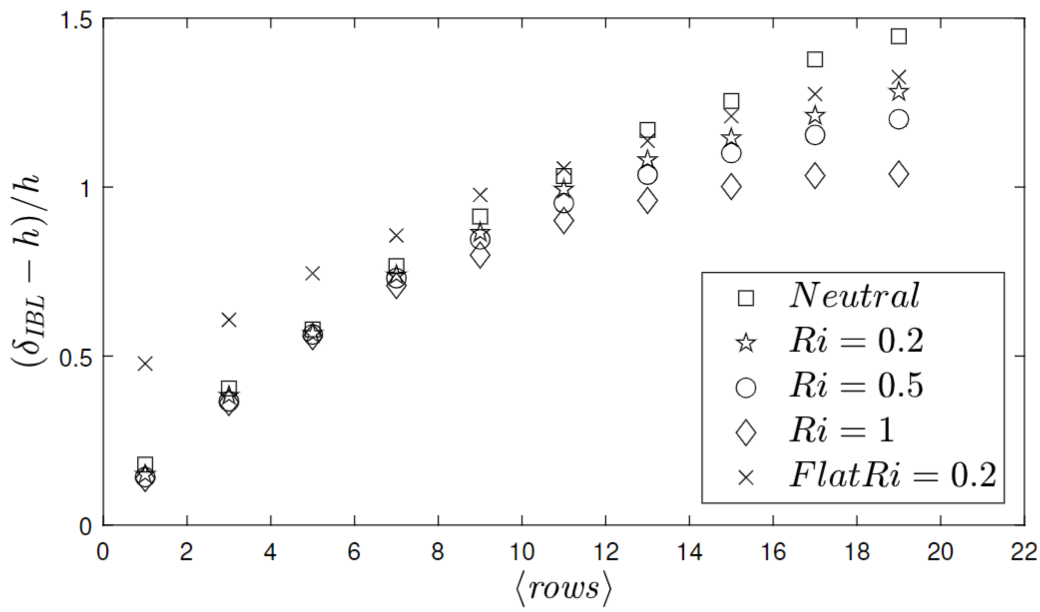

Internal boundary layer depths along the inflow domain for the simplified arrays, for neutral (pitched roof) and Stratified (flat and pitched roofs) inflow conditions, normalised by the local building's streamwise extent. Data is spatially averaged across each row, beginning at the front of the first building and averaged across the span and 2H in the streamwise direction.

Influence of vegetation on urban canyon ventilation. Part II: velocity field and turbulent mass fluxes

A. Del Ponte[1], S. Fellini[2], M. Barulli[3], L. Ridolfi[1], L. Shoulhac[2], M. Marro[4], P. Salizzoni[4]

[1] Department of Environmental, Land, and Infrastructure Engineering, Politecnico di Torino, Corso Duca Degli Abruzzi 24, 10129, Turin, Italy
[2] Univ Lyon, INSA Lyon, CNRS, Ecole Centrale de Lyon, Univ Claude Bernard Lyon 1, LMFA, UMR5509, 69621, Villeurbanne France
[3] Department of Mathematical Sciences "Giuseppe Luigi Lagrange", Politecnico di Torino, Corso Duca Degli Abruzzi 24, 10129, Turin, Italy
[4] Univ Lyon, Ecole Centrale de Lyon, CNRS, Univ Claude Bernard Lyon 1, INSA Lyon, LMFA, UMR5509, 69130, Ecully, France

Abstract

The greening of cities is one of the most encouraged mitigation strategies to face the urban heat island phenomenon, as vegetation increases the evapotranspiration and the shading. Moreover, trees enhance the pollutant deposition rate thanks to their large surface area. However, few studies on the impact of tree planting on the natural ventilation and dispersion mechanisms inside urban street canyons are available.

In this framework, we present the results of an experimental campaign carried out in the wind tunnel of École Centrale de Lyon, in France (*figure 1a*). The study was aimed at understanding how the presence and the density of trees affect the flow field inside a street canyon, and if they hinder the air exchange with the external atmosphere. Concentration, velocity, and combined concentration and velocity measurements have been performed inside a street canyon, without street intersections, oriented perpendicular to the wind direction, inserted in an urban network reproduced inside the test section of the wind tunnel. The vehicular pollution has been simulated by a linear source of ethane, which behaves as a passive scalar. The aerodynamic behavior of trees has been reproduced by inserting plastic miniatures of trees along the two long sides of the canyon, using three different tree density configurations: absence of trees inside the canyon, two low density tree rows, and two high density tree rows (*figure 1b*).

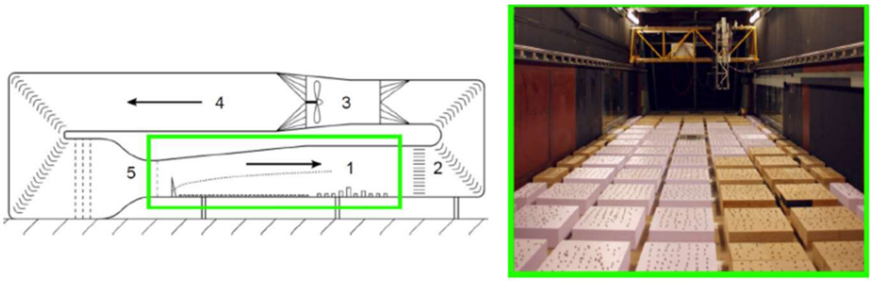

(a)

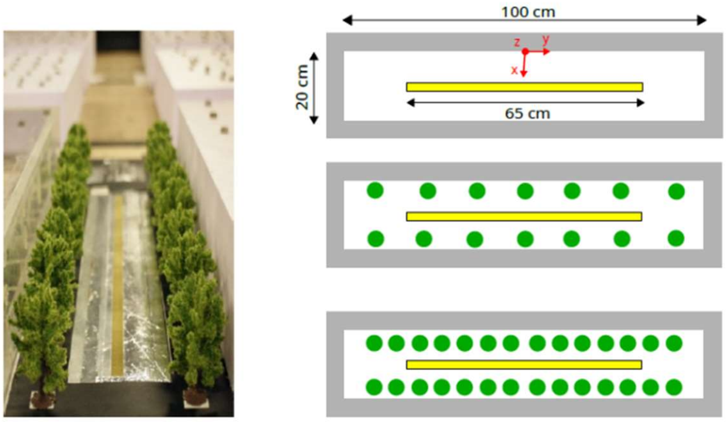

(b)

Figure 1: (a) Scheme of the wind tunnel (left): 1 test section; 2 heat exchanger system; 3 fan; 4 diverging system; 5 converging system and generating turbulence grid. Street network simulated inside the test section (right). (b) Plastic miniatures of trees placed inside the model street canyon (left). Tree density configurations (right): Zero configuration, Half configuration, Full configuration.

The measurements of the mean concentration field reveal that the presence of trees determines the transition from a two-dimensional concertation field to a three-dimensional one. Indeed, the concentration is homogeneous along the longitudinal direction of the empty canyon while, when trees are inserted, the concentration field becomes heterogeneous, with areas of accumulation of pollutant and areas of low concentration. However, the bulk vertical exchange velocity is almost constant varying the tree density. To unveil the reasons for this, we have investigated the structure of the velocity field within the canyon by performing velocity measurements with the LDA (Laser Doppler Anemometer), and we have evaluated turbulent mass fluxes using the LDA coupled with the FID (Flame Ionization Detector).

From the velocity measurements, we find that the mass transfer inside the canyon is governed by recirculating cells transporting the pollutant from the downwind wall to the upwind wall, and they are not weakened by the presence of trees. Moreover, we find that the presence of trees homogenizes the mean vertical velocity, and it decreases the turbulent kinetic energy. Turbulent mass fluxes have been evaluated both inside the canyon and at the rooftop. It is found that inside the empty canyon the turbulent mass fluxes are strongly homogeneous and negative, while they are almost negligible in the case with trees. A quadrant analysis of the turbulent mass fluxes at the rooftop reveals that the ventilation of the canyon is dominated by the entrance of clean air, and its local contribution to the total turbulent mass flux is homogeneous along the canyon, with and without vegetation.

The statistical analysis of concentration time series measured in different spatial points inside the canyon reveals that the dispersion phenomenon can be entirely modeled with a Gamma distribution, even if the Lognormal and the Weibull 2p distributions perform a good fitting as well, and that the extreme concentration events are governed by an exponential law.

References

Gromke, C. and Ruck, B. (2007). Influence of trees on the dispersion of pollutants in an urban street canyon—experimental investigation of the flow and concentration field. *Atmospheric Environment*, 41(16):3287–3302.

Gromke, C. and Ruck, B. (2009). On the impact of trees on dispersion processes of traffic emissions in street canyons. *Boundary-Layer Meteorology*, 131(1):19–34.

Gromke, C. and Ruck, B. (2012). Pollutant concentrations in street canyons of different aspect ratio with avenues of trees for various wind directions. *Boundary-Layer Meteorology*, 144(1):41–64.

Marro, M., Gamel, H., Méjean, P., Correia, H., Soulhac, L., and Salizzoni, P. (2020). High frequency simultaneous measurements of velocity and concentration within turbulent flows in wind-tunnel experiments. *Experiments in Fluids*, 61(12):1–13.

Marucci, D. and Carpentieri, M. (2019). Effect of local and upwind stratification on flow and dispersion inside and above a bi-dimensional street canyon. *Building and Environment*, 156:74–88.

Oke, T. R. (2002). *Boundary layer climates*. Routledge.

Orsi, M., Soulhac, L., Feraco, F., Marro, M., Rosenberg, D., Marino, R., Boffadossi, M., and Salizzoni, P. (2021). Scalar mixing in homogeneous isotropic turbulence: A numerical study. *Physical Review Fluids*, 6(3):034502.

Salizzoni, P., Soulhac, L., and Mejean, P. (2009). Street canyon ventilation and atmospheric turbulence. *Atmospheric Environment*, 43(32):5056–5067.

Effect of an upstream tall building on a street canyon flow

Haoran Du[1], Eric Savory[1], Laurent Perret[2]

[1]University of Western Ontario, Department of Mechanical and Materials Engineering, 1151 Richmond Street, N6A 3K7 London, Canada
[2]Nantes Université, École Centrale Nantes, CNRS, LHEEA, UMR 6598, F-44000 Nantes, France

Abstract

The wake effect caused by high-rise buildings could have a strong influence on the boundary layer and result in a strong impact on the turbulence associated with street canyon flows. A wind tunnel experiment was performed to investigate this, focusing on a realistic street canyon configuration embedded in a realistic urban fabric. A morphographic scale model of the centre of Nantes, France, at the scale of 1:200 was used, in which the Rue de Strasbourg was the investigated canyon and the nearby cathedral was identified as the local tall building. To complement this investigation, additional experiments were performed by replacing the cathedral with a block building as a comparison. Stereoscopic PIV was set up to capture the vertical plane at the centre of the street canyon for turbulence statistics. The wake caused by the cathedral affects all the flow statistics, such as the mean velocities, the Reynolds stresses, and the velocity skewnesses within the shear layer. The cathedral wake was also found to reduce the vertical exchanges at roof level. Finally, strong spanwise velocities at the pedestrian level were also observed, as a result of the complex morphology of the surrounding building layout and the presence of nearby intersections.

Introduction

With the growth of the global economy, the number of designs and constructions of tall buildings in the coming years has increased progressively. A single tall building or a cluster of tall buildings within a low-rise neighbourhood could bring multiple unexpected influences on urban climates, such as strong gusts at the pedestrian level (Tominaga & Shirzadi, 2021), poor pollutant dispersion and ventilation in street canyons (Yuan et al., 2014).

Previous *in-situ*, experimental, or computational studies of urban boundary layers and street canyons focused on flow turbulence, or pollutant dispersion using idealized homogeneous roughness elements such as bars or cubes (Bottema, 1996; Inagaki & Kanda, 2008; Salizzoni et al., 2011; Blackman et al., 2015; Basley et al., 2019; Jaroslawski et al., 2019). Basley et al. (2019) stated that the flow characteristics in the inertial layer, such as coherent structures and vortices, show independence from the wall configuration, in agreement with the smooth-wall situation (Castro et al., 2013; Squire et al., 2016) and the roughness sublayer could be penetrated by large-scale motions of the overlaying boundary layer if the packing density, which is defined by the ratio of the plan area of the obstacles to the total plan area, is below a certain threshold. Some studies used idealized heterogeneous roughness such as bars and cubes whose heights followed a normal distribution (Cheng & Castro, 2002; Goulart et al., 2019) or examined different element spacings (Choi et al., 2020; Cheng et al., 2021), or focused on the effects of the different roof shapes (Schultz et al., 2007) and orientation of the buildings in roughness (Yang & Meneveau, 2016). Although Cheng & Castro (2002) found that the upper limit of the inertial sublayer over a homogeneous roughness arrangement is almost identical to that over inhomogeneous roughness, while the roughness sublayer is much thinner and the friction velocity and roughness length are significantly smaller for the latter case, studies of heterogenous simplified arrays seldom focused on the influence on the downstream boundary layer (Cheng et al., 2021).

Furthermore, tall buildings, in accordance with their definition, are extreme outliers to the height distribution of the upstream roughness and, hence, cannot simply be represented by the normal distribution. Tall buildings protrude across the roughness sublayer which extends two or three times the mean building height above the underlying roughness (Cheng & Castro, 2002). Karman vortices, horseshoe vortices, and tip vortices are generated around and downstream of a wall-mounted finite cylinder with a high aspect ratio $AR_w = h_{cylinder}/d_{cylinder}$ (Roh & Park, 2003), and can noticeably influence the downstream boundary layer over the relatively low-height surrounding roughness. The effects of tall buildings have been, therefore, studied either in idealized roughness arrays (Brixey et al., 2009; Heist et al., 2009; Fuka et al., 2018) or morphological models (Rotach et al., 2005; Ng et al., 2011; Salizzoni et al., 2011b; Cheng et al., 2021; Hertwig et al., 2019, 2021). Cheng et al. (2021) divided the urban roughness sublayer into two layers and found that the upper layer, which is governed by tall buildings, has larger dispersive stress and smaller drag than the lower layer which contains more dense and shorter buildings. The incoming flow, influenced by the upstream low-rise canopy, strikes the tall building to generate a rooftop shear layer and the tall building's wake changes the near-wake dynamics by interacting with the downstream low-rise canopy (Lim et al., 2022). The wake caused by a tall building, therefore, could have a strong and long-distance effect on the flow and scalar field of the low-rise surrounding urban terrain and the downstream urban boundary layer (Hertwig et al., 2021).

Grimmond & Oke (1999) suggested categorizing street canyon flows into three different regimes; isolated, wake interference, and skimming, based on the building plan area density and showed that the canyon aspect ratio $AR_c = w_{canyon}/h_{canyon}$ has a large influence on street canyon flow. Studies have examined the effect of varying the geometry (2D or 3D) of the roughness elements on the boundary layer flow (Michioka & Sato, 2012; Takimoto et al., 2013) and have found that the friction velocity and shear stress increase from 2D to 3D configurations throughout the boundary layer. More detailed studies regarding both 2D and 3D arrays falling within both the skimming flow regime and the wake interference regime were studied by Blackman et al. (2015) and Jaroslawski et al. (2019), who found that the mean streamwise velocity is higher in skimming flow regime than in the wake interference regime, whilst the 2D configurations of upstream roughness yield a larger streamwise velocity than in 3D with same plan area density λ_p. They also suggested that a higher level of vertical ventilation at the roof level and larger shear stresses appear with a higher AR_c.

The same test model of the Rue de Strasbourg in Nantes, was studied in a series of experiments, either *in-situ* (Mestayer et al., 1999; Berkowicz et al., 2002; Louka et al., 2002; Vachon et al., 2002) or in wind tunnels (Kastner-Klein et al., 2004; Kastner-Klein & Rotach, 2004) to understand the turbulence and pollutant dispersion mechanism within and above the canyon considering different factors. The thermal effects caused by solar heating (Mestayer et al., 1999; Louka et al., 2002) provided insights into their influence on the pollutant concentration and wind turbulence within the street canyon and were compared with a Reynolds Averaged Navier Stokes (RANS) model that incorporated a k-ε turbulence closure named CHENSI (Sini et al., 1996). The CHENSI simulations showed two counter-rotating vortices and a small eddy at the bottom of the leeward wall which was thought to be an overestimation in comparison with the field experiment, probably due to the potential error in its wall function and the limitation of the 2D simulation. The traffic-induced turbulence and pollutant dispersion were studied (Berkowicz et al., 2002; Vachon et al., 2002) in comparison with the Danish Operational Street Pollution Model (OSPM) (Berkowicz, 2000) and Micro Scale Air Pollution Model (MISKAM) (Eichhorn, 1996). The dependence of pollutants concentration on the wind speed was found to be less obvious on the leeward side and MISKAM was shown to be in better agreement with the field experiment than the OSPM model by considering the initial mixing of vehicle exhausting at a lower height of 2 m. The wind tunnel experiments (Kastner-Klein et al., 2004; Kastner-Klein & Rotach, 2004) used the same morphographic model as this present research while measuring with Laser Doppler Velocimetry (LDA) and placing the cathedral downstream of the street canyon. Mean streamwise velocities and shear stresses were fitted within the overlying boundary layer through parameterization of length scales and friction velocities.

All these studies focusing on the effect of upstream roughness and boundary layer on the street canyon used homogeneous arrays while, as illustrated above, the rarely investigated heterogeneous terrain and, especially, the presence of a tall building would noticeably change the boundary layer characteristics and, therefore, would strongly influence the flow and scalar field of street canyons. However, such a topic lacks abundant studies and so this aspect is the focus of the present paper.

Experiment details

The experiments were conducted in the open circuit atmospheric boundary layer wind tunnel in the LHEEA at Ecole Centrale de Nantes, which has test section dimensions of 24 m (length) × 2 m (width) × 2 m (height) and a 5:1 ratio inlet contraction. To initiate the boundary layer, five vertical tapered spires of 800 mm in height and 134 mm in width were located at the intersection of the end of the contraction and the test section, followed by a 200 mm high solid fence across the working section downstream of the inlet and then a 19 m fetch of staggered cube roughness elements with height h_1 = 50 mm and a plan area density λ_{p1} = 25 %. A 1:200 scaled morphographic model part of the city of Nantes, France, centred around the rue de Strasbourg, in which the cathedral was identified as the local tall building was placed downstream of the cubic array. The model has an upstream plan area density λ_{p2} = 44 % and an overall average ridge height of approximately 100 mm (Petra Kastner-Klein & Rotach, 2004). In another experiment, the cathedral was replaced by a 200 mm × 200mm × 100mm rectangular block, named as 1-block configuration for comparison purposes. The width of the street canyon is 73 mm, and the upstream building ridge height h_2 equals 116 mm while the downstream ridge height is 114.5 mm. The distinction between the height of the upstream roughness and the street canyon is due to the different terrain categories of suburban areas and city centre.

A Dantec particle image velocimetry (PIV) system was utilized to measure the 3-component velocity field in the vertical plane at the centre of the street canyon. LaVision Laskin-Nozzle aerosol generator was used to seed the flow with olive oil aerosol with a mean droplet diameter of 1 um. A Litron double cavity Nd-YAG laser (2 × 200 mJ) was mounted on the ceiling of the wind tunnel to generate a laser light sheet. Two 2048 x 2048 CCD cameras with 105 mm objective lenses were installed under the wind tunnel floor and used for stereoscopic PIV to record pairs of images at a frequency of 7.4 Hz between pairs of pulses and a time-step of 300 µs between two images of the same pair, as shown in Fig.1. The synchronization of the cameras and laser was controlled using Dantec Dynamic Studio software, which was also used to perform the PIV analysis on the recorded images. 10,000 pairs of images were recorded for each flow configuration and the multi-pass cross-correlation PIV processing resulted in a final interrogation window size of 32 × 32 pixels with an overlap of 50 %. For all the configurations, the final spatial resolution was 1.6 and 3.2 mm in the longitudinal and vertical directions, respectively.

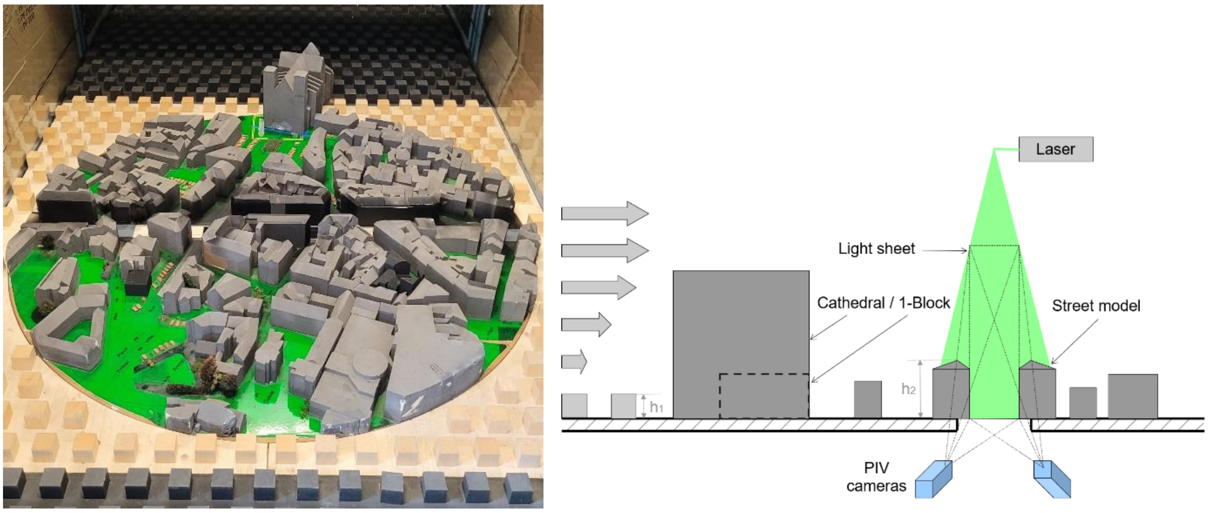

Fig 1. Left: The morphological model in the wind tunnel; Right: Stereoscopic PIV set-up

All the experiments were performed with the same free-stream velocity of U_e = 5.8 m s^{-1} measured with a pitot-static tube located 1.5 m above the wind tunnel floor and the centreline of the tunnel in the test section, without the model. The Reynolds number, based on upstream roughness height, of $Re_{h_1}=\frac{h_1 u_*}{\nu}=1.2\times 10^3$ was computed and the oncoming boundary layer parameters and scaling factors are shown in Table 1.

Table 1. Oncoming boundary layer characteristics (Blackman et al., 2018)

	U_e (m s^{-1})	u_*/U_e	h_1 (m)	δ (m)	$Re_{h_1}(u_*)$	$Re_\delta(u_*)$	d/h_1	z_0/h_1	$\frac{\partial P}{\partial x}$ (Pa m^{-1})
Cathedral / 1-block	5.8	0.07	0.05	0.975	1.2×10^3	2.4×10^4	0.64	0.08	- 0.37

Results

Contours of temporally averaged components are presented below for a comparison between the scenario with the cathedral or with the replaced block in the upstream direction. Fig. 2 shows the magnitude of streamwise, vertical, and longitudinal velocity distributions by sequence. The streamwise velocity component over the canyon is noticeably smaller if the cathedral is upstream which could be explained by the fact that the induced wake downstream the cathedral is more turbulent than the overlying boundary layer flow for the 1-block configuration. This could also be observed in the vertical velocity component contour since the zone at z/h_2 = 2 shows larger magnitudes than the surroundings, which indicates some lifting effects in the observed region. In the near-wall region, the vertical component shows a general pattern, such that the most negative region is near the downstream wall and the most positive region is near the upstream wall, while the magnitude of the latter is larger than the former. Spanwise velocities were usually regarded as negligible in long symmetrical street canyon models, while a strong spanwise effect was observed at the upstream lower corner within the canyon in this presenting morphological model. This might primarily be induced by the intersections that separated the street canyon into multiple short sections and partly be caused by the asymmetric wake generated by the upstream building since it is not situated perpendicular to the street canyon but at an angle of around 20° to the streamwise direction.

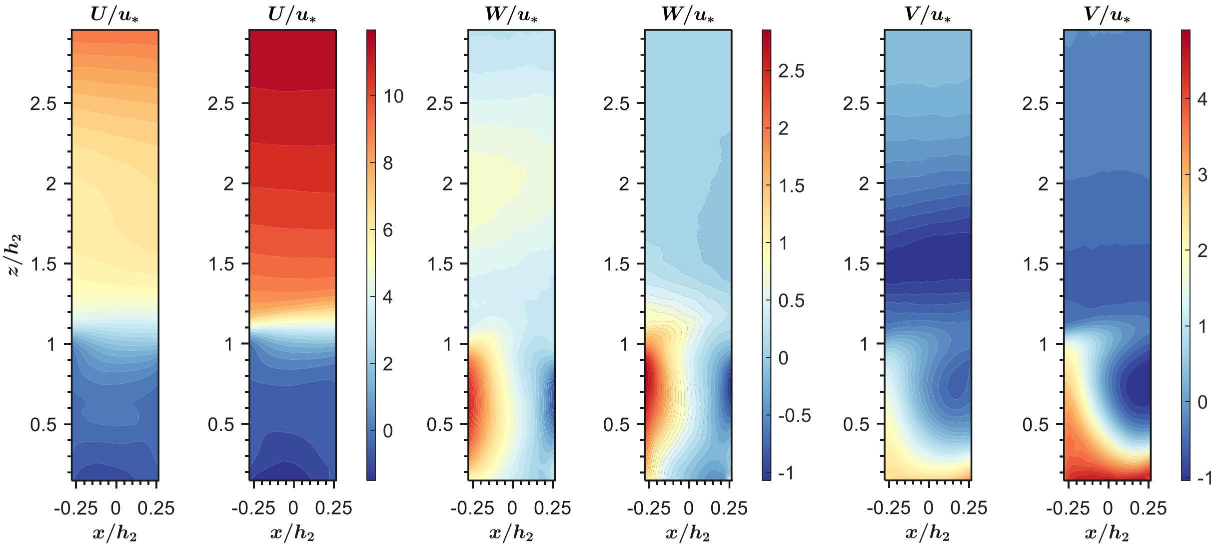

Fig 2. Comparison of contours of velocity components (Left: cathedral; Right: 1-block)

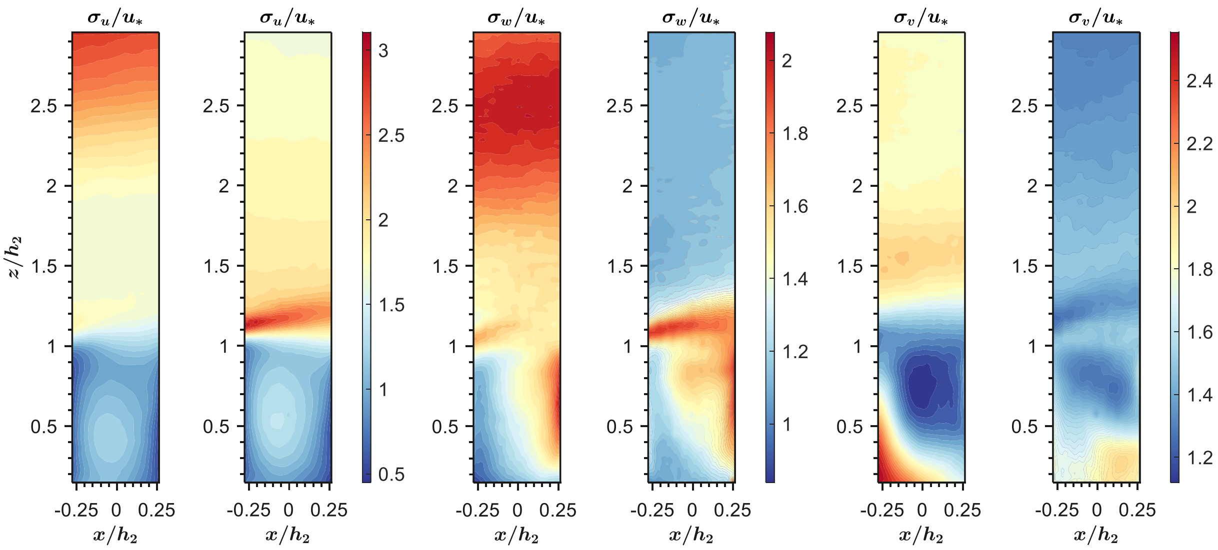

Fig 3. Comparison of contours of velocity standard deviations (Left: cathedral; Right: 1-block)

As shown in Fig 3. for the case of the cathedral, the standard deviations of velocity components in the overlying boundary layer are clearly larger while those within the shear layer are visibly smaller for the 1-block configuration. This could be explained by the wake induced by the cathedral and a relatively smaller streamwise velocity at the leading edge of the upstream canyon obstacle, respectively. Similar patterns in the streamwise and vertical components within the canyon are observed in both configurations, while those in the 1-block configuration show a slightly larger magnitude and spatial extent. The standard deviation of the vertical velocity component shows extremely distinct patterns since the regions with maximum magnitudes are at different canyon corners at the pedestrian level.

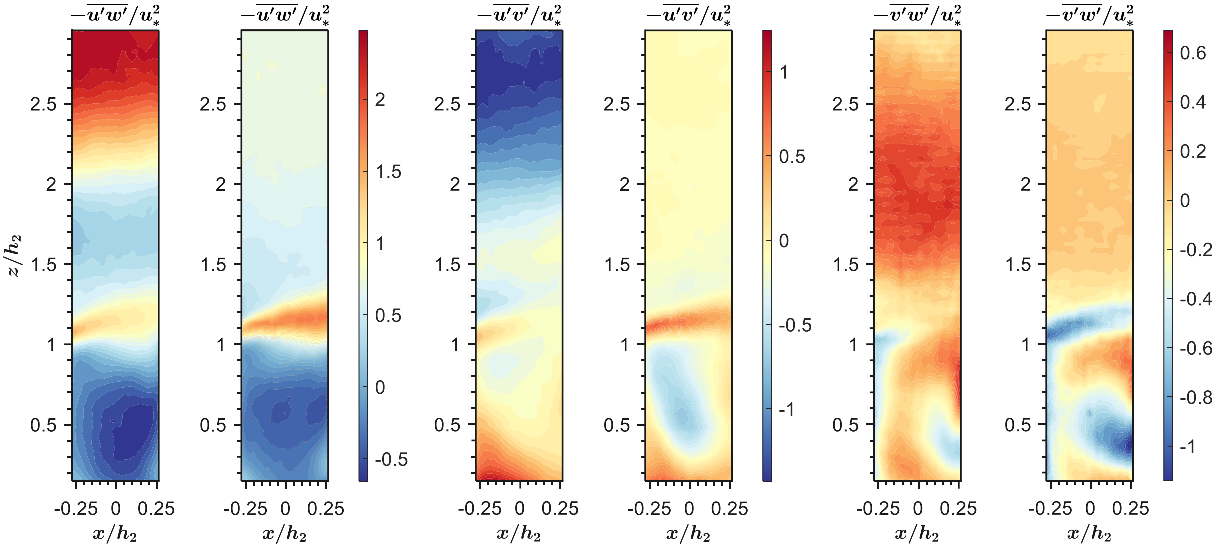

Fig 4. Comparison of contours of Reynolds stresses (Left: cathedral; Right: 1-block)

Reynolds stresses (Fig 4.), interpreted as momentum fluxes, could bring insights into turbulent kinetic energy (TKE) production. Within the shear layer caused by the upstream canyon leading-edge, $-\overline{u'w'}$ and $-\overline{u'v'}$ are positive but the $-\overline{v'w'}$ is negative. The $-\overline{u'w'}$ between $z/h_2 = 2$ and 3, and $-\overline{v'w'}$ between $z/h_2 = 1.5$ and 2.5 over the canyon in the cathedral configuration show a large positive value, but the $-\overline{u'v'}$ within the same region show a negative value. A large positive $-\overline{u'v'}$ is observed at the upstream lower corner of the canyon whilst there is an elliptical region of negative $-\overline{u'v'}$ immediately below the shear layer which penetrates deep into the canyon. The negative $-\overline{v'w'}$ extends from the shear layer along the upstream wall and also has a local minimum at the downstream wall between $z/h_2 =$ 0.2 and 0.6.

Higher-order moments of velocities such as skewness (Fig 5.) and flatness (Fig 6.) help characterize the shape of the probability density function (PDF). The value of a non-zero skewness indicates whether the probability of the existence of larger velocity excursions in one direction is greater than in the others. A larger flatness shows whether the occurrence of larger excursions from mean values is more frequent.

The streamwise skewness S_u is highly positive in the shear layer for both configurations. Positive S_u is observed in the wake-affected boundary layer in the cathedral configuration while in the 1-block configuration, the S_u shows a negative region immediately above the shear layer and stays negative in the overlying boundary layer. Within the canyon, the major part of the downstream near-wall region is positively skewed and the upstream near-wall region is negatively skewed. Similar patterns occur between the cathedral and 1-block configurations for the skewnesses of the vertical and spanwise components, although a large difference is the positive vertical skewness in the boundary layer over the canyon downstream of the block. It is worth noting that there is a strongly positive elliptical area in the canyon for the skewness of the spanwise velocity component near the downstream wall. The positive areas suggest that the PDFs of velocity in a certain direction at these locations have a peak value that is smaller than the mean value while the tail is larger, and they show that the dominant modes are slower than the mean wind speeds in this corresponding direction.

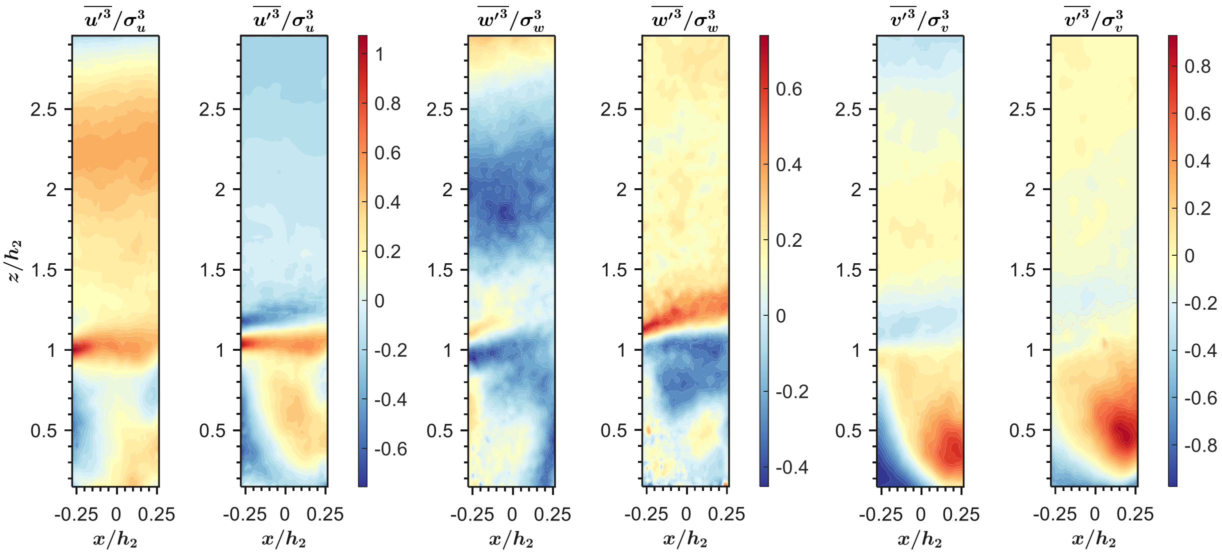

Fig 5. Comparison of contours of velocity skewness (Left: cathedral; Right: 1-block)

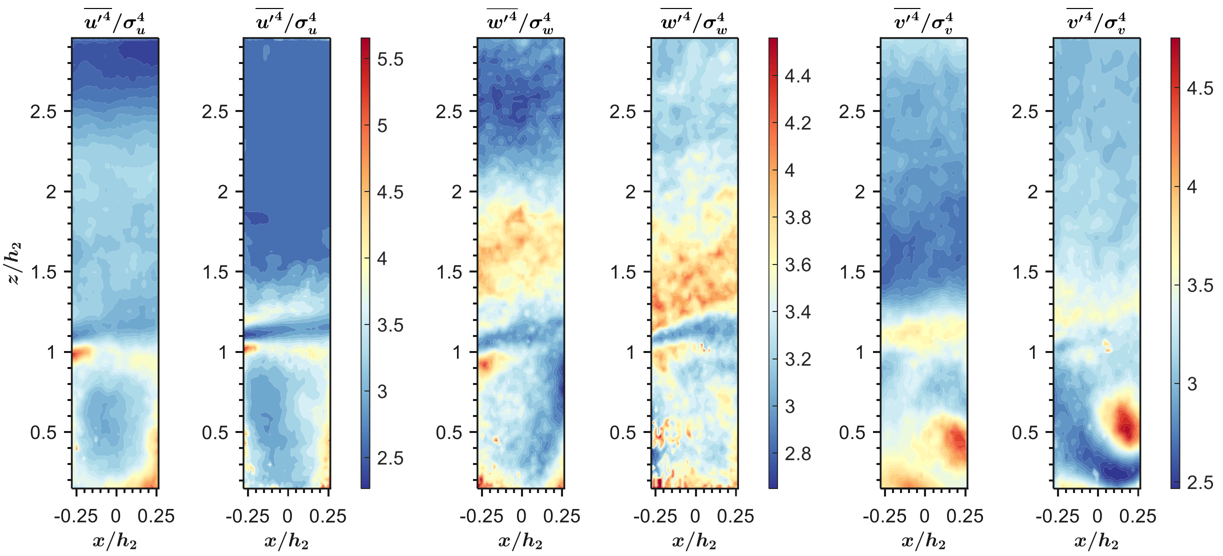

Fig 6. Comparison of contours of velocity flatness (Left: cathedral; Right: 1-block)

Differences in the velocity flatness (kurtosis) between the two configurations are not apparent. The upper limit of the shear layer shows a strongly flattening effect in the streamwise direction. The region between z/h_2 = 1.2 to 2 has a much more elevated peak in the vertical PDF than a normal distribution. A more peaked region is found at the bottom of the street canyon for the cathedral model than the 1-block model for the spanwise flatness, but a similar high-value core appears near the downstream wall.

Conclusion

In the present work, the flow within and above a street canyon immersed within a morphological model with or without an upstream tall building was investigated through the analysis of the main one-point statistics, and the following conclusions were drawn. The wake caused by the upstream cathedral has a strong effect on the turbulence statistics in comparison to the 1-block situation. The presence of the cathedral decreases the $-\overline{u'w'}$, σ_u, σ_w and S_w within the shear layer, in comparison to the 1-block configuration, and this results in weaker vertical exchanges at the roof level. Strong spanwise velocities were found at the pedestrian level at the upstream corner of the canyon in both configurations, which could be explained by the heterogeneity caused by the intersections along the canyon. However, the spanwise velocity in the cathedral configuration smaller while being more turbulent than in the 1-block configuration. The influence of the upstream tall building and the coupling between the flow within the canyon and the overlying flow will be investigated in future work.

Reference

Barlow, J., Best, M., Bohnenstengel, S. I., Clark, P., Grimmond, S., Lean, H., Christen, A., Emeis, S., Haeffelin, M., Harman, I. N., Lemonsu, A., Martilli, A., Pardyjak, E., Rotach, M. W., Ballard, S., Boutle, I., Brown, A., Cai, X., Carpentieri, M., … Zhong, J. (2017). Developing a research strategy to better understand, observe, and simulate urban atmospheric processes at Kilometer to Subkilometer Scales. *Bulletin of the American Meteorological Society*, *98*(10), ES261–ES264. https://doi.org/10.1175/BAMS-D-17-0106.1

Basley, J., Perret, L., & Mathis, R. (2019). Structure of high Reynolds number boundary layers over cube canopies. *Journal of Fluid Mechanics*, *870*, 460–491. https://doi.org/10.1017/jfm.2019.274

Berkowicz, R. (2000). OSPM - A Parameterised Street Pollution Model. *Environmental Monitoring and Assessment*, *65*(1–2), 323–331. https://doi.org/10.1007/978-94-010-0932-4_35

Berkowicz, R., Ketzel, M., Vachon, G., Louka, P., Rosant, J.-M., Mestayer, P. G., & Sini, J.-F. (2002). Examination of traffic pollution distribution in a street canyon using the Nantes'99 experimental data and comparison with model results. *Urban Air Quality — Recent Advances*, 311–324. https://doi.org/10.1007/978-94-010-0312-4_22

Blackman, K., Perret, L., & Savory, E. (2015). Effect of upstream flow regime on street canyon flow mean turbulence statistics. *Environmental Fluid Mechanics*, *15*(4), 823–849. https://doi.org/10.1007/s10652-014-9386-8

Blackman, K., Perret, L., & Savory, E. (2018). Effects of the upstream-flow regime and canyon aspect ratio on non-linear interactions between a street-canyon flow and the overlying boundary layer. *Boundary-Layer Meteorology*, *169*(3), 537–558. https://doi.org/10.1007/s10546-018-0378-y

Bottema, M. (1996). Roughness parameters over regular rough surfaces: Experimental requirements and model validation. *Journal of Wind Engineering and Industrial Aerodynamics*, *64*(2–3), 249–265. https://doi.org/10.1016/S0167-6105(96)00062-1

Brixey, L. A., Heist, D. K., Richmond-Bryant, J., Bowker, G. E., Perry, S. G., & Wiener, R. W. (2009). The effect of a tall tower on flow and dispersion through a model urban neighborhood: Part 2. Pollutant dispersion. *Journal of Environmental Monitoring*, *11*(12), 2171–2179. https://doi.org/10.1039/b907137g

Castro, I. P., Segalini, A., & Alfredsson, P. H. (2013). Outer-layer turbulence intensities in smooth- and rough-wall boundary layers. *Journal of Fluid Mechanics*, *727*, 119–131. https://doi.org/10.1017/jfm.2013.252

Cheng, H., & Castro, I. P. (2002). Near wall flow over urban-like roughness. *Boundary-Layer Meteorology*, *104*(2), 229–259. https://doi.org/10.1023/A:1016060103448

Cheng, W. C., Liu, C. H., Ho, Y. K., Mo, Z., Wu, Z., Li, W., Chan, L. Y. L., Kwan, W. K., & Yau, H. T. (2021). Turbulent flows over real heterogeneous urban surfaces: Wind tunnel experiments and Reynolds-averaged Navier-Stokes simulations. *Building Simulation*, *14*(5), 1345–1358. https://doi.org/10.1007/s12273-020-0749-4

Choi, Y. K., Hwang, H. G., Lee, Y. M., & Lee, J. H. (2020). Effects of the roughness height in turbulent boundary layers over rod- and cuboid-roughened walls. *International Journal of Heat and Fluid Flow*, *85*(June), 108644. https://doi.org/10.1016/j.ijheatfluidflow.2020.108644

Eichhorn, J. (1996). Validation of a Microscale Pollution Dispersal Model. *Air Pollution Modeling and Its Application XI*, 539–547. https://doi.org/10.1007/978-1-4615-5841-5_56

Fuka, V., Xie, Z. T., Castro, I. P., Hayden, P., Carpentieri, M., & Robins, A. G. (2018). Scalar fluxes near a tall building in an aligned array of rectangular buildings. *Boundary-Layer Meteorology*, *167*(1), 53–76. https://doi.org/10.1007/s10546-017-0308-4

Goulart, E. V., Reis, N. C., Lavor, V. F., Castro, I. P., Santos, J. M., & Xie, Z. T. (2019). Local and non-local effects of building arrangements on pollutant fluxes within the urban canopy. *Building and Environment*, *147*(July 2018), 23–34. https://doi.org/10.1016/j.buildenv.2018.09.023

Grimmond, C. S. B., & Oke, T. R. (1999). Aerodynamic properties of urban areas derived from analysis of surface form. *Journal of Applied Meteorology*, *38*(9), 1262–1292. https://doi.org/10.1175/1520-0450(1999)038<1262:APOUAD>2.0.CO;2

Heist, D. K., Brixey, L. A., Richmond-Bryant, J., Bowker, G. E., Perry, S. G., & Wiener, R. W. (2009). The effect of a tall tower on flow and dispersion through a model urban neighborhood: Part 1. Flow characteristics. *Journal of Environmental Monitoring*, *11*(12), 2163–2170. https://doi.org/10.1039/b907135k

Hertwig, D., Gough, H. L., Grimmond, S., Barlow, J. F., Kent, C. W., Lin, W. E., Robins, A. G., & Hayden, P. (2019). Wake characteristics of tall buildings in a realistic urban canopy. *Boundary-Layer Meteorology*, *172*(2), 239–270. https://doi.org/10.1007/s10546-019-00450-7

Hertwig, D., Grimmond, S., Kotthaus, S., Vanderwel, C., Gough, H., Haeffelin, M., & Robins, A. (2021). Variability of physical meteorology in urban areas at different scales: Implications for air quality. *Faraday Discussions*, *226*, 149–172. https://doi.org/10.1039/d0fd00098a

Inagaki, A., & Kanda, M. (2008). Turbulent flow similarity over an array of cubes in near-neutrally stratified atmospheric flow. *Journal of Fluid Mechanics*, *615*, 101–120. https://doi.org/10.1017/S0022112008003765

Jaroslawski, T., Perret, L., Blackman, K., & Savory, E. (2019). The Spanwise Variation of Roof-Level Turbulence in a Street-Canyon Flow. *Boundary-Layer Meteorology*, *170*(3), 373–394. https://doi.org/10.1007/s10546-018-0405-z

Kastner-Klein, P., Berkowicz, R., & Britter, R. (2004). The influence of street architecture on flow and dispersion in street canyons. *Meteorology and Atmospheric Physics*, *87*(1–3), 121–131. https://doi.org/10.1007/s00703-003-0065-4

Kastner-Klein, Petra, & Rotach, M. W. (2004). Mean flow and turbulence characteristics in an urban roughness sublayer. *Boundary-Layer Meteorology*, *111*(1), 55–84. https://doi.org/10.1023/B:BOUN.0000010994.32240.b1

Lim, H. D., Hertwig, D., Grylls, T., Gough, H., Reeuwijk, M. van, Grimmond, S., & Vanderwel, C. (2022). Pollutant dispersion by tall buildings: laboratory experiments and Large-Eddy Simulation. *Experiments in Fluids*, *63*(6), 1–20. https://doi.org/10.1007/s00348-022-03439-0

Louka, P., Vachon, G., Sini, J.-F., Mestayer, P. G., & Rosant, J.-M. (2002). Thermal Effects on the Airflow in a Street Canyon – Nantes'99 Experimental Results and Model Simulations. *Water, Air and Soil Pollution*, *2*(5), 351–364. https://doi.org/10.1023/A:1021355906101

Mestayer, P. G., Vachon, G., & Rosant, J. (1999). The nantes '99 data base for model validation of air quality in streets. *8th Int. Conf. on Harmonisation within Atmospheric Dispersion Modelling for Regulatory Purposes*, 297–300.

Michioka, T., & Sato, A. (2012). Effect of incoming turbulent structure on pollutant removal from two-dimensional street canyon. *Boundary-Layer Meteorology*, *145*(3), 469–484. https://doi.org/10.1007/s10546-012-9733-6

Ng, E., Yuan, C., Chen, L., Ren, C., & Fung, J. C. H. (2011). Improving the wind environment in high-density cities by understanding urban morphology and surface roughness: A study in Hong Kong. *Landscape and Urban Planning*, *101*(1), 59–74. https://doi.org/10.1016/j.landurbplan.2011.01.004

Roh, S. C., & Park, S. O. (2003). Vortical flow over the free end surface of a finite circular cylinder mounted on a flat plate. *Experiments in Fluids*, *34*(1), 63–67. https://doi.org/10.1007/s00348-002-0532-6

Rotach, M. W., Vogt, R., Bernhofer, C., Batchvarova, E., Christen, A., Clappier, A., Feddersen, B., Gryning, S. E., Martucci, G., Mayer, H., Mitev, V., Oke, T. R., Parlow, E., Richner, H., Roth, M., Roulet, Y. A., Ruffieux, D., Salmond, J. A., Schatzmann, M., & Voogt, J. A. (2005). BUBBLE - An urban boundary layer meteorology project. *Theoretical and Applied Climatology*, *81*(3–4), 231–261. https://doi.org/10.1007/s00704-004-0117-9

Salizzoni, P., Marro, M., Soulhac, L., Grosjean, N., & Perkins, R. J. (2011). Turbulent transfer between street canyons and the overlying atmospheric boundary layer. *Boundary-Layer Meteorology*, *141*(3), 393–414. https://doi.org/10.1007/s10546-011-9641-1

Schultz, M., Leitl, B., & Schatzmann, M. (2007). How rough is rough ? Characterization of turbulent fluxes within and above an idealized urban roughness. *International Workshop on Physical Modelling of Flow and Dispersion Phenomena*, 69–74.

Sini, J. F., Anquetin, S., & Mestayer, P. G. (1996). Pollutant dispersion and thermal effects in urban street canyons. *Atmospheric Environment*, *30*(15), 2659–2677. https://doi.org/10.1016/1352-2310(95)00321-5

Squire, D. T., Hutchins, N., Schultz, M. P., & Klewicki, J. C. (2016). Erratum: Comparison of turbulent boundary layers over smooth and rough surfaces up to high Reynolds numbers (Journal of Fluid Mechanics (2016) 795 (210-240) DOI: 10.1017/jfm.2016.196). *Journal of Fluid Mechanics*, *797*, 917. https://doi.org/10.1017/jfm.2016.307

Takimoto, H., Inagaki, A., Kanda, M., Sato, A., & Michioka, T. (2013). Length-scale similarity of turbulent organized structures over surfaces with different roughness types. *Boundary-Layer Meteorology*, *147*(2), 217–236. https://doi.org/10.1007/s10546-012-9790-x

Tominaga, Y., & Shirzadi, M. (2021). Wind tunnel measurement of three-dimensional turbulent flow structures around a building group: Impact of high-rise buildings on pedestrian wind environment. In *Building and Environment*. https://doi.org/10.1016/j.buildenv.2021.108389

Vachon, G., Louka, P., Rosant, J.-M., Mestayer, P. G., & Sini, J.-F. (2002). Measurements of traffic-induced turbulence within a street canyon during the Nantes'99 experiment. *Urban Air Quality — Recent Advances*, *1986*, 127–140. https://doi.org/10.1007/978-94-010-0312-4_10

Yang, X. I. A., & Meneveau, C. (2016). Large eddy simulations and parameterisation of roughness element orientation and flow direction effects in rough wall boundary layers. *Journal of Turbulence*, *17*(11), 1072–1085. https://doi.org/10.1080/14685248.2016.1215604

Yuan, C., Ng, E., & Norford, L. K. (2014). Improving air quality in high-density cities by understanding the relationship between air pollutant dispersion and urban morphologies. *Building and Environment*, *71*(2), 245–258. https://doi.org/10.1016/j.buildenv.2013.10.008

Use of atmospheric boundary-layer LES fields for an operational Lagrangian dispersion model

A. Emmanuelli [1], G. Lamaison[1], L.Soulhac[2]

[1]Univ Lyon, Ecole Centrale de Lyon, CNRS, Univ Claude Bernard Lyon 1, INSA Lyon, LMFA, UMR5509, 69130, Ecully, France
[2]Univ Lyon, INSA Lyon, CNRS, Ecole Centrale de Lyon, Univ Claude Bernard Lyon 1, LMFA, UMR5509, 69621, Villeurbanne, France

Abstract

SLAM (Safety Lagrangian Atmospheric Model) is a Lagrangian dispersion model developped for use in operational conditions, notably in an industrial context. To ensure quasi real time dispersion simulations, a Reynolds-Averaged Navier-Stokes (RANS) detailed simulation database is first built, for use on demand to set flow variable inputs such as mean wind and turbulence fields. Assumptions made by this RANS approach can have a strong impact on the flow and thus on the dispersion process. Large-Eddy Simulation (LES) could prove an efficient tool to limit this. The aim of this study is therefore to use LES to compute the mean flows fed into SLAM, and as such better take into account the effect of turbulence on the mean flow, all the while keeping with operational constrains. Concentration levels obtained using SLAM with both RANS and LES mean flow fields are compared, as well as the concentration computed directly using an LES simulation with dispersion. The high-fidelity simulations are run using the PALM model system, developed for LES of atmospheric and oceanic boundary-layers. The study focus on an academic configuration in the presence of obstacles. In the future, more complex configurations with realisitic obstacles and stratification effects will be insvestigated.

Introduction and objectives

Air pollution affects the quality of human life with short- and long-term health effects, especially in the respiratory and cardiovascular systems. Populations in the area surrounding industrial sites are particularly vulnarable, and there is a need to understand the extent of pollution dispersion.

Meteorological conditions and complex terrain affect flow and dispersion. The dynamics of the atmospheric boundary layer are particularly significant, with neutral, stable or unstable stratification conditions. The type of pollutant source can add to this complexity, often with multiple sources problems. For instance, in an industrial context, pollutants are often not only emitted by tall chimneys, but also by various machinery and storage tanks near to ground, with chronical pollutant sources due to leaks, but also industrial accidents. Taking into account complex configurations with buildings is thus necessary. They will also have a strong impact on the flow, so that sophisticated pollution dispersion models are needed. However, the latter should also have computational costs that allow fast response times in operational conditions.

It is in this spirit that the SLAM Lagrangian model was develloped and coupled with an operational simulation methodology called Flow'Air 3D (Vendel et al. 2010). It uses RANS (Reynolds-Averaged

Navier-Stokes) mean flow and statistical turbulence fields as inputs, in which turbulence is modeled. As the dispersion process is heavily affected by turbulence, the use of LES (Large Eddy Simulation) in which it is resolved rather than modeled could further improve pollution dispersion predictions. Indeed, a significant part of turbulence scales are resolved with this method. Furthermore, continued improvement of computational hardware could allow the use of such a method at a cost that was prohibitive until recently.

The objective of this study is therefore to evaluate whether the accuracy of SLAM can be further improved by use of LES input statistical flow fields, giving more accurate mean and turbulent flow, while keeping with operational constrains. As well as comparing SLAM predictions obtained using both RANS and LES fields, concentration levels resulting directly from LES with dispersion, as well as a wind tunnel experiment are used. In the first two sections, the operational methodology of the model and SLAM itself are presented. The experimental set-up follows, before detailing the coupling with LES.

Presentation of the operational dispersion simulation methodology

In a simulation of the flow and atmospheric dispersion with a CFD model, an important part of the computing time is devoted to modelling the flow and turbulence field. The principle of our approach, illustrated on Figure 1, is to prepare in advance a database of wind fields on the considered industrial site. In this way, only the dispersion is modeled in operational situations and time savings are considerable. The parameters that constitute the database are the wind direction and the inverse of the Monin-Obukhov length. As it was shown by Vendel et al. (2010), it is possible to overcome the wind speed by normalizing the velocity and turbulence fields by the friction velocity u_* (and the same kind of assumption can also been made for the temperature field normalized by using the potential temperature at ground level). Vendel et al. have also shown that a discretization of the database in 18 wind directions (step of 20°) and 7 values of $1/L_{MO}$ can limit the interpolation error in the database to a few percents. Once the database is ready, it is used as input for the Lagrangian model SLAM. In operational situations, a point meteorological data (measurement or forecast) is used in a meteorological preprocessor to estimate the wind direction, the inverse of the Monin-Obukhov length and the friction velocity u_*. These parameters are interpolated in the database to obtain wind, temperature and turbulence fields corresponding to the real atmospheric conditions. These fields are then used to model the dispersion with the SLAM Lagrangian model.

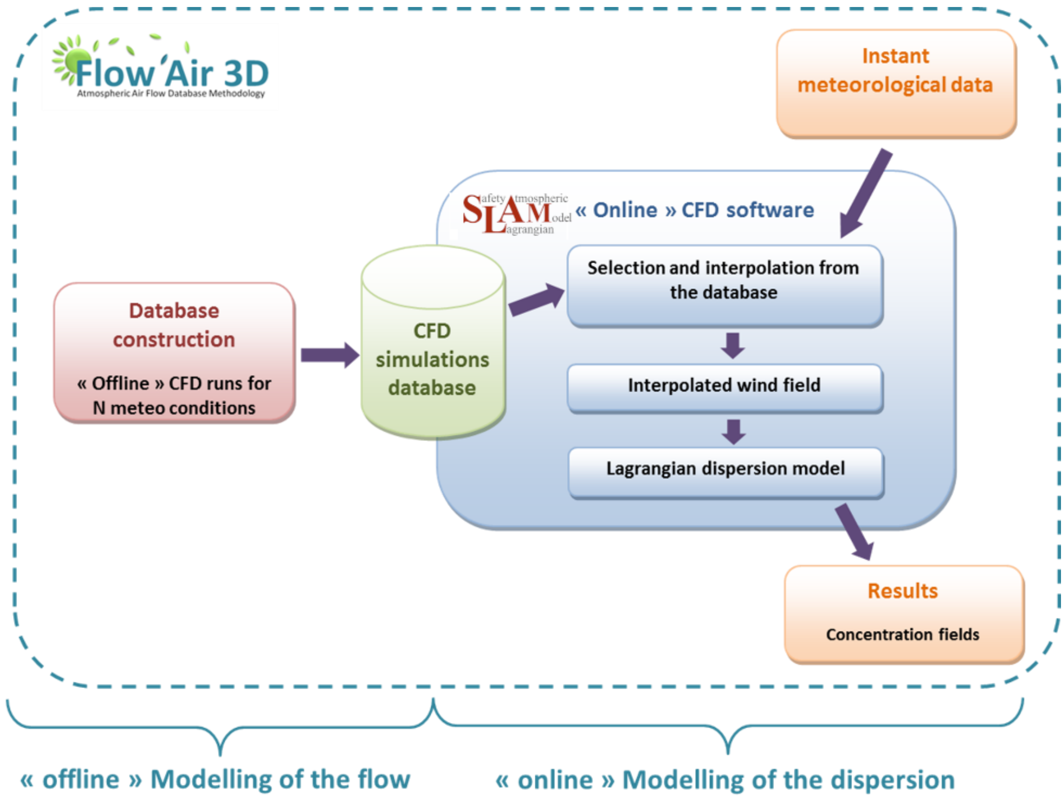

Figure 1: General decription of the Flow'Air 3D methodology

Presentation of the Lagrangian dispersion model SLAM

The Safety Lagrangian Atmospheric Model (SLAM) is a stochastic particle dispersion model, based on the tracking of Lagrangian trajectories of individual particles. The temporal evolution of the Lagrangian velocity of each particle is given by the equation:

$$U_i(t) = \overline{U_i}(t) + U_i'(t) \text{ with } U_i'(t+dt) = U_i'(t) + dU_i' \quad (1)$$

U_i is the mean velocity of the flow obtained from the CFD velocity field. The evolution of the fluctuating velocity U_i' is determined by the stochastic differential equation (Thomson, 1987):

$$dU_i' = a_i(X, U', t)dt + \sum_j b_j(X, U', t)d\xi_j \quad (2)$$

in which the terms a_i and b_j are expressed in terms of standard deviations of velocity fluctuations σ_{u_i} and of the Lagrangian times T_{L_i}. To express σ_{u_i} and T_{L_i}, we use the variables from the turbulence model of the CFD code. When using the k-ε turbulence model, we get σ_{u_i} and T_{L_i}, from an isotropic assumption by the relations:

$$\begin{cases} \sigma_u = \sqrt{\frac{2}{3}k} \\ T_L = \frac{2\sigma_u^2}{C_0\varepsilon} \end{cases} \quad \text{with} \quad C_0 = 4 \tag{3}$$

More complex turbulence models allow to take into account the anisotropy of turbulence and in particular, mean velocity and turbulence fields obtained with LES are better suited in this context than usual RANS simulations. Higher computation and storage cost which was previously prohibitive is now balanced by increasing computionnal capabilities.

Experimental set-up

The concentration levels investigated numerically in this study are compared to data from wind tunnel experiments led by Gamel et al. (2015) in the atmospheric dispersion wind tunnel of the Laboratoire de Mécanique des Fluides et d'Acoustique at the Ecole Centrale de Lyon in France, presented in Figure 3. It is a recirculating wind tunnel with a working section measuring 9 m long, 0.7 m wide and 1 m high, and it allows for a maximal wind speed of about 15 $m.s^{-1}$. The figure shows an overall sketch of the wind tunnel, as well as a row of 500 mm high Irwin spires and roughness elements, which allow to reproduce a neutral atmospheric boundary layer of height δ = 0.55 m. The latter are rods with square sections of side length of 15 mm, which are separated by 45 mm. An obstacle with a square section of side H = 0.1 m runs along the whole width of the wind tunnel, of 7H, as illustrated in Figure 2. It also shows a source is placed 1.5H downstream of the obstacle. It is a line source of ethane, which is a passive tracer. The non-intrusive velocity measurement instrumentation that are laser doppler anemometry and particle image velocimetry are used, and concentration levels are obtained with the fast flame ionizing detector technique. The Reynolds number reaches 10^5, confirming the turbulent nature of the flow.

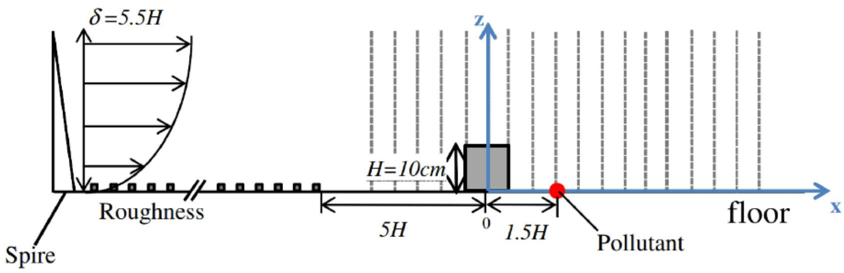

Figure 2 : Sketch of the experimental configuration (Gamel, 2015).

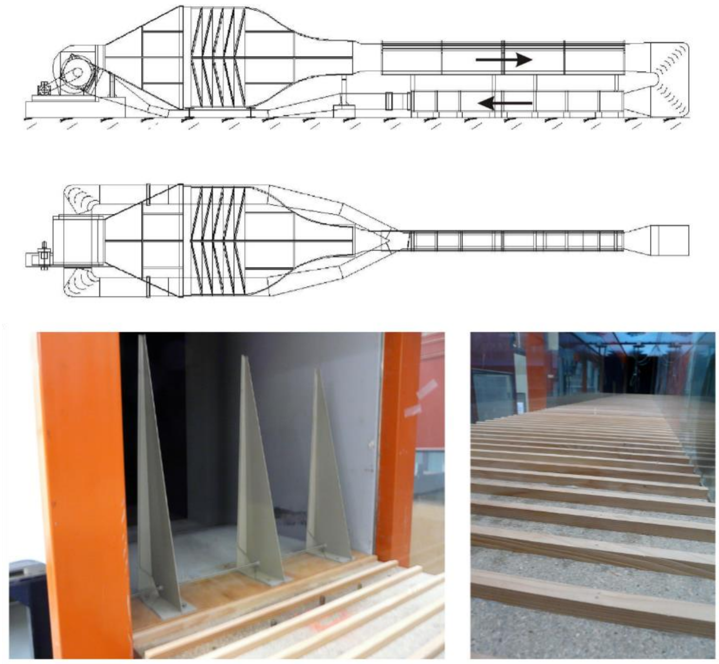

Figure 3 : Sketch of the wind tunnel at LMFA (Gamel et al. 2015) (top) and pictures of the Irwin spires and roughness generators (bottom).

Coupling with LES simulations

As explained in the introduction, the operational model SLAM is coupled with LES simulations in order to better account for the effect of turbulence. The PALM model system is used for this (Maronga et al. 2020). It is an open source code developped at the University of Hannover, in particular for LES of the atmospheric boundary layer, as well as oceanography. The non-hydrostatic, filtered incompressible Navier–Stokes equations in Boussinesq-approximated form at formally infinite Reynolds number, neglecting molecular viscous stress, are used with an advection–diffusion equation for the transport of a passive scalar. They are solved for six prognostic variables: the three velocity components, potential temperature, SGS turbulence kinetic energy and a passive scalar.

The use of such LES mean flow fields in SLAM is investigated for the bi-dimensional academic configuration described in the previous section, with a passive scalar source behind an obstacle in neutral atmospheric conditions. The numerical domain is 6*H* high, 7*H* wide, 23*H* long and the obstacle is placed 6.5*H* downstream. Figure 4 represents the mean flow obtained through both RANS and LES simulations. It shows separation of the flow and the recirculation zones are strongly affected by the simulation type, which in turn has an impact on concentration levels. These levels resulting from the use of both RANS and LES mean flow fields are compared, as well as those obtained directly from LES with dispersion, and from a wind tunnel experiment.

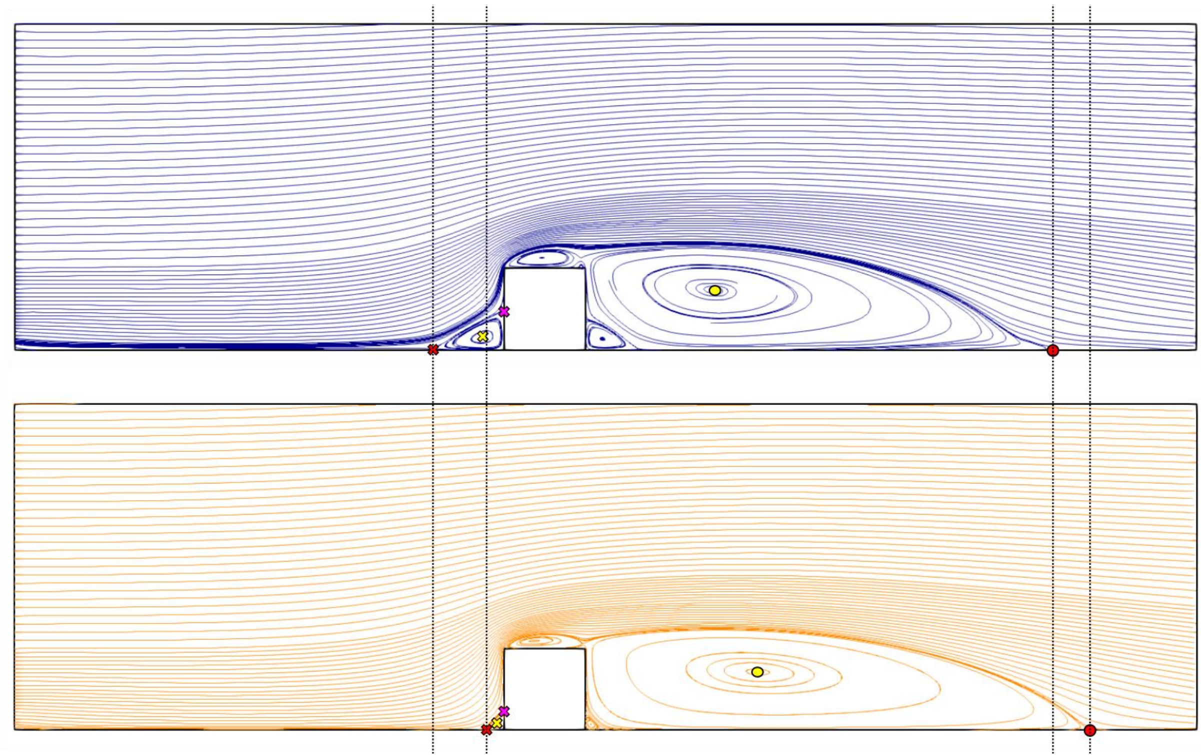

Figure 4 : Streamlines from RANS (orange) and LES (blue).

Gamel, H., 2015: *Caractérisation expérimentale de l'écoulement et de la dispersion autour d'un obstacle bidimensionnel.* Doctoral dissertation, Ecully, Ecole centrale de Lyon.

Maronga, B., Banzhaf, S., Burmeister, C., Esch, T., Forkel, R., Fröhlich, D., ... & Raasch, S., 2020: Overview of the PALM model system 6.0. *Geoscientific Model Development*, *13*(3), 1335-1372.

Thomson, D.J., 1987: Criteria for the selection of stochastic models of particle trajectories lagrangian dispersion model in turbulent flows. Journal of Fluid Mechanics, 180, 529-556.

Vendel, F., G. Lamaison, L. Soulhac, L. Donnat, O. Duclaux and C. Puel, 2010: A new operational modelling approach for atmospheric dispersion in industrial complex area. 13th Int. Conf. on Harmo. within Atmos. Disp. Modell. for Regul.Purposes, Paris, France

Lattice-Boltzmann Large-Eddy Simulations of the flow field and dispersion around a bidimensional obstacle

S. Fellini[1], G. Lamaison[2], E. Lévêque[3], P. Salizzoni[2], L. Soulhac[1]

[1]Univ Lyon, INSA Lyon, CNRS, Ecole Centrale de Lyon, Univ Claude Bernard Lyon 1, LMFA, UMR5509, 69621, Villeurbanne France
[2]Univ Lyon, Ecole Centrale de Lyon, CNRS, Univ Claude Bernard Lyon 1, INSA Lyon, LMFA, UMR5509, 69130, Ecully France
[3]Univ Lyon, CNRS, Ecole Centrale de Lyon, Univ Claude Bernard Lyon 1, INSA Lyon, LMFA, UMR5509, F-69130, Ecully, France

Abstract

Flow and dispersion dynamics in the urban atmosphere are characterized by the complex interaction between the atmosphere and the urban geometry, consisting of buildings, vegetation, and infrastructure. Furthermore, in cities, the concentration of human activities is responsible for pollution and heat emissions that are characterized by high spatial and temporal heterogeneity. The investigation and understanding of these dynamics is essential to address crucial aspects related to the urban microclimate (wind, humidity, temperature) and the air quality.

Today, the main investigation techniques are experiments and numerical simulations. Experiments allow to directly measure the turbulent flow field as well as to analyse the interaction of complex processes such as dispersion of pollutants and buoyancy effects due to solar heating. However, they provide limited spatial resolution and are used to analyse a small number of configurations (e.g., the number of geometries or external forcings). These two aspects are instead overcome by numerical approaches, and in particular by CFD (Computational Fluid Dynamics) simulations. In urban physics, most studies rely on RANS (Reynolds-averaged Navier–Stokes) simulations due to their low computational cost. For the analysis of dispersion processes and turbulent transfers, Large Eddy Simulations (LES) are more suitable as they resolve large scale turbulence. However, their great computational cost still makes them prohibitive for operational applications.

In this context, the Lattice Boltzmann Method LBM-LES approach is promising as it describes flow dynamics around complex geometries with a lower computational cost than traditional Navier Stokes approaches. Differently from Navier-Stokes equations, that macroscopically describe fluid motion, the LBM solves the Lattice Boltzmann (LB) equation which adopts a mesoscopic perspective (Kruger et al. 2015). The Boltzmann equation describes the behaviour of a collection of fluid particles by means of a distribution function, and their interactions by the BGK (Bhatnagar-Gross-Krook) collision operator. The discretized version of the Boltzmann equation is solved on a three-dimensional lattice. Once the distribution function is determined, the macroscopic density and velocity of the fluid can be easily derived. Moreover, the LES technique can be implemented in the LB equation: eddies smaller than the grid mesh are modelled by using the Smagorinsky subgrid viscosity model. To solve the conservation equations for species (passive scalar transport), an additional superimposed lattice is considered. Alternatively, a hybrid approach is adopted where the species conservation equation is solved using a standard finite volume method (Feng et al. 2019)

The LBM formulation makes the technique inherently parallel. Moreover, the use of the immersed boundary method allows to reduce the preprocessing time in the presence of complex geometry. For these reasons, in the last decade, the technique has found application in the field of urban climate and pollution. Recent applications concern the investigation of the link between urban morphology and pedestrian comfort (Ahmad et al. 2017, Jacob and Sagaut, 2018), the dispersion of pollutants in complex urban environments (Merlier et al. 2019), and in vegetated street canyons (Merlier et al. 2018).

To further examine the suitability of the method for urban applications, we evaluate in this work the performance of the LBM in predicting the velocity field and the turbulent dispersion in a boundary layer flow that develops over urban-like geometries. This is achieved by performing LBM-LES simulations using the software ProLB (CS, 2018). ProLB software is developed within an industrial and academic consortium including CS-GROUP, Airbus, Renault, Ecole Centrale Lyon, Aix-Marseille University and CNRS.

As a first step, we test the development of the turbulent boundary layer on a flat plate. We observe boundary layer indicators such as the boundary layer thickness, the logarithmic mean velocity profile, and the profiles of turbulent velocity fluctuations. The results are compared with classic experimental studies and DNS simulations.

The fully development of the turbulent boundary layer requires a long adaptation region and thus unfeasible computational cost for application to real urban geometries. This raises the necessity to inject synthetic turbulence at the entrance of the computational domain. To this aim, a tailor-made condition for synthetic inlet turbulence is implemented in the simulations. The condition is based on the method proposed by Shur et al. (2014). Velocity fluctuations are generated as a superimposition of weighted spatiotemporal Fourier modes with amplitudes designed to reproduce the actual Reynolds stress tensor. We compare the results provided by the inlet turbulent condition with those obtained from the simulated development of the boundary layer.

We then move to an idealized building geometry, and we simulate the flow around a two-dimensional obstacle. This configuration is used to assess the performance of the LBM simulation in reproducing flow recirculation around an obstacle. These circulating structures are common in the urban environment and are generated by the interaction of the wind with buildings. Furthermore, they play a fundamental role in dispersion dynamics as they can trap pollutants released at street level and delimit regions with high concentration.

The numerical results are compared with measurements from a detailed experimental characterization performed in the wind tunnel of the Ecole Centrale de Lyon. In the experiment, the flow field is measured by means of a Hot Wire Anemometer. The results show that the simulations are able to reproduce the mean velocity field (Figure 1). Furthermore, the turbulent flow field is tested with and without the application of the synthetic inlet turbulence condition.

In the last part of this work, we simulate the dispersion of a passive scalar behind the obstacle. In the wind tunnel experiment, ethane (acting as a passive tracer) is released by a line source at ground level. The concentration field is measured by means of a Flame Ionisation Detector. In ProLB, pollutant dispersion is simulated using temperature as a passive scalar. The source is reproduced as a surface (with extension equal to that of the linear source used in the experiment) at fixed temperature $T_S = T_{ref} + \Delta T$, where T_{ref} is the reference temperature and ΔT is the temperature rise at the source. A suitable non-dimensionalization of the concentration in the experiment and of the temperature in the simulation is implemented to compare the results obtained with the two techniques. Results show a good agreement between simulations and measurements for the mean concentration field. Moreover, the concentration variance and turbulent mass fluxes are assessed.

This study confirms that the LBM technique is suitable for reproducing dispersion around building-like geometries, while allowing the use of fine spatial and temporal resolution thanks to the computational efficiency. Future studies aim to simulate the effects of buoyancy due to heating of building surfaces and reproduce the flow and dispersion field in more realistic urban geometries in order to create a large dataset of numerical results for research purposes.

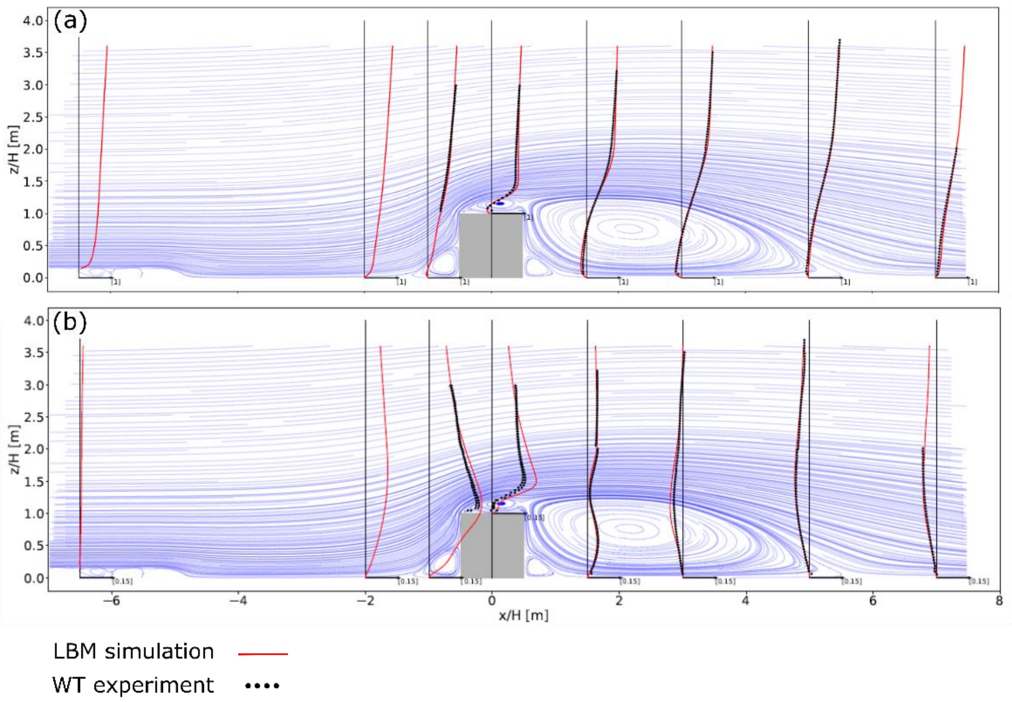

Figure 1: Comparison between the results from LBM simulations (red line) and measurements from the wind tunnel experiment (black dots). (a) Mean horizontal velocity. (b) Mean vertical velocity.

References

Ahmad, K., Khare, M., & Chaudhry, K. K. (2005). Wind tunnel simulation studies on dispersion at urban street canyons and intersections—a review. Journal of Wind Engineering and Industrial Aerodynamics, 93(9), 697-717.

CS, ProLB (2018). URL http://www.prolb-cfd.com/.

Feng, Y., Boivin, P., Jacob, J., & Sagaut, P. (2019). Hybrid recursive regularized lattice Boltzmann simulation of humid air with application to meteorological flows. Physical Review E, 100(2), 023304.

Jacob, J., & Sagaut, P. (2018). Wind comfort assessment by means of large eddy simulation with lattice Boltzmann method in full scale city area. Building and Environment, 139, 110-124.

Krüger, T., Kusumaatmaja, H., Kuzmin, A., Shardt, O., Silva, G., & Viggen, E. M. (2017). The lattice-Boltzmann method. Springer International Publishing, 10(978-3), 4-15.

Merlier, L., Jacob, J., & Sagaut, P. (2018). Lattice-Boltzmann Large-Eddy Simulation of pollutant dispersion in street canyons including tree planting effects. Atmospheric Environment, 195, 89-103.

Merlier, L., Jacob, J., & Sagaut, P. (2019). Lattice-Boltzmann large-eddy simulation of pollutant dispersion in complex urban environment with dense gas effect: Model evaluation and flow analysis. Building and Environment, 148, 634-652.

Shur, M. L., Spalart, P. R., Strelets, M. K., & Travin, A. K. (2014). Synthetic turbulence generators for RANS-LES interfaces in zonal simulations of aerodynamic and aeroacoustic problems. Flow, turbulence and combustion, 93(1), 63-92.

The influence of building structures on ground level air movement and pollutant input in courtyards

F. Harms[1], T. Szyszka[1], B. Leitl[1]

[1]EWTL, Meteorological Institute, University of Hamburg, Bundestrasse 55, D-20146, Germany

Abstract

The present study analyses flow and dispersion processes in urban areas, with a focus on air exchange between street canyons and courtyards. Particularly the effect of gateways and different building shapes was investigated by systematic wind tunnel measurements. The goal of the study was to identify parameters, which influence the air quality in inner courtyards.

Introduction

Buildings with inner courtyards are quite common for residential areas in many central European cities. They often consist of one or more green spaces that can be used by the residents of the surrounding buildings. "However, considering that courtyards represent enclosed cavities, they are often poorly ventilated spaces and pollutants from neighbouring traffic, once entrained, can pose a serious threat to human health" (Gronemeier and Sühring, 2019). Hence, many different studies have been carried out to better understand urban ventilation processes and to implement such processes in development plans for a healthier urban climate (Song et al. ,2018); Wu and Kriksic, 2012; Allard et al. ,2010).

In cities in general, there is no standard form of building structure enclosing an open space. Thus, urban blocks can differ greatly in their extension and shape. Openings of different sizes can lead into the inner courtyard, such as gateways, street entrances or a missing house in a perimeter block development. In addition, there is a wide range of diversity in roof shapes and building heights. Thus, many geometric aspects can affect the flow within a courtyard. As a result, it is difficult to perform flow or concentration measurements within two almost identical courtyards to determine the cause of measurement differences between both courtyards. A more effective comparison of different courtyards can thus be carried out using idealized urban geometries. This allows to control the composition of the surrounding buildings of the observed courtyards. Selected parameters such as a gateway into the courtyard can also be adjusted individually, while the remaining structure of the building stays the same.

Methodology

All measurements were carried out in the EWTL boundary layer wind tunnel facility 'Blasius' at the University of Hamburg. The 16 m long wind tunnel provides a 10.7 m long test section equipped with a turntable and an adjustable ceiling. The cross section of the tunnel measures 1.5 m in width and 1.1 m in height. For each wind tunnel campaign, a neutrally stratified model boundary layer flow was generated by a carefully optimized combination of turbulence generators at the inlet of the test section, and a compatible floor roughness.

The influence of gateways and differently shaped roofs to the air quality in courtyards was tested during the measurement campaign. Therefore, an idealized urban geometry comprising 38 simplified buildings in the scale of 1:500 was mounted in wind tunnel (Figure 1). All building models are square-shaped with a square courtyard in the centre. The thickness of the building walls surrounding the courtyard is 11 m in full-scale. The total height of the building from the ground to the top of the roof is 20 m for all buildings.

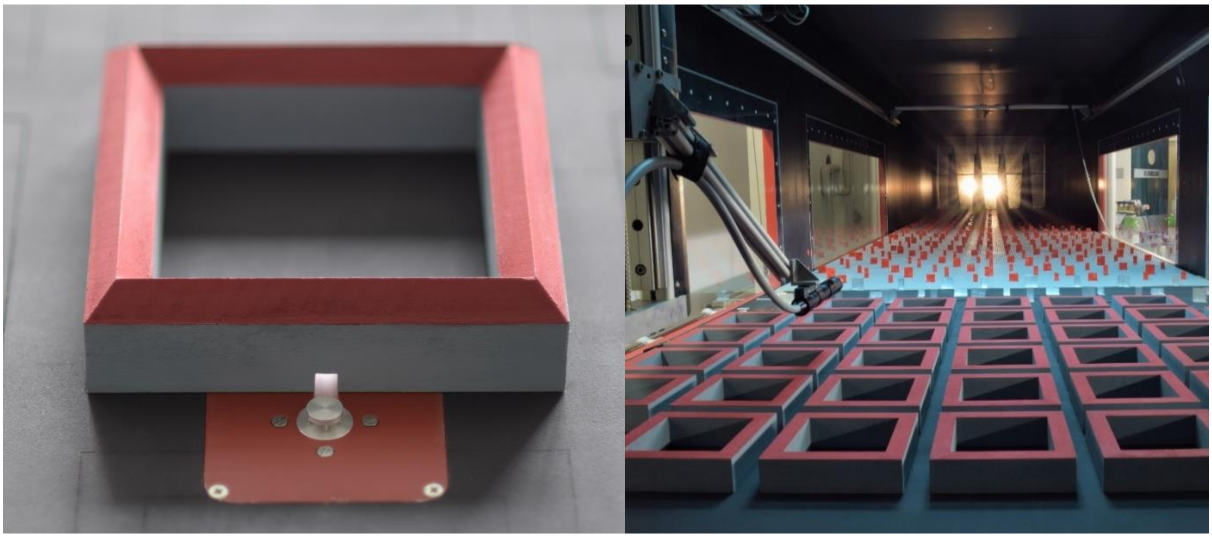

Figure 1: Gable roofed building with the standard gateway behind a ground level source (left figure). Idealized urban roughness containing 38 buildings (right figure) mounted in the boundary wind tunnel Blasius at the University of Hamburg.

While the shape of 37 buildings was kept constant during the measurement campaign, the layout of the central building was changed systematically. Figure 2 shows the three different roof shapes (a flat roofed building, a mansard roofed building and a gable roofed building) which were used.

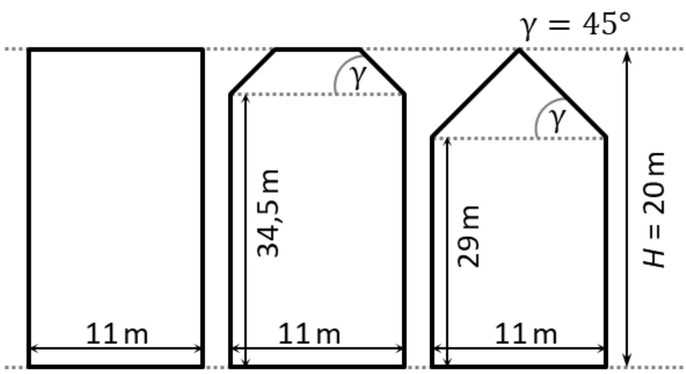

Figure 2: Side view of a flat roofed building (left), a mansard roofed building (middle) and a gabel roofed building (right). All sizes are given in full-scale.

For one building per roof type, a quadratic opening is located in the middle of one side of the building (Figure 3, red, centre). This opening represents a gateway of 4 m by 4 m. Five flat roofed buildings are designed with different gateways (Figure 3). The position of the gateway is varied in the way that the gateway is shifted once by 13.5 m to the left and once by 27 m to the left. In addition to this predominant gate shape, the gateway size is changed for three buildings. The smallest gateway meets the minimum requirements of a fire lane gateway according to DIN 14090:2003-05 as cited in Baunormenlexikon (2005) with 3 m in width and 3.5 m in height. Additionally a large opening of 10×10 m and a complete vertical opening with a width of 10 m was modelled. The lateral and longitudinal distance between all building exterior walls is 30 mm, which corresponds to 15m in full-scale.

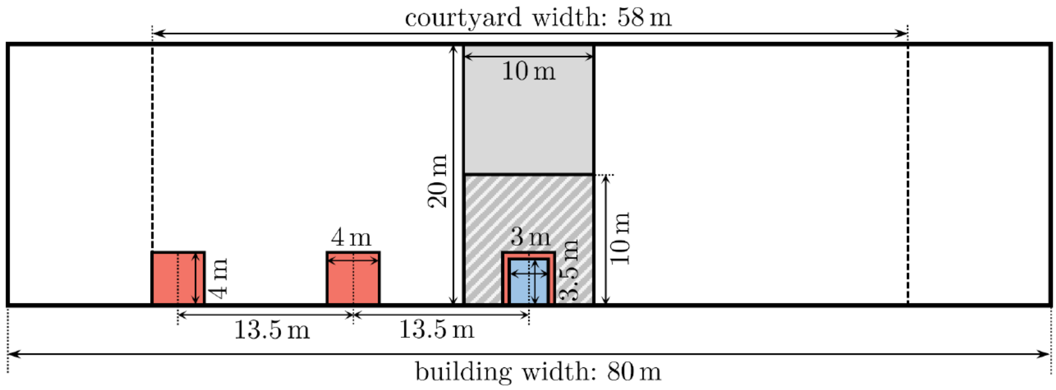

Figure 3: Front view of a courtyard building with all gate variations. Gates of the same dimensions are marked in the same color. All sizes are given in full-scale.

The measurement points investigated within each courtyard are the same for the flow and concentration measurements. Within a courtyard, two measurement grids are distinguished. A detailed grid consisting of five lateral times six longitudinal measurement points (see Figure 4, all circles) is used for the flat roof cases with and without the standard gateway. Except for the first two lateral rows, the distance between all points is equidistant (10 m full-scale). The points of the first lateral row have a distance of 5 m to the leeward wall as well as to the downstream lateral measurement row. The point distance in the lateral direction is 10 m. This grid serves to determine the general wind and concentration field in a courtyard as well as the influence of a simple gateway on the flow and the input of pollutants in a courtyard. For the remaining cases under investigation, a coarser grid of 3 × 3 measuring points, with a distance of 20 m full-scale between the individual points orthogonally was applied (see Figure 4, gray-filled circles). At each point, time series of three minutes (model-scale) were recorded for the flow measurements.

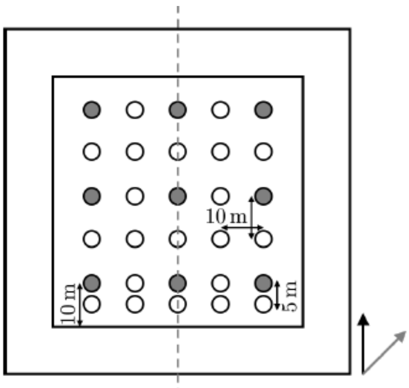

Figure 4: Top view of a courtyard. The circles indicate the measuring point positions 2m above the ground. The total points show the detailed 6 × 5 grid and the filled points the 3 × 3 grid. The dashed line represents the courtyard center axis. The arrows to the right of the courtyard represent the wind direction: black normal inflow and gray wind rotation of 45°. Measures are given in full-scale.

A 2D Laser-Doppler-Anemometry (LDA) System was used to measure component-resolved flow data at sampling rates of 100 – 500 Hz (model scale), resolving even small-scale turbulence in time. Reference wind speed was permanently monitored close to the tunnel inlet through Prandtl tube measurements.

For concentration measurements Ethane was used as tracer gas and emitted from ground-level point sources. A Fast Flame Ionization Detector (FID) measured concentration time series with 140 Hz resolution (model scale) at selected measurement locations. The background concentration was constantly monitored with an additional FID. Measurement devices were checked and calibrated frequently to maintain a high accuracy of measured data.

Selected results

In this chapter, the influence of gateways to the flow and concentration field in courtyards is shown for flat roofed buildings.

Figure 6 shows wind roses measured at 2 m height above ground (full-scale) for the scenarios Cf (flat roofed building without gateway) and scenario Gf (flat roofed building with a 4 m x 4 m gateway). The two scenarios are displayed in figure 5. A clear main axis symmetry for the wind distribution over both courtyards can be seen (Figure 6). On average, the general shape of this pattern differs only slightly between the two cases.

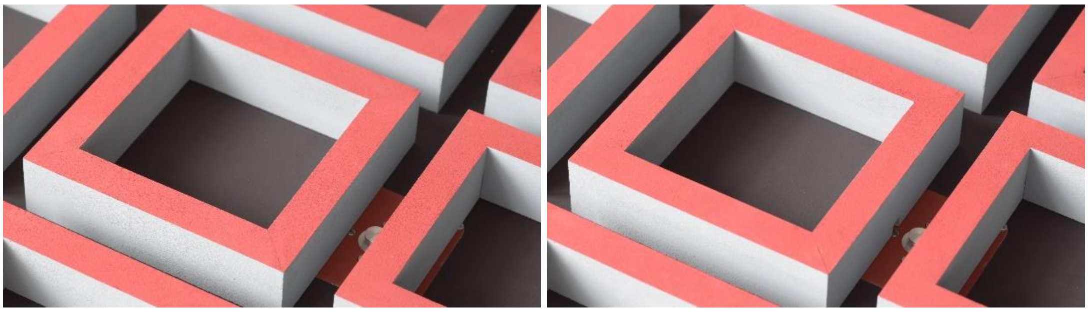

Figure 5: Flat roofed building without gateway (scenario Cf; left picture) and with a 4m x 4m gateway (scenario Gf; right picture).

For both cases, an increase of the mean wind speed downwind of the courtyards are observed. The maximum mean wind speed is reached at a longitudinal distance of about 2H from the courtyard front. On average, the longitudinal increase in the mean wind speed from 0.25H to 2H distance to the front is about 0.21 (−).

The predominant wind direction within the courtyard differs significantly from the inflow direction. In the rear half of the courtyard the mean horizontal wind direction meaured in 2 m height above ground is rotated by 180° regarding the average wind direction above building height. Towards the central axis a bimodal distribution of the wind direction was measured.

The flow pattern in the courtyard within the flat roof building with the standard gateway (Gf) generally differs only slightly from the reference scenario Cf. When comparing the wind directions, the center axis point at the longitudinal distance of 0.25H to the front stands out clearly. Two predominant wind directions can be found in case Cf. In addition, a third main wind direction is measured, corresponding to the inflow, so that a trimodal wind direction distribution is observed for case Gf. The mean wind speed increases by more than 6% at this measurement location. This increase is also evident as an increase in the skewness of the wind speed distribution.

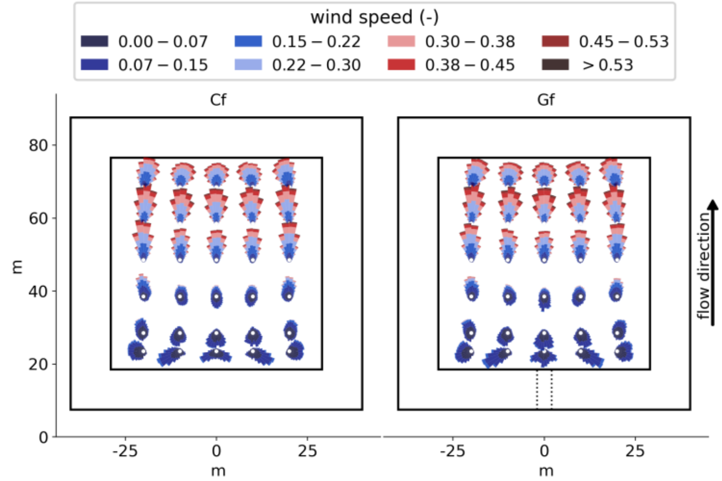

Figure 6: Wind roses at normal inflow at 2m height (full-scale) for the cases Cf (left) and Gf (right).

Results for the concentration measurements for the scenarios Cf and Gf are shown in Figure 7. In both cases the highest concentrations for the 50th percentile were measured near the front wall on the center axis of the courtyard. A general decrease in the 50th percentile of the concentration towards the side walls and with the inflow was measured for each scenario.

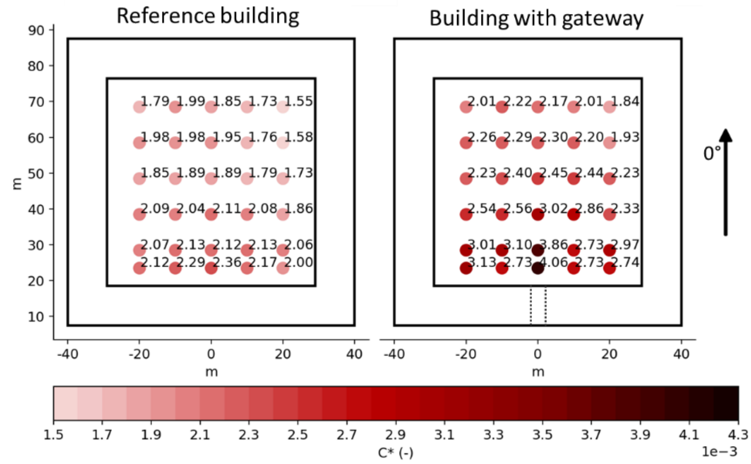

Figure 7: 50th percentiles of dimensionless concentrations for case Cf (left) and Gf (right). The values applied to the points denote 50th percentile · 10−3 (−) at the respective measuring point.

Comparing the scenarios Cf and Gf, higher concentration were measured for scenario Gf, were a gateway connects the courtyard with the surrounding street. This is true for all measurement locations. The differences of the measured 50th percentile are larger than the detected measurement uncertainty. The largest relative deviation in the 50th percentile of the concentration with respect to Cf is about 83%.

For all analysed gateway sizes, an increase in the 50th percentile with reference to Cf is measured in almost all points (see Figure 8). This increase generally is the largest in the front courtyard area.

A bigger gateway size leads to higher concentrations in the courtyard. While the small, fire-lane entrance leads to an increase in the 50th percentile of approx. 14%, the selected standard gateway results in an increase of about 30%. The large gateway leads, in the case Gf-sV, to an increase of about 58% and the complete breakthrough to about 112% in the 50th percentile.

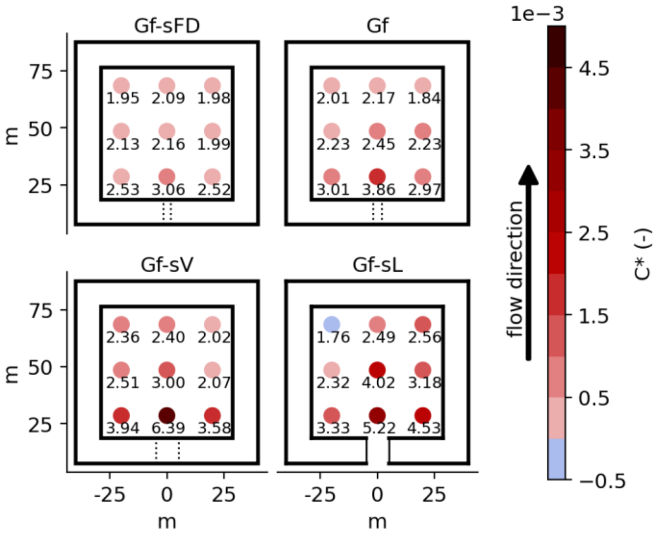

Figure 8: Differences of the 50th percentile of the dimensionless concentrations for cases with different gateway sizes with reference to the case Cf. The values applied to the points denote 50th percentile · 10−3 (−).

The largest change in the 50th percentile is observed in the point closest to the openings. However, the increase in the 50th percentile with increasing gateway size can only be observed for the cases with a continuously closed roof.

Summary

The aim of this work is to quantify the impacts of different gateway and roof shapes on the ground-level horizontal wind and mean concentration field within a courtyard. Various building structure alterations were made in order to investigate their influence on the flow and concentration field in the courtyard. Thereby, the focus was set to the relative differences to the reference building Cf. The first step in this regard was a simple gateway. In Gf the gateway is located in the front wall, upstream of the area where the two recirculating horizontal vortices meet in Cf (see Figure 6). Due to the tunnel-shaped opening, the current flowing towards the building is restricted in its space if it does not change its direction. As there is a road in front of the gateway and not a solid boundary restricting the flow, the current is not forced to pass through the gateway completely. The question arises whether any air at all passes through the gateway into the courtyard or whether air from the courtyard passes through the gateway into the street canyon due to the vortex within the courtyard. Near the gate, a change in the wind distribution is measured in the courtyard (see Figure 6). The gates influence can be seen more clearly, the closer a measurement point is to the gate, especially in the wind direction distribution. When comparing the horizontal flow pattern of case Cf and Gf, it becomes clear that a part of the flow enters the courtyard through the gate. In addition, the wind speed increases in the direct vicinity of the gateway in Gf compared to Cf. However, it decreases quickly with distance from the gateway in longitudinal direction. By the time, the flow is leaving the gateway, the available space for the flow becomes larger and the flow is slowed down accordingly. The increased wind speed compared to Cf is almost only evident in the u component of the flow velocity. This supports the conclusion that the gateway is the reason for the increase in the mean wind speed and that air enters the courtyard through the gate.

With reference to Cf, an increase in concentration in the courtyard in the vicinity of the gateway can be clearly seen in Gf. The highest concentrations directly downstream of the gateway indicate a direct pollutant transport through the gate. The fact that the concentration decreases significantly more towards the laterally adjacent measuring points than in the longitudinal direction reflects the flow pattern near the gate. A similar concentration distribution can also be seen in the study by Gronemeier and Sühring (2019). The pollutants entering through the gateway do not directly mix completely with the air in the courtyard, but are initially transported with the flow slightly into the courtyard. Not only due to the direct flow entering through the gate, but also supported by the two horizontal recirculating eddies, the concentration in the front area of the courtyard is higher than in the rear area. This also shows that a higher pollutant input into the courtyard occurs through the gateway than over the roof with a pollutant source directly upstream of the gate.

Another point of investigation is the influence of different gateway sizes on the near-ground flow and concentration. For this purpose, the flat roof basic building with the gateway position in the front centre is altered. Differences can already be observed between the two smallest gateway openings. All four flat roof cases with different sizes of the gateway in the front of the building show an increase in the wind speed near the gate. The larger the opening, the stronger the increase in the 50th percentile of the concentration in the courtyard (see Figure 8). This applies in particular to the centre of the courtyard. In the immediate vicinity of the gate, where the strongest effects in the 50th percentile are generally seen, this increase is only visible for the three gateway sizes excluding the complete vertical opening. However, for the case Gf-sL the increase in the concentration in the centre to Gf-sV is proportionally larger than in the smaller gateway enlargement steps. This suggests that in the case Gf-sL the concentration is transported immediately further into the courtyard. The present study shows that the shape of the surrounding building affects air quality in urban courtyards. Gateways connecting the courtyard with an adjacent street lead to higher concentrations in the courtyard. This is especially true for the area near the gateway.

Further studies need to be conducted for different building and source configuration to verify that the findings of the present study are generally true. In this study a point source was placed only in a central location upstream of the analysed building. A line source placed in the street canyons surrounding the courtyard could further help to understand the parameters influencing air quality in courtyards.

Reference

Allard, F., Ghiaus, C. and Szucs, A. (2010), 'Natural ventilation in high-density cities', Designing High-Density Cities for Social and Environmental Sustainability.

Baunormenlexikon (n.d.), 'DIN 14090 | 2003-05, Flächen für die Feuerwehr auf Grundstücken'. Accessed: July 01, 2021 at 13:25. URL: https://www.baunormenlexikon.de/norm/din-14090/ce645ce8-8b82-4a96-839b-142154d6ead0

Gronemeier, T. and Sühring, M. (2019), 'On the effects of lateral openings on courtyard ventilation and pollution—a large-eddy simulation study', Atmosphere 10, 63.

Song, J., Fan, S., Lin, W., Mottet, L., Woodward, H., Davies Wykes, M., Arcucci, R., Xiao, D., Debay, J.-E., Apsimon, H., Aristodemou, E., Birch, D., Carpentieri, M., Fang, F., Herzog, M., Hunt, G., Jones, R., Pain, C., Pavlidis, D. and Linden, P. (2018), 'Natural ventilation in cities: the implications of fluid mechanics', Building Research and Information 46, 809–828.

Wu, H. and Kriksic, F. (2012), 'Designing for pedestrian comfort in response to local climate', Journal of Wind Engineering and Industrial Aerodynamics s 104–106, 397–407.

PHYSMOD 2022 – International Workshop on Physical Modeling of Flow and Dispersion Phenomena
Institute of Thermomechanics of the CAS, Prague, Czech Republic – August 29-31, 2022

Prediction of turbulence generated by non-homogeneous grids for applications to experimental atmospheric boundary layer generation

HURET Thomas[1], VASSILICOS Christos[1], TANGUY Geoffrey[1], JACQUIN Laurent[2], GALLAS Quentin[3]

[1] Univ. Lille, CNRS, ONERA, Arts et Métiers Institute of Technology, Centrale Lille, UMR 9014 –LMFL – Laboratoire de Mécanique des Fluides de Lille –Kampé de Fériet, F-59000 Lille, France
[2] DAAA, ONERA, Université Paris-Saclay, F-92190 Meudon –France
[3] ONERA–The French Aerospace Lab, 31410 Mauzac, France

1. Introduction

1.1 The neutral Atmospheric Boundary Layer (ABL)

The present work focuses on the experimental generation of neutral ABL over flat surfaces of homogeneous roughness, quantified by the "roughness length" h_0. This quantity is defined through the mean velocity profile obtained in the Inertial SubLayer (ISL) of the ABL [1,2,3].

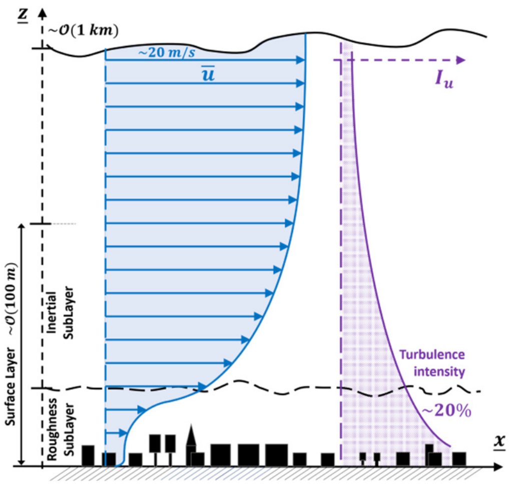

Figure 1: Schematic visualization of the neutral Atmospheric Boundary Layer. Based on [3,4].

The ISL is characterized by a logarithmic dependency of mean velocity with the altitude [3] (see Figure 1), as described by the equation:

$$\overline{u}(z) = \frac{u_*}{\kappa} \ln\left(\frac{z-d}{h_0}\right) \tag{1}$$

The friction velocity u_* is defined as $u_* := \sqrt{\frac{\tau_{friction \to wall}}{\rho}} \approx \sqrt{-\langle u'w' \rangle_{wall}}$ and $\kappa \sim 0.4$ will be considered while the displacement height d will be neglected.

The generation of atmospheric boundary layer within short aeronautic wind tunnels requires to thicken artificially the otherwise naturally growing rough-wall boundary layer. Several attempts were made to achieve this boundary layer thickening with both passive or active devices [5]. The successful Counihan-type passive configurations [6] inspired Cook (1978) [7] who presented a family of devices, named as "Roughness-Barrier-Mixing device method" (RBM), for which were suggested a general understanding of the flow generation.

However, almost all present passive devices require a trial-and-error step in their design process, which must be reproduced for each new studied configuration (i.e. new roughness condition) and each new wind tunnel setup. This was observed by Cook (1978) [7] who undertook a parametric analysis on their devices to relate the effective roughness length and integral length scales to their geometric parameter (the height of the wall component).

1.2 Objectives

The present work aims at investigating Multiscale Inhomogeneous Grids (MIGs) [8] as a new type of passive device for wind tunnel generation of ABL flows. This type of grids is expected to enable the tailoring (almost without trial-and-error) of both mean flow profile and turbulent intensity profiles with potentially no trial-and-error process. Indeed, these devices takes advantage of tools developed initially for fractal grids studies and enabling to predict turbulent intensity.

The first section describes the different considered ways to design a grid for a given mean flow profile. The two following sections presents respectively the considered wind tunnel setup and the different MIGs designed for this work. The resulting mean flow and streamwise turbulent intensity profiles are then analysed. The last section introduces the tools used for the current development of the turbulence prediction model.

2. Development of a grid design algorithm for mean flow tailoring

2.1 Multiscale Inhomogeneous Grids

Multiscale Inhomogeneous Grids are composed of regular arrays of vertical bars within several horizontal levels of varying geometric properties (w_n, g_n, h_n, as presented in Figure 3).

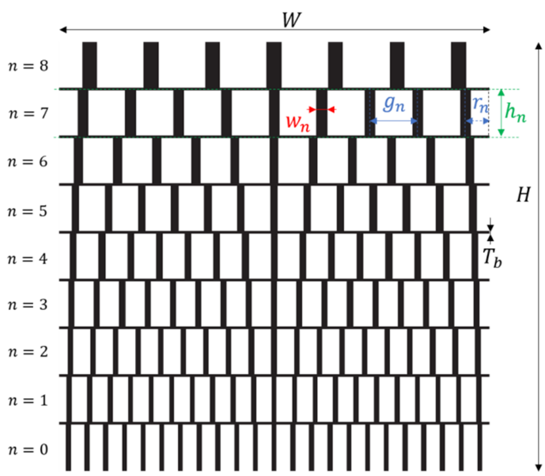

Figure 2: Several passive devices for the generation of a neutral ABL in wind tunnel

Notation	Definition
N	Number of layers
W	Width of the grid section
H	Height of the grid section
T_h	Width of the horizontal bars
d_h	Streamwise depth of the horizontal bars
h_n	Height of each layer (horizontal Bars center to center)
g_n	Distance between adjacent vertical bars (cent. to cent.)
r_n	Distance from the wall of the first vertical bar of the level
w_n	Width of vertical bars
d_n	Streamwise depth of vertical bars
c_n	Number of vertical bars
σ_n	Blockage ratio (solidity) of the layer

Table 1: Definition of the different geometric parameters of MIG grid.

2.2 Theoretical prediction of the mean flow profile

By varying the number of bars and their respective width at each level of the grid, it is possible to produce a non-uniform local blockage ratio field that generates a non-uniform pressure jump between the two sides of the grid [9,10,11,12]. This pressure jump is normalized as $K = (P_{0-} - P_{0+})/½\rho u_0^2$ in the following (see Figure 3 for notations). It produces a non-uniform pressure field upstream and downstream, both of which influencing the mean flow velocity. The grid geometry is therefore a way to convert the far upstream mean flow distribution $u^{-\infty}$ into a sheared mean flow far downstream $u^{+\infty}$ (see Figure 3).

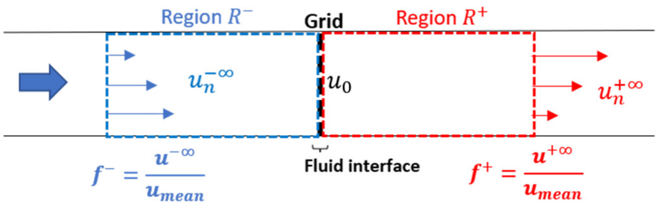

Figure 3: Schematic visualization of the upstream and downstream regions of influence of the grid within the wind tunnel. Inspired from [19]

Elder (1959) [11] and then McCarthy (1964) [12] suggested two different analytical formulations relating these far upstream and downstream mean flows with the grid geometric characteristics. Differences between these two reasonings consist in a different set of hypotheses for the analytical approximation of the main problem solution. Elder (1959) [11] derived a linearized theory with upstream flow and grid properties close to uniformity.

McCarthy (1964) model

McCarthy (1964) [12] considered the far upstream flow to be perfectly homogeneous ($du^{-\infty} = 0$ and $u^{-\infty} = u_{mean}$) so that the problem consists in solving a non-linear Ordinary Differential Equation (ODE) on $u^{+\infty}$ as a function of $\chi = \sqrt{1+K}$. This equation was solved analytically by approximating several integrals up to the second order (see [12]). The resulting relation, discretized over the N levels of the designed grid, is given in the first box of the schematic in Figure (4).

This non-linear coupled equation system is inverted by a Sequential Least Squares Programming (SLSQP) algorithm in order to find the $\{K_n\}_n$ distribution for a given objective function f_n^+.

A numerical solving model

In order to avoid the need for uniformity hypothesis (not perfectly valid due to upstream boundary layers at the wind tunnel walls), another method that we suggest consists in solving the analytical main equation from McCarthy (1964) [12] numerically. For prescribed normalized upstream and downstream mean flows, the main problem can be rewritten as an ODE on χ as a function of the altitude z. The resulting equation is given in the second box of the schematic in Figure (5), where $G_+(\chi) = 1 + \frac{\chi^2-1}{1+\frac{B}{\chi}}$; $G_-(\chi) = \frac{\frac{B}{\chi}(\chi^2-1)}{1+\frac{B}{\chi}} - 1$; $\mathcal{M}(\chi) = \frac{B}{\chi^2}\frac{\chi^2-1}{1+\frac{B}{\chi}}$ and $\mathcal{L}(\chi) = \frac{B}{\chi^2}\frac{\chi^2-1}{\left(1+\frac{B}{\chi}\right)^2} + \frac{\chi}{1+\frac{B}{\chi}}$.

The solution is numerically computed using a Runke-Kutta 4 (RK4) method. It is finally discretized by averaging over each grid level. A dichotomy algorithm is used to find the initial condition corresponding to the prescribed mean obstruction over the full section.

2.3 Grid design algorithm

Using the mean flow tailoring tools described above, a grid design algorithm was implemented in two versions depending of the modelling choice. They can be visualized schematically in Figure (4) and Figure (5) for the case of MIG grids. Choice was made to arbitrarily fix the distance g_n between two adjacent bars and the height of each grid level, since they represent extra-degrees of freedom that will become useful only for generating prescribed turbulence profiles.

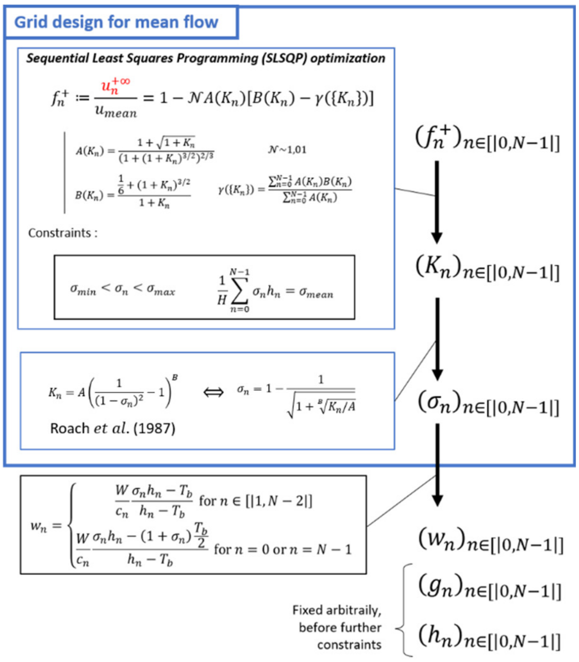

Figure 4: Schematic representation of the MIG design algorithm using the McCarthy (1964) [12] model. Relation between K_n and σ_n from [13]

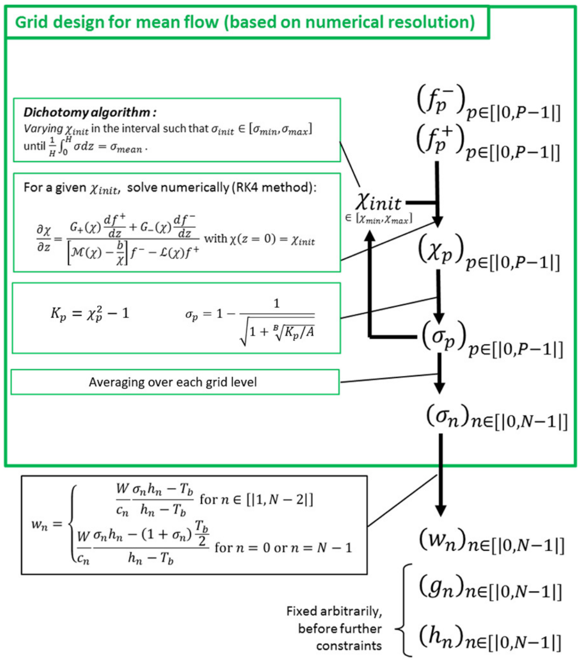

Figure 5: Schematic representation of the MIG design algorithm solving the main equation numerically through a RK4 method.

The design process for grids dedicated to the generation of a logarithmic mean flow is fully characterized by two input parameters: the mean blockage ratio σ_{mean} (averaged over the full wind tunnel section area) and the non-dimensional roughness ratio h_0/H.

3. Experimental setup

3.1 Hot-wire Anemometry in SCL-PIV wind tunnel (ONERA Lille)

The SCL-PIV wind tunnel (ONERA Lille) is dedicated to boundary layer studies. The working section of $H \times W = 0.29\,m \times 0.30\,m$ enables an exploration by both Hot-Wire Anemometry (HWA) and Particle Image Velocimetry (PIV). The operational velocity range is between $10\,m/s$ and $30\,m/s$. The current work presents HWA results obtained for a reference velocity of $U_{pitot} = 15\,m/s$ (global Reynolds number $Re = U_{pitot}H/\nu \sim 2.78 \times 10^5$).

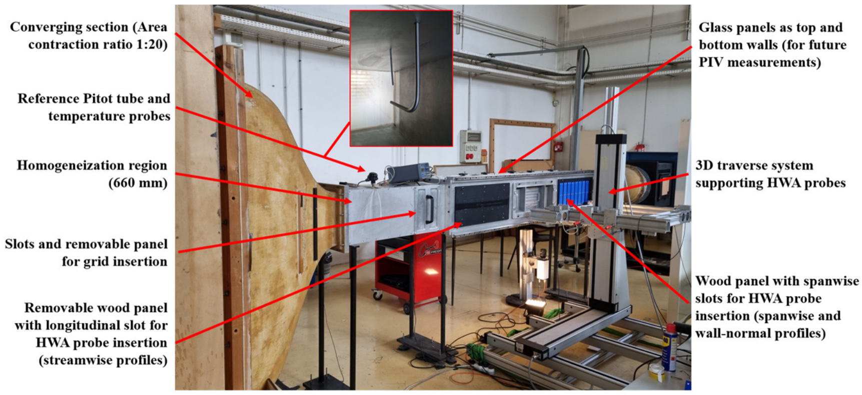

Figure 6: The SCL-PIV wind tunnel (ONERA Lille).

Two different Hot-Wire probes are considered: (i) a single Hot-Wire (Dantec 55P15) probe with frequency response up to very high frequencies for spectral studies and wall-vicinity studies, (ii) a X-cross Hot-Wires probe (Dantec 55R51) providing two velocity components and Reynolds stress measurements. For each acquisition point, a signal of $30\ s$ is acquired at $f_{acq} = 100\ kHz$ (Analog low-pass filter at $f_{cutoff} = 30\ kHz$). The current work presents results measured across the wall-normal profile visible in red in Figure (7), distant of $1950\ mm$ from the inserted grid.

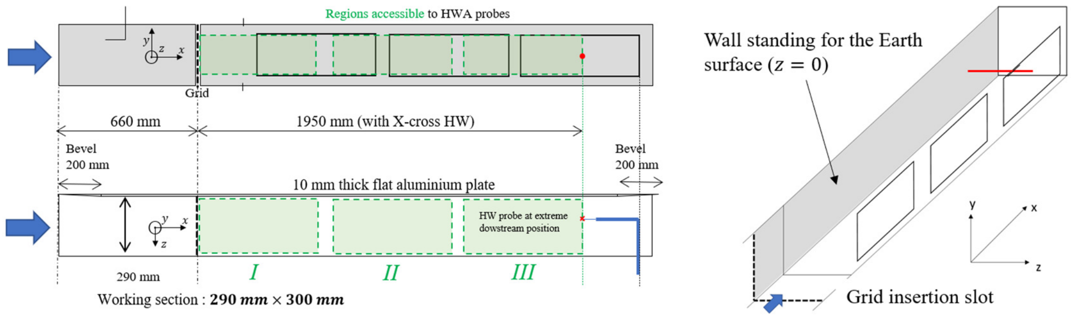

Figure 7: Schematic visualization of the wind tunnel working section. The studied profile is highlighted in red.

3.2 Roughness characterisation

In order to reproduce the surface layer of the ABL (see Figure (1)), the Jensen similarity criterium [14] requires that the "roughness length" h_0 of the considered terrain is represented at scale in the wind tunnel. By default, the wind tunnel is in a "smooth configuration" (flat aluminium plate with measured $h_0^{smooth} = 0.0025\ mm$ comparable to estimations from [15] at the considered Reynolds number). Adding LEGO® Baseboards on the flat plate leads to the "rough" configuration (characterized with $h_0^{LEGO} = 0.13$ mm, comparable with the estimation by Counihan (1969) [6]).

3.3 Definition of the 6 grids

In the present work, six different grids were designed in order to fit within the SCL-PIV wind tunnel (Fig. 8). The five first grids (a-e) are designed in order to generate the same logarithmic mean flow with an artificial roughness $h_0^{objective}/H = 4.5 \times 10^{-4}$ (compatible with the LEGO® Baseboard roughness). The grid (f) has a slightly higher artificial roughness input $h_0^{objective}/H = 10^{-3}$. All the grids, except the one in (d), are designed using the McCArthy (1964) [12] model. Grids (a-c) differs only in their prescribed distribution of levels, impacting the resulting design. The grid (d) is derived through numerical solving of McCarthy's main equation using a RK4 method. The configuration (e) is designed with the above grid design algorithm with removed horizontal structural bars and with a high number of levels (500). It is comparable in its principle with the "spires" introduced by Irwin (1981) [16].

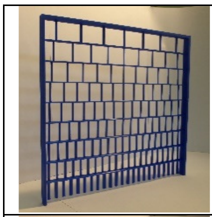	***(a) MIG-log-LEGO_N9*** 9 levels of same height. Designed with the McCarthy model (1964) [19]. $h_0/H = 4.5 \times 10^{-4}$. $\sigma_{mean} = 0.2$ $\sigma_{max} = 0.389$	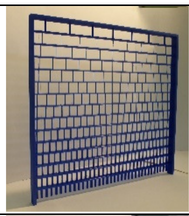	***(b) MIG-log-LEGO_N15*** 15 levels of same height. Designed with the McCarthy model (1964) [19]. $h_0/H = 4.5 \times 10^{-4}$. $\sigma_{mean} = 0.2$ $\sigma_{max} = 0.442$
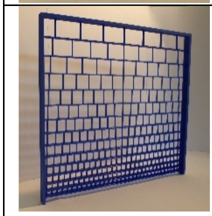	***(c) MIGnh-log-LEGO_N15*** 15 levels of increasing height (power law of the altitude). Designed with the McCarthy model (1964) [19]. $h_0/H = 4.5 \times 10^{-4}$. $\sigma_{mean} = 0.2$ $\sigma_{max} = 0.597$	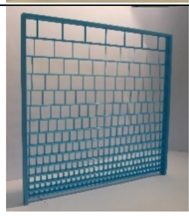	***(d) MIGnh-rk4-log-LEGO_N15*** 15 levels of increasing height (power law of the altitude). Designed with the numerical solving (RK4) of Equation (2) [19]. $h_0/H = 4.5 \times 10^{-4}$. $\sigma_{mean} = 0.2$ $\sigma_{max} = 0.630$
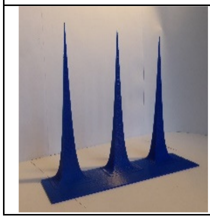	***(e) MIG-spires-log-LEGO_N500*** 500 levels. No horizontal bar. Only three vertical bars at each level, leading to three spires. Designed with the McCarthy model (1964) [19]. $h_0/H = 4.5 \times 10^{-4}$. $\sigma_{mean} = 0.2$	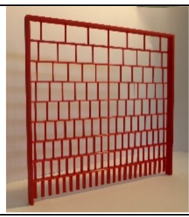	***(f) MIG-log-1e-3_N9*** 9 levels of same height. Designed with the McCarthy model (1964) [19]. $h_0/H = 10^{-3}$. $\sigma_{mean} = 0.2$ $\sigma_{max} = 0.413$

Figure 8: Main characteristics of the 6 grids designed using the algorithm of the previous section. The grids are all 3D printed in PLA with a 100% fill. $H = 290mm$.

4. First experimental investigations

4.1 Grid-generated mean flow profiles

The measurements by X-cross hot-wire at the wall-normal profile given in Figure 7 downstream of the grid *"MIGnh-rk4-log-LEGO_N15"* is presented in Figure (9). Similar conclusions can be drawn for the other grids (to the exception of the "*MIG-spires-log-LEGO_N500*").

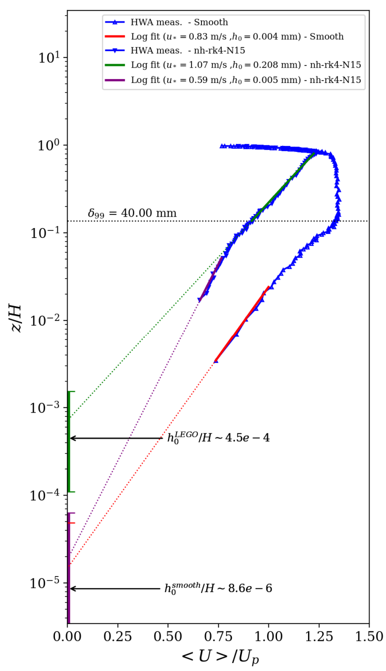

(a) Smooth wall configuration

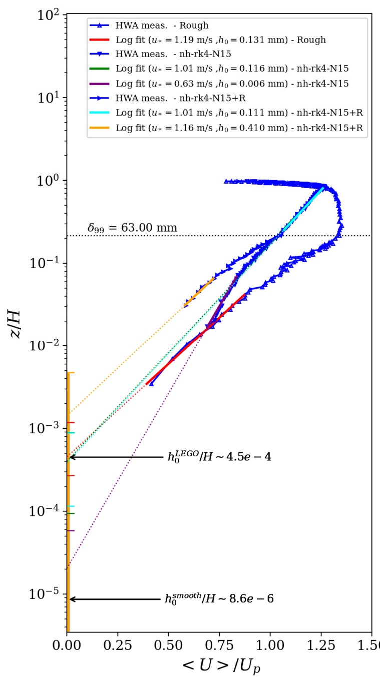

(b) Rough wall configuration

Figure 9: Mean longitudinal mean flow velocity profile measured at position $x = 1950\ m$ downstream of MIGnh-rk4-log-LEGO_N15.

In Figure (9a-b), two different regions are visible: a wall-region of approximately the same height as the natural boundary layer growing in empty vein configuration, and a center vein region (roughly between 0.2H and 0.8H). The profiles within these two regions are fitted by logarithmic laws in order to estimate their equivalent friction velocities and roughness lengths. The 95%-confidence intervals for the estimation of roughness length are presented as continuous lines on the x-axes in Figure (9).

Downstream of all the grids introduced above, the center vein region is shown to depend mainly on the grid characteristics, showing a good match with the expected mean flow profiles (i.e. the expected artificial roughness lengths).

The wall-region seems to remain almost entirely influenced by the wall itself. Surprisingly, the attempt of reaching roughness similarity lead to larger discrepancies, except for the “spires” configuration which shows a very good match with the expected mean flow even within the wall region. This reveals that the geometric differences between grid and spires have a significant influence on the interaction with roughness. This is probably due to the larger vortex structures produced by spires, which enable a coupling of flow layers over a significant range of altitudes (as explained by Cook (1978) [3]). Downstream of passive grids, turbulent structures scale with the mesh size (e.g. [17,18]) and are probably too small to produce the same mixing effect as spires.

4.3 Grid-generated turbulence intensity

The streamwise turbulence intensity measured at the same location for *“MIG-nh-rk4-log-LEGO_N15”* (d) and *“MIG-spires-log-LEGO_N500”* (e) are presented in Figure (10). Conclusions with the other grids are similar to the one with *“MIG-nh-rk4-log-LEGO_N15”*.

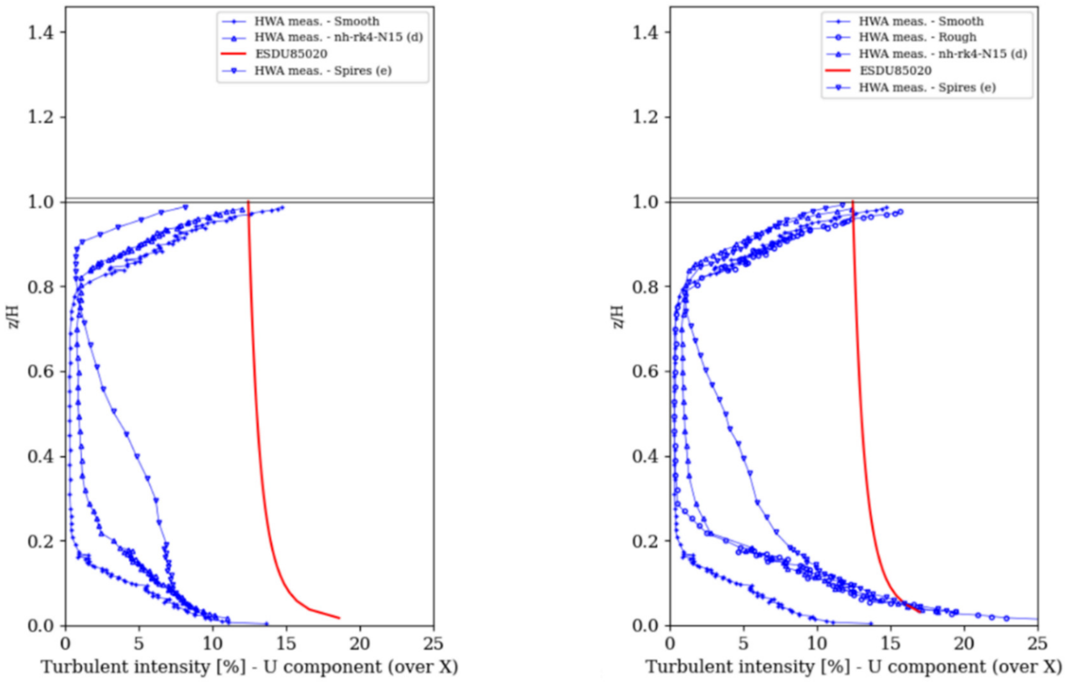

(a) Smooth configuration (b) Rough configuration

Figure 10: Streamwise turbulent intensity measured by HWA in SCL-PIV at the location of the “*IIIT9-Center*” profile. The profiles are compared to the ESDU85020 atmospheric model [19] adapted with the LEGO® Baseboard roughness length.

From Figure (10), the “Smooth configuration” presents a turbulence level too low compared to the atmospheric case even close to the wall. As expected, the turbulence intensity increases when roughness is added, even though no clear changes are visible in the grid-affected center region. Contrary to “spires”, which maintain high turbulence intensity far from the wall, the grid generated turbulence decay quickly to values smaller than 3%, in accordance with previous observations (Cook (1978) [3]). Such conclusion may be mitigated by the development a turbulence prediction model that could be taken into account within the grid design process.

5. Turbulence intensity model

5.1 Fractal grid-generated turbulence evolution

Previous studies focusing on the turbulence evolution downstream of fractal grids validated a scaling law (Equation (2)) relating turbulence intensity with the downstream distance [20].

$$\frac{\sqrt{2k}}{\bar{u}} = \frac{1}{\beta}\sqrt{\frac{C_d w_n}{x_*{}^{peak}}}\,\boldsymbol{g}\left(\frac{x}{x_*{}^{peak}},*\right) \tag{8}$$

Where $k = \frac{1}{2}\langle u'^2 + v'^2 + w'^2 \rangle$, $\beta \sim 2.88$ and C_d stands for the drag coefficient associated to one isolated grid bar. This scaling depends on the length scale $x_*{}^{peak}$ describing the position of the maximum of turbulent intensity. It can be interpreted as a characteristic streamwise interaction distance between two adjacent planar wakes. It is expressed as in Equation (9) (see [20]).

$$x_*{}^{peak} = \Gamma \frac{g_n{}^2}{\alpha C_d w_n} \tag{3}$$

Where $\Gamma \sim 0.21$ and $\alpha \sim 0.24$ are coefficients empirically deduced by Symes & Fink (1977) [21] and Gomes-Fernandes et al (2012) [20] respectively. The scaling of Equation (8) was experimentally validated for fractal and regular grids, as can be seen with the good collapse in Figure (12) obtained for several regular and fractal grids.

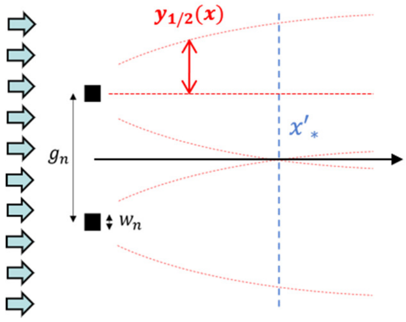

Figure (11): Two interacting wakes. By definition, $y_{1/2}$ is the spanwise distance at which the velocity defect is half of its maximum value. From planar wake theory, $x'_* = g_n^2/\alpha C_d w_n$ [20].

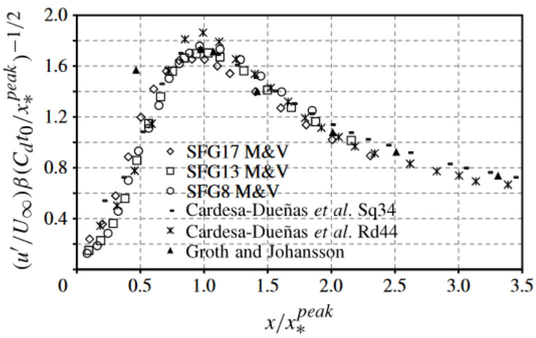

Figure (12): Downstream evolution of normalized turbulence intensity for several fractal and regular grids. Extracted from [20].

However, Equation (2) has only been validated for flows in absence of mean shear. Indeed, such collapse is not perfectly observed in Figure (13) which plots longitudinal profiles of turbulence intensity measured at the center of each grid level for grid (b).

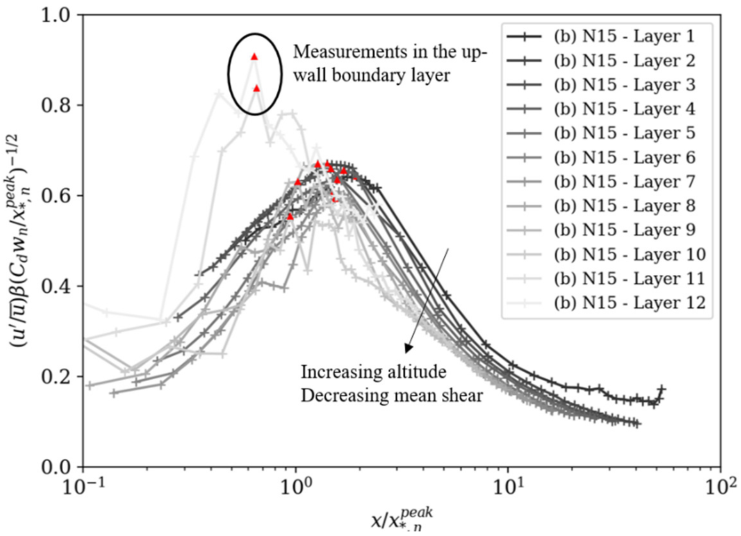

Figure (13): Longitudinal profiles of measured streamwise turbulence intensity at the center of each level of grid (b) in SCL-PIV wind tunnel, normalized according to the scaling law from equation (2).

Therefore, an analytical model has been developed from the Turbulent Kinetic Energy (TKE) equation in order to predict this behaviour, relying mainly on an hypothesis of proportionality between the turbulent transport terms and the dissipation rate. In order to close this theoretical model, it is required to model the downstream evolution of both Reynolds stress $\rho = \langle u'w' \rangle / \sqrt{\langle u'^2 \rangle}\sqrt{\langle w'^2 \rangle}$ and streamwise integral length scale $L_{uu,x}$. This work has been undertaken empirically thanks to measurements downstream of the presented grids. The resulting turbulence prediction model is finally compared to experimental results.

References

[1] R. B. Stull, An Introduction to Boundary Layer Meteorology. Springer Netherlands, 1988.

[2] J. R. Garratt, “Review: the atmospheric boundary layer,” Earth-Science Reviews, vol. 37, no. 1, pp. 89–134, Oct. 1994.

[3] A. S. Monin and A. M. Obukhov, “Basic laws of turbulent mixing in the surface layer of the atmosphere,” *Tr. Akad. Nauk. SSSR Geophiz. Inst.*, vol. 24, no. 151, pp. 163–187, 1954.

[4] J. C. Kaimal and J. J. Finnigan, *Atmospheric Boundary Layer Flows: Their Structure and Measurement*. Oxford, New York: Oxford University Press, 1994.

[5] J. C. R. Hunt and H. Fernholz, “Wind-tunnel simulation of the atmospheric boundary layer: a report on Euromech 50,” *Journal of Fluid Mechanics*, vol. 70, no. 3, pp. 543–559, Aug. 1975.

[6] J. Counihan, “An improved method of simulating an atmospheric boundary layer in a wind tunnel,” *Atmospheric Environment (1967)*, vol. 3, no. 2 : 197–200, 1969.

[7] N. J. Cook, “Wind-tunnel simulation of the adiabatic atmospheric boundary layer by roughness, barrier and mixing-device methods,” *Journal of Wind Engineering and Industrial Aerodynamics*, vol. 3, no. 2, pp. 157–176, Jan. 1978.

[8] S. Zheng, P. J. K. Bruce, J. M. R. Graham, and J. C. Vassilicos, “Weakly sheared turbulent flows generated by multiscale inhomogeneous grids,” *Journal of Fluid Mechanics*, vol. 848, pp. 788–820, Aug. 2018.

[9] G. I. Taylor, G. K. Batchelor, H. L. Dryden, and G. B. Schubauer, “THE EFFECT OF WIRE GAUZE ON SMALL DISTURBANCES IN A UNIFORM STREAM,” Q J Mechanics Appl Math, vol. 2, no. 1, pp. 1–29, Jan. 1949.

[10] P. R. Owen and H. K. Zienkiewicz, "The production of uniform shear flow in a wind tunnel," *Journal of Fluid Mechanics*, vol. 2, no. 6, pp. 521–531, Aug. 1957.

[11] J. W. Elder, "Steady flow through non-uniform gauzes of arbitrary shape," *Journal of Fluid Mechanics*, vol. 5, no. 3, pp. 355–368, Apr. 1959.

[12] J. H. McCarthy, "Steady flow past non-uniform wire grids," *Journal of Fluid Mechanics*, vol. 19, no. 4, pp. 491–512, Aug. 1964.

[13] P. E. Roach, "The generation of nearly isotropic turbulence by means of grids," *International Journal of Heat and Fluid Flow*, vol. 8, no. 2, pp. 82–92, Jun. 1987.

[14] M. Jensen and N. Franck, "Model-scale tests in turbulent wind," 1963.

[15] M. R. Raupach, R. A. Antonia, and S. Rajagopalan, "Rough-Wall Turbulent Boundary Layers," *Applied Mechanics Reviews*, vol. 44, no. 1, pp. 1–25, Jan. 1991.

[16] H. P. A. H. Irwin, "Design and use of spires for natural wind simulation," *Laboratory Technical Report (National Research Council of Canada. National Aeronautical Establishment. Low Speed Aerodynamics Laboratory)*, p. 65 p., Aug. 1979.

[17] P. C. Valente and J. C. Vassilicos, "The decay of turbulence generated by a class of multiscale grids," *Journal of Fluid Mechanics*, vol. 687, pp. 300–340, Nov. 2011.

[18] J. Nedić and S. Tavoularis, "Energy dissipation scaling in uniformly sheared turbulence," *Phys. Rev. E*, vol. 93, no. 3, p. 033-115, Mar. 2016.

[19] ESDU 85020, "Characteristics of atmospheric turbulence near the ground - Part II: singlepoint data for strong winds (neutral atmosphere)." Engineering Sciences Data Unit, 1985.

[20] R. Gomes-Fernandes, B. Ganapathisubramani, and J. C. Vassilicos, "Particle image velocimetry study of fractal-generated turbulence," Journal of Fluid Mechanics, vol. 711, pp. 306–336, Nov. 2012.

[21] C. R. Symes and L. E. Fink, "Effects of external turbulence upon the flow past cylinders," in Structure and Mechanisms of Turbulence I, Berlin, Heidelberg, 1978, pp. 86–102.

Wake Flows of a Cluster of Tall Buildings

Saad Inam*, Cung Nguyen, Davide Lasagna, Zheng-Tong Xie

*University of Southampton, Department of Aeronautics and Astronautics, Southampton SO16 7QF, UK
*s.inam@soton.ac.uk

1. Introduction

Urban immigration is increasing rapidly, and tall building (TBs) are contructed to tackle this issue. This means that cities around the world are getting bigger and taller significantly with the construction of isolated and clustered tall buildings. Such contsruction is supposed to have a huge impact on the microclimate within cities such as wind, temperatures, heat and pollutant concentration. Furthermore, a change in the microclimate directly impacts the aerodynamic performance of the building for instance wind loading. Hence, it is very important to understand the flow around these cylindrical structures. However, this comes with challenges, as studies using wind tunnel facilities require large domain scale and appropriate building size making it difficult to perform analysis. Most of the researchers have performed computational simulations in order to undertsand the impact of turbulent winds on cylindrical structures (TBs) and behaviour of the wind field within and immediately above the urban canopy. Such computational analysis requires high computational resources, which means that these studies are compromised when considering the size of urban area, number of tall buildings and spatial resolution. It is even more challenging for experiments and numerical simulations when tall buildings are considered as their wake lasts for a longer distance than low-rise buildings.

The research reported in this paper is part of the large project ``Fluid Dynamics of Urban Tall building clUsters for Resilient built Environments (FUTURE)``, which involves the University of Surrey and the University of Reading. The aim of this project is to tackle the above-mentioned challenges using a combination of different approaches such as high fidelity computational analysis, wind tunnel tests, and field observation. One of the foremost aim of this project is to gain a good undertstanding regarding the magnitude and spatial scale of the impacts of tall buidlings both single and clusters as well as the adverse effect on the microclimate and urban boundary layers.

This project is currently in its initial phase, and this paper reports the results obtained so far. These inlcudes numerical simulations performed for (i) an infinite-height single square cylinder in smooth and turbulent flows, and (ii) a cluster of 2 × 2 square cylinders with a height-to-cylinder-width ratio 4. Large Eddy Simulations (LES) embedded in OpenFOAM and PALM-4U were performed using the high-performance computing (HPC) facilities at University of Southampton, and on the national supercomputing system ARCHER2.

2. Computational Setup

Two cases are considered: (i) **Case 1** represents a single building with dimensions of b×b×h, where h is the height of the building equal to domain height 15b; (ii) **Case 2** represents 2×2 buildings with the dimensions of b×b×h where the height of building is approximately 1/4 of the domain height. Case 1 is mainly considered for the sake of validation, while Case 2 would be the focus of this paper. The considered configuration for Case 2 is shown in Fig. 1. It consists of four-square buildings present inside the domain. The width of the building is b and the height is $4b$. The domain size for both cases is $30b$×$24b$×$15b$ in streamwise, cross-stream and vertical directions, respectively. For Case 1, the origin is placed at the centre of the cylinder at $7.5b$ from the inlet, $22.5b$ from the outlet, and $12b$ from the two lateral sides. For Case 2, the origin is placed at the centre of the cluster at a distance of $8.5b$ from the inlet, $21.5b$ from the outlet, and $12b$ from the two lateral sides. The blockage ratio is 1%, which is considered suitable to avoid boundary effects.

Parallelized LES model (PALM-4U) was used (Raasch and Schröter, 2001). The model is based on the filtered, incompressible Navier-Stokes equations in Boussinesq-approximated form. A synthetic turbulence generator implemented in PALM was used to provide turbulent inflow conditions. The method is based on the work of Xie and Castro (2008) and Kim et al. (2013).

For both cases, dirichlet boundary condition was applied at the left boundary $U_\infty = 1m/s$) whereas a zero gradient boundary condition $\partial u_i/\partial x = 0$ is used at the outlet. A periodic boundary condition was applied at the two lateral (north and south) boundaries, while Neuman (free slip) boundary condition was used for the top boundary. No-slip wall boundary condition was used for the bottom boundary. For Case 1, initialization was done for 5 hours which corresponds to 10 flow passthroughs, and averaging was performed for 15 hours corresponding to 30 passthroughs. For Case 2, initialization was done for 5 hours, while averaging was performed for 10 hours (20 passthroughs).

A uniform mesh was used for both cases to acquire a good mesh quality. For both cases, a total 900 (x) × 720 (y) × 300 (z) grid cells were used, and 30 grid cells along the length b was used (See Table 1). 160 CPUs were used for all the simulations, and the wall-clock time for Case 1 was 22 hours whereas the wall-clock time for Case 2 was 20 hours.

Table 1: Grid number and domain size for the two cases.

	N_x	N_y	N_z	L_x	L_y	L_z
Case 1	900	720	300	$30b$	$24b$	$15b$
Case 2	900	720	300	$30b$	$24b$	$15b$

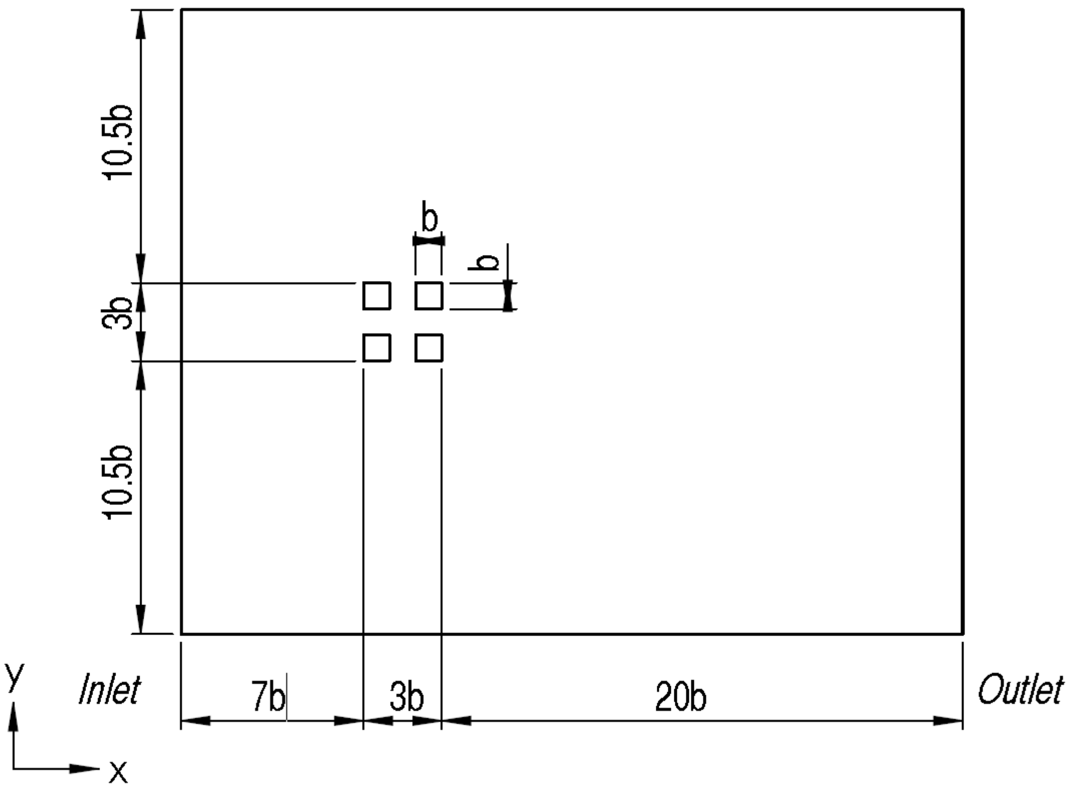

Fig. 1. Sketch of the domain with a cluster of 2×2 square buildings. The coordinate origin is on the ground at the centre of the cluster. The building height is 4*b* and the domain height is 15*b*.

3. Validation – CASE 1

For the validation purpose, two different sets of settings were used using PALM-4U. The first one considered was a single cylinder with a height equal to the domain height having a smooth inflow at the inlet. The second one considered was same as the first in terms of configuration, except a turbulent inflow condition was implemented at the inlet. For both simulations, the results obtained using PALM-4U were compared with the LES data from OpenFOAM and experimental measurements from Lyn et al., (1995) both having a smooth flow at the inlet. A much finer mesh was used for the simulation performed using OpenFOAM (i.e., 200 points along *b*). For the OpenFOAM simulation, perodic boundary conditions were used for the top and bottom boundaries with the domain height h=4*b*.

Table 2 shows detailed inflow turbulence settings. It is important to highlight that in the experiments conducted by Lyn et al. (1995) a turbulent intensity of 2% was specified at the inlet, while for the single cylinder with turbulent inflow a turbulent intensity of 10% was provided at the inlet. Figure 2 shows the mean velocity and turbulent statistics on the central horizontal plane at half height, where it is expected to have negligible effect from the top and bottom boundaries. Discrepancies are visible in Fig. 2 between different cases as the turbulence at the inlet can induce change in the flow features in the wake region of a square cylinder (Tamura and Ono, 2003). For instance, a change in the length of the recirculation bubble. For the smooth and turbulent flow cases in the current LES using PALM-4U, the lengths of the recirculation bubble are 0.82*b* and 1.22*b* respectively. For the smooth flow case, this is consistent with numerical data from OpenFOAM keeping in mind that a much finer mesh was used for the analysis performed using OpenFOAM. For the turbulent flow cases, again the agreement is good with experimental data from Lyn el al., (1995) given that the turbulent intensity is not same at the inlet. Furthermore, the increase in the bubble length for the the case of turbulent flow in comparison to smooth flow aligns with the findings of Tamura and Ono (2003), where for a square cylinder in higher turbulent intensity ($\sigma_u/U = 0.13$) flow, the reattachement of shear layer on the cylinder sides occurs at irregular intervals which results in the shifting of dividing point in the wake region.

Table 2: Comparison of the recirculation bubble length (L_f) with numerical data and reference.

Cases	L_f
Smooth Inflow (PALM-4U)	0.82*b*
FST TI=10% (PALM-4U)	1.25*b*
Smooth Inflow (OpenFOAM)	0.67*b*
FST TI=2% Experiment (Lyn et al. 1995)	1.37*b*

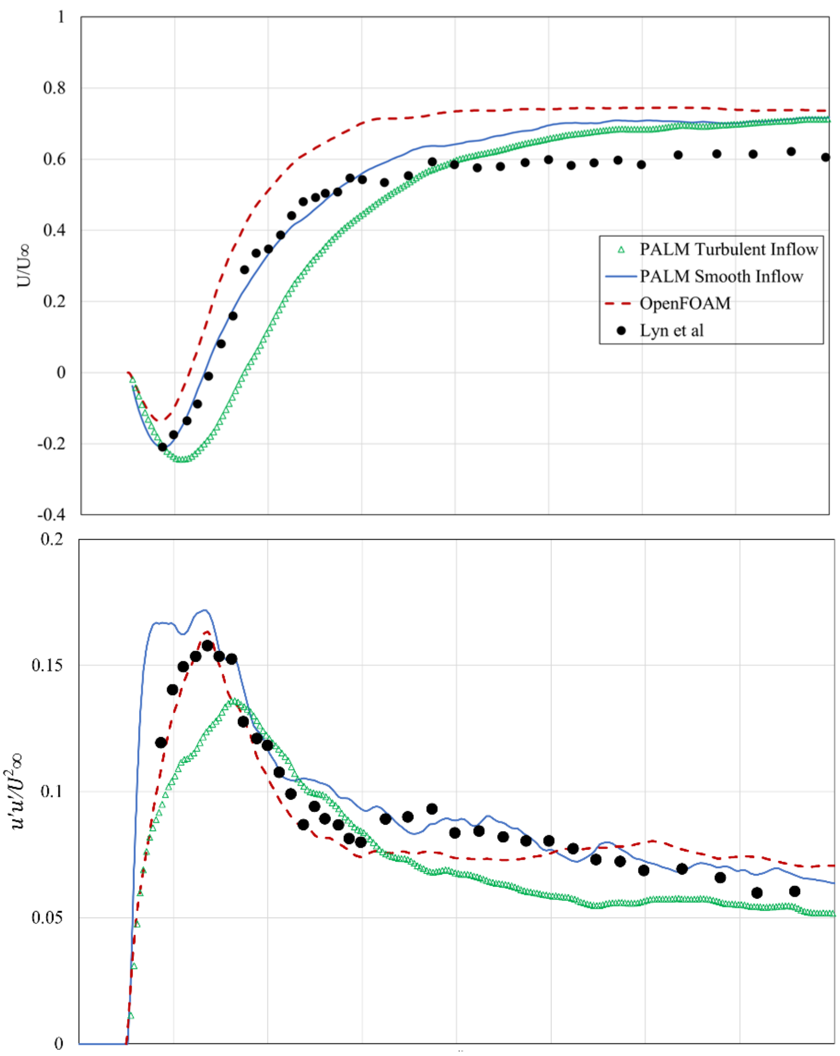

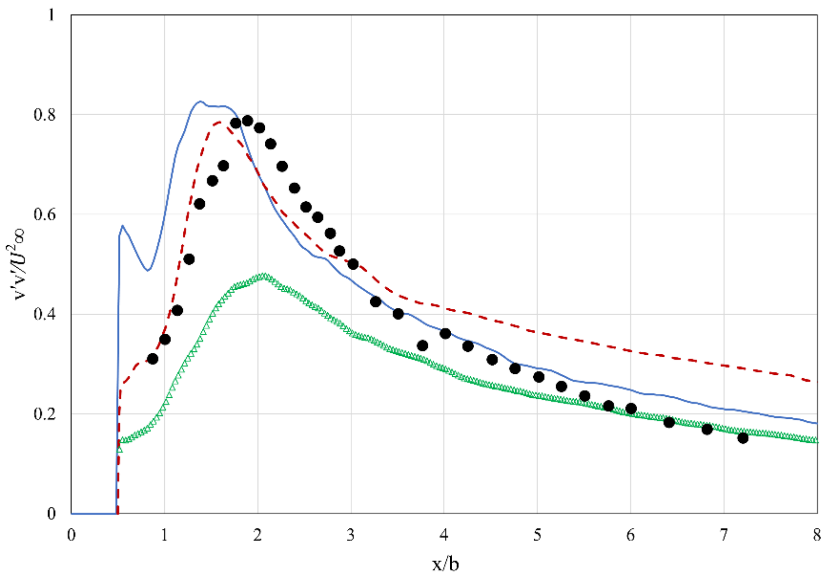

Fig. 2. Streamwise velocity $\overline{U}/U_{\infty}$ (top), Reynolds normal stress $\overline{u'u'}/{U_{\infty}}^2$ (middle) and $\overline{v'v'}/{U_{\infty}}^2$ (bottom) along the wake centreline at half height. Comparison with the experimental measurements by Lyn et al. (1995) and LES using OpenFOAM.

It can be clearly seen from Fig. 2 that the streamiwse velocity for the turbulent inflow shows a good agreement with experimental measurements of Lyn et al. (1995) in near cylinder region for *x/b* = 4. The agreement between smooth inflow cases (PALM-4U and OpenFOAM) is also good regardless of the difference in mesh size. The difference in the wake region is perhpas no surprise as according to literature (Sohankar et al., 2000, Cao and Tamura, 2016) an over-prediction of the streamwise velocity usually occurs in this region. The discrepancies between the two smooth inflow cases (PALM and OpenFOAM) are likely due to different resolutions.

Fig. 2 also highlights that the streamwise Reynolds normal stress $\overline{u'u'}/{U_{\infty}}^2$ and cross-stream Reynolds normal stress $\overline{v'v'}/{U_{\infty}}^2$ for the turbulent flow case shows a good agreement with the experimental measurements from Lyn et al. (1995), albeit the different turbulent intensities imposed the the inlet. Similarly, for the smooth inflow case, the results obtained through PALM-4U and OpenFOAM are overall consistent. However, interestingly, it could be seen that Reynolds normal stress $\overline{u'u'}/{U_{\infty}}^2$and cross-stream Reynolds normal stress $\overline{v'v'}/{U_{\infty}}^2$ for the turbulent flow case are significantly less as compared to the smooth flow case. This is due to the fact that the lead-edge vortices (LEV) which originates from the leading edge of the cylinder are broken down by the incoming freestream turbulence, particularly in the along-cylinder direction, which consequently diminishes LEV generated turbulent fluctuations (e.g. Daniels et al. 2016).

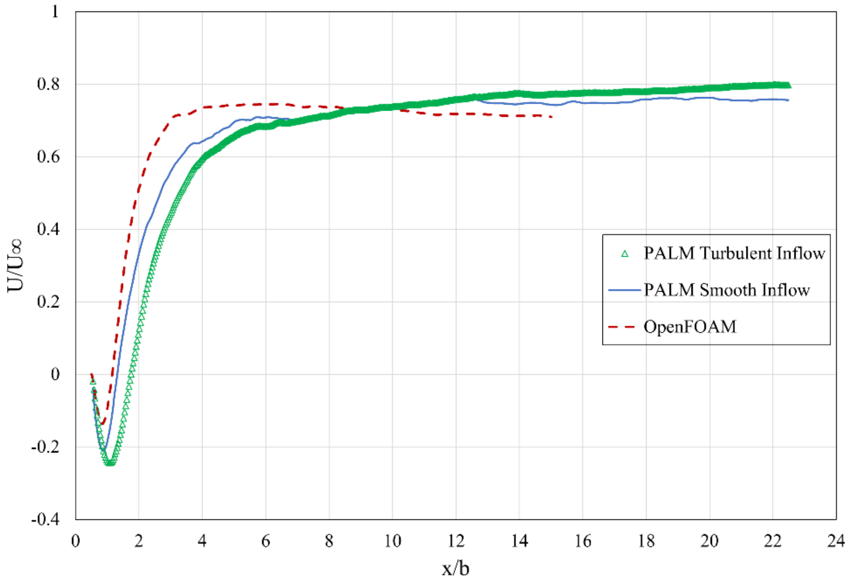

Fig. 3. Streamwise velocity $\overline{U}/U_{\infty}$ along the wake centreline (y=0) at half height.

Fig. 3 shows the streamwise velocity at z = 7.5b over much longer distance i.e x/b = 24. For turbulent flow, it can be seen that at x/b = 22, the velocity has recovered to 80% of the velocity specified at the top boundary of the inlet ($U_{\infty} = 1m/s$). Furthermore, Fig. 3 also indicates that turbulent flow recovers faster as compared to smooth inflow however a full recovery would occur over a much longer distance. As the atmospheric boundary layer is often turbluent, a turbulent intenisty of 10% considered in the paper is closer to the real-life. The results of the freestream turbulence case about the wake recovery is more realistic as comapred to the smooth flow case.

4. Results of a 2x2 building cluster

This abstract highlights the results for **Case 2** which represents a cluster of 2×2 finite-height square cylinders. Figure 4 shows the contours for the time-averaged U component of the velocity at half height (z =2b) with turbulent inflow. A jet region with a high velocity magnitude can be clearly seen at the centre of the cluster. Furthermore, two low speed wake regions are present at the leeward sides of the two rear buildings. These two low speed wakes merge at a certain distance in the wake region, which will be discussed further for Fig. 7.

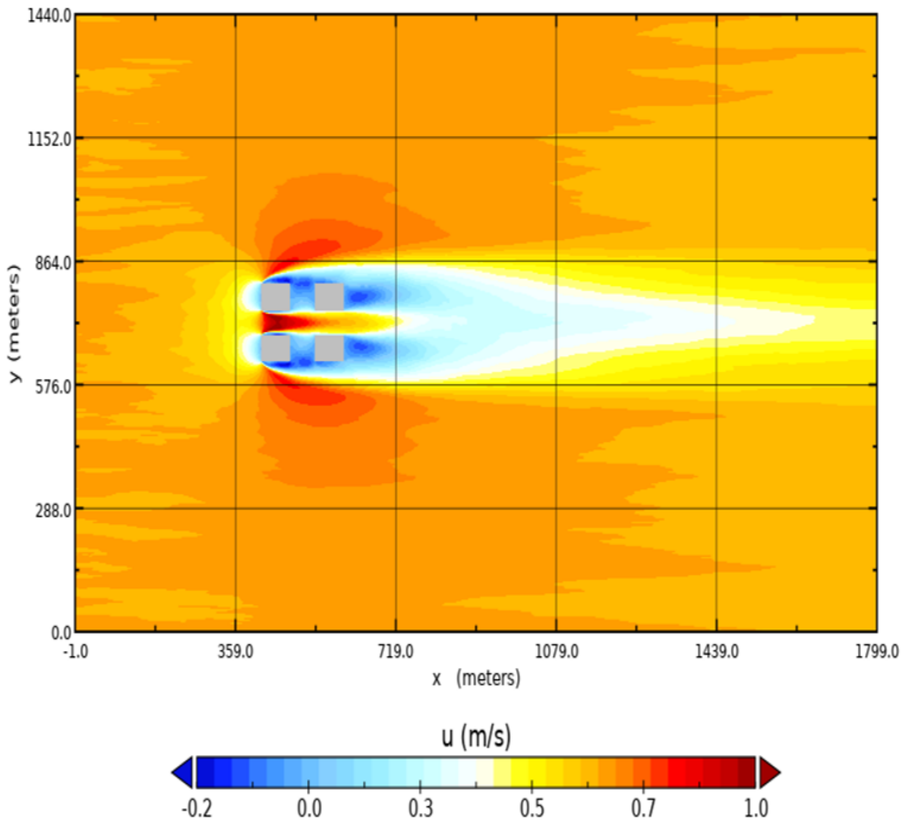

Fig. 4. Time-averaged streamwise velocity contours for a cluster of 2 × 2 finite-height square cylinders at half height.

Figure 5 show time-averaged spanwise velocity profiles which were plotted at various streamwise locations at half height of the cluster. Figure 5 shows that for x=7b, the two low-speed wake regions (i.e., at y = b and y = -b) are still visible and are not merged, while high peak velocity at y = 0 represents the end of the jet region. The two low speed wakes merge approximately at x=8b.

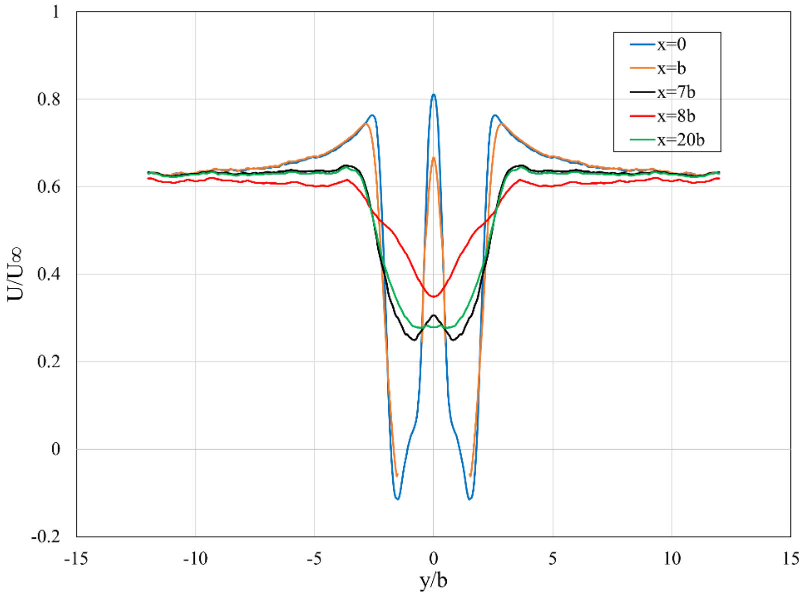

Fig. 5. Time-averaged streamwise velocity U/U_∞ along the cross-flow direction at half height (z=2b).

Figure 6 shows time-averaged streamwise velocity profiles at different cross-flow y locations at the half building height. The profile '*y* = avg of *b* and –*b'* is the averaged velocity at *y* = *b* and *y* = -*b*. Figure 6 shows that the merging location of the two low-speed wake regions (see Fig. 5) is the point where the curve for '*y* = avg of *b* and -*b*' intersects with that for *y*=0. It is important to compare Figs. 6 to 3 on the recovery of the streamwise velocity in the wake region. Figure 3 shows that the time-averaged streamwise velocity at the cylinder centre (*y*=0) recovers to approximately 70% of U_∞ at *x*=8*b* for the three cases. Figure 6 shows that at *x*=20*b*, the time-averaged streamwise velocity at the cylinder centre (*y*=0) recovers to approximately 62% of the inlet velocity at the same height, while at *x*=24*b*, the time-averaged streamwise velocity is recovered to approximately 70%. This suggests that the characteristic length scale of the cluster is between 2.5*b* and 3*b*.

Figure 7 shows the merging location of the two low-speedwake regions at different heights. In the region *z* = 2.8*b*-3.5*b* the sudden change of the reduction rate of the downstream distance (to the centre of the cluster) of the merging point is likely due to the short-time average error. This suggests that the wake flow of the cluster is highly three-dimensional, which might not be supprising. Given the cluster height is 4*b*, the characteritic length scale of the cluster in the streamwise direction is more than 2*b*, resulting in a height-to-width ratio of the cluster less than 2.

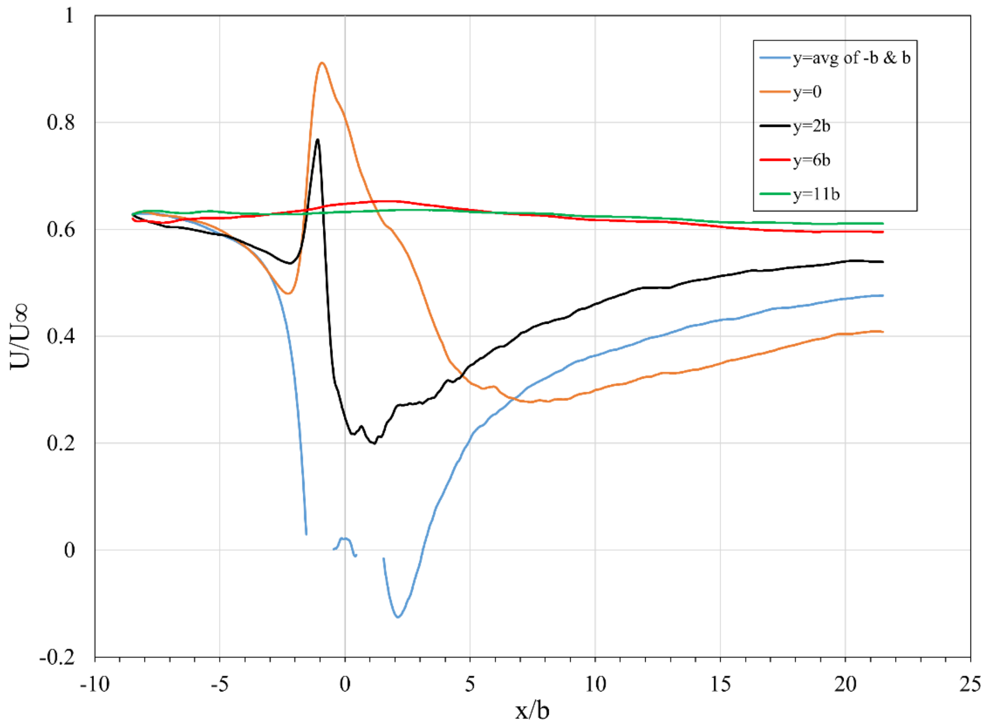

Fig. 6. Time-averaged streamwise velocity U/U_∞ at different y locations at the half building height. The discontinities in the '*y*=avg of –*b* and *b*' represent the two cylinders.

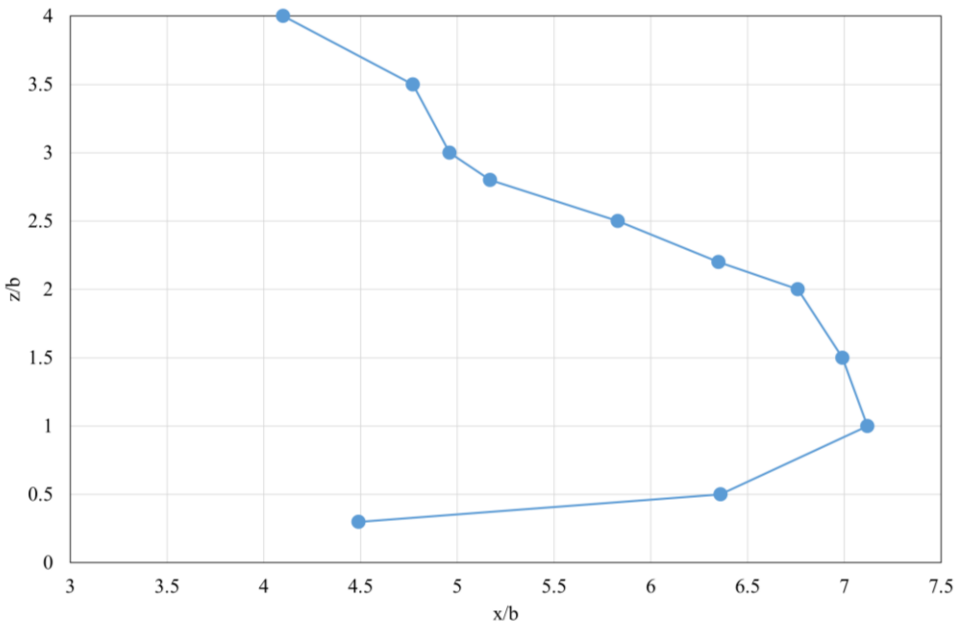

Fig. 7. The downstream distance (to the centre of the cluster) of the merging point of two low-speed wake regions at different heights.

5. Conclusion

In the first half of the paper, large-eddy simulations were performed for a single infinite length square cylinder in smooth and turbulent inflows. It was observed that for a turbulent flow, velocity recovers much faster to its original value specified at the inlet as compared to a smooth flow. This result is indeed quite realistic because in real-life the turbulent effects are dominant in atmospheric boundary layer. In the second half of the paper, large-eddy simulations were performed for a 2×2 array of finite-height square cylinders in a turbulent boundary layer. We found the streamwise characteristic scale at the half building height is between 2.5*b* and 3*b* by comparing the wake recovery to the single cylinder case. Investigation was also performed on the merging point of the two low-speed wake regions behind the two rear buildings. It was observed that the merging point tends to be delayed at the half building height, while for the building top it recovered the quickest. Further investigation will be performed on the effects of different turbulent intensities, integral length scales, atmospheric boundary layer height, and thermal stratification conditions, effects. These results will be reported in the workshop.

Acknowledgement

The research is funded by the UK Engineering and Physical Science Research Council (EPSRC)(EP/V010514/1). The computations were performed on the IRIDIS 5 supercomputer facility at the University of Southampton, UK and on the national supercomputing system ARCHER2 (supported by the UKTC).

References

Cao, Y. and Tamura, T., 2016. Large-eddy simulations of flow past a square cylinder using structured and unstructured grids. *Computers & Fluids*, *137*, pp.36-54.

Daniels, S.J., Castro, I.P. and Xie, Z.T., 2016. Numerical analysis of freestream turbulence effects on the vortex-induced vibrations of a rectangular cylinder. *Journal of Wind Engineering and Industrial Aerodynamics*, *153*, pp.13-25.

Kim, Y., Castro, I.P. and Xie, Z.T., 2013. Divergence-free turbulence inflow conditions for large-eddy simulations with incompressible flow solvers. *Computers & Fluids*, *84*, pp.56-68.

Lyn, D.A., Einav, S., Rodi, W. and Park, J.H., 1995. A laser-Doppler velocimetry study of ensemble-averaged characteristics of the turbulent near wake of a square cylinder. *JFM*, *304*, pp.285-319.

Raasch S, Schröter M (2001) PALM—a large-eddy simulation model performing on massively parallel computers. Meteor Z 10:363–372

Sohankar, A., Davidson, L. and Norberg, C., 2000. Large eddy simulation of flow past a square cylinder: comparison of different subgrid scale models. *J. Fluids Eng.*, *122*(1), pp.39-47.

Tamura, T. and Ono, Y., 2003. LES analysis on aeroelastic instability of prisms in turbulent flow. *Journal of wind engineering and industrial aerodynamics*, *91*(12-15), pp.1827-1846.

Xie, Z.T. and Castro, I.P., 2008. Efficient generation of inflow conditions for large eddy simulation of street-scale flows. *Flow, turbulence and combustion*, *81*(3), pp.449-470.

Temporal, Spatial, and Spatio-temporal correlation of the velocity fluctuations

K. Jurčáková[1]

[1]Institute of Thermomechanics, Czech Academy of Sciences, Dolejškova 1402/5, 18200, Praha 8, Czech Republic

Introduction

Taylor's hypothesis about frozen turbulence [1] says that if the turbulence intensity is small compared to the mean velocity then the advection of a turbulent flow field past a fixed point can be taken entirely due to the mean flow. This means that in the "frozen turbulent field" spatial and temporal dimensions can be interchanged. Although the main assumption of Taylor's hypothesis is not met in the atmospheric boundary layer (the intensity of turbulence is usually between 10 and 20%) the hypothesis is commonly used to calculate integral length scales of turbulent fields from point measurements. Particle image velocimetry with high temporal resolution (TR-PIV) allows us to analyze both temporal and spatial cross-correlations in the turbulent flow fields and to evaluate obtained results.

Experimental Methods

We investigated flow in 5 different boundary layers. Firstly, a set of 4 canonical boundary layers developed over homogeneous rough surfaces was studied, see Fig. 1. Setups S4_8, S4_6, S4_4, and S4_2 had the surface roughness made of thin erected plates with dimensions 4 x 4 x 1 mm (width x height x thickness) arranged in staggered rows. The distance of the roughness elements was 32, 24, 16, and 8 mm in both directions, respectively, which makes the setup S4_8 the less rough one and the setup S4_2 the roughest one. The measurement campaign was conducted in an open blowing-type wind tunnel of the dimensions 0.25 m, 0.25 m, and 4.20 m (width, height, and length). The characteristics of developed boundary layers can be found in [2].

Secondly, we investigated the model of ABL over the complex terrain in an open blowing-type wind tunnel of the dimensions 1.5 m, 1.5 m, and 25 m (width, height and, length), see Fig. 2. The meteorological observatory Kopisty and its surrounding were modeled on the scale 1:1333. The approaching atmospheric boundary layer was modeled in the same scale and its characteristics agreed with the table data of rough ABL according to [3]. The two wind direction was investigated. The 220° direction where the wind flows over a hilly and forested area and the 300° direction where the landscape is flat with some industrial and water areas.

In both cases, we used time-resolved particle image velocimetry (TR-PIV) which utilized the diode-pumped Nd:YLF laser and VEO cameras (resolution 1280 × 800 pxs). The investigated horizontal area covered 140 × 90 mm in a longitudinal and transversal direction in the case of the canonical BLs and 300 x 200 mm in the case of the Kopisty model. The spatial resolution was 0.11 mm and 0.23 mm per pixel, respectively. The data were pre-processed by an adaptive PIV algorithm with a 32 x 32 pixels interrogation area and 50% overlap. Each measurement consisted of 6200 double-frame snapshots and sampling frequency f_S varied with the free stream velocity to capture flow field dynamics. The average advection distance between two consecutive snapshots was about 1/20 of the field of view (approx. 70 pxs). The reference velocity was 14 m/s for the canonical BLs and 5 m/s for the Kopisty model.

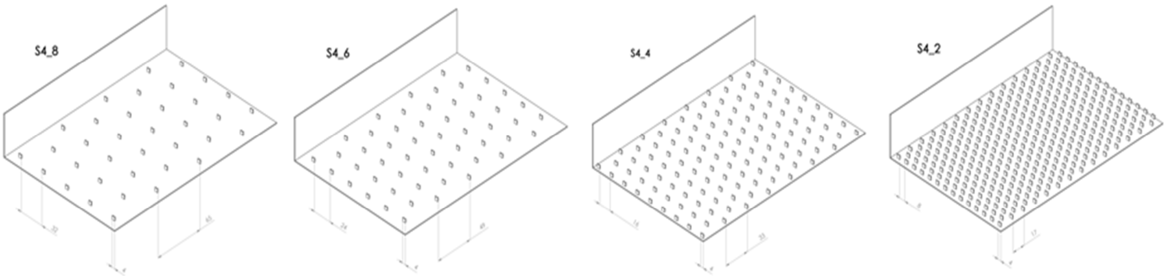

Figure 1: Rough surfaces geometry. The whole floor of the wind tunnel was covered by roughness elements.

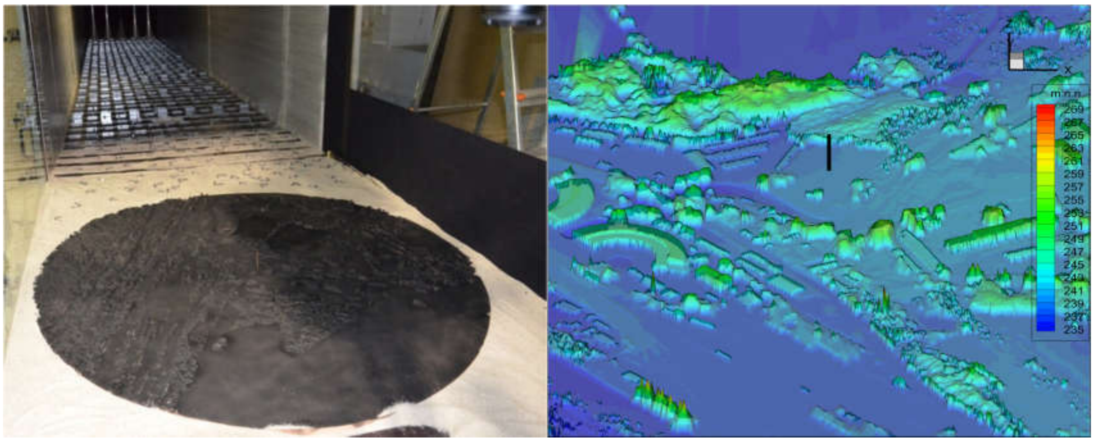

Figure 2: Model of the meteorological observatory Kopisty.

Spatial correlations

The computational methodology of the spatial and temporal correlations as well as the derivative variables will be explained in the example of the canonical BL above surface S4_4 at the height of 30 mm which corresponds to 0.3δ (δ is boundary layer height).

Two-point correlation map of longitudinal velocity fluctuations r_{uu} is shown in Fig. 3, upper figure. The correlation isolines create an oval with the longer axis oriented along the wind direction. The black bold lines depict the correlation isolines of r_{uu} = 0.5 and r_{uu} = 1/e, where e = 2.718 is the Euler number. There are distinct side minima of r_{uu} in the lateral direction. The cut of the correlation map together with the threshold values in the along-wind axis is shown in Fig. 3, lower figure. The distance where the correlation curve decreases to the value of 1/e, L_{ruu}= 0.368, is one of the definitions of the integral length scale. Another definition is the area integral of the correlation curve. In the ideal case, where the correlation curve has an exponential shape, these two definitions are equivalent. In the BL flows, the integral definitions usually give about 50% higher values.

The integral length scales L_{ruu} reaches values comparable in order of magnitudes with the BL height. The full-scale equivalent of the integral length scales measured on the Kopisty model is in order of several hundred meters.

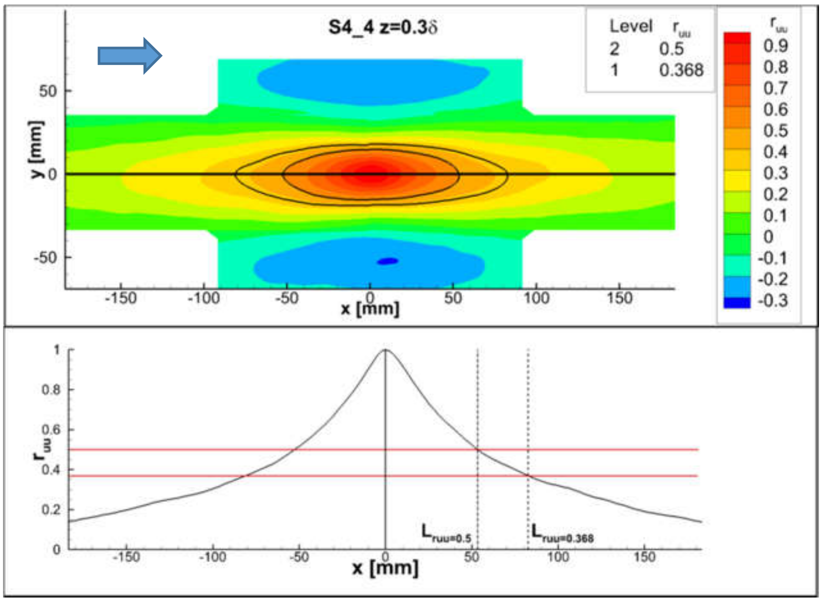

Figure 3: Spatial distribution of two-point correlations at 0.3δ above surface S4_4 (upper figure). Two-point correlation curve along the flow direction (lower figure).

Temporal correlations

Time series of longitudinal velocity fluctuations measured at point [0;0] was used to calculate the autocorrelation curve, which is shown in Fig. 4. The same correlation thresholds 0.5 and 1/e were used to obtain an integral time scale which isn't universal variables, but depends on the local wind speed. The temporal axis is therefore transformed to the spatial axis by the use of the local mean velocity U_{local}. The temporal (autocorrelation) and spatial correlation curves can be compared using the spatial axis (Fig. 4, right). The curves are very close and the difference in the integral length scales is less than 10%.

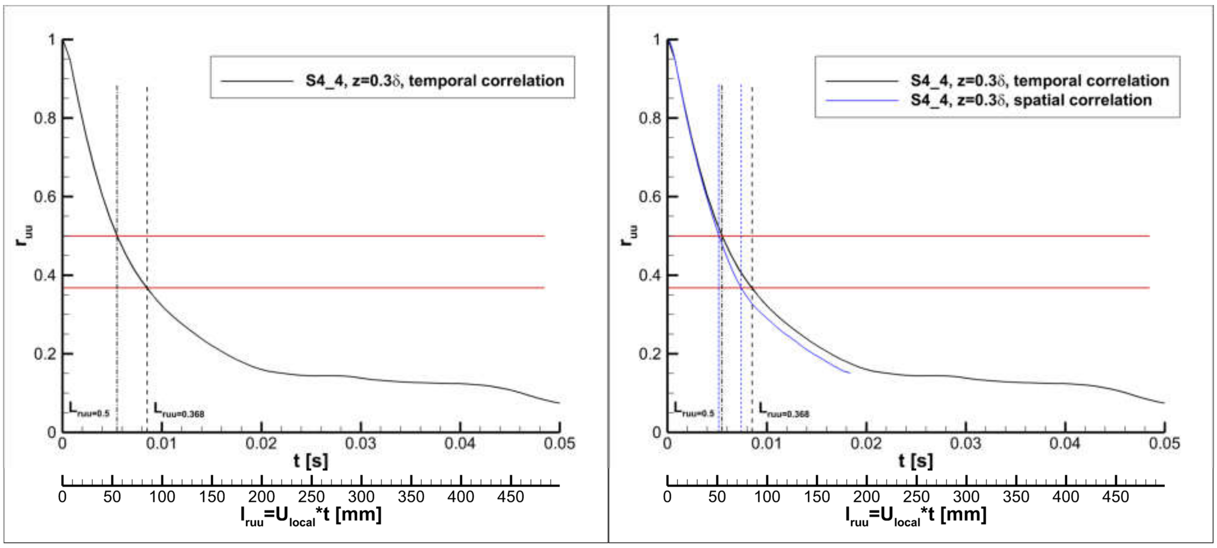

Figure 4: Autocorrelation function at at 0.3δ above surface S4_4 (left). Autocorrelation function and two-point correlation function along the flow direction (right).

Spatio-temporal correlations

Spatio-temporal correlation can be computed from the TR-PIV measurement. The maps in Fig.5 are calculated as two-point correlations of the longitudinal velocity fluctuations at each point where the first time series is fixed at the point [0; 0] and at the time t=0. The second time series are covering the whole measured field with different time lags. The maximal correlation r_{uu}=1 is reached only at the point [0;0] and time t=0. For the increasing lime lag, the maximum correlation weakens and it drifts along the flow.

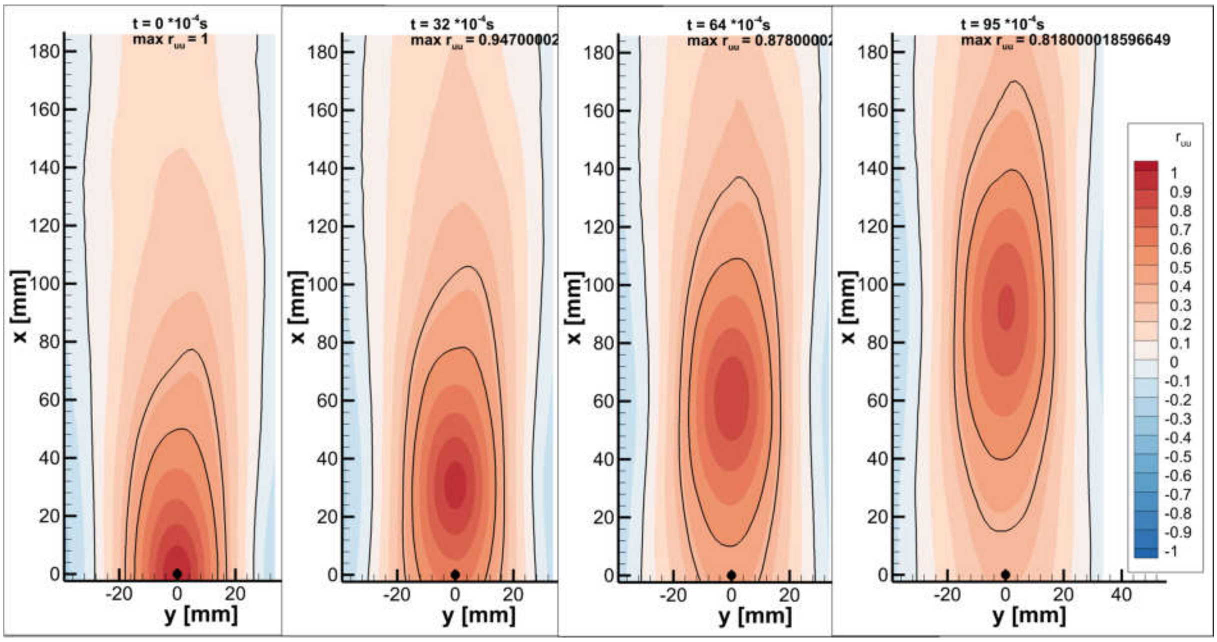

Figure 5: Two-point correlation maps with different time lags. The wind blows from the bottom, setup S4_4, z=0.3δ. The isolines depict r_{uu}=0.5 and r_{uu} =1/e.

Integral length scales

Two means how to calculate the integral length scales are compared in Fig. 6. The integral length scales were set as a distance (or the time lag multiplied by the local velocity) where the correlation curve decreases to the value 1/e (the similar results were obtained with the threshold correlation value 0.5, not shown here). It is obvious that the differences between these two modes are comparable with the overall result uncertainty. The canonical BL over smoother surfaces has longer integral length scales if scaled by the boundary layer depth. The differences between different wind directions on the model of Kopisty Observatory are negligible.

Integral velocities

Let us define the Taylor velocity U_{Taylor} which will be defined as a ratio of integral length scale L obtained from the spatial correlation field (Fig. 3) and integral time scale T obtained from the temporal autocorrelation curve (Fig. 4) at the same point.

$$U_{Taylor} = \frac{L_{ruu}}{T_{ruu}}$$

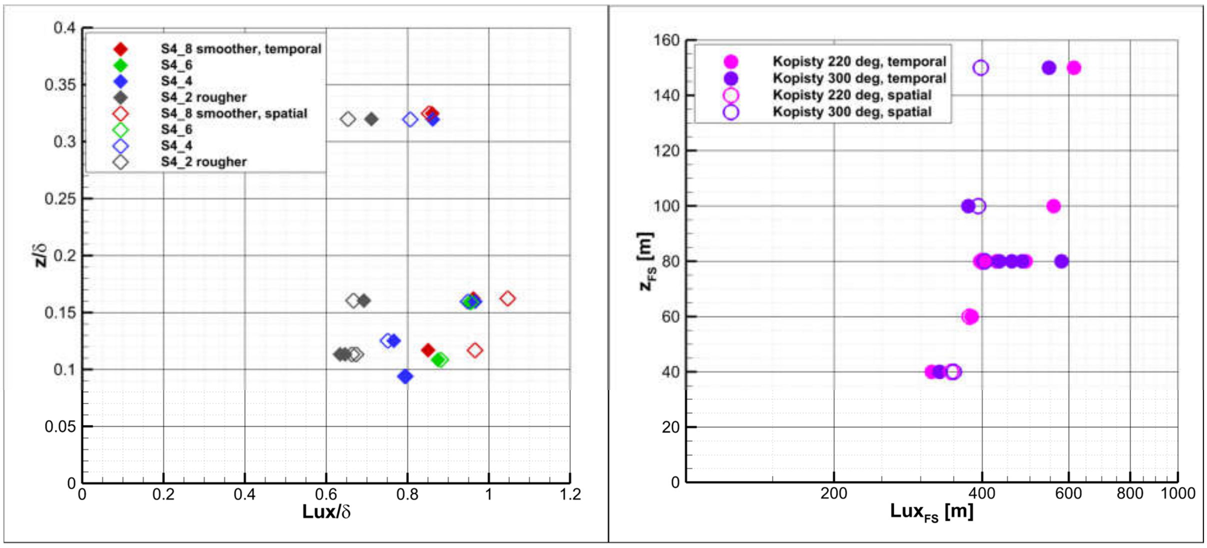

Figure 6: Integral length scales as a function of height. The full symbols depict Lux computed from autocorrelation functions, the empty symbols from the two-point correlations.

We can also define the Convective velocity U_{conv} as a velocity of the drift of the maximum spatio-temporal correlations (Fig. 5). We calculated U_{conv} as a least-square fit of a linear function to a graph of a maximal correlation distance versus correlation lag time (derived from Fig. 5). The Taylor velocity, as well as Convective velocity (together called Integral velocities) should be equal to the local velocity U_{local} in the ideal case.

Fig. 7 and 8 show the ratios of the Integral velocities U_{conv} and U_{Taylor} over U_{local} as a function of the height and surface roughness. The integral velocities tend to be slightly faster than the local velocities in the lower parts of the canonical BL (up to 0.15δ, this upper region of the inertial sublayer), while they are slightly faster in the upper part of BL. This effect is stronger above smoother surfaces than above rougher ones.

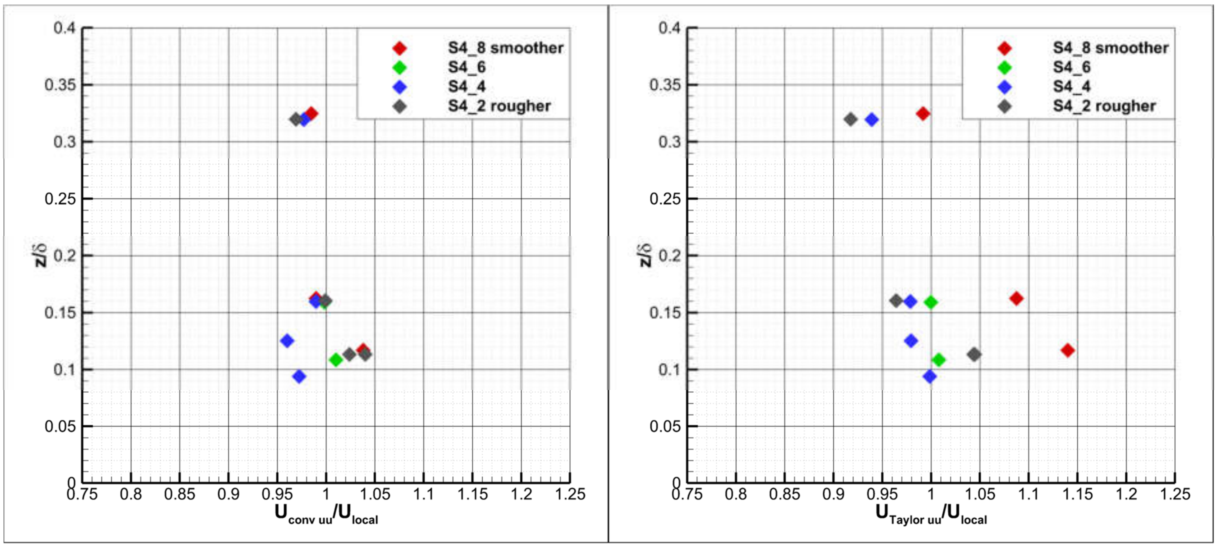

Figure 7: Convective and Taylor velocities in the canonical boundary layers as a function of the surface roughness and the height.

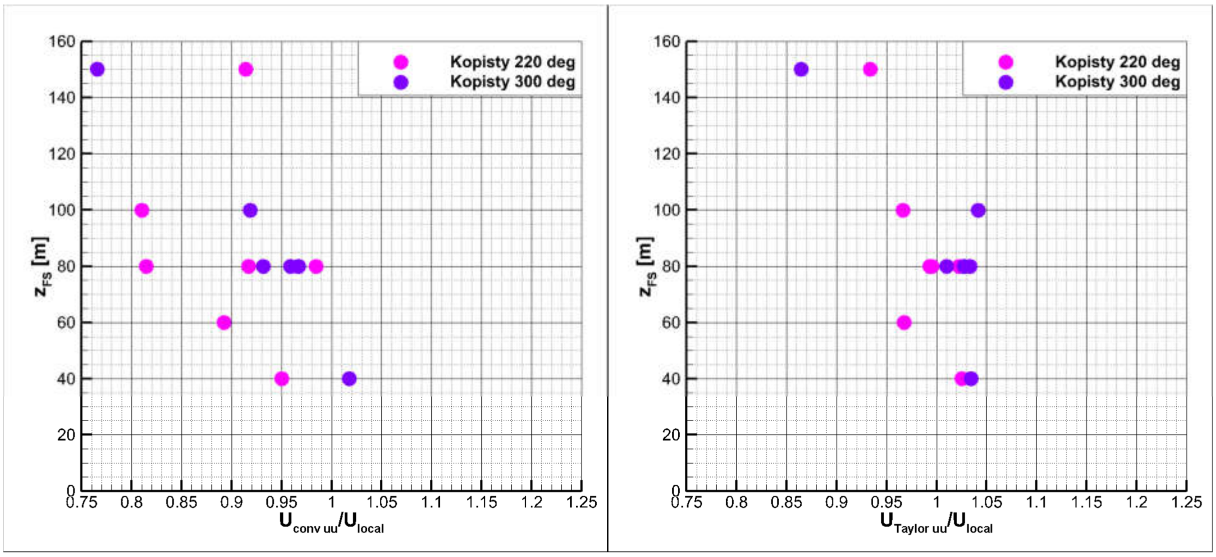

Figure 8: Convective and Taylor velocities in the ABL model (Observatory Kopisty) as a function of the full-scale height.

The data from the flow at the Kopisty Observatory confirms the previous findings, although they are more scattered. In the higher elevation, we found slower Integral velocities compared to the local velocity. The Integral velocities are higher above the smoother surface (approach wind direction 300°), which is in good agreement with our previous study (see below and [4]).

In our previous study [4], we derived the Convective velocity from the spatio-temporal correlations in the vertical plane (the TR-PIV field of view was oriented vertically and covers the whole extent of the BL, Fig. 9, left). In this case, we track the maximum of the two-point correlation field in the longitudinal direction as a function of the lag time. The Convective velocity was set as analogically. We found the same tendency as in the horizontal planes – Convective velocities were faster than local velocity close to the surface and slower in the upper part of BL, see Fig. 9, right. The differences

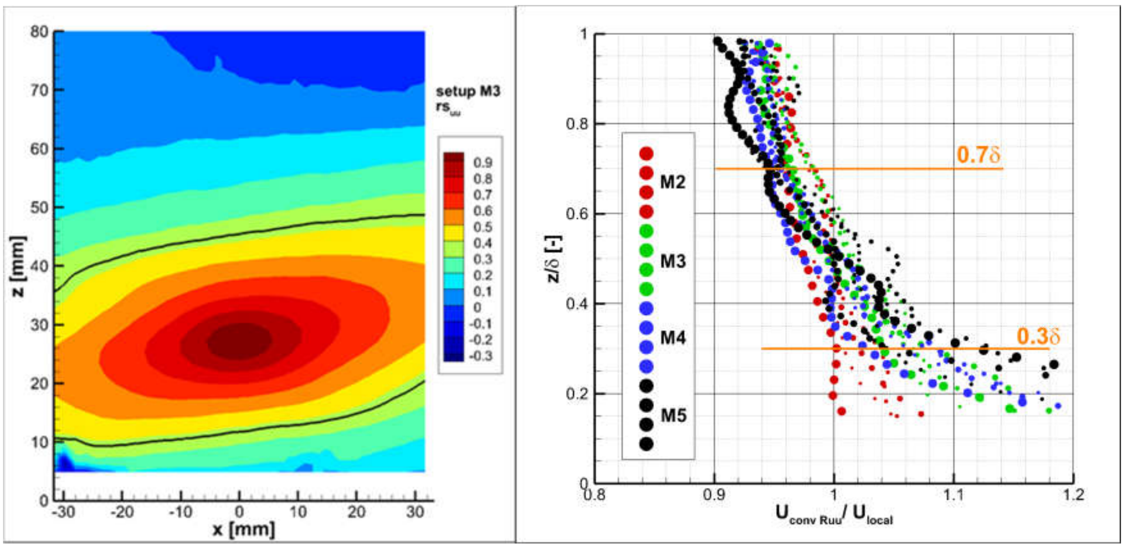

Figure 9: (left) Map of the two-point correlation functions in the vertical plane over rough surface M3. (right) Convective velocities are derived from the spatio-temporal correlations in the vertical plane. Rough surface M2 is the less rough, and M5 is the roughest. The size of the scatter is proportional to the free stream velocity. Figure adopted form [4].

between the Convective velocity and the local velocity are higher (up to 20% close to the surface) and the elevation where both velocities are equal is higher (between 0.3 and 0.7δ). The higher difference between Convective and local velocities may be caused by the biased contribution of the vertically profuse large organized structures. Those structures are connected with the fast flow in the upper of BL and bring higher momentum close to the surfaces. Such structures may have a smaller horizontal extent and therefore they may contribute less to the spatio-temporal correlation field in the horizontal plane. More investigation into this topic is needed. We plan to use 3D velocity field from the numerical simulation to reveal how different 3D organized structures appear in 2D planes (typical experimental setup of TR-PIV) and how to interpret results obtained based on 2D data.

Conclusion

We experimentally investigated a flow field over 4 different rough surfaces and over a model of a landscape on the scale 1:1333. We computed temporal, spatial, and spatio-temporal correlations and compared respective integral time and length scales. The smoother surfaces exhibit longer integral scales when scaled by the boundary layer depth. The differences between integral length scales based on spatial and temporal correlation functions was small, comparable to the overall computation uncertainty. The Convective velocity as well as Taylor velocity was faster than the local wind speed close to the ground and it was slower than the local velocity above the inertial sublayer. The effect of the surface roughness on the convective velocities was negligible.

Acknowledgement

This work was carried out thanks to the support of the Czech Science Foundation (projects no. GA18-09539S and GA15-18964S), the support of the Czech Ministry of Education, Youth, and Sports (project no. LTC 20056), and the institutional support RVO 61388998.

References

[1] Townsend A.A.: Turbulent Structure of Turbulent Shear Flow. Cambridge University Press (1976).

[2] Jurcakova, K., Prochazka, P., Kellnerova, R. (2019), Assessing quality of boundary layer flows with the diagnostic plots. Proceeding of Topical Problems of Fluid Mechanics, 2019, DOI: 10.14311/TPFM.2019.015

[3] VDI – Verein Deutcher Ingenier. (2000) Environmental meteorology. Physical modeling of flow and dispersion processes in the atmospheric boundary layer. Application of wind tunnels, VDI Standards: VDI 3783, Part 12, Dusserdorf.

[4] Jurcakova, K., Kellnerova, R. (2019), Convection velocities in turbulent boundary layers over rough surfaces, PROGRESS IN TURBULENCE VIII 226 , pp.93-98, DOI: 10.1007/978-3-030-22196-6_15

Using Doppler wind lidars to measure kinematic quantities across the lower atmosphere

Markus Kayser, Eileen Päschke, Carola Detring, Frank Beyrich, Claudia Becker, Volker Lehmann, Ronny Leinweber

Deutscher Wetterdienst, Lindenberg Meteorological Observatory – Richard Aßmann Observatory, 15848 Tauche OT Lindenberg, Germany

Abstract

Fibre-optic based Doppler wind lidars (DL) are able to retrieve vertical profiles of kinematic quantities across the lower atmosphere with high spatio-temporal resolution. Especially short-term forecasting would benefit from assimilating their data which renders these compact systems promising candidates for operational use in future observing networks. Here, we illustrate the DL measurement principle and introduce the different scan configurations and the methods which have been realized and tested at the Lindenberg Observatory. These include retrievals for mean wind, turbulent kinetic energy (TKE), eddy dissipation rate, momentum fluxes, integral length scales and wind gusts.

Assessing the mean wind product, we present results from a long-term comparison at Lindenberg using a 482 MHz radar wind profiler and 6-hourly radiosonde ascents as references, and from a side-by-side comparison of eight Halo Photonics "Streamline" DLs during the FESSTVaL 2021 field experiment (**F**ield **E**xperiment on **S**ub-mesoscale **S**patio-**T**emporal **Va**riability in **L**indenberg). The TKE and wind gust observations are compared to a sonic anemometer located at the boundary layer site Falkenberg tower in 90 m altitude. All three products – wind, TKE and gusts – show good agreement with their respective references. Additionally, case studies emphasize the potential of DLs to characterize enhanced turbulence, e.g. in the shear zone below the axis of a nocturnal low-level jet.

Keywords: Doppler Lidar application, operational observing networks, wind, TKE, gusts

1. Introduction

The first efforts to measure atmospheric winds using the Doppler frequency shift of laser light backscattered from moving atmospheric particles date back more than 50 years. These earliest Doppler instruments relied on continuous-wave lasers, detectors cooled with liquid nitrogen, and analog signal processing [1-2]. Since then, technology evolved rapidly and the Doppler lidar (DL) has been utilized to investigate various atmospheric processes, including wind shear and boundary layer turbulence. DL systems use either direct or coherent measurement methods. The latter use wavelengths in the infrared range, which allows observations over large distances with small measurement error and they require less laser power. With the help of solid-state laser transmitters for wavelengths of 2 and 10 µm, mobile systems on land, ship and aircraft platforms could be realized in 1990s with great success [3-4].

Because such instruments were expensive and needed frequent regular maintenance, they have been mainly deployed for research. But nowadays, fibre-optic based Doppler wind lidars with coherent design and with wavelengths around 1.5 µm are widely used for both meteorological research and in the wind energy sector [5-7]. These compact and rather inexpensive systems are able to obtain vertical profiles of the mean horizontal wind vector in the atmospheric boundary layer as well as in optically thin cloud layers in the free troposphere with high spatio-temporal resolution. Especially short-term forecasting would benefit from assimilating their data which renders these compact systems promising candidates for operational use in future observing networks of meteorological and environmental services, because convective-scale forecast also needs convective-scale observations [8]. Therefore, Deutscher Wetterdienst (DWD) includes the assessment of DLs in its effort to evaluate ground-based remote sensing systems for their operational readiness.

Here, we illustrate the DL measurement principle and introduce the different scan configurations and the methods which have been realized and tested at the Lindenberg Observatory. These include retrievals for mean wind, turbulent kinetic energy (TKE) and wind gusts. Further, we assess the mean wind product with a long-term comparison at Lindenberg using a 482 MHz radar wind profiler as reference. The TKE and gust observations are compared to a sonic anemometer located at the GM Falkenberg tower in 90 m altitude. Additionally, we infer challenges in using DLs to study atmospheric boundary layer processes.

2. Methods

The Doppler effect, first described by Christian Doppler in 1842 [9], describes the change in wavelength or frequency of a wave when the source and receiver move relative to each other. This change is called the Doppler shift and occurs in both sound waves and electromagnetic waves. In the case of a lidar system emitting light of frequency f_0, an observer moving at velocity v relative to the source sees light of frequency f_1.

$$f_1 = f_0(1 + {}^{v}/_{c}), \tag{1}$$

where c is the speed of light. Thus, the Doppler shift is always proportional to the relative velocity between transmitter and receiver and for changes in frequency one can write.

$$\Delta f = f_1 - f_0 = f_0({}^{v}/_{c}). \tag{2}$$

With lidar and also with sodar and radar, it should be noted that the Doppler effect occurs twice, since the photons emitted by the lidar travel the path along the line of sight twice before they are detected [10]. Thereby the scatterers act both as a moving receiver for the light emitted from the instrument, f_0 to f_1, and as a moving transmitter for the backscattered fraction of the light signal, f_1 to f_2.

$$f_2 = f_1(1 + {}^{v}/_{c}) = f_0(1 + {}^{v}/_{c})^2 \approx f_0\left(1 + {}^{2v}/_{c}\right), \tag{3}$$

which implies a Doppler shift of

$$\Delta f = f_2 - f_0 = 2f_0({}^{v}/_{c}). \tag{4}$$

For a wavelength of 1.5 µm and a line of sight (LOS) velocity of 1 ms^{-1} this shift is just 50 pm, which presents a challenge to the measurement architecture. Generally, for lidar systems parameters related to the signal strength and backscattered intensity can also be derived, which renders DLs useful as a multipurpose instrument (see Table 1). The primary quantities of interest, such as the attenuated backscatter coefficient (β), the wind speed (WS) and direction (WD) as well as turbulence measures need to be retrieved from the observed quantities, Doppler shift and signal strength. Here, we want to focus on wind related quantities but the remaining quantities can be also very helpful, especially in combination with other remote sensing instruments, e.g. in characterizing the boundary layer [11]. Note that during a measurement a large number of pulses (N, in the order of 10^3 to 10^4) needs to be accumulated and that more pulses imply a better SNR/CNR as well as higher precision velocity measurements.

Table 1: Parameters measured by Doppler lidar, adapted from [10]

Parameter	Description	Unit
LOS speed, v_{LOS}	Wind speed in direction of the laser LOS, also called radial velocity	m s^{-1}
Signal intensity	Intensity of backscattered signal	a.u. or dB
Signal-to-noise ratio (SNR), carrier-to-noise ratio (CNR)	Ratio of signal intensity (or carrier) to noise intensity	a.u. or dB

Firstly, observing the mean wind and other quantities requires a suitable scan geometry. At the Lindenberg Observatory we apply the well-known velocity-azimuth-display (VAD) technique, originally developed for radar [12] (Fig. 1). We use the VAD method in a stepped-stare setup with 24 different azimuth directions, a zenith angle of 15°, 30000 pulses per direction and a 30 min time window to reconstruct the wind field while a single scan cycle takes approx. 2 min [13]. Prior to the reconstruction, we detect the radial velocities related to the atmospheric signal according to a non-linear clustering technique, called consensus averaging [14], which is also used in the operational setup of DWD's radar wind profilers (RWP). This method shows improved data availability without a reduction in data quality compared to the conventional filter approach of using a fixed SNR/CNR-threshold [5, 13]. Additionally, we apply quality flags to the retrieved winds according to thresholds based on the algebraic inversion problem at hand, namely the coefficient of determination (R^2), the problem's condition number (CN) and also the minimum number of directions left after filtering (n_v). The algebraic problem and its solution via singular value decomposition (SVD) is explained in equations (5-7).

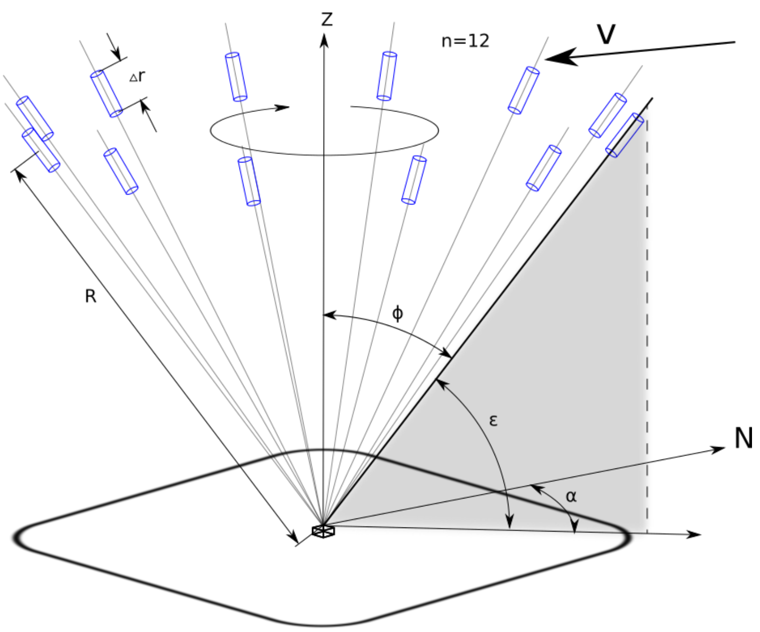

Figure 1 Stepped-stare VAD schematic for n=12 directions, adapted from [13, Fig. 1]. The blue cylinders show that the radial velocities for a single range gate are actually representative for a volume along the LOS. The length corresponds to the pulse duration, i.e. a few 100 ns.

Projection matrix (5)

$$\mathbf{A} = \begin{pmatrix} \sin\alpha_1 \sin\phi & \cos\alpha_1 \sin\phi & \cos\phi \\ \cdots & \cdots & \cdots \\ \sin\alpha_n \sin\phi & \cos\alpha_n \sin\phi & \cos\phi \end{pmatrix}$$

VAD measurement (6)

$$\vec{v}_{LOS} = \mathbf{A} \cdot \vec{V}$$

Wind field reconstruction using SVD

$$\vec{v}_{LOS} = svd(\mathbf{A}) \cdot \vec{V}$$
$$\vec{v}_{LOS} = \mathbf{UDV^T} \cdot \vec{V}$$

Estimated solution (7)

$$\Rightarrow \hat{\vec{V}} = \mathbf{VD^{-1}U^{\mathit{T}}}\vec{v}_{LOS}$$

While DLs in a vertical scanning mode are often used to measure the turbulent energy dissipation rate, it is more difficult to derive TKE with a single DL. For this purpose, we also use a conical scan geometry, but in a continuous scanning mode (CSM) and with a specific zenith angle of 54.7°, in order to scale the horizontal and vertical parts of the TKE equally (see Equation (9)). This method was originally applied to Doppler radar observations [15]. It estimates the TKE from the fluctuations in radial velocities (σ_L^2) along a scan cycle which requires small and roughly constant azimuth differences. Here, a single scan cycle takes approx. 75 seconds which amounts to approx. 210 different directions and a difference between two adjacent azimuth directions of approx. 1.7° (Fig. 2). This scan mode uses only 2000 pulses per direction, which leads to weak return signals and a reduction in data availability and quality. The TKE is related to the variance of the lidar estimated radial velocities, but the fact that the DL retrieval always represents a volume along the LOS makes a correction, σ_t^2, necessary to account unresolved small-scale wind fluctuations due to the averaging over the pulse volume, plus a correction for instrumental noise, σ_e^2 [17]. For a detailed description of this method, we refer to [15-17].

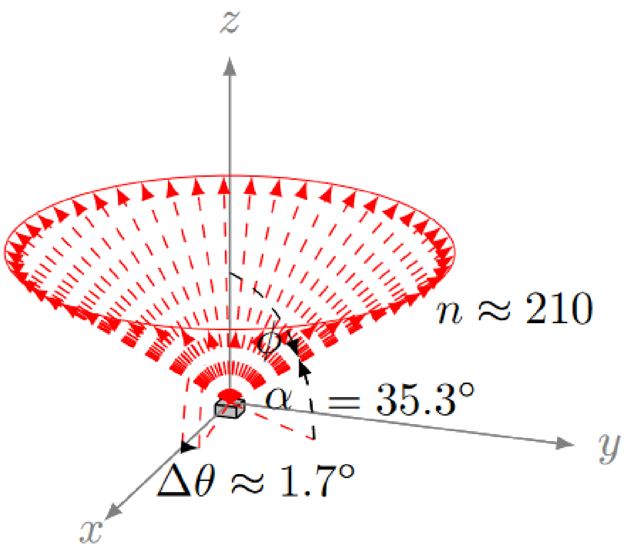

Figure 2 CSM schematic used to retrieve TKE with a single DL, adapted from [16, Fig. 3a]. In this figure, α refers to the elevation angle and the azimuth angle is described by θ.

TKE without correction, according to [15] (8)

$$TKE = \frac{3}{2}\bar{\sigma}_L^2,$$

(9)

$$\text{with } \bar{\sigma}_L^2 = \frac{1}{2\pi \sin\phi}\int_0^{2\pi} {v'_{LOS}}^2 d\alpha = \frac{1}{2}\left(\langle u'^2\rangle + \langle v'^2\rangle + \frac{2}{\tan^2\phi}\langle w'^2\rangle\right)$$

TKE with correction, according to [17] (10)

$$TKE = \frac{3}{2}(\bar{\sigma}_L^2 + \bar{\sigma}_t^2 - \bar{\sigma}_e^2)$$

Lastly, we also attempted to derive wind gusts with a scanning DL operated in CSM. Gust detection requires a fast scan cycle and measurements without the occurrence of velocity folding. Therefore, we reduce the cycle time to approx. 3.4 seconds with leaves us with approx. 11 independent azimuth directions, and in order to reduce the possibility of velocity folding the zenith angle is set to 28°. Due to the fast scanning mode, the number of pulses per direction is set to 2000, i.e. data quality and availability are also reduced. Wind gusts are identified for a chosen time window, here 10 min. Therefore, the mean wind speed within the time window as well as the wind speeds of individual cycles need to be derived. Thus, there are approx. 180 cycles per time window for CSM mode and only around 25 for stepped-stare VAD. The largest of these single-cycle wind speed values is chosen as the maximum gust. While the mean wind is more robust, the individual cycle winds present a challenge to data filtering and to the “regression problem” [16].

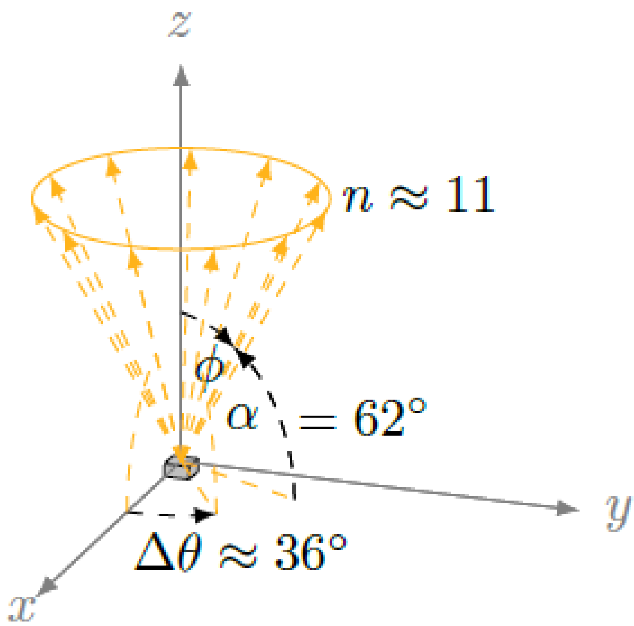

Figure 3 CSM schematic used to retrieve wind gusts with a single DL, adapted from [16, Fig. 3g]. In this figure, α refers to the elevation angle and the azimuth angle is described by θ.

3. Results and Discussion

For DWD, the long-term performance of the measured mean wind product is of high importance, because only a reliable instrument and product can be used in a future operational network.

Therefore, we compare the DL wind speeds with those observed with the operational RWP for the measurement period starting in 2016 until today. Figure 4 (top) shows high correlation between the two instruments with hardly any outliers. The height resolved difference reveal that the average difference is less than 0.5 ms^{-1} for all available heights and that the 1st and 5th percentile as well as the 99th and 95th percentile show increasing spread with decreasing data availability (Fig. 4, bottom). Overall, the instrument performance is very good and the DL mean wind product appears to be of the same quality as the RWP wind. However, the RWP's data availability (not shown) is obviously much higher throughout the year and throughout the entire troposphere, while the DL's product availability is mostly dependent on the extend of the atmospheric boundary layer with the exception of optically thin clouds in the free troposphere.

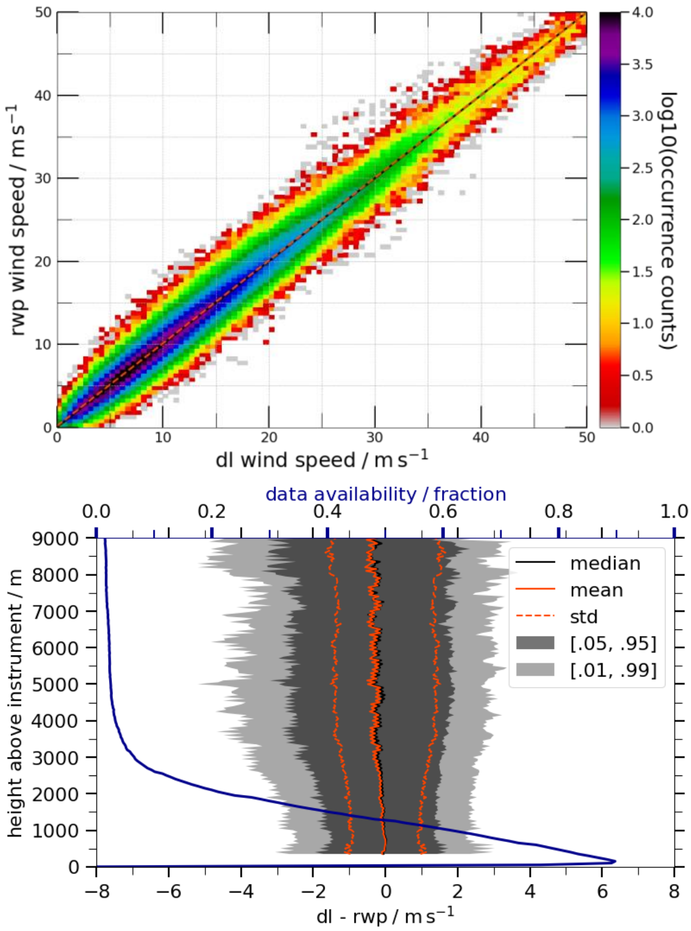

Figure 4 Longterm (2016 until today) comparison of wind speeds observed with the Halo Streamline XR system at Lindenberg with the radar wind profiler as an operational reference: (top) scatter plot with occurences (shading); (bottom) height dependent statistics of wind speed differences paired with average product data availability (blue line).

The TKE product is still in development, but Figure 5 (left) shows that the DL agrees well with the sonic anemometer at 90 m above gound level if the corrections outlined in [17] are included. If the TKE above 90 m is of the same quality, this method has not only great observational potential, but could also be used for model evaluation and development. On the downside, Figure 5 (right) shows that TKE information can only be retrieved from the lowest portion of the boundary layer which most often does not include processes at the top of the boundary layer.

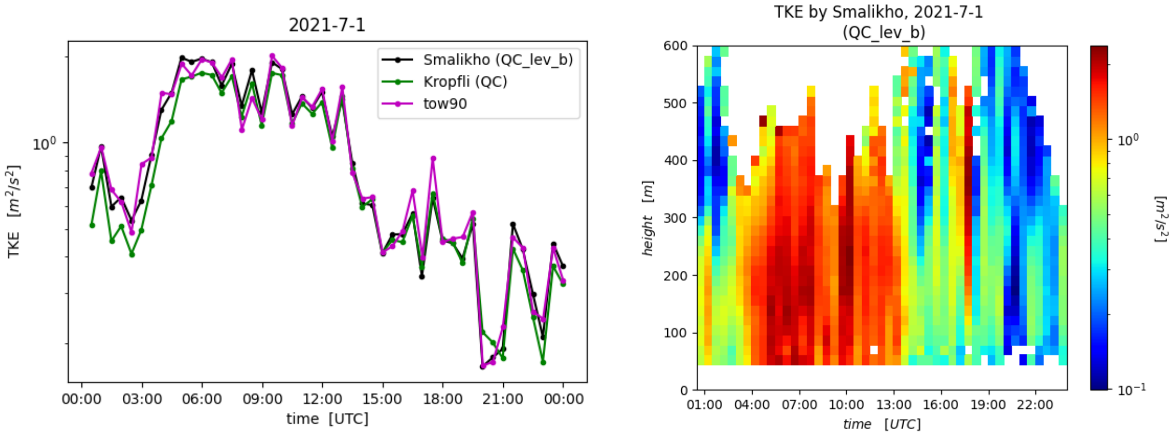

Figure 5 (left) Comparison of TKE derived from the Halo Photonics Streamline DL measurements, without (green) and with (purple) correction, at the Falkenberg measurement site and from the sonic anemometer (black) mounted at the mast at 90 m above ground level for 1st July, 2021. (right) Time-height cross-section of TKE derived with from the DL for the same day.

Last but not least, the wind gust detection and speed, also a product in development, can be validated with the same sonic anemometer located at the Falkenberg tower. Figure 6 compares the speed of mean wind and wind gusts observed with both instruments, respectively. Both depict a high correlation, even though the spread around the regression line of gusty winds is larger. This is highlighted by the slightly smaller R^2 and RMSD values of the gust wind speeds compared to the mean wind speed. However, an RMSD of 0.58 ms^{-1} for gust speeds can be considered a very good agreement, considering the different measurement principles of the two instruments and it certainly illustrates the potential of the method. Through the measurements of vertical gust profiles, we hope to improve our understanding of events, such as frontal passages or thunder storms.

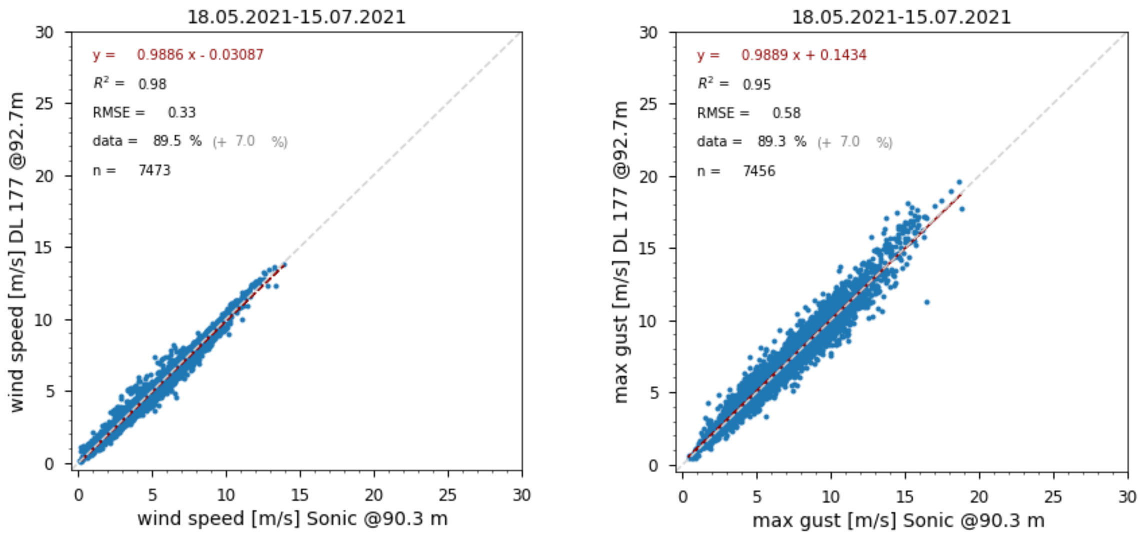

Figure 6 Comparison of wind speed (left) and wind gust speed (right) at the Falkenberg measurement site measured with a Halo Photonics Streamline DL and with a sonic anemometer mounted at the mast at 90 m above ground level for the period between 18th May to 15th July, 2021.

4. Challenges

All in all, the examples presented give just a glimpse of the capabilities of ground-based DLs. So far, we have restricted ourselves to single instrument retrievals and their validation. But multi-DL retrieval, such as virtual tower measurements, are another important use case. However, even though we can rely on reference instruments as the RWP for mean wind applications, finding references for TKE and wind gusts is a challenging on its own. In the future, we think that UAVs will help with this task. In addition, we note that a full overview of DL applications also needs to consider process studies.

But, we want to point out that the advanced use cases presented today, e.g. the TKE retrieval, inevitably lead to weak backscattered signals. This increases the influence of noise, both instrumental and atmospheric, on the observations. New filter methods need to be developed and tested in order to deal with problems created by these setups [16].

5. Acknowledgements

The authors acknowledge the work and support of DWD’s technical staff members.

Further, we gratefully acknowledge the support by the European Cooperation in Science and Technology (COST) action “PROBE” (CA18235) in the form of a travel grant to attend this meeting.

6. References

[1] Benedetti-Michelangeli, G., Congeduti, F., and Fiocco, G.. Measurement of Aerosol Motion and Wind Velocity in the Lower Troposphere by Doppler Optical Radar, *J. Atmos. Sci.,* 29, 5 (1972): 906-910. doi: 10.1175/1520-0469(1972)029<0906:MOAMAW>2.0.CO;2

[2] Post, M. J., Schwiesow, R. L., Cupp, R. E., Haugen, D. A., and Newman, J. T.. A Comparison of Anemometer- and Lidar-Sensed Wind Velocity Data, *J. Appl. Meteorol. Climatol.,* 17, 8 (1978): 1179-1181. doi: 10.1175/1520-0450(1978)017<1179:ACOAAL>2.0.CO;2

[3] Henderson, S. W., Suni, P. J. M., Hale, C. P., Hannon, S. M., Magee, J. R., Bruns, D. L., et al. (1993). Coherent Laser Radar at 2 Mu M Using Solid-State Lasers. *IEEE Trans. Geosci. Remote Sensing,* 31 (1), 4–15. doi:10.1109/36.210439

[4] Targ, R., Steakley, B. C., Hawley, J. G., Ames, L. L., Forney, P., Swanson, D., et al. (1996). Coherent Lidar Airborne Wind Sensor II: Flight-Test Results at 2 and 10 µm. *Appl. Opt.,* 35 (36), 7117–7127. doi:10.1364/ao.35.007117

[5] Pearson, G. N. and Eacock, J. R.. Fiber-based coherent pulsed Doppler lidar for atmospheric monitoring. In Upendra N. Singh, editor, Lidar Remote Sensing for Industry and Environment Monitoring II, volume 4484, pages 51 – 57. International Society for Optics and Photonics, *SPIE*, 2002. doi: 10.1117/12.452799.

[6] O’Connor E. J., Illingworth A. J., Brooks I. M., Westbrook C. D., Hogan R. J., Davies F., and Brooks B. J.. A method for estimating the turbulent kinetic energy dissipation rate from a vertically pointing doppler lidar, and independent evaluation from balloon-borne in situ measurements. *J. Atmos. Ocean. Technol.*, 27(10):1652–1664, 2010. doi: 10.1175/2010JTECHA1455.1.

[7] Wildmann N., Vasiljevic N., and Gerz T.. Wind turbine wake measurements with automatically adjusting scanning trajectories in a multi-doppler lidar setup. *Atmos. Meas. Tech.*, 11(6):3801–3814, 2018. doi: 10.5194/amt-11-3801-2018.

[8] Gustafsson, N., Janjić, T, Schraff, C., et al. Survey of data assimilation methods for convective-scale numerical weather prediction at operational centres. *Q. J. R. Meteorol. Soc.,* 2018; 144: 1218– 1256. doi: 10.1002/qj.3179

[9] Doppler, C.. Ueber das farbige Licht der Doppelsterne und einiger anderer Gestirne des Himmels: Versuch einer das Bradley'sche Aberrations-Theorem als integrirenden Theil in sich schliessenden allgemeineren Theorie. K. Böhm Gesellschaft der Wissenschaften, 1903.

[10] Reitebuch, O. and Hardesty, R.M. (2021). Doppler Wind Lidar. In: Foken, T. (eds) Springer Handbook of Atmospheric Measurements. Springer Handbooks. Springer, Cham. doi: 10.1007/978-3-030-52171-4_27

[11] Kotthaus, S., Bravo-Aranda, J. A., Collaud Coen, M., Guerrero-Rascado, J. L., Costa, M. J., Cimini, D., O'Connor, E. J., Hervo, M., Alados-Arboledas, L., Jiménez-Portaz, M., Mona, L., Ruffieux, D., Illingworth, A., and Haeffelin, M.: Atmospheric boundary layer height from ground-based remote sensing: a review of capabilities and limitations, *Atmos. Meas. Tech. Discuss.* [preprint], https://doi.org/10.5194/amt-2022-14, in review, 2022.

[12] Browning, K. A., and Wexler, R.. The Determination of Kinematic Properties of a Wind Field Using Doppler Radar, *J. Appl. Meteorol. Climatol.,* 7, 1 (1968): 105-113. doi: 10.1175/1520-0450(1968)007<0105:TDOKPO>2.0.CO;2

[13] Päschke, E., Leinweber, R., and Lehmann, V.: An assessment of the performance of a 1.5 μm Doppler lidar for operational vertical wind profiling based on a 1-year trial, *Atmos. Meas. Tech.*, 8, 2251–2266, 2015. doi: 10.5194/amt-8-2251-2015

[14] Fischler, M. A. and Bolles R. C.. 1981. Random sample consensus: a paradigm for model fitting with applications to image analysis and automated cartography. *Commun. ACM 24*, 6 (June 1981), 381–395. doi: 10.1145/358669.358692

[15] Kropfli, R. A. Single Doppler Radar Measurements of Turbulence Profiles in the Convective Boundary Layer, *J. Atmos. Ocean. Technol.,* 3, 2 (1986): 305-314. doi: 10.1175/1520-0426(1986)003<0305:SDRMOT>2.0.CO;2

[16] Steinheuer, J., Detring, C., Beyrich, F., Löhnert, U., Friederichs, P., and Fiedler, S.: A new scanning scheme and flexible retrieval for mean winds and gusts from Doppler lidar measurements, *Atmos. Meas. Tech.*, 15, 3243–3260. doi: 10.5194/amt-15-3243-2022, 2022.

[17] Smalikho, I. N. and Banakh, V. A.: Measurements of wind turbulence parameters by a conically scanning coherent Doppler lidar in the atmospheric boundary layer, *Atmos. Meas. Tech.*, 10, 4191–4208, https://doi.org/10.5194/amt-10-4191-2017, 2017.

Evaluation of differences between DMD and OPD in detection of coherent structures

Zuzana Kluková[1, 2], Štěpán Nosek[1], Zbyněk Jaňour[1]

[1]Institute of Thermomechanics, Czech Academy of Sciences, Department of Fluid Dynamics, Dolejškova 1402/5, 18200, Praha 8, Czech Republic
[2]Charles University, Faculty of Mathematics and Physics, Department of Atmospheric Physics, Ke Karlovu 3, 12116, Praha 2, Czech Republic

Abstract

It is well known that flow within the Atmospheric boundary layer is not absolutely chaotic, but it contains some structures (so called coherent structures). Using mathematical methods, it is possible to reveal these structures in time-resolved data obtained for instance from PIV measurements or numerical modelling. Next to the widely used proper orthogonal decomposition (POD) arising from the singular value decomposition, there are methods producing complex eigenvalues and eigenvectors containing information about the cyclic propagation or pulsation of the coherent structures, frequency of their excitation, and decay time of the amplitude oscillation. As an example, we can mention dynamic mode decomposition (DMD) and oscillating pattern decomposition (OPD). Both the methods (DMD and OPD) are based on computing the POD modes, but following algorithm is different. Within this contribution, I will evaluate the differences between these two methods on the PIV data and I will show how the paremeters choice within the algorithm influence the results.

Transient Wind Forcing: a method for modelling wind shear in building-scale Large Eddy Simulations

M. Koren[1], M. Balogh[1], K. Gergely[1]

[1]Department of Fluid Mechanics, Faculty of Mechanical Engineering, Budapest University of Technology and Economics. Bertalan Lajos u. 4 – 6, H-1111 Budapest, Hungary. E-mail: koren.marton@gpk.bme.hu, balogh.miklos@gpk.bme.hu, kristof.gergely@gpk.bme.hu,

Abstract

The Transient Wind Forcing (TWF) wind-shear coupling method is tested by performing Large Eddy Simulation in two spherically periodic domains of different sizes. According to the TWF method, the velocity-time series extracted from a single observation point in the large model was used for controlling the horizontal components of the spatially distributed driving force in the small model. Turbulent flow over an idealized city was investigated. The model consists of square-based buildings arranged in a staggered configuration. The long-distance dispersion from ground level point sources was examined by attributing the numbers of periodic jumps (in x and y directions) to the tracked mass-less particles. The effects of building height and mesoscale atmospheric phenomena, e.g., the Coriolis force and stability, were studied. As a result of the Coriolis force, the wind direction changed significantly in the space between the buildings and at roof level. The performance of TWF coupling is assessed based detailed statistical comparison of the velocity and tracer concentration fields obtained from the large and small models. Both the flow and the concentration fields are successfully reproduced in the small model with the help of the TWF technique.

Coarse grid and implicit LES for urban pollutant dispersion

T. Lauriks[1,2], W. Munters[2], J. van Beeck[2] and S. Denys[1]

[1] University of Antwerp, Faculty of Science, Department of Bioscience Engineering, Groeneborgerlaan 171, 2020 Antwerpen, Belgium
[2] von Karman Institute for Fluid Dynamics, Environmental and Applied Fluid Dynamics Department, Waterloosesteenweg 72, 1640 Sint-Genesius-Rode, Belgium

Abstract

Improving urban air pollution remains important, for which CFD is a powerful tool. However, RANS is insufficiently accurate and LES is too computationally costly. Monotonicity preserving implicit LES (MILES) is implicit LES using non-oscillatory finite volume methods. Both coarse grid LES and MILES might lower the computational cost, at an acceptable accuracy. Dispersion around an array of cuboids was simulated (CEDVAL B1-1 case), to determine the accuracy of coarse grid LES, MILES, and RANS, using OpenFOAM. Three grid resolutions were used. The finest marginally resolved 80 % of the turbulent kinetic energy. It was necessary to also perform the conventional LESs with a non-oscillatory scheme. Even on the coarse grids, in general, both LES and MILES simulated the concentration more accurately than a well tuned unsteady RANS simulation on the finest grid. The difference between switching the subgrid scale model on or off was insignificant, but MILES was slightly faster than LES. MILES on the coarsest grid was only 1.6 times slower than RANS.

1 Introduction

Reducing urban air pollution levels remains imperative [7], but an accurate prediction of pollutant dispersion in urban areas is not straightforward [18, 19]. CFD is considered a powerful tool for the prediction of urban wind and dispersion patterns [6, 15, 18]. However, it is well known that the faster Reynolds-averaged Navier-Stokes (RANS) method is insufficiently accurate [3] and that large eddy simulation (LES) has a too high computational cost [2].
Using coarse grids reduces the computational cost of LES [4], which – luckily – seems possible at acceptable accuracy for urban dispersion cases [21, 13]. Moreover, indications exist that implicit LES (ILES), more specifically monotonicity preserving ILES (MILES), is a suitable simulation method for marginally resolved flows. In MILES, non-oscillatory finite volume methods (FVMs) are used, e.g. flux limiting schemes such as the total variation diminishing (TVD) schemes. Theoretical indications exist, that such methods result in the presence of an implicit mixed subgrid scale (SGS) model (i.e. SGS viscosity and scale-similar) [11]. Mixed SGS models are suitable for complex geometries and marginally resolved flows (e.g. [1] and [16]). Several large scale urban dispersion MILES studies (e.g. [21]) attained high simulation speeds and achieved a good accuracy using coarse grids. These studies were performed using the FAST3D-CT code. Despite this success, no recent similar studies were published, likely due to the fact that FAST3D-CT is not publicly accessible.

2 Research summary and goals

The CEDVAL wind tunnel experiment of flow and dispersion over a regular array of cuboids, the B1-1 case (Figure 1), was simulated with RANS, LES, and MILES. The first goal was to determine how coarse the grid can be, so that a wall-modeled LES still significantly outperforms RANS and to determine the resulting computational cost. To achieve this goal, RANS and LES were applied on a grid that marginally resolved 80 % of the turbulent kinetic energy in the LES. Subsequently, two coarser grids were used for LES. The second goal was determining whether MILES, as implementable using the standardly available tools in the open source CFD software OpenFOAM (mostly TVD schemes), is a valuable strategy. In contrary to what was performed in the theoretical analysis of MILES in [11] and the convection algorithm of FAST3D-CT [5], it is impossible in OpenFOAM to apply a flux limiting scheme to both instances of the velocity in the convection term, which might result in a significant difference in accuracy as compared to the FAST3D-CT code. However, the rationale for using OpenFOAM, is that it is free and open source, and hence accessible to a large CFD community.

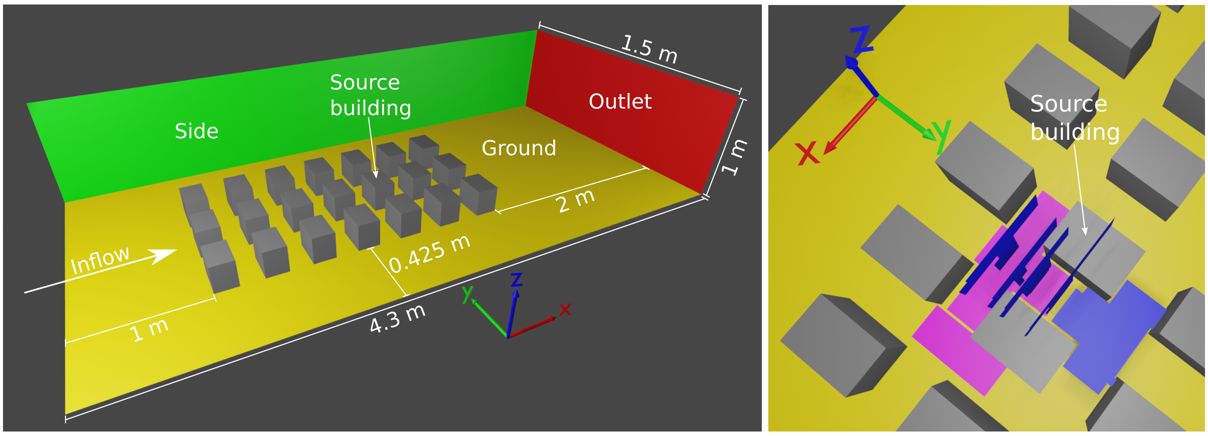

(a) Computational domain. A tracer was emitted from 4 inlets at the bottom part of the leeward wall of the source building. The origin of the coordinate system coincided with the source building bottom face center. All buildings have the same dimensions, spanwise: 0.15 m, streamwise: 0.1 m, and vertical: 0.125 m. All spacings between the buildings are equal: 0.1 m. The model scale is 1:200.

(b) CEDVAL measurement and model sampling locations. The concentration was measured and sampled in the magenta plane, at $z = 0.0075$ m. The mean velocity and stresses were measured and sampled in the blue planes, at respectively $z = 0.0625$ m, $y = 0$ m, $y = -0.05$ m, $y = -0.075$ m, and $y = -0.125$ m.

Figure 1: CEDVAL experiment and computational domain.

3 Governing equations

Simulations were performed with OpenFOAM v2012. For RANS and LES, respectively, the incompressible LES and unsteady RANS equations were solved, supplemented with a scalar transport equation. In all MILESs, the governing equations were identical to the LESs, but the SGS model was switched off. Unsteady RANS was performed, because the values of several variables, e.g. the mean vertical velocity $\langle w \rangle$, at the sampling locations (Figure 1 (b)) differed substantially between iterations in a converged steady RANS simulation (the residual decreases were also very small). For LES, the WALE SGS model was used. The cube root of the cell volumes was selected as filter width. For RANS, the $k - \omega$ SST turbulence model was selected, because it previously demonstrated a good accuracy on the CEDVAL B1-1 case [23]. In the scalar transport equation, the standard gradient diffusion hypothesis was applied, with a turbulent Schmidt number, Sc_t, value of 0.2, the best performing setting among different tested values by [23]. It should however be noted that said authors point out themselves, that Sc_t varies with height in the atmospheric boundary layer (ABL) [12], while all concentration measurement points are located at a very low height. Hence, adjusting Sc_t to obtain good concentration results at the single measurement height likely reduces the accuracy at other heights. Even so, the eddy resolving methods on the coarsest grid obtain much more accurate dispersion results than RANS performed on the finest grid (see section 8.2).

4 Computational methods, domain and mesh

The domain dimensions can be viewed in Figure 1 (a). The base mesh was designed to be coarse but at the same time accommodate an appropriate simulation of the approach flow, the ABL, and to be nearly fully orthogonal. It was constructed in blockMesh, with x, y, and z spacings of 0.02, 0.01, and 0.0125 m respectively, without grading. The corresponding z^+ value in the ABL was 140. A total of 3 meshes derived from the base mesh was used, where the grid spacing of mesh 1 to 3 increased sequentially from finest to coarsest (Table 1). If in this research a local refinement was performed in a mesh, this means that the grid spacings in all directions of the concerning part of the domain were halved. For mesh 1, one refinement around the buildings was performed. This allowed the LES to marginally resolve 80 % of the turbulent kinetic energy (TKE). Besides, the average z^* values on the buildings and the streets were approx. 166 and 128, respectively, for the LES. Mesh 2 was the base mesh, where only the surfaces of the tracer inlets were refined once. Mesh 3 was similar to mesh 2, except for the ABL grid spacings, which were increased by a factor 1.25 in each direction. The average z^* values in the LES on mesh 3 were 373 on the buildings and 255 on the streets.
With regard to the eddy resolving methods, it was observed that reaching steady state and obtaining statistically converged mean variables and Reynolds stresses was possible, after reaching a simulation time of 1800 s and averaging over 1600 s. For RANS, a simulation time of 600 s and an averaging time of 200 s was necessary.

Table 1: Grid spacings of the meshes used for the CEDVAL case.

	mesh 1	mesh 2	mesh 3
Δx ABL [m]	0.02	0.02	0.025
Δy ABL [m]	0.01	0.01	0.0125
Δz ABL [m]	0.0125	0.0125	0.015625
refinements around buildings	1	0	0
refinements of tracer inlets	0	1	1

5 Boundary conditions

A symmetry plane was applied at the top of the domain (Figure 1 (a)). A symmetry plane was also applied at the lateral sides in the RANS model. In the eddy resolving models, periodic boundary conditions were applied at the lateral sides. The pressure, p, at the outlet was set to a constant static pressure and the

other variables were set to zero gradient. At the bottom surface around the buildings, a rough wall function (atmNutkWallFunction) was applied, with a surface roughness length, z_0, of 0.00045 m. At the buildings and the bottom surface between the buildings, a smooth wall function (nutkWallFunction) was applied. At the tracer inlets in the RANS model, the average of the experimental velocity was set (0.024 m/s). In the LES model, a synthetic turbulence generation method was applied to the tracer inlets, namely the divergence free synthetic eddy method (DFSEM). The settings applied to this method were: a uniform average velocity of 0.024 m/s and isotropic turbulence with an intensity of 10 %. A value of 1e-3 kg/m^3 was set for the tracer concentration, at the tracer inlets.
In this research, it was possible to largely avoid the well-known problem of horizontal inhomogeneities in ABL RANS simulations, which can also occur in LES when the computationally efficient method of synthetic turbulence generation is applied [14]. In fact, the solution for this problem in LES from the latter authors was applied in this research, where the input parameters of the turbulence generator – in this research the DFSEM was applied at the inflow boundary – are changed, so that the correct mean velocity and turbulence profiles are obtained at the location of interest in the domain. By using as input the log law fitted profile of the mean velocity (friction velocity, u_*, equal to 0.33393 m/s and z_0 = 0.00045 m), the fitted profile of the shear stress $\langle u'w' \rangle$ – where u, v, and w are respectively the x, y, and z velocity, $'$ signifies the fluctuating part, and $\langle \rangle$ the mean – and alterations of the fitted profiles of the normal stresses, it was possible to obtain good ABL characteristics at the location of the center of the first building row in the empty domain. Concerning the RANS simulation, it was possible to generate a good ABL at the location of interest, using the $k - \omega$ SST turbulence model, the above mentioned wall function, and the standard ABL inflow boundary conditions available in OpenFOAM (atmBoundaryLayer). The turbulent kinetic energy, k, profile expression of the OpenFOAM ABL inflow boundary condition was fitted to the CEDVAL data.

6 Numerical methods

This first attempted strategy was to use second order schemes for all terms of all equations, except for the convection of the velocity in the MILESs. It was however observed that even on mesh 1, the velocity and concentration field of the LES were highly oscillatory. Therefore, flux limiting schemes were applied to the convection of the scalar and the velocity in all simulations. This was also applied to the RANS simulation, since it was observed that this greatly improved the RANS concentration results. An overview of all simulations is available in Section 7. The observed oscillatory behavior of the LES with full second order discretization on mesh 1 can in fact be expected, since mesh 1 is still coarse, which can render the simulation unstable. To resolve this issue, a fine and computationally very expensive grid can be used to obtain a local Peclet number ≤ 2. However, the upwind component of a flux limiting scheme also solves this problem [17, 8, 20].
Concerning MILES, three TVD schemes were selected for assessment: the Superbee, OSPRE, and Minmod scheme. The rationale for selecting these schemes, is that the behavior of their flux limiter covers a large area of the allowed second order TVD region. Since the behavior of the flux limiter influences the implicit SGS model, this hence boils down to a calibration of the implicit SGS model [21]. These three schemes were applied on mesh 1 (Table 1), while only the Superbee scheme was applied on the coarser meshes, because it is the least diffusive TVD scheme and was already identified as suitable for MILES [10].
Finally, the additional backscatter based on information from the applied flux limiting scheme described

by [21] was applied. This was achieved by perturbing the resolved velocity in each mesh element:

$$\boldsymbol{u}_P, \text{per} = \boldsymbol{u}_P + \text{sign}\left(\boldsymbol{u}_P\right) \odot m\boldsymbol{r} \sum_f |1 - \Psi_f| \left\|\boldsymbol{u}_f^H - \boldsymbol{u}_f^L\right\| \quad (1)$$

where $\boldsymbol{u}_P$, per is the perturbed velocity at the cell centroid, $\boldsymbol{u}_P$ the unperturbed velocity as calculated by the solver, $\odot$ signifies element wise multiplication, $||$ the absolute value, $\|\|$ the magnitude, m is a constant that can be altered to change the magnitude of the perturbation, $\boldsymbol{r}$ is a vector whose 3 components are random numbers drawn from [0,1], Ψ_f is the flux limiter at face f of the mesh element, and $\boldsymbol{u}_f^H$ and $\boldsymbol{u}_f^L$ are the velocities at face f, respectively obtained with the high and low order parts of the scheme. The derivation of Eq. 1 from the description of [21] required some interpretation, since this description is not entirely unambiguous. On each mesh, adding backscatter to MILES was applied, making use of Superbee and two values of m, 0.173 and 0.3.
Both for the RANS and LES models, the upper limit of the residuals was set to 1e-5 for p and to 1e-8 for all other variables.

7 Overview of all simulations

In Table 2, an overview can be found of all performed simulations.

Table 2: Overview of simulations of the CEDVAL B1-1 case. See Table 1 for the meshes. LES: turbulence model on, MILES: turbulence model off.

	Mesh 1	Mesh 2	Mesh 3
RANS	v		
$\text{LES}_{\text{Superbee}}$	v	v	v
MILES: Superbee	v	v	v
MILES: OSPRE	v		
MILES: Minmod	v		
MILES: Superbee, backscatter: 0.3	v	v	v
MILES: Superbee, backscatter: 0.173	v	v	v

8 Results and discussion

This section begins with some general observations, remarks, and conclusions that can easily be summarized, so that the more detailed discussion in the following subsections can be kept as concise as possible. Firstly, it was observed that the solution of the eddy resolving methods was asymmetrical on mesh 1. Also the RANS results and the results on the coarser meshes were slightly asymmetrical. The cause for this seemed to have been the fact that the nature of the mesh refinements in OpenFOAM used in this research introduces asymmetries in the grid and that the DFSEM synthetic turbulence generator in OpenFOAM seems to not generate an entirely symmetrical inflow over the spanwise direction. Therefore, in the comparison of the results to the measurements, all model results were averaged over the symmetry axis wherever possible. Also, the overview of the flow field (Figure 2) are results on mesh 2 instead of the finest mesh, since these results were less asymmetrical but qualitatively similar to the results on mesh 1.

Besides, a lot of measurements, at many locations and of several variables, are available for the CEDVAL B1-1 case. For all available locations and variables, data was extracted from every simulation. In this short paper, however, only a small selection, believed to be representative for the drawn conclusions, can be shown. For all simulations and variables, root mean square errors (RMSEs) and mean absolute errors (MAEs) were also calculated, for each individual measurement plane and over all locations. Again, only a small selection of the available errors can be shown in this paper.
For all simulations, the difference between results of LES (with the Superbee scheme) and MILES with the Superbee scheme is insignificant for all variables. Results of both are shown in the plots, but for conciseness, henceforth mostly only LES will be discussed in the text. In addition, on mesh 1, MILES with the Minmod scheme performs clearly worse than LES for the concentration concerning the overall MAE and RMSE (result not shown). OSPRE, on the other hand, performs better than LES concerning the overall RMSE. However, it performs worse than LES for the mean velocity components. It was hence concluded that the Superbee scheme has the best performance – being the least diffusive scheme – as previously established in the literature [10]. Finally, it can be concluded from these observations, that the choice of the TVD scheme has a much larger influence than switching the turbulence model on or off in OpenFOAM. Results obtained with the Minmod and OSPRE scheme will not be discussed further.

8.1 Flow field

As explained in Section 6, LES on the finest mesh (Table 1) in combination with second order convection disretization resulted in a highly oscillatory velocity (and concentration) field. Mesh 1 was still rather coarse and as expected, applying a TVD scheme to the convection solved the issue of the oscillations. Hence, a first important conclusion is, that applying non-oscillatory schemes allows to extract sensible results from LES on coarse meshes, which is in fact basic knowledge.
Figure 2 shows an overview of the mean flow field close to the source building, in the volume where the tracer is emitted. A typical mean flow field for street-canyon-like structures occurs. At each building corner, a vortex is present in the horizontal plane (Figure 2 (a)). In the vertical plane at $y = 0$, a vortex is also present (Figure 2 (b)).

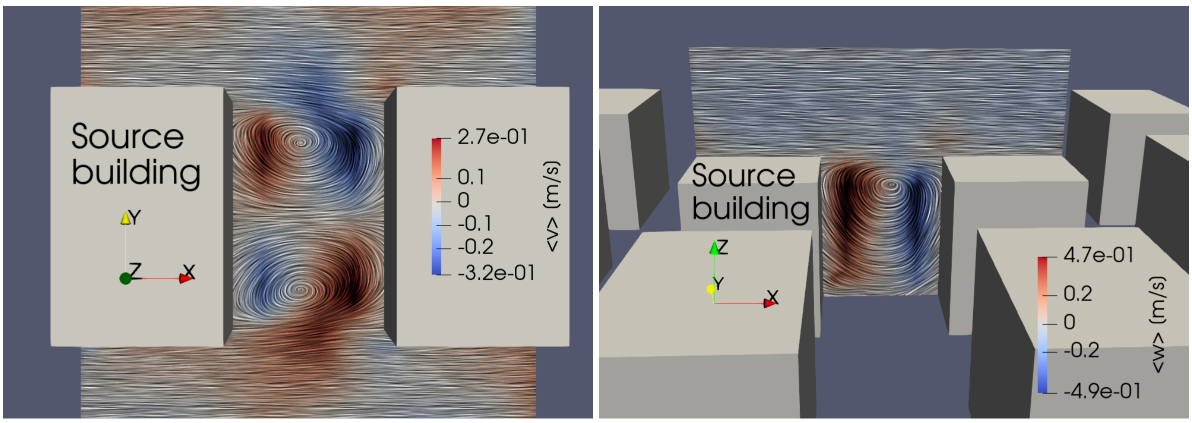

(a) LES results on mesh 2 at $z = 0.0625$ m. (b) LES results on mesh 2 at $y = 0$ m.

Figure 2: Line integral convolution and mean velocity components close to the source building.

When considering the MAE (Table 3), in general, LES on mesh 1 performs better than RANS regarding the mean velocity (see also Figure 3), while it is less clear which method performs better for the Reynolds stresses. However, the MAE is slightly deceiving, since LES captures the trends in the shear stresses better than RANS, of which two examples are shown in Figure 3. As the grid coarsens, for LES in general, results first improve and then worsen again. The backscatter tends to have a favorable effect on the velocity results, but clearly delivers worse stress results. It can be concluded that the LES results are reasonable, but can certainly use improvements. This is likely achievable using a finer grid. However, due to the already substantial computation time on mesh 1 (20.13 days, see further), this was not applied in this research, which tries to obtain simulation speed in LES.

Table 3: MAEs of the mean velocity components and available Reynolds stresses. SB: MILES with Superbee, BS: backscatter.

	$\langle u \rangle$	$\langle v \rangle$	$\langle w \rangle$	$\langle u'v' \rangle$	$\langle u'w' \rangle$	$\langle u'u' \rangle$	$\langle v'v' \rangle$	$\langle w'w' \rangle$
Mesh 1								
LES	3.5e-01	2.6e-01	2.1e-01	1.3e-01	9.3e-02	3.5e-01	2.3e-01	2.0e-01
SB	3.5e-01	2.7e-01	2.1e-01	1.3e-01	9.1e-02	3.4e-01	2.3e-01	2.0e-01
BS 0.3	3.6e-01	2.4e-01	2.0e-01	1.8e-01	1.8e-01	5.6e-01	6.2e-01	4.3e-01
BS 0.173	4.1e-01	2.5e-01	2.0e-01	1.4e-01	1.3e-01	4.3e-01	3.4e-01	3.1e-01
RANS	5.0e-01	2.8e-01	2.1e-01	1.3e-01	7.9e-02	8.3e-01	2.9e-01	1.0e-01
Mesh 2								
LES	3.1e-01	2.7e-01	2.1e-01	1.2e-01	8.9e-02	3.1e-01	2.1e-01	1.2e-01
SB	3.0e-01	2.7e-01	2.0e-01	1.2e-01	8.7e-02	3.1e-01	2.1e-01	1.2e-01
BS 0.3	2.0e-01	2.5e-01	1.9e-01	1.3e-01	2.1e-01	4.5e-01	2.3e-01	3.0e-01
BS 0.173	3.0e-01	2.6e-01	2.0e-01	1.2e-01	1.5e-01	3.5e-01	2.0e-01	2.2e-01
Mesh 3								
LES	4.6e-01	2.8e-01	2.1e-01	1.2e-01	8.9e-02	3.4e-01	2.3e-01	1.2e-01
SB	4.6e-01	2.8e-01	2.1e-01	1.2e-01	8.4e-02	3.4e-01	2.3e-01	1.1e-01
BS 0.3	3.6e-01	2.7e-01	2.0e-01	1.3e-01	1.7e-01	4.4e-01	2.1e-01	2.2e-01
BS 0.173	4.6e-01	2.8e-01	2.1e-01	1.3e-01	1.3e-01	3.8e-01	2.1e-01	1.8e-01

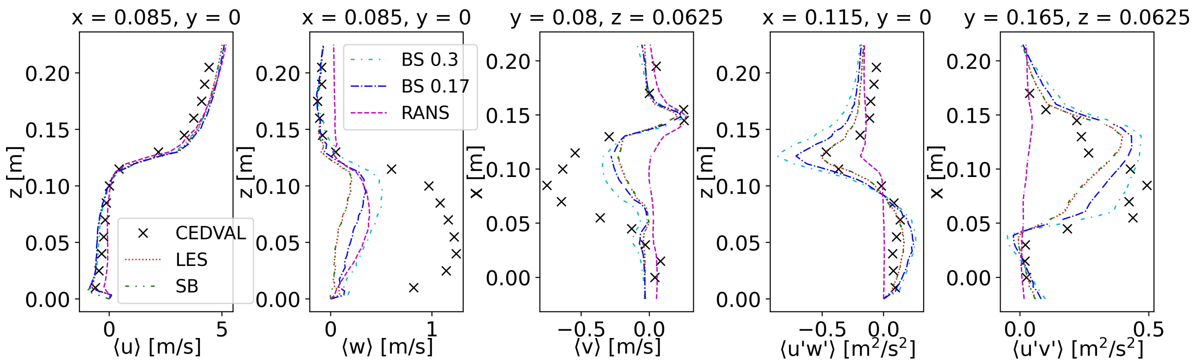

Figure 3: Selection of flow field results on mesh 1. SB: MILES with Superbee, BS: backscatter.

8.2 Concentration field

In Table 4, the MAEs and RMSEs of the concentration of all discussed simulations can be found. It is clear that LES performs much better than RANS on mesh 1. On mesh 2, it performs worse than RANS regarding the RMSE, but the MAE is lower. However, from Figure 4 it is clear that RANS is not able to capture the pronounced concentration peak in the area beside the source building, while LES simulates this peak very well. (In fact, LES captures all the important trends in the concentration profiles on all the grids.) It is hence concluded that LES still performs better than RANS on mesh 2. On mesh 3, LES remains better than RANS. It can be concluded that LES performance is very robust – delivering reasonable concentration results and capturing all important trends – on grids that are rougher than what is advised in wind engineering guidelines [9, 22]. In addition, the advantage of LES is that it does not need tuning, while it was observed that the RANS performance deteriorated for many tested settings that were not applied. Besides, when looking at the errors, it seems that the backscatter has an advantageous effect on the concentration results on the coarser grids. It is hence worthwhile to include the backscatter in future validation studies of coarse grid MILES.

Regarding the computational cost, all simulations were calculated with a similar and nearly optimal number of cells per processor (approx. 2e4 cells/CPU). It is likely that this level of parallellization is rather close to the maximal level. After reaching the maximum level, the computation time can not be reduced anymore and depends entirely on the maximally allowable time step. The computation time of RANS was 3.18 days. LES took 20.13, 8.42, and 5.76 days, respectively on mesh 1, 2, and 3. Switching off the turbulence model caused a speed-up of 13 % on average, with a computation time of 5.11 days for MILES on mesh 3. The backscatter caused a slowdown of 14 % on average, due to a decrease of the time step as a consequence of the applied velocity perturbations.

Table 4: MAEs and RMSEs of the concentration. SB: MILES with Superbee, BS: backscatter.

	LES	SB	BS 0.3	BS 0.173	RANS
			Mesh 1		
RMSE	8.4	8.5	6.3	6.5	19
MAE	1.9	1.9	2.9	2.3	4.3
			Mesh 2		
RMSE	21	22	13	16	
MAE	3.8	3.9	3.3	3.1	
			Mesh 3		
RMSE	12	13	9.6	11	
MAE	2.9	2.9	2.9	2.6	

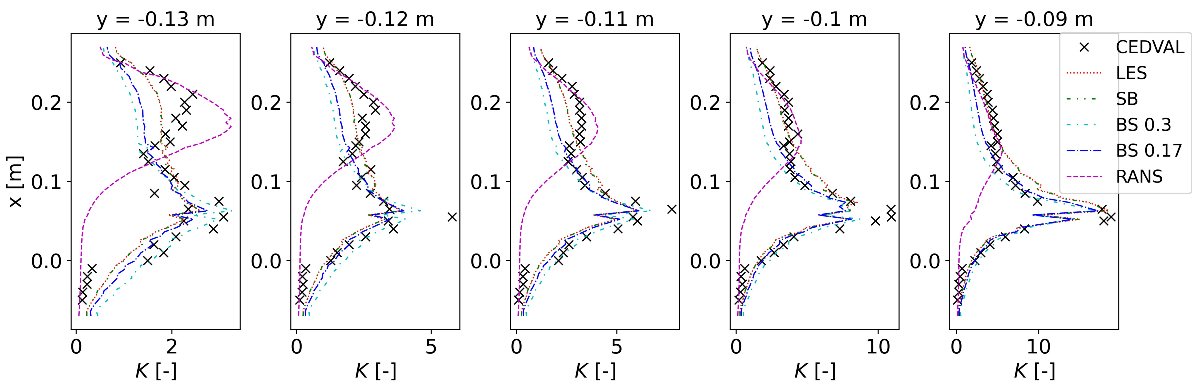

Figure 4: Selection of concentration results. Eddy resolving methods: mesh 2, RANS: mesh 1. SB: MILES with Superbee, BS: backscatter.

9 Conclusion

The performance of LES and MILES on reasonable to coarse grids was compared to an unsteady RANS simulation on a reasonable grid. Firstly, it was observed that non-oscillatory FVMs allow to extract sensible results using eddy resolving methods on coarse grids. Also for RANS, results were greatly improved using non-oscillatory methods.
The Minmod, OSPRE, and Superbee TVD scheme were tested in OpenFOAM for their capability of performing MILES. It was found that the effect of switching the turbulence model on or off in OpenFOAM is insignificant, while the choice of the scheme has an important influence. As previously established in the literature, the Superbee scheme – being the least diffusive TVD scheme – was found to deliver the highest accuracy.
LES performance was very robust, delivering reasonable concentration results and capturing all important trends in the concentration profiles, on grids rougher than advised in wind engineering guidelines. Switching off the turbulence model further reduced the computation time. In addition, an enormous advantage of LES is that it does not need tuning, as opposed to RANS. The computation time for RANS was 3.18 days, while MILES on the coarsest grid took 5.11 days and delivered better concentration results than RANS. It has to be noted, however, that using coarse grids is not ideal. The results were reasonable, but can certainly be improved. The only way of achieving lower computation times using higher resolution conventional LES, instead of e.g. the lattice Boltzmann method, seems to be the parallellization of the time integration.

References

[1] R. Akhavan, A. Ansari, S. Kang, and N. Mangiavacchi. Subgrid-scale interactions in a numerically simulated planar turbulent jet and implications for modelling. *Journal of Fluid Mechanics*, 408:83–120, 2000.

[2] B. Blocken. LES over RANS in building simulation for outdoor and indoor applications: A foregone conclusion? *Building Simulation*, 2018.

[3] Bert Blocken, Rob Vervoort, and Twan van Hooff. Reduction of outdoor particulate matter concentrations by local removal in semi-enclosed parking garages: A preliminary case study for eindhoven city center. *Journal of Wind Engineering and Industrial Aerodynamics*, 159:80–98, dec 2016.

[4] J. Boris. Flux-Corrected Transport looks at forty. *Computers & Fluids*, 84:113–126, 2013.

[5] J. P. Boris and D. L. Book. Flux-Corrected Transport. I. SHASTA, A Fluid Transport Algorithm That Works. *Journal of Computational Physics*, 11:38–69, 1973.

[6] V. Busini and R. Rota. Influence of the shape of mitigation barriers on heavy gas dispersion. *Journal of Loss Prevention in the Process Industries*, 29(13-21):13–21, 2014.

[7] EEA. Air quality in Europe – 2020 report. Technical report, European Environment Agency, 2020.

[8] J. H. Ferziger, M. Perić, and R. L. Street. *Computational Methods for Fluid Dynamics*. 2020.

[9] JÃűrg Franke, Antti Hellsten, Heinke SchlÃijnzen, and Bertrand Carissimo. Best practice guideline for the CFD simulation of flows in the urban environments. Technical report, 2007. COST Action 732.

[10] F. Grinstein and C. Fureby. Recent progress on MILES for high Reynolds number flows. *Journal of Fluids Engineering*, 2002.

[11] F. F. Grinstein, L. G. Margolin, and W. J. Rider. *Implicit Large Eddy Simulation. Computing Turbulent Fluid Dynamics*. Cambridge University Press, 2007.

[12] K. Koeltzsch. The height dependence of the turbulent Schmidt number within the boundary layer. *Atmospheric Environment*, 34:1147–1151, 2000.

[13] D. A. Köse, D. Fauconnier, and E. Dick. ILES of flow over low-rise buildings: Influence of inflow conditions on the quality of the mean pressure distribution prediction. *Journal of Wind Engineering and Industrial Aerodynamics*, 99:1056–1068, 2011.

[14] G. Lamberti, C. García-Sańchez, J. Sousa, and C. Gorlé. Optimizing turbulent inflow conditions for large-eddy simulations of the atmospheric boundary layer. *Journal of Wind Engineering & Industrial Aerodynamics*, 177:32–44, 2018.

[15] R. Longo, M. Fürst, A. Bellemans, M. Ferrarotti, M. Derudi, and A. Parente. Cfd dispersion study based on a variable schmidt formulation for flows around different configurations of ground-mounted buildings. *Building and Environment*, 154:336–347, 2019.

[16] C. Meneveau and J. Katz. Conditional subgrid force and dissipation in locally isotropic and rapidly strained turbulence. In *International Conference on Turbulence*, 1999.

[17] H. Ono. Implicit large eddy simulation of flow and dispersion around a building. In *14th Conference of International Building Performance Simulation Association*, 2015.

[18] A. Parente, R. Longo, and M. Ferrarotti. *CFD boundary conditions, turbulence models and dispersion study for flows around obstacles*. VKI LS 2017-01, 2017. Editors: Benocci, C. and van Beeck, J. P. A. J.

[19] A. Parente, R. Longo, and M. Ferrarotti. *Turbulence model formulation and dispersion modelling for the CFD simulation of flows around obstacles and on complex terrains*. VKI LS 2019-03, 2019. Editor: van Beeck, J. P. A. J.

[20] S. V. Patankar. *Numerical Heat Transfer and Fluid Flow*. series in computational methods in mechanics and thermal sciences. 1980.

[21] G. Patnaik, J. P. Boris, F. F. Grinstein, and J. P. Iselin. *Large Scale Urban Simulations with FCT*, pages 105–130. 2005.

[22] Yoshihide Tominaga, Akashi Mochida, Ryuichiro Yoshie, Hiroto Kataoka, Tsuyoshi Nozu, Masaru Yoshikawa, and Taichi Shirasawa. Aij guidelines for practical applications of cfd to pedestrian wind environment around buildings. *Journal of Wind Engineering and Industrial Aerodynamics*, 96(10-11):1749–1761, 2008.

[23] H. Yu and J. Thé. Validation and optimization of sst $k-\omega$ turbulence model for pollutant dispersion within a building array. *Atmospheric Environment*, 145:225–238, 2016.

PHYSMOD 2022 – International Workshop on Physical Modeling of Flow and Dispersion Phenomena
Institute of Thermomechanics of the CAS, Prague, Czech Republic – August 29-31, 2022

New guideline – better guideline? The new VDI code of practice for wind tunnel modeling of atmospheric flow and dispersion processes

B. Leitl[1], W. Bächlin[2], W. Theurer[3], F. Harms[1], R. Lieb[4], R. Höffer[5], C. Kalender-Wevers[5], V. Hildebrand[6], B. Bauhofer[7]

[1] EWTL, Meteorological Institute, University of Hamburg, Bundesstrasse 55, D-20146 Hamburg
[2] Ingenieurbüro Lohmeyer, An der Roßweid 3, D-76229 Karlsruhe
[3] Ingenieurbüro Theurer, Händelweg 4, D-67346 Speyer
[4] I.F.I. Institut für Industrieaerodynamik GmbH, Welkenrather Straße 120, D-52074 Aachen
[5] Ruhr-Universität Bochum, Windingenieurwesen/Strömungsmechanik, Universitätsstr. 150, D-44801 Bochum
[6] TU Dresden, ILR, AG Experimentelle Aerodynamik, Marschnerstr. 28, D-01307 Dresden
[7] GfA Gesellschaft für Aerophysik mbH, Aidenbachstraße 52, D-81379 München

Abstract

Guidelines or codes of practice have a long tradition in wind tunnel modeling of atmospheric flow and dispersion phenomena. Amongst others, they define essential requirements for proper physical modeling and aim for reasonable quality, repeatability and comparability of model results originating from different wind tunnel facilities. The latter is of special importance when wind tunnel modeling is used in the context of licensing procedures, where court-proof results are needed. However, the application range of physical modeling was changing with time, at least in Germany. The use of wind tunnels in applied consultancy work related to flow and dispersion in the lower atmospheric boundary layer is now gradually replaced by computational modeling. Wind tunnel data are now used more frequently either as independent model results in case of conflictive numerical predictions or as reference for validation of corresponding numerical modeling tools. This change in wind tunnel application called for an update and extension of the VDI 3783/12 code of practice. The contribution will introduce the new version of the guideline and aims for an open discussion of the more demanding documentation requirements and best practice recommendations. By the time of PHYSMOD 2022, the new document will be open for comments from practitioners/users.

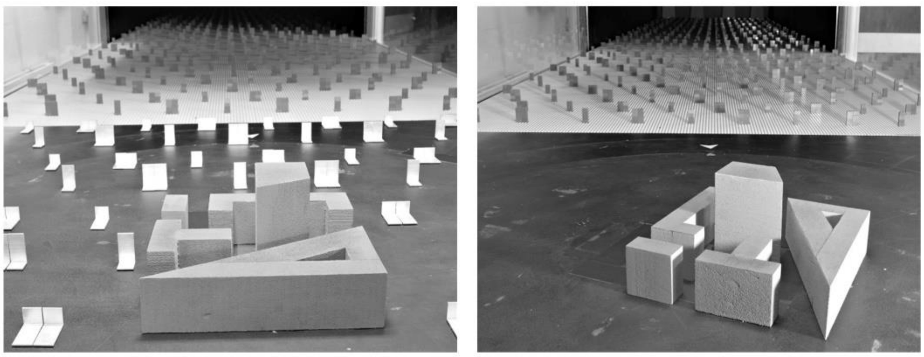

Experimental setup in agreement (left) or not in agreement (right) with VDI 3783/12.

PHYSMOD 2022 – International Workshop on Physical Modeling of Flow and Dispersion Phenomena
Institute of Thermomechanics of the CAS, Prague, Czech Republic – August 29-31, 2022

Scale analysis of turbulent statistics over real urban surface: A wind tunnel study

Fei Li[1], Ziwei Mo[2,3] and Chun-Ho Liu[1]

[1]Department of Mechanical Engineering, The University of Hong Kong, Pokfulam Road, Hong Kong, CHINA

[2]School of Atmospheric Sciences, Sun Yat-sen University, and Southern Marine Science and Engineering Guangdong Laboratory (Zhuhai), Zhuhai, CHINA

[3]Key Laboratory of Tropical Atmosphere-Ocean System, Ministry of Education, Zhuhai, CHINA

Abstract

Dynamics and turbulence structure in the roughness sublayer (RSL) and inertial sublayer (ISL) of atmospheric surface layer (ASL) over roughness elements are quite different. In this study, the ASL flows over real urban morphology are measured in wind tunnel experiments. Quadrant-hole and frequency analyses are adopted to examine the ASL momentum transport and how the processes are influenced by different motion scales. The downtown Kowloon Peninsula, Hong Kong is fabricated by 3D printing that is adopted as the reduced-scale model. Notable variations in mean wind speed u, fluctuating velocities u'' and w'' together with vertical momentum flux $u''w''$ in the ISL and RSL are observed. With increasing motion scales, the efficiency of momentum transfer increases in the RSL top and ISL. Moreover, the contribution from sweep Q4 gradually increases while from ejection Q2 decreases with increasing motion scale. Whereas, the phenomenon is reversed in the ISL. In the RSL, the contribution from eddies in the frequency range of 0.1 Hz to 10 Hz decreases then increases thereafter with increasing frequency. On the other hand, the momentum contribution from high-frequency motions increases monotonically with increasing frequency in the ISL. It is thus suggested that large turbulence scales would be beneficial to aged air removal.

1 Introduction

Atmospheric surface layer (ASL) consists of the inertial sublayer (ISL) and roughness sublayer (RSL), and the dynamics characteristics in ISL and RSL are quite different [1]. There are numerous studies have been conducted to study the winds, ventilation and pollutant dispersion over idealized urban surfaces [2-4]. Beside, the turbulent structures can also be influenced by turbulent scale, and there are also some investigations concentrating on the turbulent scale [5, 6]. While there is a lack of investigation on turbulence scale inflence to the ISL and RSL over real urban. The characteristics and momentum transport variations between ISL and RSL over real urban morphology still need to be characterized.

This study aims to investigate the differences between ISL and RSL over real urban morphology and how the momentum transport is influenced by different motion scales and frequency in

ISL and RSL, which would be useful to understand the momentum transport mechanism in real urban and apply to the air pollution removal.

2 Methodology

2.1 Real urban model

The downtown Kowloon Peninsula, Hong Kong is selected as the reduced-scale model. Its physical model (1:1200) is fabricated by 3D printing to simulate the flow structure over the complicated urban morphology. The size of the reduced-scale model in floor area is 2 m (length) × 0.55 m (width), which is corresponding to 3.6 km (length) × 0.5 km (width) in real scale.

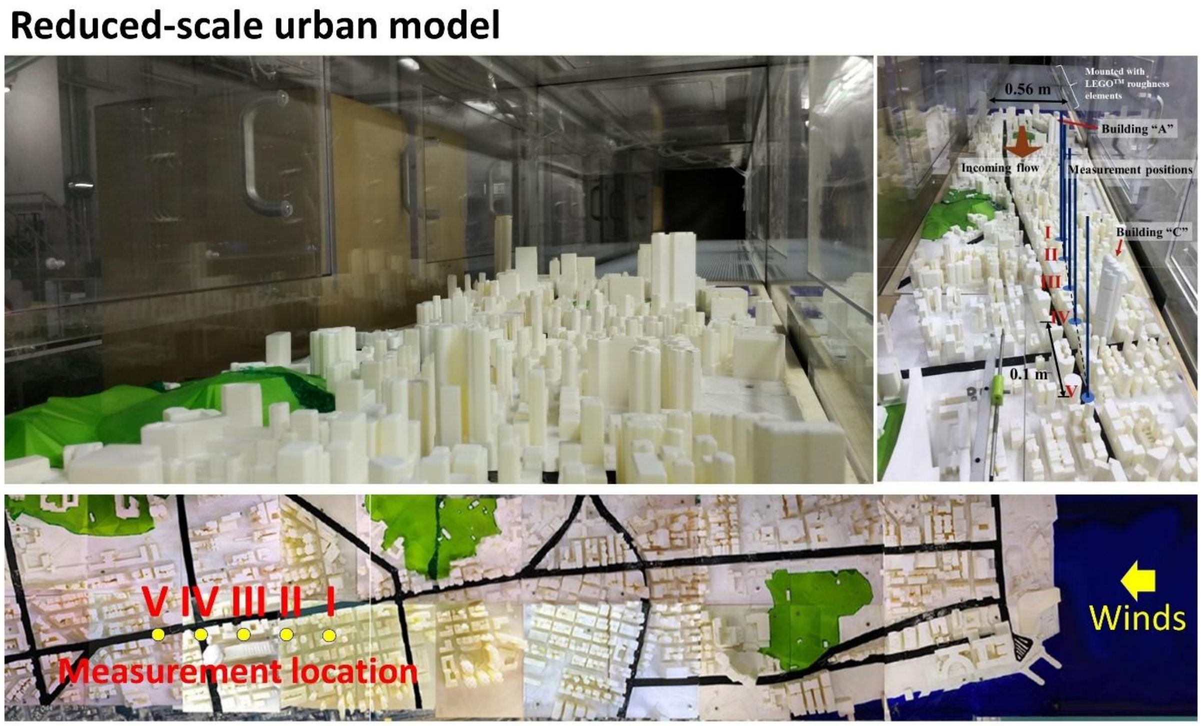

Figure. 1. The reduced-scale urban model fabricated by 3D printing.

2.2 Wind tunnel measurements

The experiments are carried out in the wind tunnel in the Department of Mechanical Engineering, The University of Hong Kong. The size of the test section in wind tunnel is 6 m (length) × 0.56 m (width) × 0.56 m (height). The free-stream wind speed U_∞ ranges from 8.8 m s^{-1} to 9.6 m s^{-1} and the friction velocity is 0.62 m s^{-1} ≤ u_τ ≤ 0.67 m s^{-1}. The thickness of turbulence boundary layer (TBL) δ is about 0.18 × 10^{-3} m. The Reynolds numbers Re_∞ (= $U_\infty\delta/v$; where v is the kinematic viscosity of air) is about 170 × 10^3 which is large enough to neglect the effect of molecular viscosity and the similarity principle is also satisfied when modeling in wind tunnel. In this experiment, the spanwise velocity v is neglected due to its small value.

Constant-temperature (CT) hot-wire anemometry (HWA) is adopted to measure the velocities in streamwise and vertical directions. The sampling frequency of HWA is 2000Hz and the sampling duration is 50 thus 10^4 data can be got at each point.

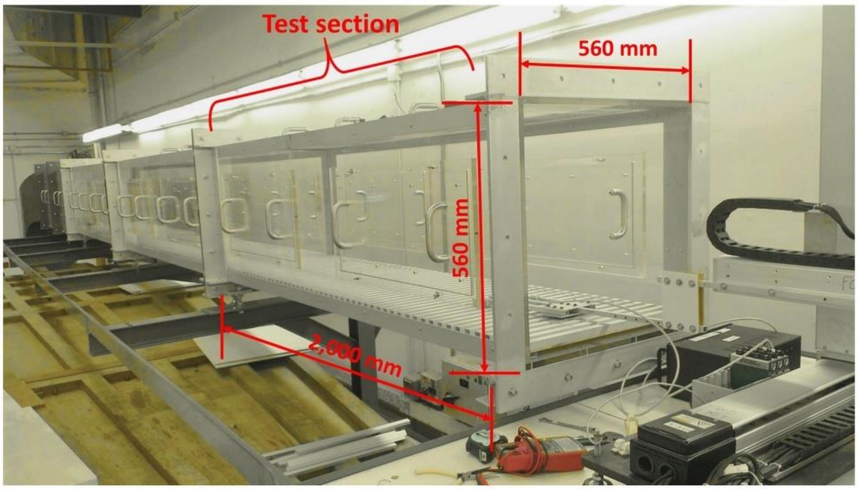

Figure 2. The wind tunnel and dimensions.

2.3 Quadrant-hole and frequency analyses

Quadrant analysis has been developed to evaluate the turbulence statistical characteristics, and the first quadrant analysis was adopted by Wallace et al. [7] to analyze the Reynolds shear stress. According to the direction of the motions, the fluctuating velocity, *u'' and w''* are classified into four groups, Q1: outward interaction (+*u''*, +*w''*), Q2: ejection (-*u''*, +*w''*), Q3: inward interaction (-*u''*, -*w''*) and Q4: sweep (+*u''*, -*w''*).

Based on the quadrant analysis, quadrant-hole analysis was introduced [8]. By introducing a filter factor *H*, $|u''w''|$ in each quadrant can be filtered. Then conditional sampling is used to measure the contributions from different motion scales [9, 10]. The size of the hole was defined by filter size *H*, and the points (*u''*, *w''*) on the hole boundary satisfy

$$|u''w''| = H\left|\overline{u''w''}\right| \tag{1}$$

The importance to the total flux of $|u''w''|$ can be identified by the increasing filter factor *H*.

According to the conditional function with i ranging from 1 to 4,

$$I_{i,H} = \begin{cases} 1, (u'', w'') \text{ lies in ith quadrant and } |u''w''| \geqslant H\left|\overline{u''w''}\right| \\ 0, otherwise. \end{cases} \tag{2}$$

the conditional flux fraction is defined as

$$S_{i,H} = \frac{\overline{u''w''I_{i,H}}}{\overline{u''w''}} \tag{3}$$

It can be observed that $S_{2,H}$ and $S_{4,H}$ are positive and $S_{1,H}$ and $S_{3,H}$ are negative.

To measure the coherent structure of turbulence, exuberance is widely adopted, which is defined as

$$Ex_H = \frac{S_{1,H} + S_{3,H}}{S_{2,H} + S_{4,H}} \tag{4}$$

There would be more efficient transfer of momentum with increasing Ex_H.

The time fraction of each quadrant with motion scale $|u''w''|$ is defined as

$$T_{i,H} = \frac{I_{i,H}(u'', w'')}{I_{total}} \tag{5}$$

The differences in the fractions of time and momentum flux between sweep Q4 and ejection Q2 are

$$\Delta T_H = T_{4,H} - T_{2,H} \tag{6}$$

Then the importance of sweep Q4 and ejection Q2 can be compared by ΔT_H.

Besides, to investigate how the momentum transport is influenced by different eddy frequencies, the low-pass filter is adopted to process the data by different cutt-off frequencies. Then the $u''w''$ covariance with different eddy frquencies can be calculated.

3 Result and discussion

3.1 Wind and turbulence profiles

In the wind tunnel experiment, the free-stream wind speeds U_∞ are up to 8 m s^{-1}. The TBL thickness δ over the real urban model is defined at the height z where the time-averaged wind speed converges to 99% of the free-stream level $u|_{z=\delta} = 0.99U_\infty$. Its range is 167×10^{-3} m $\leq \delta \leq 191 \times 10^{-3}$ m in the wind tunnel experiments. The Reynolds number Re ($= U_\infty\delta/\nu$) is over 10^4 that is sufficiently large for turbulent flows in the wind tunnel.

To characterize the turbulence over the real urban model, the time-averaged wind speed u, streamwise and vertical fluctuating velocity, and vertical momentum flux $-\overline{u''w''}$ in the streamwise direction on the three measurement planes are depicted in Figure 3. It can be observed there exists flow inhomogeneity caused by the roughness elements below the RSL top $z \leq 0.4\delta$ on the 1st plane. The bulk aerodynamic properties would be influenced by the arrangements and height of building elements.

The mean wind speeds u in RSL increases in the streamwise direction on the 1st plane from $0.4U_\infty$ to $0.7U_\infty$. Besides, the shear $\partial u/\partial z$ is smaller in the lower RSL while this value is larger in the upper RSL, suggesting the momentum entrainment from the ISL to the roof level. There are also large variations in the streamwise and vertical fluctuating velocities.

On the contrary, the vertical profiles on the 2nd and 3rd planes do not exist large variations. It is mainly because their surface roughness variations in the streamwise direction are not noticable.

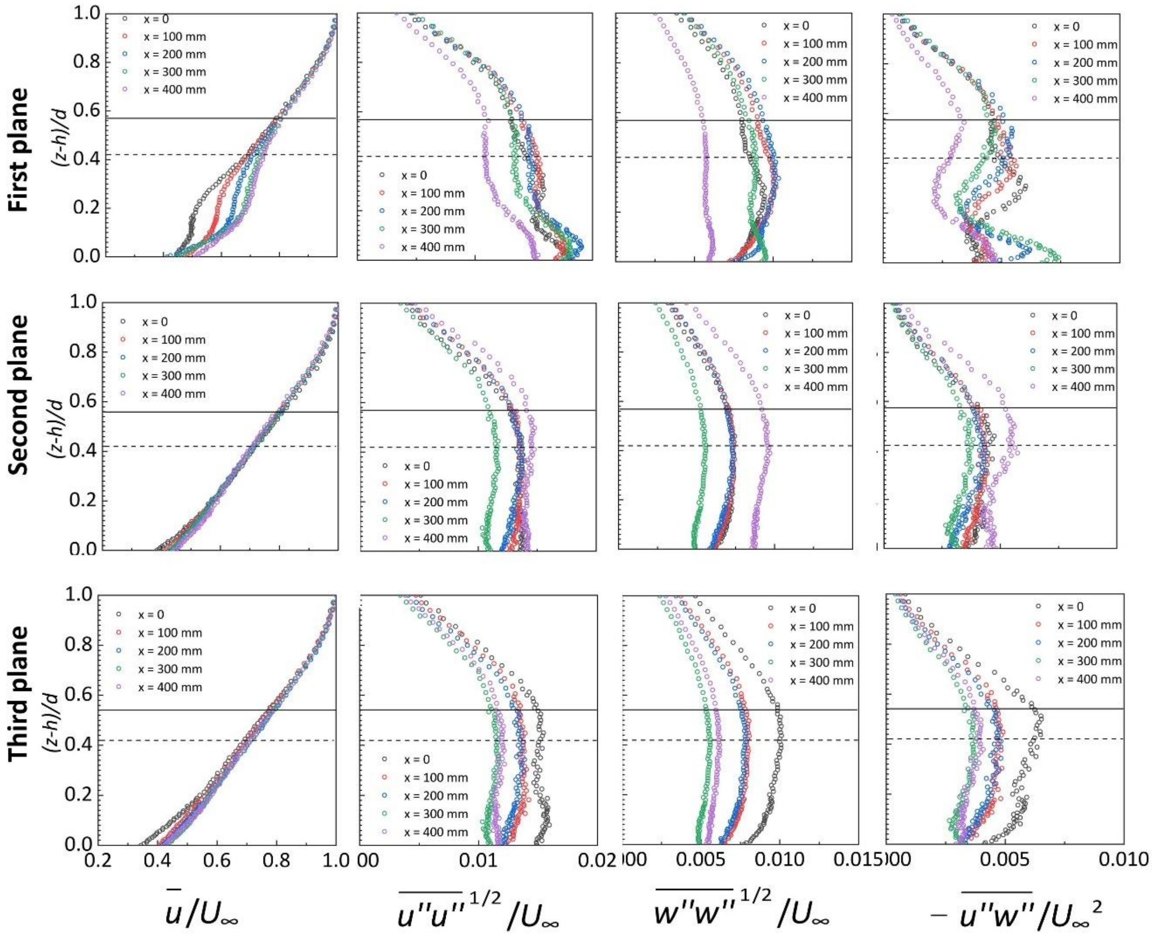

Figure 3. The wind profiles for three planes.

3.2 Quadrant-hole analysis

By quadrant-hole analysis, the average Ex_H for each plane over the real urban is calculated and depicted (Figure 4) to investigate the characteristics of momentum transfer influenced by different motion scales.

In the RSL and ISL, Ex_H increases with the increasing hole size for all three planes, which means the momentum transfer efficiency increases with the intensifying motion scales. The Ex_H is peaked in the ISL regardless of the strength of motions, which suggests the largest momentum transfer efficiency appears in the ISL. For the first plane, there is a large area that displaying worse momentum transfer efficiency in the ISL with small motion, which is not found in other two planes. It is mainly caused by the large element variations in the first plane combined with wind speed profile in Figure 3.

Figure 5 displays the variations of ΔT_H with elevated height and hole size of three planes. The ΔT_H gradually increases with the increasing hole size in RSL, suggesting the strengthening motion scales result in an increasing and decreasing contributions from sweep Q4 and ejection Q2 to momentum transport, respectively. However, the phenomenon is opposite in the ISL, where ΔT_H decreases with the enlarging hole size. From the phenomenon above, it can be concluded that the sweep Q4 dominates the momentum transport in large motion scale in RSL and ejection Q2 plays a more important role than sweep Q4 in small motion scale in ISL.

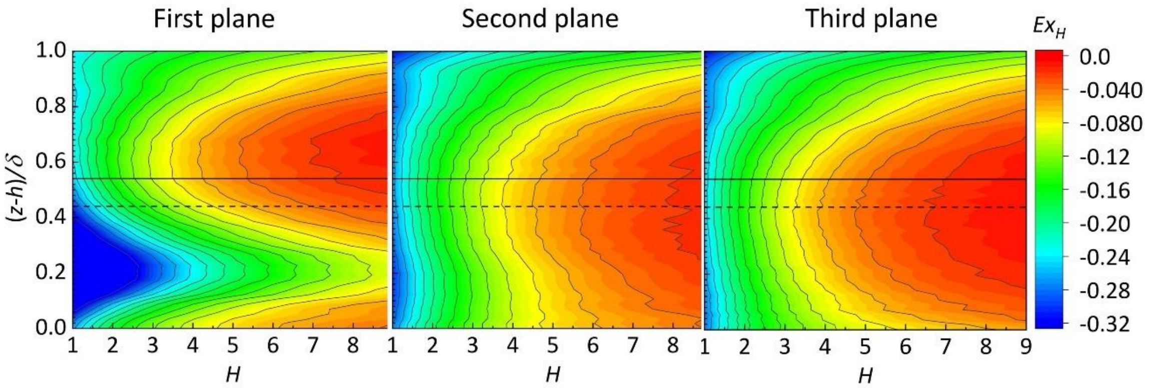

Figure 4. The ExH variation with with different hole sizes.

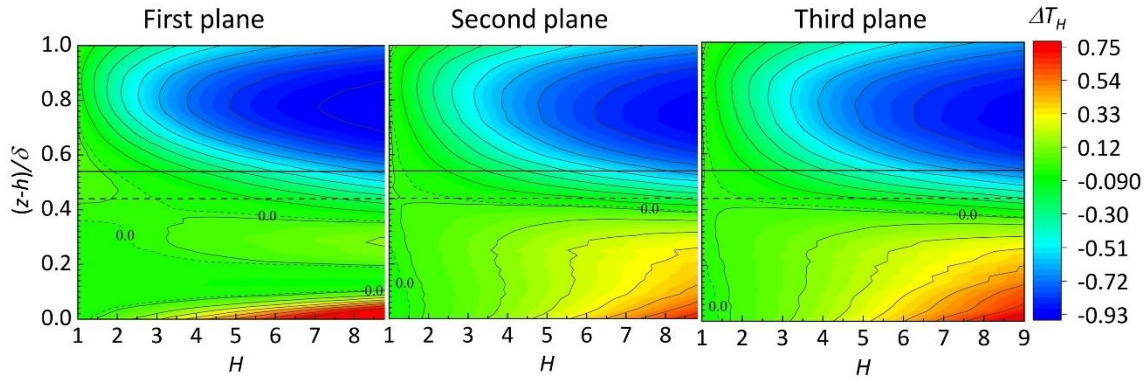

Figure 5. The ΔT_H distribution with different hole sizes.

3.3 Frequency scale analysis

To analysize the momentum tranport influenced by frequency, the *u′′ w′′* covariance contribution to the momentum is calculated by different frequency. From Figure 6, the negative contribution mainly apears in the RSL. In the ISL, the momentum contribution from high-frequency motions increases monotonically with increasing frequency in the ISL, while the contribution from eddies in the frequency range of 0.1 Hz to 10 Hz decreases then increases thereafter with increasing frequency in the RSL. It can be concluded that a larger frequency scale would result in a more intense momentum contribution from the eddy.

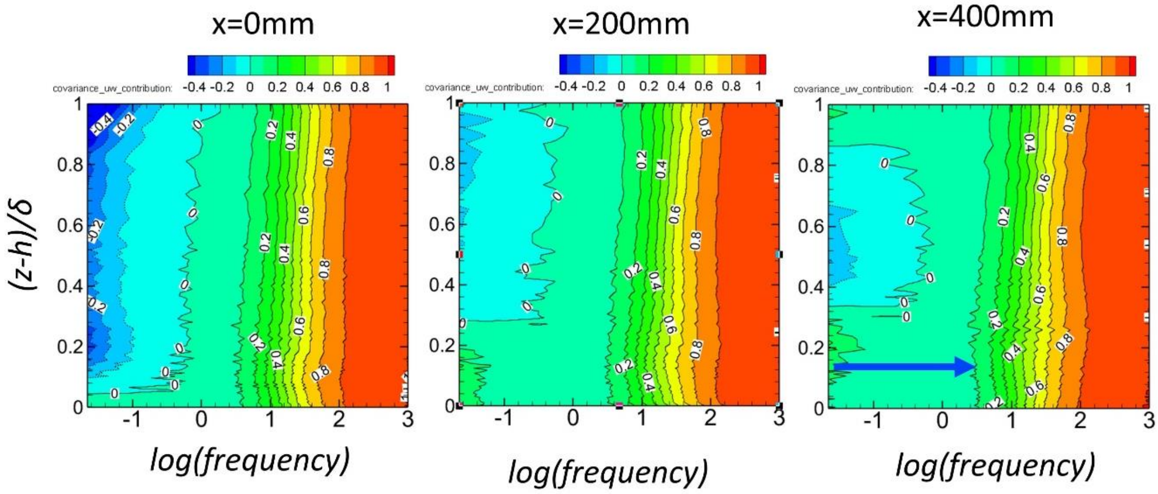

Figure 6. The u’’w’’ covariance contribution with different frequencies.

4 Conclusion

In this work, wind tunnel experiments are carried out to measure the ASL flows over the reduced-scale model of real urban morphology. Quadrant-hole and frequency analyses are used to examine the ASL momentum transport and how the processes are influenced by different motion scales. Major findings are:

(1) Notable variations of mean wind speed *u*, fluctuating streamwise *u’’* and vertical *w’’* velocities together with vertical momentum flux *u’’w’’* exist in the ISL and RSL.

(2) With increasing motion scales, the efficiency of momentum transfer increases in the RSL top and the ISL. The largest momentum transfer efficiency appears in the ISL for all motion scales. Moreover, the strengthening motion scales result in an increasing contribution from sweep Q4 and a decreasing contribution from ejection Q2 to momentum transport respectively in RSL. Whereas, the phenomenon is opposite in the ISL.

(3) The contribution from eddies in the frequency range of 0.1 Hz to 10 Hz is decreasing with the increasing frequency, then the contribution increases with the increasing frequency large than 10 Hz in the RSL. On the other hand, the contribution increases monotonically with increasing frequency in the ISL.

It is thus suggested that large turbulence scales dominate aged air removal of urban areas.

5 Reference

[1] Y.-K. Ho, C.-H. Liu, Street-Level Ventilation in Hypothetical Urban Areas, Atmosphere 8(12) (2017).
[2] D. Cui, G. Hu, Z. Ai, Y. Du, C.M. Mak, K. Kwok, Particle image velocimetry measurement and CFD simulation of pedestrian level wind environment around U-type street canyon, Building and Environment 154 (2019) 239-251.
[3] J. Hang, Y. Li, M. Sandberg, R. Buccolieri, S. Di Sabatino, The influence of building height variability on pollutant dispersion and pedestrian ventilation in idealized high-rise urban areas, Building and Environment 56 (2012) 346-360.

[4] Z. Mo, C.-H. Liu, A wind tunnel study of ventilation mechanism over hypothetical urban roughness: The role of intermittent motion scales, Building and Environment 135 (2018) 94-103.
[5] G. Iacobello, L. Ridolfi, S. Scarsoglio, Large-to-small scale frequency modulation analysis in wall-bounded turbulence via visibility networks, Journal of Fluid Mechanics 918 (2021).
[6] S. Chowdhuri, G. Iacobello, T. Banerjee, Visibility network analysis of large-scale intermittency in convective surface layer turbulence, Journal of Fluid Mechanics 925 (2021).
[7] J.M. Wallace, H. Eckelmann, R.S. Brodkey, The wall region in turbulent shear flow, Journal of Fluid Mechanics 54(1) (1972) 39-48.
[8] W.W. Willmarth, S.S. Lu, Structure of the Reynolds stress near the wall, Journal of Fluid Mechanics 55(1) (1972) 65-92.
[9] J.M. Wallace, Quadrant Analysis in Turbulence Research: History and Evolution, Annual Review of Fluid Mechanics 48(1) (2016) 131-158.
[10] M.R. Raupach, Conditional statistics of Reynolds stress in rough-wall and smooth-wall turbulent boundary layers, Journal of Fluid Mechanics 108 (1981) 363-382.

PIV-PLIF measurements of pollutant dispersion in atmospheric boundary layer flow in a water channel

H.D. Lim[1], C. Vanderwel[1]

[1]University of Southampton, Faculty of Engineering and Physical Sciences, Department of Aeronautical and Astronautical Engineering, Boldrewood Innovation Campus, Burgess Road, SO16 7QF, United Kingdom

Abstract

The scalar dispersion of pollutant from a ground level source in a neutral atmospheric boundary layer (ABL) is experimentally investigated by releasing Rhodamine 6G fluorescent dye in a recirculating water channel. Smooth-wall turbulent boundary layer flow developed over ~46 boundary layer thicknesses (δ) is used to simulate a rural ABL. The flow and turbulence properties of the oncoming ABL flow are characterised using multiple overlapping Particle-Image Velocimetry (PIV) measurements which provided insight into the velocity profile, friction velocity and turbulence intensity. Simultaneous Planar Laser-Induced Fluorescence (PLIF) measurements of the dye plume are compared to the rural flow results of Robins, *Atmos. Environ*., 1978, with the plume vertical half-width, concentration profiles and concentration decay rate agreeing well with the analytical model far from the source despite several key differences in the methodologies. Interpolating the velocity measurements onto the concentration measurements allows two-dimensional maps of the turbulent scalar fluxes and turbulence diffusivity to be calculated and compared with theory. We discuss the significance of these results and the capability of PIV-PLIF measurements in the water tunnel for studies of pollutant dispersion in the ABL.

Introduction

Atmospheric boundary layers (ABL) have been simulated in laboratories for plume dispersion studies. Using ground level sources of negligible buoyancy and momentum in wind tunnel experiments, plume properties such as the concentration decay, vertical concentration profile and plume spread (based on half-widths at half-max) were shown to collapse reasonably well with analytical gradient-transfer and similarity theories, and comparisons with full-scale data suggest good agreement with a slightly unstable ABL [1]. Spatially and temporally resolved concentration and velocity measurements of sources at various source heights in a canonical smooth-wall turbulent boundary layer were performed in a wind tunnel [2], and revealed the concentration profiles of ground level plumes exhibit an exponential distribution while elevated plumes displayed a reflected Gaussian distribution, consistent with the results observed in an artificially thickened urban boundary layer flow [3] and rural flow [1]. The initial source conditions (such as source size) has been observed to affect concentration fluctuations in the near-source region of an elevated source where fluctuations were mostly produced by the meandering of the instantaneous plume [4]. The mean plume spread was observed to become independent much quicker than the instantaneous plume width. For ground level sources, however, the source conditions were found to have a negligible effect on the concentration fluctuations.

Taylor's dispersion theory approaches the turbulent diffusion problem using the Lagrangian approach instead of the Eulerian approach adopted in the studies discussed earlier, and identified three main regimes of diffusion [5]. In the molecular diffusion regime, the dispersion rate is dominated by molecular diffusion actions. In the turbulent convection regime, turbulent diffusivity grows linearly, and in the turbulent diffusion regime, turbulent diffusivity reaches an asymptote that is dependent on

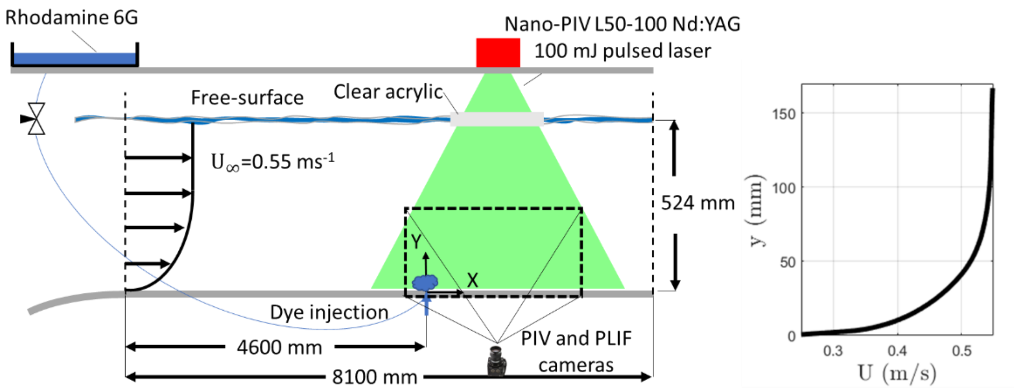

Figure 1: Sketch of experimental setup and incoming velocity profile

the Lagrangian integral timescale and velocity fluctuations. Taylor's theory suggests in the near-source region, the choice of tracer concentration and working medium which determines the Schmidt number (ratio of momentum diffusivity to molecular diffusivity) has an effect on scalar transport. The literature on plume dispersion is currently heavily focused on field measurements or gaseous tracers in wind tunnels which has a typical Schmidt number of Sc~1. In this study, we use Rhodamine 6G dye in a water tunnel (Sc=2500) to study the plume dispersion of a ground-level source in a rural boundary layer flow. We compare our experimental results to analytical gradient-transfer theory and comment on the suitability of using water tunnels for studies on plume dispersion in ABL.

Methodology

Two-dimensional Particle-Image Velocimetry (PIV) and Planar Laser-Induced Fluorescence (PLIF) experiments were performed in the University of Southampton's new recirculating water tunnel which has a test section of 8,100 mm in length and 1,200 mm in width. The freestream velocity and boundary layer thickness were U_∞=0.55 ms^{-1} and δ=100 mm respectively. The ground level plume was simulated using a neutrally buoyant Rhodamine 6G fluorescent dye introduced at the ground level through a 4 mm tube machined into an internal channel of the false floor. The dye Schmidt number is Sc=2500 [6], which indicates negligible molecular diffusion effects as compared to diffusion by momentum. The dye flow rate was maintained at Q=10 cm^3 min^{-1} using a needle valve and was carefully selected to match the vertical velocity component of the incoming flow in order to minimise disturbance. A sketch of the experimental setup and incoming flow velocity profile is presented in Figure 1.

For the PIV-PLIF measurements, illumination was provided by a 100 mJ Nd:YAG double-pulsed laser operated at 10 Hz, with an emission wavelength of 532 nm. A 5.4 MP 16-bit depth sCMOS camera fitted with an optical long-pass filter (sharp cutoff at 540 nm) was used for PLIF. Since the absorption and emission peaks of the dye are at 525 nm and 554 nm, the PLIF camera records only the fluorescence emitted from the excited dye. Two 4 MP CMOS cameras in a side-by-side configuration were used for PIV and fitted with optical bandpass filters to block out the fluorescence signal from the dye, enabling them to record only the 50 µm polyamide seeding particles in the flow. The PIV-PLIF field-of-view was approximately 200 mm streamwise × 130 mm vertical. To achieve a longer streamwise field-of-view, the cameras were shifted downstream sequentially, and the dye concentration was increased from 0.3 to 50 mg L^{-1} to provide optimal signal to noise ratio while avoiding overexposure. PLIF post-processing was performed with an inhouse code and PIV post-processing using LaVision's DaVis 10 software package, details on the procedures and PLIF calibration are available in an earlier study [7]. A summary of the test cases is presented in Table 1.

Table 1: Summary of test cases

Test case	Measurement location	No. of samples	Dye concentration
P1	-25 mm < x < 186 mm	6000	C_s=0.3, 1, 5 mg L^{-1}
P2	173 mm < x < 385 mm	2000	C_s=50 mg L^{-1}
P3	372 mm < x < 583 mm	2000	C_s=50 mg L^{-1}

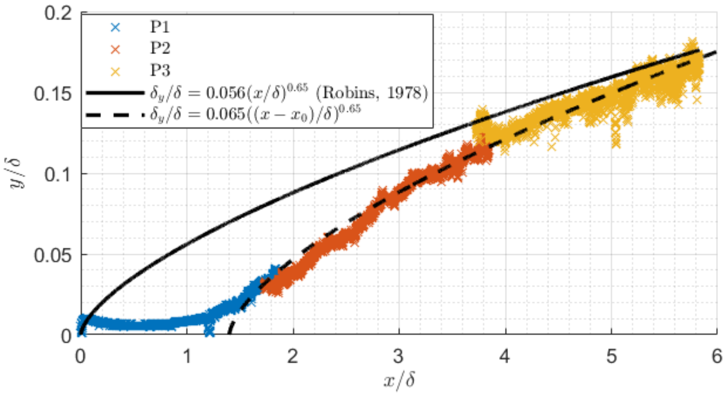

Figure 2: Plume growth rate

Results and discussions

The plume growth rate presented in Figure 2 shows there is a huge deviation of the plume width in the near-source region when compared to the analytical form and empirical constants used by Robins [1]:

$$\frac{\delta_y}{\delta} = 0.056\left(\frac{x}{\delta}\right)^{0.65} \tag{1}$$

where δ represents boundary layer thickness and δ_y represents plume half-width based on the distance from ground when concentration reaches half maximum.

There are two key differences in our study as compared to Robins. Firstly, the Schmidt number of the plume tracer is 2500 which is around three orders of magnitude higher than Robins' study in the wind tunnel. Secondly, our plume injection to freestream velocity ratio was 0.025 which is one order of magnitude lower than Robins. In this study, it is likely the injected dye remained within the viscous sublayer of the flow and was unable to diffuse into the logarithm layer initially due to its high Schmidt number. As a result, the half width remained small and did not grow for a significant downstream fetch of more than 1 boundary layer thickness. Our data fits well if we introduce a virtual origin by shifting the source downstream by x_0=-140 mm (or shifting the data upstream) and adjusting the empirical constant to:

$$\frac{\delta_y}{\delta} = 0.065\left(\frac{x-x_0}{\delta}\right)^{0.65} \tag{2}$$

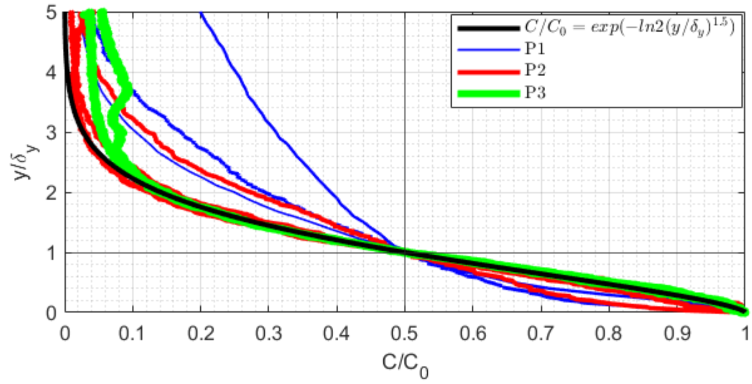

Figure 4: Vertical concentration profiles. Line width increases with downstream distance from source

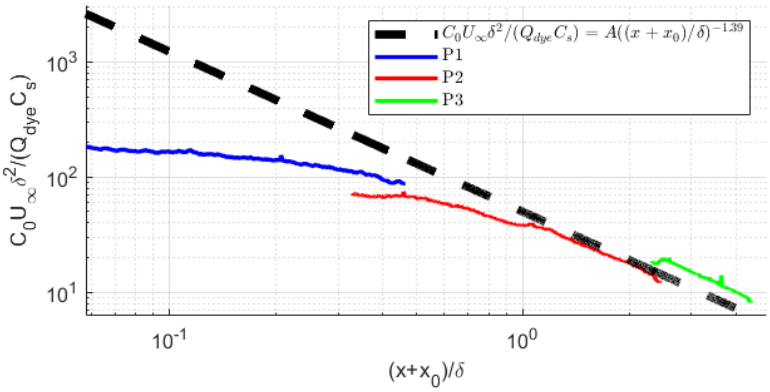

Figure 3: peak Centreline concentration decay

Figure 3 presents the concentration vertical profile in the same self-preserving form presented by Robins [1] which is based on the analytical gradient transfer theory:

$$\frac{C}{C_0} = exp\left(-\ln(2)\left(\frac{y}{\delta_y}\right)^{1.5}\right) \tag{3}$$

where C_0 represents the peak centreline concentration. The experimental profiles collapse with wind tunnel studies [1] at approximately $\frac{x}{\delta} > 3$, which is consistent with the results in Figure 2 (good agreement of the experiments with the virtual origin analytical line for $\frac{x}{\delta} > 3$). Hence, the plume is fully developed and self-similar in the far-field.

Finally, the mean centreline peak concentration decay is presented in Figure 4 and follows the power law,

$$\frac{C_0 U_\infty \delta^2}{Q} = A\left(\frac{x + x_0}{\delta}\right)^{-1.39} \tag{4}$$

where A is a scaling constant. At approximately $\frac{x+x_0}{\delta} > 1.6$ (or $\frac{x}{\delta} > 3$), the plume decay rate has an exponent of -1.39 which matches Robins' observations.

Conclusions

In this study, PIV and PLIF measurements were performed on a Rhodamine 6G dye source passively released in a canonical turbulent boundary layer in a water tunnel. We compare our results to the analytical gradient transfer theory and empirical constants used in Robins' study [1]. One of the key differences is at the near-source region, with the analytical solution overpredicting the plume half-width, and this was attributed to negligible molecular diffusion of the dye. We show this can be easily corrected by introducing a virtual origin. In the far source region, the vertical concentration profile was shown to be in self-preserving form and agreed well with Robins. Using the virtual origin correction, the mean centreline peak concentration decay also matched Robins' rural flow observations. These results indicate the suitability of the water tunnel to simulate plume dispersion in an ABL. We discuss velocity-concentration statistics, such as turbulent scalar fluxes, in our presentation.

References

1. Robins, A.G., *Plume dispersion from ground level sources in simulated atmospheric boundary layers.* Atmospheric Environment (1967), 1978. **12**(5): p. 1033-1044.
2. Talluru, K.M., J. Philip, and K.A. Chauhan, *Local transport of passive scalar released from a point source in a turbulent boundary layer.* Journal of Fluid Mechanics, 2018. **846**: p. 292-317.
3. Fackrell, J.E. and A.G. Robins, *Concentration fluctuations and fluxes in plumes from point sources in a turbulent boundary layer.* Journal of Fluid Mechanics, 1982. **117**: p. 1-26.
4. Fackrell, J.E. and A.G. Robins, *The effects of source size on concentration fluctuations in plumes.* Boundary-Layer Meteorology, 1982. **22**(3): p. 335-350.
5. Castro, I.P. and C. Vanderwel, *Turbulent Flows: an Introduction.* 2021.
6. Vanderwel, C. and S. Tavoularis, *Measurements of turbulent diffusion in uniformly sheared flow.* Journal of Fluid Mechanics, 2014. **754**: p. 488-514.
7. Lim, H.D., D. Hertwig, T. Grylls, H. Gough, M.v. Reeuwijk, S. Grimmond, and C. Vanderwel, *Pollutant dispersion by tall buildings: laboratory experiments and Large-Eddy Simulation.* Experiments in Fluids, 2022. **63**(6): p. 92.

Struggles of Heavy Gas Dispersion Experiments

Simon Michel[1], Dr. Frank Harms[1], Prof. Dr. Bernd Leitl[1]

[1] EWTL, Meteorological Institute, University of Hamburg, Bundesstrasse 55, D-20146 Hamburg, Germany

Abstract

Heavy gas dispersion experiments in boundary layer wind tunnels are subject to a large number of challenges and difficulties. Due to the smaller scale of models inside wind tunnels the matching of similarity numbers is not trivial. Issues with measurement equipment, model geometries, quality of the inflow boundary layer, changes in roughness and others difficulties need to be addressed. In the talk different struggles with heavy gas dispersions and how they have been overcome will be presented.

Introduction

Accidental releases of hazardous materials remain a concern and pose safety risks in factories or during transport. Especially in cases of releases of toxic or flammable heavy gases, major safety and health risks can emerge. Simulating dense gas dispersion with numerical models is still challenging and reliable and robust reference data for heavy gas dispersion in complex terrain like industrial sites is still rare. However, proper physical modelling of realistic heavy gas dispersion is a challenge as well and poses several difficulties and pitfalls.

To achieve scalability of wind tunnel results Reynolds and densimetric Froude number must maintained sufficiently. Modelling a Froude number as small as possible is desired for generating substantial heavy gas effects. To achieve a Froude number as small as possible either a low wind speed, a high density gas or a large source flow is needed. The margin for low wind speeds is however limited by the necessity to achieve Reynolds number independence. The selection of the dense gas is also not trivial. Gases with a high density are often toxic, flammable or have a high global warming potential. Depending on the dispersion scenario the source flow also can only be varied over a certain range of values. Source flows which are too big can influence the overall flow inside the model area and result in unrealistic dispersion patterns. An adequate source design is needed, minimising the emission velocity and reducing jet effects interfering the dense gas behaviour. Maximising the wind tunnel model scale allows a larger range of possible combinations of wind speeds, density of released gas and source flow rate.

Wind tunnel measurements

In the last three years heavy gas dispersion experiments were carried out in the large boundary layer wind tunnel 'WOTAN' of the University of Hamburg. These heavy gas dispersion experiments were part of a project to investigate accidental releases of gaseous hazardous materials from industrial sources. The measurement data is used as a reference data set for RANS and LES dispersion models. This chapter including the figures is mostly based on the publication of (S. Michel, 2021).

For the creation of the reference data set three models with increasing complexity were used. A horizontal homogenous rough boundary layer without obstacles (Fig. 1a), a simplified commercial area (Fig. 1b) and a complex industrial site (Fig. 1c). All models have a scale of 1:100. The commercial area and the industrial site have a horizontal extent of approx. 300 m x 300 m. The buildings inside the commercial area model all have a height of 15 m, the horizontal sizes of the buildings range from 15 to 40 m. In the middle of the model area a larger building with a size of 30 m by 60 m is placed. This building has three openings on the sides and one opening on the top which are used as sources.

In case of the complex industrial area model the buildings have greatly varying sizes of up to 150 m. The buildings are 10 m or 25 m high. Furthermore in the middle of the model area cylindrical shaped tanks are placed. Gas is released from a ground source in the middle of the model area.

Two different boundary layer inflows were modelled. One moderately rough boundary layer and one rough boundary layer. Both boundary layers were checked for similarity to nature according to the VDI guideline (VDI, 2000).

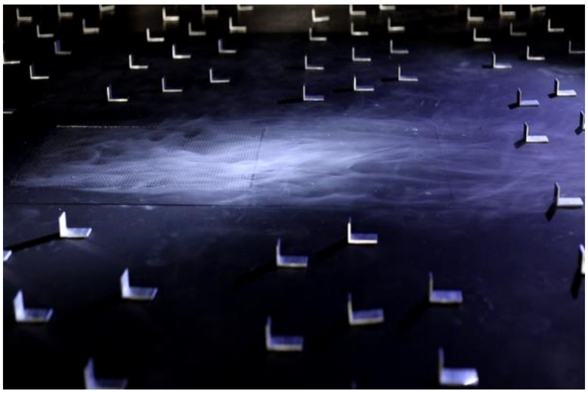

Fig. 1. Left: (a) Heavy gas dispersion from a ground source in a homogenous rough boundary layer without obstacles, **Right**: (b) View into the wind tunnel with the simplified commercial area model, **Bottom**: (c) View into the wind tunnel with the model of a part of the chemical industrial park of BASF in Ludwigshafen in Germany

In all three configurations flow measurements, neutral gas dispersion and heavy gas dispersion experiments were performed. For the simplified commercial area model three different inflow directions were realized (0°, 30°, 90°). For the flow measurements a Laser Doppler Velocimeter (LDV) and for the concentration measurements a flame ionization detector (FID) was used. As an example for the flow measurements the wind statistics inside the simplified commercial area model for the inflow direction of 0° are shown in Figure 2. Clearly visible is the strong influence of the buildings on the flow which result in recirculation zones and bimodal wind direction distributions.

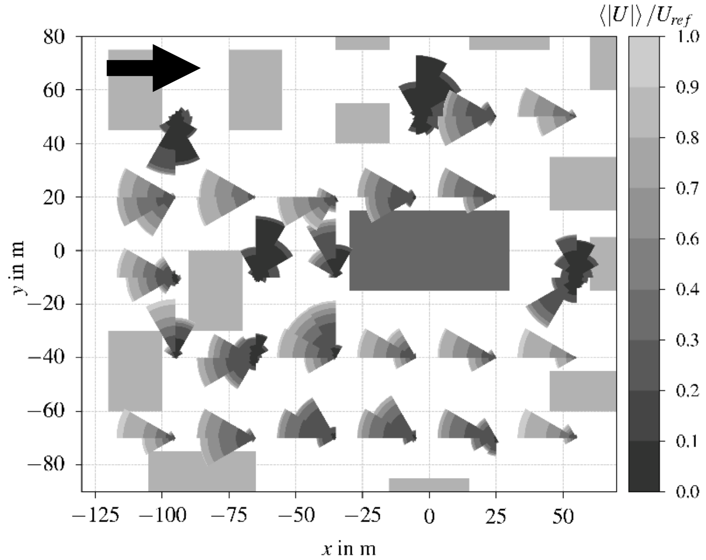

Fig. 2. Distribution of wind speeds and wind directions in the simplified commercial area model. Measurement height is 4 m. Inflow wind direction is marked with the black arrow.

An example for the gas dispersion experiments a neutral gas dispersion and a heavy gas dispersion is shown in Figure 3. Here the used source is in the middle of the right side of the large dark grey building on the left side of the figure. Shown in Figure 3 are the mean relative concentrations of the released gases. The heavy gas effect is visible close to the source where relative concentrations exceed 10% and are much higher than the relative concentrations of the neutral gas release.

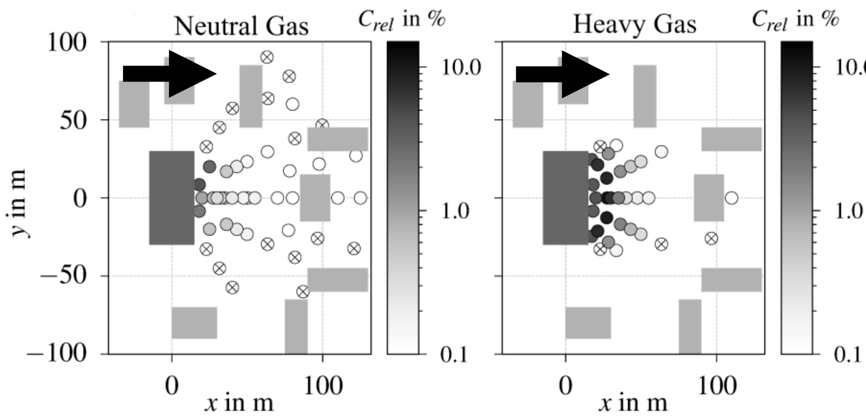

Fig. 3. Relative concentrations of neutral gas (left) and heavy gas (right) releases in the simplified commercial area model. Measurement height is 1 m. Inflow wind direction is marked with the black arrow.

Instrumentation

As previously described a low reference wind speed is desired to maximise the reference wind speed. Previously the reference wind speed was measured with a Prandtl tube connected to a pressure transducer. However due to the length of tubing and the measurement setup the lower limit of measureable reference wind speed of the Prandtl tube was slight above 1 m/s. Thus a new ultra sonic anemometer was bought and installed. With the new USA the desired low reference wind speeds could be measured.

A major issue was the selection of the dense gas. In previous wind tunnel measurement campaigns sulphur hexafluoride (SF_6) was used as the dense gas. SF_6 has lots of advantages, it has a high density of approx. 6 kg\m³ and it is neither toxic nor flammable. It however has a huge global warming potential of 23,900 times of CO_2 over a 100-year period (Forster, 2007) and is expensive. The use of SF_6 also poses an issue with the used instrumentation. To measure gas concentrations inside the wind tunnel a FID type HFR400 is used. The combustion of the SF_6 inside the FID creates corrosive compounds which damage the inside of the FID and render it unusable just after a few hours of operation.

Due to these factors a different heavy gas was needed. An obvious choice was CO_2. CO_2 is much cheaper than SF_6 and is also not toxic nor flammable. However its density of approx. 2 kg/m³ is way smaller than the density of SF_6. Therefore the potential heavy gas effect will also be reduced. In very high concentrations above 10% CO_2 can pose severe health risks which can lead to death (NJ, 2005). Due to the well-designed ventilation system of the wind tunnel and a better planning of the measurements the toxicity of CO_2 was not an issue. Beside the reduced heavy gas effect due to the lower density of CO_2 another peculiar issue arose with its use.

FID CO_2 sensitivity

Depending on the specific setting of the FID a temperature sensitivity due to presence of CO_2 was observed. Especially during calibration of the FID this was a big issue. Under normal circumstances one expects that the FID reaches a steady temperature after approx. 30 minutes of operation. However if CO_2 was present inside the combustion chamber of the FID the temperature changed drastically. This behaviour was unexpected. Normally one would expect a rise in temperature only from high concentrations of combustible gases like propane or butane.

This temperature change posed quite the challenge since the calibration of the FID was performed with self-mixed concentrations of butane and CO_2 and the change in temperature interfered with the calibration. However by changing the parameters of the FID, like increasing the negative pressure or changing the amount and mixing of the oxygen and hydrogen, the temperature difference changed as well. This is shown in Figure 2. For two different mixing ratios of oxygen and hydrogen the influence of a negative pressure change on the temperature change is shown.

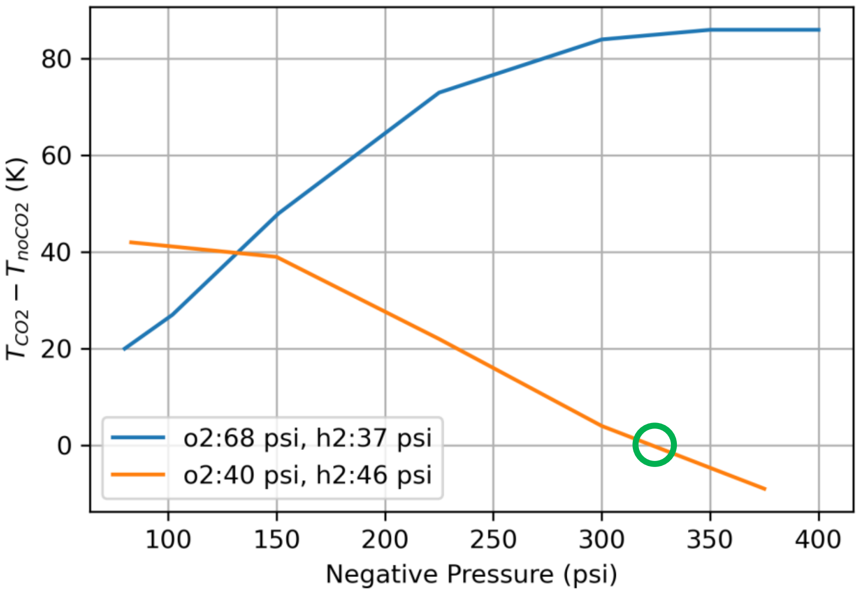

Fig. 4. Influence of CO_2 on the combustion chamber temperature of the FID

Desirable is the point where the temperature of the FID does not change with the addition of CO_2. For the specific settings of the blue line (O_2 68 psi, H_2 37 psi) there was no possible setting found. For the other curve (orange line) a point of optimal settings was found at approx. 325 psi negative pressure. The optimal settings vary from FID to FID, change with a different cannula and change over time. Depending on the cannula optimal settings without a temperature change might not be possible to find since the settings are not freely selectable and might lead to unstable flame conditions.

With the settings without temperature change with CO_2 the FID calibration was stable and produced satisfying results.

Influence of individual roughness elements on the heavy gas cloud

Performing dispersion experiments from ground sources in horizontal homogeneous rough boundary layers without obstacles begs the question whether to remove individual roughness elements or not. There are pro and con arguments regarding this topic. During the measurement campaign the influence of individual roughness elements on the flow and the heavy gas cloud was investigated.

Since the measurement data was taken to be used as reference data for dispersion models intensive exchange with dispersion modellers was maintained. One of the most important aspects was that inside the area of dispersion the roughness and the flow does not change significantly. Mainly because the new roughness is unknown. To investigate the influence of individual roughness elements on the heavy gas cloud two individual dispersion experiments with the ground source were performed. One without roughness elements in the plume (Fig. 5) and one with roughness elements in the plume (Fig. 1a).

The presence of individual roughness elements has a significant effect on the heavy gas cloud. This is mainly due to relatively large size of the roughness elements compared to the gas cloud. The roughness elements have a full scale size of 2 m x 2 m and a length of 5 m. In the vicinity of the source the heavy gas cloud also has a height of 2 to 4 m. Due to the relatively large size of the roughness elements the elements act like individual obstacles and influence the local flow and the dispersion around the roughness elements. This resulted in lower concentrations of heavy gas close to the ground. To test the absence of roughness elements on the flow, roughness elements inside the heavy gas plume were removed and boundary layer measurements were carried out. Over a full scale distance of approx. 100m the influence of missing roughness elements on the flow was observable but acceptably small.

Therefore the gas dispersion measurements were performed with locally removed roughness elements so the heavy gas cloud was not influenced by the presence of individual roughness elements.

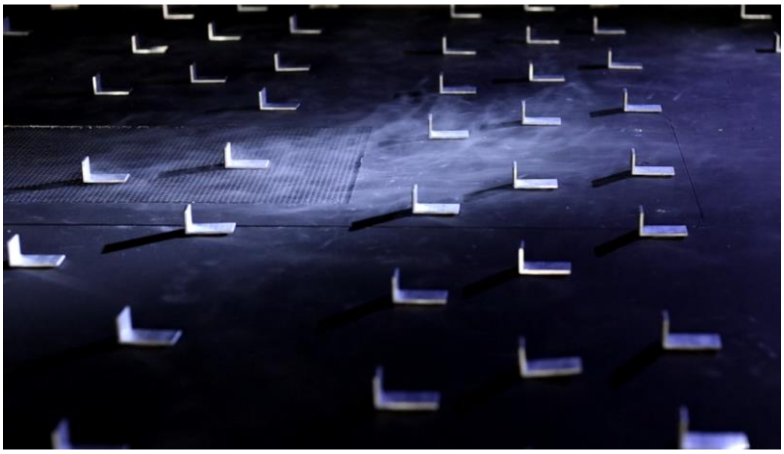

Fig. 5. Heavy gas dispersion from a ground source in a homogenous rough boundary layer without obstacles but with roughness elements

Conclusion

Heavy gas dispersion experiments pose a number of challenges and difficulties, however with good planning and the right instrumentation the difficulties can be overcome. In the past three years a large reference data set of flow measurements, neutral and heavy gas dispersion experiments were carried out in models with rising complexity. In all models a heavy gas effect was observable.

Bibliography

Forster, P. a. (2007). *Changes in Atmospheric Constituents and in Radiative Forcing.*

NJ, L. (2005). Carbon dioxide poisoning. *Toxicol Rev.*, 229.

S. Michel, H. P. (2021). Simulation kurzzeitiger Gefahrstofffreisetzungen aus Industrieanlagen - Herausforderungen und mögliche Lösungen. *Gefahrstoffe Reinhaltung der Luft*, 257-269.

VDI. (2000). *VDI 3783 Blatt 12: Environmental meteorology - Physical modelling of flow and dispersion processes in the atmospheric boundary layer - Application of wind tunnels.* Berlin: Beuth Verlag.

Turbulent Flows in the Inertial- and Roughness-sublayer over Real Urban Morphology: A Comparison of Wind tunnel Experiment and Large-eddy Simulation

Ziwei Mo[1], Chun-Ho Liu[2]

[1]School of Atmospheric Sciences, Sun Yat-sen University, Southern Marine Science and Engineering Guangdong Laboratory (Zhuhai), Zhuhai, China
[2]Department of Mechanical Engineering, The University of Hong Kong, Hong Kong

Abstract

Wind tunnel experiment (WT) and large-eddy simulation (LES) are widely used to investigate the turbulent flows over urban surfaces. Most of the computational fluid dynamics (CFD) model validations only compare the vertical profiles of mean and fluctuating velocities. Few studies look into the higher-order moments of velocity and turbulent structures. In this paper, we contrast the flows in inertial-sublayer (ISL) and roughness-sublayer (RSL) over the real urban surface in Hong Kong using both WT and LES. The results obtained by these two approaches agree favorably in terms of mean and fluctuating velocity, skewness and kurtosis, as well as quadrant-hole analysis. Both WT and LES reveal that ejection Q2 and sweep Q4 dominate the turbulent transport, especially sweep Q4 in the RSL. We also found that the rare, large-scale high-speed downward flows are enhanced in the RSL. These results could help understand the dissimilar flow structure in ISL and RSL, as well as the implications for CFD validation exercises.

PHYSMOD 2022 – International Workshop on Physical Modeling of Flow and Dispersion Phenomena
Institute of Thermomechanics of the CAS, Prague, Czech Republic – August 29-31, 2022

Statistical assessment of the ventilation of street canyons based on time-resolved wind tunnel experiments

B. Papp [1], B. Istók [1], M. Koren [1], M. Balczó [1], G. Kristóf [1]

[1] Department of Fluid Mechanics, Faculty of Mechanical Engineering, Budapest University of Technology and Economics. Bertalan Lajos u. 4–6, H-1111 Budapest, Hungary. E-mail: papp.balint@gpk.bme.hu, istok.balazs@gpk.bme.hu, koren.marton@gpk.bme.hu, balczo.marton@gpk.bme.hu, kristof.gergely@gpk.bme.hu

Abstract

Time-resolved experimental pollutant concentration results are reported for a series of parallel street canyons of uniform and variable building height, subjected to perpendicular approach flow. The velocity field was mapped using Laser Doppler Anemometry (LDA), and the tracer gas concentration distribution was sampled using Fast Flame Ionization Detection (Fast FID) in more than 1000 measurement points altogether. In addition to the time-averaged data, the measurement points are further characterized by the concentration probability distribution and the concentration power spectra. Based on the results obtained by the statistical analysis, the ventilation of the three examined periodic building patterns – uniform canyons, matrix (aligned) towers, and staggered towers on the top of shorter continuous buildings – was analyzed in terms of the mean exposure and the extreme values of the concentration fluctuations. It was shown that although both tower configurations can effectively decrease the mean concentration compared to the uniform canyons, the extreme values reached and sometimes exceeded those of the baseline case in the source canyon. It was also demonstrated that the probability distribution of the concentration in a single point can be accurately modeled by the Exponentially Modified Gaussian distribution both in the near-field and in the far-field.

1. Introduction

The ventilation efficiency of an urban area is commonly characterized by the time-averaged mean normalized concentration, either at street level, corresponding to the pedestrian exposure to traffic-related air pollutants, or below roof height, which indicates the exposure of the residents of the buildings. This metric is sufficient for studying sustained hazards and risks, such as exposure to nitrogen oxides or particulate matter, as the accumulation process filters the temporal concentration fluctuations (see **Cassiani et al., 2020** and the references therein). On the other hand, for the assessment of the exposure to toxic, infectious, or explosive substances, the probability of their concentration exceeding a specific threshold and expected the mean time above the threshold must be known (**Hilderman et al., 1999**; **Gant et al., 2011**; **Gant and Kelsey, 2014**; **Sze To and Chao, 2009**).

A detailed review of toxicity models for realistic atmospheric applications is provided by **Gunatilaka et al (2014)**, compiling and comparing models from the simplest linear dose-toxicity response approach (for which knowing the mean concentration is enough) towards more elaborate methods considering the peak values and time statistics of the concentration fluctuations (e.g., **Yee, 1999**), and ones which even include the saturation and the biological recovery time of the human body. It was also demonstrated by **Kikumoto and Ooka (2012)** the correlation between the time fluctuations of reactive substances' concentrations strongly affects the reaction rates; therefore, the assessment of the mean concentration is not enough.

Modeling the probability distribution of the concentration is an efficient way to characterize the magnitude and the probability of its fluctuations (various modeling approaches are reviewed by **Cassiani et al., 2020**). It was found that the lognormal and gamma distributions gave the best agreement with the experimental data in short and far ranges as well, regarding the concentration fluctuations in a plume released from a point source for stable, near-neutral, and unstable stability conditions (**Yee et al., 1993, 1994, 1995**). Other previous proposals are listed by **Cassiani et al. (2020)** in Table 2). The two-parameter gamma distribution has become an accepted model for modeling the concentration fluctuations of pollutants released from point sources (**Nironi et al., 2015**; **Ardeshiri et al., 2020**), which is able to produce their exponential-like probability distribution in the near-field, the Gaussian-like PDF in the far-field, and the lognormal-like blending between them.

In this paper, statistically processed concentration results of a well-known model for the urban canopy, a series of parallel street canyons of H/W = 1 aspect ratio; and two more complex building arrangements (matrix and staggered towers) of the same total building volume and identical floor area density are compared in order to give detailed insight to their ventilation characteristics. Furthermore, the concentration time statistics obtained within and above the buildings can serve as reference (validation) data when studying transient CFD-based dispersion models for air quality and local-scale emergency prediction purposes. (The measurement results are available on request.)

2. Materials and methods

2.1. Experimental setup

Wind tunnel experiments were performed using the closed-circuit horizontal (Göttingen-type) wind tunnel of the Kármán Wind Tunnel Laboratory of the Department of Fluid Mechanics at Budapest University of Technology and Economics. The wind tunnel, shown in **Fig. 1a**, has a circular cross-section of 2.6 m in diameter at the open test section of 3.8 m in length, and it is equipped with a 2.5 m wide horizontal table. Further details on the presented wind tunnel experiments, including the measurement instrumentation, can be found in **Papp et al. (2021)** in Table 1.

For the measurements, three building arrangements were constructed from styrofoam. The *uniform street canyons (UC)* form the baseline case with 23 small-scale (M = 1:200) buildings positioned perpendicular to the wind direction. The buildings have a $B \times H$ = 100×100 mm (breadth by height) rectangular cross-section, and they are positioned W = 100 mm distance one after another; hence, the offset between two adjacent streets is S = 200 mm. The 22 canyons are numbered from -10 to +11 in the streamwise direction, with tracer gas sources located in the 0th canyon.

Two additional building patterns were constructed with roof height modifications. The middle part of each building row was divided into six segments, each of $B \times T$ = 100 × 208.33 mm plan area. The roof height of the segments was alternately raised and lowered by 0.5H; thus, the total building volume remained unchanged. In the *matrix tower (MT) arrangement*, the tall buildings are aligned with each other in the streamwise direction, while in the *staggered tower (ST) arrangement*, the tall towers are shifted laterally relative to the neighboring rows, causing both lateral and streamwise building height inhomogeneity. The building configurations are illustrated in **Fig. 1b-c-d** below.

The incoming flow was homogeneous with a low turbulence level of <1%; this way, the building arrangements were able to generate their own boundary layer. 4.75*H* upstream of the test section, a 0.6*H* tall baffle was placed (shown in **Fig. 1a**), in order to reduce the size of the separation bubble forming over the first few rows of buildings. It was found that after 11 street canyons, the flow was fully developed below 3*H* height (see **Fig. 2**); thus, after that, it can be considered periodic. (The 0^{th} number was assigned based on this result.) Two identical tracer gas sources (of 28 mm diameter) were constructed from pumice in brass housings and were flush-mounted in the base plate of the model. As shown in **Fig. 1b-c-d**, the sources are located in the middle of the 0^{th} canyon with a lateral offset of half a tower width (x/S = 0, y/T = ±0.5, where y > 0 is named the "left side").

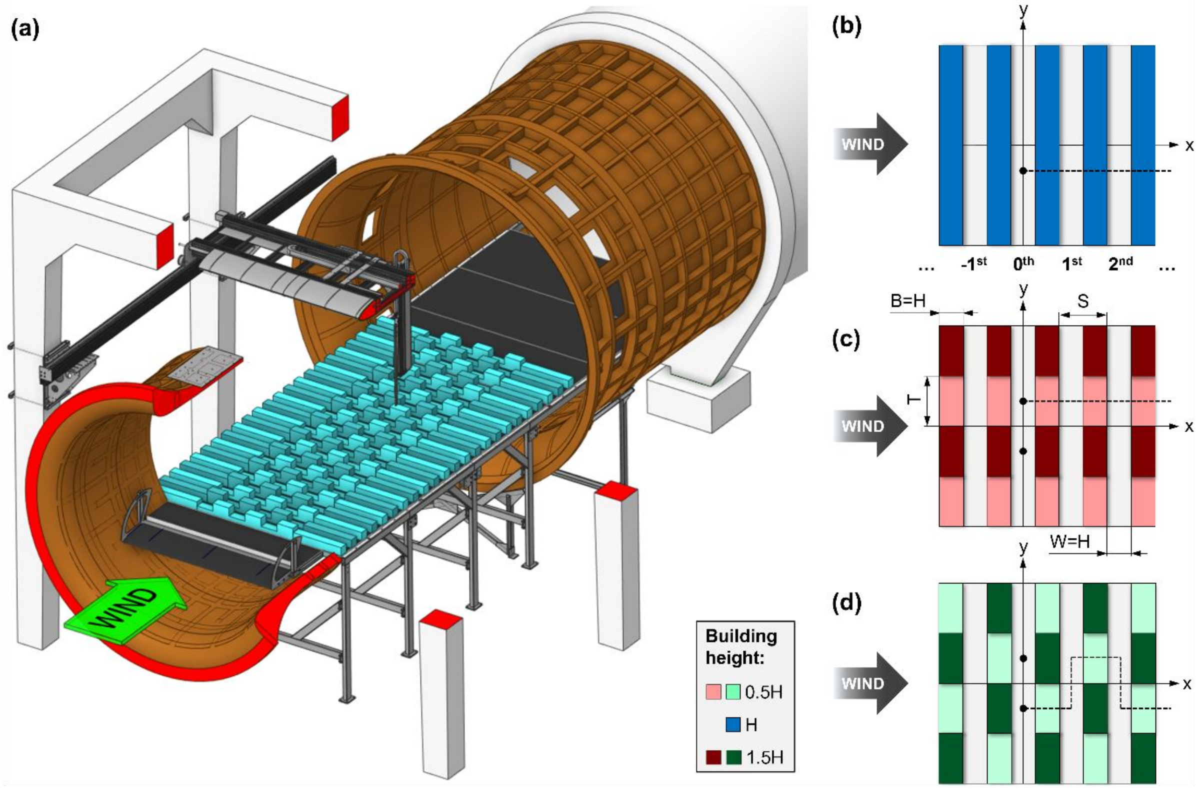

Fig. 1. Experimental setup (a) and the investigated building patterns: uniform street canyons (UC; b), matrix/aligned towers (MT; c), staggered towers (ST; d). The black dots designate the sources, and the dashed lines indicate the locations of the measurement points at z/H = 1.2.

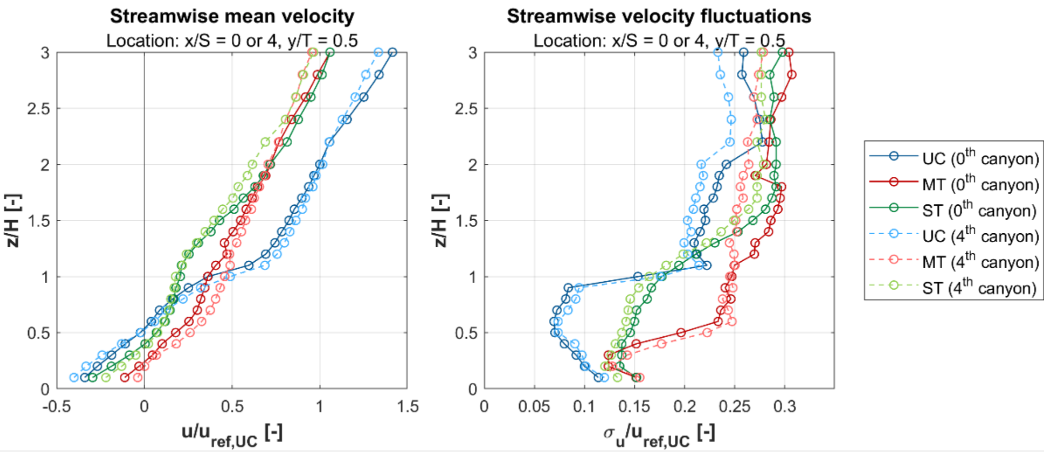

Fig. 2. Normalized streamwise mean and fluctuating velocity components measured along a vertical line in the 0th and in the 4th canyons for the three investigated building patterns.

2.2. Measurement techniques

The horizontal velocity component distribution was measured using two-component Laser Doppler Anemometry in the 0th and 4th canyons using a TSI LDA system; for the details, see **Papp et al. (2021)**. The velocity measurement in each gauging point took 150 s with a sampling frequency range of 100…1000+ Hz. The absolute measurement uncertainty is 0.1 m/s. The bulk velocity of the wind tunnel was monitored with a Pitot-static probe, and its minor changes were compensated during the normalization process.

The characteristic Reynolds number based on the reference mean velocity at 2H in the uniform canyons case ($u_{ref,UC}$ = 4.74 m/s) and the roof height H was calculated around Re_H = 31 800, which exceeds the threshold of Re = 11 000, above which the flow can be considered Reynolds-insensitive for H/W = 1 aspect ratio street canyons; furthermore, the flow field can also be assumed Re-independent for the matrix and staggered tower arrangements (H/W = 0.5 and 1.5) as well (**Chew et al., 2018**).

The pollutant distribution between and above the buildings was mapped using a Cambustion HFR400 FID (Flame Ionization Detection) device. The applied tracer gas representing the traffic-induced air pollutants was pure methane (100% CH_4), continuously emitted from one of the two sources (left or right) at a time. Pre-calibrated smart mass flow meters were applied to control the volume flow rate. The resultant dispersion field was sampled for 30 s in each measurement point, with a sampling frequency of 5000 Hz and a response time of 2.05 ms, resulting in 12% relative and (0.28·c*) absolute uncertainty, based on 4 reproduced measurements. The relative uncertainty is calculated as the 90th percentile of the coefficient of variation (relative standard deviation), and the absolute uncertainty is obtained as the mean of the coefficient of variation in the far-field.

2.3. Signal processing and statistical analysis

The voltage time signal produced by the FID device was first calibrated to obtain the tracer gas concentration (in part per million, ppm), using two calibration mixtures of pre-defined concentrations (100 ppm and 4950 ppm) and by subtracting the background concentration of the wind tunnel, which was gradually increasing during the measurements due to the continuous methane emission. (Remark: instantaneous negative concentrations can result from measurement errors as well as from being below the background concentration momentarily.) The measured concentration time series were normalized according to

$$c^*(t) = \frac{c(t)}{10^6} \cdot \frac{u_{ref,UC}}{Q/A}, \tag{1}$$

in which c^* [–] is the normalized concentration, t [s] is time, c [ppm] is the measured concentration, $u_{ref,UC}$ [m/s] is the reference mean velocity (at z/H = 2 in the uniform canyons configuration), Q [m^3/s] is the volume flow rate of the tracer gas, and $A = 2 \times S \times T$ [m^2] is the reference area. Note that for the different geometries (UC/MT/ST), the undisturbed flow velocity was identically 9 m/s. Using the same velocity and area for the normalization for all building patterns allows a "fair" comparison of the concentration fields: as the urban boundary layer is generated by the buildings themselves, this approach also includes the effect of surface drag corresponding to the installation length used in the model, as in the case of rough surfaces (i.e., more heterogeneous roof height), a better mass transfer is achieved at the cost of greater surface drag.

Based on the normalized concentration time series, the statistical parameters describing each measurement point, such as the mean, the standard deviation, and the nth percentile can be assessed, with the 0th percentile corresponding to the minimum, the 50th to the median, and the 100th to the maximum value. It is expected that the measurements contain outliers; therefore, the representative extreme values are calculated after removing the top and bottom 1% of the data: the minimum is represented by the 1st percentile, and the maximum is given by the 99th percentile of the time series. These quantities can be visualized using a box plot (with six parameters), as shown in **Fig. 3**, indicating the peak values and the magnitude, and the relation between the mean and the median concentration, based on which the skewness of the data set can be estimated.

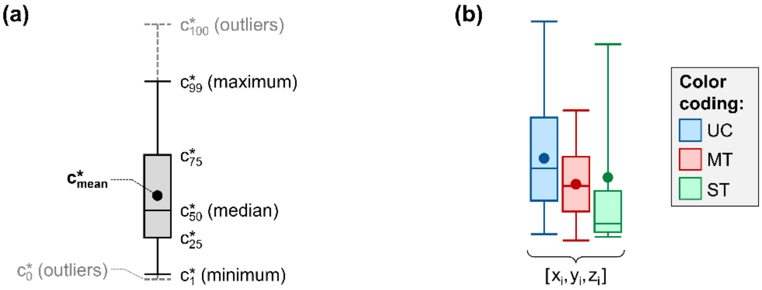

Fig. 3. (a) Box plot representation of the time statistics characterizing a single normalized concentration time series c*(t). (b) Comparison example of the concentration statistics between the three building patterns (UC, MT, ST) at a single (the ith) measurement point.

The number of parameters can be further reduced, without losing information about the time series, if a suitable probability density function (PDF) is fitted to the original data set. In the present paper, the three-parameter Exponentially Modified Gaussian distribution (also termed as EMG or ex-Gaussian distribution) is fitted to the data sets, which describes the sum of independent normal and exponential random variables. Note that the domain of the EMG PDF – conversely to that of the widely used gamma distribution – can include negative values as well. The fitting is carried out using the method and its MATLAB implementation of **Lacouture and Cousineau (2008)**, whose paper also provides the equation of the EMG PDF. As the aforementioned fitting algorithm is only able to handle positive input data; therefore, to avoid inaccuracies due to the truncation, the time series were first shifted to have purely positive values, and after the fitting, the previous offset was subtracted from the Gaussian mean parameter (μ) of the EMG PDF, while the Gaussian standard deviation (σ) and the exponential scale (τ, defining the length of the exponential tail) parameters were left unchanged.

While the statistics derived from the fitted PDF can provide valuable information about the magnitude of the fluctuations, their dominant frequency can only be assessed if spectral information is available. In this paper, the power spectra of the time series – each sampled at 5000 Hz for 30 s – are computed following Welch's method (**Welch, 1967**), using a window size of 10 000 points with a symmetric Hanning window function and a 50% overlap.

3. Results and discussion

During the discussion of the results, we are going to focus on the 0th canyon (containing the point sources) as this is the most polluted area. To analyze the far-field effects, concentration distributions in the 1st canyons are also shown in this paper. Note that the concentration field was also sampled in the 4th canyon; for the list of measurement locations, see **Table A1** in the **Appendix**.

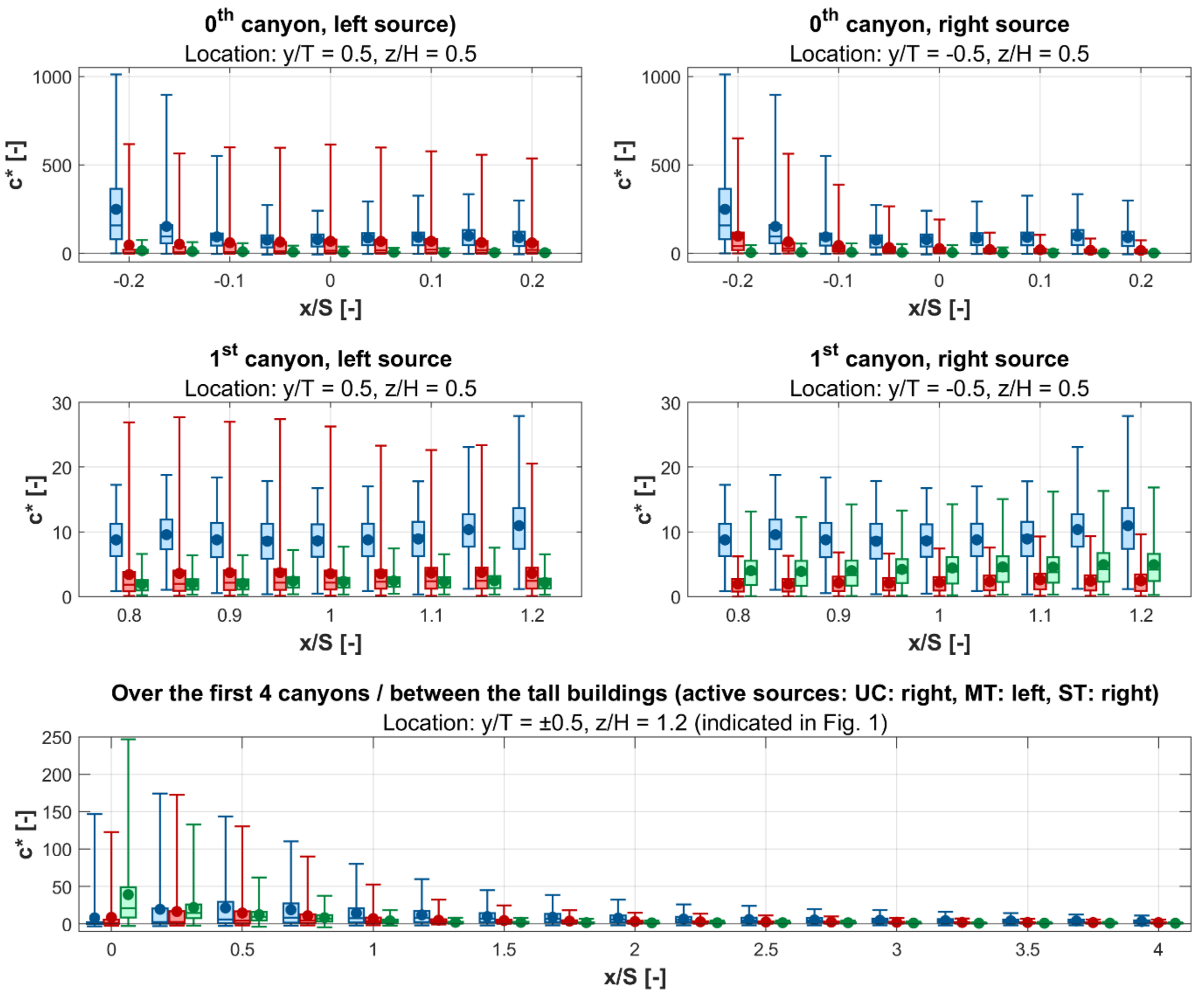

Fig. 4. Concentration statistics along several streamwise (x) profiles.

It can be observed in **Fig. 4** that in terms of the mean concentration, the uniform canyons display the highest values in the 0^{th} and 1^{st} canyons along a streamwise line between the walls at *z/H* = 0.5 (UC:

half building height; MT/ST: the height of the short buildings). For the UC case, in the 0^{th} canyon, the known asymmetry between the leeward and windward sides can be clearly identified (concentration surplus at *x/S* = -0.2 compared to *x/S* = 0.2). A similar asymmetric tendency can be observed over the right source of the MT case (at *z/H* = 0.5 between two tall buildings), which is caused by the present backflow induced by the downwash at the windward face of the tall buildings. Note that the "windward downwash" phenomenon is also present for the staggered tower arrangement (**Papp et al., 2021**). The MT and especially the ST case produce substantially lower mean concentrations; however, the peak concentration values of the MT case can reach and at some points exceed those measured between the uniform canyons, most likely as a consequence of the more intensive turbulent mixing within the towers, especially when a shear layer is present (MT, left source).

It is also shown in **Fig. 4** that in the 1^{st} canyon, the pointwise concentrations are an order of magnitude smaller, and in the UC case their distribution is symmetric, while in the case of either of the tower arrangements, they are rather skewed. This can be attributed to the fact that the pollutants reach this location indirectly, and they are mixed more evenly along the way due to turbulent diffusion. Regarding the concentration distribution at *z/H* = 1.2, the three investigated building arrangements show similar tendencies, with the exception of the ST case, where at the first point significantly higher mean concentration was measured. This is due to the fact that this point is located in the wake of a building, in which the pollutants are quickly transported upwards.

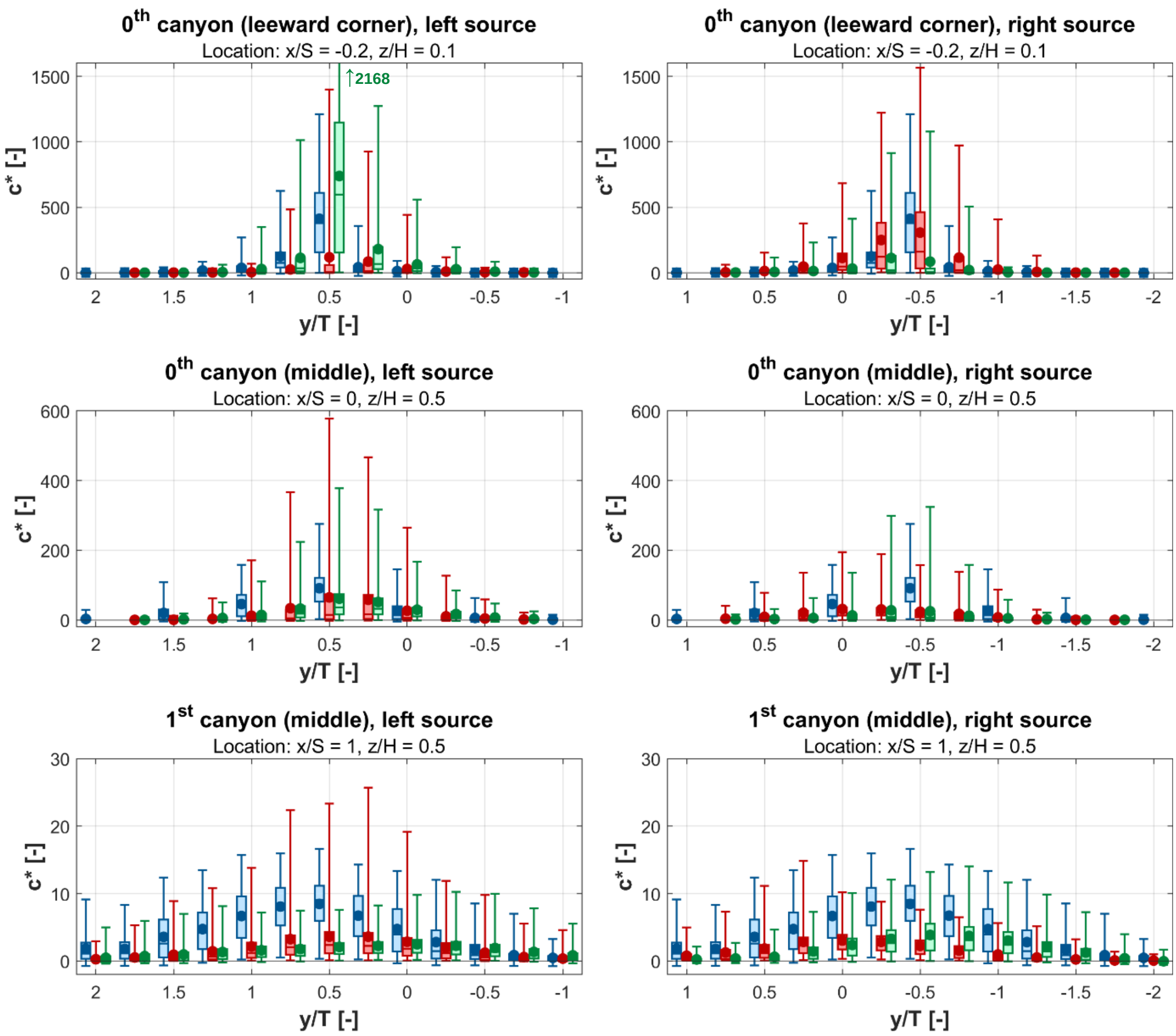

Fig. 5. Concentration statistics along several lateral (crosswise, y) profiles.

The lateral concentration distributions presented in **Fig. 5** reveal that at the leeward corner of the 0th canyon – which is the most critical location in terms of pedestrian exposure –, the highest mean concentration in the case of the staggered towers (ST) arrangement exceeds that of the baseline case (UC) near the left source (i.e., in front of a tall building). When the source is located behind the tall building – in our case, on the right side –, the mean concentration is significantly smaller for the ST case; although on this side, in the MT case, the mean concentration is nearly as high as in the reference configuration (UC). It is also visible in **Fig. 5** that in the middle of the 0th canyon (x/S = 0, z/H = 0.5) – which is a better representation of the canyon average – the mean concentrations are the highest for the UC case and the lowest for the ST case. It is important to note, however, that the peaks of the concentration fluctuations induced by the heavily turbulent flow between the towers are reaching and many times exceeding those of the baseline case in the near-field. It can also be seen in **Fig. 5** that in the far-field (i.e., in the middle of the 1st canyon), the mean concentration is 30 times lower compared to the 0th canyon, and they are even lower in the case of heterogeneous roof height (MT, ST); although, the peak concentrations are in the same order of magnitude in all cases.

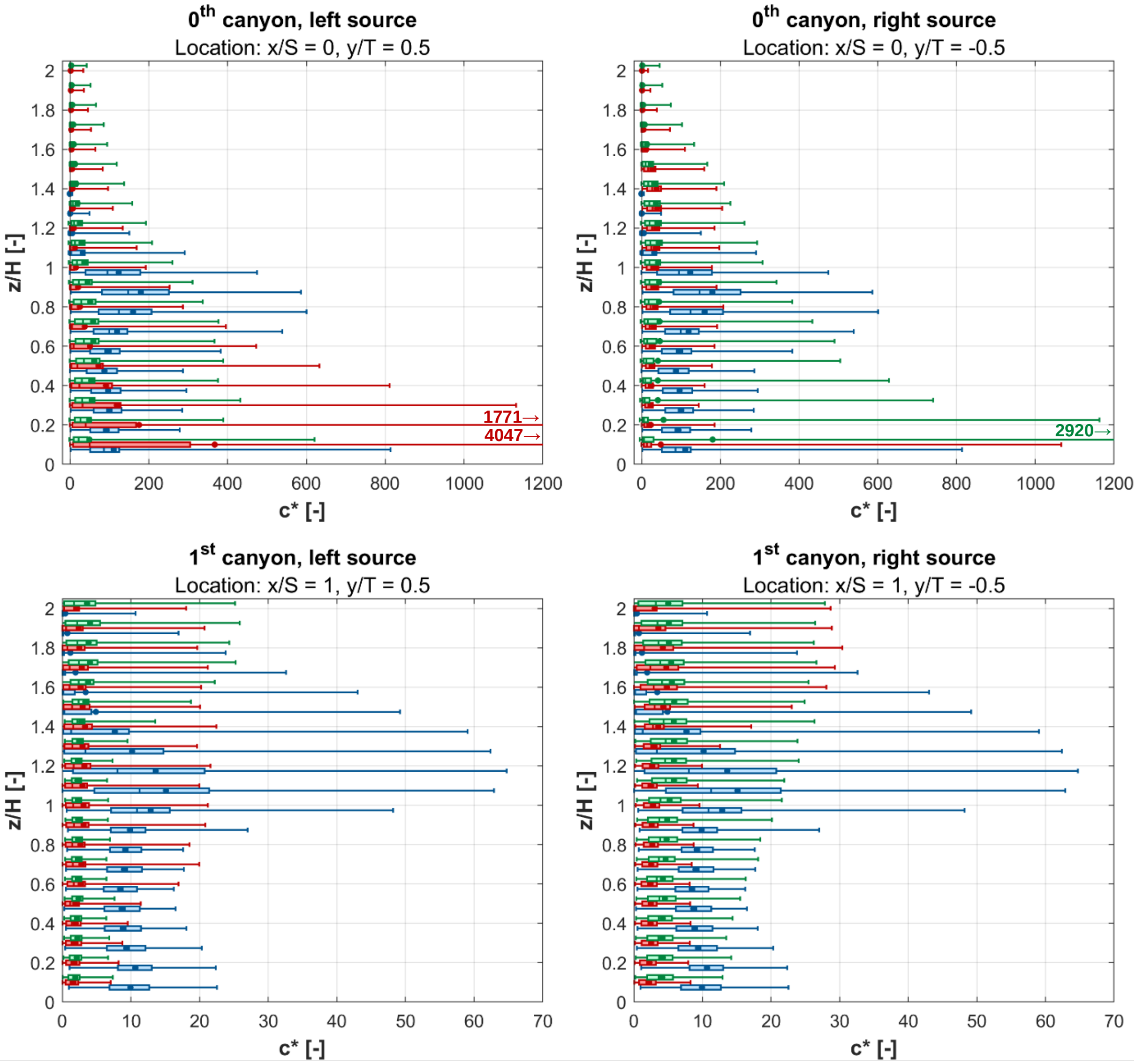

Fig. 6. Concentration statistics along several vertical (z) profiles.

The above-described tendencies can be observed in the vertical concentration profiles presented in **Fig. 6** as well. In the source canyon, the mean concentrations are generally higher for the UC arrangement compared to the towers, with two exceptions: for the MT arrangement, on the left side ($y > 0$, between two short buildings) particularly high average concentrations are present below z/H = 0.5, which can be attributed to the fact that a tight, closed vortex structure – similar to the canyon vortex in the UC case – is formed between the short buildings, hindering the upward transport of the pollutants. Conversely, in the ST case, high concentrations above the source can only be found over the right source, at z/H = 0.1. It can also be seen in **Fig. 6** that in the 1st downstream canyon, the mean exposure is significantly lower in the presence of the towers compared to the UC case. The peak concentration values can reach (and exceed) those of the uniform canyons only above street level; hence, the pedestrian exposure is not compromised in the far-field.

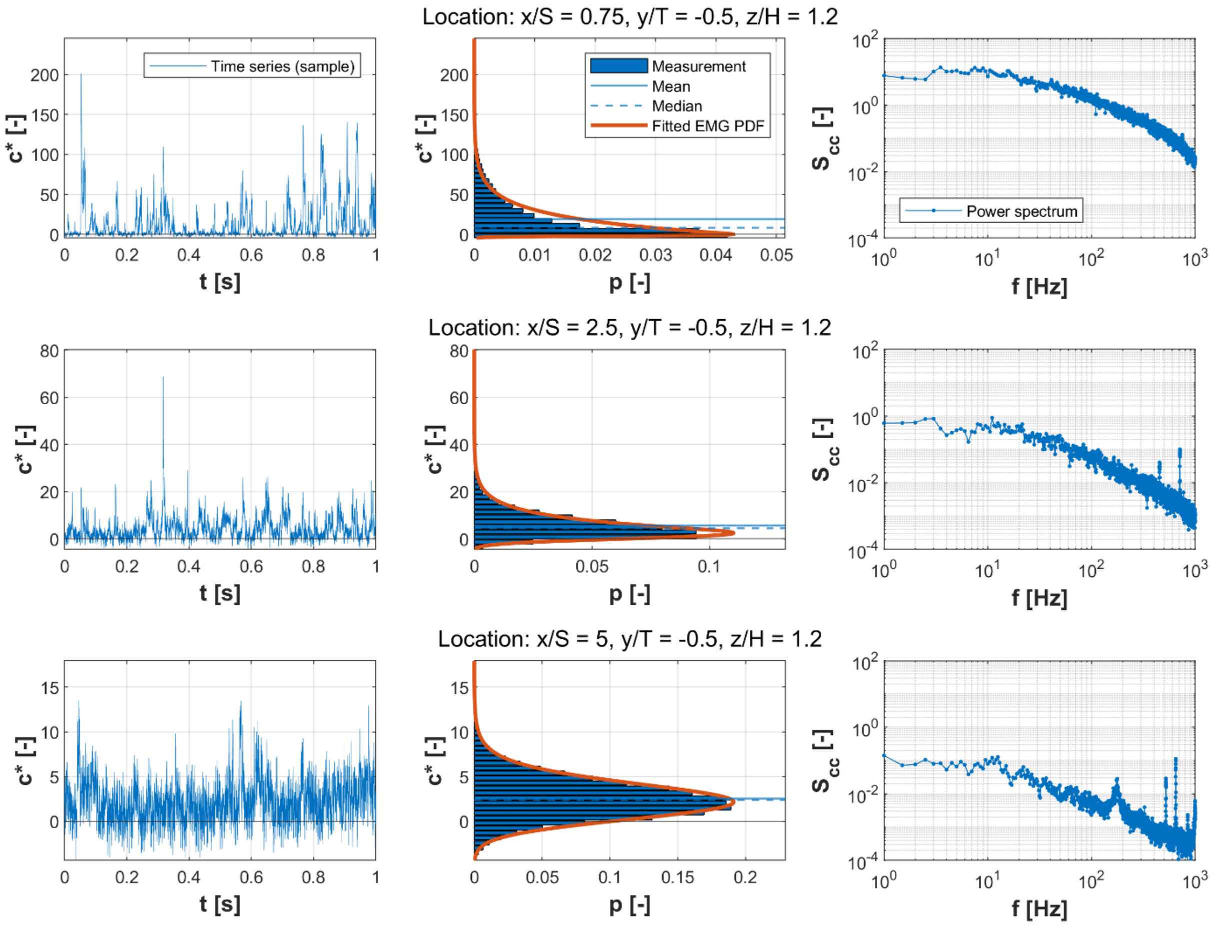

Fig. 7. Characteristics of three measurement points located at different distances from the (UC case). Left: 1 s long samples of the time series. Middle: histograms with the Exponentially Modified Gaussian PDF fitted to the original time series. Right: power spectra of the original time series.

Fig. 7 shows the time statistics for three measurement points above the uniform canyons at z/H = 1.2. It can be observed that as we move away from the source, the probability distribution blends from an exponential to a Gaussian PDF, which can be explained by the fact that in the near-field high, pulse-like concentration peaks (caused by the turbulent flow) are superimposed on top of an essentially zero background concentration (known as meandering); while in the far-field, the tracer gas is evenly mixed, resulting in a more symmetric, normal-like behavior around a significantly lower mean value, with clearly noticeable peaks in the spectrum. The parameters of the fitted EMG distributions are compared with the statistics derived from the experimental data in **Table 1** below.

Table 1. Statistics corresponding to Fig. 7. (Italic numbers denote the statistics derived from the fitted PDF.)

Measmt. point	x/S [–]	μ [–]	σ [–]	τ [–]	c^*_{mean} [–]	c^*_{std} [–]	c^*_{1} [–]	c^*_{25} [–]	c^*_{50} [–]	c^*_{75} [–]	c^*_{99} [–]
#1	0.75	-2.015	0.965	20.723	18.71 *18.71*	25.12 *20.75*	-2.53 *-2.68*	1.41 *3.81*	8.12 *12.06*	27.26 *25.54*	110.31 *93.22*
#2	2.5	0.408	1.715	5.215	5.62 *5.62*	5.39 *5.49*	-2.08 *-2.08*	1.80 *1.83*	4.49 *4.20*	8.12 *7.85*	24.00 *24.64*
#3	5	1.082	1.706	1.471	2.55 *2.55*	2.25 *2.25*	-2.27 *-2.10*	1.03 *1.01*	2.37 *2.37*	3.89 *3.86*	8.84 *8.82*

4. Conclusions

In the present paper, the concentration distribution of three periodic building arrangements was analyzed using statistical tools. It was shown that the mean concentration within the urban canopy could be effectively decreased by introducing heterogeneity to the building height, i.e., by constructing towers in either matrix or staggered arrangement, while keeping the total building volume and plan area density identical to the reference case of uniform H/W = 1 street canyons. It was also demonstrated that the temporal probability distribution of the concentration – showing an exponential-like behavior in the near-field and a normal-like behavior in the far-field – can be accurately represented using the Exponentially Modified Gaussian distribution.

Acknowledgements

This study was funded by grant no. K 124439 from the National Research, Development, and Innovation Office, Hungary. The research reported in this paper and carried out at BME has been supported by the NRDI Fund (TKP2020 NC, Grant No. BME-NCS) based on the charter of bolster issued by the NRDI Office under the auspices of the Ministry for Innovation and Technology. The research reported in this paper is part of project no. BME-NVA-02, implemented with the support provided by the Ministry of Innovation and Technology of Hungary from the National Research, Development and Innovation Fund, financed under the TKP2021 funding scheme. Bálint Papp's contribution to this paper was supported by the Gedeon Richter Talent Foundation (registered office: Gyömrői út 19-21, 1103 Budapest, Hungary), established by Gedeon Richter Plc., within the framework of the Gedeon Richter PhD Scholarship. Márton Balczó gratefully acknowledges the support of project PD 127919 of the Hungarian Scientific Research Fund (NKFI), entitled 'Application and validation of measurement techniques related to the physical modeling of the atmospheric boundary layer in a new boundary layer wind tunnel'.

References

Ardeshiri, H., Cassiani, M., Park, S. Y., Stohl, A., Pisso, I., & Dinger, A. S. (2020). On the convergence and capability of the large-eddy simulation of concentration fluctuations in passive plumes for a neutral boundary layer at infinite reynolds number. Boundary-Layer Meteorology, 176(3), 291-327. [DOI]

Cassiani, M., Bertagni, M. B., Marro, M., & Salizzoni, P. (2020). Concentration fluctuations from localized atmospheric releases. Boundary-Layer Meteorology, 177(2), 461-510. [DOI]

Chew, L. W., Aliabadi, A. A., & Norford, L. K. (2018). Flows across high aspect ratio street canyons: Reynolds number independence revisited. Environmental Fluid Mechanics, 18(5), 1275-1291. [DOI]

Gant, S. E., & Kelsey, A. (2012). Accounting for the effect of concentration fluctuations on toxic load for gaseous releases of carbon dioxide. Journal of Loss Prevention in the Process Industries, 25(1), 52-59. [DOI]

Gant, S. E., Pursell, M. R., Lea, C. J., Fletcher, J., Rattigan, W., Thyer, A. M., & Connolly, S. (2011). Flammability of hydrocarbon and carbon dioxide mixtures. Process safety and environmental protection, 89(6), 472-481. [DOI]

Gunatilaka, A., Skvortsov, A., & Gailis, R. (2014). A review of toxicity models for realistic atmospheric applications. Atmospheric Environment, 84, 230-243. [DOI]

Hilderman, T. L., Hrudey, S. E., & Wilson, D. J. (1999). A model for effective toxic load from fluctuating gas concentrations. Journal of Hazardous Materials, 64(2), 115-134. [DOI]

Kikumoto, H., & Ooka, R. (2012). A numerical study of air pollutant dispersion with bimolecular chemical reactions in an urban street canyon using large-eddy simulation. Atmospheric environment, 54, 456-464. [DOI]

Lacouture, Y., & Cousineau, D. (2008) How to use MATLAB to fit the ex-Gaussian and other probability functions to a distribution of response times, Tutorials in Quantitative Methods for Psychology, 4(1), 35-45. [DOI] [GitHub]

Nironi, C., Salizzoni, P., Marro, M., Mejean, P., Grosjean, N., & Soulhac, L. (2015). Dispersion of a passive scalar fluctuating plume in a turbulent boundary layer. Part I: Velocity and concentration measurements. Boundary-layer meteorology, 156(3), 415-446. [DOI]

Papp, B., Kristóf, G., Istók, B., Koren, M., Balczó, M., & Balogh, M. (2021). Measurement-driven Large Eddy Simulation of dispersion in street canyons of variable building height. Journal of Wind Engineering and Industrial Aerodynamics, 211, 104495. [DOI]

Sze To, G. N., & Chao, C. Y. H. (2010). Review and comparison between the Wells–Riley and dose-response approaches to risk assessment of infectious respiratory diseases. Indoor air, 20(1), 2-16. [DOI]

Welch, P. (1967). The use of fast Fourier transform for the estimation of power spectra: a method based on time averaging over short, modified periodograms. IEEE Transactions on audio and electroacoustics, 15(2), 70-73. [DOI]

Yee, E. (1999). An impact–effect mathematical model incorporating the influence of exposures to fluctuating concentrations in a dispersing plume of pollutant in the atmosphere. Journal of Exposure Science & Environmental Epidemiology, 9(4), 300-311. [PDF]

Yee, E., Chan, R., Kosteniuk, P. R., Chandler, G. M., Biltoft, C. A., & Bowers, J. F. (1994). Concentration fluctuation measurements in clouds released from a quasi-instantaneous point source in the atmospheric surface layer. Boundary-layer meteorology, 71(4), 341-373. [DOI]

Yee, E., Chan, R., Kosteniuk, P. R., Chandler, G. M., Biltoft, C. A., & Bowers, J. F. (1995). The vertical structure of concentration fluctuation statistics in plumes dispersing in the atmospheric surface layer. Boundary-Layer Meteorology, 76(1), 41-67. [DOI]

Yee, E., Kosteniuk, P. R., Chandler, G. M., Biltoft, C. A., & Bowers, J. F. (1993). Statistical characteristics of concentration fluctuations in dispersing plumes in the atmospheric surface layer. Boundary-Layer Meteorology, 65(1), 69-109. [DOI]

Appendix

The geometrical position and the range of the measured concentration profiles are compiled below.

Table A1. Details of the concentration measurements.

Name	x/S [–]	y/T [–]	z/H [–]	Active source*	In this paper
X distribution in the 0th canyon	**-** **0.2…0.2**	-0.5 0.5	0.5	Right Left	**Fig. 4.**
X distribution in the 1st canyon	**0.8…1.2**	-0.5 0.5	0.5	Right Left	**Fig. 4.**
X distribution over the roofs (UC) / between the tall buildings (MT, ST)	**0…6**	±0.5 *(see Fig. 1.)*	1.2	Right (UC, ST) Left (MT, ST)	**Fig. 4., Fig. 7.**
Y distribution in the leeward corner of the 0th canyon	-0.2	**-1.75…0.75** **-0.75…1.75**	0.1	Right Left	**Fig. 5.**
Y distribution in the middle of the 0th canyon	0	**-2.75…1.75** **-1.75…2.75**	0.5	Right Left	**Fig. 5.**
Y distribution in the middle of the 1st canyon	1	**-2.75…1.75** **-1.75…2.75**	0.5	Right Left	**Fig. 5.**
Y distribution in the middle of the 4th canyon	4	**-2.75…1.75** **-1.75…2.75**	0.5	Right Left	*Not shown*
Y distribution over the 4th canyon	4	**-2.75…1.75** **-1.75…2.75**	0.5	Right Left	*Not shown*
Z distribution in the 0th canyon	0	-0.5 0.5	**0.1…2.5**	Right Left	**Fig. 6.**
Z distribution in the 1st canyon	1	-0.5 0.5	**0.1…3.5**	Right Left	**Fig. 6.**
Z distribution in the 4th canyon	4	-0.5 0.5	**0.1…3.5**	Right Left	*Not shown*

* For the uniform canyons (UC) the left source was not active at all. In **Figs. 4-6**, the results from the right side are displayed on the left as well, utilizing the geometrical similarity.

SCALE INTERACTION AND THE LARGE-SCALES INFLUENCE IN THE URBAN CANOPY

L. Perret[1]

[1]Nantes Université, Centrale Nantes, CNRS, LHEEA, UMR 6598, F-44000 Nantes, France

Abstract

Recent investigation of turbulent boundary layer flows developing over urban-like roughness has evidenced the strong similarities of their spatio-temporal organization with that of smooth-wall boundary layers. In particular, the presence of large and very-large scale structures (VLSMs) has been shown in flow at high Reynolds numbers. The objective of the present contribution is to review some of the aspect of the interaction between these boundary-layer large scales and the most energetic structures existing in the roughness sublayer (RSL). In addition to superimpose onto the RSL scales, VLSMs are shown to modulate canopy turbulence, leaving their imprint in high order moments and participating to the transport of kinetic energy turbulence through inter-scale energy transfer.

1. Introduction

Understanding and modeling the flow dynamics over urban terrain still represent a challenge due to the high geometrical complexity of built areas, the existence of numerous interacting thermodynamic processes that take place in the urban canopy, and the mutual influence of atmospheric processes. From a purely aerodynamic point of view, the atmospheric flow over the urban canopy can be considered as a high Reynolds number boundary-layer flow developing over a heterogeneous and multi-scale surface. This flow has therefore an important multi-scale character in both space and time with strong and complex inter-scale interactions. The resulting high complexity limits our ability both to understand the dynamics of urban flows and to model these flows.

Decades of research on the turbulent boundary layer that develops over a flat smooth wall has brought general consensus across the scientific community regarding its organization (Marusic et al. 2010): the turbulent structures existing in such a flow are the well-known near-wall streaks and hairpin vortices, the latter assembling into vortex packets to form a third type of coherent structures, the large-scale motions (LSMs). The fourth type of structures has been identified as very large-scale motions (VLSMs) consisting of narrow low-momentum regions meandering in the horizontal plane and flanked by regions of high momentum (Hutchins & Marusic, 2007). While smaller structures such as streaks and hairpin vortices scale in wall units, LSMs and VLSMs are found to scale with δ, the depth of the boundary layer. VLSMs and near-wall turbulence have been found to interact through a non-linear mechanism that resembles amplitude modulation. Despite the drastic modification of the near-wall turbulent cycle by the roughness elements in flow over very rough surfaces similar to urban terrain, similar types of coherent structures have been shown to exist in direct numerical simulation (DNS) (Coceal et al., 2007), large-eddy simulation (LES) (Kanda et al., 2004), wind-tunnel experiments (Castro et al., 2006), and field experiments (Inagaki & Kanda, 2010). Building upon these past studies and based on the last decade of experimental research conducted at the LHEEA lab in Nantes, France, the objective of the present contribution is to review some of the aspect of the interaction between the most energetic large scales existing in the boundary layer and those from the roughness sublayer (RSL). Section 2 describes the experimental setup and methodologies. Section 3 is devoted to the presentation of the main results. Discussion and conclusions are presented in Section 4.

2. Methods

2.1. Experimental setup

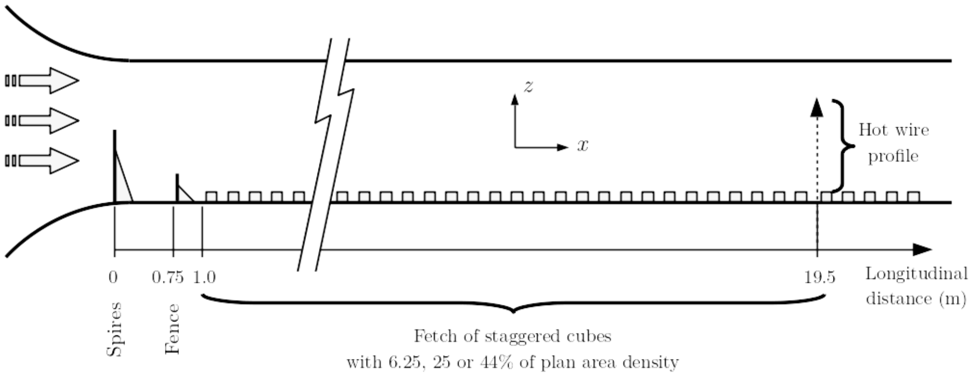

Fig. 1: Wind-tunnel set-up (sketch not to scale).

Experiments were conducted in the boundary-layer wind tunnel of the Laboratoire de recherche en Hydrodynamique, Energétique et Environnement Atmosphérique of Ecole Centrale de Nantes (LHEEA, Nantes, France), which has test-section dimensions of 24 m × 2 m × 2 m (Fig. 1). A reproduction of the lower part of a suburban-type ABL developing over an idealized urban canopy model was achieved by using five vertical, tapered spires of height of 800 mm and width of 134 mm at their base, a 200 mm high solid fence across the working section located 0.75 m downstream of the inlet, followed by a 22 m fetch of staggered cubic roughness elements of various density (6.25%, 25%, 44.4%) or two-dimensional bars. The obstacle height was $h = 50$ mm. Extensive details on this facility and set-up can be found in Blackman et al. (2014, 2018b) and Perret et al. (2019).

Measurements were conducted using hot-wire anemometry (HWA) (Perret et al., 2019) and stereoscopic Particle Image Velocimetry (PIV) (Basley et al., 2018, 2019, Blackman et al., 2014, 2017, 2018b). In some of these studies, the two measurement techniques were combined and synchronized to allow for the time-resolved estimation of the coherent structures detected in the boundary layer.

2.2. Method for large scales – small scales separation

The method for the detection and separation of the large scales from the boundary layer and the smaller scales existing within the RSL is briefly presented here. For more details, the reader is referred to the work of Blackman & Perret (2016) and Perret et al. (2019).

Given the strong geometrical heterogeneity of the urban canopy, in most of the results presented here, PIV was retained as a measurement technique to enable the analysis of the spatial variation and features of both the flow and the existing coherent structures within the RSL. However, standard PIV systems suffer from a low temporal acquisition frequency (on the order of 10Hz), too low to correctly sample the time evolution of the flow. From a spatial point of view, given the typical depth of the

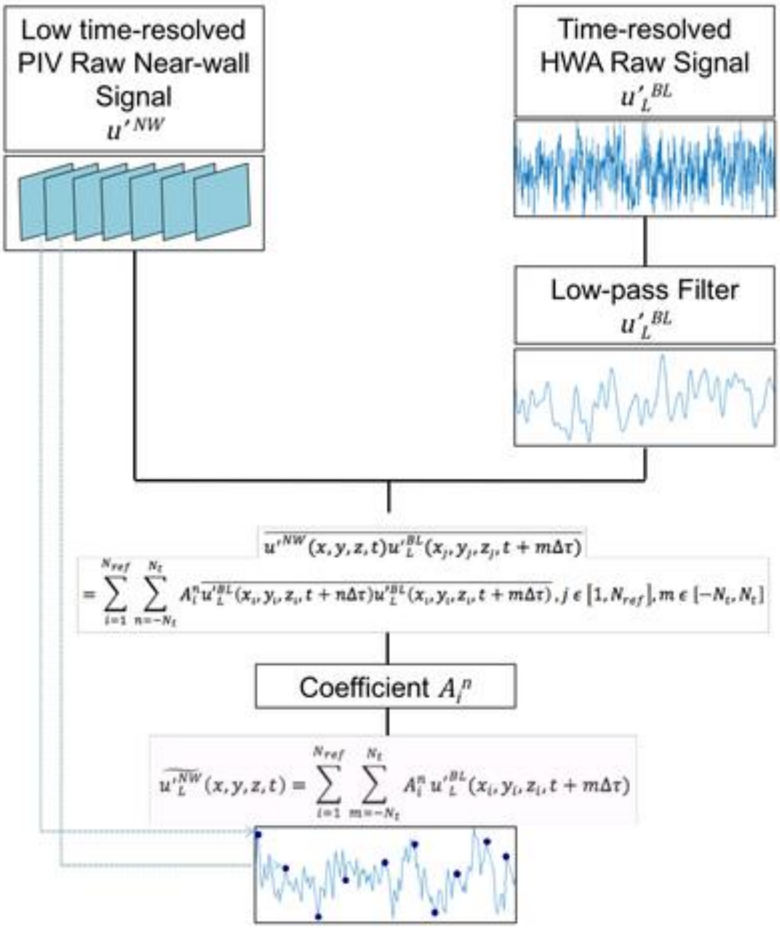

Fig. 2: Schematic of process used for large-scale eduction (Blackman & Perret, 2016).

boundary layers generated in the LHEEA's wind tunnel (on the order of 1m), the PIV field of view is generally too small to capture the spatial extent of the largest scales existing in the boundary layer.

A method using synchronized HWA (to measure the large-scales) and PIV (to capture the flow characteristics within the RSL) has been designed, based on the use of the Linear Stochastic Estimation (LSE). This method enables the estimation of the part of the velocity field that is the most correlated with a given reference signal. In the present case, the reference signal is u'^{BL} the low-pass filtered streamwise velocity component measured using HWA in the logarithmic region of the boundary layer characterizing the large-scales. The large-scale contribution $\tilde{u'}_L$ to the velocity field measured via PIV is estimated using LSE as described in figure 2, and is written as a linear combination of the large-scale signal measured at different time intervals. The coefficients A_i^mdirectly depend on the temporal correlation between the velocity measured by PIV and the time-resolved HWA signals, a statistics that can be measured as the two measurement systems are synchronized. A spectral version of this approach has been proposed by Perret et al. (2019), based on the use of the cross-spectra between two HWA located in the RSL and in the log-region, respectively. Note that an

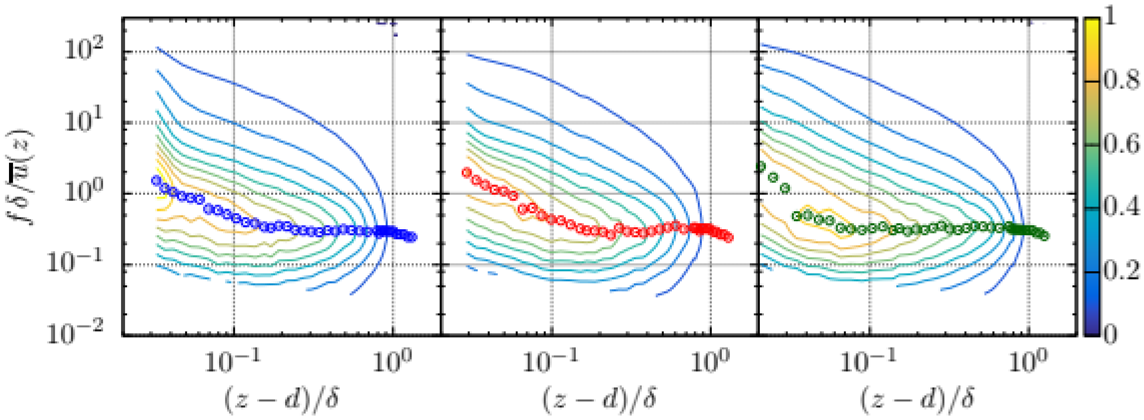

Fig. 3: Pre-multiplied spectra of the streamwise veocity component as a function of the distance from the wall z and the normalized frequency by $\langle u(z)\rangle$ and δ. Symbols show the energy maxima (Perret et al, 2019).

alternative approach based on the use of the Proper Orthogonal Decomposition (POD) with a modified kernel has been proposed and validated by Perret & Kerhervé (2019) for the large-scale extraction from PIV data only.

3. Results

3.1. Evidence of the presence of very large-scale structures

VLSMs in the smooth-wall turbulent boundary layer have been identified as turbulent structures similar to high- and low-speed streaks of very large streamwise extent (several times δ) and that scale with δ and the local mean streamwise velocity $\langle u(z)\rangle$. Their contribution to the variance and the Reynolds shear-stress in the near-wall region remains small.

Studying the most energetic structures of the streamwise velocity component in the boundary layer developing over cube arrays of different packing density, Perret et al. (2019) evidenced the presence of VLSMs. In the outer region of the boundary layer, these structures have a streamwise extent of 3.3δ, independent of the distance from the wall and of the packing density (Fig. 3). Their two-point analysis of the spectral coherence between a fixed point within the log-region and a moving point within the RSL showed the large vertical extension of these structures. The part of the velocity signal correlated between the two points indeed corresponded to the VLSMs wavelengths.

The characteristics of the VLSMs have been further investigated in the horizontal plane by Basley et al. (2019), confirming the associated wavelengths and their meandering behavior. VLSMs were also detected within the RSL, through the presence of a secondary energy peak in the spectra at low wavenumbers.

Blackman et al. (2018b) evidenced the presence of VLSMs in boundary layers developing of two-dimensional obstacles (i.e a series of street canyons) with different spacing. They showed the same characteristics as those detected in flow over cube canopies (Fig. 4). It is worth noting here that the same type of coherent structures have also been educed from boundary layers developing over vegetation canopies (Perret & Ruiz, 2013), confirming that are a key ingredient common to all turbulent boundary layer types.

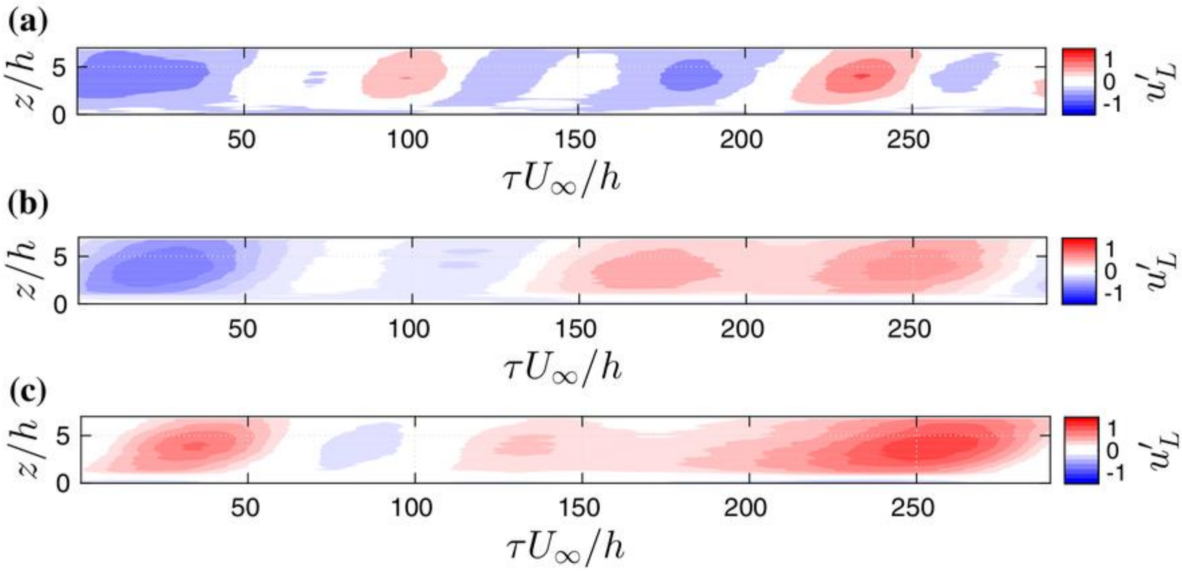

Fig. 4: temporal evolution of the VLSMs associated with the streamwise velocity component in flows over (a) a 25% cube array, (b) and (c) two-dimensional obstacles with spacing of $W/h = 1$ and$W/h = 3$, respectively (Blackman et al, 2018).

3.2. Boundary layer – canopy flow scale interaction.

Studies of smooth boundary layers have shown that the VLSMs contribution becomes prominent in the outer region of the flow with increasing Reynolds number. In addition to the superimposition mechanisms described above, the interaction between the VLSMs and the near-wall turbulence has been shown to resemble an amplitude modulation (AM) mechanism, through which the smaller-scales near the wall are amplified or attenuated by the very-large scale high- or low-speed streaks, respectively (Hutchins & Marusic, 2007; Mathis et al., 2009). The identification of such a mechanism is based on the decomposition of the velocity field into a large- and a small-scale contributions, as $u = u_L + u_S$. In the present case, this decomposition has been performed using the method described in section 2.2. This decomposition is then used to compute the statistics $\langle u_L u_S^2 \rangle$ (one of the four components of the scale-decomposed skewness), which serves as a diagnostic tool to identify non-linear scale interactions such as amplitude modulation (Mathis et al., 2011). This statistics, being similar to the correlation coefficient between the large scales and the envelope of the small scale, takes positive values when large-scale high- (low-) speed streaks are correlated with high (low) level of near-wall turbulence. Conversely, negative values correspond to attenuated small scales in the presence of high-speed VLSMs. An example of the one-point version of $\langle u_L u_S^2 \rangle$ estimated in the RSL of turbulent boundary layers developing of staggered arrays of cubes is shown in figure 5. It shows that, in addition to the above-mentioned superimposition effect, most of the RSL turbulence is under the influence of the VLSMs (which do not correspond to the most energetic structures in this region of the flow) through an AM-like mechanism, independent of the canopy-flow regime (Blackman et al., 2019). Similar results were found in flows over two-dimensional obstacle arrays (Blackman et al., 2018b).

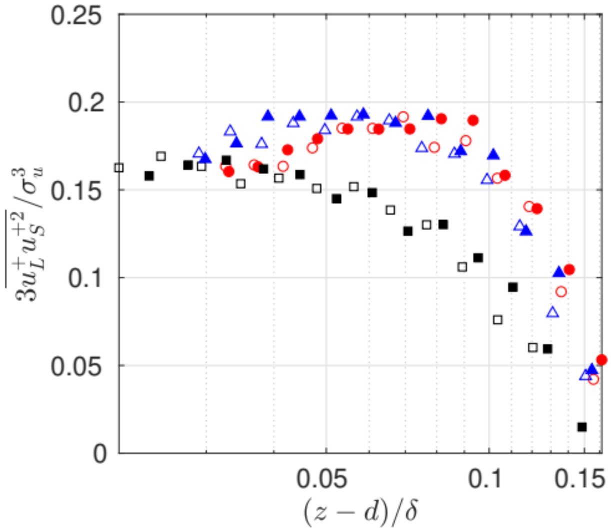

Fig. 5: Influence of the packing density λ_p of cube canopies on the amplitude modulation mechanism. Red symbols: $\lambda_p = 6.25\%$, blue symbols:$\lambda_p = 25\%$, black symbols: $\lambda_p = 44.4\%$ (filled symbols:$\delta^+ = 45000$, open symbols: $\delta^+ = 30000$) (Blackman et al., 2019).

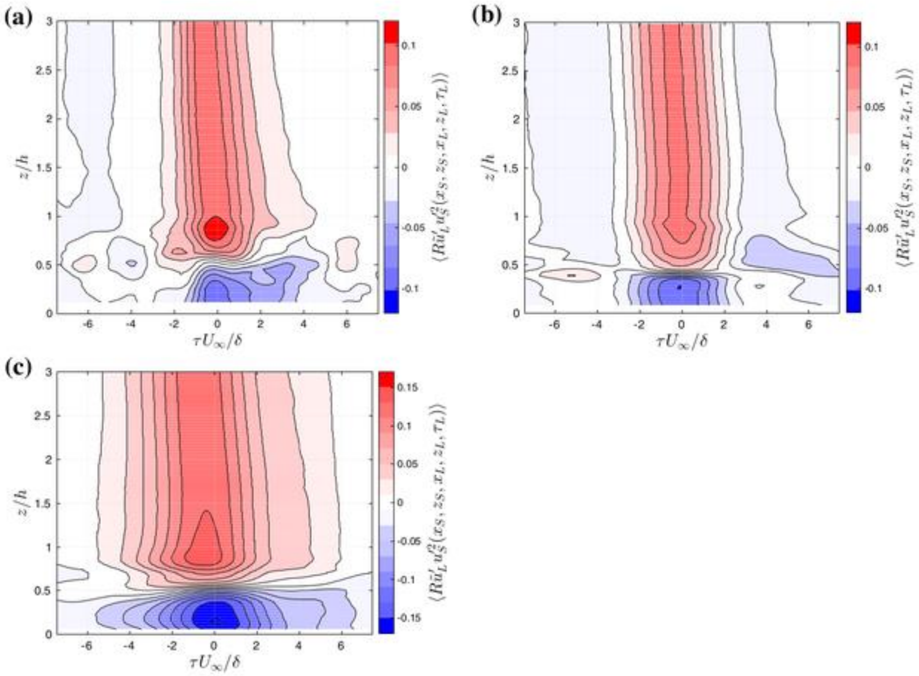

Fig. 6: Spatio-temporal two-point correlation $R_{u_L u_S^2}(z_L, z_S, \tau_L)$: fixed point $z_S = 0.75$: small scales, moving point z_L: large-scales ($x_S = x_L$) for (a) 25% cube canopies, (b) and (c) two-dimensional obstacles with spacing of $W/h = 1$ and $W/h = 3$, respectively (Blackman et al., 2018).

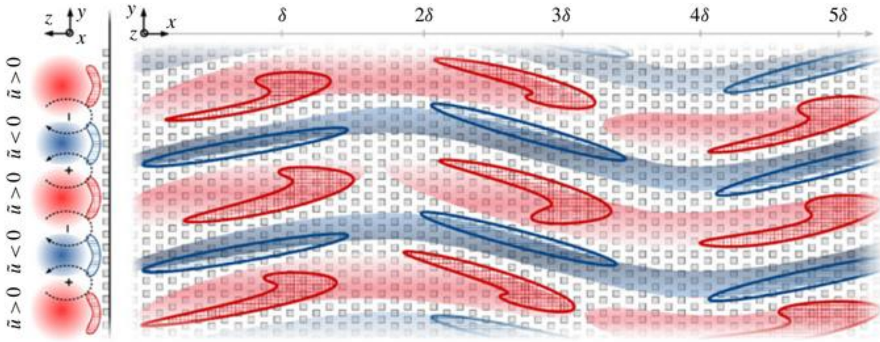

Fig. 7: spatial organization of the coherent structures of in a horizontal plane within the RSL. Red and blue shaded areas correspond to large-scale high- and low-speed regions, red and blue hatched areas correspond to locations of amplification or attenuation, respectively, of the small scales by the large through the AM-like mechanism (Basley et al., 2018).

To further investigate the spatial structure of the interaction and allow for the study of the interaction between the VLSMs and the inner-canopy flow, the two-point version (both in time and space) of the statistics $\langle u_L u_S^2 \rangle$ has also been used. Results from figure 6 show that the RSL and the top half of the canopy, the flow is under the positive influence of the VLSMs (i.e high-streaks correspond to amplified small-scale turbulence), in the bottom part of the canopy, u_L and u_S are out of phase (i.e negative values of $\langle u_L u_S^2 \rangle$) (Blackman et al., 2018b). Overall, the influence of the large scales onto the smaller scales is independent of the nature of the canopy, the differences being attributed to the change of flow regime and the subsequent small-scale turbulence modification rather than a change in the interaction mechanism (Blackman et al., 2018b).

The spatial structures of the large-small scale interaction has been further investigated in the horizontal plane within the RSL by Basley et al. (2018). By taking into account the sign of both the streamwise and spanwise large-scale velocity components u_L and v_L, respectively, they computed conditional two-point AM coefficients. By doing so, they broke the symmetry imposed by the spanwise statistical homogeneity of the flow and accounted for the meandering behavior of the VLSMs. They evidenced the preferred spatial organization of the AM mechanism (Fig. 7): the VLSMs influence is non-symmetric, the maximum influence being on their flank, and on their upstream portion, in agreement with the literature finding that small scales are phase-leading.

These findings are summarized in figures 8. Strong similarities with the interaction mechanisms identified in smooth-wall flows are found, in particular regarding the nature and the organization of coherent structures in the logarithmic and outer regions of the boundary layer and the existence of a superimposition – amplitude modulation mechanism of the near-wall canopy flow by the VLSMs. The only differences (from a qualitative point of view) seem to be due to the obvious change of the structure of turbulence within the RSL due to the presence of the canopy obstacles and the change of in flow regimes induced by the canopy morphology. Despite the apparent strong decoupling of the lower portion of the canopy flow from the outer flow induced by the canopy itself (not discussed here), the upper half of the canopy and the portion of the RSL above, are influenced by the mechanisms discussed above. It therefore suggests an influence of the larger scales of the boundary layer onto the instantaneous exchange processes between the canopy and the flow above.

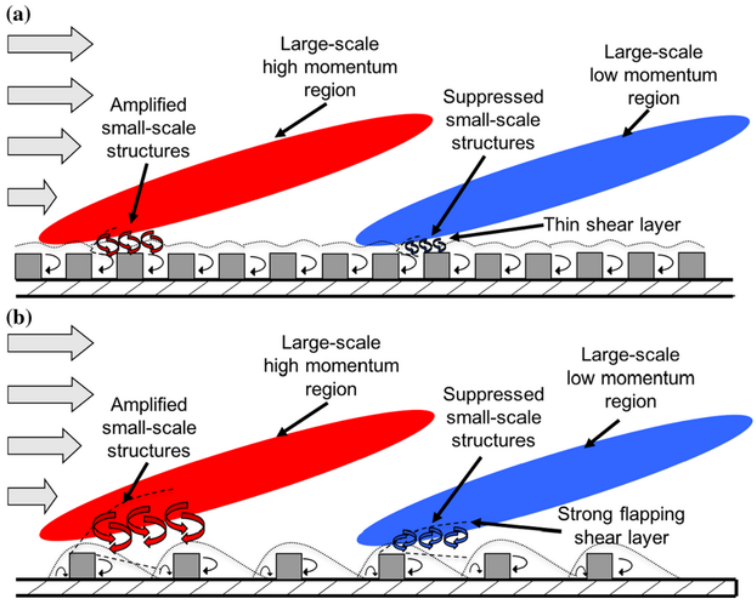

Fig. 8: Influence and interaction of the VLSMs with the canopy flow for (top) skimming flow and (bottom) wake-interference flow regimes (Blackman et al., 2018b).

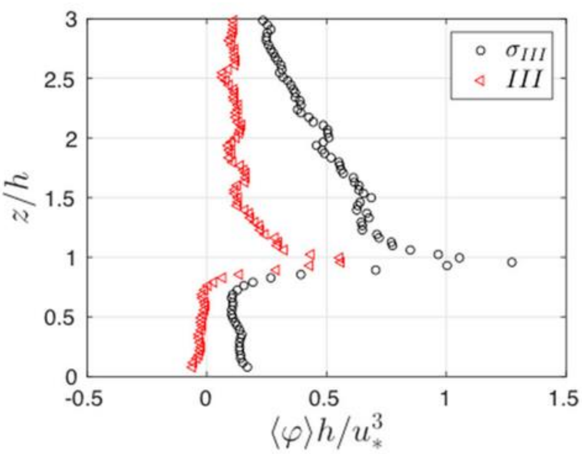

Fig. 9: Mean (red) and standard deviation (black) of the inter-scale energy transfer term between the VLSMs and the canopy turbulence in the boundary layer developing over a 25% staggered cube array (positive values indicate energy transfer from the VLSMs to the smaller scales) (Blackman et al., 2018a)

3.3. Amplitude modulation and inter-scale energy transfer

Besides leaving their imprint on the smaller-scales and modulating their amplitude, the large most energetic coherent structures from the boundary layer do interact with the RSL turbulence via an energy transfer mechanism. This point has recently been investigated by Blackman et al. (2018a) by estimating the inter-scale turbulent kinetic energy transfer between the VLSMs and the RSL flow in the boundary layer developing over a 25% staggered cube array. As expected, the average energy transfer is from the VLSMs toward the smaller scales (i.e classical forward scatter of energy). Interestingly, instantaneous energy transfer were found of larger magnitude and were found from VLSMs to small scales but also the other way around (i.e backscatter of energy), implying a more complex interaction mechanism than what can be observed in average. This energy transfer has been found to be well correlated with the amplitude modulation mechanism firstly observed, confirming the non-linear nature of the latter. Similar findings have been obtained in atmospheric boundary layers developing over vegetation canopies for various atmospheric stability regimes by Perret & Patton (2021). The extension of this analysis to various of urban-like canopies is the subject of ongoing research.

4. Conclusion

Recent results obtained at LHEEA, Nantes, and based on wind tunnel investigation on the interaction between the most energetic large scales existing in the outer region of boundary layers developing over urban-like canopies and those existing in the RSL have been presented. Focusing first on the identification of these coherent structures, it has been shown that despite the strong disruption of the near-wall flow by the presence of the obstacles, the spatio-temporal organization of the turbulent boundary layers over very rough wall share many features with those developing over smooth walls. In particular, it has been shown that the interaction between the inner and the outer region of the flow is driven by the same type of mechanism, namely the combination of the superimposition of the large scales onto the RSL turbulence with a non-linear interaction that resembles an amplitude modulation mechanism, influencing all three velocity components. This feature has been found in all the investigated flow configurations with different types of canopy morphology: cube arrays of different packing densities, arrays of two-dimensional obstacles with different streamwise spacing and vegetation-like canopies. This amplitude modulation mechanism, being non-linear, leaves its imprint into the third-order moment of the velocity components (i.e their skewness) and is directly linked to inter-scale energy transfer.

The modulation of small-scale turbulence by larger scales discussed in this paper clearly demonstrates the importance of large-scale turbulence on higher-order velocity statistics and the instantaneous dynamics of smaller-scale turbulence in the RSL. It therefore reinforces the need for the proper physical modeling of all the relevant scales within the wind tunnel if one wants to perform accurate wind-tunnel simulations of flows relevant to atmospheric processes. Furthermore, the VLSMs being an order of magnitude larger than the RSL scales, the amplification/attenuation of the latter by the former can lead to long-standing spatial heterogeneity in the RSL flow characteristics. Even if this will average out in the case of horizontally homogeneous terrains, presence of surface heterogeneity caused for instance by topography, preferential roughness obstacle distribution, presence of tall isolated building will induce a locking effect of the location of those VLSMs and therefore of their influence.

Acknowledgments
The author warmly thank the colleagues and students who contributed to the presented work.

References

Basley J, Perret L, Mathis R (2018) Spatial modulations of kinetic energy in the roughness sublayer. J Fluid Mech 850:584–610

Basley J, Perret L, Mathis R (2019) Structure of high Reynolds number boundary layers over cube canopies. J Fluid Mech 870:460-491.

Blackman K, Perret L (2016) Non-linear interactions in a boundary layer developing over an array of cubes using stochastic estimation. Phys Fluids 28(095):108

Blackman K, Perret L, Calmet I, Rivet C (2017) Turbulent kinetic energy budget in the boundary layer developing over an urban-like rough wall using PIV. Phys Fluids 29(085):113

Blackman K, Perret L, Calmet I (2018a) Energy transfer and non-linear interactions in an urban boundary layer using Stochastic Estimation. J Turb 19.10:849-867

Blackman K, Perret L, Mathis R (2019) Assessment of inner-outer interactions in the urban boundary layer using a predictive model. J Fluid Mech 875:44-70

Blackman K, Perret L, Savory, E (2014) Effect of upstream flow regime on street canyon flow mean turbulence statistics. Env Fluid Mech 106:139-153

Blackman K, Perret L, Savory E (2018b) Effect of upstream flow regime and canyon aspect ratio on non-linear interactions between a street canyon flow and the overlying boundary layer. Boundary-Layer Meteorol.

Castro IP, Cheng H, Reynolds R (2006) Turbulence over urban-type roughness: deductions from wind-tunnel measurements. Boundary-Layer Meteorol 118:109–131

Coceal O, Dobre A, Thomas TG, Belcher SE (2007) Structure of turbulent flow over regular arrays of cubical roughness. J Fluid Mech 589:375–409

Hutchins N, Marusic I (2007) Evidence of very long meandering features in the logarithmic region of turbulent boundary layers. J Fluid Mech 579:1–28

Inagaki A, Kanda M (2010) Organized structure of active turbulence over an array of cubes within the logarithmic layer of atmospheric flow. Boundary-Layer Meteorol 135:209–228

Kanda M, Moriwaki R, Kasamatsu F (2004) Large eddy simulation of turbulent organized structure within and above explicitly resolved cubic arrays. Boundary-Layer Meteorol 112:343–368

Marusic I, McKeon BJ, Monkewitz PA, Nagib HM, Smits AJ, Sreenivasan K (2010) Wall-bounded turbulent flows at high Reynolds numbers: recent advances and key issues. Phys Fluids 22(6):065,103

Mathis R, Hutchins N, Marusic I (2009) Large-scale amplitude modulation of the small-scale structures in turbulent boundary layers. J Fluid Mech 628:311–337

Mathis R, Hutchins N, Marusic I, Sreenivasan K (2011) The relationship between the velocity skewness and the amplitude modulation of the small scale by the large scale in turbulent boundary layers. Phys. Fluids 23, 121702.

Perret L, Basley J, Mathis R, Piquet T (2019). The Atmospheric Boundary Layer Over Urban-Like Terrain: Influence of the Plan Density on Roughness Sublayer Dynamics. Boundary-Layer Meteorol 170:205-234

Perret L, Kerhervé F (2019) Identification of very large scale structures in the boundary layer over large roughness elements. Exp Fluids 60:97-113

Perret L, Ruiz T (2013) SPIV analysis of coherent structures in a vegetation canopy model flow. In Coherent Structures in Flows at the Earth's Surface. John Wiley and Sons, Ltd.

Perret L, Patton E (2021) Stability influences on inter-scale transport of turbulent kinetic energy and Reynolds shear stress in atmospheric boundary layers interacting with a tall vegetation canopy J Fluid Mech 921:1-49

Takimoto H, Inagaki A, Kanda M, Sato A, Michioka T (2013) Length-scale similarity of turbulent organized structures over surfaces with different roughness types. Boundary-Layer Meteorol 147(2):217–236

PHYSMOD 2022

PHYSMOD 2022 – International Workshop on Physical Modeling of Flow and Dispersion Phenomena
Institute of Thermomechanics of the CAS, Prague, Czech Republic – August 29-31, 2022

The control of buoyant smoke in transversally ventilated tunnels with the presence of a longitudinal flow

P. Salizzoni[1], C. Peruzzi[1], M. Marro[1], P. Cingi[1,2,3], D. Angeli[2,3], T. Kubwimana[4], A. Mos[4]

[1]Université de Lyon, Ecole Centrale de Lyon, CNRS, Université Claude Bernard Lyon 1, INSA Lyon, Laboratoire de Mécanique des Fluides et d'Acoustique (LMFA), UMR5509, 36 Avenue Guy de Collonge, 69130 Ecully, France.
[2]Università degli Studi di Modena e Reggio Emilia, Dipartimento di Scienze e Metodi dell'Ingegneria (DISMI), Via Amendola 2, 42122 Reggio Emilia, Italy.
[3]Mimesis s.r.l., Via Contrada 309, 41125 Modena, Italy.
[4]Centre d'Études des Tunnels (CETU), Avenue Francois Mitterrand 25, 69500 Bron, France.

Abstract

Ventilation systems are fundamental in preventing disastrous consequences after road tunnel accidents. To improve our understanding, we have experimentally studied the ventilation conditions required to control the propagation of smoke produced by a tunnel fire in presence of a transversal extraction system and a longitudinal flow. Within a reduced scale tunnel, we have simulated the release of hot smoke during a fire by using a mixture of air and helium, while the buoyant flow dynamic has been analysed with flow visualisation techniques. We have focused our attention on studying the conditions that guarantee the confinement of the buoyant flow between two adjacent extraction vents. Experiments have involved various source conditions, different shapes and positions of the extraction vents as well as the use of barriers. In this way, it has been possible to quantify the increase of the extraction velocity needed to confine the buoyant flow by overcoming the effect of an imposed longitudinal current. Vents with a rectangular shape, and spanning over the whole tunnel width, provide the best performance while the squared off-centred ones have the worst performance. Finally, we studied the stratification conditions of the flow, individuating four different regimes due to the flow asymmetry.

Introduction

Road tunnels are environments where the control of smoke and fire emitted during accidents is potentially difficult to control. A recent study that has analysed more than 150 tunnel fire accidents (Bai et al., 2020) reposts that, on average, tunnel accidents are three times more lethal than accidents occurring on open roads. To prevent the occurrence of these dramatic events, forced tunnel ventilation systems are a pivotal strategy, permitting to safely evacuate the tunnel and reducing damage as much as possible.

Depending on the traffic mode (one- or bi-directional) and traffic flow (congested and uncongested), different ventilation strategies can be adopted. With bi-directional road and/or congested traffic, transverse ventilation systems are the most appropriate. With this apparatus, the toxic smoke is extracted by vents displaced at the tunnel ceiling and the smoke should be confined within the extraction zone that is delimitated by two adjacent vents (Li & Chow, 2003). Along with the confinement of the hot smoke, transverse ventilation systems should keep the flow in stratified conditions, namely with the hot smoke lying on the tunnel ceiling. In real operational situations, the achievement of smoke confinement in stratified conditions is demanding, especially because of the flow asymmetry due to not perfect airflow regulation or the presence of natural ventilation currents, driven by the wind-induced pressure difference between the two tunnel portals induced by meteorological effects (Kubwimana et al., 2018).

In order to study transverse ventilation systems operating in asymmetry conditions (i.e. subject to a longitudinal flow), we performed an experimental campaign where the flow in the tunnel is induced by a buoyant release simulating a fire (Vauquelin, 2008) and by mechanical forcings due to the extraction vents at the tunnel ceiling and the longitudinal flow imposed by a longitudinal pressure gradient.

Experimental set-up

The experimental campaign was conducted in a 1/25 reduced tunnel facility (Figure 1a) installed at the Fluid Mechanics and Acoustics Laboratory (LMFA) of the Ecole Centrale de Lyon. The reduced tunnel is 8.4 m long with a rectangular cross-section (0.36 m broad and 0.18 m high). The flow within the tunnel was studied using flow visualisation, i.e. oil drops were injected into the buoyant flow (a mixture of air and helium) and, if excited with a green laser sheet, allowed for the direct visualisation of the buoyant release. The inlet flow rate (and in turn the mean longitudinal velocity U_t) was measured by using a Pitot tube placed at the tunnel entrance.

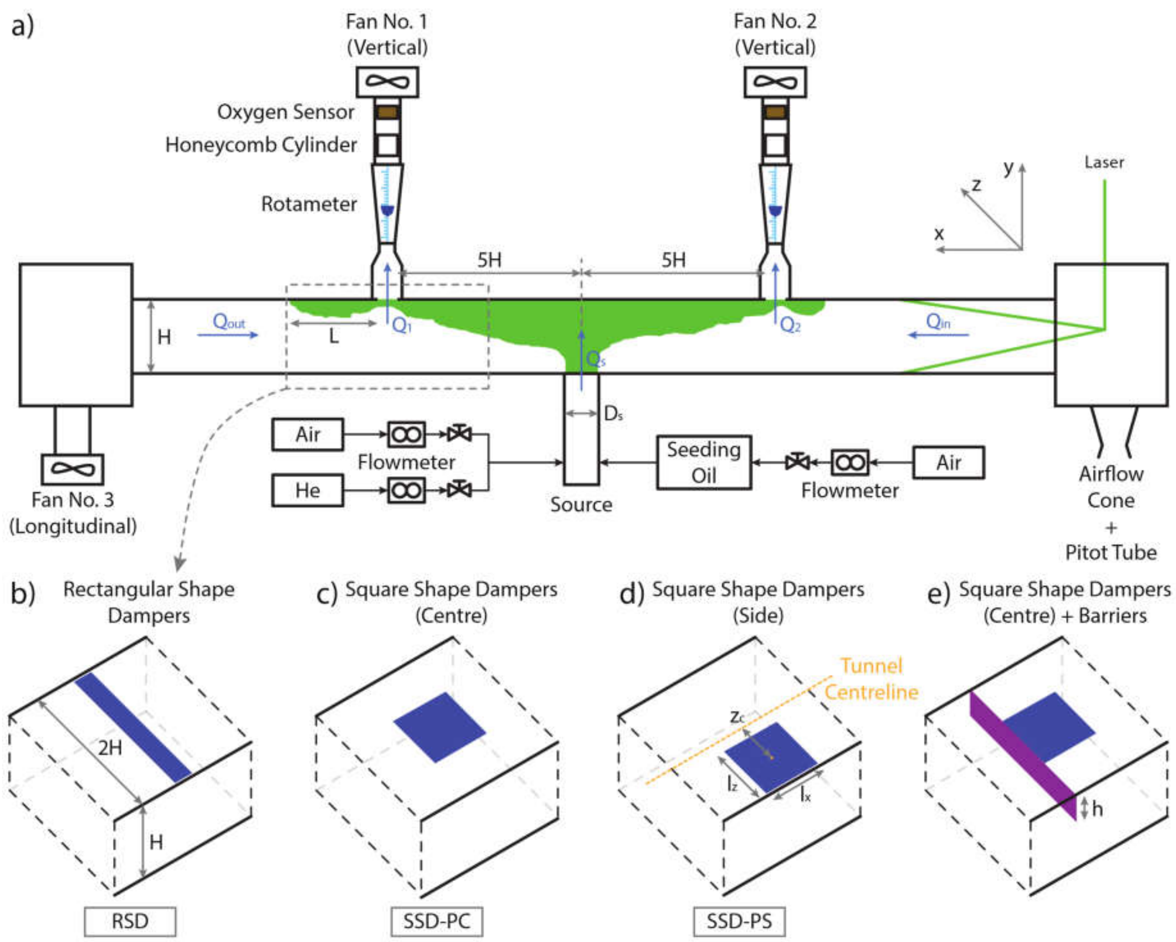

*Figure 1: **a)** Overview of the tunnel facility used for the experiments thogheder with the instrumentation. Panels **b)** to **d)** report the shape and disposition of the different dampers displaced in the tunnel ceiling: **b)** rectangular shape damper (RSD); **c)** square shape damper positioned in the centre of the tunnel (SSD-PC); **d)** square shape damper positioned in the side of the tunnel (SSD-PS). Finally, panel **e)** shows the disposition of barriers ($h = H/3$) in the representative case of SSD-PC.*

Run	Γ_s	ρ_s/ρ_0	Fr_t	$Fr_{e,c}$	Vents	Barriers
Test 1	1.6	0.74	0.35 - 2.39	2.09 - 9.92	RSD	×
Test 2	3.0	0.74	0.46 - 2.78	2.31 - 10.26	RSD	×
Test 3	1.9	0.72	0.60 - 2.10	3.60 - 8.91	RSD	×
Test 4	3.7	0.72	0.25 - 2.49	1.95 - 9.64	RSD	×
Test 5	7.4	0.72	0.31 - 3.16	2.01 - 11.77	RSD	×
Test 6	3.7	0.45	0.35 - 1.36	2.35 - 6.09	RSD	×
Test 7	14.8	0.72	0.27 - 3.32	2.13 - 12.18	RSD	×
Test 8	3.7	0.26	0.32 - 1.57	2.31 - 6.55	RSD	×
Test 9	3.7	0.72	0.32 - 2.52	2.60 - 10.73	RSD	✓
Test 10	3.7	0.72	1.33 - 2.57	7.12 - 11.32	SSD-PC	×
Test 11	3.7	0.72	0.49 - 2.93	3.31 - 10.88	SSD-PC	✓
Test 12	3.7	0.72	2.27	11.28	SSD-PS	×
Test 13	3.7	0.72	1.26 - 2.73	6.76 - 11.20	SSD-PS	✓

Table 1: Summary of experiments and associated fluid dynamics conditions.

Three different vent (or damper) shapes were employed during the experiments, all having the same opening area $A_d = 0.011$ m^2 (Figure 1b-d). We used the same dampers adopted by Chaabat et al. (2020), notably:

- A damper with a transverse rectangular shape (0.32 x 0.034 m) which occupies almost the entire width of the tunnel, hereinafter called RSD (Figure 1b);
- A damper with a square shape (0.104 x 0.104 m) centred with respect to the tunnel centreline, hereinafter called SSD-PC (Figure 1c);
- A damper with a square shape (0.104 x 0.104 m) positioned on a side with respect to the tunnel centreline, hereinafter called SSD-PS (Figure 1d).

Note that side positioned squared shape dampers (SSD-PS) are the most common configuration in actual tunnels (e.g. the Trans-Alpine Fréjus Road Tunnel connecting France and Italy), since a fresh air duct is often present next to the smoke extraction duct. Additionally, we tested the effect of vertical barriers in order to enhance the vents' capture efficiency (Figure 1e). Two planar barriers were hung at the tunnel ceiling close to the vents' extremity. The height and width of the barriers were $h = H/3$ and $2H$ (i.e. equal to the tunnel width), respectively, and were sufficiently rigid to withstand the aerodynamic forces induced by the flow.

Table 1 reports the carried out experiments together with the values of the controlling parameters. In particular, $\Gamma_s = 5B_s/4\pi\alpha D_s W_s^3$ is the plume Richardson number (where B_s is the buoyancy flux at the source, α is the top-hat entrainment coefficient, D_s is the souce diameter and W_s is the flow velocity at the source), ρ_s/ρ_0 is the ratio between the souce density and the air density, $Fr_t = U_t/(B_s/H)^{1/3}$ is the tunnel Froude number (H is the tunnel high) and $Fr_{e,c} = U_{e,c}/(B_s/H)^{1/3}$ is the extraction Froude number (where $U_{e,c}$ is the mean extraction velocity). As reported in Salizzoni et al. (2018), Γ_s is generally used to distinguish between forced plumes ($\Gamma_s < 1$) lazy plumes ($\Gamma_s > 1$), pure plumes ($\Gamma_s = 1$) and jets ($\Gamma_s = 0$), depending on the relative importance between the momentum and buoyancy flux (Morton, 1959; Hunt & Kaye, 2005).

Each test started by turning on all three fans at the minimum regime (Figure 1a). Once the longitudinal velocity at the tunnel inlet became stable, the flowmeters controlling the buoyant release were also turned on. At this stage, the extraction velocity was weak, so the released buoyant fluid could spread within the whole tunnel. The extraction velocity of the vertical fans was then progressively increased, always checking that the flow extracted by both fans was the same. When the confinement condition was attained, i.e. with the buoyant release bounded between the two vents, we registered the value of the extraction velocities at the two vents, as well as the value of U_t. The extraction velocity in confinement conditions $U_{e,c}$ was then computed as the average between the values registered at fan no. 1 and fan no. 2 (Figure 1a). To further explore the relationship between U_t and $U_{e,c}$, the longitudinal velocity was slightly increased and the above procedure was repeated. A test was stopped when the flow rate at the extraction vents exceeded the rotameter measurement range.

Main Results

First of all, based on the visualisations of the distribution of the buoyant flow, we could identify four different flow stratification conditions or regimes (Figure 2):

- Regime I (Figure 2a): the flow is stratified, with the light gas lying close to the tunnel ceiling, since the buoyancy effects prevail over turbulent mixing;
- Regime II (Figure 2b): the buoyant fluid is unstratified on the upwind side, due to the growing role of Kelvin-Helmholtz instabilities, and stratified on the downwind side;
- Regime III (Figure 2c): the turbulent fluctuations overcome the density gradients, so that the light gas mixes with the ambient air, on both sides of the source;
- Regime IV (Figure 2d): the buoyant fluid is present only downwind of the source due to the
- overwhelming effect of the longitudinal velocity.

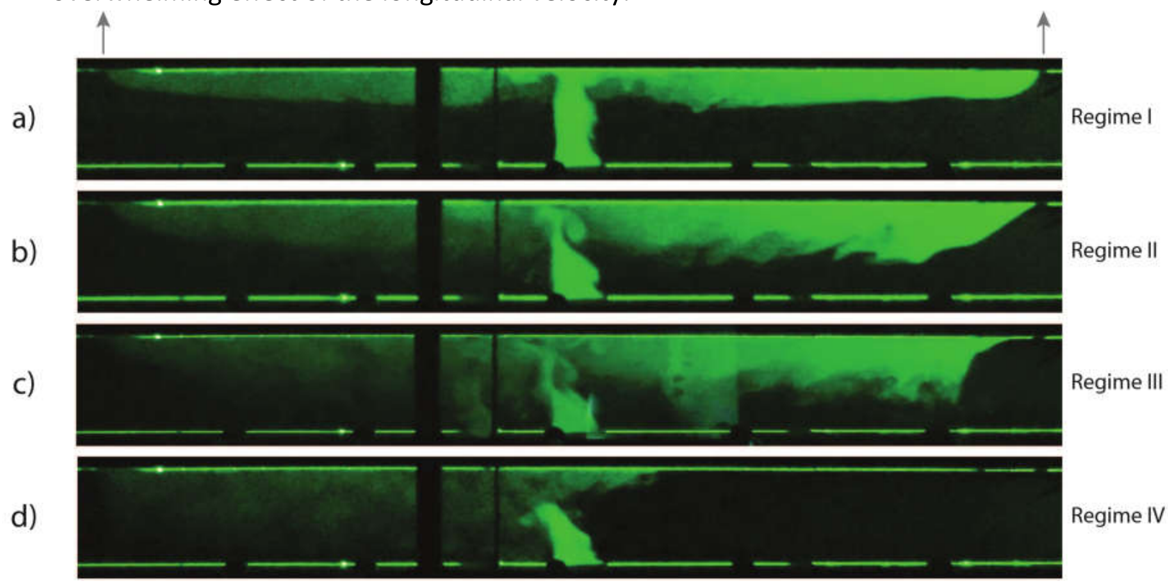

Figure 2: Example of stratification conditions of the buoyant release in the tunnel with RSD: a) Regime I – stratified flow; b) Regime II – intermediate condition; c) Regime III – unstratified flow; d) Regime IV – strong longitudinal velocity. The grey arrows indicate the position and direction of extraction of the vents.

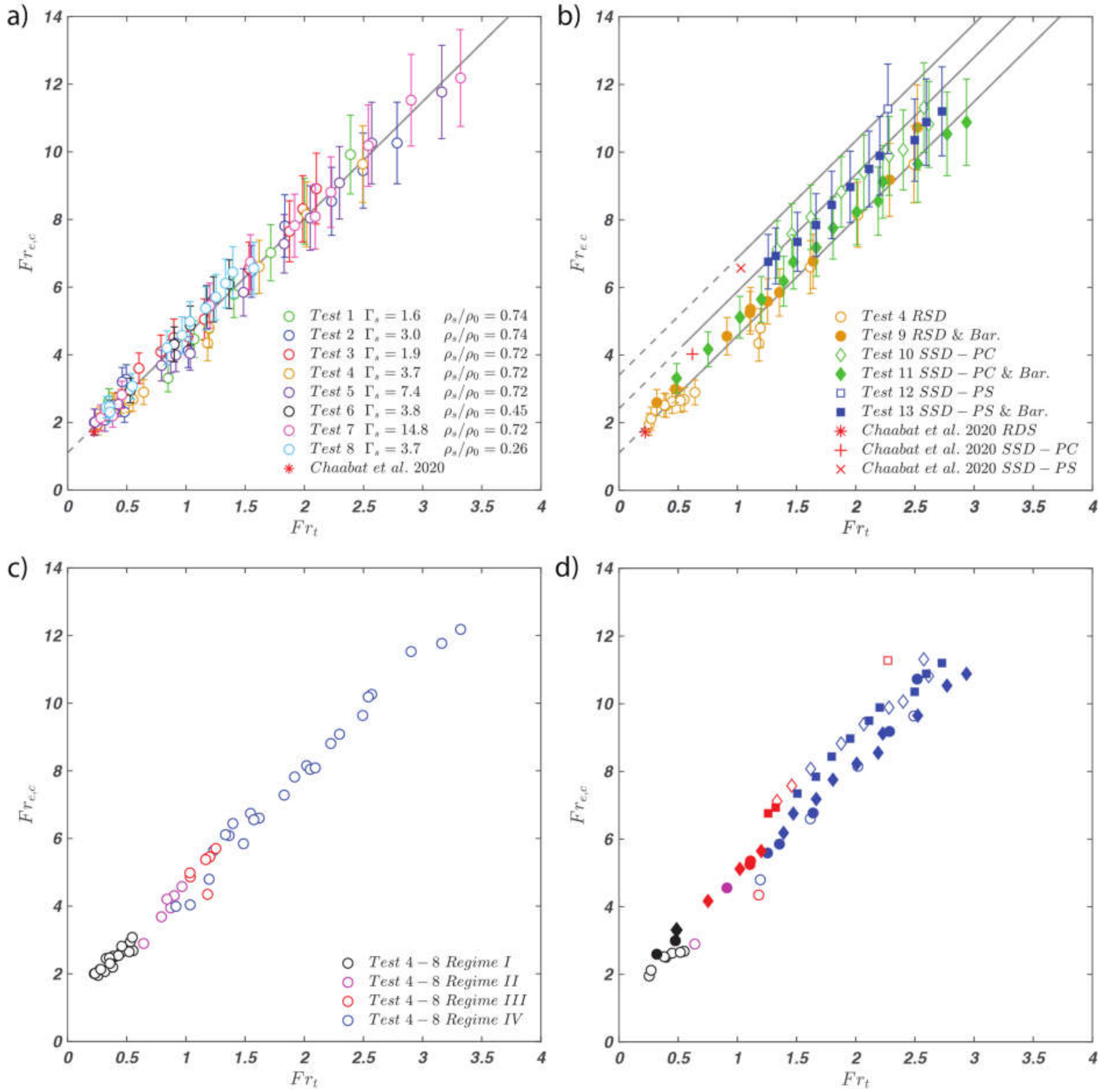

*Figure 3: Relationship between the tunnel Floude number Fr_t and the extraction Froude number $Fr_{e,c}$ using **a)** RSD and different source conditions ($\Gamma_s = 1.6 - 14.8$ and $\rho_s/\rho_0 = 0.26 - 0.74$); **b)** different vent arrangements (hollow markers) and barriers (filled markers). In panels **c)** and **d)** the flow regimes are reported as follows: black markers indicate Regime I, purple markers indicate Regime II, red markers indicate Regime III while blue markers indicate Regime IV.*

Regime IV (Figure 2d): the buoyant fluid is present only downwind of the source due to the overwhelming effect of the longitudinal velocity. The functional dependence between Fr_t and $Fr_{e,c}$ is unveiled in Figure 3a for RSD and Figure 3b for also SSD-PC and SSD-PS as well as the usage of barriers. Considering the same damper shape, the data follow a curve of the form $Fr_{e,c} = aFr_t + b$, where the coefficient a seems to be unsensitive of the damper shape and position while the coefficient b depend on the damper configuration. Interestingly (Figure 3a), the flow dynamic is insensitive to the source conditions (Γ_s and ρ_s/ρ_0), as already figured out in longitudinal and pure transverse tunnel ventilation systems (Jiang et al., 2019; Chaabat et al., 2020). Looking at Figure 3b, we can state that the shape and position of the dampers have a significant impact on the conditions required to confine the buoyant smoke. As already exposed by Chaabat et al. (2020), the rectangular shape damper (RSD) leads to the best performance, while the off-centred square damper (SSD-PS) can confine the buoyant plume only with very high velocities. A possible way to improve the effectiveness of on existing ventilation system is the deployment of solid barriers at the tunnel ceiling (Seike et al., 2014) and in Figure 3b it can be seen that when barriers are used in combination with square-shaped dampers, they are effective in reducing the extraction velocity required to impose confinement conditions, compared to the case of an empty tunnel. Instead, with rectangular-shaped dampers, the beneficial action of the barriers is limited or negligible, since their opening already spans the whole tunnel width.

Finally, we focus on the flow regimes within the tunnel and their occurrence as a function of the two control parameters Fr_t and $Fr_{e,c}$, which we present in Figure 3c a for the rectangular-shaped dampers (RSD) and Figure 3d for the square-shaped dampers (SSD-PC and SSD-PS) as well as with the deployment of barriers. Interestingly, we observe an almost perfect succession of the four regimes, as identified in Figure 2, as both the longitudinal and extraction velocities increase. The implementation of dampers with a different shape highly affects the buoyant flow regime (Figure 3d). Indeed, placing both the SSD-PC and the SSD-PS prevents the occurrence of a stratified flow (Regimes I and II), so that only Regimes III and IV can occur. The situation can be somehow improved using the barriers.

Conclusions

The conditions required to confine a buoyant release within a tunnel were studied by means of flow visualisation technique in a reduced tunnel facility equipped with a transverse ventilation system subject to a longitudinal airflow. First, we have noted that the confined buoyant flow can exhibit four distinct regimes, i.e. stratified (Regime I), intermediate condition (Regime II), unstratified (Regime III), or an extreme condition where the plume is deviated by the strong longitudinal velocity towards the downstream vent (Regime IV). Second, we have pointed out the functional dependence that exists between the controlling parameters Fr_t and $Fr_{e,c}$. Finally, we have found that rectangular-shaped dampers guarantee the best performance in confining the buoyant release while the squared off-centred ones have the worst performance.

References

Bai, J., Liao, H., & Xia, Y. (2020). Study on fire accidents in tunnels. In *IOP Conference Series: Materials Science and Engineering* (Vol. 741, No. 1, p. 012095). IOP Publishing.

Chaabat, F., Salizzoni, P., Creyssels, M., Mos, A., Wingrave, J., Correia, H., & Marro, M. (2020). Smoke control in tunnel with a transverse ventilation system: An experimental study. *Building and Environment*, *167*, 106480.

Hunt, G. R., & Kaye, N. B. (2005). Lazy plumes. *Journal of Fluid Mechanics*, *533*, 329-338.

Jiang, L., Creyssels, M., Hunt, G. R., & Salizzoni, P. (2019). Control of light gas releases in ventilated tunnels. *Journal of Fluid Mechanics*, *872*, 515-531.

Kubwimana, T., Salizzoni, P., Bergamini, E., Mos, A., Méjean, P., & Soulhac, L. (2018). Wind-induced pressure at a tunnel portal. *Environmental Fluid Mechanics*, *18*(3), 769-786.

Li, J. S., & Chow, W. K. (2003). Numerical studies on performance evaluation of tunnel ventilation safety systems. *Tunnelling and Underground Space Technology*, *18*(5), 435-452.

Morton, B. (1959). Forced plumes. *Journal of Fluid Mechanics*, *5*(1), 151-163.

Salizzoni, P., Creyssels, M., Jiang, L., Mos, A., Mehaddi, R., & Vauquelin, O. (2018). Influence of source conditions and heat losses on the upwind back-layering flow in a longitudinally ventilated tunnel. *International Journal of Heat and Mass Transfer*, *117*, 143-153.

Seike, M., Kawabata, N., & Hasegawa, M. (2014). The effect of fixed smoke barriers on evacuation environment in road tunnel fires with natural ventilation. In *7th International Conference 'Tunnel Safety and Ventilatio* (pp. 126-132).

Vauquelin, O. (2008). Experimental simulations of fire-induced smoke control in tunnels using an "air–helium reduced scale model": Principle, limitations, results and future. *Tunnelling and Underground Space Technology*, *23*(2), 171-178.

Wake flows of wind turbines in stably stratified boundary layers

C. Deebank [*], M. Bastankhah [+], M. Placidi [*]

[*]University of Surrey, Faculty of Engineering and Physical Sciences, Centre for Aerodynamics and Environmental Flow, Guildford, GU2 7XH, United Kingdom
[+]Durham University, Department of Engineering, Durham, DH1 3LE, United Kingdom

Abstract

The inevitability of climate change[1] and the rise of net-zero policies are driving unprecedented growth in wind energy technologies, with the UK pledging to generate "40 GW from offshore wind–enough to power every home in the UK" by 2030[2]. This requires understanding and modelling, to a greater degree than at present, the temporal and spatial behaviour of the wind within each wind farm, to enable more accurate performance predictions and wind farm optimisation. In turn, this means a better grasp of turbine wakes both in terms of mean velocity deficit (i.e., steady wind component) and turbulence quantities, which can lead to loss of energy production, raised fatigue loads, and shorter machine life. Both the steady and unsteady properties of wake flows are affected by the stability state of the atmospheric boundary layer. In this talk, we will discuss a set of wind tunnel measurements performed in the EnFlo thermally stratified wind tunnel at the University of Surrey, on two models: a porous disk and a scaled wind turbine of matched size in both neutral and stably stratified winds. The talk will focus on the spatial evolution of high-order turbulence quantities in the wake flow of a single wind turbine.

[1] Climate Change 2021: the Physical Science Basis. Intergov. Panel on Climate Change (IPCC). UN.

[2]Energy white paper: Powering our net-zero future (2020). Dep. for Business, Energy & Industrial Strategy.

Measuring wall shear forces with a simple pressure transducer?

Nikhil Raghuvanshi[1], Frank Harms[1], Bernd Leitl[1], Thomas Glanert[1]

[1]Meteorological Institute, EWTL, University of Hamburg, Bundesstrasse 55, D-20146 Hamburg, Germany

Abstract

Despite the fact that a variety of force balance and sensor systems are available for use in wind tunnels, measuring small drag forces at low wind speeds remains to be an challenging task. Measuring the drag forces acting on relatively small and relatively smooth surfaces, particularly in low-speed boundary layer wind tunnels, often becomes expensive as far as the costs of force sensors and the force balance are concerned. A desire for systematic modelling and measurement of the drag forces acting on varying sea ice roughness motivated the study reported here.

Introduction

The Aerodynamic roughness length (z_0) is one of the most important parameters in modelling the regional ice motions, however there are a lot of uncertainties around its measurement. The values of z_0 obtained from field measurement are often not accurate and this can be attributed to multiple reasons. One of the main reasons is that, at most field stations, wind speeds were only measured at a few level heights and bears much statistical uncertainty in measuring z_0. Also, the field instruments are exposed to harsh atmospheric conditions, which inherently leads to error in estimating z_0. Uncertainties in estimating z_0 leads to error in evaluating drag forces over ice sheets. In order to overcome the inaccuracies associated with the field experiments, wind tunnel experiments are carried out in a controlled environment. In order to quantify the drag forces, a one component force measurement device for a boundary layer wind tunnel has been developed.

A one component, pressure based force balance device has been proposed to measure the drag forces for a boundary layer wind tunnel. The main idea to build such a device is to provide an alternative to the already existing Piezoelectric Force Sensors for wind tunnels. One advantage for such a device is that it would be cost-effective compared to the Piezoelectric Force Sensors and is made from the transducers which are generally available at any wind tunnel facility. The other advantage for building such a device is that the measurement range capabilites is not restricited to its inbuilt stiffness, which is in the case of the Piezoelectric Force Sensors for wind tunnels. Figure 1 shows a 2-D illustration of the proposed pressure based force device.

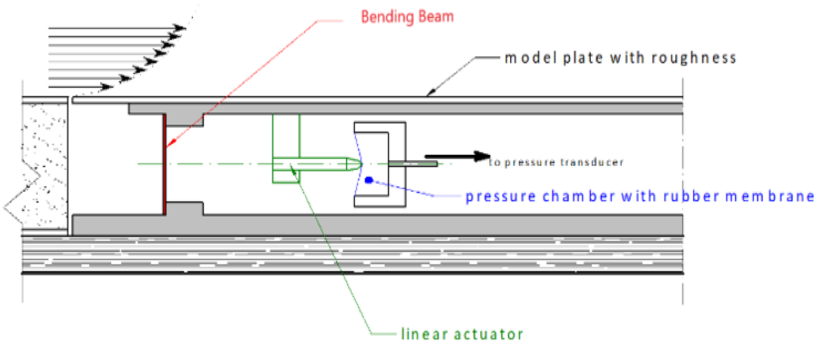

Fig 1: Diagram of the Proposed Device

Design of Pressure based 1D Drag Force Balance

The device consists of two rectangular 40 by 35 mm aluminium frames which are attached vertically by four flexible bending beams (see Figure 2). A 'pressure chamber' is mounted at the centre of the bottom frame. In a similar fashion, a linear actuator is mounted on the upper frame of the device. The pressure chamber is composed of a small circular aluminium cup covered by a flexible membrane. The pressure signal generated by the movement of the actuator is transferred to a regular laboratory grade pressure transducer via tubing. The Pressure chamber and the linear actuator are aligned in such a way that it is perpendicular to the wind direction in the wind tunnel. The entire device is installed underneath the test section of the wind tunnel and the test section plate is mounted on the upper frame of the force balance. The advantages for such a design is that

- Compact size – easy to install in a wind tunnel
- Flexibility in choosing the materials for bending beams and the membrane sensors for the pressure chamber
- Simple design - Requires less maintenance

Figure 2 shows the force balance device installed underneath the test section of the Blasius wind tunnel at the EWTL. A 'moderately rough' boundary layer was modelled in the wind tunnel following the VDI 3783-12 guidelines.

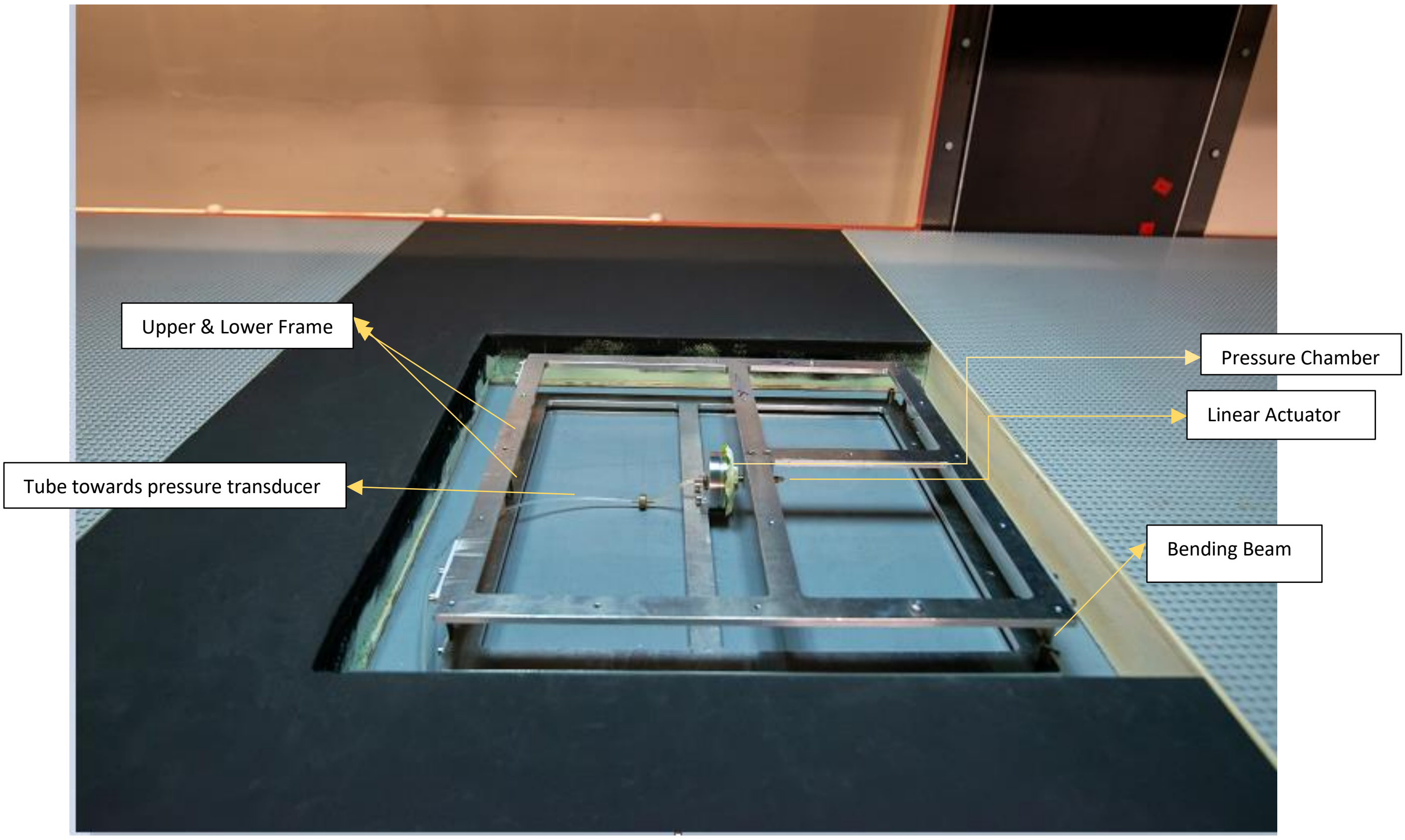

Figure 2: Force Balance device installed underneath the test section of the Blasius wind tunnel

Working Principle

As the wind is blown over the test section plate, the upper frame on which the linear actuator is mounted is moving, the actuator is deforming the membrane of the 'sensor cup' which in turn generates pressure signals. Pressure signals can be assigned to corresponding force values by a calibration of the whole setup before measurements. With the current setup, it is possible to quantify the drag forces in only one direction. However, the principle can easily extend to measure both of the horizontal drag force components simultaneously. Figure 3 shows the close up of the linear actuator and the pressure chamber

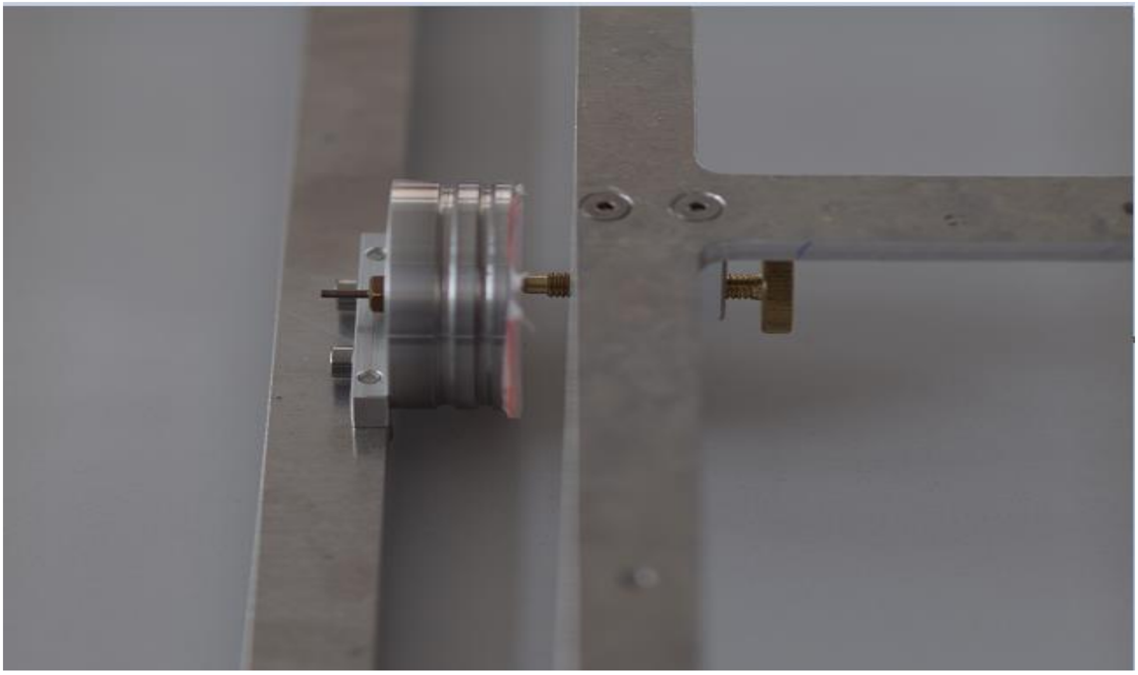

Figure 3: Close up view of the Pressure Chamber and Linear Actuator

Performance/Measurement Capabilities

One of the main performance objectives for building such a device is that it would be able to quantify the drag forces due to low wind speeds and to have a good repeatability of the results. Currently different configurations of bending beams and pressure chamber sensors are being carried out to optimize the performance of the device. Preliminary results showed that changing the bending beams influences the stability of the device. It was also found out that the output signal is strongly influenced by the sensor material. As of now, there are a few open end questions like which configuration have a very good repeatability of the output signal, what measurement times are needed for a certain repeatability, how good is the sensitivity of a particular pressure chamber sensor and so on. Exemplary results available by the time of the conference will illustrate the performance of the easy to replicate device.

References

1. Highly variable aerodynamic roughness length (z_0) for a hummocky debris-covered glacier, Miles et al. 2017
2. VDI 3783-12 guideline, December 2000

PHYSMOD 2022 – International Workshop on Physical Modeling of Flow and Dispersion Phenomena
Institute of Thermomechanics of the CAS, Prague, Czech Republic – August 29-31, 2022

DIFFERENT BOUNDARY CONDITIONS FOR LES SOLVER PALM 6.0 USED FOR ABL IN TUNNEL EXPERIMENT

Hynek Řezníček[1,3], Jan Geletič[1], Martin Bureš[1], Pavel Krč[1], Jaroslav Resler[1], Kateřina Vrbová[2], Arsenii Trush[2], Petr Michálek[2], Luděk Beneš[3], Matthias Sühring[4]

[1] Institute of Computer Science, Czech Academy of Sciences, Prague (cs.cas.cz - reznicek@cs.cas.cz)
[2] Institute of Theoretical and Applied Mechanics, Czech Academy of Sciences, Prague (itam.cas.cz)
[3] Faculty of Mechanical Engineering, Czech Technical University in Prague (fs.cvut.cz)
[4] Institute of Meteorology and Climatology, Leibniz University in Hanover (meteo.uni-hannover.de)

section: Validation of numerical (and analytical) models

1 Introduction

Our work is motivated by modelling of pollutants and dust spread in the urban canopy which is one of the major problem for human health in inhabited areas. Majority of the pollutants can be considered as passive contaminants (driven by the flow), therefore we need to find the correct flow field for best prediction of their concentration. The talk is focused on dynamical core of the model PALM which is responsible for the best possible capture of the flow.

The computational results for the velocity magnitude and turbulent intensity are compared to measurements in a wind tunnel (Vincenc Strouhal) at Institute of Theoretical and Applied Mechanics (ITAM) which calibration is documented in [Kuznetsov et al.,2017]. The flow similar to urban Atmospheric Boundary Layer (ABL) is simulated in the tunnel by three elements: castellated barrier wall and vortex generators at the entrance of the aerodynamic section and surface roughness elements on its floor. The question is how to prescribe the boundary condition at the enter of the domain which can't be completely simulated.

The realistic buildings layout from Prague-Dejvice quarter is chosen as the testing domain. It has been 3D-printed * and placed to the test section of the tunnel. The choice of this particular domain is motivated by existing validation for the model in Dejvice quarter [Resler et al.,2021] and because the buildings contain some passageways which serves for testing the new 3D structures in our model.

PALM model is capable to simulate turbulent air-flow within the lowest part of the ABL. By default, it uses the Large Eddy Simulation (LES) approach in which the bulk of the turbulent motions is explicitly resolved [PALM]. The core was already validated according to tunnel measurements in [Gronemeier et al.,2021], therefore our expectations were high. The air simulated is considered as incompressible (due to much lower velocities in comparison to the speed of sound), viscid (the molecular viscosity is neglected everywhere except for the turbulent dissipation) and neutrally stratified (for testing the dynamical core only without unfavourable stratification effects).

*3D-geometry kindly provided by Operátor ICT, a.s. (operatorict.cz)

2 Mathematical model

The dynamical core of PALM model is based on Navier-Stokes equations in Boussinesq approximation for filtered quantities (filtering usually denoted with overbar is omitted here due to readability)

$$\begin{aligned} \nabla \cdot \mathbf{u} &= 0 \\ \frac{\partial \mathbf{u}}{\partial t} + (\mathbf{u} \cdot \nabla)\mathbf{u} &= -\frac{1}{\rho_0}\nabla \pi + \mathbf{g} - \nabla \cdot \underline{\underline{\tau}} \end{aligned} \tag{1}$$

The velocity vector $\mathbf{u} = u_i = (u, v, w)$ describes the movement of air which is assumed to be dry with constant density ρ_0. The gravitational acceleration denoted as $\mathbf{g} = -g\delta_{i3}$ is acting only in vertical direction (here written using Kronecker's delta δ_{ij} in third component), its value is set to $g = 9.81$ m/s^2. The modified pressure fluctuation can be expressed as $\pi = p + \frac{2}{3}\rho_0 e$ using the pressure fluctuation p and sub-grid-scale (sgs = unresolved) turbulent kinetic energy e. The residual stress tensor $\underline{\underline{\tau}} = \tau_{ij}$ symbolises the turbulent part of the flow.

The modified Deardorff's model is employed for turbulent closure (Einstein summation convention)

$$\begin{aligned} \tau_{ij} = \overline{u_i''u_j''} - \frac{2}{3}e\delta_{ij} &= -K_m\left(\frac{\partial u_i}{\partial x_j} + \frac{\partial u_j}{\partial x_i}\right) \\ \frac{\partial e}{\partial t} + u_j\frac{\partial e}{\partial x_j} &= 2K_m\nabla^2 e \quad + \quad \overline{u_i''u_j''}\frac{\partial u_i}{\partial x_j} \quad - \quad \epsilon \end{aligned} \tag{2}$$

The local (sgs) eddy diffusivity coefficient of momentum is approximated as $K_m \approx 0.1\Delta\sqrt{e}$, where distance $\Delta = \min\{\Delta_{x_i}\}$ is minimal grid spacing. This distance serves also as implicit filter for large eddies. The dissipation rate is approximated as $\epsilon \approx 0.93\frac{\sqrt{e^3}}{\Delta}$. For more details please see the documentation in [PALM]. Further the dimensions are referenced as $x_i = (x, y, z)$.

2.1 Numerical solver

The equations are spatially discretized by using finite differences at equidistant horizontal grid spacing while the vertical grid is stretched above the surface layer to save CPU-time. The stretching factor applied above 100 m height set to 1.01 is limited by maximal vertical step ($\max \Delta_z = 2\Delta_x$). Arakawa staggered C-grid is used for velocity $\mathbf{u}$ defined at edges of the grid cell while the scalars are defined in the grid cell center (see fig. 1). The Upwind-biased 5^{th} order advection scheme based on flux formulation according to [Wicker&Skamarock,2002] is used.

The time integration is done by 3^{rd} order low-storage (3 stages) Runge-Kutta method according to [Baldauf,2008]. It is proved that the CFL condition in such case can be $C_{CFL} = \frac{\max_i\{u_i\}\Delta_t}{\Delta} < 1.4$ which limits the maximal time step Δ_t.

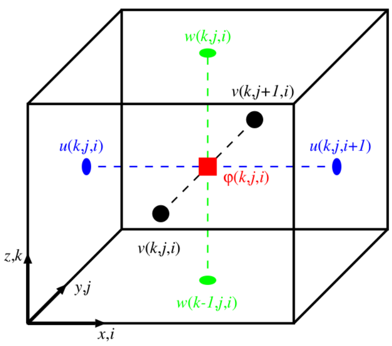

Fig. 1: Arakawa staggered C-grid [PALM]

To enforce incompressibility (divergence free velocity field needed by Bouissinesq approx.) a predictor-corrector method is used where Poisson equation is solved for the modified perturbation pressure (π) after every time step. The resulting system of linear equations is solved via multi-grid scheme (if number of cells per core is even) with Gauss-Seidel method. The detailed description can be found in [PALM].

3 Set-up and boundary conditions

As mentioned above, the measurement was done in Vincenc Strouhal)wind tunnel at the Institute of Theoretical and Applied Mechanics (ITAM), detailed description can be found in [Kuznetsov et al.,2017] and its references. What is important to notice here is the arrangement of elements generating the ABL flow before the aerodynamic test section as can be seen in the fig. 2, because the castellated barrier wall and vortex generators can't be part of the model domain. Due to their placement too close to the inlet, it would caused some serious instabilities in the model.

The real world building configuration in Prague-Dejvice between streets Jugoslavskych partyzanu and Terronska was chosen as testing area (serves as inner domain in the model). The fig. 3 shows the map of the area with blue circle indicating the passage-way in the building in Rooseveltova street. The area is rotated clockwise to adjust the air flow with x-direction. The situation in the atmospheric test section (inner domain in the model) is shown in the fig. 4 with marked measuring point locations.

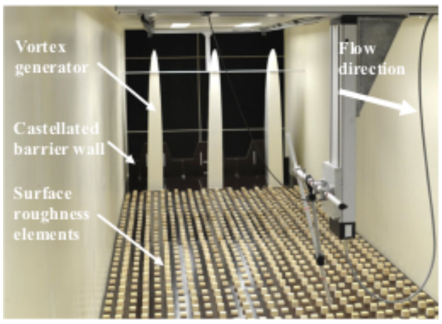

Fig. 2: View from the aerodynamic test section backwards (against the flow).

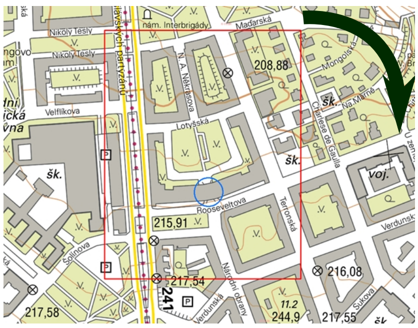

Fig. 3: Map of chosen area. The domain is rotated clockwise in the model.

Fig. 4: The same area as inner domain with measuring points.
.

The scale of the model is 1:300 which holds for time and space meaning that the 1 min. average in the tunnel is 5 hours average in real. A characteristic length is chosen as the height of the vortex generator which is $H = 1.5$ m in the tunnel which corresponds to 450 m in reality. The advantage of the scale setting is that the velocities can be compared 1:1. If the reference velocity $U_{ref} = 6.6$ m/s is considered, the Reynolds number in the tunnel is $Re \approx 10^6$ which is large enough. If Townsend's hypothesis applies, the flow in the wind tunnel should be dynamically comparable to the real one.

The computational domain contains all the roughness elements (simulated directly) as can be seen in the fig. 5. The whole domain 3000×600 m large includes the test section with dimensions 600×500 m (all listed as real here). The resolution of the grid is set to $\Delta = 1$ m.

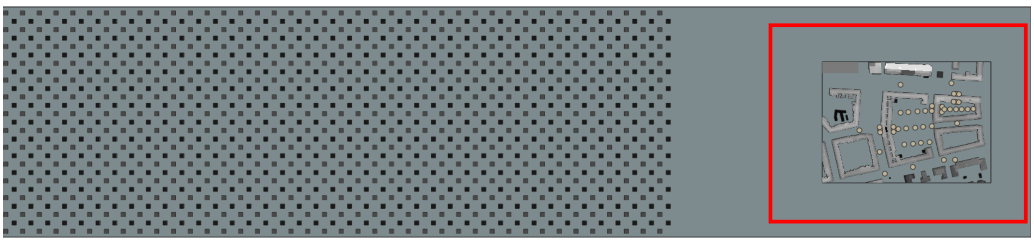

Fig. 5: Computational domain with buildings in the aerodynamic test section (marked in red).

3.1 Boundary conditions

The boundary conditions (b.c.) are set as follows:

On **inlet** the vertical velocity profile driven by $U_{ref} = 6.6$ m/s is prescribed for the first velocity component $u = u(z)$ with statistically created disturbances every 60 s with amplitude ± 0.25 m/s from the mean velocity. The other components are set to $v = w = 0$. Homogeneous Neumann b.c. is prescribed for the other quantities (e, p).

On **outlet** a radiation b.c. is used for all velocity components where a constant phase velocity is considered as maximum value allowed by CFL condition. Homogeneous Neumann condition is assumed for scalar quantities (e, p).

At the **bottom** homogeneous Dirichlet b.c. for velocity vector $\mathbf{u}(0) = \mathbf{0}$ (no slip) is used. Homogeneous Neumann b.c. is prescribed for the other quantities (e, p).

At the **top** boundary Dirichlet b.c. for the first velocity component is given by the inlet profile as $u(z_{max}) = \max u(z)$. For the other components and the pressure perturbation the homogeneous Dirichlet b.c. is utilized. Homogeneous Neumann condition is assumed for sgs-tke (e).

On **sides** the cyclic b.c. is prescribed for all quantities.

4 Results

The whole aerodynamic section (including the roughness elements in front of the test section) of the wind tunnel was simulated and the results were compared to the measurements. The main comparison was done for velocity components in the given points (see fig. 4) obtained by five-hole probe for three different heights: 3, 10 and 30 m (listed as real dimensions). Nevertheless, the agreement of the velocity and turbulent intensity profiles measured by hot-wire probe in the tunnel axes in front of the test section was also important. The values for the profiles were taken from wind tunnel validation measurement provided in [Kuznetsov et al.,2017] since the measurement of these profiles during our experiment wasn't accomplished.

The first numerical experiment was performed with uniform inlet velocity profile $u(z) = U_{ref}$ and was considered as naive attitude serving as technical preview. The flow was decelerated and its turbulent intensity was also decreased within the roughness elements section. The example of such horizontal velocity field (u) in 9 m height captured in a moment when the simulation time hits 1 hour is shown in the fig. 6.

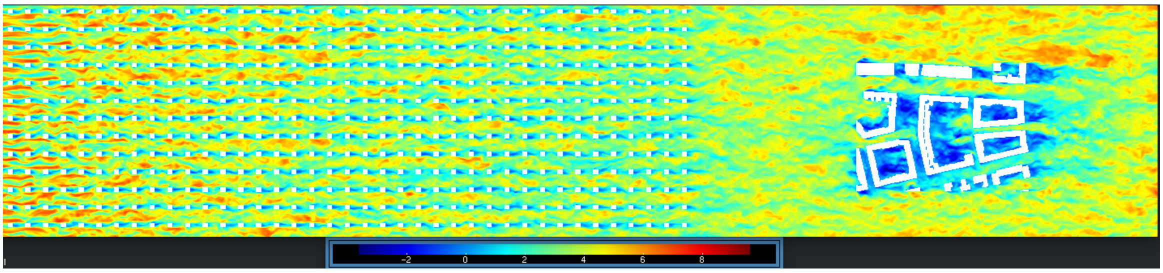

Fig. 6: Horizontal velocity field in $z = 9$ m captured after 1 hour simulation (u - instantaneous values).

The model outputs were mainly saved every 30 minutes as time averages and then their mean over 5 hours simulation were computed. Example of such output for velocity component u in the test section is rendered in the fig. 7. There, one can easily identify the influences of the buildings and their recirculation zones. Also, the influence of the passageway in the middle of the U-shaped building, which allows some air to go through, therefore the flow behind it is fasted than its surrounding area. In fig. 8 the vertical profiles of u velocity in the tunnel axes in front the test section are plotted (in

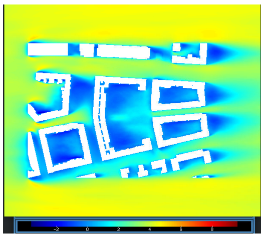

Fig. 7: 30 minutes average for u, in $z = 9$ m, $t = 1$ h (In the test section).

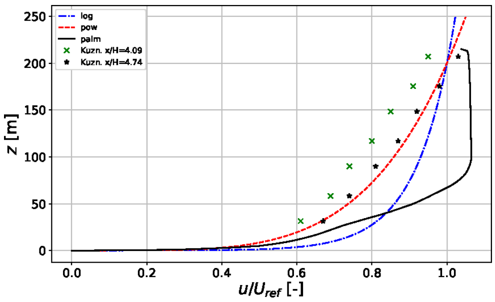

Fig. 8: Velocity profiles at the enter of the test section.

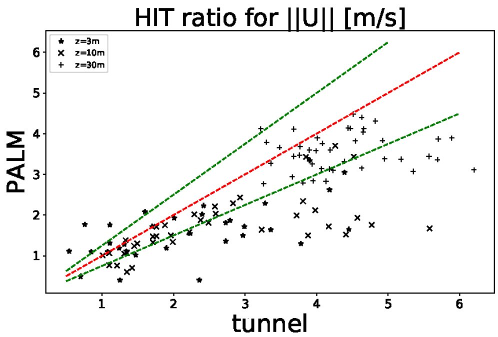

Fig. 9: Mean velocity magnitudes hit.

the distance x/H = 4.74). For illustration, two possible theoretical profiles are plotted in the graph as well as experimental profile in the different distance (x/H = 4.09). The profile from PALM (black line) behaves differently than the experimental profile (exp.). The different behaviour of the simulated profile is probably given by different boundary conditions at the inlet (castellated barrier wall and vortex generators at the entrance of the aerodynamic section aren't in the simulation). However, the hit ratio for velocity magnitudes displayed in the fig. 9 isn't as bad as expected. The values are seriously under-predicted by the model in some points but in several points the model predicts surprisingly correct values.

The first numerical experiment confirmed that convergence of the model is achieved relatively quickly. As fig. 10 shows, the steady state in terms of kinetic energy and resolved Turbulent Kinetic Energy (TKE) conservation is reached approximately after 15 min. of the simulation. The spectral density of TKE corresponds well to the Kolmogorov's cascade as plotted in the graph of fig. 11.

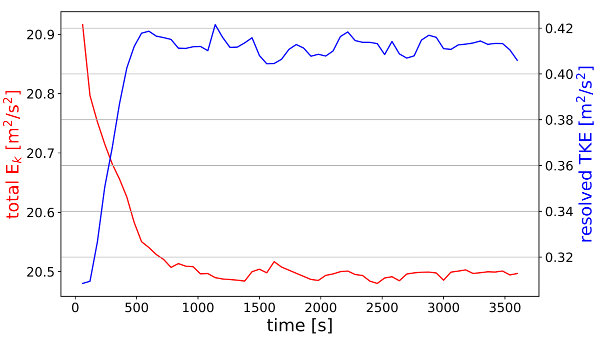

Fig. 10: Convergence for kinetic energy and Turbulent Kinetic Energy (TKE) conservation.

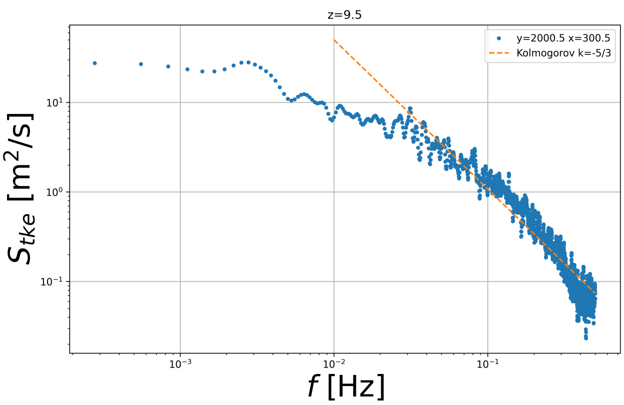

Fig. 11: Spectral density of resolved TKE.

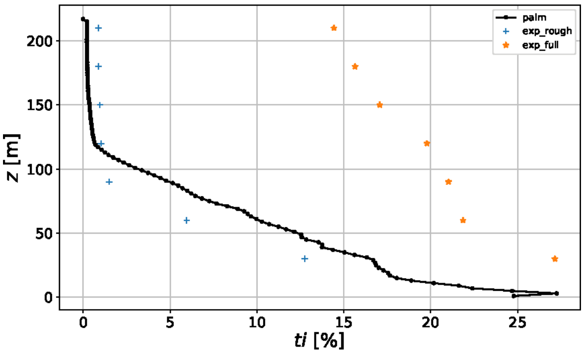

Fig. 12: Vertical profiles of Turbulent Intensity at the enter of the test section.

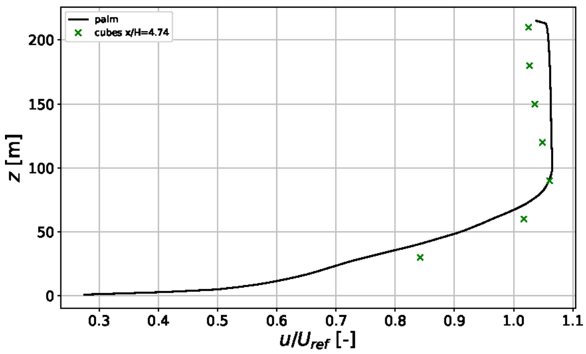

Fig. 13: Velocity profile compared to empty tunnel with roughness elements only (cubes).

The comparison of Turbulent Intensity (TI) profiles in the fig. 12 for the PALM outputs and calibration measurement with hot-wire (in the tunnel axes ahead of the test section) indicates the good ability of the model to capture well the empty tunnel with roughness elements only (when the castellated barrier wall and the vortex generators weren't present). On the other hand the fully developed profiles of turbulence and velocity (will be described further) of the fully equipped wind tunnel (with all three elements generating similar flow to ABL) are difficult to get from the model. Probably they have to be prescribed as an inlet b.c. When the dimensionless velocity profiles are compared to the empty tunnel profiles with roughness elements (cubes) only in the fig. 13, they fit quite well.

The second numerical experiment should used the known velocity profile to obtain results closer to the experiment. The power law velocity profile

$$u(z) = U_{ref} \left(\frac{z}{z_{ref}} \right)^{\alpha}, \tag{3}$$

with coefficient $\alpha = 0.22$ and $z_{ref} = 200$ m, was prescribed on the inlet. Unfortunately, the turbulence on the inlet was again generated by the disturbances since PALM can't use synthetic turbulent generator without meteorology from meso-scale model. As shown in fig. 14 the profile still doesn't match fully developed state. The flow is decelerated near the ground much more than expected.

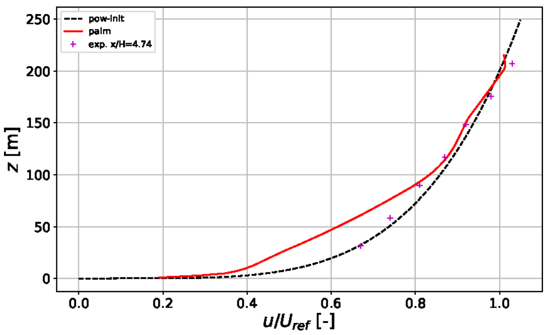

Fig. 14: Velocity profiles for the second numerical experiment.

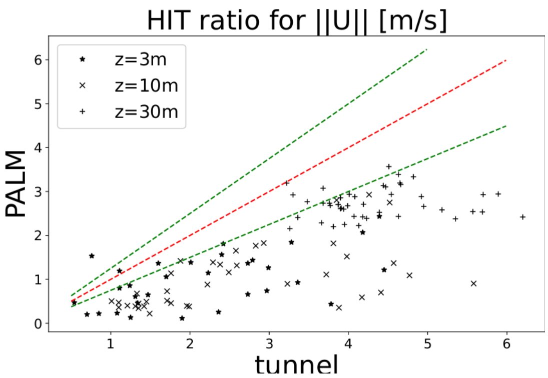

Fig. 15: Mean velocity magnitudes hit.

The hit ratio in that case is even worse as is indicated in the fig. 15. However, it is not surprising because the simulated flow entering the testing domain in this case is much slower than the physical flow in the wind-tunnel.

Since simulation of whole atmospheric domain is time consuming and CPU costly, the third set of experiments was done as a parametric study where the inlet b.c. were prescribed directly to the test section. Variety of reference velocities were tested within the power law profile (eq. 3), but none of them showed any improvement.

The scattering of the hit ratio is even bigger than in the first experiment. The fig. 16 displays a situation inside the test section for reference velocity $U_{ref} = 7$ m/s. The points in height 30 m are coloured according to formula $\left(\frac{u_{palm}}{u_{exp.}} - 1\right) \cdot 100\%$, which means how accurately they hit the experimental value. Some patterns can be identified in the figure, such that the velocities inside the closed building block fit well and the values in front of the closed building block are very under-predicted, but the rest seems quite random. That leads us to consideration of wrong turbulent structure in the simulation probably caused by lacking of right tools and information how to prescribe it at the inlet (as the results from the first experiment suggested).

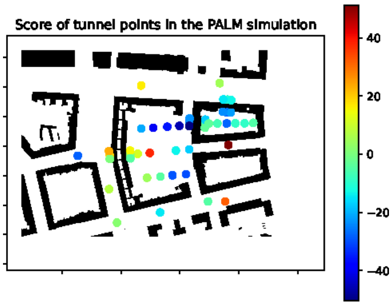

Fig. 16: Measuring points colored according to $(u_{palm}/u_{exp.} - 1) * 100\%$

5 Conclusions

A large simulation (containing circa 25×10^8 cells) of the whole wind-tunnel atmospheric section was performed by atmospheric LES model PALM and its results were compared to the measurements. It was shown that kinetic energy conservation is achieved relatively quickly and the calculated turbulence spectrum corresponds to the theory. The results obtained for the "naive" uniform initial velocity profile were promising but not satisfying. The model was able to develop the correct profile over the roughness elements quite well in the case of velocity and even of turbulent intensity. The functionality of 3D structures inside PALM was also tested and nothing has been discovered to prove that they didn't work correctly.

The attempts of improving the hit ratio by prescribing different (assumed developed) velocity profiles failed and actually leaded to more scattered graphs. To conclude that the results of the model are limited with prescription of correct turbulent structure and the known (well developed) velocity profile. Unfortunately, such profile wasn't provided by the experimenters and during our numerical experiments it wasn't found. The question, how to impose the correct profile (even if we know it), remains for the future testing.

The future endeavors are pointed to the simulation of cyclic domain (infinite) with smaller part serving as precursor where the correct profile could be developed. Also we hope that we can adopt some knowledge obtained by testing original code provided by [Gronemeier et al.,2021]. If it was possible we would ask for the new measurements with the empty tunnel with roughness element to see whether the well defined inlet improved our hit ratio.

Acknowledgement

This work was supported by the Strategy AV21 projects “Energy interactions of buildings and the outdoor urban environment” and “City as Lab of changes”, financed by the Czech Academy of Sciences. The measurements were possible due to the support of grant GACR 22-08786S financed by The Czech Science Foundation (GACR).

References

[Baldauf,2008] Baldauf M.: Stability analysis for linear discretisations of the advection equation with Runge-Kutta time integration. *J. Comput. Phys.* 227 (2008)

[Gronemeier et al.,2021] Gronemeier T., Surm K., Harms F., Leitl B., Maronga B and Raasch S.: Evaluation of the dynamic core of the PALM model system 6.0 in a neutrally stratified urban environment: comparison between LES and wind-tunnel experiments *Geosci. Model Dev.* 14 (2021)

[Kuznetsov et al.,2017] Kuznetsov S., Ribičić M., Pospíšil S., Plut M., Trush A. and Kozmar H.: Flow and Turbulence Control in a Boundary Layer Wind Tunnel Using Passive Hardware Devices *Experimental Techniques* 41/6 (2017)

[PALM] PALM online documentation. `https://palm.muk.uni-hannover.de/trac`. accessed: 30.06.2022.

[Resler et al.,2021] Resler, J., Eben, K., Geletič, J., Krč, P., Roseckỳ, M., Sühring, M., Belda, M., Fuka, V., Halenka, T., Huszár, P., et al.: Validation of the palm model system 6.0 in a real urban environment: A case study in dejvice, prague, the czech republic. *Geoscientific Model Development*, 14 (2021)

[Wicker&Skamarock,2002] Wicker L.J., Skamarock W.C.: Time-splitting methods for elastic models using forward time schemes *Mon. Weather Rev.* 130 (2002)

PHYSMOD 2022 – International Workshop on Physical Modelling of Flow and Dispersion Phenomena
Institute of Thermomechanics of the CAS, Prague, Czech Republic – August 29-31, 2022

Aspects of dosage from short and long duration emissions

Alan Robins[1], Paul Hayden[1], David Gallacher[1,2], Sam Pace[2], Hana Chaloupecka[3]

1, Department of Engineering Science, University of Surrey, GU2 7 XH, UK
2, Guys and St Thomas' Hospital NHS Foundation Trust, UK
3, Institute of Thermomechanics, Czech Academy of Sciences, Czech Republic
Contact: a.robins@surrey.ac.uk

Abstract

The objectives of this work were to use wind tunnel concentration measurements to describe the structure of dispersing clouds from an elevated source in a deep turbulent boundary layer and to develop scaling rules that reduce the results to a universal form. The experiments were carried out in the EnFlo meteorological wind tunnel at the University of Surrey. Ensembles of between 100 and 200 repeat emissions were used, emission durations between 0.067 and 1.02s and a reference flow speed of 2ms^{-1}. The fetch studied extended to about six source heights downwind (about two boundary layer depths). The structure of the evolving clouds was analysed to determine time of flight, along-wind spread and dosage and to compare the dosage behaviour with the concentration field in a plume from the same source. This illustrated how the two were related and how cloud dosage statistics (mean and standard deviation) could be derived from plume data. It also demonstrated that much larger ensembles were required to reduce the statistical uncertainty in the mean cloud properties. The next steps involve testing these conclusions in a wider range of flow and dispersion conditions, in the presence of obstacles or complex urban areas.

Introduction

The literature relating to short duration emissions is slight. Robins and Fackrell (1998) carried out a wind tunnel study of the dispersion of short duration, ground level emissions in a deep turbulent boundary layer. This focused on comparison with the analytical theory developed by Chatwin (1968) and characterised the structure of the dispersing cloud. Although published in 1998, this was part of a wider investigation of concentration fluctuations in plumes and clouds, as reported in Fackrell and Robins (1982a, b). Subsequent experimental work with short duration emissions can be conveniently divided between field work at the US Army Dugway Proving Ground (Yee et al. 1994a, 1994b, 1999) and in Oklahoma City (Doran et al., 2007; Zhou and Hanna, 2007; Hanna et al., 2019), and wind tunnel simulations in Europe (e.g. Berbekar et al., 2015; Chaloupecka et al., 2017, 2021).

The objective of the present work was to use wind tunnel concentration measurements to describe the structure of dispersing clouds from an elevated source in a deep turbulent boundary layer and to develop scaling rules that reduce the results to a universal form. Here, we concentrate on dosage.

Methodology

The experiments were carried out in a 1 m deep simulated atmospheric boundary layer in the EnFlo meteorological wind tunnel at the University of Surrey. Ensembles of between 100 and 200 repeat emissions were used in most cases, with emission durations between 0.067 and 1.02s and a reference flow speed at the boundary edge of 2ms^{-1}. The fetch studied extended to about six source heights downwind (roughly, two boundary layer depths). Figure 1 shows an example of an ensemble-averaged emission profile, as $C(t)$, and explains some relevant terminology.

Analysis

The structure of the evolving clouds was analysed to determine time of flight, along-wind spread and dosage and to compare the dosage behaviour with the concentration field in a plume from the same source. This illustrated how the two were related and, therefore, how cloud dosage statistics (mean and standard deviation) could be derived from plume data. It also demonstrated that much larger ensembles were required to reduce the statistical uncertainty in the mean cloud properties.

Figure 2 shows ensemble averaged concentration time series at x/h = 1.125 to 5.625, y = 0, z/h = 1, for an 0.066s emission, weighted by $(x/h)^{2.8}$, for an ensemble size, N = 196; h is the source height. Note that the weighting results in similar maximum concentrations at all four locations.

The concentration time series in a plume from the same source was divided into a number of sub-series of lengths corresponding to the effective cloud release durations. The ensembles thus obtained were then processed in the same manner as the cloud data. The results could be compared directly as the emission rates were the same in both cases. The outcome is shown in Figure 3, a scatter plot of mean and standard deviation of the dosage and equivalent measures derived from the plume data. Data for all values of release duration and downwind fetches are included.

Conclusions

1. Near the source, where the emission duration exceeds the time of flight, $T_{eff} > T$, and the cloud has a plateau region – defined as plume-like, but with end regions. Downwind, where $T \gg T_{eff}$, the structure becomes puff-like. Between these two limiting regions, there is an intermediate cloud dispersion regime.

2. A high degree of variability was apparent in ensemble averages formed from 100 to 200 repeat experiments; analysis showed that ensembles of between 400 and 900 repeats would be needed to reduce the variability to more generally acceptable levels. The high levels of intermittency in individual time series or in the plume from a continuous release disappeared under ensemble averaging and fluctuation levels decreased relative to those in the plume by factors of $\sqrt{N}$, N being the number of observations forming the ensemble.

3. The time of flight increased linearly with fetch but was slightly greater than that implied by the mean wind speed at the source height. Fluctuation levels were only weakly dependent on emission duration and were of the order of a standard deviation of 15% of the time of flight. The along-wind spread in the time series was shown to be reasonably well predicted from the turbulence intensity at source height in the approach flow.

4. The cloud peak or plateau concentrations decayed as $(x/h)^{-n}$, with n varying from 2.8 in the puff regime, to 2 in the plume-like regime.

5. A reliable estimate of centreline dosage from a passing cloud can be made from the product of concentration in a plume, with the same emission rate, and the emission duration. Dosage fluctuation levels depended on the dispersion regime, being greatest for puffs (standard deviation of

150%) and least for long emissions (50%). It is expected that these values will converge once along-wind spread dominates emission duration and all releases enter the puff regime. This analogy can be extended to the standard deviation of the dosage.

6. Ensemble sizes required to drive the standard error in the mean dosage to below 10% varied from about 300 for the shortest emission duration to 50 for the longest.

7. As a good working hypothesis, the travel time is independent of lateral position, and by supposition vertical position and the profile on D/D_o in a cloud the same as that of C/C_o in a plume. The ensemble average concentration time series on the centreline can be used to derive that at an off-centreline location.

The main caveats on these conclusions are:

- They apply to a source well above the surface, where shear can be ignored, at least to first order. This also implies that the surface boundary condition has no significant impact on the dispersion process and that, in turn, implies a fetch limit, typical that x/h is less than about 10.

- Only one source diameter was investigated, and it is well-known that concentration fluctuation levels in plumes are very sensitive to source size. Here, dosage fluctuation levels also depend on emission duration.

The next steps involve testing these conclusions in a wider range of flow and dispersion conditions, for example in the presence of obstacles or complex urban areas. Such flows generally introduce additional time scales into the dispersion process that are defined by interaction between the boundary layer and the geometry. One such is the residence time scale in the near-wake of a cuboid. Do the scaling relationships discussed above continue to hold?

References

Berbekar, E, Harms, F, and Leitl, B, 2015. Dosage-based parameters for characterization of puff dispersion results. Journal of Hazardous Materials 283 (2015) 178–185.

Chaloupecká, H, Janˇour, Z, Miksˇovský́, J, Jurcˇáková, K and Kellnerová, R, 2017. Evaluation of a new method for puff arrival time as assessed through wind tunnel modelling. Process Saf. Environ. Prot. 111, 194–210.

Chaloupecká, H, Kluková, Z, Kellnerová, R and Janˇour, Z, 2021. Characteristics of Toxic Gas Leakages with Change in Duration. Atmosphere 2021, 12, 88.

Chatwin, PC, 1968. The dispersion of a puff of passive contaminant in the constant stress region. Quart. J. R. Met. Soc., 94, 350-360.

Doran, JC, Alwine, KJ, Flaherty, JE, Clawson, KL and Carter, RG, 2007. Characteristics of puff dispersion in an urban environment. Atmos. Environ. 41, 3440–3452.

Fackrell, JE and Robins, AG, 1982a. Concentration fluctuations and fluxes in plumes from point sources in a turbulent boundary layer. J. Fluid Mech., 117, 1-26.

Fackrell, JE and Robins AG, 1982b. The effects of source size on concentration fluctuations in plumes. Boundary Layer Met., 22, 335-350.

Robins, AG and Fackrell, JE, 1998. An experimental study of the dispersion of short duration emissions in a turbulent boundary layer. Transactions on Ecology and the Environment vol 21, 697-707.

Yee, E, Chan, R, Kosteniuk, PR, Chandler, GM, Biltoft, CA and Bowers, JF, 1994a. Experimental measurements of concentration fluctuations and scales in a dispersing plume in the atmospheric surface layer obtained using a very fast response concentration detector. J. Appl. Meteorol. 33, 996–1016.

Yee, E, Chan, R, Kosteniuk, PR, Chandler, GM, Biltoft, CA and Bowers, JF, 1994b. Concentration fluctuation measurements in clouds released from a quasi-instantaneous point source in the atmospheric surface layer. Bound. Layer Meteorol, 71, 341-373.

Yee, E, Kosteniuk, PR and Bowers, JF, 1998. A study of concentration fluctuations in instantaneous clouds dispersing in the atmospheric surface layer for relative turbulent diffusion: basic descriptive statistics. Bound. Layer Meteorol. 87, 409–457.

Zhou, Y and Hanna, SR, 2007. Along-wind dispersion of puffs released in a built-up urban area. Bound. Layer Meteorol. 125, 469–486.

Figures

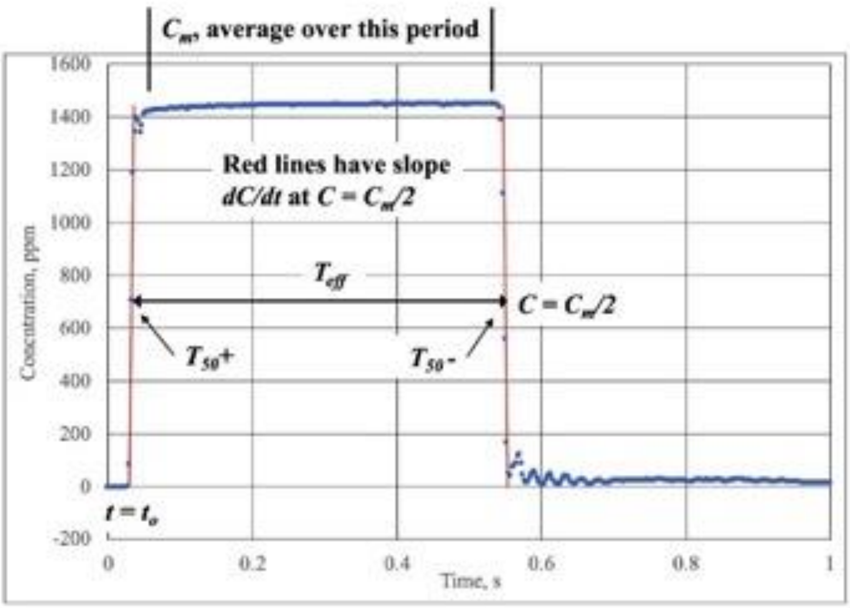

Figure 1. Ensemble averaged source concentration profile for the nominal 0.5s release duration showing definition of the derived properties.

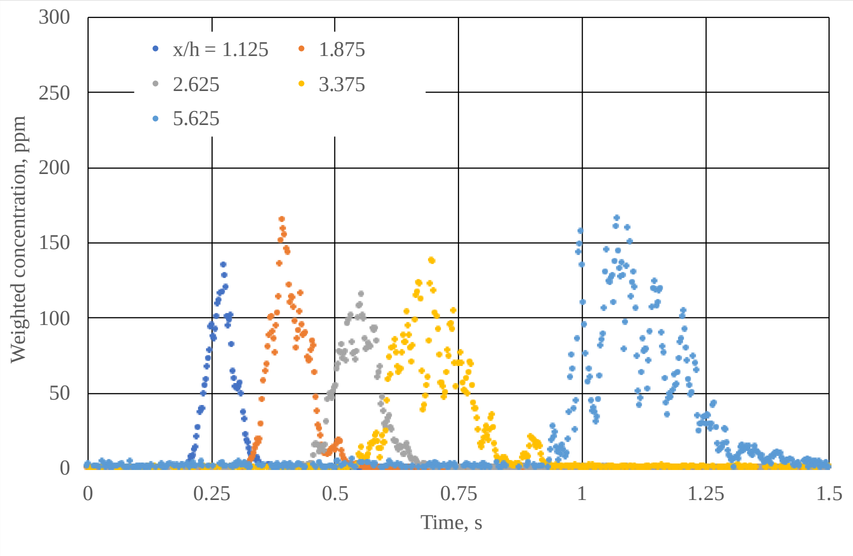

Figure 2. Ensemble averaged concentration time series at x/h = 1.125 to 5.625, y = 0, z/h = 1, for a 0.066s emission, weighted by $(x/h)^{2.8}$, N = 196.

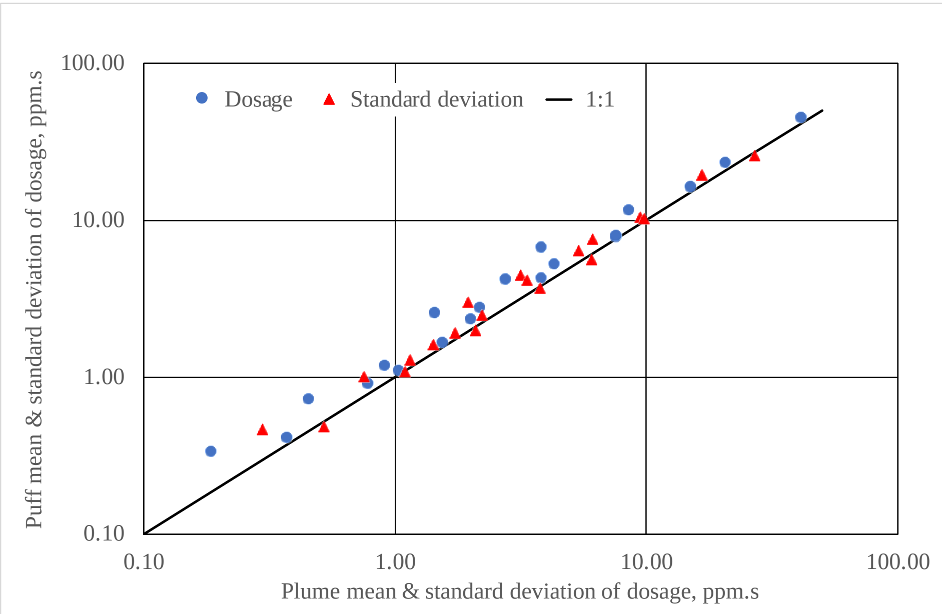

Figure 3. Scatter plot of mean and standard deviation of the dosage and equivalent measures derived from plume data. Data for all values of release duration and downwind fetches are shown.

Concentration fluctuations in atmospheric boundary layer

C. Schiavini[1], L. Soulhac[1] , P. Salizzoni[1], M. Marro[1]

[1]Univ Lyon, CNRS, Ecole Centrale de Lyon, INSA Lyon, Univ Claude Bernard Lyon 1, LMFA, UMR5509, 69134 Ecully, France

Abstract

The prediction of concentration statistics from a localised source in turbulent atmospheric flows is essential to determining health and environmental hazards. In case of an accidental release of dangerous compounds, the risk assessment can not be realised by evaluating the mean concentration merely, but we need to estimate also the local probability and mean time of exceeding of toxicity. To that purpose we analyse a wind-tunnel dataset related to concentration of a passive scalar released from a localised source within neutral boundary layers. We propose a simple analytical model inspired by Chatwin & Sullivan (1990) to compute the high-order statistics as a function of the lower order moments whose spatial distribution can be easily determined by means of simple well-assessed models.

Introduction

Dispersion phenomena of a scalar such as pollutant concentration in a turbulent boundary layer have important consequences for environmental and industrial purposes. Health and environmental hazards can be generated, for instance, by accidental releases in the atmospheric boundary layer of pollutants in industrial environments, during terrorist attacks or natural events such as volcanic eruptions. Even when the mean concentration in the plume is under concerning limits, pollutants can locally reach toxicity and flammability thresholds generating hazards for populations and the environment. Actually, concentration fluctuations are a key aspect since scalar instantaneous values can exceed the average concentration of 10-1000 times (Gurka et al., 2010).

Here, we are interested in the probability to cross hazard threshold as well as the mean time above the threshold (Cassiani et al., 2020). Previous works on concentration fluctuations included the experiments led by Fackrell & Robins, (1982) and modelling works (Bertagni et al., 2019; Jørgensen et al., 2010; Schopflocher et al., 2005) which were mainly empirical due to the difficulty to model concentration fluctuations.

Currently, various shape of probability density functions (PDF) have been tested in different situations, such as the Gamma, lognormal and exponential distributions. Nevertheless, high uncertainties remain and all the previous distributions fail to provide accurate results both close and far to the source.

A very simple analytical model tested against experimental data was proposed by Chatwin & Sullivan (1990) and further studied by Sawford & Sullivan (1995), taking into account the source distribution and adding parameters for high order moments.

The aim of this work is to develop an analytical model linking fluctuations to the mean scalar field in the case of a continuous point source in the surface boundary layer. We choose to study non-central moments instead of the more common strategy focusing on central moments.

A simple analytical model

Chatwin & Sullivan (1990) proposed an analytical model for statistical moments of concentration validated up to order 4, following a very simple framework, by analysing several experiments with a source of pollutant in a turbulent flow for various configurations. In a first time, they did not consider molecular diffusion. Dispersion was then only due to advection (particles of pollutant are moved away but keep their concentration). Particles reaching a given point downstream of the source either come from the source or from the environment, and thus have respectively a concentration of pollutant C_s (pure pollutant) or a null concentration (pure air). Due to this pure advection hypothesis, fluctuations are simplified to the extreme case in which only one maximal value and one minimal value can be reached at a given point and a given time. For the sake of simplicity, we normalize the concentration values by the source concentration $\chi = C/C_s$. Variable χ is thus either $\chi_s = 1$ when $C = C_s$ or 0 when $C = 0$. This corresponds to a Bernoulli distribution whose probability density function (PDF) is given by:

$$PDF(\chi,\vec{x},t) = p(\vec{x},t)\delta(\chi-\chi_s) + \left(1-p(\vec{x},t)\right)\delta(\chi) \qquad (1)$$

with p the probability that the particle at position $\vec{x}$ and time t originates from the source and $\delta(-)$ the Dirac delta function (Abramowitz & Stegun, 1965). The spatial coordinate $\vec{x}$ consists in the x coordinate following the wind direction, y the transverse coordinate, and z the vertical one.

Experiments and results

To find relations between non central moments of concentration, we analysed a wind-tunnel experimental dataset from Nironi et al. (2015) and Bertagni et al. (2019) as well as new experimental data. We consider a pollutant source of height h_s and diameter σ_0 releasing continuously a gas in a turbulent boundary layer with free-stream velocity $u_\infty = 5$ m/s. Turbulence is generated by spires at the entrance of the test section and roughness elements on the ground, creating a boundary layer of depth δ. The gas used in the experiments is ethane due to its density similar to air. In the experiments we analysed hitherto, only the neutral stability case was considered. Further experiments are programmed to study the impact of thermal stratification. Five different configurations were studied, with variations of the source diameter (σ_0 = 1, 3 and 6 mm) and height (h_s/δ = 0.19 and 0.06). Transversal and vertical concentration profiles were measured with a fast flame ionisation detector with frequency 1000 Hz at various distances downwind. Statistical moments up to order 4 were retrieved from instantaneous concentration measurements.

Dimensionless distances are obtained by division by the boundary layer depth while dimensionless concentrations are as C/C_s. We limited our analysis to statistical moments up to order 4 due to enhanced sampling errors on high order moment measurements (Chatwin & Sullivan, 1990). Since several orders of magnitude separate the different orders of moments, we normalise each profile by its maximum, reached closed to the plume centreline.

Figure 1 presents the results for one configuration with a source of diameter 3 mm elevated at 0.19 δ from the ground. Concentration moments divided by the source concentration are shown as dots of different colours, whereas the source position is shown as black dotted lines. The spatial coordinates y and z are respectively divided by the plume spreads σ_y and σ_z that are computed as parameters from the Gaussian profiles of the concentration moments. Red dotted lines demarcate the plume borders, arbitrarily chosen as a constant times the spatial standard deviations of concentration: $2.5\sigma_y$ and $2.5\sigma_z$. The first row shows vertical profiles for various distances from the source along the x axis downstream of the source. The second row presents the corresponding transversal profiles. For all orders of moments, we observe no variation in shape for transversal profiles, contrary to vertical profiles for which there is a clear change of behaviour at x* = 2.5. The symmetrical close-to-the-source profiles become asymmetrical due to the ground effect far from the source, which increases the concentration in the lower part of the plume over the ground. Except in this asymmetrical part of vertical profiles, concentration moments seem to scale between each others when they are divided by their maximums.

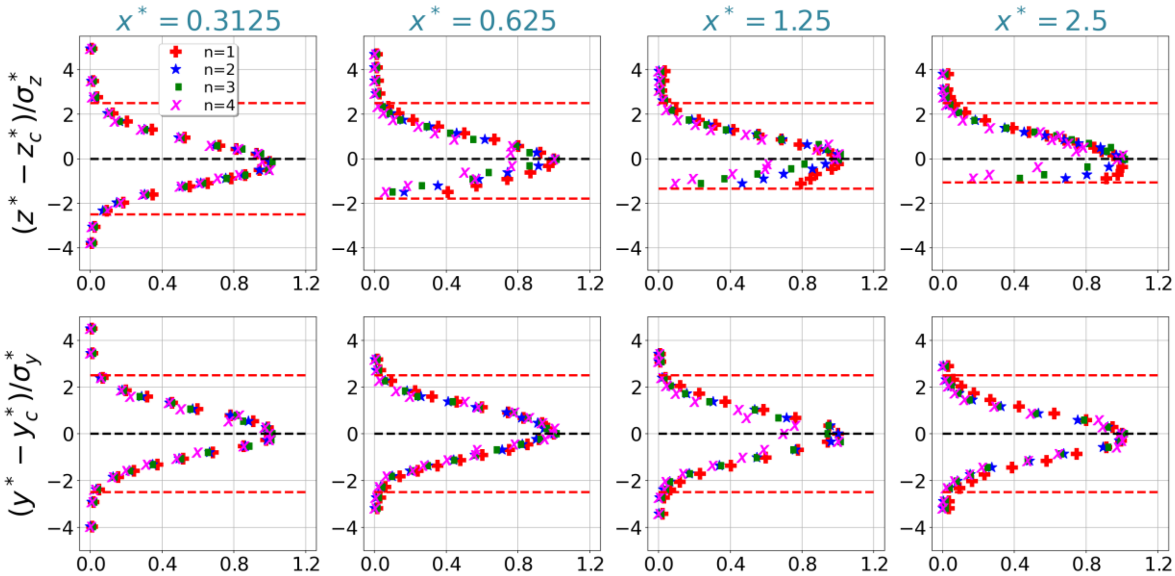

Figure 1: Non central concentration moments (red: order 1, blue: 2, green: 3, pink: 4) normalised by their maximum value (reached at the plume centreline), at several distances downwind (dimensionless distance x*) for one continuous point source in neutral turbulent boundary layer at height 0.19δ (boundary layer height). Vertical profiles in the upper part of the image are scaled by the spatial vertical standard deviation of the concentration distribution σ_z, while the transversal standard deviation σ_y is used for transversal profiles in the lower part of the figure. Black dotted lines show the source position while red dotted lines correspond to the

limit of plume borders over which uncertainties exceed concentration measurements, arbitrarily chosen at $2.5\sigma_y$ (σ_z respectively). The ground effect is visible for vertical profiles at x* >= 2.5, for which the lower red dotted line reaches the ground level.

Conclusion

We analysed scalar fluctuations obtained experimentally from wind-tunnel measurements and we proposed a simple Bernoulli PDF to predict the concentration statistics. We find relationships between non central moments of scalar up to order 4 experimentally and we then tested a simple analytical model derived from Chatwin & Sullivan (1990) against wind-tunnel data collected from a point source in turbulent neutral boundary layer. We investigate further relationships between high order moments with the aim to express them as a function of the mean concentration field and some known aditional parameters. In particular, futur works would enable the concentration fluctuation maximum to vary perpendicularly to the wind direction, include ratios of moments that are constant experimentally and consider thermal stratification. Evolutions of the simple Bernoulli model including a larger range of possible concentration values will also be compared to experimental data, for which the source height and size impact will be detailed.

References

Abramowitz, M., & Stegun, I. A. (1965). *Handbook of Mathematical Functions, With Formulas, Graphs, and Mathematical Tables* (United States Department of Commerce, National Bureau of Standards). https://www.abebooks.fr/9780486612720/Handbook-Mathematical-Functions-Formulas-Graphs-0486612724/plp

Bertagni, M. B., Marro, M., Salizzoni, P., & Camporeale, C. (2019). Solution for the statistical moments of scalar turbulence. *Physical Review Fluids*, *4*(12), 124701. https://doi.org/10.1103/PhysRevFluids.4.124701

Cassiani, M., Bertagni, M. B., Marro, M., & Salizzoni, P. (2020). Concentration Fluctuations from Localized Atmospheric Releases. *Boundary-Layer Meteorology*, *177*(2), 461-510. https://doi.org/10.1007/s10546-020-00547-4

Chatwin, P. C., & Sullivan, P. J. (1990). A simple and unifying physical interpretation of scalar fluctuation measurements from many turbulent shear flows. *Journal of Fluid Mechanics*, *212*, 533-556. https://doi.org/10.1017/S0022112090002087

Fackrell, J. E., & Robins, A. G. (1982). Concentration fluctuations and fluxes in plumes from point sources in a turbulent boundary layer. *Journal of Fluid Mechanics*, *117*, 1-26. https://doi.org/10.1017/S0022112082001499

Gurka, R., Liberzon, A., Sarathi, P., & Sullivan, P. J. (2010). Diffusion of scalar concentration from localized sources in turbulent flows. *Reviews in Chemical Engineering*, *26*(1-2), 13-27. https://doi.org/10.1515/REVCE.2010.004

Jørgensen, H. E., Mikkelsen, T., & Pécseli, H. L. (2010). Concentration Fluctuations in Smoke Plumes Released Near the Ground. *Boundary-Layer Meteorology*, *137*(3), 345-372. https://doi.org/10.1007/s10546-010-9532-x

Marro, M., Nironi, C., Salizzoni, P., & Soulhac, L. (2015). Dispersion of a Passive Scalar Fluctuating Plume in a Turbulent Boundary Layer. Part II : Analytical Modelling. *Boundary-Layer Meteorology*, *156*(3), 447-469. https://doi.org/10.1007/s10546-015-0041-9

Nironi, C., Salizzoni, P., Marro, M., Mejean, P., Grosjean, N., & Soulhac, L. (2015). Dispersion of a Passive Scalar Fluctuating Plume in a Turbulent Boundary Layer. Part I : Velocity and Concentration Measurements. *Boundary-Layer Meteorology*, *156*(3), 415-446. https://doi.org/10.1007/s10546-015-0040-x

Sawford, B. L., & Sullivan, P. J. (1995). A simple representation of a developing contaminant concentration field. *Journal of Fluid Mechanics*, *289*, 141-157. https://doi.org/10.1017/S0022112095001273

Schopflocher, T. P., Smith, C. J., & Sullivan, P. J. (2005). *The interdependence of some moments of the PDF of scalar concentration*. 312-318. Scopus.

Turbulent flows around multi-scaled buildings - a comparative study of wind tunnel experiments and Large Eddy Simulations

B. Seitzer[1], F. Harms[1], B. Leitl[1]

[1]EWTL, Meteorological Institute, University of Hamburg, Bundesstr. 55, 20146 Hamburg, Germany

Introduction

Obstacle-resolving Large Eddy Simulations (LES) are increasingly applied in urban climate studies. This development stems from the fact that over decades, larger and faster computing systems have made it possible to model the urban climate at higher resolutions (Letzel et al. 2012; Tolias et al. 2018; Gronemeier and Sühring 2019; Auvinen et al. 2020). Whereas major urban structures can be resolved by LES in general, details like aerodynamically rough surface structures cannot be resolved explicitly due to limitations in computational resources or the lack of detailed building data. On the other hand, boundary conditions and sub-grid parameterisations in Large Eddy Simulations were initially formulated for surfaces of homogeneous roughness and for wall distances much larger than the roughness sublayer thickness, where turbulence is homogeneous and isotropic. Grid resolution, surface-boundary conditions and the choice of subgrid-scale models in obstacle-resolved Large Eddy Simulations should thus be a question of scales studied and have to be chosen carefully.
We will now further discuss the difficulties of object-resolved LES in urban climate simulations. Our analysis is first based on general considerations about length scales in urban environments, resolution requirements of numerical grids in LES and basic physical prerequisites for LES parameterisations. For this purpose, in a second step a comparison of experimental wind tunnel data obtained at the **EWTL** in Hamburg with corresponding Large Eddy Simulations using the urban climate LES model **PALM** is carried out.

Dominating length scales and grid-resolution requirements within the urban canopy layer

Figure 1 shows schematically which length scales are apparent and how they influence the wind within the urban canopy layer (UCL). A distinction is made between two flow regimes, namely the UCL flow and the near-wall flow. Both regimes naturally depend on ambient conditions such as temperature, humidity and pressure at synoptic scales. These variables are not to be examined in our distinction, which rather concerns geometric length scales.
The large-scale UCL flow is mainly influenced by the length scales $\boldsymbol{H_b}$, which corresponds to the building dimensions. This affects, for example, eddies in front and behind of buildings and flows through street canyons. In addition to the ambient conditions, the near-wall flow is mainly influenced by small-scale objects of size $\boldsymbol{h_r}$. These small-scale objects, as for example chimneys or balconies, generate turbulence and lead to roughness-dependent deviations in wind shear in the near-wall region.

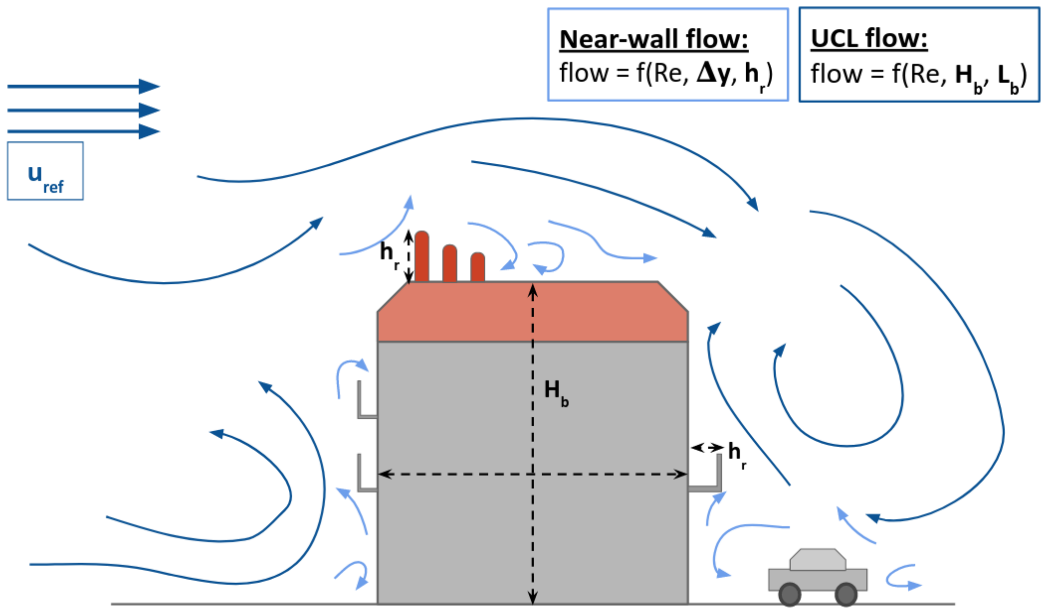

Figure 1: The sketch schematically shows the flow around a multi-scaled building. It is important to distinguish between two geometric length scales. On the one hand, large-scale objects of scale $\mathbf{H_b}$ such as buildings influence the large-scale flow structures. On the other hand, there are small-scale objects of scale $\mathbf{h_r}$ such as balconies, chimneys or cars which generate turbulence in the near-wall region.

In contemporary LES, the boundary conditions applied between the first grid level and ground surfaces or building facades are commonly based on the Monin-Obukhov Similarity Theory (MOST) with smaller or larger modifications (Hultmark et al. 2013).
Basu and Lacser (2017) discussed the choice of evaluation height for this class of boundary conditions and justify their recommendation for the smallest possible grid size $min(\Delta)=50 \cdot z_0$ by observations in laboratory and field measurements (Garratt 1980; Raupach et al. 1991). The roughness length z_0 usually is about one tenth of the roughness element height, which in the case of building facade roughnesses would be $z_0=0.1 \cdot h_r$ and thus $min(\Delta)=5 \cdot h_r$. Maronga et al. (2020) tried to solve this issue by raising the evaluation height of boundary conditions to higher grid levels. Nevertheless it is questionable if this approach is feasible within for example a street canyon.
While there are limitations for a minimum grid size due to boundary conditions, there are also limitations for the maximum possible grid size within the UCL. The effective resolution of an eddy in LES models is about 6 to 10 times the grid width (Cabot & Moin 2000). This depends on the actual flow situation as well as on the SGS-parameterisation in the model (Skamarock 2004). The largest eddies within the UCL are in recirculation zones behind freestanding buildings or in flows in street canyons. An estimate for the maximum possible grid size can thus be made and $max(\Delta)=0.1 \cdot H_b$.
Figure 2 illustrates the considerations on length scales in the urban canopy layer and their implications on numerical grid sizes in LES. It is apparent that in most cases, the maximum possible resolution is smaller than the minimum allowed resolution. This makes the task of properly resolving UCL flows at all length scales impossible and grid resolution should be chosen according to the phenomenon studied and the questions to be answered.

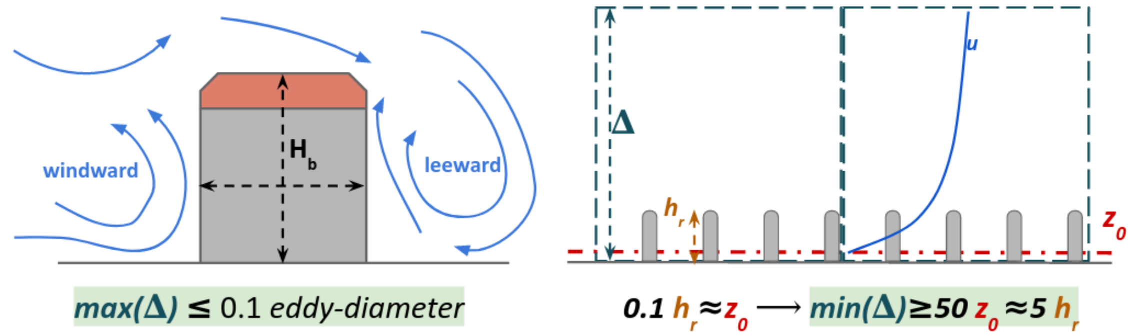

Figure 2: The urban canopy flow can be distinguished into two regimes from which, in turn, requirements for grid resolution can be derived. The maximum allowed resolution depends on building sizes and thus on the length scale $\boldsymbol{H_b}$. The minimum possible resolution depends on boundary condition requirements (Basu and Lacser 2017) and thus on the length scale $\boldsymbol{h_r}$. In most urban cases, the maximum possible resolution is smaller than the minimum allowed resolution.

Wind tunnel experiment of single multi-scaled buildings with varying facade roughnesses

At the wind tunnel **WOTAN** located at **EWTL** in Hamburg, we conducted wind tunnel experiments of three single multi-scaled building models. These model buildings have the same large dominating length scales as the building height and lengths, but differ in the smaller length scales as roughnesses attached to the building facade. The aim is to show that the flow around a multi-scaled building can be distinguished into two regions, each dominated by the length scales mentioned above. By varying the smaller facade roughnesses and keeping the larger scales the same for every setup a direct comparison is possible. All lengths will be given in full scale. The scale of the experiment was *1:500*.

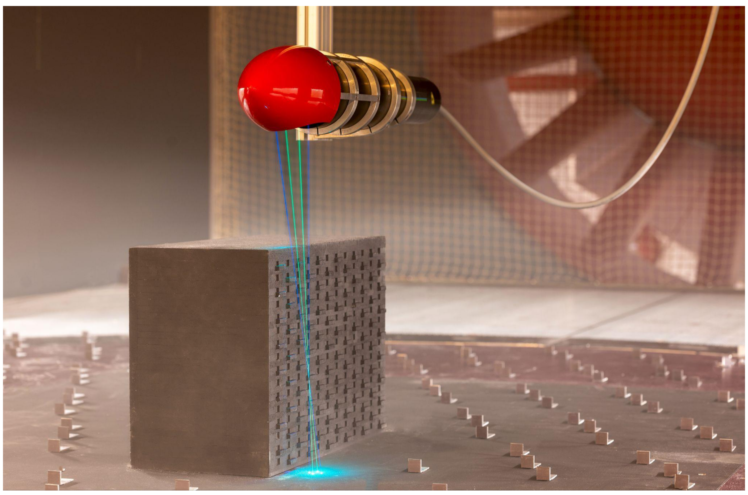

Figure 3: Multi-scaled building model with height $\boldsymbol{H_b}$=*50.4*m, length $\boldsymbol{L_b}$=*76.5*m and width $\boldsymbol{W_b}$=*34.5*m. The much smaller balcony-like facade roughnesses of depth $\boldsymbol{h_r}$=*0.9*m are visible on the facade next to the laser beams. The LDA-probe measuring the near-wall wind in U-V-mode is visible above the model building. The *u*-component is the main wind direction and *v* is the wall-normal horizontal component.

The model buildings were placed into a boundary layer flow and the long edge was aligned with the longitudinal, main wind direction *u*. The approach boundary layer flow has a roughness length of

$z_{0,b}=(0{,}071\pm0{,}003)$m and was tested for lateral homogeneity. The used reference velocity u_{ref} was calculated by scaling the velocity u_{in} measured at the inlet of the windtunnel with the ratio of the boundary layer velocity $u_{BL,ref}$ at reference height $z_{ref}=45$m and the corresponding inlet velocity of that measurement $u_{BL,in}$ such that $u_{ref} = u_{in} \cdot u_{BL,ref} / u_{BL,in} = 0.738 \cdot u_{in}$. All shown measurements were obtained as wall-normal profiles at mid-building-height $z=25{,}2$m. The measurement time for each point was $T_{mes}=7.5$h.

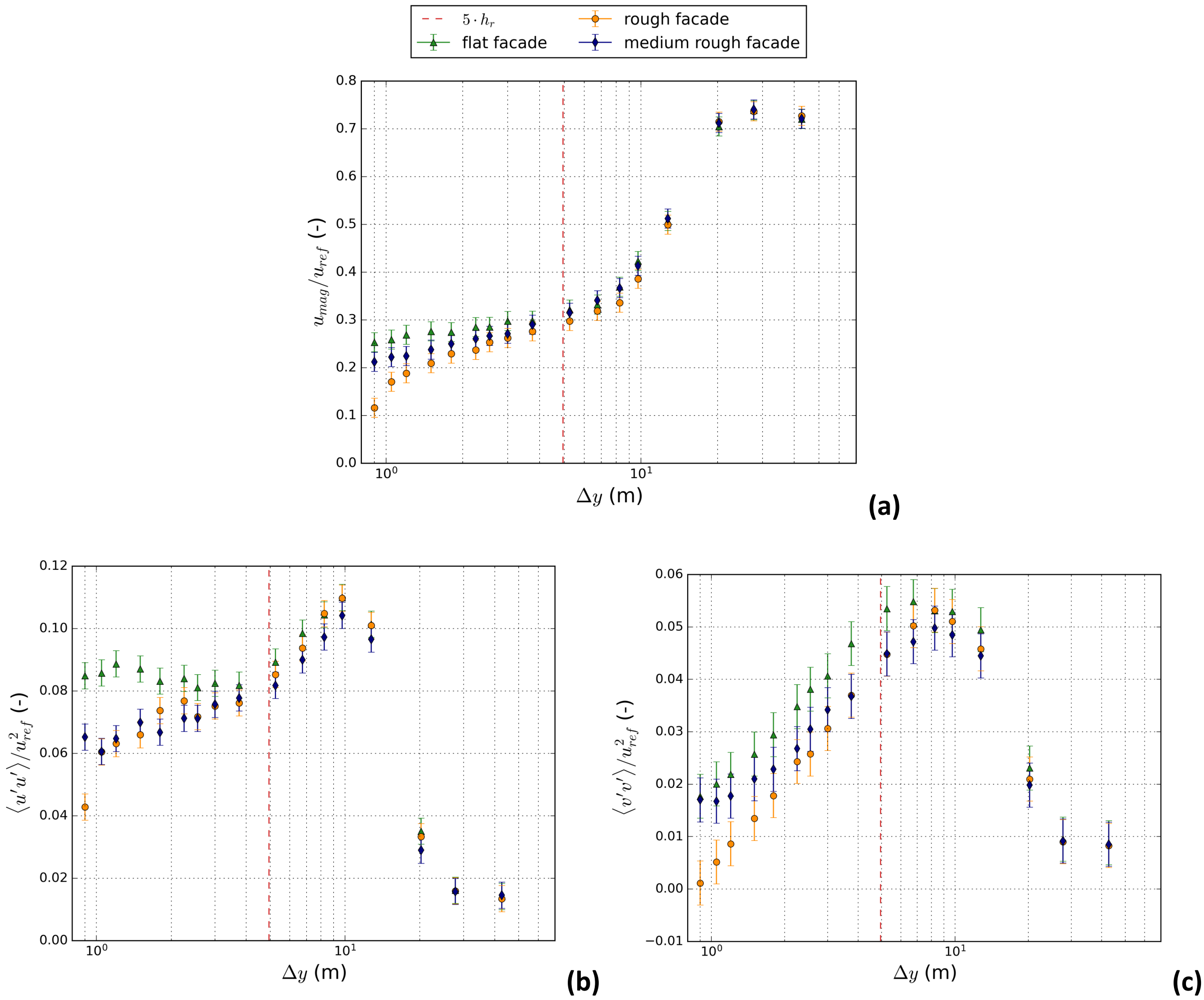

Figure 4: Shown are the fractional velocity magnitude (a), and the variances of the two measured wind components *u* (b) and *v* (c) as a function of the wall distance Δy. The vertical dashed line marks the wall distance $5 \cdot h_r=4.5$m at which a change in flow regimes is expected.

The results depicted in Fig. 4 clearly show that a distinction of flow regimes into near-wall flow and UCL flow is possible even at more complex flow cases than simple boundary layer flows over horizontal surfaces of uniform roughness. The fractional velocity magnitudes are calculated from the *u* and *v* components. As can be seen in Fig. 4 (a), the near-wall velocities are highest for the flat facade (green) with no small-scale obstacles attached to the wall. The wind shear is higher for the medium rough (blue) and rough facade (orange) and thus, velocity-magnitudes are lower in the near-wall region. At $\Delta y>5 \cdot h_r$, the wind magnitudes do not differ significantly any more and at $\Delta y=20$m onwards, the values stay constant. The horizontal variances shown in Fig. 4 (b) and (c) show similar behaviour concerning roughness dependent variations in the near-wall region. One would expect the variances to increase at higher facade roughnesses since they cause higher wind shear. This is not the case, which speaks for a strong three-dimensionality of the flow as only the horizontal components were measured. As a matter of fact, also the co-variances $\langle u'v' \rangle$ do show similar behaviour as the variances.

The effect of near-wall wind shear is not only visible in variances and wind magnitude profiles. Turbulence cospectra show deviations from the classical Kolmogorov-scaling in the inertial subrange (see Fig. 5 (a)). Whereas larger eddies do not show strong variations in the near-wall region, smaller energies (high frequencies) vary strongly in the inertial subrange dependent on the facade roughness. This effect is also visible as a function of the wall distance Δy. Figure 5 (b) shows the scaling factor m - the slope of the cospectra in the inertial subrange - as a function of Δy. In the near-wall region spectral scalings differ. With increasing wall distance, the spectral scaling factor m approaches Kolmogorov-scaling. There might be several possible reasons for the increased energy-production in the near-wall region and thus the scaling-deviations. The first reason could be that the increased wind shear leads to a faster transfer of kinetic energy to smaller vortices. Another source for the differences could be a roughness-dependent anisotropy of the near-wall turbulence. In both cases, this flow behaviour has implications on SGS-models used in LES, which are based on assumptions from isotropic turbulence.

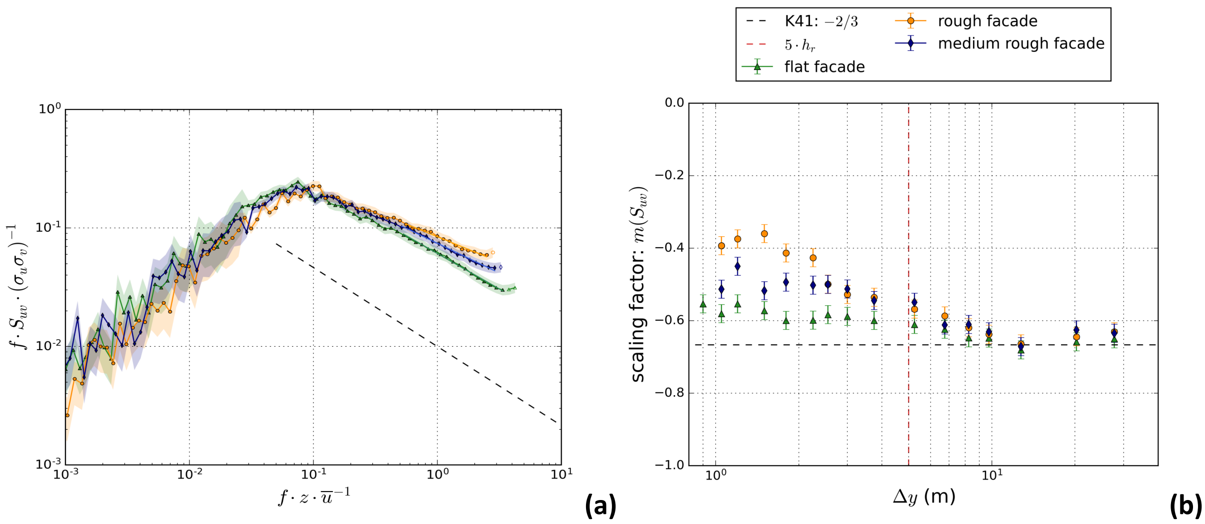

Figure 5: Spectral scaling deviates from Kolmogorov-scaling (grey dashed line) depending on facade roughness and wall distance. The spectra shown in (a) are turbulence cospectra at wall distance Δy=*2.25*m in the near-wall region. The slope m in the inertial subrange approaches the Kolmogorov-scaling further away from the wall (visible on the right in (b)). The red dashed line again shows the wall distance at which the transition between near-wall and UCL flow is expected

Numerical Large Eddy Simulations of the single buildings case

The wind tunnel experiments will be compared to LES simulations of a single building case using **PALM** (Maronga et al. 2020). The numerical setup uses cyclic boundary conditions and a conserved volume flow as forcing. The approaching boundary layer is taken from the wind tunnel experiments and prescribed to the numerical model. In the middle of the *1024*m long domain, the single building is placed. The domain needs to be long enough such that the effect of the building does not replicate itself at the cyclic boundaries and the approach flow in front of the building is not affected. The grid is cartesian, uniform and of a grid size of Δ=*1*m. Figure 6 shows a x-z-cross section of the longitudinal velocity *u* at one timestep.

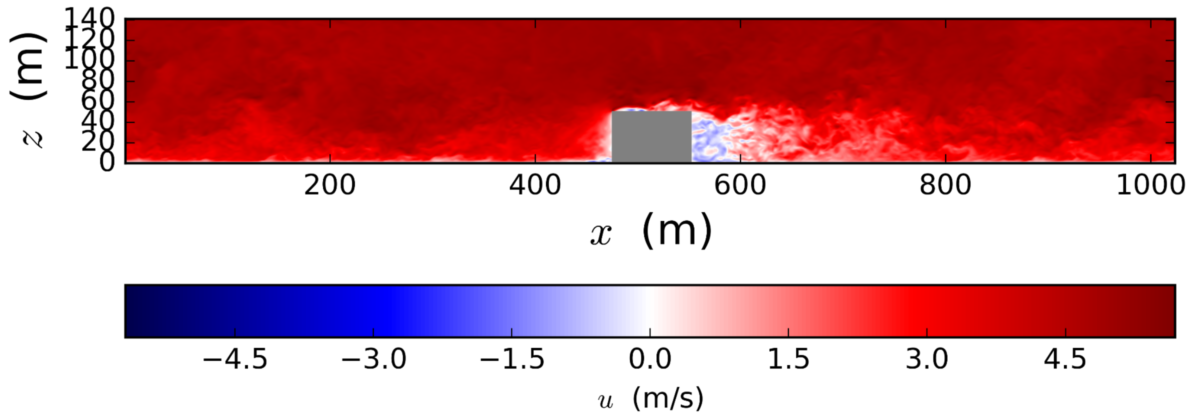

Figure 6: A x-z-cross section of the longitudinal velocity *u*. The building effect on the flow is visible in front, over and especially behind the building. The computational domain needs to be long enough such that building effects vanish before being replicated at the cyclic domain boundary.

The numerical simulations are not finalised until submission of this extended abstract, but will be by the time of the Physmod conference. Because of these circumstances, a direct comparison is not yet possible.

Conclusions and Outlook

A dimensional analysis of flow regimes in a generic representation of the urban canopy layer has been done and two flow regimes could be identified. First, there is the UCL flow, which is dominated by large scale motions and eddy sizes which scale with building heights or street canyon widths. Another regime is the near-wall region, where the flow scales with small scale obstacles and varying building facade roughnesses. As a result, a single multi-scaled building experiment was designed to test if these two flow regimes actually can be distinguished in experimental data in a complex setting. The wind tunnel data shows strong roughness-dependent deviations in all flow measures in the near-wall region. By looking at turbulence cospectra, deviations from the Kolmogorov scalings can be found, depending on the facade roughness. These deviations are likely to be caused by wind-shear and flow-anisotropy close to the facade. These deviations are expected to be one of the reasons why obstacle-resolving LES-models in urban climate simulations tend to become inaccurate close to building surfaces.
A comparison with numerical data will be done in the upcoming months until the time of the Physmod conference.

References

Auvinen M, Boi S, Hellsten A, Tanhuanpää T, Järvi L (2020) Study of realistic urban boundary layer turbulence with high-resolution Large Eddy Simulation. Atmosphere 11(2):1–41

Basu S, Lacser A (2017) A Cautionary Note on the Use of Monin-Obukhov Similarity Theory in Very High-Resolution Large Eddy Simulations. Boundary-Layer Meteorology, 163(2):351–355

Cabot, W., & Moin, P. (2000) Approximate wall boundary conditions in the Large Eddy Simulation of high Reynolds number flow. Flow, Turbulence and Combustion, 63(1), 269-291.

Garratt JR (1980) Surface influence upon vertical profiles in the atmospheric near-surface layer. Q J R Meteorological Society 106(450 , Oct. 1980):803–819

Gronemeier T, Sühring M (2019) On the effects of lateral openings on courtyard ventilation and pollution-A Large Eddy Simulation study. Atmosphere 10(2):63

Hultmark M, Calaf M, Parlange MB (2013) A new wall shear stress model for atmospheric boundary layer simulations. Journal of Atmospheric Sciences 70(11):3460–3470

Letzel MO, Helmke C, Ng E, An X, Lai A, Raasch S (2012) LES case study on pedestrian level ventilation in two neighbourhoods in Hong Kong. Meteorologische Zeitschrift 21(6):575–589

Maronga, Björn, et al. (2020) Overview of the PALM model system 6.0. Geoscientific Model Development 13.3: 1335-1372.

Maronga, B., Knigge, C., & Raasch, S. (2020). An improved surface boundary condition for Large Eddy Simulations based on Monin–Obukhov similarity theory: Evaluation and consequences for grid convergence in neutral and stable conditions. Boundary-Layer Meteorology, 174(2), 297-325

Raupach MR, Antonia RA, Rajagopalan S (1991) Rough-wall turbulent boundary layers. Appl Mech Rev 44(1):1–25

Skamarock, W. C. (2004) Evaluating mesoscale NWP models using kinetic energy spectra. Monthly weather review, 132(12), 3019-3032.

Tolias IC, Koutsourakis N, Hertwig D, Efthimiou GC, Venetsanos AG, Bartzis JG (2018) Large Eddy Simulation study on the structure of turbulent flow in a complex city. J Wind Eng Ind Aerodyn 177(February):101–116

Wind tunnel measurement on the flow and traffic emission dispersion around roadside building with green vegetation belt

B.S. Shiau[1, 2], H.P. Huang[2], P.H. Cao[2], W.P. Huang[2]

[1]Institute of Physics, Academia Sinica, Taipei, Taiwan
[2]Department of Harbor and River Engineering, National Taiwan Ocean University, Keelung, Taiwan

Abstract

The green vegetation belt has been shown reductive effects on air-borne pollutants concentrations, therefore is usually designed to use as improving the local air quality in roadside buildings. In the present study, the wind tunnel model experiments were performed to investigate the flow and traffic emission of air borne pollutants dispersion around roadside building with different heights of green vegetation belts under a turbulent boundary layer flow. Flow measurements of the canopy of green vegetation belt and roadside buildings incorporated with smoke flow visualization by laser light sheet were made. Methane mixing with pure air was adopted to simulate the air borne pollutant. Line source was employed to simulate the road traffic emission. The sampled tracer was analysed by the flame ionization detector (FID) to yield the mean concentration. The leaf area density (LAD) of green vegetation belt model was $2m^2m^{-3}$ which represented the medium dense vegetation. Measured wind speed profile shows that wind speed changes significantly with increasing the green vegetation belt height. The distribution of the concentration is strongly affected by the cavity flow in the region between the green vegetation belt and building. The higher the green vegetation belt, the induced updraft motion became more significant. The updraft motion lofts the traffic emission plume. Concentration distribution measurements exhibited the vertical dispersion parameter (dispersion length scale) of each downwind distance of source decreased as the height of green vegetation belt increased in the region between green vegetation belt and building. As increasing the height of green vegetation belt leads to lower the vertical location of centroid of pollution cloud due to accumulation.

Introduction

Due to the significant impact of traffic emissions of urban roads on the public health of nearby region polulation, this motivated the study of feasible method to reduce exposure to these pollutants. The traffic emissions including fine particulate matters and gaseous pollutants will caused serious impact on air quality around the roadside environment. James *et al.* (2016) have shown that green infrastructure and vegetation have overall health benefits, such as lower obestity, increased physical activity, mental health improving, lower adverse cardiovascular illness, decreased mortality. Trees or green infrastructure can filter the fine particulate matters and gaseous pollutants, thus the green infrastructure or vegetation is usually designed to use as improving the local environment air quality around roadside. Baldauf (2017) indicated one of feasible ways to improve local or near road air quality was to plant trees or other vegetation which reduced regional air quality pollution levels through the interception of airborne particles or through the uptake of gaseous air pollutions through leaf stomata on the plant surface. Diener and Mudu (2021) made a critical review on how vegetation can protect us from air pollution and green spaces' mitigation abilities for air-borne particles from a public health perspective. Podhajska *et al.* (2020) had developed a scheme for shaping urban plantings which acts as barriers against particulate pollution. Their method has rather complex. Zheng, *et al.* (2021) performed field measurements on three common street vegetation configurations for particle pollution concentrations in the near-by region. Ghasemian *et al.* (2017) applied numerical simulations on the roadside solid and vegetation barriers on near-road air quality. Tong *et al.* (2016) applied numerical method of CTAG and LES models to investigate the effects of vegetation and wall barriers on near-road air quality of size-resolved particle concentrations.

The main purpose of this wins tunnel study is aim at the medium dense green vegetation belt height affects the wind flow and dispersion of airborne pollution around the roadside building. Flow measurements of the canopy of green vegetation belt and roadside buildings incorporated with smoke flow visualization by laser light sheet were made. Methane mixing with pure air was adopted to simulate the air borne pollutant. Line source was employed to simulate the road traffic emission. The measured pollution concentration distributions were applied to analyse the statistical dispersion characteristics, such as pollution plume centroid and dispersion parameter. Results can offer to assess the roadside building air pollution impacts and to provide the effective suggestions and guidance in achieving better urban air quality environment for roadside vegetation planning and design strategies.

Experimental set-up

The experiments are conducted in the wind tunnel which had a cross section of 2 m wide by 1.4 m high and 12.6 m long. The tunnel is an open suction type and it contracts to the test section with an area ratio of 4:1. The turbulence intensity of empty tunnel in test section is less than 0.5% at the mean velocity of 5 m/s. our spires of 100 cm height were set up laterally with equal spaces. The roughness elements (0.05 m x 0.05 m x 0.05 m) were succeeded to the spires and they were properly deployed 9 m long on the test section. Such arrangement was to generate a fully developed turbulent boundary layer which was used as the approaching flow.

The model scale was 1:100. The green vegetation belt models are with length of 60cm, width of 3cm and heights of 9cm, 6cm, and 3cm. Fig.1 is picture of the green vegetation belt model. Roadside building model has the dimension of 24cm high, 10cm wide, and 60cm in length. The averaged leaf area density (LAD) of green vegetation model is $2m^2m^{-3}$ as suggested by Gromke and Blocken (2015) for medium dense vegatation.

Fig.1. The green vegetation belt models with different heights; medium dense vegetation of LAD= $2m^2m^{-3}$

Methane was used as tracer gas and it mixed with the standard gas. The tracer gas was a mixture of volume ratio of 1:9 for methane and standard gas. So tracer gas was slightly lighter than the ambient environment of air. The collected tracer gas concentration was measured by using FID (Flame Ionization Detector) device.

For dimensional analysis, the control dimensioness parameters for the wind tunnel model study is shown as following:

$$\pi = F\left(\frac{x}{W}, \frac{z}{\sqrt{H_t H_b}}, \frac{H_t}{W}, \frac{H_b}{W}, \frac{W_r}{W}, Fr, R_e\right) \tag{1}$$

Where *x* is downwind distance form the line source, *z* is the vertical distance from the ground, H_t is green vegetation height, H_b is the building height, W_r is the road width, *W* is the width of building, *Fr* is the densimetric Froude number of line emission, *Re* is the Reynolds number of approaching flow. In the wind tunnel model experiment, we choose Fr=40, Re=3*10^5, H_t/W=0.3, 0.6, 0.9, H_b/W=2.4, W_r/W=2. The distance between green vegetation belt and building is 0.5*W*. and U_{ref} is the free stream velocity of approaching flow.

Smoke flow visualization and Canopy Flow Velocity Profiles

The smoke flow visualization with laser light sheet on flow pattern between green vegetation and building for different vegetation belt heights are shown in Fig.2. The flow pattern shown in the figures revealed that the higher the green vegetation belt is, the induced updraft motion becomes more significant. The downwash flow was also clearly shown on the facade of building.

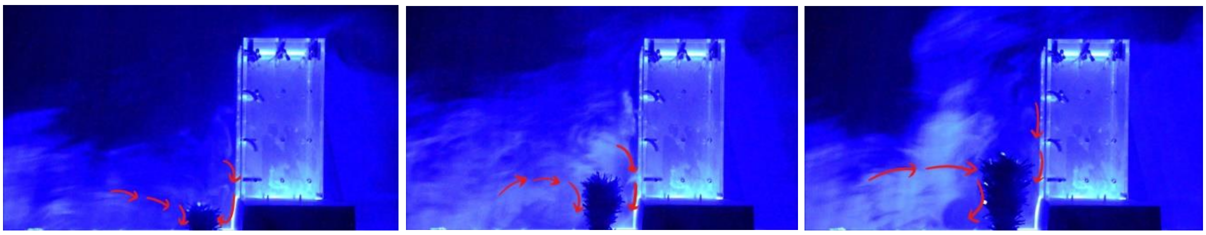

Fig.2. Smoke flow visualization of flow pattern between green vegetation belt and building; green vegetation belt heights form left to right are 0.3W, 0.6W, and 0.9W, respectively; W is building width

The mean velocity profiles above the green vegetation belt canopy along downstream of emission source for green vegetation belt height 0.3W are shown as Fig.3. The canopy flow velocity profiles varies significantly between the stations x/W=1 and x/W=1.5. The velocity variations are due to the building inducing updraft motion. Therefore, the mean velocity increased considerably. At x/W=2 of building roof centre, the canopy flow velocity decreased sharply because of flow recirculation.

Fig.4 shows the canopy flow mean velocity profiles at upstream of green vegetation belt (x/W=0.5) station and facade of building (x/W=1.5) station for different heights of green vegetation belt.

The figure exhibits that when the heights of green vegetation belt varies, the mean velocity profiles changes unsignificantly at upstream of green vegetation belt (x/W=0.5) station. At the facade of building (x/W=1.5) station, the lower portion of canopy flow mean velocity profiles indicates the mean velocity increasing as the height of green vegetation belt increasing. For the upper portion of canopy flow mean velocity profiles, the variations of mean velocity become unsignificantly for varying he height of green vegetation belt. That is a higher of green vegetation belt lofts the wind flow, therefore the lower portion of canopy flow around the facade of building was significantly affected due to circulation region flow lofing and increasing the velocity. Ahangar *et al.* (2017) studied reduction of air pollution levels downwind of aroad with an upwind noise barrier, they obtained the circulation region becomes larger as the height of noise barrier increasing. And circulation region lofts wind flow and affected canopy flow velocity. This induces the canopy flow velocity increasing as circulation region becoming larger.

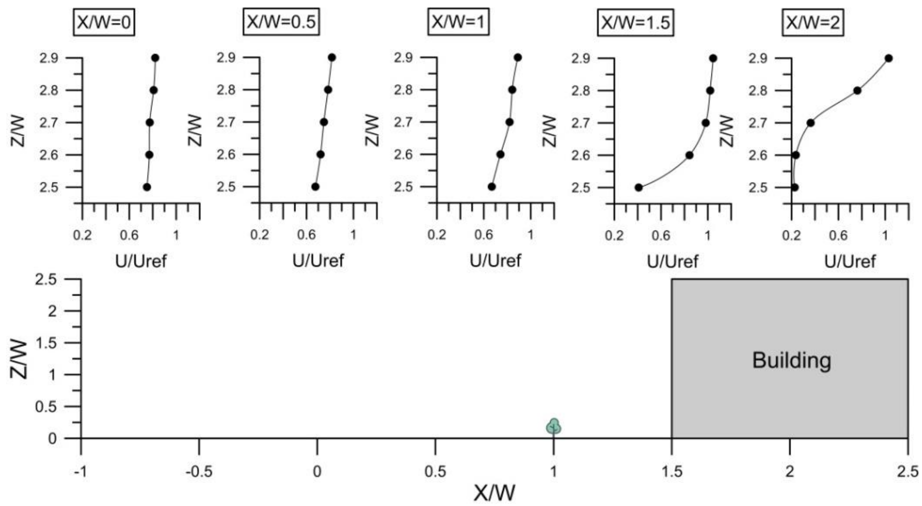

Fig.3. Mean velocity profiles along the downwind stations; green vegetation belt height 0.3W

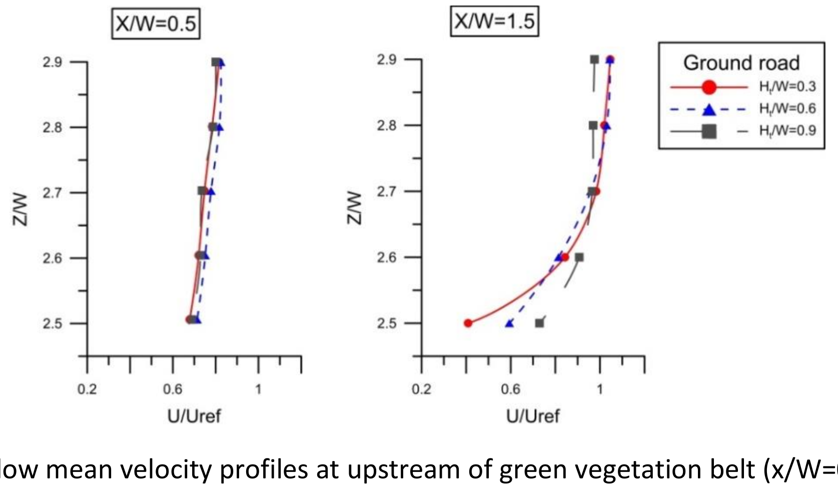

Fig. 4. Canopy flow mean velocity profiles at upstream of green vegetation belt (x/W=0.5) station and facade of building (x/W=1.5) station for different heights of green vegetation belt

Concentration distribution

The measured concentration C is in nondimesional parameter, K which is expressed as:

$$K = \frac{C L_x L_y U}{Q^*} \tag{2}$$

where L_x is the length of line source, L_y is the width of line source, Q^* is the emission flow rate, U is the characteristic reference velocity.

Fig.5 shows the concentration contour around the green vegetation belt and building with green vegetation belt height of 0.3W. Due to the obstruction of green vegetation belt and building on the oncoming flow, it leads to the pollution concentration accumulation occurred at regions ahead of the green vegetation belt and facade of building (Refer to Fig.5). The pollution concentration contours for green vegetation belts with heights of 0.6W and 0.9W also have revealed the similar results, i.e. pollution was found to accumulate around the regions ahead of the green vegetation belt and facade of building.

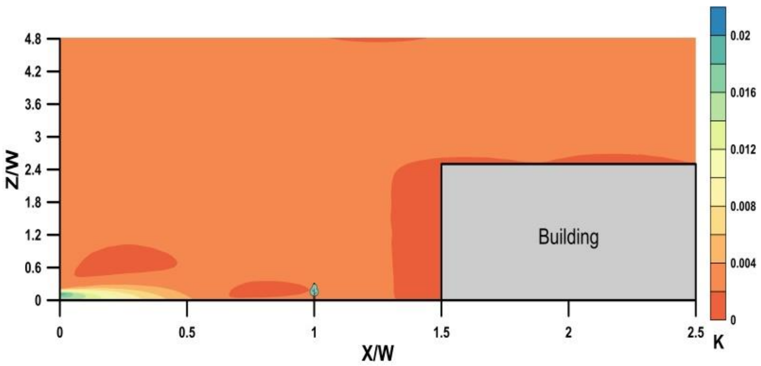

Fig.5. The concentration contour around the green vegetation belt and building; green vegatation belt height 0.3W

Fig.6 are the concentration vertical profiles for downwind stations of source with (green vegetation belt heights 0.3W, 0.6W) and without (no barrier) green vegetation belt. As comparing the concentration profiles at x/W=1 (green vegetation location) for with and without green vegetation belt, it shows that shelter effect the green vegetation caused significantly reduction of the pollution concentration at positions lower than the green vegetation belt height. Lin *et al*. (2016) made a field study on the effects of vegetation barriers on the near-road ultrafine particle number and carbon monoxide concentrations. They found that without foliage shelter on the road-side will have higher ultrafine particle and CO concentrations. That is green vegetation belt is favourable to reduce and lower the concentration of air pollution.

Emission plane plume characteristics

The emission formed a plane plume. The plume interacted with the green vegetation belt and the building. To investigate the effects of the green vegetation belt and building on the pollution dispersion, the plume characteristics are necessary and they are able to show how the affection of the green vegetation and building barriers on the pollution dispersion. The pollution cloud of plume statistical characteristics, such as centroid of pollution cloud $Z_c(x)$, plume dispersion parameter $\sigma(x)$ can be obtained from the wind tunnel measurement of the tracer concentration distributions at different downwind distances of line source. Calculations of the centroid and dispersion parameter of plume along downwind distance of source are as follows:

$$Z_C(x) = \int_0^\infty zC(x,z)dz \,/\, \int_0^\infty C(x,z)dz \tag{3}$$

$$\sigma_z(x) = \left[\int_0^\infty (z - Z_C)^2 C(x,z)dz \,/\, \int_0^\infty C(x,z)dz\right]^{1/2} \tag{4}$$

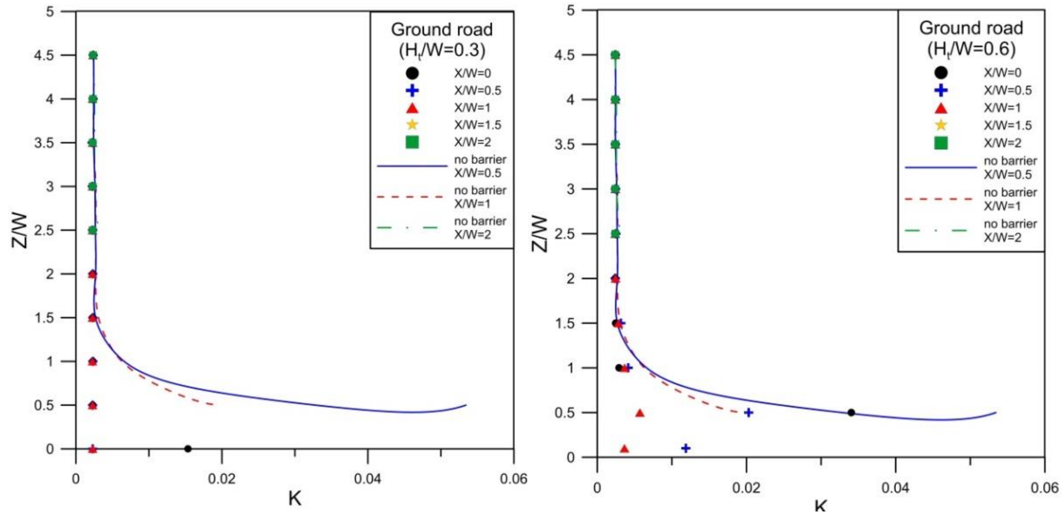

Fig.6. Comparison of the concentration vertical profiles for downwind stations of source with and without (no barrier) green vegetation belt; Left figure green: vegetation belt height 0.3W, Right figure: green vegetation belt height 0.6W

Both the heights of green vegetation (H_t) and building (H_b) have effects on the flow and pollution dispersion, the centroid location, Z_c and dispersion parameter, σ_z are scaled by $\sqrt{H_t * H_b}$. The plume centroid along the downwind distance of source for different heights of green vegetation belt are shown in the Fig.7. Fig.7 shows that plume centroid location around the region between the green vegetation and building ($1 \leq$ x/W$\leq$ 1.5) becomes lower as increasing the height of the green vegetation. This implies that higher green vegetation belt reduced larger reverse flow area in the region of $1 \leq$ x/W$\leq$ 1.5, such that pollution concentration accumulated, therefore the centroid location of the concentration distribution become lower. Fig.8 is the dispersion parameter as functions of downwind distance of source for various heights of green vegetation belt and without green vegetation belt. The plume dispersion parameter is an indicator of the extent of pollution dispersing. Results of Fig.8 show that the dispersion parameters along the downwind distance of source for various heights of green vegetation belt and without green vegetation belt. At the region of downwind distance of source 1≤ x/W≤ 1.5, dispersion parameters decrease as incresing the heights of green vegetation belt due to circulation effect inducing concentration accumaulation. Steffens *et al.* (2014) study on effects of the roadway configurations on the near-road air quality. Their results also show the barriers on the near road induce the flow circulation zone behind the barriers causing the pollution accumulation.

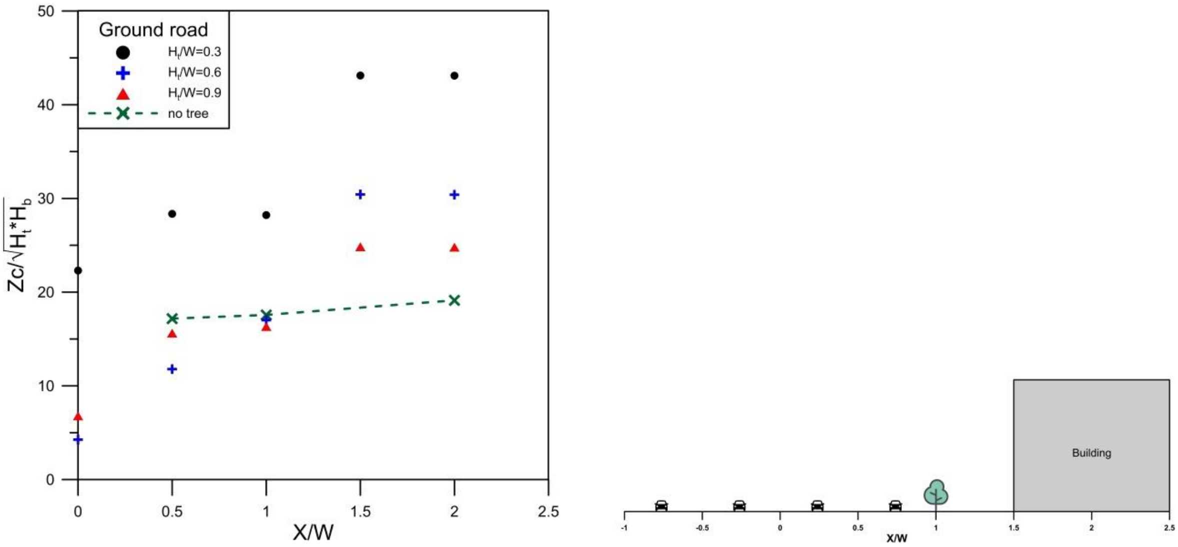

Fig.7. Centeroid of concentration distribution along downwind distnace for various heights of green vegetation belt

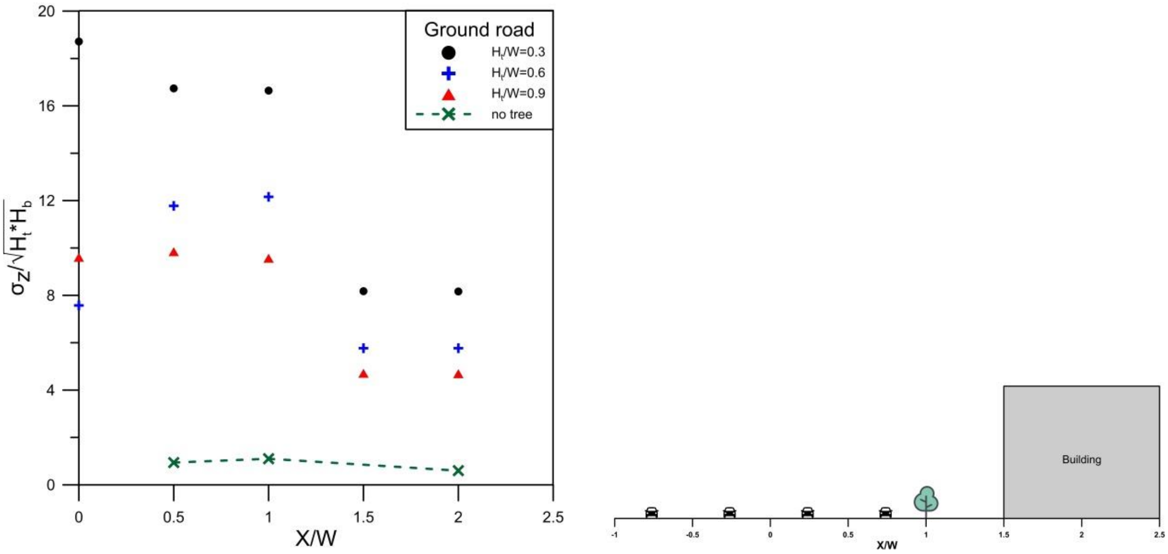

Fig.8. Dispersion parameter as functions of downwind distnce of source for various heights of green vegetation belt and without green vegetation belt

Conclusion

Wind tunnel model experiments were performed to investigate the flow and traffic emission of air borne pollutants dispersion around roadside building with different heights of green vegetation belts under a turbulent boundary layer flow. Measured wind speed profile shows that wind speed changes significantly with increasing the green vegatation belt height. The distribution of the concentration is strongly affected by the cavity flow in the region between the green vegatation belt and building. The higher the green vegetation belt, the induced updraft motion became more significant. The udraft motion lofts the traffic emission plume. Concentration distribution measurements exhibited the vertical dispersion parameter (dispersion lenth scale) of each downwind distance of source decreased as the height of green vegetation belt increased in the region between green vegetation belt and building. As incerasing the height of green vegetation belt leads to lower the vertical location of centroid of pollution cloud due to accumulation.

References

1. Ahangar, F.E., Heist, D., Perry, S., Venkatram, A., 2017, Reduction of air pollution levels downwind of a road with an upwind noise barrier, *Atmospheric. Enviroment,* Vol. 155, pp. 1-10.

2. Baldauf, R., 2017 Roadside vegatation design to improve local, near-road air quality, T*ansportation Research D Transportation Environment*, Vol.52, No.11, pp.354-361.

3. Diener, A., and Mudu, P., 2021 How can vegetation protect us from air pollution ? Acritical review on green spaces‘ mitigation abilities for air-borne particles from a public health perspective – with implications fro public urban planning, *Science of Total Environment*, Vol.796, 148605

4. Ghasemian, M., Amini, S., and Princevac, M., 2017, The influence of roadside solid and vegatation barriers on near-road aie quality, *Atmospheric Environment*, Vo. 170, pp.108-117.

5. Gromke, C., Blocken, B., 2015, Influence of avenue-trees on air quality at the urban neighborhood scale. Part I: Quality assurance studies and turbulent Schmidt number analysis for RANS CFD simulations, *Environment Pollution*, Vol. 196, pp. 214-223.

6. James, P., Hart, J.E., Banay, R.F., and Laden, F., 2016 Exposure to greenness and mortality in a nationwide , Prospective Cohort Study of Women Environ Health Perspect.

7. Lin, M.Y., Hagler, G., Baldauf, R., Isakov, V., Lin, H.Y., and Khlystov, A., 2016, The effects of vegetation barriers on near-road ultrafine particle number and carbon monoxide concentrations, *Science of the Total Environment*, Vol.553, pp.372-379.

8. Podhajska, E., Halarewicz, A.A., Zienowicz, M., Deszcz,R., and Podhajski, B., 2020, Structural and parametric aspects of plnt barriers as a paasive method for improving urban air quality, *City and Environment Interactions*, Vol.8, 100048.

9. Steffens, J.T., Heist, D.K., Perry, S.G., Isakov, V., Baldauf, R.W., and Zhang, K.M., 2014, Effects of roadway configurations on near-road air quality and the implications on roadway designs, *Atmospheric Environment*, Vol. 94, pp. 74-85.

10. Tong, Z., Baldauf, R., Isakov, V., Deshmukh, P., and Zhang, K.M., 2016, Roadside vegetation barrier design to mitigate near-road air pollution impacts, *Science of the Total Environment*, Vol.541, pp.920-927.

11. Zheng, T., Jia, Y.P., Zhang, S., Li, X.B., Wu Y., Wu, C.L., He, H.D., and Peng, Z.R., 2021, Impacts of vegetation on particle concentrations in roadside environments, *Environmental Pollution*, 282, 117067.

Tall buildings drag: the effect of multiscale urban morphologies

C. Southgate-Ash[*], M. Placidi[*]

[*]University of Surrey, Faculty of Engineering and Physical Sciences, Centre for Aerodynamics and Environmental Flow, Guildford, GU2 7XH, United Kingdom

1. Introduction

Experts estimate that by 2050, more than half of the world's population will live in cities, where tall buildings will be ever more prominent (DESA, 2019). How these tall buildings affect the wind and temperature fields within cities is important for both air quality and pedestrian comfort. It is therefore crucial to be able to understand their effect and provide reference data for policymakers and regulators to ultimately contribute to more accurate weather and air quality modelling. Modern tall buildings are characterised, by nature, by several length scales. For example, a tall building will have its largest length scale in height - this can often be an order of magnitude larger than its width, which in turn has a length scale an order of magnitude larger than its external roughness features (e.g., balconies). Despite the multiscale nature of real-world urban flows, much of the previous work (both experimental and computational), for simplicity, has considered cuboid buildings with a single length scale (Castro, 2002; Coceal, et al., 2006). There has been an effort to relate the aerodynamic parameters of urban morphologies to measures of surface morphometry, most commonly frontal and plan solidities (λ_f and λ_p, respectively) with some success (Macdonald, 2000; Grimmond & Oke, 1998). However, these methods are often only applicable to simplified cuboid models with the results extrapolated to non-cubic arrays lacking physical justification (Barlow & Coceal, 2009).

Work on multiscale roughness has aimed at quantifying the effect of the smaller scales on the flow, particularly in respect to aerodynamic properties such as drag (Vanderwel & Ganapathisubramani, 2019). They showed that the smallest geometric scales, which were an order of magnitude smaller than the largest, had a negligible impact on the overall drag generated by the surface. It is important to note that their work considered heterogeneous roughness patches and not tall buildings showcasing multiscale characteristics. However, work on drag and wake characteristics of flat plates with multiscale fractal geometries has shown that the smallest scales can have a non-negligible impact on the drag of up to 7% (Nedic, et al., 2013). They also showed that the size of the wake has some dependence on the smaller scales with an increase in fractal dimension leading to a decrease in wake volume. These plates were not submerged in an urban boundary layer, but nonetheless showed that a significant change in drag and wake characteristics can be seen without changing the frontal area of the bluff body.

In this study, we consider a set of buildings characterised by multiscale roughness immersed in an atmospheric boundary layer (where the relative height of the buildings to the boundary layer thickness is approximately z/δ=0.25 and 0.4). A simple cuboid and square cylinder building (with aspect ratio, AR, of 1 and 3 respectively) were used, with two fractal iterations that each added a roughness scale an order of magnitude smaller than the previous; for a total of 6 basic building shapes. Through these six buildings, the frontal and plan solidities remain the same, isolating the effect of the various length scales on the wake flow structure. The drag around each building was measured using an independent floating-element (FE) force balance. These results will be used to validate pressure measurements obtained via static pressure ports embedded in the buildings themselves. The talk will present pressure fields around multiscale buildings in isolation and in small clusters.

2. Experimental Details and Setup

2.1 Fractal Building Models

The six building models are shown in Figure 1. These are designed to be arranged such that the frontal and plan solidity of all building models is fixed at nominally $\lambda_f = 0.24$ and $\lambda_p = 0.2$, respectively.

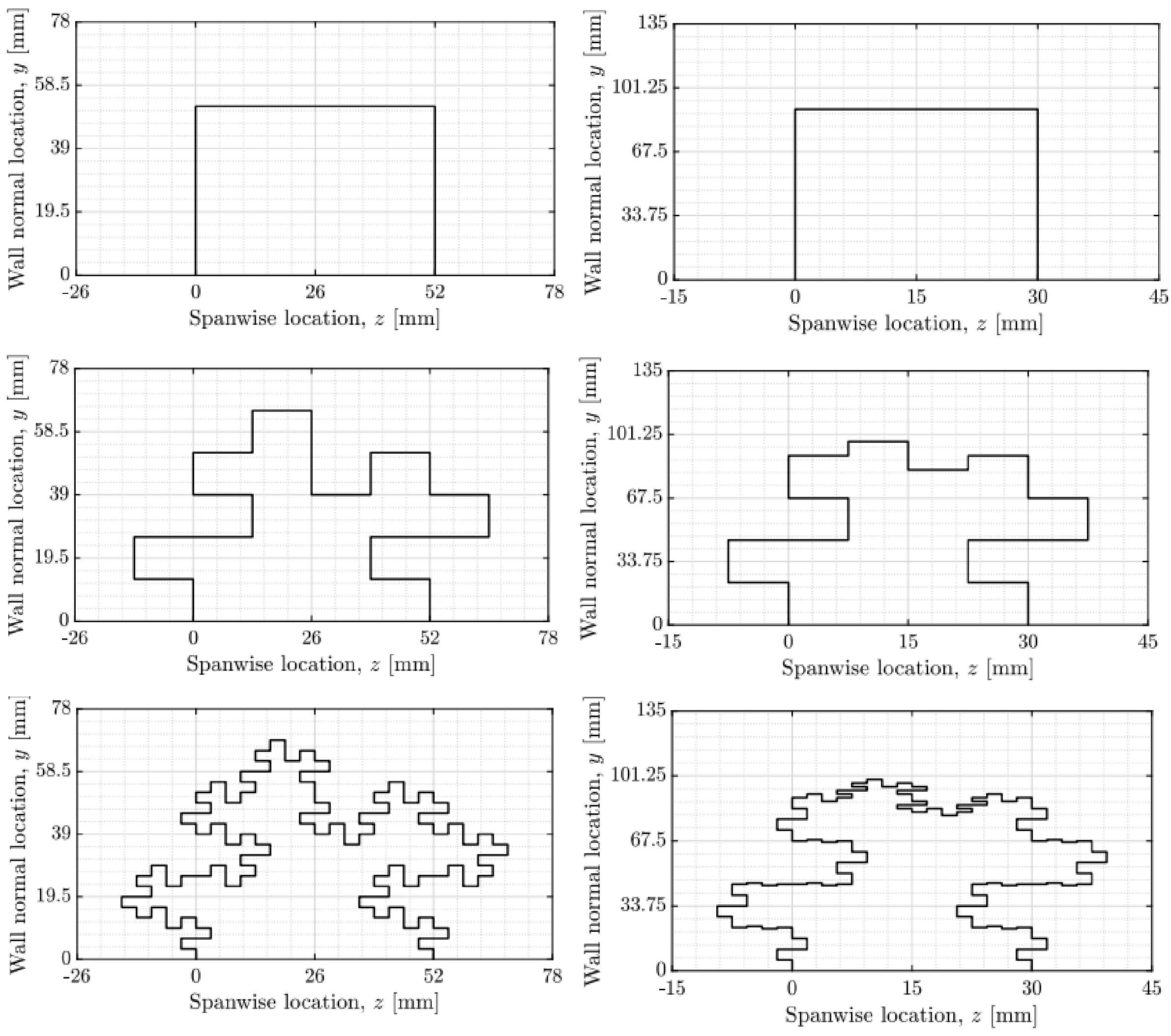

Figure 1 Geometry of standard (left) and tall (right) buildings with their first and second fractal iterations in the middle and bottom, respectively

The main characteristics for the models are shown in Table 1. The fractal iterations are obtained by means of Makowski Sausage-type generator and are introduced to decrease the minimum length scale of the building for each iteration. This process could, of course, be continued for further iterations, but the length scales would soon become smaller than the measurement spatial resolutions.

Table 1 Main geomtrical statistics for building models

Building Model	λ_f	λ_p	Max Height (mm)	Max Width (mm)	Depth (mm)	Min Length Scale (mm)
Standard Iteration 0	0.24	0.20	52.00	52.00	36.00	52.00
Standard Iteration 1	0.24	0.20	65.00	78.00	24.00	13.00
Standard Iteration 2	0.24	0.20	68.25	84.50	22.15	3.25
Tall Iteration 0	0.24	0.20	90.00	30.00	36.00	30.00
Tall Iteration 1	0.24	0.20	97.5	45.00	24.00	7.50
Tall Iteration 2	0.24	0.20	99.38	48.75	22.15	1.88

All building models, both the set used with the FE force balance and those instrumented with pressure taps were 3D printed.

2.2 FE Force Balance

The FE force balance system used an optical non-contact displacement transducer (Micro-epsilon model optoNCDT 1420), accurate to $\pm 0.5 \mu m$, to record the displacement of the floating plate, from which the drag force was calculated. The force balance was calibrated before and after the experiment, using a pulley which was hard mounted to the tunnel floor and hanging known masses from a 3D-printed hook. The hook was attached to the building model via fishing wire. This set up, and the optical non-contact displacement transducer, are shown in Figure 2.

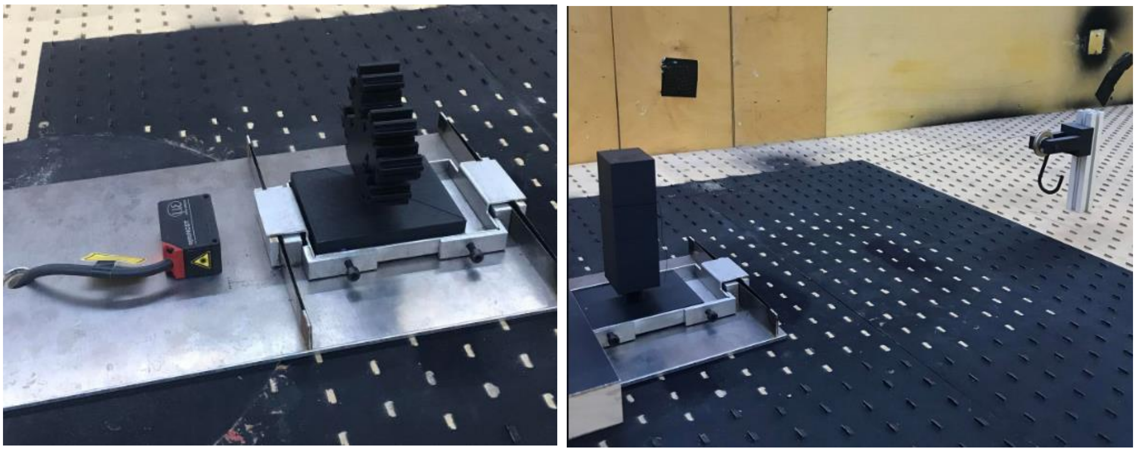

Figure 2 FE force balance and calibration set up

A range of known weights of up 500mN were used during calibration. The drag was estimated to reach close to 200mN for each building assuming a coefficient of drag, C_d, of 1.05, which is standard for a simple cube (Carvill, 1993). The results of the pre and post calibrations can be seen in Figure 3.

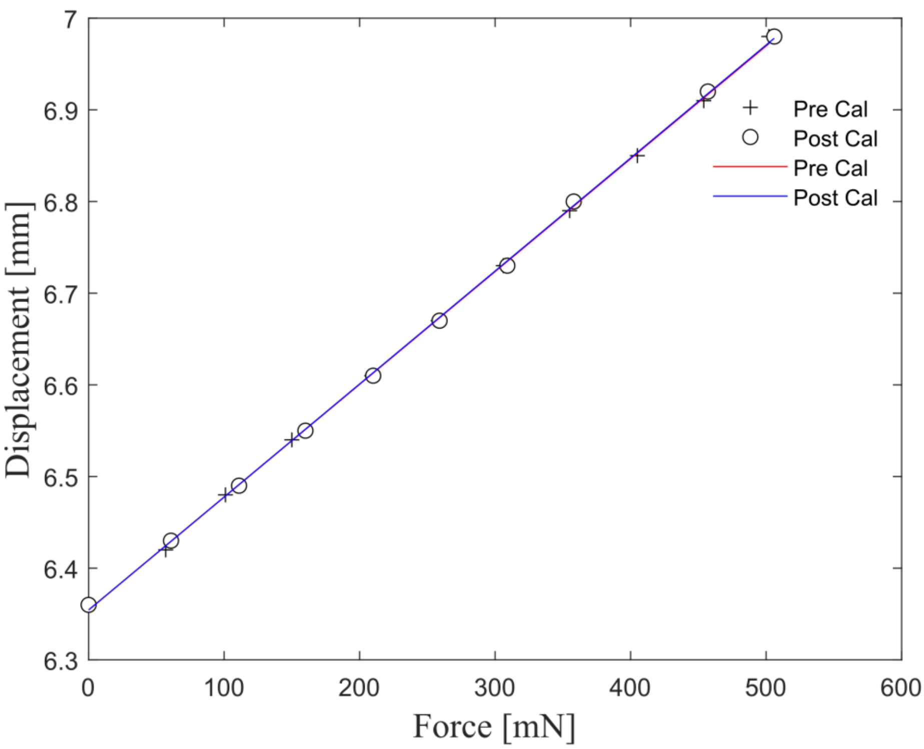

Figure 3 Pre and post calibration results. Symbols indicate measured data, lines reppresent linear best fits

A best fit line was calculated for both data sets using the least squares method. The coefficients for both lines were identical to 4 decimal places showing good reliability/repeatability. The FE force balance sat on the floor of the tunnel, and was covered by a shroud (not shown in Figure 2), to minimise its effect of the flow. This results in the buildings being raised by 20mm off the surface of the tunnel. The effect this has on the drag the buildings experience is expected to be small but will be quantified in later experiments.

2.3 Static pressure ports

The 3D printed models to be used for the pressure measurements have a range of static pressure ports on their front and rear faces depending on the available space at the base of each model. The Standard 0 iteration model has a total of 128 static pressure ports, the Standard 1 iteration model has 64 pressure ports due to the reduced base space, and the Standard 2 iteration model has 80. For the latter, this was achieved by using two separate models to allow for the pressure on the small outer scales to be more accurately resolved. The tall models have an even larger geometric reduction in base space with the tall building iteration 0 and 1 models having 42 and 52 ports respectively. The Tall 2 iteration building model has 66 ports, again in an attempt to capture the effect of the smaller scales. Each static pressure port has an internal barb which is connected to a length of silicone tubing. This is fed out of the base of the buildings and the wind tunnel floor to a connector from Surrey Sensors Ltd (model QC-66). The connectors screw onto a case containing 8 64-channel pressure scanners with a full-scale range of 160Pa, these are also from Surrey Sensors Ltd (model DPS14-160P). Comparison from static port and FE balance measurements will shed light on the necessary spatial resolution (i.e., the number of pressure ports) to accurately capture drag of tall buildings with multiscale character.

2.4 Wind Tunnel Setup

The experiments were carried out in the ‘A’ wind tunnel in the Environmental Flow Research Centre (EnFlo) at the University of Surrey. This tunnel has a working section of 5000mm (length) x 900mm (width) x 600mm (height). It is a blow down, open circuit wind tunnel with a maximum velocity of 25 m/s and a free-stream turbulence intensity below 0.1%. A Pitot-static probe was used to calculate the freestream velocity. The data was acquired at 500Hz and averaged over 18 seconds. The velocities considered were 2m/s, 4m/s, 6m/s, 8m/s, 10m/s, 12m/s, and 14m/s. These resulted in a Reynolds number range, based on defining the Reynolds number as $Re = {}^{\rho U x}/_{\mu}$, where ρ is the air density, U is the free stream velocity, x is the fetch of the incoming boundary layer and μ is the dynamic viscosity, of Re=3×10^5-2.3×10^6. The tunnel used a LabView code that automatically changed the tunnel velocity, allowing enough setting time between each measurement point. Every building model was run through each velocity 3 times, and the tunnel was set back to 0m/s between runs.

Irwin spires, along with floor roughness elements were employed to produce a thick velocity profile similar to that of an urban boundary layer, see Figure 4. The spires were 245mm in height with a base width of 35mm and spaced 130mm from their centre lines. The floor roughness elements were 2mm in height and 8mm in width and were fitted to wooden board, which essentially replaced the regular flooring in the wind tunnel.

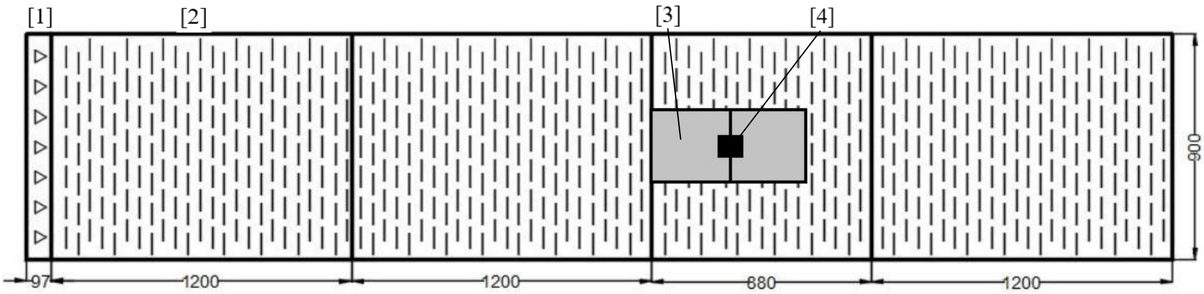

Figure 4 Wind set up showing Irwin spires [1], roughness elements [2], shroud [3] and building model [4]. Measurements in mm

3. Preliminary Results

The drag on each building is shown in Figure 5 for buildings with *AR=1* and *AR=3*. All results show good repeatability (where the 3 runs show good concurrence). A line of best fit was produced for each data set using the least squares method for a second order polynomial. Each fractal iteration showed a clear change in drag from the previous, with the tall building models experiencing a larger drag than the standard models (up to 20%). For the tall buildings, each iteration increased the drag by a non-negligible amount, which supports some of the previous findings in (Nedic, et al., 2013). For the standard model instead, the second iteration showed a drop in drag to below that of even the base cuboid model after the increase from the previous iteration. The cause for this is not yet known, however, the pressure distribution experiments are hoped to provide more insight into this. It is also plausible that the smaller scales are causing a quicker wake recovery, reducing the drag. Wake measurements should provide an answer to this – see section 4.

Figure 6 shows similar data to that in Figure 5, but in terms of the drag coefficient, C_d. It is shown that, for each building, the drag coefficient is independent of the Reynolds number for approximately Re > $1.2\text{x}10^6$. These figures also allow to quantify the effect of the addition of smaller length scales. The difference between each iteration were found to be significant, even when considering the experimental uncertainty of the measurements. For the tall buildings, the first iteration provides an increase in drag coefficient of approximately 8%, and the second provides an increase of approximately 13% from the base iteration. For the standard models, the first iteration results in an increase of approximately 5%, and the second a decrease of approximately 5% from the base iteration. This shows that the small scales, at least when looking at an isolated building, can have a significant effect of the aerodynamics properties.

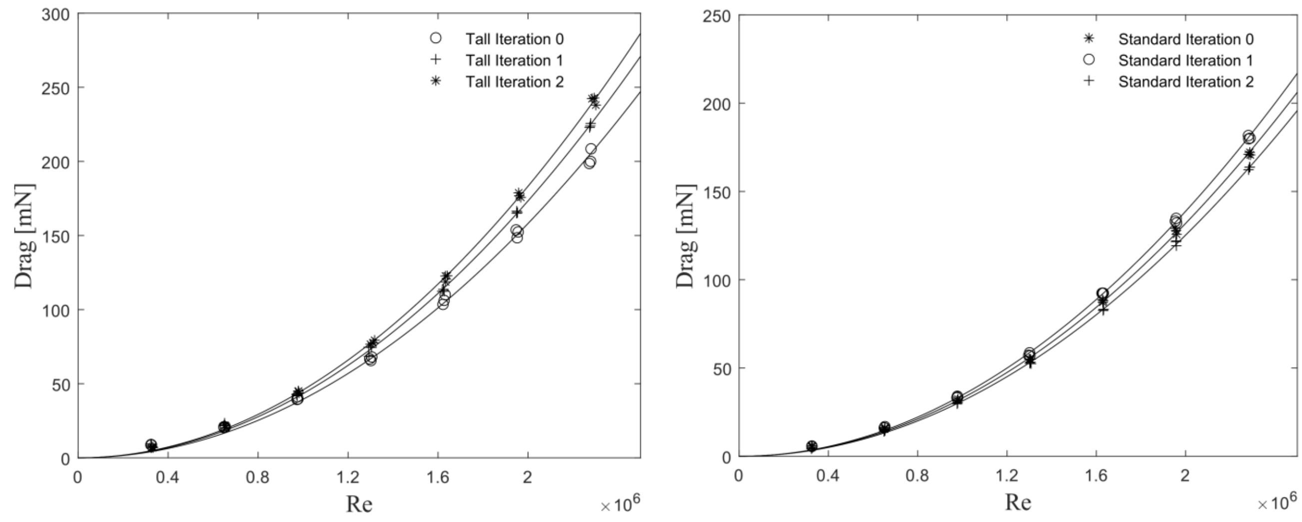

Figure 5 Drag [mN] as a function of Reynolds number on tall (left) and standard (right) building models

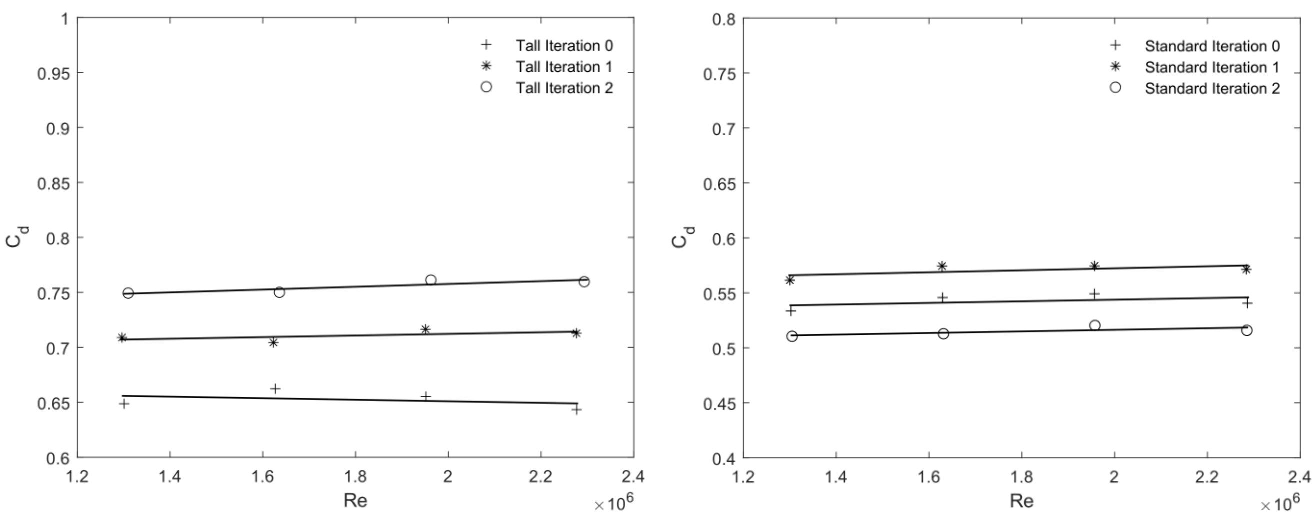

Figure 6 Drag coefficent as a function of Reynolds number for tall (left) and standard (right) building models

4. Future Work

Pressure measurements across the front and back faces of each building model will be taken via static pressure ports. This will be compared to the FE balance drag measurements and provide some insight into the significant drag change seen through each fractal iteration. These pressure measurements will be taken for buildings in isolation and in small clusters of up to 5x5, to show if the smaller scales still affect the aerodynamic properties for buildings in arrays which are more representative of real-world cities. This comparison will all be presented at the conference.

Following this, the wake of each building, in isolation and in clusters, will be examined via 3-D Laser Doppler Anemometry. This will allow the characterisation of the wake and provide further understanding into the change in drag seen by each iteration. This will also allow the turbulent kinetic energy behind each building to be quantified. Later on in this project, considerably larger arrays will be employed to simulate full city-scale morphologies. Fast flame ionisation detection will also be used to take concertation measurements and inform the urban dispersion phenomenon as a function of the various length scales. Finally, we ultimately aim to incorporate the effects of thermal stability on the quantities of interest.

Acknowledgments

The authors would like to thank Mr Josh Minien for his early work on the fractal geometries. We would also like to thank NERC Postgraduate Centre in the Science of the Environment: Natural & Anthropogenic Processes, Impacts & Opportunities (SCENARIO) DTP coordinated by the University of Reading, and the School of Mechanical Engineering Sciences at the University of Surrey for funding this research (NERC grant research number NE/S007261/1).

References

Barlow, J. & Coceal, O., 2009. *A review of urban roughness sublayer turbulence,* Reading: Met Office.

Carvill, J., 1993. 4 - Fluid mechanics. In: J. Carvill, ed. *Mechanical Engineer's Data Handbook.* s.l.:Butterworth-Heinemann, pp. 146-171.

Castro, I., 2002. Near wall flow over urban-like roughness. *Boundary Layer Meteorology* , 104(2), pp. 229-259.

Coceal, O., Thomas, T., Castro, I. & Belcher, S., 2006. Mean flow and turbulence statistics over groups of urban-like cubical obstacles. *Boundary Layer Meteorology,* Volume 121, pp. 491-519.

DESA, 2019. *World Population Prospects.* New York, United Nations.

Grimmond, S. & Oke, T., 1998. Aerodynamic properties of urban areas derived from analysis of surface form. *Journal of Applied Meterology,* Volume 38, pp. 1262-1292.

Macdonald, R., 2000. Modelling the mean velocity profile in the urban canopy layer. *Boundary-Layer Meteorology,* Volume 97, pp. 25-45.

Nedic, J., Ganapathisubramani, B. & Vassilicos, J., 2013. Drag and near wake characteristics of flat plates normal to the flow with fractal edge geometries. *Fluid Dynamics Research,* 45(6).

Tatebe, K., 2005. *Combining Mutliple Averaged Data Points and Their Errors.* [Online]
Available at: https://www.yumpu.com/en/document/view/37147068/combining-multiple-averaged-data-points-and-their-errors
[Accessed 26 06 2022].

Vanderwel, C. & Ganapathisubramani, B., 2019. Turbulent Boundary Layers Over Multiscale Rough Patches. *Boundary-Layer Meteorology,* 172(1), pp. 1-16.

Wind Tunnel Modelling of the Jack Rabbit II Mock Urban Environment Chlorine Releases

T. Spicer[1] and C.T. Smith[1]

[1]University of Arkansas/Ralph E. Martin Department of Chemical Engineering/3202 Bell Engineering Center/Fayetteville, AR, 72701/USA

Abstract

Led by the U.S. Department of Homeland Security Science & Technology (DHS S&T) Chemical Security Analysis Center (CSAC), the Jack Rabbit II (JR II) chlorine release trials were conducted at the U.S. Army Dugway Proving Ground in 2015 and 2016. A 50:1 scale model of the 2015 JR II Mock Urban Environment (MUE) was built in the Chemical Hazards Research Center (CHRC) ultra-low speed wind tunnel. Between the two test seasons, a sonic anemometry study was made in the MUE, and field measurements were compared to wind tunnel LDV measurements to confirm the validity of the wind tunnel model. In the wind tunnel model, the simulated source gas cloud (a mixture of carbon dioxide, sulfur hexafluoride, and air) was made visible by mixing with commercial theater fog to compare with field videos. The wind tunnel model flow was modified to be consistent with Trial 4 observations. The approach was validated using JR II Trial 5 conditions. Repeated concentration measurements were made using an NDIR gas sensor, which showed similar times to cloud arrival and duration of exposure as observed in the JR II near-field JAZ™ measurements.

Introduction

The Jack Rabbit II (JR II) test program was undertaken to address critical knowledge gaps for assessment of the consequences of a large-scale release of chlorine, an important toxic inhalation hazard (TIH) chemical. In addition to outdoor releases of chlorine in 2015 and 2016 of sufficient scale to be representative of potential releases from rail cars and other large-scale storage and transport, the project aimed to improve understanding and modeling of hazards and consequences to affected population and infrastructure from the release of chlorine. Conducted at Dugway Proving Ground (DPG), the JR II program was developed to provide the opportunity to improve hazard assessment capabilities as well as guidance for emergency response, particularly involving evacuation and shelter-in-place guidance. At roughly 10:1 scale with current transportation practices for chlorine, the JR II program was planned to address questions involving the interaction of a chlorine cloud with a mock urban environment (MUE) in the 2015 test season and in an open environment in the 2016 test season. An overview of the test program is available (Fox et al., 2022).

The scope of this work includes preparation for and conduct of experiments in a wind-tunnel scale model of the five JR II field releases conducted in the MUE, particularly to consider the interaction of a dense gas cloud with obstacles. The wind tunnel experiments were conducted at a sufficient scale (50:1) to ensure that field scale phenomena were modeled appropriately. The sonic anemometry study conducted between the 2015 and 2016 JR II test seasons was used to confirm that the wind tunnel model was representative of the wind field (including the friction velocity), particularly in the vicinity of the MUE. Video records from JR II Trial 4 were used to develop the wind tunnel methodology to describe the near field behavior of the chlorine cloud in the MUE. The wind tunnel methodology was verified by comparison with a second trial (Trial 5). Finally, point-wise concentration measurements in the wind tunnel model were compared to JAZ field-scale measurements.

Wind Tunnel Model

The Chemical Hazards Research Center (CHRC) wind tunnel is an ultra-low-speed boundary layer wind tunnel capable of producing airflows that simulate the constant stress layer of the atmospheric boundary layer. It was designed and constructed specifically for the study of atmospheric dispersion of denser-than-air gases at wind speeds below 2 m/s (Havens et al., 1994). The tunnel is centered laterally in a larger room to ensure a symmetrical return space for the re-circulating air. An isolated control/observation room is situated adjacent to the tunnel housing data acquisition systems and control instrumentation. During the course of an experiment, the tunnel room is isolated so as to prevent extraneous effects that would disrupt the tunnel flow and measurements. Airflow produced by the fans passes through a circular-to-rectangular transition from the fans to the working area of the wind tunnel. The working area is 2.1 m high, 6.1 wide, and 24 m long, and is divided into two sections:

- The boundary-layer generation section is downwind from the circular-to-rectangular transition. A uniform airflow across the cross-sectional area of the wind tunnel is generated as the airflow passes through a honeycomb with 1.2 cm cells followed by a series of four seamless nylon screens. Fourteen Irwin spire-shaped turbulence generators (13.2 cm base, and 92.7 cm height), positioned 30 cm downwind from the last seamless screen with 46.3 cm between adjacent spires, induce an approximately 1 m high turbulent boundary layer.
- The test section begins at six spire heights (approximately 5.5 m) downwind from the last screen. For this program, this region also included a 50:1 scale model of the MUE (Figure 1) as well as instrumentation.

In these tests, aluminum angles (3.8 cm wide and tall) were placed in staggered rows spaced 61 cm apart with lateral spacing of 61 cm in each row. Another seamless screen and a back-pressure device consisting of vertical Plexiglass strips (7.6 cm wide spaced 8.1 cm apart) were installed at the end of the working section of the wind tunnel. Froude number scaling was used to set the tunnel wind speed based on observed wind speeds at DPG.

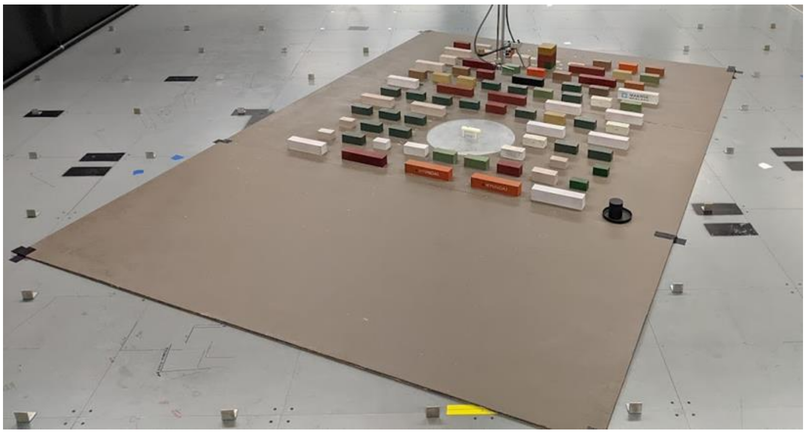

Figure 1. Wind tunnel model of MUE looking downwind

As shown modeled in Figure 1, the JR II tests were conducted on a gravel pad built on the surrounding playa (approximate elevation of 61 cm above the playa) and aligned with the historical wind direction. Because of the change in elevation, the MUE was constructed 200 ft (61 m) downwind of the leading edge of the gravel pad. The MUE consisted of CONEX containers of various sizes numbered by row (upwind to downwind) and position (left to right), so the left most CONEX on the third row was 3.1. Inside the MUE, the release area consisted of a chlorine tank (capacity of 7.7 m^3 liquid) placed in the center of a circular concrete pad (25 m diameter). At the downwind edge of the MUE, a stack of six CONEX containers (in three levels) was built to mimic a tall urban structure (CONEX 11.4) which was the focus of the sonic anemometry study.

Wind Tunnel Model of Sonic Anemometry Field Tests

A special study between the two seasons of the JR II field tests was conducted using three-component sonic anemometers to examine the flow and turbulence characteristics within the MUE used in the 2015 tests. Measurements during the JR II Special Sonic Anemometry Study (JR II-S) were completed in March 2016, and the study is summarized by Pirhalla, et al. (2020). The MUE used in 2015 was modified during JR II-S by removing three CONEX containers from Row 12 so that additional anemometers could be placed downwind of CONEX 11.4. Wind tunnel velocity and turbulence measurements were made with a 3D LDV system (Lopes, 2023).

With measurements from MET Tower 3 upwind of the gravel pad, six time periods were identified as having constant wind field properties (denoted A-F in Spicer and Smith, 2021). Since the overall objective was to verify the ability to model conditions in the JR II field tests, two time frames were chosen for further study because those agreed best with JR II test conditions (shown in Table 1). (The historical average wind direction is 165°.)

Table 1 Sonic Anemometry Study Conditions

Time Frame	Date and Time	Height (m)	Wind Speed (m/s)	Average Wind Direction
C	3/24/2016 11:00 am	2 4	3.35 3.79	164°
E	3/27/2016 7:00 am	2 4	4.38 4.96	166°

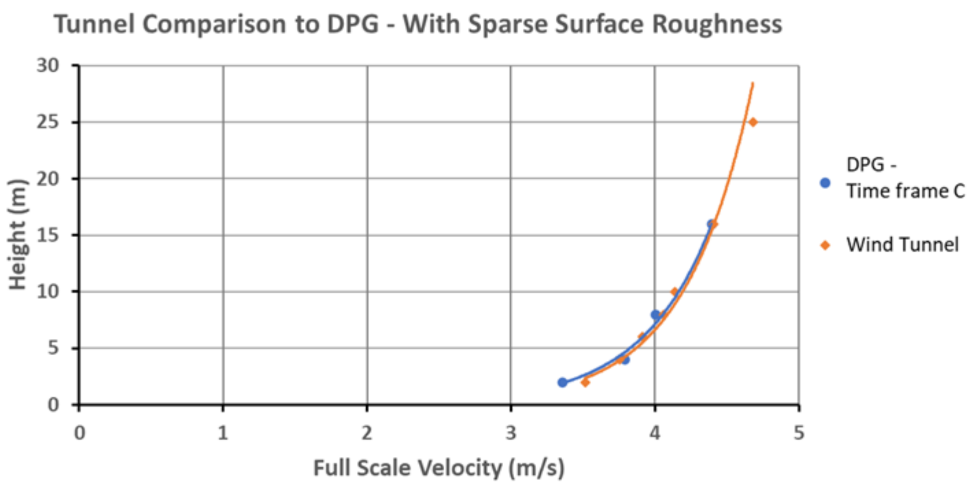

Figure 2. MET Tower 3 velocity profile comparison for Time Frame C.

Velocity measurements made at the MET Tower 3 location for Time Frames C and E are shown in and Figure 3. MET Tower 3 velocity profile comparison for Time Frame E., respectively. Using Froude number scaling, the wind tunnel velocity profiles agreed closely with velocity profiles from JR II-S.

Velocity measurements were made at selected sonic anemometer locations within the MUE model. Figure 4 illustrates the comparison between measured u and w velocity components at selected locations along the centerline of the MUE around the tall container for Time Frame C. All wind tunnel measurements were in good agreement with field-scale measurements. The vectors show the effect of a dividing stream line where below a certain elevation, the flow tends to go around the sides of the obstacle, and above that elevation, the flow goes over the top of the obstacle. This effect has been observed and quantified in water tunnel studies conducted by Snyder et al. (1985). This effect can result in higher that expected concentrations of gas on the roof of a tall building as was observed in an urban environment as discussed by Hanna and Chang (2015).

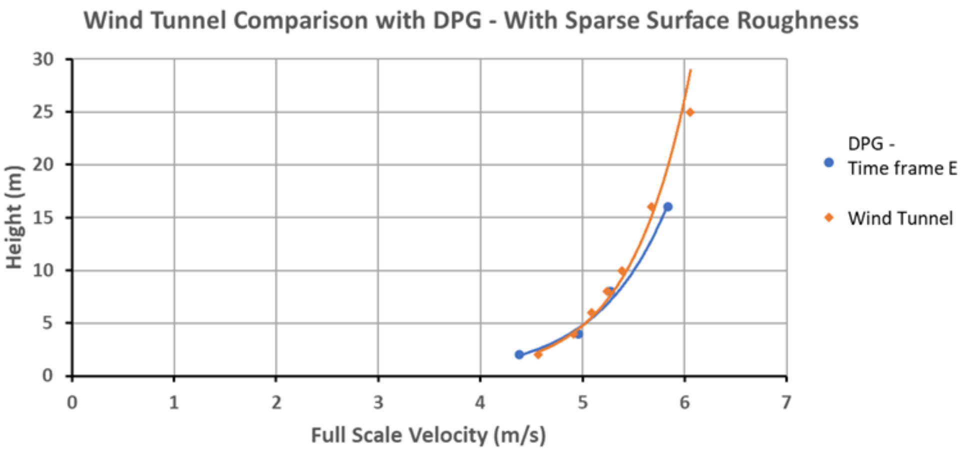

Figure 3. MET Tower 3 velocity profile comparison for Time Frame E.

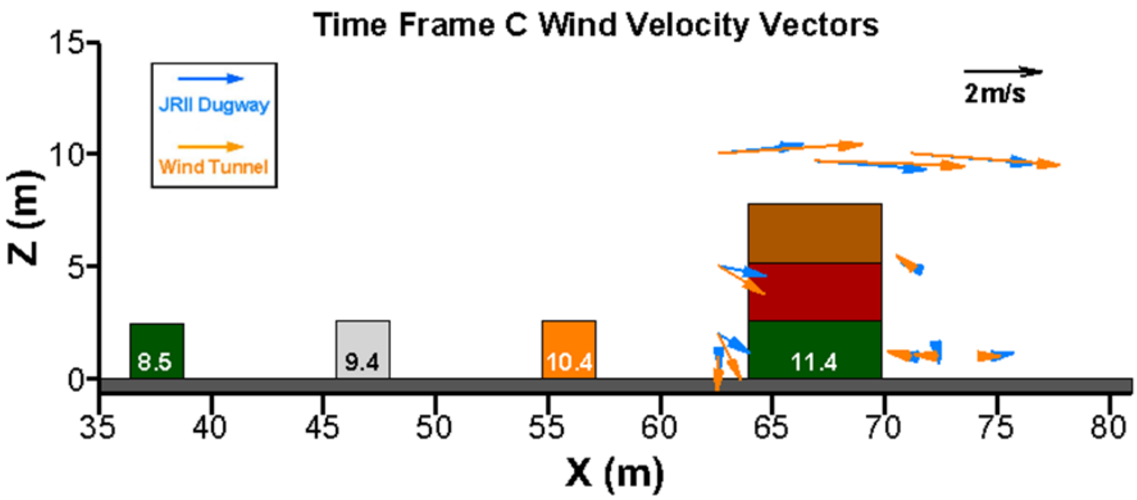

Figure 4. Comparison of centerline u and v velocity vectors for the wind tunnel and field study for Time Frame C.

Figure 5 shows a top view of CONEX containers and measured velocity vectors in the xy-plane (u and v components) for Time Frame C at locations near CONEX 11.4 at 1 m elevation. As indicated in the figure, the wind tunnel measurements are generally consistent with field-scale measurements. The flow in the lee of the obstacle would be expected to show more variability, and in this region, the agreement between field-scale and these wind tunnel measurements is not as good.

Measurements of the friction velocity ($U_* = \sqrt[4]{(u'v')^2 + (u'w')^2}$) were made in JR II-S and in the wind tunnel model and are shown in Table 2. As can be seen in the table, the agreement between field and tunnel scaled friction velocity is good. Tunnel measurements were also made at (scaled) heights of 10 and 6 m, and using the simple average from the wind tunnel measurements, the average (scaled) frcition velocity was found to be 0.177 and 0.227 m/s for Time Frames C and E, respectively. For these velocity profiles, the surface roughness (z_0) was estimated to be 0.7 mm at field scale which is consistent with Hanna's recommendation of 0.5 mm (Hanna, 2020). At wind tunnel scale, the roughness Reynolds number ($Re_* = U_* z_0/\nu$ where ν is the kinematic viscosity)

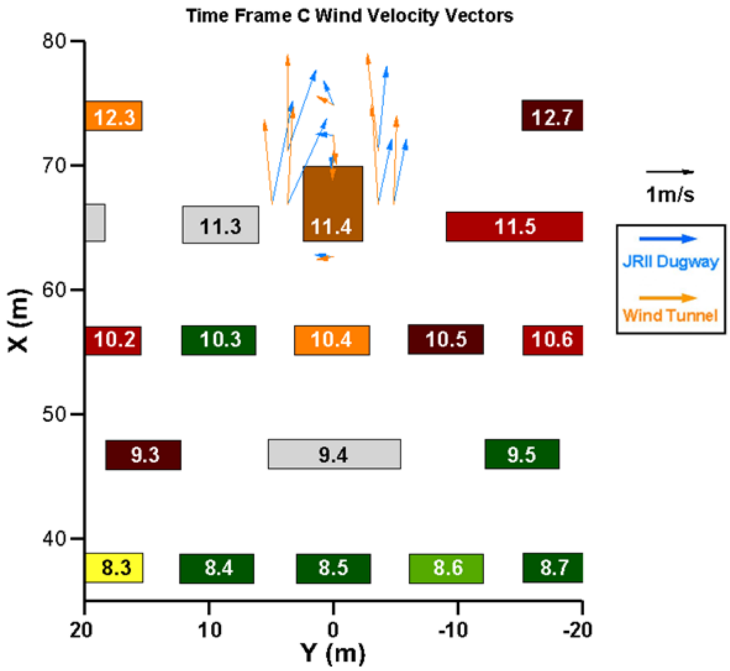

Figure 5. Comparison of xy-plane velocity vectors at 1 m elevation measured at wind tunnel and field scale in Time Frame C

Table 2 Comparison Between Field and Scaled Tunnel Friction Velocity for Time Frames C and E.

	Time Frame C		Time Frame E	
Field Scale Height (m)	JR II-S U_* (m/s)	Scaled Tunnel U_* (m/s)	JR II-S U_* (m/s)	Scaled Tunnel U_* (m/s)
16	0.165	0.185	0.204	0.203
8	0.183	0.196	0.239	0.217
4	0.177	0.163	0.244	0.211
2	0.182	0.133	0.228	0.169

would be approximately 0.2. This value of Re_* is less than the criteria of 1 recommended by Snyder and Castro (2002), but exceeds the value of 0.135 for a smooth wall. (It is worth noting the the field scale flow has a $Re_* \approx 6$.) Despite this concern, the wind tunnel measurements are consistent with field measurements. The main focus of this work to model the JR II chlorine releases, and the turbulence of the approach flow was not as important as the momentum of the release.

Physical Model of the JR II MUE Chlorine Releases

All of the MUE chlorine releases were vertically downward from a 15.2 cm circular hole (1 m above grade) made instantaneously in the bottom of the horizontal chlorine dissemination vessel. The flashing-two phase flow jet impacted the concrete pad and formed a wall jet that flowed radially from the release. The mass remaining in the vessel was measured by load cells which allowed accurate determination of the release rate as a function of time. As summarized by Spicer and Tickle (2021), the mass rate of chlorine leaving the vessel was constant during most of the release, but the amount of chlorine that moved downwind was impacted by aerosol rainout on the concrete pad. To facilitate comparison between atmospheric dispersion models, the rate chlorine moved downwind was simplified in two alternative ways including (i) a constant rate of aerosol and (ii) a lower constant rate of aerosol with susbequent release of gas from the liquid rainout that remained. In the physical model developed in this work, the constant release rate approximation was used.

A physcial model of this release starting from the initial two-phase jet was considered impractical because of the inability of creating such a flow in the wind tunnel. Due to the violent nature of the flow as well as the corrosive behavior of chlorine, only thermocouples were deployed on (and in) the concrete pad. The thermocouple measurements confirmed that a thin film of liquid chlorine was deposited on the concrete surface which subsequently evaporated. Thermocouple measurements along with video records of the tests were used to develop a model to quantify the amount of chlorine rained out (Spicer et al., 2019). However, since no other measurements were made on the concrete pad, the concentration, density, and velocity of the chlorine/air aerosol cloud was unknown. The aerosol cloud properties would be required to conserve the mass of chlorine released since the mass release rate had been measured. Because the chlorine liquid rainout was found to be limited to the concrete pad, the physcial model was conceptualized to model the outward flowing aerosol wall jet at the edge of the concrete pad.

In the physical model, there were three parameters that were identified as unknowns at the edge of the concrete pad including the depth, velocity, and density of the wall jet. The wall jet in the physical model was made by suspending a circular disk over an area source in the floor of the wind tunnel which was the same (scaled) diameter as the concrete pad (see Figure 1). The area source top was fabricated using three perforated sheets. The holes in the top and bottom sheet are aligned and fixed. When the middle sheet is also aligned, test gas flows into the tunnel from the area source. When the middle sheet is moved so that the holes are not aligned, slots on the side of the area source under the tunnel are opened so that a continuoius supply of gas can be maintained from mass flow controllers. The gas supply was made visible using theater fog for comparison with field video records. Test gas from the mass flow controllers goes through a manifold that injects gas into the theater fog machine thereby allowing the gas supply to be marked with fog so that the density and volumetric rate of the gas supply could be controlled. By controlling the volumetric rate of supply gas and the gap between the circular disk and the model surface, the velocity of supply gas leaving the concrete pad could be controlled. With the ability to control the wall jet depth, velocity, and density in the physical model, visulaization tests were used to determine the wind tunnel gas release conditions to re-create various aspects of the visual record from the field tests.

Visual Test Comparison with Field Scale Video Record

The video record of the JR II field tests consists of recordings from a set of high definition cameras (numbered 1 – 12) at various locations around the MUE. Videos were not available for all cameras for all release trials. Two upwind camera locations (designated Cameras 3 and 4) were selected to best show the upwind and lateral motion of the chlorine cloud. Vehicles were parked at various locations inside the MUE during different tests, and the location of vehicles is reported in Spicer and Smith (2021). All wind tunnel simulations used the vehicle locations from trials 1-3 for all trials. (Subsequent wind tunnel simulations of trial 5 with three vehicles near the source were made, and the observations were largely unchanged except for deviations between field and tunnel observations at times after the primary release was complete.)

In the wind tunnel model, Trial 4 conditions were used to experimentally determine the optimum parameters to model the release, and Trial 5 was used to validate the test parameters. To quantify the agreement between wind tunnel and field tests, the time required for the gas cloud to reach certain locations in the videos was measured. For Trial 5 using multiple releases, the average time to reach locations A-L in the wind tunnel are compared with field observations in Figure 6. Average arrival times for wind tunnel videos are somewhat too fast for locations nearest to the release point (A – C and G) with better agreement for arrival times at locations D – F and H – K. The arrival time at location L for the wind tunnel tests is slightly later. Overall, arrival times agree quite well considering the complex and turbulent nature of the gas flow within the MUE. Unlike pointwise velocity and concentration measurements, comparison of video records provides a global confirmation that the model is an effective representation of the field scale tests.

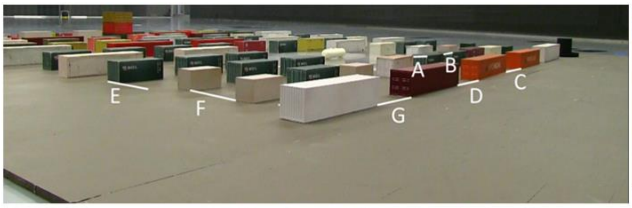

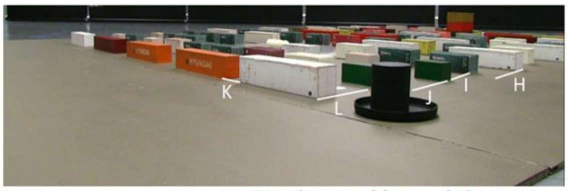

Time (in seconds) to reach the Location:

			A	B	C	D	E	F	G
Locations:			A	B	C	D	E	F	G
Official JRII Trial 5 time:			2.9	3	6.8	6.2	11.2	18.1	18
Run Examples	Run 6	680 LPM 49% Cl_2	1.5	1.5	5.75	6	11.25	14.25	17
	Run 9		1.5	1.75	5.5	7	11.5	13.75	15.25
	Run 12		1.5	1.5	5.75	6.5	11.5	15.25	16.75
15 Repeated Runs									
Average Times			1.43	1.50	5.45	6.45	11.72	14.48	16.30
Standard Deviation			0.148	0.164	0.302	0.343	0.452	0.658	0.819

Time (in seconds) to reach the Location:

Locations:			H	I	J	K	L
Official JRII Trial 5 time:			8.3	8.2	11.6	13.7	16
Run Examples	Run 5	680 LPM 49% Cl_2	7.75	8.25	10.25	13.5	18
	Run 9		7.75	7.75	10.75	12.75	17.5
	Run 12		7.75	8.25	11	13.5	19
15 Repeated Runs							
Average Times			7.82	8.08	10.77	12.92	18.37
Standard Deviation			0.200	0.336	0.417	0.479	0.574

Figure 6. Trial 4 time of cloud arrivalto reach locations A-L

The optimal fog fluid composition was determined to be 21.4 mL/min of Rosco Clear Fog Fluid to provide good visualization of the releases. Using a tunnel disk spacing of 7 mm (0.35 m field scale), the optimum flow rate of the source gas was determined experimentally to be 680 L/min with a density of 1.96 g/L (which accounted for the fog mass). While a single set of conditions were determined to be optimal, there is no doubt that a range of test conditions would have been representative of the observed phenomenon.

In each of the comparison video frames in Figure 7, the color of the chlorine cloud has been detected digitally and enhanced (with addition of green) at pixel level to facilitate the comparison between field and tunnel clouds. In the field releases, portions of the chlorine cloud that include aerosol are opaque, and portions of the cloud that are transparent are chlorine gas only (no aerosol present).

Comparison of Field Scale and Wind Tunnel Scale Concentration Measurements

During the field-scale MUE experiments, JAZ concentration sensors were deployed to measure chlorine concentrations. As with all other concentration measurement instruments in the test, the JAZ were calibrated before and after each test. The JAZ were deployed within the MUE because their upper limit of measurement was 100,000 ppm chlorine.

In the wind tunnel model, SF_6 was used as one component in the source gas to obtain the needed initial gas density to model the field scale releases. However, SF_6 is known to create issues with concentration measurement systems such as a flame ionization detector (FID), so an alternate approach was tested. The Cambustion NDIR500 Fast Carbon Monoxide and Carbon Dioxide Analyzer was developed to measure CO and CO_2 in internal combustion engines using an NDIR sensor. Because the instrument was on loan from Cambustion, no changes to the instrument could be made to tailor it to our application. For the wind tunnel tests, the sample probe attached was placed inside the wind tunnel with the main control unit and vacuum pump outside the wind tunnel. For each location tested, the sampling probe was placed approximately 0.6 cm AGL. For these concentration measurements, the source gas was composed of SF_6, CO_2 , and air. The concentration of CO_2 was maximized to improve measurement sensitivity, and the presence of SF_6 was determined to not interfere with the measurements even though SF_6 is IR active. Figure 8 shows an example of one comparison between the J91 field scale measured concentration, and the average wind tunnel

Figure 7. Trial 5 comparison between wind tunnel and JR II video frames at selected times.

measured concentration from multiple releases. Figure 8 also includes wind tunnel measurements from two separate releases.

To complete the NDIR measurements in a timely fashion with available mass flow meters, the molecular weight of the source gas was reduced from 1.96 g/L to 1.79 g/L because this was the maximum density gas mixture that could be delivered while also containing sufficient carbon dioxide for adequate measurement with the NDIR. To accommodate this change in density, a higher volumetric flow rate was required, but at the time of the NDIR experiments, an error was made when setting flowrates, so a flowrate of 794 L/min was used (approximately 17% larger than desired). In all of the comparisons that follow, model-scale concentration is presented as a concentration of chlorine gas (in ppm) assuming that chlorine gas (without aerosol) was used in the field experiments. Taking aerosol behavior into account would require that a larger model molecular weight be used (to account for the aerosol density increase) for comparison which would reduce model measured concentrations when compared to field scale measurements. Consequently, the model gas concentrations are expected to be higher near the source where aerosol behavior would be more important.

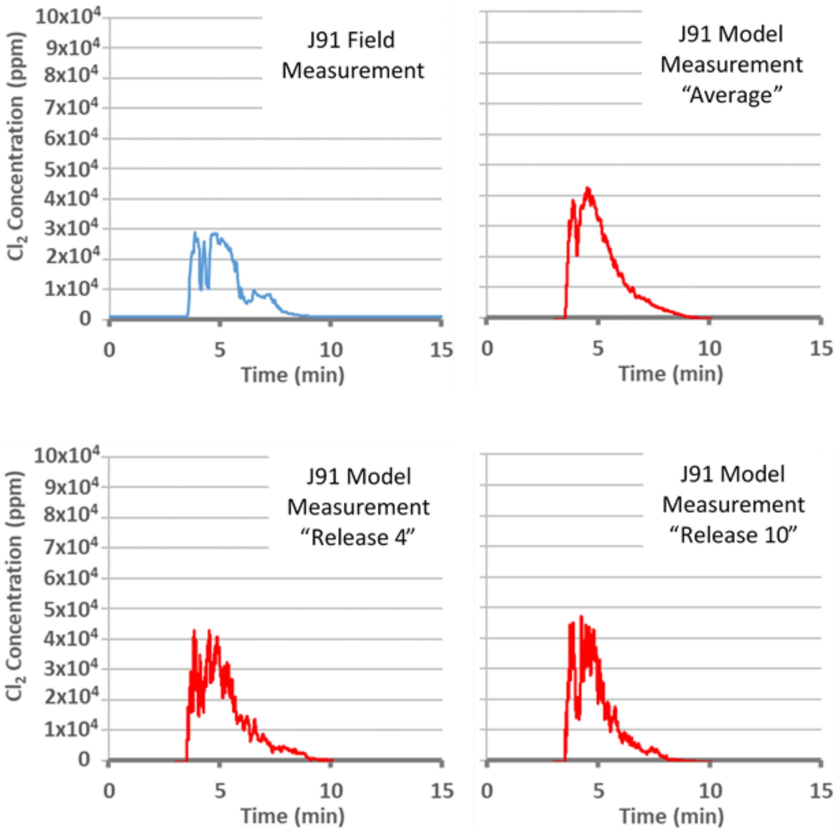

Figure 8. Comparison of Jaz J91 measurements in Trial 4 with averaged NDIR model measurements along with two individual model measurements. Plot scales are the same between field and model measurements.

Conclusions

The JR2 chlorine field tests conducted in 2015 and 2016 were modeled in the CHRC wind tunnel. In the 2015 test season, a mock urban environment (MUE) was built in the field tests, and a 50:1 scale model of the MUE was built in the wind tunnel. The model work focused on the Special Sonic Anemometry study in the MUE between test seasons to validate the ability to model field scale turbulence and velocity in the wind tunnel. Using the upwind MET 3 measurements to set the wind speed, the chlorine releases were modeled in the wind tunnel as a gas wall jet at the edge of the (field scale) 25 m diameter concrete pad. Model parameters of the wall jet (depth, density, and volumetric flow rate) were experimentally determined so that cloud time of arrival between field and model scale at various locations were in good agreement using the field conditions for Trial 4. Model parameters of the wall jet were validated by comparison with observations in Trial 5. Scale up of these model parameters provided an estimate of field scale flow conditions which could not be measured due to the complexity of the flow (e.g., jet density and velocity). Field scale concentration measurements were compared with wind tunnel measured concentrations using a novel application of the Cambustion NDIR instrument.

Acknowledgements

This project was based upon work conducted under contract HDTAT FA8075-14-D-0003 DO FA807517F1402 with the U.S. Department of Homeland Security Science & Technology (DHS S&T) Chemical Security Analysis Center (CSAC), and their support and guidance is appreciated. David Cotsman at Transport Canada also provided useful guidance on the project. Cambustion, Ltd. loaned the NDIR500 Fast Carbon Monoxide and Carbon Dioxide Analyzer and provided support in making measurements with the system under novel circumstances. Several students including Mr. Paulo Lopes, Mr. Samuel Gallimore, and Mr. Sami Fares were critically important in the conduct, analysis of the wind tunnel work in this report including preparation of figures. In previous experimental work, Dr. Jessica Morris developed the use of the area gas source so that it could be promptly started and stopped.

References

Fox, S., S. Hanna, T. Mazzola, T. Spicer, J. Chang, and S. Gant, „Overview of the Jack Rabbit II (JR II) field experiments and summary of the methods used in the dispersion model comparisons," Atmospheric Environment, 269, 118783, 2022.

Hanna, S., „Meterological data recommendations for input to dispersion models applied to Jack Rabbit II trials," Atmospheric Environment, 235, 117516, 2020.

Hanna, S., and J. Chang, „Skyscraper rooftop tracer concentration observations in Manhattan and comparisons with urban dispersion models," Atmospheric Environment, 106, 215-222, 2015.

Havens, J., T. Spicer, and H. Walker, "Regulatory Application of Wind Tunnel Models and Complex Mathematical Models for Simulating Atmospheric Dispersion of LNG Vapor," Gas Research Institute Report No. 92-0257, August 1994.

Lopes, P.V., „Experimental and Computational Study of a Scale Model of the Jack Rabbitt II Special Sonic Anemometry Study," University of Arkansas Martin Department of Chemical Engineering, PhD Dissertation, 2023 (in preparation).

Pirhalla, M., D. Heist, S. Perry, S. Hanna, T. Mazzola, S. Pal Arya, and V. Aneja, "Urban wind field analysis from the Jack Rabbit II Special Sonic Anemometer Study," Atmospheric Environment, 243, paper 117871, 2020.

Snyder, W.H., The EPA Meteorological Wind Tunnel: Its Design, Construction, and Operating Characteristics," Environmental Sciences Research Laboratory, Fluid Modeling Report No. 6, EPA-600/4-79-051, 1979.

Snyder, W.H., and I.P. Castro, „The critical Reynolds number for rough-wall boundary layers," Journal of Wind Engineering and Industrial Aerodynamics, 90, 41-54, 2002.

Spicer, T., A. Feuvrier, and S.B. Fox, „Transient large-scale chlorine releases in the Jack Rabbit II field tests: Rainout source data analysis from video records," Journal of Loss Prevention in the Process Industries, 59, 35-43, 2019.

Spicer, T. and C.T. Smith, Jack Rabbit II Mock Urban Environment Trials: Wind Tunnel Model Investigation and Validation, U.S. Department of Homeland Security Science & Technology Chemical Security Analysis Report CSAC 21-005, 2021.

Spicer, T.O., and G. Tickle, „Simplified source description for atmospheric dispersion model comparison of the Jack Rabbit II chlorine field experiments,“ Atmospheric Environment, 244, 117866, 2021.

PREDICTING MEAN WIND PROFILES AND POLLUTANT DISPERSION INSIDE URBAN CANOPIES

Huanhuan Wang[1], Eden Furtak-Cole[2], Keith Ngan[1]

[1]School of Energy and Environment, City University of Hong Kong, Kowloon, Hong Kong, China
[2]Division of Atmospheric Sciences, Desert Research Institute, Reno, NV, USA

Abstract

Mean wind profiles within urban canopies can be predicted by assuming that the velocity is controlled by intense layers of vorticity, i.e., by solving the three-dimensional Poisson equation for a set of discrete vortex sheets. A fast pollutant dispersion model is developed by coupling mean wind profiles to a parameterisation of turbulent fluctuations and solving the time-dependent three-dimensional advection–diffusion equation. Improved agreement with large-eddy simulation results is obtained when the spatial dependence of the wind profiles is accounted for. Parameterisations based on an explicit specification of the turbulent fluctuations or the associated effective diffusivities yield nearly identical results. The fast model shows much better agreement with LES than does the Gaussian plume model (e.g. the normalized mean square error is reduced by ~80%), especially in the near field. The current implementation of the fast model is approximately 50 times faster than LES. With its combination of computational efficiency and moderate accuracy, the fast model may be suitable for applications like emergency dispersion modelling.

A comparison of turbulent flows over idealized urban and vegetation canopy

Ruiqi Wang[1], Ziwei Mo[2,3] and Chun-Ho Liu[1]

[1]The Department of Mechanical Engineering, The University of Hong Kong, Pokfulam Road, Hong Kong, China

[2]School of Atmospheric Sciences, Sun Yat-sen University, and Southern Marine Science and Engineering Guangdong Laboratory (Zhuhai), Zhuhai, China

[3]Key Laboratory of Tropical Atmosphere-Ocean System, Ministry of Education, Zhuhai, China

Abstract

Atmospheric flows in the inertial sublayer (ISL) and the roughness sublayer (RSL) are largely affected by the urban and vegetation canopies beneath. In this study, the turbulent flows over idealized urban and vegetation canopies are modeled by wind tunnel experiments. The effect of aerodynamic resistance on the RSL and ISL turbulence structure is contrasted. Vertical profiles of velocity and turbulence statistics are sampled by hot-wire anemometry (HWA) to examine the flows over different configurations of urban and vegetation canopies so as to elucidate the transport processes. A new analytical solution to the mean wind profiles of RSL and ISL is proposed that is verified by the wind tunnel measurements. The influence of aerodynamic resistance on the RSL turbulence structure is evaluated by quadrant analysis. Further to the quadrant analysis, a series of frequency analysis is carried out to examine how turbulence eddies with different scales contribute to the transport processes.

1. Introduction

The inertial sub-layer (ISL) and roughness sublayer (RSL) air flows can be strongly impacted by the surface roughness of the urban and vegetation canopy. The Monin-Obukhov similarity theory(MOST), which is based on the well-characterized and homogenous ISL winds and turbulence, applies to the flux-gradient connection[1]. But above the canopy of vegetation, the classical flux-gradient relationship is invalid[2]. Therefore, further understanding of the wind and turbulence structure in the RSL is required.

In view of the complicated surface morphology, understanding the aerodynamic effects induced by the rough surfaces is still inadequate. Many studies have used wind tunnel experiments to investigate the effect of urban roughness on the flow above the street canyon[3], [4]. More investigations over different arrangements of vegetation roughness are therefore needed. Statistical analysis of RSL turbulence over urban and vegetation canopies found strong sweeps and jets dominating transport processes[5]. However, these studies have only investigated the RSL characteristics over limited configurations of surface roughness. There is thus a need to advance our understanding of RSL dynamics.

The purposes of this paper are to (1) verify the newly proposed analytical solution to mean-wind profile for RSL and ISL; (2) analyse the RSL turbulence statistics over idealized urban and vegetation canopies.

2. Methodology

The experiments were carried out in an open circuit in a wind tunnel working in neutral stratification at the Department of Mechanical Engineering, The University of Hong Kong[6].The flows are driven by a centrifugal fan and the power is regulated by a frequency converter (design wind speeds of 0.5 m sec-1 to 15 m sec-1). After the fan, a diffuser, a settling chamber, a flow straightener and a contraction cone are built for the control of winds and turbulence. Moreover, a honeycomb filter is installed before the test section to reduce the background turbulence intensity (≤ 5%). Its test section is made of acrylic and its dimensions are 6 m (L) x 0.56 m (W) x 0.56 m (H), in which the roughness elements are placed.

The roughness elements are dispersed across the entire test-section floor to initiate fully-developed TBLs. The streamwise u and vertical w velocities are measured at a frequency of 2000 Hz using an X-wire probe with an angle of 100° of constant-temperature (CT) hot-wire anemometry (HWA).

Sensor positioning on the vertical centerplane of the test section is controlled by a digital traverse system driven by the National Instruments (NI) motion controllers (PCI-7390). Through the use of a digital computer and the NI CompactDAQ system (NI cDAQ-9188), the control module digitizes the analog CT HWA signals. The automated data acquisition and data conversion programs for the measurements are then set up using the LabVIEW software.

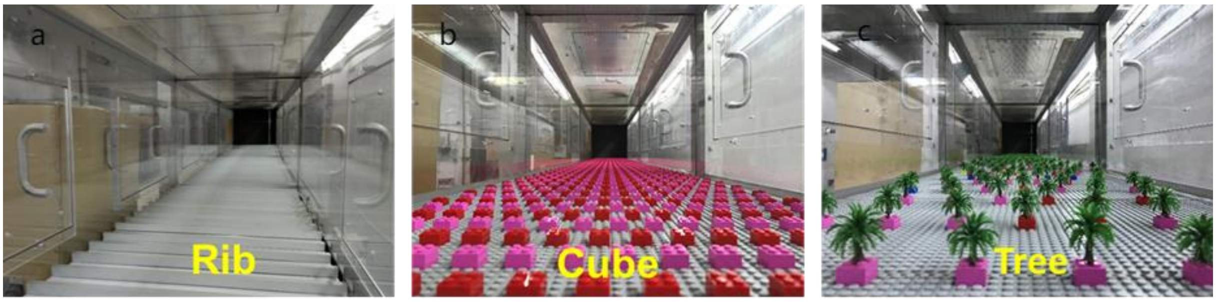

Figure 1. Photos of idealized urban canopy constructed by rib and cube elements together with vegetation canopy by tree models.

The idealised city table consists of two types of roughness elements: aluminium square bars (ribbed elements) and plastic LEGO® blocks (cube-shaped elements). The aluminium bars in crossflows with roughness-element-height-to-spacing (aspect) ratios h/b = 1,1/2,1/3,1/4,1/5,1/6,1/8,1/10,1/12 and 1/15 arrangement(Figure 1a). Arrays of LEGO® bricks are arranged in the ratio of obstacle-height-to-separation h:l, h:2l, h:3l, h:4l, h:5l, h:6l, h:7l, h:9l, h:4l-D (double LEGO® bricks), h:4l-T (triple LEGO® bricks) and h:4l-T (quadruple LEGO® bricks) (Figure 1b). The vegetation canopy is configured in a staggered and aligned pattern with flow spacing variations of h/b = 0.63, 0.31 and 0.16 (Figure 1c).

3. Results and Discussion

3.1 Parameterization of mean wind profile

The conventional ISL logarithmic mean-wind profiles do not predict RSL flows well. An analytical formulation for the mean wind speed is derived over idealised urban roughness, and a RSL function is introduced into the conventional ISL logarithmic profile[7].

$$\frac{\langle\overline{u}\rangle|_{z-d}}{u_\tau} = \frac{1}{\kappa}\left\{\underbrace{ln\left(\frac{z-d}{z_0}\right)}_{\text{ISL}} - \underbrace{\left[\gamma + ln\left(\mu\frac{z-d}{z_*}\right) + \sum_{n=1}^{\infty}\frac{(-1)^n\left(\mu\frac{z-d}{z_*}\right)^n}{n\times n!}\right]}_{\text{RSL}}\right\} \tag{1}$$

Here the κ (=0.4) is the von Karman constant,z is vertical height, u_τ is the friction velocity, z_0 is the roughness length, d is zero-displacement height, z* is RSL thickness, μ is a constant depending on the RSL configuration and γ (=0.577) is the Euler constant.

Equation (1) can be rearranged in the following form to compare the effect of surface roughness on aerodynamic resistance.

$$\frac{\langle\overline{u}\rangle|_{z-d}}{u_\tau} = -\frac{1}{\kappa}\left[\underbrace{\gamma + ln\left(\mu\frac{z_0}{z_*}\right)}_{y\text{-intercept}} + \underbrace{\sum_{n=1}^{\infty}\frac{(-1)^n\left(\mu\frac{z-d}{z_*}\right)^n}{n\times n!}}_{\text{series expansion}}\right] \tag{2}$$

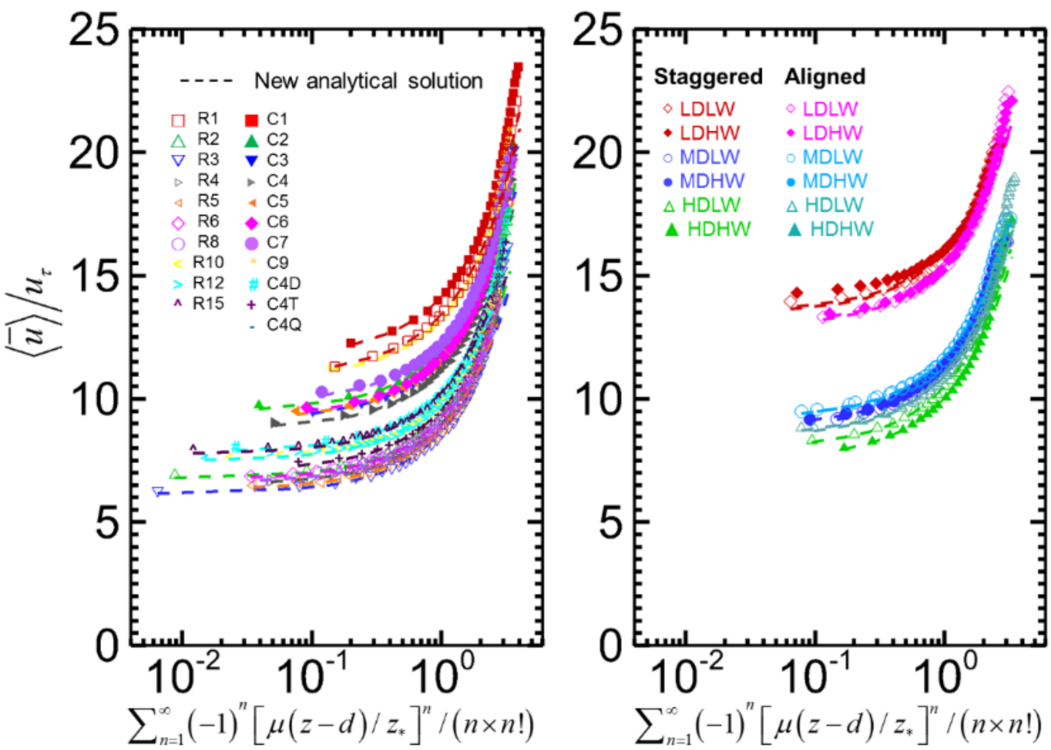

Figure 2. Dimensionless spatially averaged mean wind speed $\frac{\langle\overline{u}\rangle}{u_\tau}$ plotted against series expansion Equation (2) over (a) urban canopies (ribs and cubes) and (b) vegetation canopies (staggered and aligned).

The newly-derived mean wind profile analysis solution (Figure 2), which is continuously applied to both RSL and ISL, is validated by wind tunnel data. And the new analytical formulation describes the RSL wind profile more accurately than the traditional logarithmic form of ISL in the urban and vegetation canopy.

3.2 Turbulent Statistic

Quadrant analysis divides the velocity domain into four quadrants in the (u″,w″) plane based on the sign of the fluctuating velocity, which are outward interaction Q1 (u″> 0 and w″> 0), ejection Q2 (u″< 0 and w″> 0), inward interaction Q3 (u″ < 0 and w″ < 0) and sweep Q4 (u″> 0 and w″ <0) [8].
The occurrence fraction can be calculated as

$$N_i = \frac{Q_i}{\sum_{i=1}^{4} Q_i} \tag{3}$$

to contrast the occurrence from a particular quadrant.
And the momentum flux fraction can be calculated as

$$S_i = \frac{< \overline{u''w''} >_{Q_i}}{< \overline{u''w''} >} \tag{4}$$

to quantify the contribution from a particular quadrant.
Exuberance [9]as an indicator of transfer efficiency is defined as

$$E_x = \frac{S_1 + S_3}{S_2 + S_4} \tag{5}$$

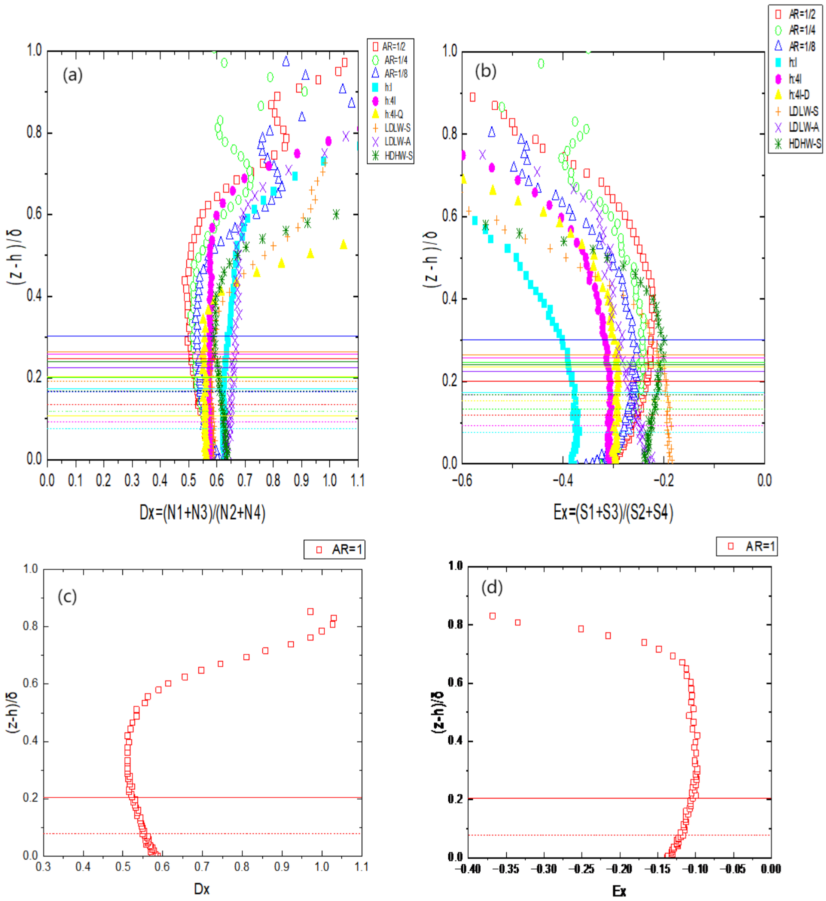

Figure 3. Dimensionless vertical profiles of spatio-temporal average of (a)D_X (b)E_x over urban canopies (ribs and cubes) and vegetation canopies, (c) (d) plotted at AR=1 of rib-type array.

Figure 3 implies in general that the occurrence of Q2 and Q4 are much more frequent than that of Q1 and Q3. Q2 and Q4 are the dominant events in turbulent transport. Take the rib-type array as an example (Figure 3 c, d). Q1 and Q3 in RSL occur more frequently than their ISL counterparts. Q2 and Q4 contribute more to the ISL than the RSL, and hence the transfer of momentum is more efficient in the ISL.

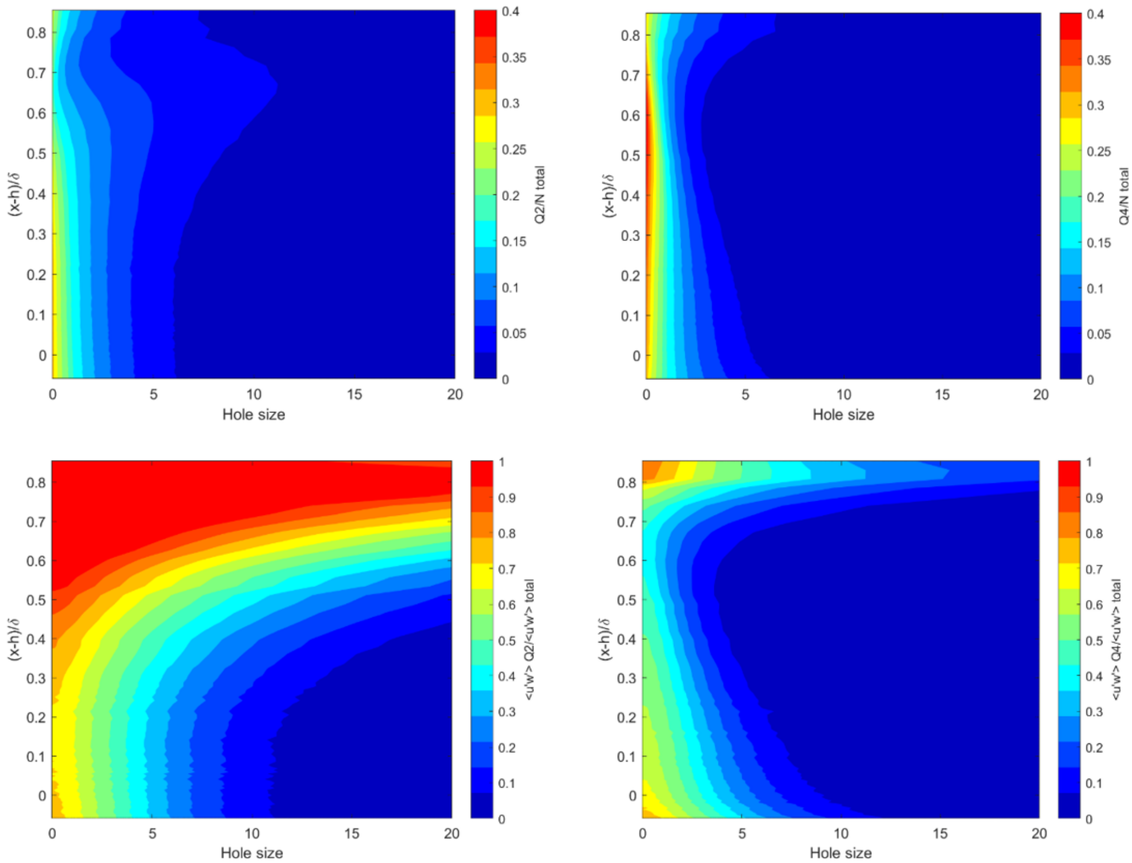

Figure 4. Occurrence fraction of Q2(a) and Q4(b) as a funtion of hole size and vertical height; momentum flux contribution of Q2(c) and Q4(d) as a funtion of hole size and vertical height

To isolate the contribution of extreme events within each quadrant, a hyperbolic hole or threshold H to identify [10].

$$H = \frac{< u''w'' >}{|< \overline{u''w''} >|} \tag{6}$$

Quadrant hole analysis examines the relative importance of Q2 and Q4.In general, Q2 occurs more frequently than Q4. Q4 contributes more momentum flux in the RSL than ISL, which is due to the strong motion scale. It means that the scale of turbulence in the RSL of Q4 is larger which contributes more to the momentum flux transport.

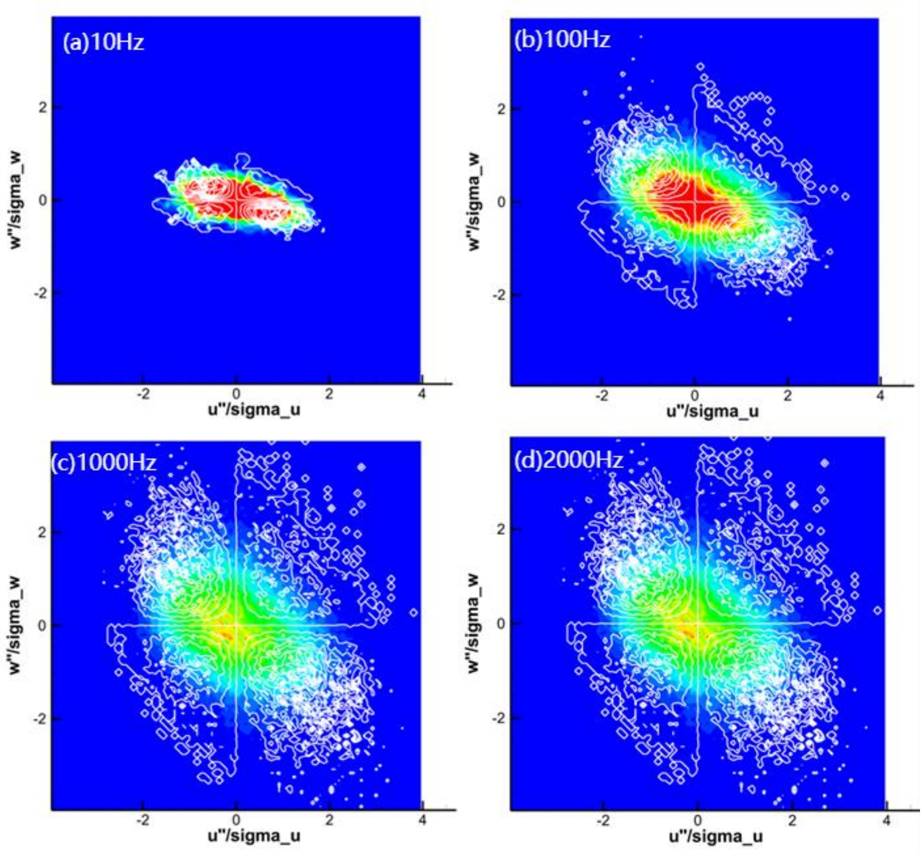

Figure 5. Shaded contour lines of the joint probability density function (JPDF) at different filter frequencies.

Frequency filter is introduced to examine quadrant analysis. Using the sampling frequency as a filter, more extreme events are found at Q2 and Q4 as the filter frequency is increased. With a sampling frequency greater than 1000hz, the full spectrum of turbulence characteristics can be captured.

4. Conclusion

A new analytical scheme for RSL and ISL mean wind profiles, verified by wind tunnel measurements, has a significant function in predicting mean wind speeds in urban and vegetation canopies. The influence of aerodynamic resistance on the RSL and ISL turbulence structure is evaluated by quadrant analyse,the results showed that ejection Q2 and sweep Q4 are the dominant events in turbulent transport. The quadrant hole analysis examined the relative importance of Q2 and Q4. These results also demonstrate the dissimilar transport mechanism between the ISL and RSL. Based on quadrant analysis, frequency analysis investigates the contribution of different scales of turbulent eddies to the transport process and derives critical frequencies that reflect the characteristics of turbulence.

Reference

[1] M. R. Raupach and B. J. Legg, 'The Uses and Limitations of Flux-Gradient Relationships in Micrometeorology', in *Developments in Agricultural and Managed Forest Ecology*, vol. 13, M. L. Sharma, Ed. Elsevier, 1984, pp. 119–131. doi: 10.1016/B978-0-444-42250-7.50011-2.

[2] P. Cellier and Y. Brunet, 'Flux-gradient relationships above tall plant canopies', *Agricultural and Forest Meteorology*, vol. 58, no. 1–2, pp. 93–117, Mar. 1992, doi: 10.1016/0168-1923(92)90113-I.

[3] P. Salizzoni, L. Soulhac, P. Méjean, and R. Perkins, 'Influence of a Two-scale Surface Roughness on a Neutral Turbulent Boundary Layer', *Boundary-Layer Meteorology*, vol. 127, pp. 97–110, Apr. 2008, doi: 10.1007/s10546-007-9256-8.

[4] H. Cheng and I. P. Castro, 'Near Wall Flow over Urban-like Roughness', *Boundary-Layer Meteorology*, vol. 104, no. 2, pp. 229–259, Aug. 2002, doi: 10.1023/A:1016060103448.

[5] M. R. Raupach, J. J. Finnigan, and Y. Brunei, 'Coherent eddies and turbulence in vegetation canopies: The mixing-layer analogy', *Boundary-Layer Meteorol*, vol. 78, no. 3, pp. 351–382, Mar. 1996, doi: 10.1007/BF00120941.

[6] Z. Mo and C.-H. Liu, 'Wind tunnel measurements of pollutant plume dispersion over hypothetical urban areas', *Building and Environment*, vol. 132, pp. 357–366, Mar. 2018, doi: 10.1016/j.buildenv.2018.01.046.

[7] Y.-K. Ho and C.-H. Liu, 'A wind tunnel study of flows over idealised urban surfaces with roughness sublayer corrections', *Theor Appl Climatol*, vol. 130, no. 1–2, pp. 305–320, Oct. 2017, doi: 10.1007/s00704-016-1877-8.

[8] W. W. Willmarth and S. S. Lu, 'Structure of the Reynolds stress near the wall', *Journal of Fluid Mechanics*, vol. 55, no. 1, pp. 65–92, Sep. 1972, doi: 10.1017/S002211207200165X.

[9] R. H. Shaw, J. Tavangar, and D. P. Ward, 'Structure of the Reynolds Stress in a Canopy Layer', *J. Climate Appl. Meteor.*, vol. 22, no. 11, pp. 1922–1931, Nov. 1983, doi: 10.1175/1520-0450(1983)022<1922:SOTRSI>2.0.CO;2.

[10] X. Shao, N. Zhang, Z. Peng, K. Zhao, Y. Luo, and X. Song, 'Observed Surface Drag Coefficient Under High Wind Speed Conditions and the Relationship With Coherent Structures', *JGR Atmospheres*, vol. 127, no. 3, Feb. 2022, doi: 10.1029/2021JD035301.

Cyclists Exposure to Vehicle Emissions in Urban Canyons

J. Wingrave (Schmeer) [1], D. M. Birch[1], M. Placidi[1]

[1]Centre for Aerodynamics, and Environmental Flow, School of Mechanical engineering Sciences, Faculty of Engineering and Physical Sciences, University of Surrey, Guildford, GU2 7XH, United Kingdom

1. Introduction

According to Transport for London, polluting vehicles are the single biggest contributor to London's air pollution, responsible for nearly half the total air pollution in London (Transport for London, 2022). Cycling is encourgaged in cities such as London to reduce traffic emissions, it is therefore important to ensure the advantages of cycling exceed the health risks of cycling in polluted areas. Studies such as those by Seaton et al. (1995) and Zuurbier et al. (2009) show a direct link between particulate matter in the air and respiratory related hospital visits. Cyclists are also at greater risk compared to pedestrains due to their extended proximity to polluting traffic and the increased inhalation rate due to the physical activity. Ning et al. (2005) and Shi et al. (2020) reveal why cyclists proximity to pollutiong vehicles is significant; an exponential decrease in pollutant concentration with increased distance from a polluting vehicle in both physical and numerical studies is observed. Pollutant dispersion is also affected by the environment into which it is emitted, Wang et al. (2008) shows that pollution concentration is elevated in street canyons due to the recirculation that occurs when a road is flanked by tall buildings, typical in urban settings.

Vehicles and bicycles often share the same space on the road which forces riders into a line behind one another. There are some studies investigating the effect of pollution exposure on cyclists but very little research on the effect of cycling in a group, as is often the case in congested areas.

2. Experimental facility and details

The experiments were carried out in the University of Surrey's Environmental Flow Meteorological Wind Tunnel (EnFlo) within the Centre for Aerodynamics and Environmental Flow. The tunnel's internal test section measures 20m x 3.5m x 1.5m (length x width x height) and is equipped with two three-dimensional traversing gears and an automatic turntable of diameter 1.4m.

To create the desired boundary layer replicating atmospheric conditions in an urban area, a set of five Irwin spires were placed at the tunnel inlet followed by approximately an 11m-long fetch of roughness elements. A 1:50 scale street model, representing a typical urban canyon was placed on a 2m x 2m square plate fixed to the turntable. Throughout this work, the x direction is defined to be parallel with the tunnel length, y indicates the spanwise direction, and z is height normal to the tunnel floor. One traverse was used for moving the source and the other for moving the fast flame ionisation detector (FFID) concentration measurement probe.

The source, modelling a car exhaust, released a mixture of air and propane, and was emitted at a height representative of a car exhaust and directed downstream, parallel to the orientation of the street canyon. This approximates to a passive release.

2.1 Experimental model

21-52 Clapham road is part of Cycle Superhighway No. 7 and has been selected becuase it is particularly straight with relatively small buildings and simple geometry, these factors render the stretch of road ideal for a scaled wind tunnel model (see Figure 1). The 1:50 scale model ensures that even when the buildings are angled to simulate the effect of wind direction, the blockage is well below 10%.

The design of the model bicycle used in these experiments uses a simplified geometry. The dimensions of the rider that sits on the bicycle are taken from an average male. A scale of 1:40 is used for the dimensions of both the bicycle and the rider (Bierkens, 2019). Each cyclist stands on a thin chamfered square mounting plate which measures 40mm x 40mm. The length of a single cyclist, l, is therefore equal to 40mm. A configuration of four cyclists in line is modelled, where the cyclists are positioned one behind the other equidistantly spaced as if they are riding adjacent to the traffic in the Cycle Superhighway.

The model car was designed based on the commonly-used Ahmed model as it reproduces the basic aerodynamic features of a car with a simplified geometry for experimental and numerical modelling (Ahmed et al., 1984). The dimensions used to create the model were inspired by a London black cab taxi, the TX4, using the same 1:40 scale used for the cyclists. To establish the prevailing wind direction, data was obtained from the nearest weather station. This is located in the borough of Brixton, approximately 1.7km from the physical measurement site. The relative angle between the absolute wind and the bearing of the modelled section of Clapham Road can be estimated to be 12°. This is therefore referred to as the prevailing wind direction.

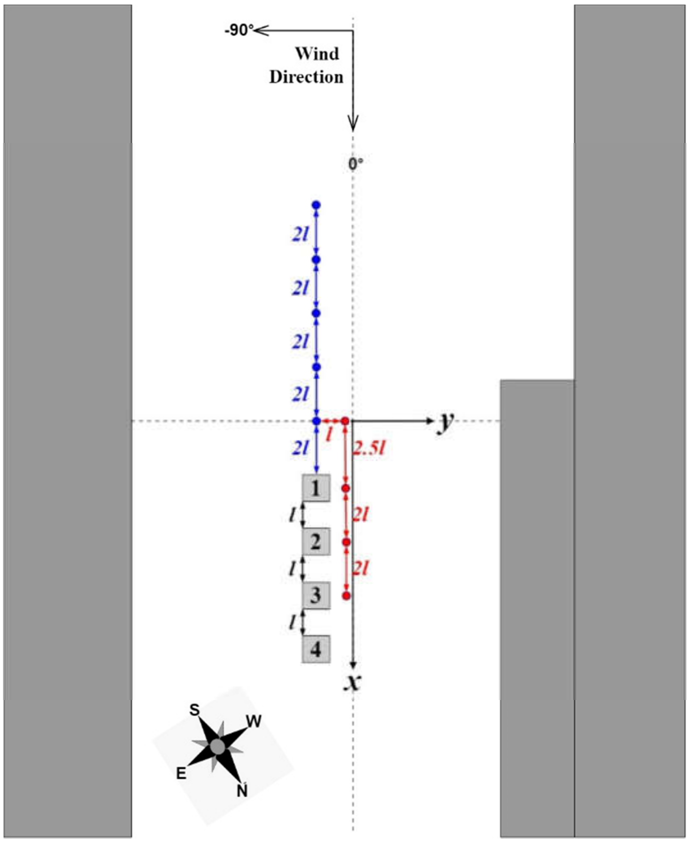

Figure 1: Diagram of the street canyon model. Buildings are in dark grey, cyclists are represented with light grey squares and dots indicate the source position. Case 1 (in blue) refers to the car positioned upstream of the cyclists and Case 2 (in red) is when the car is adjacent to the cyclists. The cases are discussed in Section 2.2.

2.2 Measurements

The FFID measurement probe was used to measure the propane concentration in front of each of the four cyclists, at a distance of $0.25l$ upstream of the rider‘s head, the values presented are averaged over a four minute sampling time with an acquisition frequency of 400Hz. The tested configurations can be split into two cases where the source is moved around the group of riders. In Case 1, the source and cyclist are in-line, the *y* position of the source is aligned with the centre of the line of cyclists. The source is moved increasingly upstream as if a car were progressively further away from the group of cyclists. In Case 2, the source is offset to the right hand side of the cyclists by a distance of l. The initial *x* source position is also set to a distance of $2l$ upstream of Cyclist 1 but is then moved downstream and so positioned adjacent to each cyclist numbered 1 - 3.

Case 1 is simulated both with and without the Ahmed model at a wind incidence angle of 0°, i.e. when the street canyon is orientated parallel to the tunnel. Case 1 and 2 are subsequently simulated with the Ahmed model with a sweep of wind incidences from -12° to +180°.

3. Preliminary results

Preliminary results only cover Case 1; Case 2 will be discussed during the presentation. The concentration measurements are rendered non dimensional, by

$$c^* = \frac{C_{ppm} H_b^2 U_b}{q_p \times 10^6} \tag{1}$$

where C_{ppm} is the concentration measured by the FFID in ppm, H_b=216mm is the average building height of the two tallest buildings in the canyon, U_b=1.44m/s is the average wind velocity measured upstream at the top of the same buildings, and q_p=0.125 x 10^{-6} m^3/s is the volumetric flow rate of the propane released through the source.

The separation distance between the source and the measurement position, *d**, was non dimensionalised using the characteristic lengthscale of a single bicycle, as given by

$$d^* = \sqrt{(d_x^*)^2 + \left(d_y^*\right)^2} \tag{2}$$

where d_x^* and d_y^* are the non-dimensional distances between the source and measurement position in the *x* and *y* directions respectively. $d^*$is, therefore, given as a number of bicycle lengths.

3.1 Case 1 results

Case 1 models a vehicle directly upstream of a line of cyclists. Case 1 is simulated at 0° wind incidence, i.e. wind parallel to the canyon, both with the Ahmed model and without, where the source is a free point source. The set up at 0° is also modelled with a Gaussian point source plume model, the results of which are plotted with the experimental results in Figure 2.

An exponential decrease of concentration with increased separation distance between source and receptor is observed when the Ahmed model is used, as expected. Without the Ahmed model however, concentration tends to zero for shorter separation distances, this is becasue without the wake effects of the Ahmed model, the plume does not disperse sufficiently within the measurement region. This reveals the importance of modelling a vehicle’s bluff body to simulate a vehicle exaust dispersion.

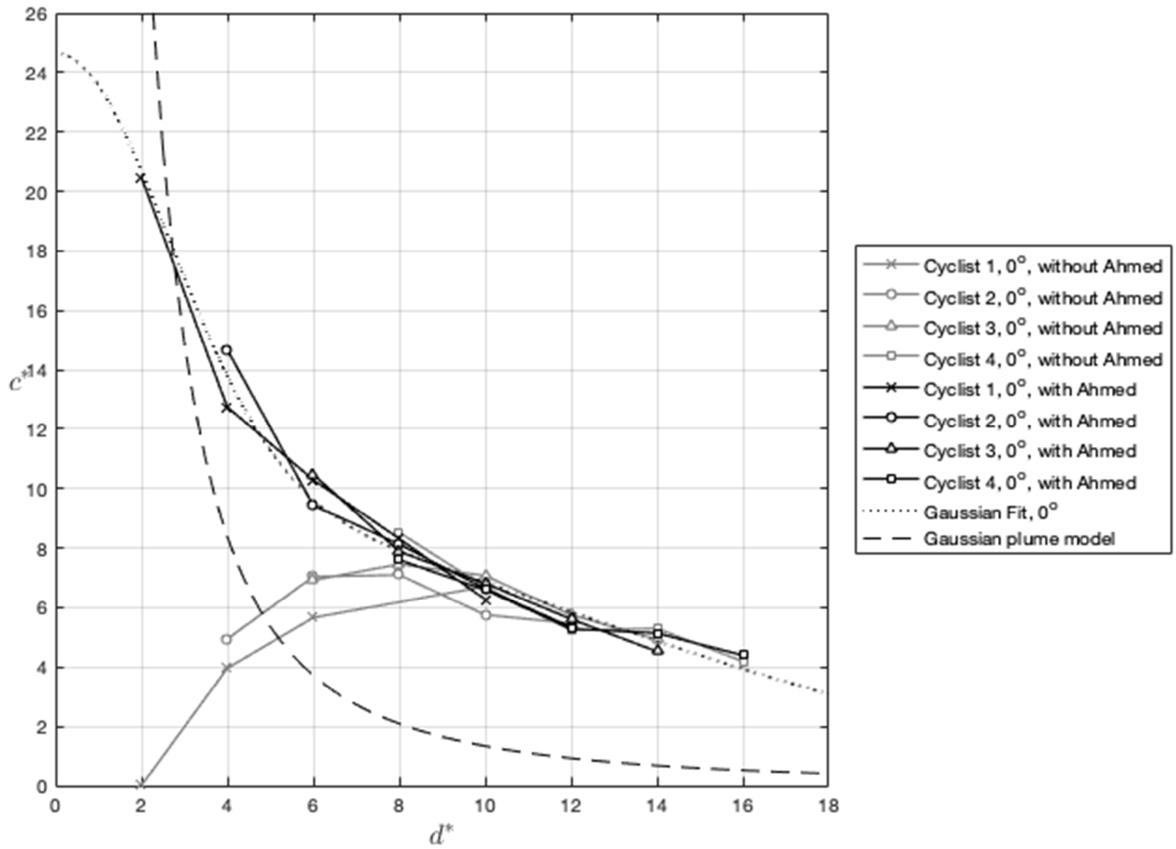

Figure 2: Normalised concentration *c** as a function of distance *d*:* Case 1, 0°, with and without Ahmed body in black and grey, respectively.

Wind incidences from 0° to -45° are simulated with the Ahmed model, this revelas that wind incidence is only significant at large separation distances, where the concentration decreases as the incidence angle increases. At -45° a larger disparity between concentration exposure between cyclists in the group is observed. The further back in the configuration of cyclists, the lower the exposure. This is likely a result of the transverse velocity in the canyon sweeping the concentration away from the cyclists.

A 180° wind incidence is simulated by reversing the orientation of the cyclists and vehicle, rather than the canyon, therefore modelling a dominant tail wind. There is little difference in concentration exposure as a function of cyclist position within the group, but the exposure is much higher in the 180° case than the 0° case. This is believed to be due to the reversed orientation of the bluff body as the exhaust is now facing upstream.

To summarise the results for Case 1, where the vehicle is in line with cyclists, the pollutant concentration decreases exponentially with increasing relative distance between the source and the cyclist. This is in agreement with previous literature and with simple prediction of Gaussian plume dispersion models. Furthermore, when the wind is largely in line with the canyon (up to 30°), there is little to no difference of concentration exposure between the positions within the group of cyclists. More substantial differences appear for wind incidences greater than 30°, for which riding at the back of the group can be beneficial regardless of the relative distance from the vehicle.

4. Conclusions and future work

The work herein is unique in combining the variables to simulate a realistic urban canyon; the bluff body aerodynamic features of a vehicle and the implications of group riding which can affect a rider's exposure to pollution in an urban area.

The findings presented also show that the presence of an Ahmed model (to simulate the presence of a vehicle) is crucial to determine accurate plume dispersion in the near field. Case 1 simulations showed that, provided the wind incidence is below 30°, the plume concentration decreases exponenetially with the separation distance between the riders and source, this is the most influential factor in determining pollutant exposure.

Case 2, where the source is adjacent to the riders at a series of downstream distances, will also be simulated at a series of wind incidence angles. The effect of distance from the source in addition to rider position within the group of cyclists on exposure level will be assessed.

The aim of this work is to be able to advise cyclsits and drivers how to reduce concentration exposure for bicycle riders in urban areas given their close proximity to pollutant emissions. Further investigations are required to fully capture the effects of different configurations of group riding, a feature of high relevance for urban riding with narrow cycle lanes.

Acknowledgements

We would like to thank the University of Surrey's Urban Living Award that provided funding to perform this research. We would also like to acknowledge Mr Floris M. Bierkens who designed the experimental rig and participated in the original data acquisition. Finally, we would like to thank Transport for London for providing us a 3D virtual map of the London borough under examination.

References

Ahmed, S., Ramm, G., Faltin, G., 1984. Some salient features of the time averaged ground vehicle wake. SAE International 93, 473–503.

Bierkens, F., 2019. Effect of Cycle Superhighways on cyclists' exposure to pollution due to road vehicles. University of Surrey, Faculty of Engineering and Physical Sciences, Mechanical Engineering MEng, Final Year Project Report .

Ning, Z., Cheung, C., Lu, Y., Liu, M., Hung, W., 2005. Experimental and numerical study of the dispersion of motor vehicle pollutants under idle condition. Atmospheric Environment 39.

Seaton, A., MacNee, W., Donaldson, K., Godden, D., 1995. Particulate air pollution and acute human health. The Lancet 345, 176–178.

Shi, T., Ming, T., Wu, Y., Peng, C., Fang, Y., de Richter, R., 2020. The effect of exhaust emissions from a group of moving vehicles on pollutant dispersion in the street canyons. Building and Environment 181.

Transport for London, 2022. About TFL, Air Quality. URL: https://tfl.gov.uk/corporate/about-tfl/air-quality?intcmp=45806

Wang, G., Van Den Bosch, F., Kuffer, M., 2008. Modelling urban traffic air pollution dispersion. Int Arch Photogramm Remote Sens Spat Inf Sci .

Zuurbier, M., Hoek, G., van den Hazel, P., Brunekreef, B., 2009. Minute ventilation of cyclists, car and bus passengers: an experimental study. Environmental Health DOI: 10.1186/1476-069X-8-48.

Experimental investigation of the heat removal and air ventilation in an urban area using simultaneous PIV-LIF measurement in a water tunnel

Y. Xue [1, 2], Y. Zhao [2], S. Mei [3], Y. Chao [3], J. Carmeliet [2]

[1] Singapore-ETH Centre, Future Resilient Systems, Singapore.

[2] Department of Mechanical and Process Engineering, ETH Zurich, Zurich, Switzerland

[3] Department of Architecture, National University of Singapore, Singapore

Abstract

The urban climate, in particular, the urban heat island effect, has been widely focused due to its significant impacts on energy consumption, air pollution level, and human health and comfort, etc. It is such a complex issue that is dominated by urban configuration, wind, temperature and human activities. To mitigate the negative impacts, it is essential to understand the fundamental physics of the urban climate, particular the flow behavior and heat transfer or energy budget of individual physical process. Therefore, the current work reposts an experimental investigation of the local urban microclimate using simultaneous PIV-LIF measurement in a water tunnel. Flow mechanism and temperature gradient are captured from the high-resolution experimental results, based on which air ventilation and heat fluxes can be calculated.

1. Introduction

The urban climate, in particular, the urban heat island effect is such a complex issue that is dominated by urban configuration, wind, temperature and human activities [1, 2]. With the increase in population, global warming and heat waves, the temperatures in cities are known to increase further, thereby having a detrimental effect on human comfort, health and increased energy demands for cooling in cities [3].

To advance the understanding, it is essential to study the urban flow behavior and heat transfer of individual physical processes and also the interactions among them [4]. Insights into factors contributing to urban heat island have been obtained, including the formation of heat dome [5] energy budget of soil [6], impact of urban morphology [7], anthropogenetic heat [8], cooling effect of plant transpiration [9], etc. Among those factors, urban airflow is a determinant one which connects dominant physical processes involving moisture and heat transport. Most urban microclimate studies in the past have focused on urban airflows driven by the wind on generic building geometries [10-12]. In the present work, we performed simultaneous PIV-LIF measurements in a large closed-circuit water tunnel to understand the potential effect of approaching flow and buoyancy in the analysis of urban flows in an urban model that developed to be representative of the real urban morphology based on the urban density analysis.

2. Experimental configurations

In this study, urban flows are studied in a water tunnel setup where both temperature and flow fields are simultaneously measured by PIV-LIF measurements in the ETH Zurich Atmospheric Boundary Layer

Water Tunnel operated at Empa (Swiss Federal Laboratories for Materials Science and Technology). The water tunnel is equipped with a 110-kW pump to produce a flow ranging from 0.03 to 1.5 m/s, and the tunnel is comprised of a 6-m long development section and a measurement section with a cross area of 0.6 × 1 m^2. The water tunnel is equipped with two sCMOS 16-bit dual frame cameras with a resolution of 2048 × 2048 $pixels^2$ at 25 Hz. The two cameras are aligned in the spanwise direction of the tunnel, focusing on the two sides of the same calibration target (CT). A Litron 100 Hz Nd-YAG laser (532 nm) is used to excite the dye for LIF measurements and illuminate the field-of-view for PIV measurements.

To reduce laser intensity fluctuation due to waves on the free air-water surface, an optical boat is mounted above the free surface of water, and the bottom of the boat is immersed about 5 mm into the water. LIF images obtained from isothermal tests are used to determine the fluctuation in laser intensity equal to 2.02%. Given the minor pulse-to-pulse intensity variation of our laser, Uranine is used in our LIF system. Since the emission peak of the Uranine is located at the wavelength of 510 nm when the excitation is at 532 nm, a bandpass filter of 535-630 nm is adopted. The concentration of the Uranine is chosen to be 2 mg/L. The experimental setup is presented in Fig. 1 and Fig. 2.

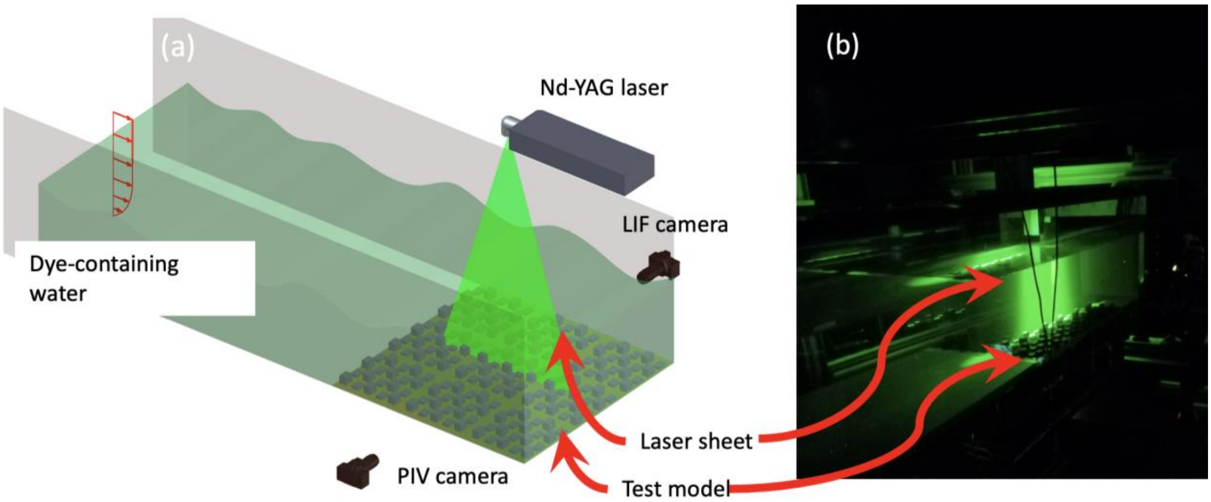

Figure 1. (a) Water tunnel filled with dye-containing water and equipped with a PIV-LIF measurement system, and (b) actual measurement process illuminated by the laser sheet.

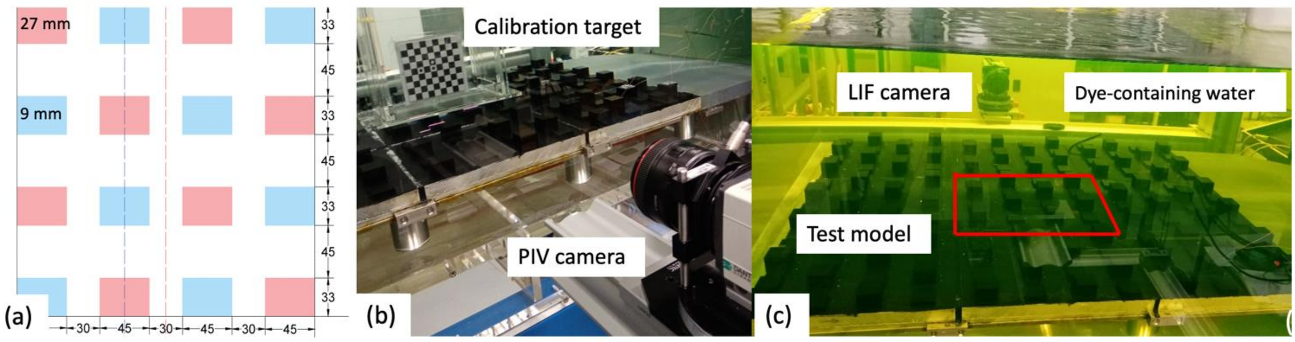

Figure 2. (a) A unit of the tested building model as indicated by the red square in (c), (b) PIV camera and a target for PIV calibration and (c) LIF camera and test model immersed in the dye-containing water.

To generate buoyant flows, the test section floor is covered with nine heating plates and the surface temperature of these heating plates can be controlled individually, as shown in Fig. 1 and 2. Conductive building models with different heights (9 and 27 mm) are mounted on the plate as presented in Fig. 2 (a). The site cover ratio (λ_p) of the current configuration is $\lambda_p = \frac{4\times4\times9\times45\times33}{1000\times1000} = 0.21$. With a constant water temperature of 21°C, the temperature of the heating plates is set at 30°C and 40°C as the partial heating and maximum heating conditions, respectively. The measurement conditions are summarized in Table 1. The Reynolds number, $Re = \frac{UH}{\gamma}$, is defined with respect to the model height (H), the freestream velocity (U) and the kinematic viscosity of water (γ). The Richardson number is defined as $Ri = \frac{g\beta\Delta TH}{U^2}$, where ΔT is the temperature difference between the ground surface and the freestream water, β is the thermal expansion coefficient of water, g is the acceleration due to gravity.

Table 1. Measurement matrix, where U is the free stream velocity and T_s denotes the plate surface temperature.

Free stream velocity, U (m/s)	Plate temperature, T_s (°C)	Reynolds number, Re	Richardson number, Ri	Remarks
0.03	20	540	0	Isothermal
0.06	20	1080	0	Isothermal
015	20	2700	0	Isothermal
0.03	30	540	1.05	Partial heating
0.03	40	540	2.58	Max heating
0.06	40	1080	0.63	Max heating
0.15	40	2700	0.08	Max heating

Velocity fields are obtained through PIV particle images which are post-processed using cross-correlation with an integration window of 32 × 32 pixels². Temperature fields are obtained by post-processing LIF images. The simultaneous velocity and temperatures are obtained by superimposing the two fields of the same FOV of the central block. 1500 pairs of images are captured at the frequency of 15 Hz for each test configuration for statistical analysis. To compensate for the spatial distribution of laser intensity, a spatial profile of the laser intensity is obtained by taking images with isothermal dye-containing water. This spatial profile is then used to normalize the intensity profiles captured in the measurements of non-isothermal flow.

3. Results and discussion

Figure 3 shows an instantaneous temperature field at Re = 540 for the maximum heating case (Ri = 2.58). Clear thermal plumes that develop and shed from the heated ground and building surfaces can be seen in the figure, which leads to a maximum water temperature rise of approximate 1.8°C. Some of the accumulated heat is carried away by the updraft and flushed downstream by the approaching flow above the rooftop.

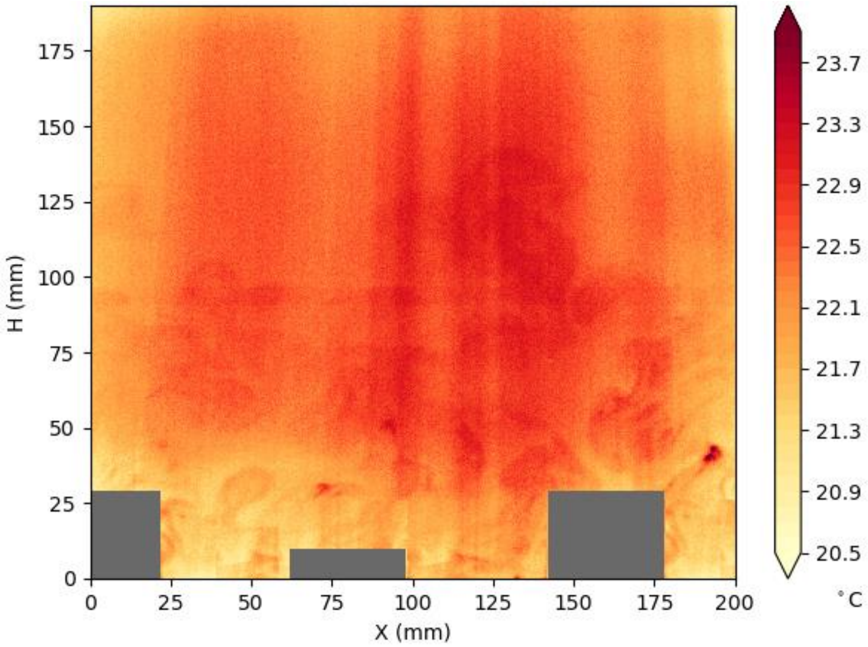

Figure 3. An example of the instantaneous temperature field across the street canyon at Ri = 2.58.

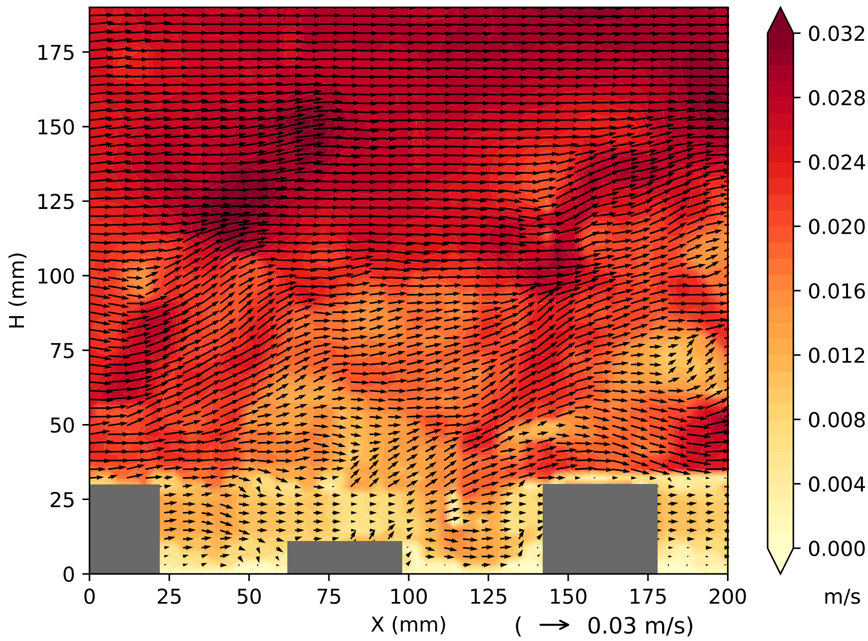

Figure 4. The corresponding instantaneous velocity vector field and velocity magnitude field across the street canyon at Ri = 2.58.

Figure 4 presents the corresponding velocity vector field and velocity magnitude field at the same moment. The significant impact of the heating plate on the flow is clearly shown by the updraft flow and the induced fluctuation near the ground. This impact is decreasing with the increase of the height as indicated by the free stream flow observed 150 mm above the ground. The flow in the street canyon is most likely three-dimensional, however, the two-dimensional experiments do not allow for analyzing the three-dimensional aspect of the flow. This drawback is however counteracted by the advantage to be able to perform simultaneous measurements of flow and temperature fields at a high spatial and temporal resolution, allowing for correlation between both fields.

To understand the impacts of the approaching flow and heating plate, figure 5 summarizes the time-averaged velocity vector fields for six runs with a particular focus on the central street canyon region where the flow is significantly influenced. The first column is the velocity vector field and velocity magnitude field in isothermal conditions and normalized by the free stream velocity, namely 0.03, 0.06 and 0.15 m/s, respectively. While the second column lists the normalized velocity fields under heating conditions for a clear comparison. Canyon vortex can be easily seen in the isothermal cases, particularly with low free stream velocity. In non-isothermal conditions, the approaching flow becomes more buoyant by convective heating from the heated plate, which stops the formation of the canyon vortex and leads to significant updraft flow. The updraft flow and thermal plumes as shown in Fig. 3 indicate the heat removal process from the ground. It is also noted that with an increase in the free stream velocity, the formation of canyon vortex and updraft buoyant flow components are weakened.

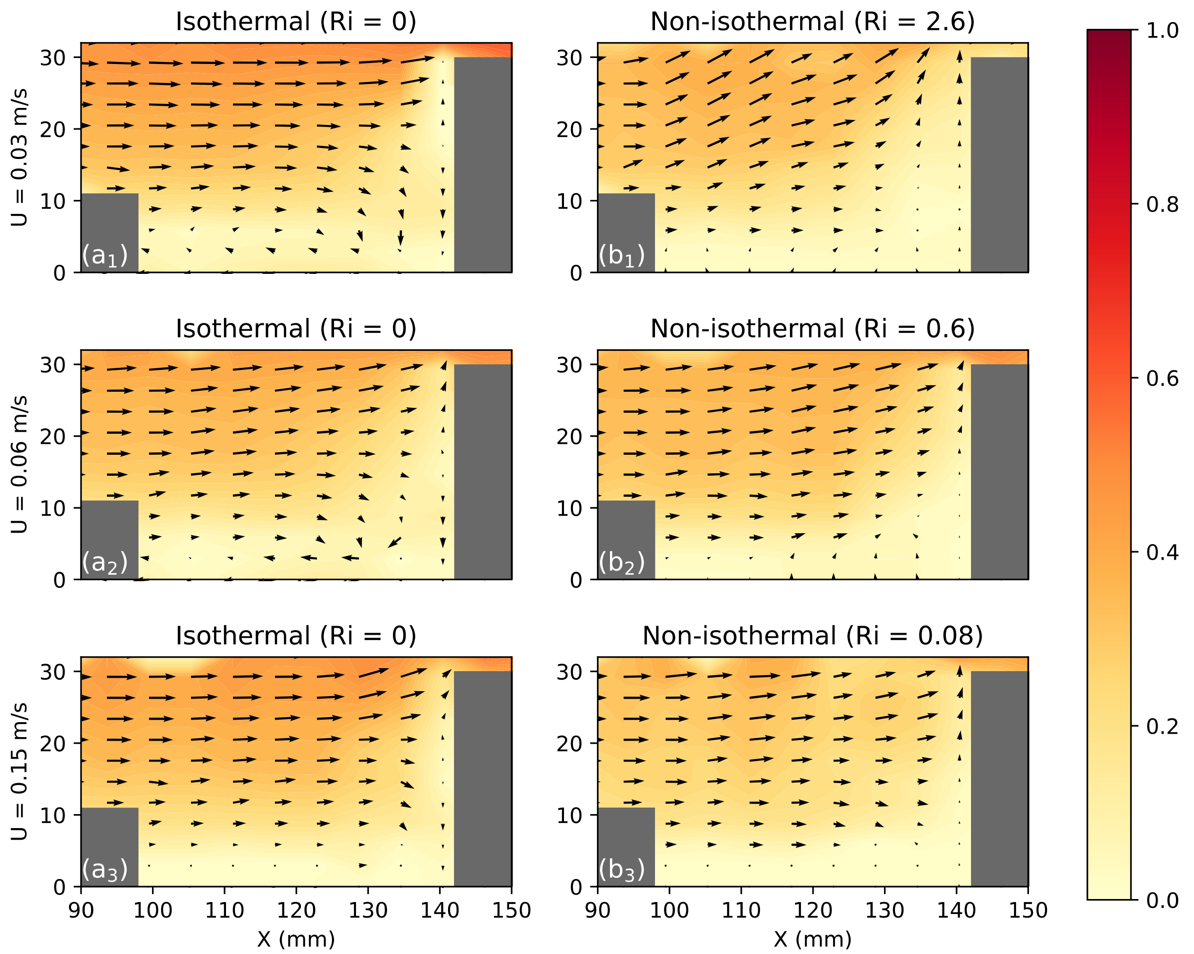

Figure 5. Time-averaged velocity vector fields and velocity magnitude fields for different configurations are normalized by the free stream velocities, respectively.

Canyon volumetric ventilation rate, Q', which plays an important role in heat removal, is calculated based on the instantaneous vertical velocity at the roof level (W), given as

$$Q' = \frac{\tau}{V_c}\int_A W dA \tag{1}$$

where τ is the reference time and calculated as $\tau = 2(H+S)/(2U_f/3)$, V_C is the unit volume of the canyon, and A is the ventilation area of interest. By integrating the ventilation rate over the canyon width, we obtain the time series of the canyon-wise ventilation rate as shown in figure 6. As mentioned above, the 3-D flow behavior can be also concluded from this high spatial and temporal two-dimensional measurement. The positive ventilation indicates the flow enters the canyon from the two sides of the canyon and exists the canyon from the roof level. It can be concluded from the figure that with a higher ground temperature, the ventilation rate over the street canyon increases regardless of the flow velocity. For instance, when the approaching flow is set at 0.03 m/s, the ventilation rate increases from 0.084 at the isothermal condition to 1.584 at plate temperature of 30 °C and further to 1.813 at plate temperature of 40 °C. When the plate is set at 40 °C, buoyant updraft flow dominates the ventilation at the canyon roof level at a velocity of 0.03 m/s. Hence, with an increased flow velocity (0.06 m/s), the impact of the buoyant flow on the ventilation rate is weakened. The approaching flow is becoming the dominating factor with a further increase in the velocity, which results in an increase in the ventilation rate from 1.25 to 1.56. This is also seen in the isothermal condition which the ventilation rate increases with an increase in the free stream velocity.

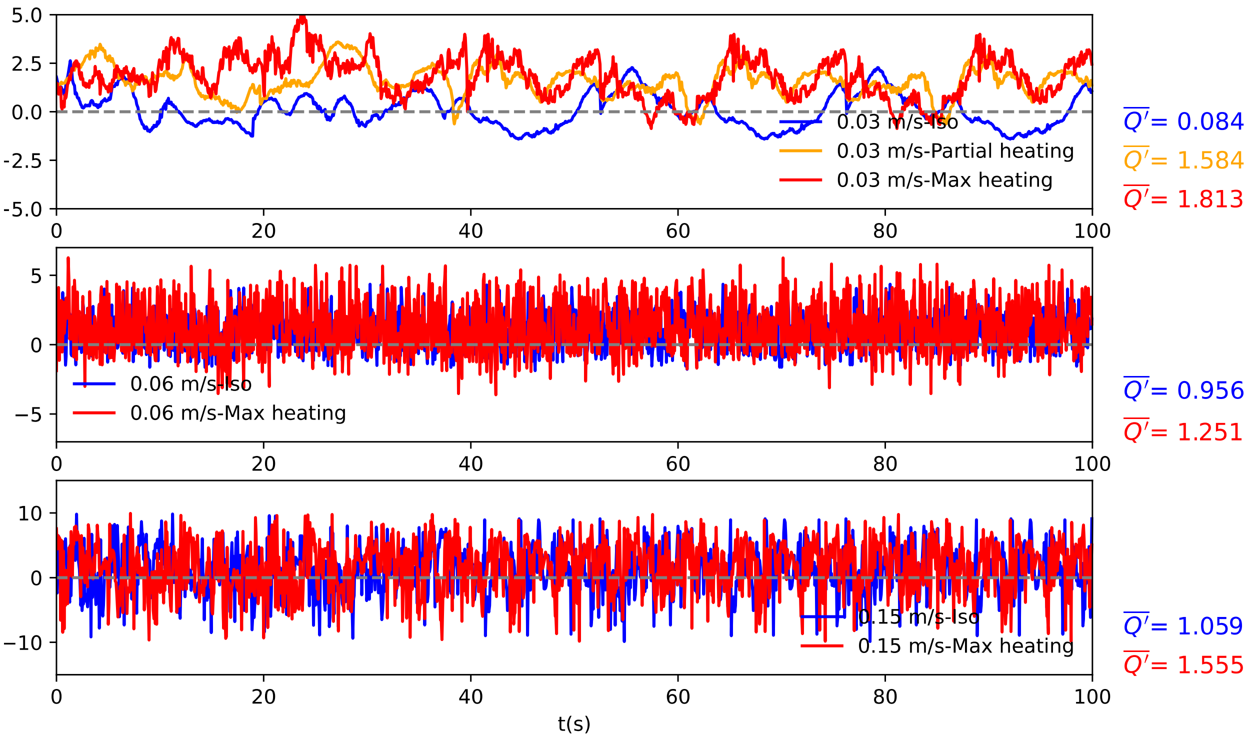

Figure 6. Ventilation rates at the canyon roof level in the different configurations as a function of time.

Figure 7 shows the time-averaged fluid temperature profiles along the canyon centerline (X = 120 mm) and canyon roof level (H = 30 mm) at different test conditions. It is shown that both the temperatures along the canyon centerline and canyon roof level decrease with an increase in the free stream velocity. As heat is carried away by the approaching flow from the plate, a flow at a higher velocity has greater heat removal capability and hence results in a lower temperature.

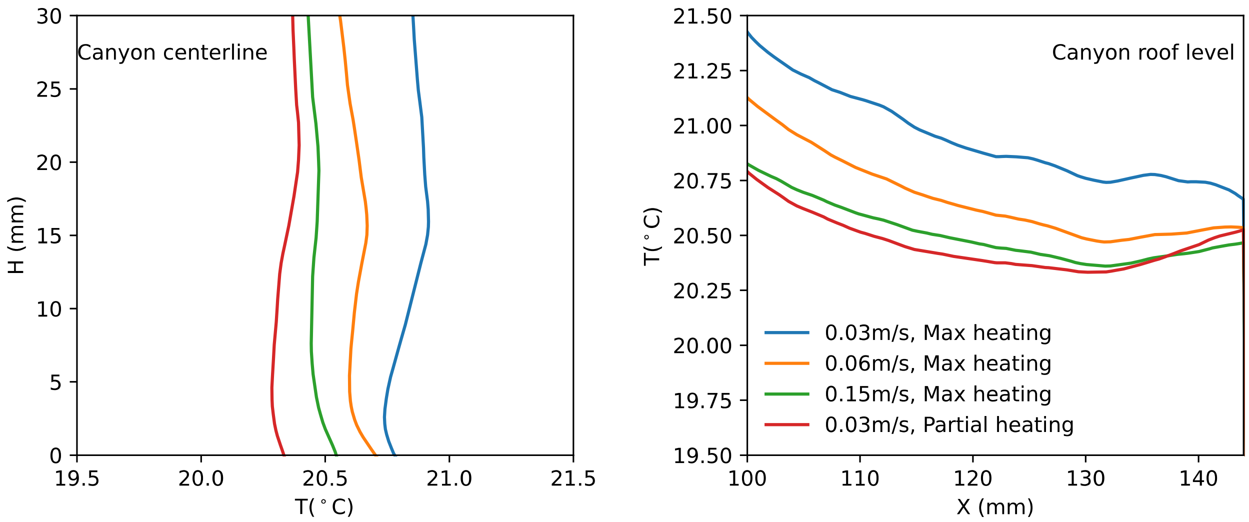

Figure 7. Time-averaged temperature distribution along the canyon centerline (left) and temperature distribution at the canyon roof level in different test configurations.

4. Conclusion

This work reports simultaneous PIV and LIF measurements conducted in the ETH Zurich Atmospheric Boundary Layer Water Tunnel to study the urban microclimate. The PIV-LIF technique makes it possible to analyze the temporal development of the concurrent velocity and temperature fields of the flows. The updraft buoyant flow and turbulence induced by the heating plate are captured. Impacts of the approaching flow velocity and heating condition of the ground plate on the flow behavior and ventilation rate from the canyon are compared. Both the flow velocity and heating condition of the ground contribute to the canyon ventilation rate and at the low velocity, the buoyant updraft flow caused by the heating plate dominates the ventilation flow.

5. Reference

1. Manoli, G., et al., *Magnitude of urban heat islands largely explained by climate and population.* Nature, 2019. **573**(7772): p. 55-60.
2. Zhao, L., et al., *Strong contributions of local background climate to urban heat islands.* Nature, 2014. **511**(7508): p. 216-219.
3. Arnfield, A.J., *Two decades of urban climate research: a review of turbulence, exchanges of energy and water, and the urban heat island.* International Journal of Climatology, 2003. **23**(1): p. 1-26.
4. Kong, J., et al., *Urban Heat Island and Its Interaction with Heatwaves: A Review of Studies on Mesoscale.* Sustainability, 2021. **13**(19): p. 10923.
5. Fan, Y., Y. Li, and S. Yin, *Non-uniform ground-level wind patterns in a heat dome over a uniformly heated non-circular city.* International Journal of Heat and Mass Transfer, 2018. **124**: p. 233-246.

6. Miralles, D.G., et al., *Mega-heatwave temperatures due to combined soil desiccation and atmospheric heat accumulation.* Nature Geoscience, 2014. **7**(5): p. 345-349.
7. Li, Y., et al., *On the influence of density and morphology on the Urban Heat Island intensity.* Nature Communications, 2020. **11**(1): p. 2647.
8. Yuan, C., et al., *Mitigating intensity of urban heat island by better understanding on urban morphology and anthropogenic heat dispersion.* Building and Environment, 2020. **176**: p. 106876.
9. Manickathan, L., et al., *Parametric study of the influence of environmental factors and tree properties on the transpirative cooling effect of trees.* Agricultural and Forest Meteorology, 2018. **248**: p. 259-274.
10. Princevac, M., et al., *Lateral channeling within rectangular arrays of cubical obstacles.* Journal of Wind Engineering and Industrial Aerodynamics, 2010. **98**(8): p. 377-385.
11. Neophytou, M.K.-A., C.N. Markides, and P.A. Fokaides, *An experimental study of the flow through and over two dimensional rectangular roughness elements: Deductions for urban boundary layer parameterizations and exchange processes.* Physics of Fluids, 2014. **26**(8): p. 086603.
12. Allegrini, J., V. Dorer, and J. Carmeliet, *Wind tunnel measurements of buoyant flows in street canyons.* Building and Environment, 2013. **59**: p. 315-326.

Computational Simulations of Gases Dispersion in Built-up Environment under Changes in Roof Shape Configurations

M. F. Yassin, M. Jasem, M. Shlash

Environment & Life Sciences Center, Kuwait Institute for Research and Science, Kuwiat

Abstract

Gases pollution dispersion in a built-up environment is a significant problem where many people live. This study investigates the impact of the building's roof shape configurations on the gases pollutant emission from vehicle exhausts within the street canyon using computational simulation with a computational fluid dynamics model (CFD). The simulations are conducted based on the Reynolds Averaged Navier Stokes (RANS) models with k–ε turbulence model (Standard, Realizable, and renormalization group (RNG) k–ε models) under neutral atmospheric conditions. Five roof shape configurations are applied in this study: (a) flat roof-shaped, (b) 45^0 sides roof-shaped, (c) 90^0 lift side roof-shaped, (d) 90^0 right side roof-shaped, and (e) Trapezoid roof-shaped. The computational results are compared and validated with the wind tunnel results. The results obtained indicate that the standard k–ε turbulence model yielded the best agreement with experimental data. The wind velocity increases with the flat, 45^0 Sides, and trapezoid roofs-shaped and decreases with the 90^0 lift side and lift side roofs-shaped. The pollutant concentration decreases with the 450 sides roof-shaped and trapezoid roof-shaped and increases with the flat roof-shaped.
Keywords: Atmospheric diffusion; Computational Fluid Dynamics; Roof building

Introduction

There are many situations where it would be helpful to compute pollutant concentrations in street canyons within an urban area. Local authorities need such information better to understand the impact of urban air quality on health and assess the likely impact of urban planning and traffic control measures on population exposure and health. The building cavity recirculation region in an urban environment is the region above the roof bounded by the separation streamline originating at the upwind roof edge and downwind of the building bounded by the reattached streamline. The cavity is bounded laterally by streamlines separating from the corners. Depending on building configurations, there can be distinct rooftop and downwind cavities or a single recirculation cavity. There is an urgent need for a better understanding of hazardous gas dispersion inside the building cavity to assess and optimally respond to any release of toxic materials near the building.

One of the most dominant parameters for pollutant dispersion in building cavity recirculation regions is building orientation and roof configuration, including roof shape, geometry, and architectural design (Yassin et al., 2005, 2008a, b; Yassin, 2009, 2010, 2011; Kellnerova et al., 2012; Yassin and ohab, 2012a,b, 2013a,b,c,d; Yassin and Kassem, 2014; Yassin et al., 2021). The influence of roof shape on flow and pollutant dispersion has been described in studies evaluating the air quality of indoor and outdoor environments, e.g., Rafailidis (1997), Kastner-Klein and Plate (1999), Louka et al. (1998), and Theodoridis and Moussiopoulos (2000). For instance, using physical simulations, Guirguis et al. (2007) investigated wind flow and pollutant dispersion around a single building with an upward wedge-shaped roof. In addition to physical simulation studies, computational simulations have been performed using the standard, RNG, and Chen-Kim k–ε models. Xie et al. (2005) and Huang et al. (2007; 2009) found that building configurations and geometries are essential determinants of flow patterns and pollutant dispersion in street canyons. Flow over regular arrangements of buildings with slanted roofs was numerically studied, and its impact on pollutant dispersion was analyzed by Takano and Moonen (2013). They showed that pollutant concentration in a street canyon decreases with the increase of roof slope. The characteristic of air pollutant dispersion around a high-rise building was investigated by Zhang et al. (2015). They compared experimental measurements in a numerical simulation of a turbulent boundary layer wind tunnel. They show a similar trend to the outcomes of self-conducted experimental measurements that the pathways of pollutant migration for windward and leeward pollutant emission are different. The use of the CFD approach for pollutant dispersion around building in urban environments was reviewed by Lateb et al. (2016). They tried to establish a common methodology for verifying and validating CFD models. At the same time, Cui et al. (2016) investigated the effect of an upstream building on the inter-unit dispersion in a multi-story building in two wind directions using CFD models. Their results show that the presence of an upstream building greatly changes the path lines of the downstream target building, which will change the pollutant transportation routes around the downstream building. The main goal of this research is to simulate the dispersion of vehicle emissions in a street canyon within an urban environment. In particular, the investigation is made into the effect of the roof configurations on the street canyon.

Methodology

The ANSYS FLUENT CFD package has been configured to solve the Navier Stokes equations for the mean flow in street canyons for various roof-shaped and its height using the three κ-ε turbulence models: standard κ-ε model, RNG κ-ε model, and Realizable κ-ε model. The conservation equation for species concentration of pollutants must also be solved with the abovementioned equations, which describe the flow characteristics. The governing equations of the model are shown below. A two-dimensional computational domain was used with the wind flow direction assumed perpendicular to the street canyon. The street canyon width to height ratio is W/H=1, and both sides of the buildings have the same height. Eight identical street canyons were aligned horizontally to facilitate fully developed and periodic street canyon turbulent flow. Five different roof shapes of building structures were considered; (1) a flat roof-shaped, (2) 45o sides roof-shaped, (3) 90o lift side roof-shaped, (4) 90o right side roof-shaped, and (5) trapezoid roof-shaped. Velocity boundary layer conditions were used in the main inlet wind flow and the vehicle exhaust. The initial wind speed is uniform (5 m/s) with low turbulence intensity. A user-defined subroutine for including the turbulence 0.28 the power-law inlet velocity profile into FLUENT code was developed and used in the analysis.

Results and Discussions

The variability of the roof-shaped produced different wind vortex structures inside the street canyon that caused a change in the dispersion characteristics. Fig. 1 shows contour lines of the normalized pollutant concentration fields inside the street canyon of the different roof-shaped windward and leeward walls for the three k-ε turbulence models with the three roof heights. A clockwise vortex circulation was generated within the street canyon when wind flow was blown across the street canyon from the left of the upstream building. Then, the pollutant was carried to the leeward wall from the line source and dispersed further in the street canyon. The pollutant concentration on the leeward wall was higher than that on the windward wall building at the lower region of the street canyon. This is because the horizontal velocity of the lower area of the street canyon was negative, where the vortex was clockwise. Moreover, as the rotation velocity was small in the lower region of the street canyon, it was tough to remove the pollutant discharged from the line source out of the street canyon. On the other hand, the mean horizontal velocity of the upper region of the street canyon was upbeat and had a larger rotation velocity.

Hence, it could transport the pollutant out of the canyon from the windward wall of the buildings. For this reason, the pollutant concentration at the leeward wall was higher than that at the windward wall in the higher region of the street canyon. Under these circumstances, pollutant dispersion was solely removed vertically from the street canyons to the free surface layer by the vertical mean flux and vertical turbulent flux. There were some uniform characteristics of pollutant dispersion, although the wind flow varied depending on the street intersection. On the other hand, it shows clearly that the dispersion pollutant transports to the windward wall when the horizontal velocity is positive.

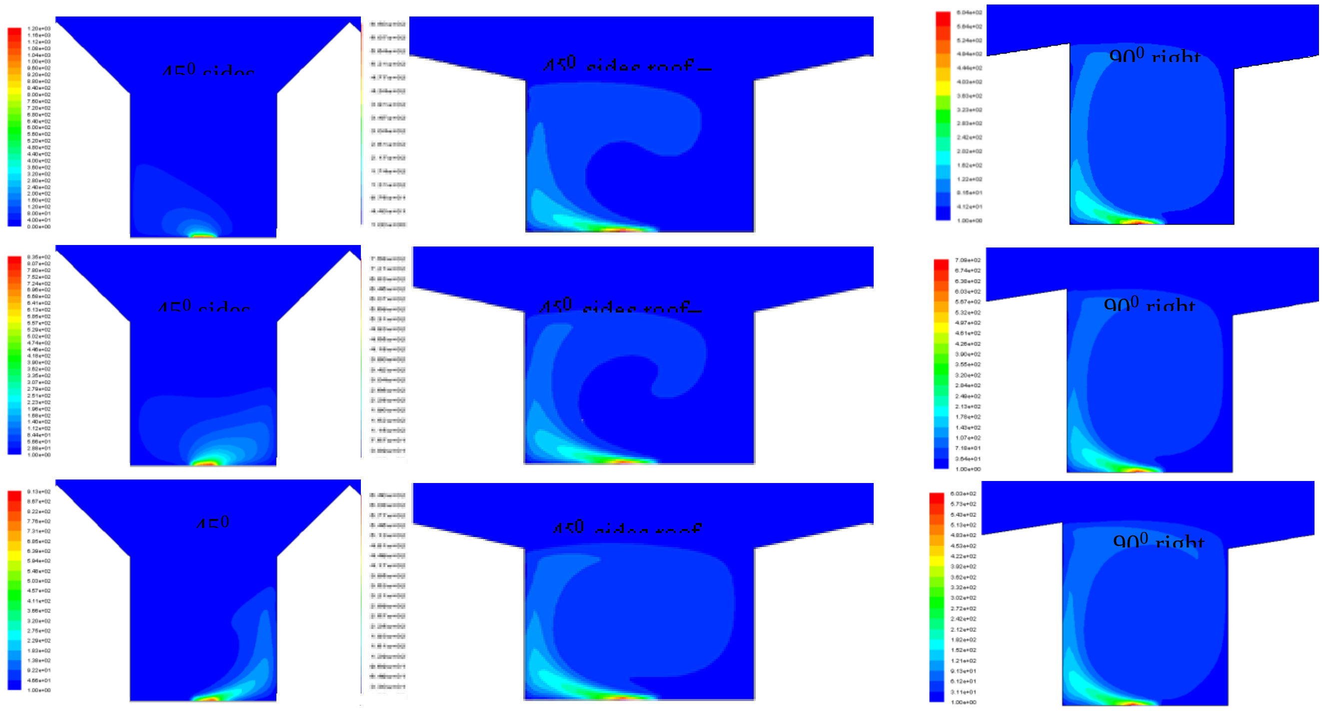

Fig. 1. Contour lines of non-dimensional mean concentration *k* in the *x-z* plane

Conclusions

The pollutant concentration increases with the flat roof-shaped. The pollutant concentration decreases with the 450 sides roof-shaped and trapezoid roof-shaped. The concentration decreases exponentially in the vertical direction. The pollutant concentration inside the street canyon increased towards the ground surface and decreased up to the roof canyon.

References

Cui, D.J., Mak, C.M., Kwok, K.C.S. and Ai, Z.T., 2016. CFD simulation of the effect of an upstream building on the inter-unit dispersion in a multi-story building in two wind directions. Journal of Wind Engineering and Industrial Aerodynamics, 150, pp.31-41.

Guirguis N. M., AbdEl-Aziz, A. A., Nassief M. M. 2007. Study of wind effects on different buildings of pitched roofs. Desalination 209: 190–198.

Huang Y., Hu X., Zeng N. 2009. Impact of wedge-shaped roofs on air flow and pollutant dispersion inside urban street canyons. Build. Environ. 44: 2335–2347.

Huang Y., Jin M., Sun Y. 2007. Numerical studies on air flow and pollutant dispersion in urban street canyons formed by slanted roof buildings. J. Hydrodyn. 19(1): 100–106.

Kastner-Klein P., Plate E. J. 1999. Wind-tunnel study of concentration fields in street canyons. Atm. Environ. 33: 3973–3979.

Kellnerova, R., Kukacka, L., Jurcakova, K., Uruba, V., Janour, Z., 2012. PIV Measurement of Turbulent Flow Within a Street Canyon: Detection of Coherent Motion. J Wind Eng Ind Aerodyn 104-106, 302-313.

Lateb, M., Meroney, R.N., Yataghene, M., Fellouah, H., Saleh, F. and Boufadel, M.C., 2016. On the use of numerical modelling for near-field pollutant dispersion in urban environments− A review. Environmental Pollution, 208, pp.271-283.

Louka P., Belcher S. E. Harrison R. G. 1998. Modified street canyon flow. J. Wind Eng. Ind. Aerodyn. 74–76: 485–493.

Rafailidis S. 1997 .Influence of building area ldensity and roof shape on the wind characteristics above a town. Boundary-Layer Meteorol. 85: 255–271.

Takano Y. , Moonen P. 2013. On the influence of roof shape on flow and dispersion in an urban street canyon J. WindEng.Ind.Aerodyn.123:107–120

Theodoridis G., Moussiopoulos N. 2000. Influence of building density and roof shape on the wind and dispersion characteristics in an urban area: a numerical study. Environ. Monit. Assessment 65: 407–415.

Xie X., Huang Z., Wang J. 2005. Impact of building configuration on air quality in street c canyon. Atm. Environ. 39: 4519 – 4530.

Yassin M.F., Kato S., Ooka R., Takahashi T. and Kouno R. (2005) "Field and Wind Tunnel study of the pollutant diffusion in built-up area under variable meteorological Conditions" Journal of Wind Engineering and Industrial Aerodynamics, 93(5), 361-382

Yassin M.F., Ohba M., and Tanaka H. (2008a) “Experimental Study on Gaseous Diffusion behind an isolated building” Environmental Monitoring and Assessment. 147 (1-3), 149-158.

Yassin M.F., Kellnerova *R.* and Janour Z. (2008b) “Impact of Street Intersections on Air Quality in an Urban Environment” Atmospheric Environment. Vol. 42/20, 4948-4963

Yassin M. F. (2009) “Numerical Study of Flow and Gas Diffusion in the Wake behind an Isolated Building” Advances in Atmospheric Sciences, 26(6), 1241-1252.

Yassin M.F. (2010) “ Study on Pollutant Dispersion Within Urban Area: Under Changes of Atmospheric Stability and Wind Direction.” VDM Publishing House Ltd, ISBN 978-3-639-27279-6

Yassin, M.F., 2011. Impact of height and shape of building roof on air quality in urban street canyons. Atmospheric Environment, 45(29), pp.5220-5229.

Yassin M.F., Ohba M. (2012a) "Experimental Simulation of Air Quality in Street Canyon under Changes of Building Orientation and Aspect Ratio" J. of Exposure Science and Envir. Epidemiology; 22(5) 502-515

Yassin M.F. and Ohba M. (2012b) "Experimental Study of the Impact of Structural Geometry and Wind Direction on Vehicle Emissions in Urban Environment" Transp. Res. P.t D: Transp. & Envir., 17, 181-189

Yassin M.F (2013a) "A wind tunnel study on the effect of thermal stability on flow and dispersion of rooftop stack emissions in the near wake of a building" Atmospheric Environment, 65, 89-100.

Yassin M.F. 2013b: Experimental Study on Contamination of Building Exhaust Emissions in Urban Environment under Changes of Stack Locations and Atmospheric Stability. Energy and Build., 62, 68-77.

Yassin M.F. (2013c) Numerical simulation of the impact of street geometry on vehicle emissions in the urban area, Int. J. of Environment and Pollution, 53(1/2), 46-63

Yassin M.F (2013d) "Numerical Modeling on Air Quality in an Urban Environment with changes of the Aspect Ratio and Wind Direction" Environmental Science and Pollution Research, 20, 3975-3988

Yassin M.F., Ohba M. (2013) "Effect of Street Geometrical Layout on Dispersion emissions of Traffic Exhaust: Experimental Simulation" Clean Technologies and Environmental Policy, 15(1) 167-177.

Yassin M.F., Kassem M. A. (2014) Effect of Building Orientations on Gaseous Dispersion in Street Canyon: a Numerical Study, Environmental Modeling & Assessment, 19(4), 335-344.

Yassin, M.F. , Alhajeri N.S., Elmi A. A., Malek M. J., Shalash M., (2021). Numerical simulation of gas dispersion from rooftop stacks on buildings in urban environments under changes in atmospheric thermal stability. *Environ Monit Assess*, **193**, 22. https://doi.org/10.1007/s10661-020-08798-x

Zhang, Y., Kwok, K.C.S., Liu, X.P. and Niu, J.L., 2015. Characteristics of air pollutant dispersion around a high-rise building. Environmental Pollution, 204, pp.280-288.

Wind tunnel measurements of airflows and gas concentrations downwind a naturally-ventilated pig building model

Qianying Yi[1], David Janke[1], Lars Thormann[1], Sabrina Hempel[1], Barbara Amon[2, 3], Thomas Amon[1, 4]

[1]Leibniz Institute for Agricultural Engineering and Bioeconomy (ATB), Department of Engineering for Livestock Management, Max-Eyth-Allee 100, 14469 Potsdam, Germany
[2]Leibniz Institute for Agricultural Engineering and Bioeconomy (ATB), Department of Technology Assessment and Substance Cycles, Max-Eyth-Allee 100, 14469 Potsdam, Germany
[3]University of Zielona Góra, Faculty of Civil Engineering, Architecture and Environmental Engineering, Licealna 9/9, 65-417 Zielona Góra, Poland
[4]Free University Berlin, Institute of Animal Hygiene and Environmental Health, Department of Veterinary Medicine, Robert-von-Ostertag-Str. 7-13, 14163 Berlin, Germany

Abstract

As a new type of pig housing system, naturally ventilated pig buildings with outdoor exercise yards (NVPBOYs) have better animal well-being and thus are receiving increasing interest. However, there is lack of information on the transport and dispersion characteristics of air pollutants for this type of pig house. Therefore, the aim of this study was to investigate the dispersion of air pollutants from a NVPBOY. Experiments with a scaled NVPBOY model were carried out in a large boundary layer wind tunnel. Air velocities and concentrations of a tracer gas were measured at a vertical plane downwind the scaled model using a Laser Doppler Anemometer and a fast Flame Ionisation Detector. A tracer gas concentration accumulation area was observed in the wake of the scaled model at the height where air vortex and peak turbulent kinetic energy occurred. The results contribute to a better understanding of air pollutants dispersion characteristics in relation to airflows.

1. Introduction

Open-type pig buildings with natural ventilation have the advantages of better animal welfare, low operation and maintenance cost, energy saving and low noise to animals. With these benefits, naturally ventilated pig buildings with outdoor exercise yards (NVPBOYs) are receiving increasing attention worldwide (Park et al., 2017).

One important issue concerning NVPBOYs is the environmental impact of air contaminants produced from the buildings. The transport and dispersion of airborne pollutants from an open-type livestock buildings are strongly related to the airflows, which are in turn mainly influenced by the building configurations (e.g. openings, roofs, building internal structures), animals, outdoor climate conditions, etc. (Sauer et al., 2011). Therefore, it is essential to understand the dispersion characteristics of air pollutants from NVPBOYs in relation to the airflows around the buildings.

Physical modelling in a wind tunnel has advantages of providing comprehensive measurements under controlled boundary conditions, and has been widely applied in emission dispersion research (Ahmad et al., 2005; Vidali et al., 2022).

The objective of this study was to investigate the transport and dispersion characteristics of air pollutants from NVPBOYs to the surrounding environment. To achieve this, air velocities and gas concentrations at downwind of a scaled model of a NVPBOY were measured in a boundary layer wind tunnel. The airflows in terms of air speed and turbulent characteristics and the distribution of gas concentrations were analysed.

2. Methodology

2.1. Experimental setup

The measurements were conducted in a large atmospheric boundary layer wind tunnel at the Leibniz Institute for Agricultural Engineering and Bioeconomy (ATB), Germany. The wind tunnel is used for the research on ventilation airflows and dispersion processes in agricultural buildings, as well as for generating dataset for CFD validations. The total length of the wind tunnel is 28.5 m. The dimensions of the test section of the wind tunnel are Length × Width × Height = 19.5 m × 3 m × 2.3 m. The spires and roughness elements placed in the upstream are used to generate a moderately rough boundary layer with a power layer exponent of 0.14, which was documented in the publication (Yi et al., 2020). All measurements were performed at a free-stream wind speed of 8 m/s.

A 1:50 scaled model of an experimental NVPBOY located in Wehnen, northwest Germany was used in this study, as shown in Fig. 1. It was consisted of a housing area with eight pigpen boxes and an outdoor exercise yard. Since the exercise yard is expected to produce most ammonia emissions, a tracer gas release surface made of porous media stone was built at the floor of the exercise yard. The dimensions of the scaled model were Length × Width × Height = 0.427 m × 0.256 m × 0.130 m, resulting in a blockage ratio of 0.8%. The height of the inlet openings was 0.020 m.

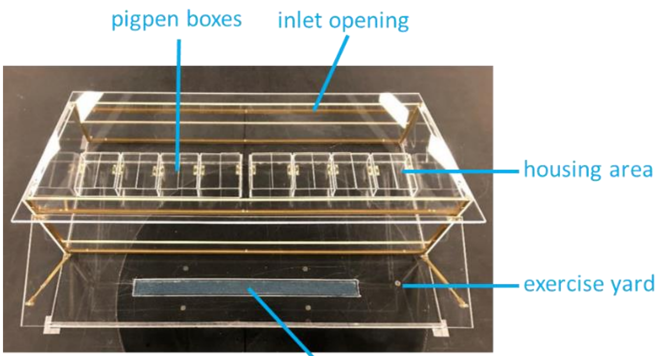

Fig. 1. A 1:50 scaled model of a naturally ventilated pig building with an outdoor exercise yard.

2.2. Measurement positions

Air velocity and concentration of tracer gas were measured at 14 vertical lines (10 points at each line) downwind the scaled pig building model. The 14 lines were at the same vertical plane along the centreline of the scaled model, located from 0.17 m to 1 m away from the scaled model. In order to capture the detailed airflow and concentration fields at the wake of the building, the measurement lines were densely distributed close to the building. Detailed measurement positions are illustrated in Fig. 2.

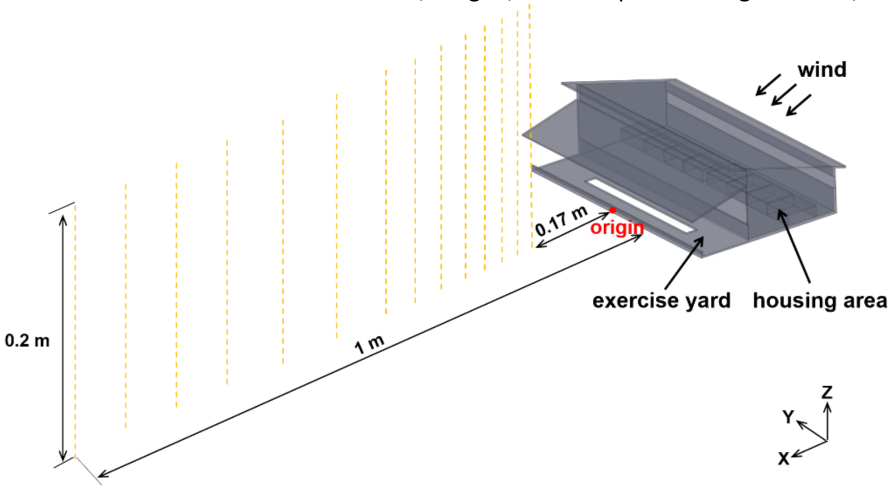

Fig.2. Sketch of the scaled pig building model with air velocity and gas concentration measurement positions represented by yellow dash lines.

2.3. Velocity and concentration measurements

Stream-wise (in X direction) and vertical (in Z direction) air velocity components were measured by a 2D Laser Doppler Anemometer, which was installed on a computer-controlled traverse system. The measurements were taken continuously at each point until the sampling number reached 40,000. Time-averaged mean velocities and standard deviations were recorded.

Concentration of the tracer gas was measured at the same positions as the velocity measurements. Ethane has a density similar to air, and was therefore used as the tracer gas in this study. The pure ethane was continuously emitted from the floor of the exercise yard of the scaled model with a mass flow rate of 250nl/h. The concentration of the tracer gas was measured using a fast response Flame Ionisation Detector (fast FID). The sampling frequency was 1,000 Hz. The sampling number at each measurement position was 30,000. The fast FID was calibrated with certified calibration gases of different concentrations before measurements.

3. Results and discussion

3.1. Air velocity and turbulence contours

Fig. 3a shows the time-averaged air speed contour with streamlines at the vertical centre plane downwind the scaled pig building model. A stagnant zone occurred in the wake of the building model up to the distance of 0.42 m (i.e. 3.23H_b, where H_b is the building height). An air vortex was observed above the leeward roof of the building model, at the height ranged from 0.072 m to 0.108 m, determined by visual inspection of the streamline plot. The air accelerated over the top of the building model at the height above 0.17 m.

Fig. 3b shows contour of the turbulent kinetic energy (TKE) at the same measurement plane. It was seen that a large portion of TKE was generated around the ridge height (from 0.12 m to 0.16 m), which was probably caused by the flow separation above the roof. The length of the main TKE production area was close to the length of the stagnant zone due to the turbulent flow structure in this area.

(a)

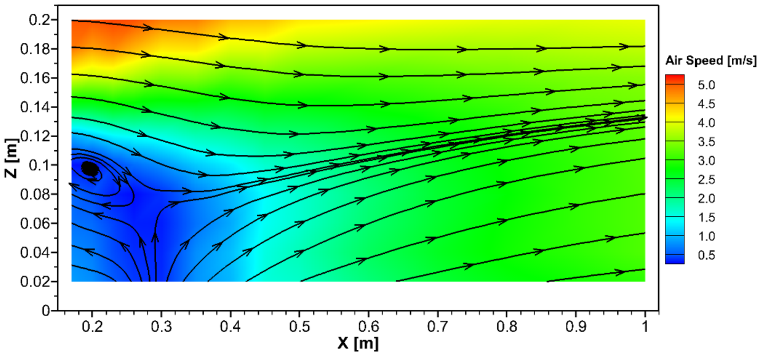

(b)

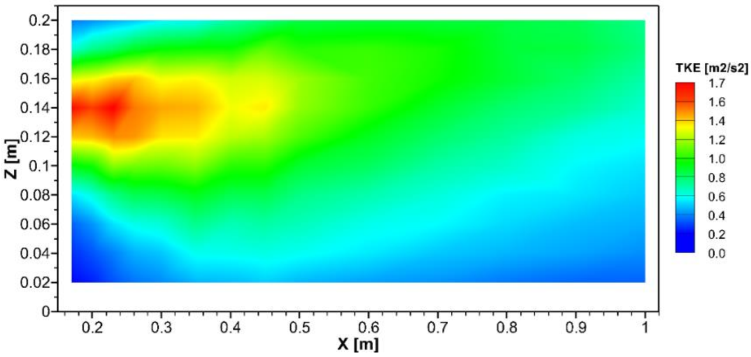

Fig. 3. Air speed contour with streamlines (a) and turbulent kinetic energy (TKE) contour (b) at the vertical plane downstream along the centreline of the scaled pig building model. X represents distance away from the scaled model, and Z represents the height from the wind tunnel floor.

3.2. Concentration contours

Fig. 4 shows the contour of time-averaged concentration of the tracer gas at the same vertical plane as velocity measurements. It was seen that the width of the plume in Z direction was 0.2 m (1.54H_b), and the length of the plume in X direction was over 1 m. This indicates that the air pollutants produced from the scaled NVPBOY are supposed to diffuse further over 1 m (i.e. 7.69H_b) at the experimental condition. Within the plume, a high concentration area (1400 – 1600 ppm) was observed at the height from 0.05 m to 0.14 m, where the air recirculation and peak of TKE occurred. This was because the tracer gas was trapped in the air vortex, and then it dispersed by turbulent flow. As a result, the tracer gas accumulated in this area. Around this area, the tracer gas transported and dispersed quickly by the mean air speed.

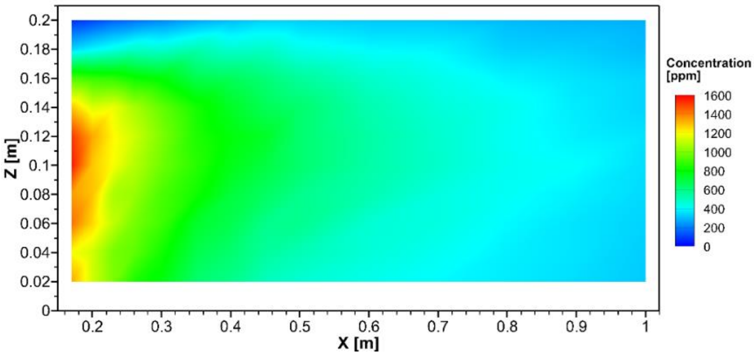

Fig. 4. Gas concentration contour at the vertical plane downstream along the centreline of the scaled pig building model. X represents distance away from the scaled model, and Z represents the height from the wind tunnel floor.

4. Conclusion

Airflows in terms of velocity and turbulence as well as concentration of a tracer gas at a vertical plane downwind a scaled-down naturally ventilated pig building with an outdoor exercise yard (NVPBOY) were measured in a large boundary layer wind tunnel. A stagnant zone with an air vortex was observed at the wake of the building up to the distance of $3.23H_b$. The size of the plume of air pollutants from the scaled NVPBOY model was $1.54H_b$ and over $7.69H_b$ in vertical and stream-wise airflow directions respectively under the experimental conditions. The gas concentration accumulated in an area at the height where air vortex and peak of TKE occurred. The results showed a close link between air pollutants dispersion and airflows.

References

Ahmad, K., Khare, M., Chaudhry, K., 2005. Wind tunnel simulation studies on dispersion at urban street canyons and intersections – a review. Journal of Wind Engineering and Industrial Aerodynamics 93, 697-717.
Park, H.-S., Min, B., Oh, S.-H., 2017. Research trends in outdoor pig production – a review. Asian-Australasian Journal of Animal Sciences 30, 1207-1214.
Sauer, T., Hatfield, J., Haan, F., 2011. A wind tunnel study of airflow near model swine confinement buildings. Transactions of the ASABE 54, 643-652.
Vidali, C., Marro, M., Correia, H., Gostiaux, L., Jallais, S., Houssin, D., Vyazmina, E., Salizzoni, P., 2022. Wind-tunnel experiments on atmospheric heavy gas dispersion: Metrological aspects. Experimental Thermal and Fluid Science 130, 110495.
Yi, Q., Janke, D., Thormann, L., Zhang, G., Amon, B., Hempel, S., Nosek, Š., Hartung, E., Amon, T., 2020. Airflow characteristics downwind a naturally ventilated pig building with a roofed outdoor exercise yard and implications on pollutant distribution. Applied Sciences 10, 4931.

PHYSMOD 2022 – International Workshop on Physical Modeling of Flow and Dispersion Phenomena
Institute of Thermomechanics of the CAS, Prague, Czech Republic – August 29-31, 2022

Dry deposition of particulate matter on urban green infrastructure with parameterised drag effects

Tess Ysebaert[1], Roeland Samson[2], Siegfried Denys[1]

[1]University of Antwerp, Faculty of Science, Department of Bioscience engineering, Sustainable Energy, Air & Water Technology (DuEL), Groenenborgerlaan 171, 2020 Antwerp, Belgium
[2]University of Antwerp, Faculty of Science, Department of Bioscience engineering, Laboratory of Environmental and Urban Ecology, Groenenborgerlaan 171, 2020 Antwerp, Belgium

Abstract

Urban green infrastructure offers opportunities as nature-based solution to urban particulate matter (PM) pollution, but the uncertainty of their effectiveness is hampering their implementation. Computational fluid dynamics (CFD) models of PM capture by vegetation are useful tools to increase their applicability. In CFD models, the correct description of the vegetation-wind interaction is key and the accuracy of the modelled wind flow is highly linked to the uncertainty about the drag coefficient. The Wilcox revised k-ω model with adapted momentum and turbulence sink terms was parameterised by comparison with wind tunnel experiments and this led to improved results of the aerodynamic statistics. Next, the scalar tranport equation was employed to model PM dispersion. The mechanisms leading to PM deposition on vegetation were implemented and the optimised drag coefficient was used in these equations. The model was validated with other wind tunnel experiments making use of labscale generated PM. Moreover, the particles consisted of Arizona fine test dust with a diameter of 1-10 µm, thus real particle dynamics were studied. All simulations were performed with Comsol Multiphysics® (version 5.6).

Keywords: Green walls, CFD, Drag force, Size-resolved deposition model, Wind tunnel validation

1 Introduction

Air pollution caused by particulate matter (PM) poses a serious health risk among citizens worldwide. Urban green infrastructure, in particular green walls, is increasingly regarded as a nature-based solution to PM pollution in cities (Ysebaert et al., 2021). The correct description of the vegetation-wind interaction is key in describing the effect of vegetation in CFD models including dispersion. Plant elements reduce momentum and turbulence by both viscous and form drag, which are represented by the permeability (represented as K, m^2) and drag coefficient (represented as C_d, unitless), respectively. The accuracy of the modelled wind flow is highly linked to the uncertainty about the drag coefficient. In addition, at low wind speeds viscous drag is not negligible and it should be regarded in CFD models (Ysebaert et al., 2022). This research aims to address the uncertainty related to C_d and K by including the effect of climbers on both the momentum and turbulence equations in CFD models. In addition, this research concerns the removal of PM from the atmosphere by dry deposition on leaf surfaces of green wall species. The optimised aeodynamic model was used to model the air flow around an through the vegetation and a scalar transport equation was extended with two often cited analytical dry deposition models (Petroff and Zhang, 2010; Zhang et al., 2001). The outcome of the two models was compared with data from wind tunnel experiments. This article discusses the results for an incoming wind speed of 1.2 ± 0.2 m s^{-1} and a PM concentration of 100 µg m^{-3}.

2 Materials and methods

2.1 Experimental set-ups

Two different wind tunnel setups were used to obtain high quality data for model validation for (1) accurate aerodynamic characterisation of vegetation in urban CFD models, and (2) validation of a size-resolved deposition model. The first setup consisted of a closed loop wind tunnel with an inner diameter of 103 mm and a total length of 6 m (Figure 1, upper picture). Plant material was hung in the middle of a removable duct part of 0.55 m in quantities corresponding with the real branch scale (Huang et al., 2013). Wind speeds between 0.40 ± 0.01 up to 3.81 ± 0.04 m s^{-1} were obtained in an empty wind tunnel with an inline duct fan (Ruck RS-series) and were measured with an air velocity transmitter (CTV 110, Kimo Instruments) in front of the plant section. Pressure drops were measured across the plant section with a pressure module (700 PD2, Fluke) and a pressure calibrator (717 30G, Fluke).

A second wind tunnel setup was built as an open-circuit system to study PM deposition on green wall species (Figure 1, bottom picture). It was equipped with a hexagonal honeycomb-screens combination after the inlet bend and another identical honeycomb (nominal cell size of 6.4 mm and thickness of 60 ± 0.25 mm, Corex) in front of the fan to straighten the flow. An extraction ventilator (MPS 355 EC 30) resulted in wind speeds between 0.55 and 5 m s^{-1} in the plant compartment, which had a size of 1 x 0.5 x 0.5 m. Climbers were grown against a wire mesh and were placed in the middle of the test section with ramps at both sides to guide the air flow. Wind speeds were measured at the in- and outlet of the test section with a hot wire anemometer (PCE-009, PCE Instruments) and the pressure drop was measured across the test section with the same pressure module.

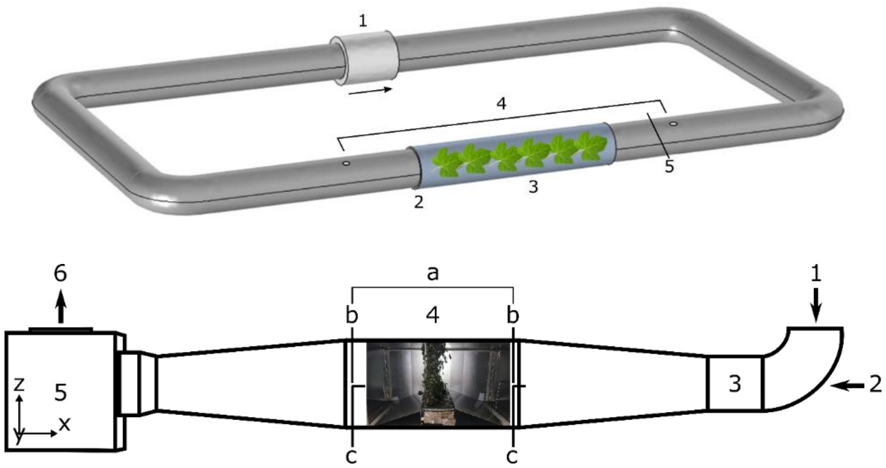

Figure 1 - Upper picture: Closed-circuit wind tunnel setup with 1, an inline duct fan, 2, a mesh to prevent the plants to move, 3, a removable plant section, 4, a differential pressure sensor, and 5, an air velocity transmitter. Bottom picture: Open-circuit wind tunnel setup with 1, an inlet with air from outside, 2, an inlet of Arizona fine test dust coming from a dust aerosol generator, 3, a honeycomb-screen combination, 4, a plant section, 5, an extraction ventilator and 6, an outlet of the wind tunnel to the outside. The letters represent the measurement points with a, a differential pressure, b, a hot wire anemometer, and c, an optical particle sizer.

PM in the size range of 0.37-10 µm was generated with a Dust Aerosol Generator (3410U, TSI) using Arizona fine test dust A1 Ultrafine (Fiatec). The concentration of PM was measured at the in- and outlet of the test section with an Optical Particle Sizer (3330, TSI). At the start of each experiment, the wind speed and PM concentration were set so that the same conditions were obtained for each repetition. In addition, PM deposition on the wind tunnel walls was considered by measuring the difference in PM concentration at the in- and outlet of an empty wind tunnel and correcting for this difference when handling the data of the climbers.

Common ivy (*Hedera helix*), Boston ivy (*Parthenocissus tricuspidata*) and Virginia creeper (*Parthenocissus quinquefolia*), climbers commonly found in Western Europe, were introduced in the first wind tunnel setup (Figure 1, upper picture) to obtain pressure-velocity data. *H. Helix* was used to study PM deposition in the second wind tunnel setup (Figure 1, bottom picture).

2.2 Numerical methods

2.2.1 Fluid flow model

The free stream flow field was modelled by solving the steady state 3D steady-state incompressible, Reynolds-averaged Navier-Stokes (RANS) equation together with the continuity equation using a finite element method in Comsol Multiphysics® (version 5.6). Nothwithstanding the higher accuracy of large eddy simulation (LES) models, RANS was chosen because of its lower computational cost, easier convergence and the avoidance of additional input parameters that have to be calibrated in the case of LES models (Kormas et al., 2016). The Reynold stress tensor was modelled using the Wilcox revised $k-\omega$ turbulence model with k, the turbulent kinetic energy (TKE, kg m^{-1} s^{-3}), and ω, the specific dissipation rate (SDR, kg m^{-3} s^{-2}) (Wilcox, 2008), assuming the Boussinesq approximation.

The effect of vegetation on air flow was modelled by considering both viscous (called viscous drag, represented by permeability K) and pressure (called form drag, represented by drag coefficient C_d) forces created by the vegetation elements. This so-called drag force, gives rise to a momentum sink in which both forces are implemented ($S_{\mathbf{u}}$, equation 1). For this end, vegetation was regarded as a uniform, porous medium and its effect on fluid flow was modelled on average for this volume. The amount of vegetation was introduced as leaf area density (LAD, m^2 m^{-3}), which is the one-sided leaf area per unit volume. In addition, the drag force created by plants gives rise to a source and sink term in the TKE and SDR equations, which come with additional model coefficients which need to be defined carefully (Sogachev and Panferov, 2006; Zeng et al., 2020). For this end, the assumptions of Sogachev and Panferov (2006) were assumed, which results in equations 2 and 3 for the vegetation terms in k and ω, respectively. For the derivation of these equations, the reader is referred to Ysebaert et al. (2022).

$$S_u = -\frac{\mu}{K}\boldsymbol{u} - \rho LAD C_d U \boldsymbol{u} \qquad \textit{Equation 1}$$

$$S_k = 0 \qquad \textit{Equation 2}$$

$$S_\omega = 0.313\rho LAD U \boldsymbol{u} \qquad \textit{Equation 3}$$

With μ, the air dynamic viscosity (kg m^{-1} s^{-1}), K, the permeability (m^2), ρ, the air density (kg m^{-3}), LAD, the leaf area density (m^2 m^{-3}), C_d, the drag coefficient (-), U, spatially averaged wind speed (m s^{-1}), $\boldsymbol{u}$, the wind velocity (m s^{-1}).

K and C_d are the parameters under study and they were determined by a Nelder-Mead optmisation study for *H. helix*, *P. Tricuspidata* and *P. quinquefolia* for a wide range of bulk mean wind speeds (U) from 0.04 ± 0.01 to 3.81 ± 0.04 m s^{-1} corresponding with Reynolds numbers (Re) from $3 \cdot 10^3$ up to $2.5 \cdot 10^4$.

2.2.2 Dispersion and deposition model

The dispersion of PM in the wind tunnel setup was modelled with the 3D steady-state convection diffusion-equation for a passive scalar and deposition was included by a sink term S_d, as follows:

$$S_d = -LADv_dC \quad \textit{Equation 4}$$

With v_d, the deposition velocity (m s^{-1}), which includes all mechanisms leading to PM deposition (Figure 2) and which was specified by Zhang et al. (2001) and Petroff and Zhang (2010). v_d is dependent on the particle diameter.

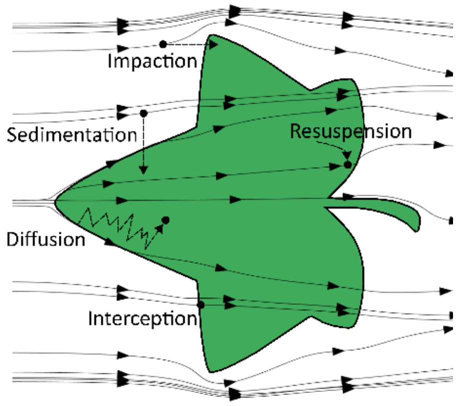

Figure 2 - The different mechanisms of PM dry deposition on a leaf surface (from the article of Ysebaert et al. (2020).

3 Results

3.1 Aerodynamic characterisation of climbers

The optimisation of permeability, K (m^2), and drag coefficient, C_d (-), demonstrated that with increasing Reynolds number, three regions could be identified and the results are depicted in Figure 3. A first region where Re < 4,000 and U < 0.6 m s^{-1}, showed only a significant effect of viscous drag on air flow. Between a Re of 4,000-10,000 (0.68-1.56 m s^{-1}), both viscous and form drag forces are at play, but form drag overtakes viscous drag at around 0.8 to 1.5 m s^{-1} depending on the type of climber and its LAD. Beyond this region, drag force is dominated by form drag. However, C_d decreased with increasing wind speed owing to the sheltering effect of consecutive vegeation elements. Increasing the wind speed even more, would result in a constant C_d value. The outcome of this optimisation clearly showed that (1) viscous drag is not neglible at wind speeds below 1.5 m s^{-1}, and (2) the drag coefficient is dependent on the wind speed in CFD models. Hence, the common practice to model the aerodynamic effect of vegetation as $C_d = 0.2$ leads to deviations, and these deviations are greatest at low wind speeds (not shown here). The latter is important when studying air flow in urban areas, since urban areas are charactised by stagnation zones of wind speeds at locations behind buildings and in street canyons (Lauriks et al., 2021).

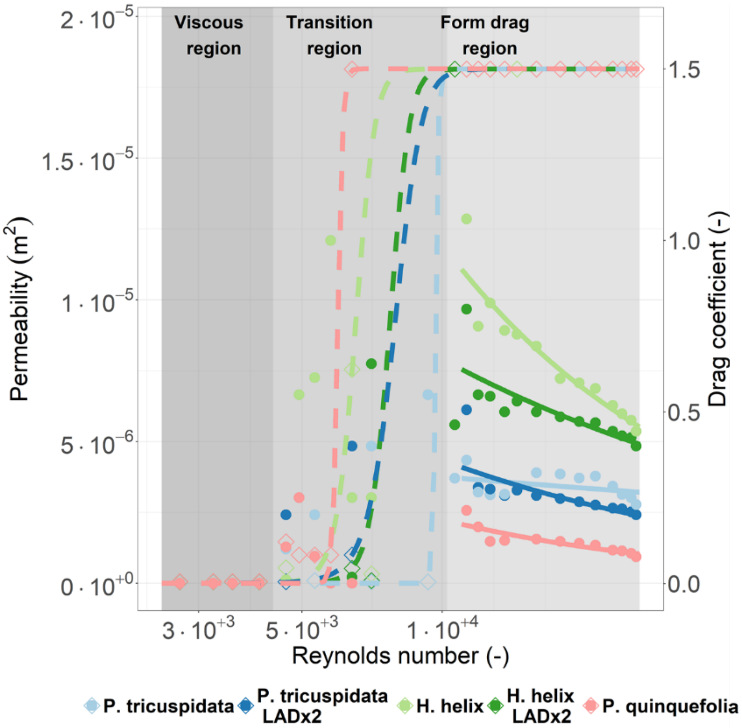

Figure 3 - Permeability (m^2) (left axis, represented by open diamond symbols) and drag coefficient (-) (right axis represented by bullet symbols) obtained with model optimisation as a function of the Reynolds number. The colour legend refers to the combination of climber species and LAD.

3.2 PM deposition

Only a small selection of the results will be discussed, namely the PM deposition on *H. Helix* for an incoming PM_{10} (PM fraction with an aerodynamic diameter smaller than 10 µm) concentration of approximately 100 µg m^{-3} and an incoming wind speed of 1.2 ± 0.2 m s^{-1}. Figure 4 shows the collection efficiency (the difference in concentration at the in- and outlet of the test section divided by the concentration at the inlet, CE, %) as a function of the particle diameter for both deposition models and the experimental data. Between 0.37 and 0.58 µm, CE of the experimental data increased with particle diameter, as is reflected by the model of Petroff, however not by the model of Zhang. At higher particle diameters, the experimental data corresponded better with the model of Zhang. Further validation of both deposition models is necessary to understand the reason behind the deviations and to find the parameters of key influence. The authors of this abstract believe that the integration of the optimised aerodynamic characterisation of vegetation improved the current size-resolved models, since the impact of air flow was better represented. Furthermore, the deposition model of Zhang includes the drag coefficient and, therefore, more accurate model results are foreseen. In addition, the wind tunnel setup will allow to test various PM concentrations and wind speeds, so that model parameters can be tuned for a wide range of environmental conditions.

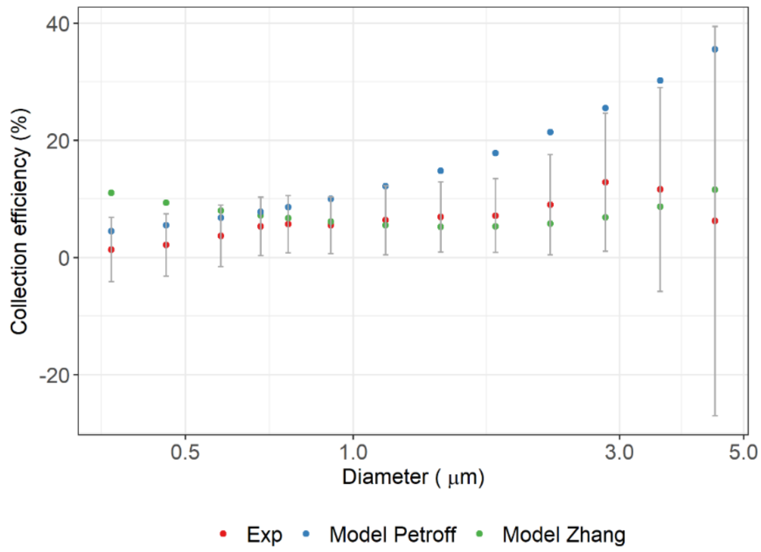

Figure 4 - Collection efficiency of H. Helix of Arizona fine test dust partciles as a function of particle diameter determined with experiments and with the size-resolved deposition model of Petroff and Zhang (2010) and Zhang et al. (2011). Error bars show the standard deviation of the experimental data.

4 Conclusions

This study demonstrated in the first place that inclusion of a varying viscous drag (i.e. permeability, K) and form drag (i.e. drag coefficient, C_d) with wind speed improved the aerodynamic characterisation of vegetation and models using a constant C_d will result in less acurate results. The correct description of the vegetation-wind interaction is critical when modelling the urban heat island effect and pollution dispersion in cities. Secondly, pollutant dispersion and deposition was studied with a wind tunnel setup with input from labscale generated PM. Two widely cited size-resolved deposition models were implemented in the previous developed CFD model and compared with experimental results. Further validation is requested to obtain an accurate deposition model for all particle sizes. Future study should include turbulence kinetic energy measurements behind the plants to verify if the parametrisation is also resulting in correct simulation of the turbulence statistics. Furtermore, more environmental conditions should be experimentally studied to fully understand the driving parameters leading to PM deposition on green walls and vegetation in general. In the end, both models could be implemented in an urban CFD model at real scale to simulate scenarios that optimise PM mitigation by green walls.

Acknowledgments

T.Y. is supported as doctoral candidate (Strategic basic research) from the Research Foundation Flanders, Belgium (FWO, 1S88919N).

References

Huang, C., Lin, M., Khlystov, A. and Katul, G. (2013) The Effects of Leaf Area Density Variation on the Particle Collection Efficiency in the Size Range of Ultrafine Particles (UFP). *Environmental Science and Technology*, 47 11607–11615.

Kormas, A., Prospathopoulos, J.M., Chaviaropoulos, P.K. and Yakinthos, K. (2016) Wind flow simulation over forested areas using a 3D RANS solver with a tree - scale approach. *Journal of*

Wind Engineering and Industrial Aerodynamics, 155 149–158.

Lauriks, T., Longo, R., Baetens, D., Derudi, M., Parente, A., Bellemans, A., van Beeck, J. and Denys, S. (2021) Application of Improved CFD Modeling for Prediction and Mitigation of Traffic-Related Air Pollution Hotspots in a Realistic Urban Street. *Atmospheric Environment*, 246(December 2020) 118127.

Petroff, A. and Zhang, L. (2010) Development and validation of a size-resolved particle dry deposition scheme for application in aerosol transport models. *Geoscientific Model Development*, 3(2) 753–769.

Sogachev, A. and Panferov, O. (2006) Modification of two-equation models to account for plant drag. *Boundary-Layer Meteorology*, 121(2) 229–266.

Wilcox, D.C. (2008) Formulation of the k-ω turbulence model revisited. *AIAA Journal*, 46(11) 2823–2838.

Ysebaert, T., Koch, K., Samson, R. and Denys, S. (2021) Green walls for mitigating urban particulate matter pollution—A review. *Urban Forestry and Urban Greening*, 59 127014.

Ysebaert, T., Samson, R. and Denys, S. (2022) Parameterisation of the Drag Effect of Climbers Depending on Wind Speed and LAD. *Sustainable Cities and Society*,.

Zeng, F., Lei, C., Liu, J., Niu, J. and Gao, N. (2020) CFD simulation of the drag effect of urban trees: Source term modification method revisited at the tree scale. *Sustainable Cities and Society*, 56.

Zhang, L., Gong, S., Padro, J. and Barrie, L. (2001) A size-segregated particle dry deposition scheme for an atmospheric aerosol module. *Atmospheric Environment*, 35 549–560.